PHYSICAL CHEMISTRY 2024

17th International Conference
on Fundamental and Applied Aspects of
Physical Chemistry

Proceedings
Volume II



This conference is dedicated to the 100th anniversary of the birth of Professor Slobodanka Caca Veljković

September 23-27, 2024
Belgrade, Serbia



PHYSICAL CHEMISTRY 2024

17th International Conference
on Fundamental and Applied Aspects of
Physical Chemistry

Proceedings
Volume II

This conference is dedicated to the 100th anniversary of the birth of Professor Slobodanka Caca Veljković

September 23-27, 2024
Belgrade, Serbia

Title: PHYSICAL CHEMISTRY 2024, 17th International Conference on Fundamental and Applied Aspects of Physical Chemistry (Proceedings) ISBN-978-86-82475-44-6
Volume II: ISBN-978-86-82475-46-0
Editors: Željko Čupić, Slobodan Anić and Ana Ivanović-Šašić
Published by: Society of Physical Chemists of Serbia, Studentski Trg 12-16, 11158, Belgrade, Serbia
Publisher: Society of Physical Chemists of Serbia
For Publisher: S. Anić, President of Society of Physical Chemists of Serbia
Printed by: ″Jovan″, <Printing and Publishing Company, Ilije Đuričića 19, Belgrade, 50 Copies
Number of pages: 6+368, Format A4, printing finished in December 2024

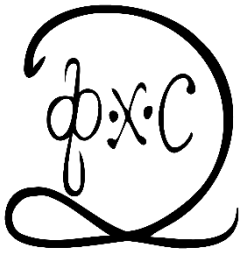
Text and Layout: ″Jovan″

Neither this book nor any part may be reproduced or transmitted in any form or by any means, including photocopying, or by any information storage and retrieval system, without permission in writing from the publisher.

50 - *Copy printing*

CONTENT

Volume II
Organizer IV
Comittes V
Sponsors VI
Macromolecular Physical Chemistry 403
Environmental Protection, Forensic Sciences, Geophysical Chemistry, Radiochemistry, Nuclear Chemistry 441
Phase Boundaries, Colloids, Liquid Crystals, Surface-Active Substances 543
Complex Compounds 555
General Physical Chemistry 585
Pharmaceutical Physical Chemistry 591
Food Physical Chemistry 671
Physico-Chemical Analysis 693
Photochemistry, Radiation Chemistry, Photonics 699
Free topic 713
Education 743
Index 753
List of reviewers 766
List of International Scientific Committee 769



PHYSICAL CHEMISTRY 2024

17th International Conference on
Fundamental and Applied Aspects of
Physical Chemistry

Organized by

The Society of Physical Chemists of
Serbia

in co-operation with

Institute of Catalysis, Bulgarian Academy of Sciences

and

Boreskov Institute of Catalysis, Siberian Branch of
Russian Academy of Sciences

and

University of Belgrade, Serbia:

Faculty of Physical Chemistry
Institute of Chemistry, Technology and Metallurgy
Vinča Institute of Nuclear Sciences
Faculty of Pharmacy

and

Institute of General and Physical Chemistry, Belgrade, Serbia

International Organizing Committee

Chairman: S. Anić (Serbia)
Vice-chairman: Z. Petkova Cherkezova-Zheleva (Bulgaria)
Oleg N. Martyanov (Russia)
S. N. Blagojević (Serbia)
Members: N. Cvjetićanin (Serbia), S. M. Blagojević (Serbia), M. Daković (Serbia), J. Dimitrić-Marković (Serbia), T. Grozdić (Serbia), Lj. Ignjatović (Serbia), A. Ivanović-Šašić (Serbia), D. Jovanović (Serbia), N. Jović-Jovičić (Serbia), M. Kuzmanović (Serbia), S. Maćešić (Serbia), D. Marković (Serbia), B. Milosavljević (USA), M. Mojović (Serbia), N. Pejić (Serbia), M. Petković (Serbia), A. Popović Bijelić (Serbia), B. Simonović (Serbia), B. Šljukić (Serbia), G. Tasić (Serbia), S. Veličković (Serbia), N. Vukelić (Serbia)

International Scientific Committee

Chairman: Ž. Čupić (Serbia)
Vice-chairman: V. Bukhtiyarov (Russia)
S. Minkovska-Dodova (Bulgaria)
B. Adnađević (Serbia)
Members: S. Anić (Serbia), A. Antić-Jovanović (Serbia), A. Clayton (Australia), P. Banković (Serbia), M. Fronczak (Poland), Lj. Gavrilovic (Norway), M. Jeremić (Serbia), E. Kiš (Serbia), A.V. Knyazev (Russia), L.I. László (Hungary), G. Lente (Hungary), S. Macura (USA), Z. Marković (Serbia), K. Novaković (UK), V. Parmon (Russia), D. Peddis (Italy), M.B. Plavšić (Serbia), L. J. Prins (Italy), J. Savović (Serbia), G. Schmitz (Belgium), I. Schreiber (Czech), L. Schreiberova (Czech), D. Stanisavljev (Serbia), N. Stepanov (Russia), Z. Šaponjić (Serbia), S. Tosti (Italy) Á. Tóth (Hungary), N. Vasilyeva (Russia), V. Vukojević (Sweden), A. De Wit (Belgium), A. Yüksel (Türkiye), M. Žabić (Bosnia and Herzegovina)

Local Executive Committee

Chairman: S. N. Blagojević
Vice-chairman: A. Ivanović-Šašić
Members: M. Ajduković, S. Bulatović, J. Dostanić, J. Đuričić-Milanković, M. Jelić, S. Jovanović, Z. Jovanović, N. Jović-Jovičić, B. Marković, J. Maksimović, S. Maćešić, S. Marinović, D. Milenković, T. Mudrinić, N. Nedić, M. Pagnacco, B. Stanković, I. Stefanović, T. Tadić, J. Parlić, M. Pejčić, G. Stevanović, H. Šalipur

SPONSORS

Ministry of Education, Science and Technological Development of the Republic Serbia

Institute of General and Physical Chemistry, Belgrade

University of Belgrade, Institute of Chemistry, Technology and Metallurgy, National Institute of Republic of Serbia, Belgrade

University of Belgrade, Faculty of Physical Chemistry, Belgrade

J *– Macromolecular Physical Chemistry*

THERMAL DEGRADATION KINETICS OF URETHANE AND UREA LINKAGES OF WATERBORNE POLYURETHANES

J. V. Džunuzović [1,2], I. S. Stefanović [1], E. S. Džunuzović [3] and C. Marega [4]

[1]*University of Belgrade, Institute of Chemistry, Technology and Metallurgy, National Institute of the Republic of Serbia, Njegoševa 12, 11000 Belgrade, Serbia. (ivan.stefanovic@ihtm.bg.ac.rs)*
[2]*University of Belgrade, Institute of Chemistry, Technology and Metallurgy, Center of Excellence in Environmental Chemistry and Engineering, Njegoševa 12, 11000 Belgrade, Serbia.*
[3]*University of Belgrade, Faculty of Technology and Metallurgy, Karnegijeva 4 ,11020 Belgrade, Serbia.*
[4]*University of Padova, Department of Chemical Sciences, via Marzolo 1, 35131, Padova, Italy.*

DOI: https://doi.org/10.46793/Phys.Chem24II.405DZ

ABSTRACT

In this study, thermal degradation of urethane and urea bonds in waterborne polyurethanes (WBPUs) based on poly(dimethylsiloxane) (PDMS), isophorone diisocyanate (IPDI) and 2,2-bis-(hydroxymethyl)propionic acid (DMPA), was investigated. Three WBPUs with different DMPA/PDMS molar ratio were prepared using simplified procedure, without chain extension step. The kinetic of the first step of thermal degradation of WBPUs, during which the weakest urethane and urea linkages decomposed, was explored in detail. It was established that the average apparent activation energy of this step ranged from 139 to 168 kJ/mol, according to the model-free Ozawa-Flynn-Wall method. Coats-Redfern model-fitting method and different kinetic models were tested to find the one that gives the best fit to the experimental data.

INTRODUCTION

The constant urge of scientist all over the world to reduce the usage of volatile organic compounds, contributed to the development of eco-friendly waterborne polyurethanes (WBPU) with high performances. These polyurethane dispersions represent safer alternative to the classic solvent based polyurethanes and have therefore found widespread application in modern adhesives and coatings industries. Different manufacturing approaches can be chosen for the WBPUs preparation, such as acetone process, prepolymer mixing process, melt dispersion process and ketamine/ketazine process [1]. Among these, acetone and prepolymer process are the most widely applied in industry for the WBPUs preparation. In each process, the synthesis of the prepolymer is done by the reaction of macrodiols with excess of diisocyanates and adequate amount of internal emulsifier. The difference between these processes lies in the applied solvent (organic solvent in prepolymer mixing process or acetone in acetone process), chain extension and dispersion step.

The knowledge about thermal stability, and particularly thermal degradation kinetics of WBPUs, is crucial factor that defines their application area. The study of thermal degradation kinetics of polymers is based on determination of the kinetic triplet, i.e. apparent activation energy of thermal degradation (E_a), pre-exponential factor (A) and the most probable kinetic model, usually using combination of model-free and model-fitting methods [2]. Model-free methods, such as Ozawa-Flynn-Wall (OFW), are usually applied to calculate E_a at different conversion degree (α), since they do not presume thermal degradation mechanism [2]. By combining E_a determined using model-free approach with model-fitting method which gives good fit to the experimental data and has similar E_a value, the correct kinetic model of thermal degradation of examined polymer and pre-exponential factor should be obtained.

METHODS

WBPUs based on poly(dimethylsiloxane) (PDMS), isophorone diisocyanate (IPDI) and 2,2-bis-(hydroxymethyl)propionic acid (DMPA), with 0.2, 0.35 and 0.5 DMPA/PDMS molar ratio, were synthesized using acetone process, described elsewhere [3].

Thermogravimetric analysis (TGA) of WBPUs was performed in nitrogen atmosphere, at four different heating rates (5, 10, 15 and 20 °C/min), in a temperature range of 25-700 °C, using a TA Instrument SDT 2960 simultaneous TG/DSC system.

RESULTS AND DISCUSSION

In our previous papers it has been shown that thermal degradation of these WBPUs is complex, three-step process. In the first step, thermal decomposition of urethane and urea linkages took place, in the second PDMS chains degraded, while during the third step residual components decomposed [3,4]. Furthermore, after running TGA data obtained at different heating rates through model-free OFW equation, it was established that, despite similar structure, each WBPU has distinct profile of $E_a = f(\alpha)$ and that diverse mechanisms were involved in their decomposition reactions. Also, it has been determined that average E_a of the first step of decomposition for WBPU-0.2, WBPU-0.35 and WBPU-0.5 is 139, 145 and 168 kJ/mol, respectively [4]. In order to study thermal degradation kinetics of urethane and urea bonds in WBPUs, values of E_a calculated by OFW method were combined with Coats-Redfern (CR) method and different kinetic model functions to find the one that gives similar E_a value and has good fit to the experimental data. CR method represents commonly applied model-fitting method for determination of the most correct kinetic model which can describe mechanism of the degradation process [2]:

$$\ln \frac{g(\alpha)}{T^2} = \ln \frac{AR}{\beta E_a} - \frac{E_a}{RT} \tag{1}$$

where $g(\alpha)$ is the integral conversion function, R is the universal gas constant, T is the absolute temperature and β (= dT/dt) is constant linear heating rate. If the correct form of $g(\alpha)$ is selected, a straight line should be obtained by plotting $\ln(g(\alpha)/T^2)$ vs. $1/T$. From the slope of straight lines, E_a can be calculated for each thermal degradation step, and if it has similar value as E_a evaluated by OFW method, then $g(\alpha)$ is correctly chosen. Then, using calculated values of E_a and obtained straight lines, value of the ln$A$ can be evaluated. Forty different kinetic models were tested in this work and they all gave different profiles. However, only two listed in **Table 1** can be considered as appropriate to explain degradation kinetics of urethane and urea bonds in these WBPUs.

Table 1. Algebraic expressions for $g(\alpha)$ for established kinetic model functions. [2]

Symbol	$g(\alpha)$	Mechanism
J2	$[1-(1-\alpha)^{1/2}]^2$	Jander equation
D3	$[1-(1-\alpha)^{1/3}]^2$	Three-dimensional diffusion

Namely, for all investigated samples, E_a calculated using other kinetic models is much lower than value determined by OFW method, although the values of correlation coefficient R^2 were sufficiently large. Therefore, besides high value of the R^2, i.e. good fit to the obtained data, the following condition was also applied to check the correctness of the used model:

$$\left| \frac{E_0 - E_a}{E_0} \right| \leq 0.1 \tag{2}$$

where E_0 is E_a value determined by OFW method, while E_a is calculated from the slope of the $\ln(g(\alpha)/T^2)$ vs. $1/T$ straight line [5]. After applying criterion given by Eq. (2), it was concluded that

the first step of thermal degradation reaction of WBPUs is consistent with the diffusion model and Jander equations (also considered as diffusion model). At this step thermal degradation of urethane and urea bonds occurred, followed by diffusion of volatile decomposition products to the surface. Król et al. have also observed that the first step of thermal degradation reaction of polyurethane-siloxane anionomers, has diffusion-controlled nature [6]. Using CR method, Wan and Huang have concluded that the first step of WBPU waste pyrolysis goes through the D3 reaction model [7]. Also, Wang et al. revealed that the whole thermal degradation process of coating based on aliphatic WBPU is mainly governed by three-dimensional diffusion [8].

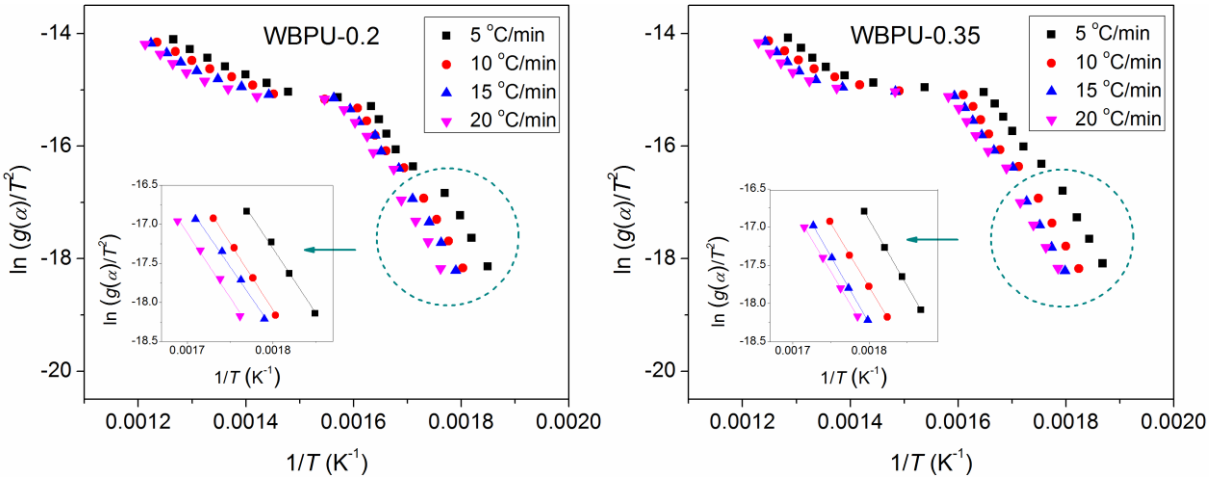


Figure 1. Application of J2 kinetic model on the whole thermal degradation process of WBPU-0.2 and WBPU-0.35 using CR equation. Inset shows fitting of TGA data for the first degradation step.

Table 2. The best fitting kinetic models, values of apparent activation energy (E_a), pre-exponential factor (ln$A$) and correlation coefficient (R^2) for the first step of WBPUs thermal degradation, calculated at different heating rates by Coats-Redfern method.

β **(°C/min)**	**Kin. model**	***E*a (kJ/mol)**	**ln*A***	**R^2**
WBPU-0.2 (0.10 <α< 0.25)				
5	J2	143	21	0.9988
10		144	20	0.9997
15		144	20	0.9991
20		146	20	0.9999
WBPU-0.35 (0.10 <α< 0.25)				
5	J2	144	22	0.9998
10		148	21	0.9996
15		148	21	0.9994
20		148	21	0.9995
WBPU-0.5 (0.10 <α< 0.45)				
5	D3	154	23	0.9990
10		156	23	0.9994
15		156	22	0.9982
20		158	22	0.9997

As an example, application of J2 kinetic model on the whole thermal degradation process of WBPU-0.2 and WBPU-0.35 using CR equation is shown in **Figure 1**. It is obvious that for these two WBPUs, J2 kinetic model can be applied only at low conversions, i.e. during the thermal decomposition of urethane and urea linkages, since only data in this range was possible to fit with straight lines (inset in **Figure 1**). Similar results were obtained for WBPU-0.5 using D3 kinetic model. The range of α for each thermal degradation step was determined from the slope change of OFW regression lines at different α [4], and for the first degradation step it is listed in **Table 2** together with values of E_a, ln$A$ and correlation coefficient.

From the results presented in **Figure 1** and **Table 2**, it can be seen that application of J2, i.e. D3 kinetic model gave good fit to the TGA data obtained for the first thermal degradation step of investigated WBPUs, and that calculated values of the apparent activation energy follow the same trend as values evaluated by OFW method.

CONCLUSION

The kinetic of the first step of thermal degradation reaction of WBPUs, based on PDMS, IPDI and DMPA, was evaluated. Using TGA data obtained at different heating rates in nitrogen atmosphere, and combination of model-free and model-fitting methods, values of E_a and ln$A$, and the most probable kinetic model were determined. According to the obtained results, thermal decomposition of urethane and urea bonds in WBPUs is governed by diffusion process, which can be for WBPU-0.2 and WBPU-0.35 described with the Jander equation, and for WBPU-0.5 with the three-dimensional diffusion model.

Acknowledgment

This work was supported by the Ministry of Science, Technological Development and Innovation of Republic of Serbia (Grant No. 451-03-66/2024-03/200026 and 451-03-65/2024-03/200135).

REFERENCES

[1] D. Dieterich, Prog. Org. Coat., 9 (1981) 281.
[2] A. Omrani, S. M. M. Hasankola, J. Non-Cryst. Solids, 358 (2012) 1656.
[3] I. S. Stefanović, J. V. Džunuzović, E. S. Džunuzović, S. J. Brzić, E. Jasiukaitytė-Grojzdek, A. Basagni, C. Marega, Prog. Org. Coat., 161 (2021) 106474.
[4] J. V. Džunuzović, I. S. Stefanović, E. S. Džunuzović, A. Basagni, C. Marega, J. Polym. Res., 31 (2024) 139.
[5] Y. Li, J. Zheng, Y. Luo, H. Zhou, Q. Wang, J. Appl. Polym. Sci., 132 (2015) 42374.
[6] P. Król, K. Pielichowska, Ł. Byczyński, Thermochim. Acta, 507-508 (2010) 91-98.
[7] H. Wan, Z. Huang, Polymers, 14 (2022) 1501.
[8] Y. C. Wang, J. Deng, J. P. Zhao, H. Shi, Prog. Org. Coat., 147 (2020) 105758.

APPLICATION OF MODEL FITTING METHODS TO STUDY THERMAL DEGRADATION OF WATERBORNE POLYURETHANES AT LATE STAGES

J. V. Džunuzović [1,2], I. S. Stefanović [1], E. S. Džunuzović [3] and C. Marega [4]

[1]University of Belgrade, Institute of Chemistry, Technology and Metallurgy, National Institute of the Republic of Serbia, Njegoševa 12, 11000 Belgrade, Serbia. (ivan.stefanovic@ihtm.bg.ac.rs)
[2]University of Belgrade, Institute of Chemistry, Technology and Metallurgy, Center of Excellence in Environmental Chemistry and Engineering, Njegoševa 12, 11000 Belgrade, Serbia.
[3]University of Belgrade, Faculty of Technology and Metallurgy, Karnegijeva 4 ,11020 Belgrade, Serbia.
[4]University of Padova, Department of Chemical Sciences, via Marzolo 1, 35131, Padova, Italy.

DOI: https://doi.org/10.46793/Phys.Chem24II.409DZ

ABSTRACT
The thermal degradation of the waterborne polyurethanes (WBPUs) based on poly(dimethylsiloxane) (PDMS), isophorone diisocyanate (IPDI) and 2,2-bis-(hydroxymethyl)propionic acid (DMPA) is a complex, three-step process. Study of the kinetics of the second and third degradation steps of these WBPUs has been presented here. During the second step, PDMS chains decomposed, while in the third step degradation of residual components occurred. A comprehensive analysis of the obtained results revealed that the Zhuravlev-Lesokin-Tempelman and Avrami-Erofeev equations represent the best kinetic models that describe degradation mechanism of the examined decomposition steps of WBPUs.

INTRODUCTION
Waterborne polyurethanes represent a class of polyurethanes which are prepared using water as a dispersion medium instead of traditional toxic organic solvents. In this way, the exposure to volatile and harmful organic solvents during the synthesis is reduced. Therefore, WBPUs are considered as environmentally friendly polymers. However, WBPUs have relatively poor thermal stability, which can be considered as deficiency, especially if these polyurethanes are preferred to be used as coatings. One of the possible ways to overcome this is to use PDMS for the synthesis of WBPUs. PDMS can have a positive influence on the thermal stability of polyurethanes, since it has low glass transition temperature, high heat resistance, higher Si-O bond energy, low thermal conductivity, etc. Thermal degradation of the WBPUs is complex process, with multiple degradation steps, and each step needs to be fully explored. The knowledge of the kinetics of thermal degradation process can help to design and improve synthetic pathways, in order to achieve the desired properties and enhance endurance and lifetime of WBPUs [1,2].

METHODS
Waterborne polyurethanes were prepared from poly(dimethylsiloxane) (PDMS), isophorone diisocyanate (IPDI) and 2,2-bis-(hydroxymethyl)propionic acid (DMPA) according to the procedure described by Stefanović et al. [3]. By changing DMPA/PDMS molar ratio (0.2, 0.35 and 0.5), three WBPU samples were synthesized (WBPU-0.2, WBPU-0.35 and WBPU-0.5, respectively). Kinetics of thermal degradation of prepared WBPUs were examined using results gained by TA Instrument SDT 2960 simultaneous TG/DSC system. Experiments were carried out from 25 °C to 700 °C, at different heating rates (5, 10, 15 and 20 °C/min), in nitrogen atmosphere.

RESULTS AND DISCUSSION

Model-fitting methods are based on fitting experimentally obtained thermogravimetric (TG) data with chosen mathematical function, i.e. kinetic model, that describes mechanism of the thermal degradation reaction ($g(\alpha)$ - integral conversion function, α - degree of conversion) [4]. Most frequently applied kinetic models, which can be found in the literature, describe mechanism of the solid state thermal degradation reactions obtained by non-isothermal TG measurements [5]. Each of these equations describes certain type of thermal degradation process that control degradation rate: nucleation and growth of nuclei, phase boundary reaction, diffusion or chemical reaction [6].

In order to determine the kinetic model at late stages of thermal degradation of WBPUs investigated in this work, i.e. for the second and third thermal degradation step, it was necessary to apply model-fitting approach by testing different reactions. For that purpose, Coats-Redfern (CR) method [4] and forty different equations for $g(\alpha)$ were tested. Straight lines, obtained after plotting different $\ln(g(\alpha)/T^2)$ vs. $1/T$ (T is the absolute temperature), with the highest correlation coefficient R^2 and similar value of the apparent activation energy of thermal degradation (E_a) as evaluated by model-free isoconversional Ozawa-Flynn-Wall (OFW) method [7], were selected. Equations for $g(\alpha)$ applied to obtain these straight lines are listed in **Table 1**, and are considered to be the best kinetic models that describes degradation mechanism of the second and third thermal decomposition step of WBPUs.

Table 1. Algebraic expressions for the best fitting $g(\alpha)$ kinetic model functions. [3]

Symbol	$g(\alpha)$	Mechanism
D5	$[(1-\alpha)^{-1/3}-1]^2$	*Diffusion model* Zhuravlev-Lesokin-Tempelman (Z-L-T) equation
A1/4	$[-\ln(1-\alpha)]^4$	*Random nucleation and growth of nuclei* (Avrami-Erofeev equation)

In **Figure 1** are as an example presented results obtained after fitting TG data of WBPU-0.35 and WBPU-0.5 in the whole thermal degradation region, using D5 kinetic model and CR equation. The range of degree of conversion for the second and third thermal degradation step of WBPUs was determined in our previous work from the change of OFW regression lines slope at different α [7].

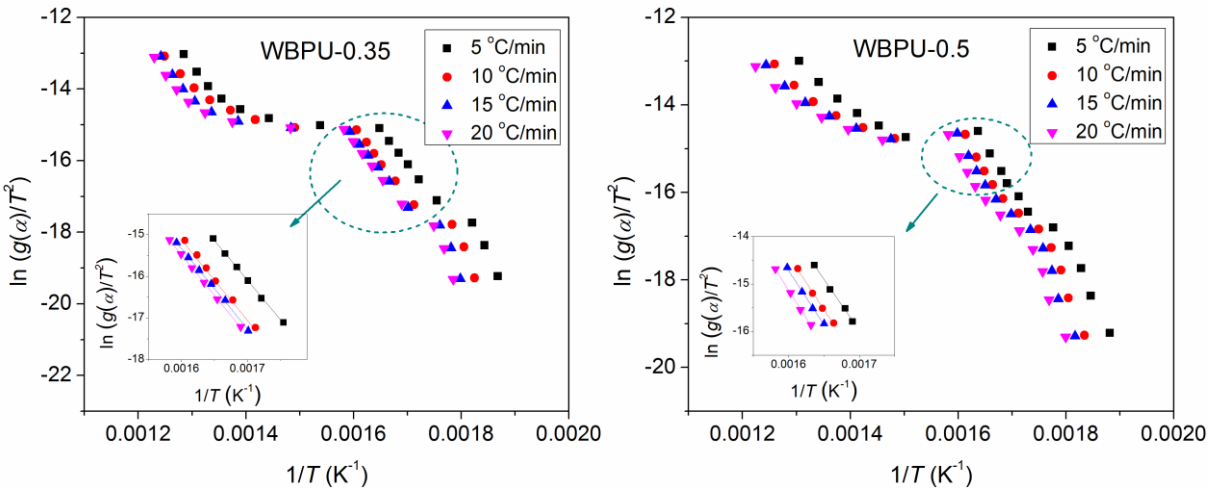


Figure 1. Application of D5 kinetic model on the whole thermal degradation process of WBPU-0.35 and WBPU-0.5 using CR equation. Inset shows fitting of TGA for the second degradation step.

It can be seen that D5 kinetic model cannot be applied on the whole thermal degradation region, i.e. linear fitting was for all examined WBPUs obtained only for the second thermal decomposition step, which corresponds to the degradation of the soft PDMS segments. From the slope of obtained

straight lines, E_a was calculated and listed in **Table 2** together with values of ln$A$ and correlation coefficient R^2. These results revealed that decomposition of PDMS chains is diffusion controlled process and its E_a depends on the PDMS content.

Table 2. The best fitting kinetic models, values of apparent activation energy (E_a), pre-exponential factor (ln$A$) and correlation coefficient (R^2) for the second step of WBPUs thermal degradation, calculated at different heating rates by Coats-Redfern method.

β (°C/min)	Kin. model	E_a (kJ/mol)	ln$A$	R^2	Kin. model	E_a (kJ/mol)	ln$A$	R^2
WBPU-0.2								
0.30 < α < 0.55					0.60 < α < 0.90			
5	D5	259	44	0.9982	A1/4	172	24	0.9996
10		264	44	0.9992		168	23	0.9994
15		266	44	0.9995		161	21	0.9995
20		266	44	0.9998		176	22	0.9993
WBPU-0.35								
0.30 < α < 0.60					0.65 < α < 0.90			
5	D5	158	24	0.9993	A1/4	162	22	0.9997
10		160	23	0.9998		158	21	0.9992
15		160	23	0.9990		166	22	0.9998
20		161	23	0.9998		164	20	0.9995
WBPU-0.5								
0.50 < α < 0.65					0.70 < α < 0.90			
5	D5	196	32	0.9991	A1/4	160	24	0.9997
10		199	32	0.9982		159	23	0.9993
15		201	31	0.9999		157	22	0.9997
20		202	31	0.9993		157	21	1.0000

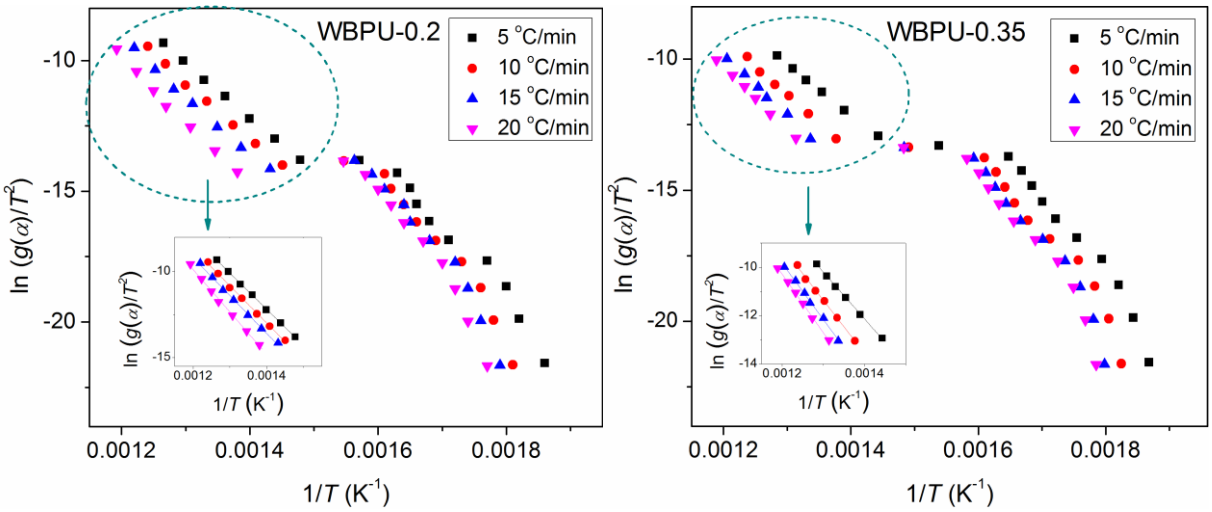


Figure 2. Application of A1/4 kinetic model on the whole thermal degradation process of WBPU-0.35 using CR equation. Inset shows fitting of TGA data for the third degradation step.

On the other hand, the best fitting kinetic model for the third step of thermal degradation of all three WBPUs is A1/4 (**Figure 2**, **Table 2**), since all other models had to be excluded due to the lack

of linearity or much lower E_a value than E_a calculated by OFW method. In this step, decomposition of residual mass, which contains different, the most stable components formed during the previous degradation steps, occurred. The obtained value of the Avrami exponent is lower than one (n=1/4), indicating inhomogeneous distribution of nuclei and diffusion controlled growth rate of nuclei [8].

CONCLUSION

According to the obtained results, thermal degradation of the WBPUs is a complex, three-step process. The second and third thermal degradation steps of the synthesized WBPUs have been investigated in this study. It was found that in the second degradation step PDMS chains decomposed through diffusion controlled process described by the Zhuravlev-Lesokin-Tempelman equation, whichs E_a depends on the PDMS content. In the third step residual components decomposed, and Avrami-Erofeev equation gave the best fitting results to the experimental TGA data. In this step, inhomogeneous distribution of nuclei and diffusion controlled growth rate of nuclei occurs.

Acknowledgment

This work was supported by the Ministry of Education, Science and Technological Development of the Republic of Serbia (Grant No. 451-03-66/2024-03/200026 and 451-03-65/2024-03/200135).

REFERENCES

[1] I. S. Stefanović, M. Špírková, S. Ostojić, P. Stefanov, V. B. Pavlović, M. V. Pergal, Appl. Clay Sci., 149 (2017) 136.
[2] M. V. Pergal, I. S. Stefanović, D. Gođevac, V. V. Antić, V. Milačić, S. Ostojić, J. Rogan, J. Djonlagić, J. Serb. Chem. Soc., 79 (2014) 843.
[3] I. S. Stefanović, J. V. Džunuzović, E. S. Džunuzović, S. J. Brzić, E. Jasiukaitytė-Grojzdek, A. Basagni, C. Marega, Prog. Org. Coat., 161 (2021) 106474.
[4] P. E. Sánchez-Jiménez, L. A. Pérez-Maqueda, A. Perejón, J. M. Criado, Resour. Conserv. Recycl., 74 (2013) 75.
[5] P. Budrugeac, Polym. Degrad. Stab., 74 (2001) 125.
[6] S. Żołtowska, I. Koltsov, K. Alejski, H. Ehrlich, M. Ciałkowski, T. Jesionowski, Polym. Test., 97 (2021) 107148.
[7] J. V. Džunuzović, I. S. Stefanović, E. S. Džunuzović, A. Basagni, C. Marega, J. Polym. Res., 31 (2024) 139.
[8] N. X. Sun, X. D. Liu, K. Lu, Scr. Mater., 34 (1996) 1201.

MORPHOLOGY OF THE POLYURETHANE COMPOSITES BASED ON TiO_2 NANOPARTICLES

I. S. Stefanović [1], J. V. Džunuzović [1,2], D. V. Randjelović [1], E. S. Džunuzović [3], A. Basagni [4] and C. Marega [4]

[1]*University of Belgrade, Institute of Chemistry, Technology and Metallurgy, National Institute of the Republic of Serbia, Njegoševa 12, 11000 Belgrade, Serbia. (ivan.stefanovic@ihtm.bg.ac.rs)*
[2]*University of Belgrade, Institute of Chemistry, Technology and Metallurgy, Center of Excellence in Environmental Chemistry and Engineering, Njegoševa 12, 11000 Belgrade, Serbia.*
[3]*University of Belgrade, Faculty of Technology and Metallurgy, Karnegijeva 4 ,11020 Belgrade, Serbia.*
[4]*University of Padova, Department of Chemical Sciences, via Marzolo 1, 35131, Padova, Italy.*

DOI: https://doi.org/10.46793/Phys.Chem24II.413S

ABSTRACT
Polyurethane composites based on polycaprolactone (PCL), Boltorn® aliphatic hyperbranched polyester of the second pseudo generation (BH-20) and isophorone diisocyanate (IPDI) and unmodified and surface modified TiO_2 nanoparticles, were successfully prepared. The surface modification of TiO_2 nanoparticles was performed with lauryl gallate (LG). The impact of added TiO_2 nanoparticles and their content on the morphology of the polyurethane network (PU) were examined. The obtained results show that the addition of both, unmodified and modified TiO_2 nanoparticles, has significant impact on the cross-sectional and surface morphology of PU.

INTRODUCTION
Polyurethane networks (PU) are polymeric materials with a three-dimensional, chemically crosslinked structure, usually constructed of hard (HS) and soft (SS) segments. These segments are thermodynamically incompatible, which leads to the creation of two phase morphology and their mutual separation, which is greatly reflected in the final properties of PUs. Although the PUs have good mechanical properties, chemical and weathering resistance, and good surface properties, there is a constant need for their improvement. One of the possible ways to enhance the aforementioned properties is the preparation of polyurethane composite materials, using inorganic metal oxide nanoparticles. For this purpose, nano-sized TiO_2 is often applied as a filler, because it has a handful of good properties, such as excellent chemical stability, eco-friendliness, easy processing, high specific surface area, anti-aging and antioxidant properties, good antibacterial properties, etc. Still, for the best utilization of these positive features of TiO_2 nanoparticles, their uniform and homogenous dispersion within the polyurethane structure is essential. That can be achieved by using adequate preparation methods [1, 2].

In this study, polyurethane composites based on PCL, BH-20, IPDI and different content of unmodified or surface modified TiO_2 were prepared. The surface modification of TiO_2 nanoparticles was done with lauryl gallate. The cross-sectional and surface morphology of the neat PU and prepared composites was investigated.

METHODS
Poly(ε-caprolactone) diol (PCL, $M_n \approx 2000$ g/mol, from Sigma-Aldrich), Boltorn® hydroxy-functional aliphatic hyperbranched polyester of the second pseudo generation (BH-20, $M_n = 1340$ g/mol, from Perstorp Specialty Chemicals AB), isophorone diisocyanate (IPDI, from Sigma-

Aldrich) were used for the preparation of neat PU and its composites. The stannous octoate ($Sn(Oct)_2$, from Sigma-Aldrich, purity 95%) was used as catalyst, while *N*,*N*-dimethylacetamide (DMAc, from Sigma-Aldrich, purity 99%) and tetrahydrofuran (THF, from J. T. Baker, purity 99.99%) were used as solvents. A commercially available TiO_2, Aeroxide P25 (80% of anatase and 20% of rutile, surface area 52 m^2/g, mean diameter ~30 nm) was purchased from Evonik Degussa GmbH [3]. Two series of PU composites with different content (0.5, 1 and 2 wt.%) of unmodified or surface modified TiO_2 nanoparticles were prepared. For the surface modification of TiO_2 nanoparticles lauryl (dodecyl) gallate (LG, from Sigma-Aldrich) was applied.

Neat PU and its composites were prepared by a two-step solution polymerization. In order to achieve homogenous distribution of nanoparticles in the polymer, they were added in the first step of reaction, after sonification of TiO_2/THF mixture in ultrasonic bath. For all samples, the stoichiometric ratio between –NCO and –OH groups was kept constant at 1.1. Prepared composites were labeled as PU/xx, where "xx" represents the numbers 0.5, 1 and 2 (weight percentages), followed by a mark of added nanoparticles (TiO_2 or TiO_2-LG), while neat polyurethane was labeled as PU.

Cross-sectional surface of the PU and its composites was investigated by scanning electron microscopy (SEM) using the XL30 scanning electron microscope (Philips), which contains a Gemini column (Zeiss Supra 35 VP). All samples were previously coated with gold in a high-vacuum evaporator.

Atomic force microscopy (AFM) examinations were performed on an atomic force microscope (NTEGRA Prima atomic force microscope, NT-MDT, Moscow, Russia), equipped with the NT-MDT NSGO1 silicon cantilevers. The 3D height AFM images of the surfaces of PU and its composite films were measured at the room temperature, using intermittent-contact mode.

RESULTS AND DISCUSSION

SEM analysis was done in order to investigate and compare the cross-sectional morphology of the neat PU and its composites. Based on the obtained micrographs (**Figure 1**), the clear difference in the morphology between neat PU and its composites is obvious. According to the obtained SEM micrographs, neat PU has rough and irregular cross-sectional morphology, while in the structure of both series of composites small cavities and certain micro-structures, such as clusters or agglomerates, can be observed. These microstructures are more pronounced in composites with higher amounts of added modified and unmodified TiO_2 nanoparticles (1 and 2 wt.%).

AFM analysis was applied to explore the surface topography and roughness of the neat PU and its composites. The obtained 3D height images, at scan size 10×10 μm^2, in intermittent-contact mode, are shown in **Figure 2**, while obtained roughness values are listed in **Table 1**. According to the obtained 3D height images, it is observed that all samples have two phase morphology (HS and SS phase). Moreover, the surface of PU became rougher with the addition of nanoparticles, and its roughness increases with increasing amount of TiO_2 nanoparticles (**Table 1**). In addition, it is also noticeable that composites prepared with unmodified TiO_2 nanoparticles have higher roughness values than composites with modified TiO_2 nanoparticles. This occurs due to the modification of TiO_2 nanoparticles with LG, since LG has long alkyl chain that reduces interfacial bonding between TiO_2 nanoparticles and simultaneously improves their dispersion in polymer [4].

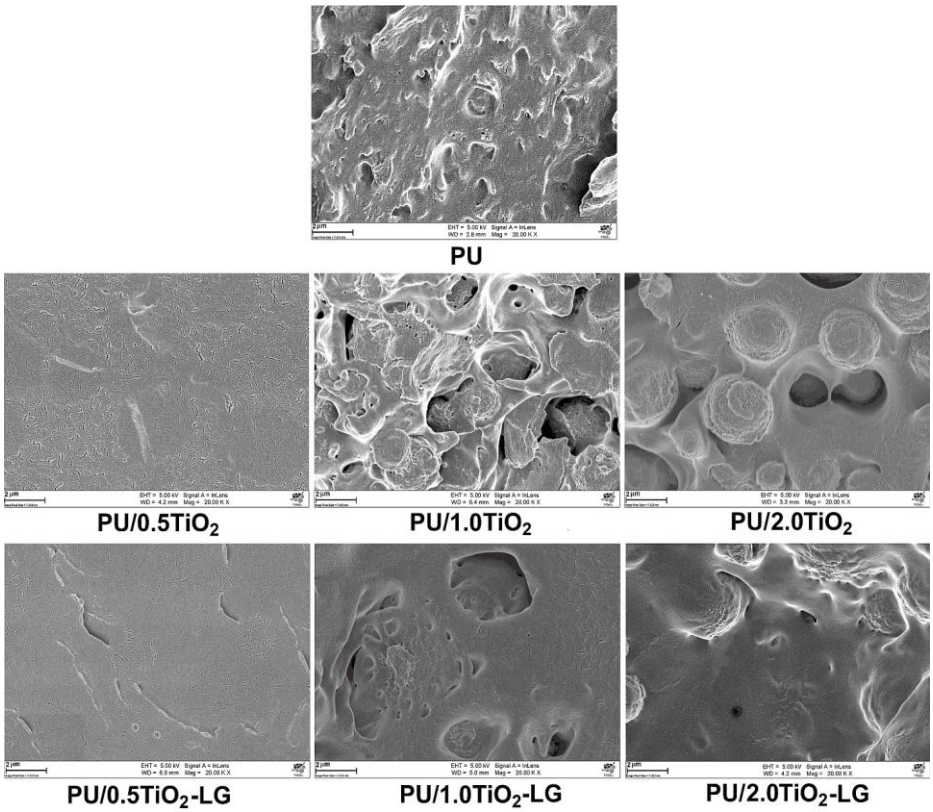


Figure 1. SEM micrographs taken at the cross-sectional surface of the neat PU and its composites (magnification 20k ×).

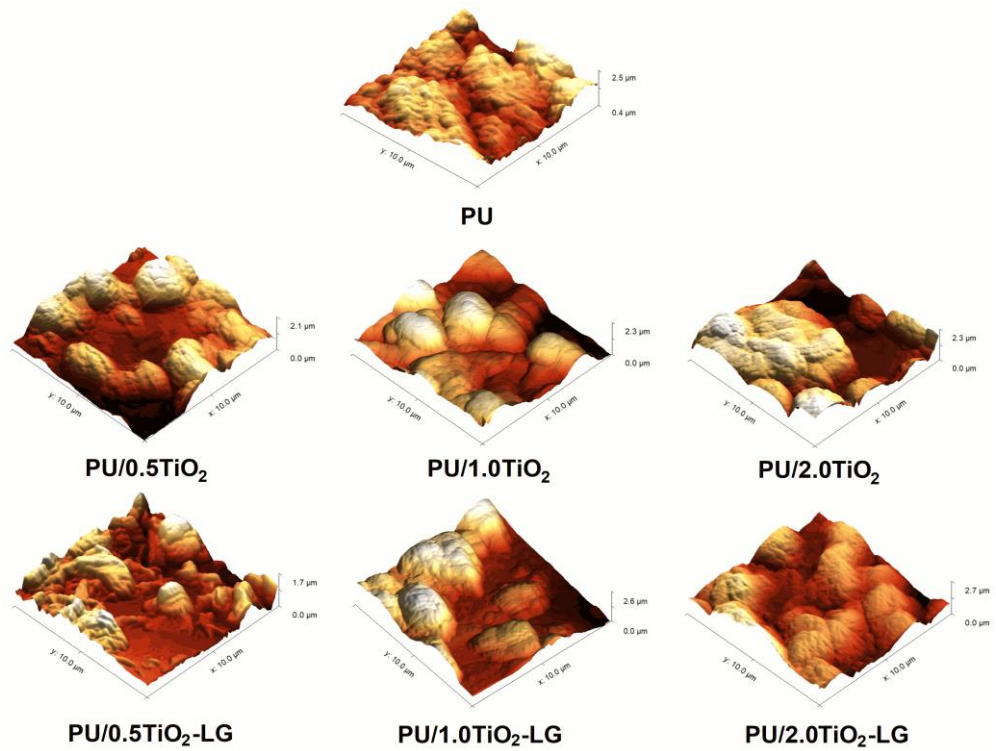


Figure 2. 3D height AFM images of the neat PU and its composites. Scan size 10×10 μm^2.

Table 1. Surface roughness of neat PU and its composite films (scan sizes 10 × 10 μm^2).

Sample	R_a [a)] (nm)	R_q [b)] (nm)
PU	270	330
PU/0.5TiO_2	415	490
PU/1.0TiO_2	427	520
PU/2.0TiO_2	576	640
PU/0.5TiO_2-LG	289	350
PU/1.0TiO_2-LG	340	408
PU/2.0TiO_2-LG	365	445

[a)] R_a – (average roughness) the average of the absolute values of surface height deviations from the arithmetical mean of the scanned area surface

[b)] R_q – (RMS - root mean square) standard deviation of the height values within a presented area

CONCLUSION

Polyurethane composites were prepared using different content (0.5, 1.0 and 2.0 wt.%) of unmodified and surface modified TiO_2 nanoparticles. The cross-sectional and surface morphology of the prepared neat PU and its composites was examined by SEM and AFM analyses. SEM micrographs showed that neat PU has rough and irregular cross-sectional morphology, while micrographs of both series of composites have small cavities and certain micro-structures, such as clusters or agglomerates. AFM analysis established that all samples have two phase morphology and that the surface of PU became rougher with the addition of TiO_2 nanoparticles. Prepared PU and its composites can be used as coatings for specific purposes.

Acknowledgment

This work was supported by the Ministry of Science, Technological Development and Innovation of Republic of Serbia (Grant No. 451-03-66/2024-03/200026 and 451-03-65/2024-03/200135) and Science Fund of the Republic of Serbia, Program PRISMA, Grant No. 5354 − HYDIS.

REFERENCES

[1] H. Nawaz, M. Umar, R. Maryam, I. Nawaz, H. Razzaq, T. Malik, X. Liu, Adv. Eng. Mater. 24 (2022) 2200844.

[2] T. S. Radoman, J. V. Džunuzović, K. B. Jeremić, B. N. Grgur, D. S. Miličević, I. G. Popović, E. S. Džunuzović, Mater. Design 62 (2014) 158.

[3] I. S. Stefanović, J. Dostanić, D. Lončarević, D. Vasiljević-Radović, S. Ostojić, S. Marković, M. V. Pergal, Hem. Ind. 73 (2019) 13.

[4] L. M. Hamming, R. Qiao, P. B. Messersmith, L. C. Brinson, Compos. Sci. Technol. 69 (2009) 1880.

AN EXAMINATION OF Cr DOPPED $ZnMn_2O_4$ IN NA AQUEOUS SOLUTION OF $ZnCl_2$

J.Senćanski[1], N.Nikolić[2], J. Jovanović[1], S.Blagojević[1], M.Pagnacco[3] and I.Stojković Simatović[4]

[1] *University of Belgrade, Institute of General and Physical Chemistry, Studentski trg 12-15, 11000 Belgrade, Republic of Serbia(jelenasencanski@gmail.com)*
[2] *University of Belgrade, Institute for Multidisciplinary Research, Kneza Višeslava 1, 11030 Belgrade, Republic of Serbia*
[3]*University of Belgrade, Institute of Chemistry, Technology and Metallurgy, Njegoševa 12, 11000 Belgrade, Serbia*
[4]*University of Belgrade, Faculty of Physical Chemistry, Studentski trg 12-15, 11000 Belgrade, Republic of Serbia.*

DOI: https://doi.org/10.46793/Phys.Chem24II.417S

ABSTRACT

This study examines the diminishing Jahn-Teller effect on the cathode material $ZnCr_{0.15}Mn_{1.85}O_4$ and its capacity increase when adding 1M $Mn(NO_3)_2$ in an aqueous solution of $ZnCl_2$. Following the addition of the 1M $Mn(NO_3)_2$, the capacity increased from ~2 mAh g^{-1} to ~14 mAh g^{-1} at a polarization rate of 5mV s^{-1}. The addition of $Mn(NO_3)_2$ effects the balance of Mn^{3+} and Mn^{4+}, which diminishes the Jahn Teller effect, thus increasing the capacity of $ZnCr_{0.15}Mn_{1.85}O_4$.

INTRODUCTION

The Jahn-Teller effect itself is present in systems containing electrons that possess equal energies. When some perturbation occurs, the energy of electrons is not equal for each electron and some electrons' energy is added to the nuclei of a compound [1]. Due to the presence of Mn^{3+} and its disproportion to $2Mn^{3+} = Mn^{2+} + Mn^{4+}$), it leads to the Jahn-Teller effect; consequently, the cores to other sites are replaced, resulting in the Zn-ions not being able to intercalate to their original sites. Hence, there is a capacity decrease [2]. Thereafter, the material obtained is examined in an aqueous solution of pure $ZnCl_2$ as well as with the addition of 1ml 1M $Mn(NO_3)_2$ in order to diminish the Jahn-Teller effect.

METHODS

The synthesis of the material $ZnCr_{0.15}Mn_{1.85}O_4$ was done using the glycine-nitrate procedure by mixing $Mn(NO_3)_2x6H_2O$ and $Zn(NO_3)_2x6H_2O$ and $Cr(NO_3)_2$ in stoichiometric ratio. The glycine was added in a ratio of glycine/nitrates=1.2. After drying the solution at 200°C until complete combustion, the sample was annealed for four hours at 800°C in atmosphere. An aqueous solution of $ZnCl_2$ was used for the experiment firstly. After the capacity of the cathode material obtained was measured, the same material was tested after adding 1 ml of 1M $Mn(NO_3)_2$ into the aqueous solution of 10 ml $ZnCl_2$.

The XRPD (x-ray powder diffraction) recording was done with a Rigaku Ultima IV powder diffractometer equipped with Ni-filtered Cu Kα radiation at an interval of 4 to 90° 2θ at steps of 0.02 ° (at a scanning speed 2° min^{-1}). The Le Bail full pattern profile fitting method [3] implemented in FullProf software [4] determined unit cell refinement.

The scanning electron microscope Tescan VEGA TS 5130MM operating at 20 kV accelerating voltage analyzed the sample morphology.

Ivium Potentiostate/Galvanostate performed the cyclic voltammetry. The polarization rates were 5, 10, 20, 50 and 100 mV s^{-1}. The counter electrode was platinum, reference SCE, while the working electrode was a glassy carbon electrode. The cathode material, carbon black as well as polyvinildiendifluoride in a ratio 85:10:5 were created following the instructions set out in Sencanski et al [5] and pasted onto the glossy carbon electrode.

RESULTS AND DISCUSSION

As shown in Fig 1.(a), the XRPD profile was refined using the Le-Bail full profile matching mode in which there were no un-indexed reflections indicating Cr-doped $ZnMn_2O_4$ present as a single phase. The Cr-doped $ZnMn_2O_4$ unit cell was refined to a I41/amd space group with lattice parameters: a=b=5.7390(5) Å, c=9.2116(10) Å. Compared to previously reported undoped single phase $ZnMn_2O_4$ (S.G. I41/amd, a=b=5.7185(8) Å, c=9.268(2) Å) [6] Cr doping results in increasing both a and c lattice parameters, consequently increasing in volume.

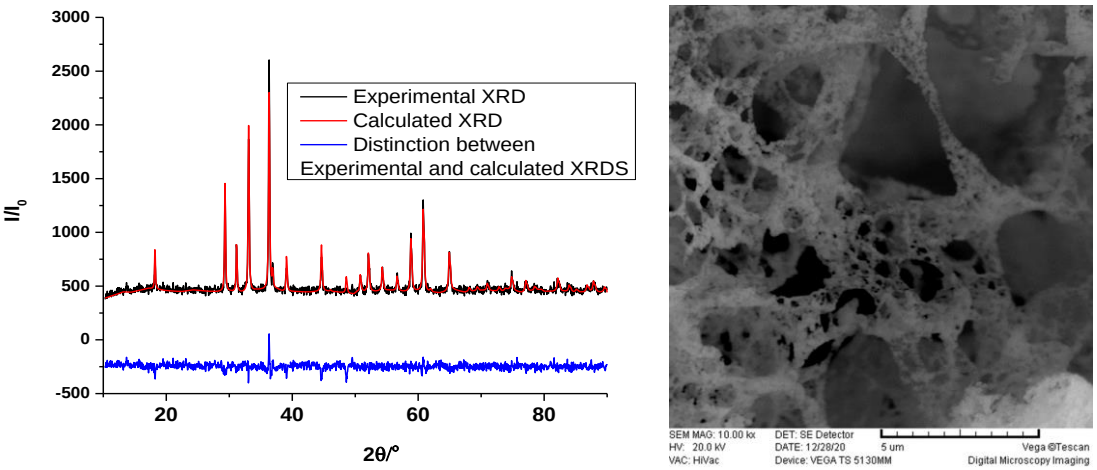


Figure 1. a) XRPD and b) SEM of the material $ZnCr_{0.15}Mn_{1.85}O_4$.

Figure 1b) displays the SEM image of the cathode material synthesized, presenting a sponged structure containing agglomerated particles. The particles' size were, therefore, not detectable. Due to the agglomerated particles, a low capacity may be predicted, as shown by measuring the cyclic voltammetry.

Figure 2. presents the electrochemical measurements.The same positions of the peaks in the cyclic voltammogrammes for each scanning rate, as observed from Fig 2 a) and b), indicate that a stable structure of the material is obtained. According to Fig 2. a) and b), the peak positioned at 0.95V vs SCE appeared after adding 1ml $Mn(NO_3)_2$. Moreover, the main intercalation peak moved to the lower potential when the capacity increased, as observed in Fig 2 a) and b). Therefore the sites for the intercalation of Zn ions are not the same after adding $Mn(NO_3)_2$, as well as the de-intercalation from those places are active. Fig 2 c) presents the capacity values for all the scanning rates applied for an aqueous solution of $ZnCl_2$ as well as after the addition of 1 ml of 1M $Mn(NO_3)_2$.

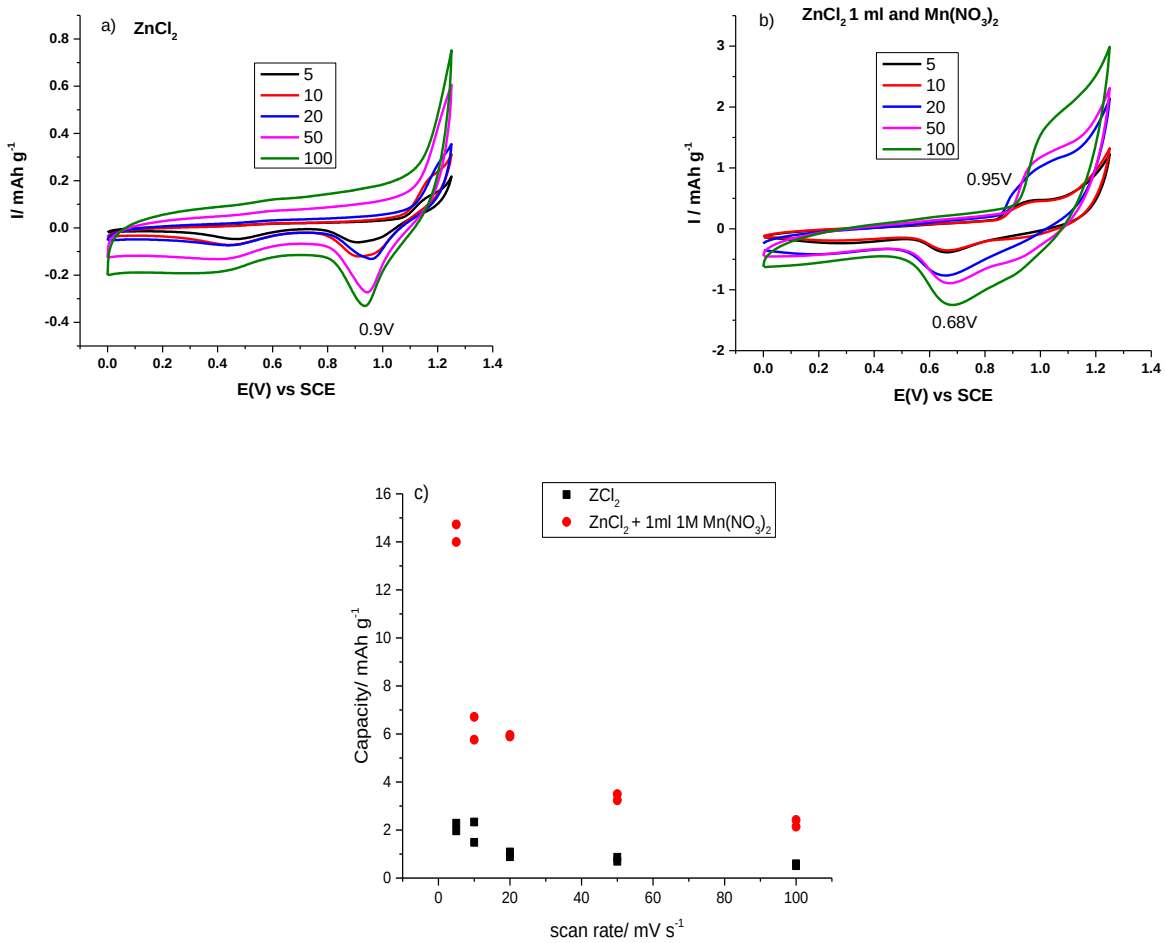


Figure 2. a) and b) the cyclic voltamogrammes of the $ZnCr_{0.15}Mn_{1.85}O_4$ material before a) and after b) the addition of 1M $Mn(NO_3)_2$, c) the capacities before and after adding the solution of 1M $Mn(NO_3)_2$.

CONCLUSION

This paper presents the influence of the addition of Mn^{2+} ions into an aqueous solution of $ZnCl_2$ to keep the Mn^{3+}/Mn^{4+} in balance, thus diminishing the Jahn-Teller effect and increasing the capacities of the $ZnCr_{0.15}Mn_{1.85}O_4$ material for all the applied scanning rates ranging from 5 to 100 mV s^{-1}. To further increase capacity, research in future should direct itself into investigating doping the material with a higher fraction of Cr or doping it with another like metal.

Acknowledgment

This work was supported by the Ministry of Education, Science and Technological Development of the Republic of Serbia (grants no. 451-03-65/2024-03/200146, 451-03-66/2024-03/200051, 451-03-66/2024-03/200053, 451-03-66/2024-03/200026). M.P. acknowledges the support of the EU: the EIC Pathfinder Challenges 2022 call through the Research Grant 101115149 (project ARTEMIS), as well as the support of the Office of Naval Research Global through the Research Grant N62902-22-1-2024.).

REFERENCES

[1] The Jahn-Teller Effect: Fundamentals and Implications for Physics and Chemistry (Springer Series in Chemical Physics, 97) 2010th Edition.
[2] L. Dai, Y. Wang, L. Sun, Y. Ding, Y. Yao, L. Yao, N. E. Drewett,W.i Zhang, J. Tang,and W. Zheng, Advanced Science 2021, 8 (2021) 2004995.
[3] A. Le Bail, H. Duroy, J. L. Fourquet, Materials Research Bulletin 1988, 23, 447-452.
[4] J. Rodriguez-Carvajal, Physica B, 192, (1993) 55-69.
[5] J. Senćanski, D. Bajuk-Bogdanović, D. Majstorović, E. Tchernychova, J. Papan, M. Vujković, Journal of Power Sources, 342 (2017) 690-703.
[6] J. Senćanski, N. Nikolić, S. Blagojević, M. Marinković, and I. Stojković Simatović. Russian Journal of Physical Chemistry A, 2022, 96 (2022) 2788.

PRODUCTION OF EXOPOLYSACCHARIDES USING BIS(2-HYDROHYETHYL) TEREPHTALATE DEGRADING BACTERIA

B. Lončarević [1], G. Gojgić Cvijović [1], M. Lješević [1], N. Lugonja [1], N. Petronijević [2], V. Beškoski [2] and J. Nikodinović-Runić [3]

[1]*University of Belgrade, Institute of Chemistry, Technology and Metallurgy, Njegoševa 12, 11000 Belgrade, Serbia. (branka.loncarevic@ihtm.bg.ac.rs)*
[2]*University of Belgrade - Faculty of Chemistry, Studentski trg 12-16, 11000 Belgrade, Serbia*
[3]*University of Belgrade, Institute of Molecular Genetics and Genetic Engineering, 11000 Belgrade, Serbia*

DOI: https://doi.org/10.46793/Phys.Chem24II.421N

ABSTRACT

Long lasting use of plastic material leads to the accumulation of waste and environmental concerns. Therefore, it is necessary to find novel polymers which can be used as substitutes for non-degradable plastic. Levan is a fructose based polymer with great potential for use in different industries due to its convenient properties such as flexibility, biocompatibility, biodegradability and non-toxicity. In this study, six microorganisms were selected based on their degradation of bis(2-hydroxyethyl) terephtalate (BHET) and for the production of exopolysaccharide (EPS). The highest yield of EPS was obtained using two strains, namely *Pseudomonas* sp. 53 and *Bacillus* sp. 47 in media containing sucrose as carbon source. Strain *Pseudomonas* sp, 53 can also synthetize EPS in the presence of BHET. FTIR analysis showed that obtained EPS in high yield correspond to levan type of polysaccharide.

INTRODUCTION

Plastic pollution has become a significant global problem. Most plastics are made for single-use, which further increases the amount of plastic waste in soil and water. Due to the overload of plastic waste, it is necessary to develop processes that will efficiently reduce waste and find acceptable polymers that can be used as substitutes for non-degradable plastic [1]. Levan is an extracellular polysaccharide (EPS) and it can be microbially produced. It consists of β-D-fructofuranosyl units connected by β(2→6) glycosidic bonds with branching at β(2→1) bond. Microbial levans generally have higher molecular masses compared to the ones in plants, up to several millions Da (105 to 108 Da) [2,3].

Levan synthesis begins with sucrose hydrolysis into its monomers, glucose and fructose, and forming of fructose polymer. Levansucrase (EC 2.4.1.10) is the main enzyme involved in biosynthesis reactions and it catalyzes hydrolysis of sucrose and formation of β(2→6) glycosidic bond. Various microorganisms have this enzyme, such as *Acetobacter*, *Bacillus*, *Lactobacilllus*, *Zymomonas* and others [2,3,4]. Microbial levan production is mainly based on sucrose fermentation as the main carbon source, and is isolated mainly by 96 % ethanol precipitation after cell centrifugation [5]. Major advantages of this polymer include adhesion, flexibility, biocompatibility, biodegradability, non-toxicity, solubility in water, and film formation, making it potentially great for industrial applications [2,3]. It can be used in cosmetics, as a hair care product, whitener, and medical applications such as healing wounds and burned tissue, as prebiotics, or as films for packaging [6]. It is observed that the LD_{50} (lethal dose for 50% of individuals) for levan is 7.5 ± 0.5 g/kg body weight and the no observed effect level (NOEL) is 1.5 g/kg/day. The safety of levan from *B. subtilis* strain was confirmed in 2000 by the Ministry of Health of Japan. Also, levan isolated

from *Z. mobilis* has been approved as a food by the Korean Food and Drug Administration, and levan under the trade name "Fructan" is permitted as a food additive in the USA, EU, Japan, Australia, and New Zealand [7].

In this study, we focused on bacteria which can degrade BHET (model compound used for polyethylene terephthalate (PET) and the one that is often released upon biocatalytic degradation of PET) while producing other valuable polymers such as levan.

METHODS

Microbial strains used in this work were: strain 47, which belongs to the *Bacillus* genera, strains 53, 61 and 95 (*Pseudomonas* sp), and strains 94 and 96 (*Rhodococcus* sp). Firstly, they were tested on Petri dishes using mineral medium containing BHET as a carbon source. If a microorganism has the capacity to degrade BHET, the halo zone occurs. After that, to test for the production of EPS, microorganisms were cultivated in sucrose medium for 6 days at 28 ^{o}C [8]. After removal of biomass the crude polysaccharide was isolated from fermentation culture by precipitation with two volumes of ethanol. Effect of pH on EPS precipitation was investigated at 6.5, 7.0 and 7.5. The production of EPS in the presence of both sucrose and BHET as carbon sources was also investigated using highest EPS producer. The ATR-IR spectra of EPS for highest producer were obtained using Thermo Nicolet 6700 FT-IR Spectrophotometer with Smart Orbit Diamond ATR (attenuated total reflectance) accessory.

RESULTS AND DISCUSSION

Results of the screening test for the utilization of BHET are represented at Figure 1. Based on the halo zones, it can be concluded that all microorganisms can utilize BHET as carbon source.

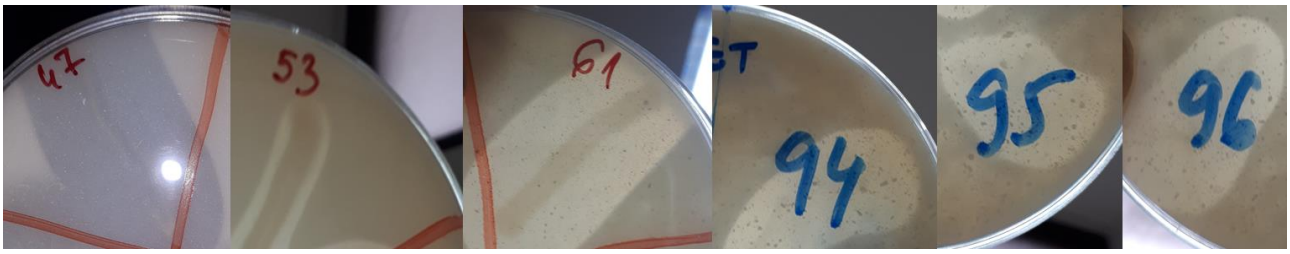


Figure 1. Test on Petri dishes with mineral medium and BHET. Halo zones for all investigated microorganisms appeared.

Microorganisms were grown in liquid media rich in sucrose and yield of EPS was measured gravimetrically (Figure 2). It can be observed that change in levan yield depended on the pH of precipitation and that the best EPS producers were strains 53 (*Pseudomonas* sp.) and 47 (*Bacillus* sp.). The strain 53 has the highest production of EPS and as the pH increases, the yield for this microorganism increases, with the highest yield of 31.83 g/L at pH 7.5. Therefore, this microorganism was chosen for investigation of EPS synthesis in the presence of BHET, in addition to sucrose. The yield obtained was one third lower (20.90 g/L).

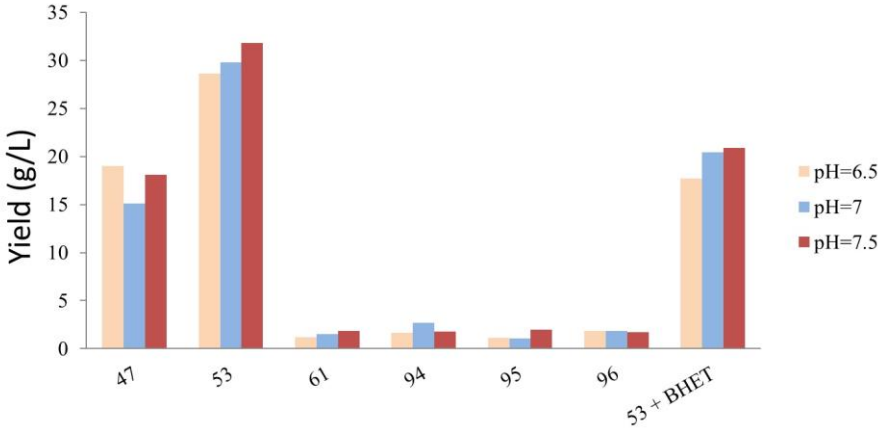


Figure 2. Changes in EPS yield as a function of pH.

The FT-IR spectra of the obtained EPS are shown in Figure 3 and can be divided into three parts: 3000-2700 cm^{-1}, 1200-900 cm^{-1} and 900-600 cm^{-1}. Broad bands with a maximum around 3300 cm^{-1} belong to O-H stretching vibrations. At the wavelength between 3000-2840 cm^{-1}, signals originating from C-H stretching vibrations can be observed and appear most often in the form of two signals. Signals at 1650 and 1652 cm^{-1} originate from water, while signals between 1500 and 1200 cm^{-1} were from C-H deformation vibrations. The highest signals in this area are located at the wave number 1050-1010 cm^{-1} and they indicate the presence of C-O-C asymmetric stretching vibrations originating from the glycosidic bond, and signals at around 926 cm^{-1} belong to C-O-C symmetric stretching vibrations. The bands at 925-927 cm^{-1} and at 811-812 cm^{-1} indicate the presence of a furanoid ring. Also, signals at 1125/1126 cm^{-1} belong to C-O stretching vibrations [9, 10]. Based on the results of FTIR analysis, it can be concluded that EPS produced by strain 53 (*Pseudomonas* sp.) corresponds to levan.

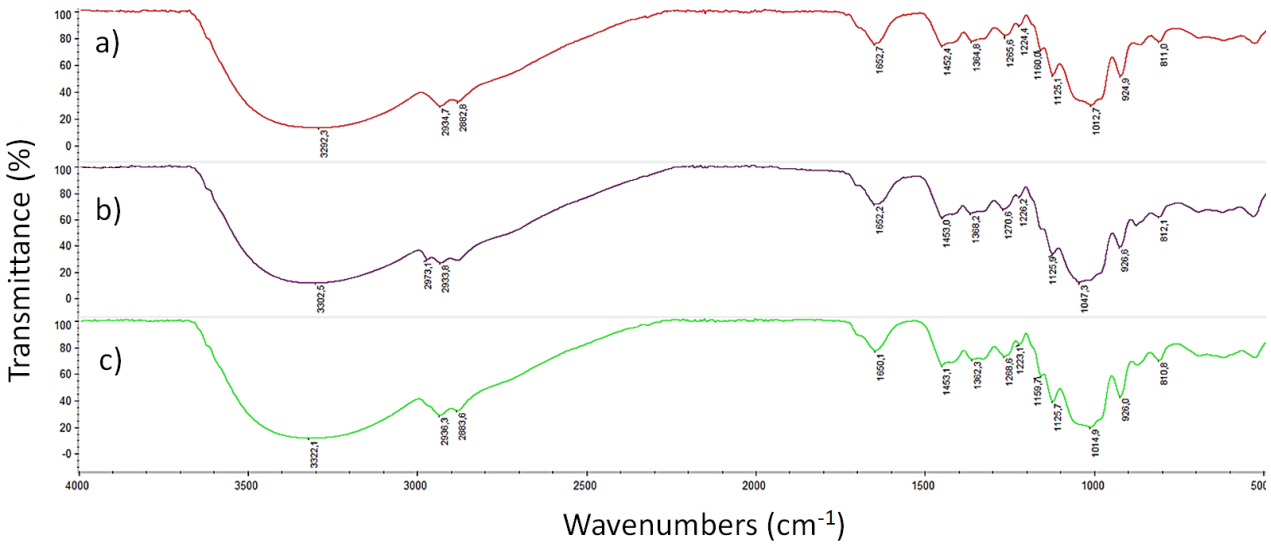


Figure 3. FTIR spectra of isolated EPS after fermentation of microorganism 53 at different carbon source and precipitation conditions: a) sucrose, pH 6.5; b) sucrose + BHET, pH 7; sucrose + BHET, pH 6.5.

CONCLUSION

All investigated microorganisms can efficiently use BHET as carbon source and therefore can be potentially used for PET degradation. The highest yield of EPS was obtained using strains 53 (*Pseudomonas* sp.) and 47 (*Bacillus* sp.) by fermentation fermentation. Also, strain 53 can produce EPS in the presence of BHET. FTIR analysis showed that EPS produced by strain 53 correspond to levan type of EPS.

Acknowledgment

This work is supported by the European Union within the Horizon 2020 program for research and innovation (number 870292, BioICEP) and Ministry of Education, Science, and Technological Development of the Republic of Serbia (number: 451-03-66/2024-03/200026 and 451-03-66/2024-03/200168).

REFERENCES

[1] Z. Yan, L. Wang, W. Xia, Z. Liu, L. Gu and J. Wu, Appl. Microbiol. Biotechnol., 105 (2021) 4551.
[2] C. Tomulescu, R. Stoica, C. Sevcenco, A. Căşărică, M. Moscovici, A. Vamanu, Scientific Bulletin. Series F. Biotechnologies, 20 (2016) 309.
[3] M. Domżał-Kędzia, M. Ostrowska, A. Lewińska, M. Łukaszewicz, Molecules, 28(14) (2023), 5407.
[4] H. Yildiz, N. Karatas, Process Biochemistry, 72 (2018), 41.
[5] S. Silbir, S. Dagbagli, S. Yegin, T. Baysal, Y. Goksungur, Carbohydrate Polymers, 99 (2014), 454.
[6] E. T. Öner, L. Hernández, J. Combie, Biotechnology Advances, 34(5) (2016), 827.
[7] O. Ates, E. T. Öner in: Microbial Functional Foods and Nutraceuticals, V. K. Gupta, H. Treichel, V. Shapaval, L. A. de Oliveira, M. Tuohy, (Eds.), John Wiley & Sons, Chichester UK, 2018.
[8] J. Liu, J. Luo, Y. Sun, H.Ye, Z. Lu, X. Zeng, Biores. Technol., 101 (2010) 6077-6083.
[9] E. Pretsch, P. Buhlmann, M. Badertscher, Springer, 4 (2009), 288.
[10] B. Kekez, G. Gojgić-Cvijović, D. Jakovljević, V. Pavlović, V. Beškoski, A. Popović, M. M. Vrvić, V. Nikolić, Carbohydrate Polymers, 154 (2016), 20.

INVESTIGATION OF FRUCTOOLIGOSACCHARIDES PREPARED BY PARTIAL HYDROLYSIS OF MICROBIAL LEVAN

G. Gojgić Cvijović [1], B. Lončarević [1], B. Nastasijević [2], N. Lugonja [1], A. Žerađanin [1], N. Petronijević [3] and V. Beškoski [3]

[1]*University of Belgrade, Institute of Chemistry, Technology and Metallurgy, Njegoševa 12, 11000 Belgrade, Serbia. (branka.loncarevic@ihtm.bg.ac.rs)*
[2]*University of Belgrade, Vinca Institute of Nuclear Sciences, 11000 Belgrade, Serbia*
[3]*University of Belgrade - Faculty of Chemistry, Studentski trg 12-16, 11000 Belgrade, Serbia*

DOI: https://doi.org/10.46793/Phys.Chem24II.425GC

ABSTRACT

Fructans are a group of complex carbohydrates that exert microbiota-stimulating and immunomodulating effects. The biological activity of fructans depends on their molecular weights and linkage type. Fructooligosaccharides are short-chain fructans with a degree of polymerization from 3 to 10. While inulin-type, β-(2,1) fructooligosaccharides are well studied and commercially exploited, the potential of levan-type, β-(2,6) fructooligosaccharides is still intensively studied. This work aimed to optimize conditions for preparing fructooligosaccharides by mild acid treatment using polysaccharide levan obtained by fermentation with *B. licheniformis* NS032. The optimum time for hydrolysis at 80 °C was 15 minutes. Based on MALDI analysis, it was shown that the obtained preparation contained oligosaccharides with degree of polymerization in the range 3-7. Also, the biological activity of prepared fructooligosaccharides was retained.

INTRODUCTION

Fructans are complex carbohydrates that hold a significant role in human health, exerting a multitude of beneficial effects. Composed of D-fructose residues linked by β-(2,1) or β-(2,6) bonds, they form structures of varying chain lengths and molecular weights. Inulin-type fructans, those with β-(2,1) bonds, are abundant in many plants. Levan-type fructans, with β-(2,6) linkages, are found in both plants and microorganisms. Also, the graminarin-type fructans, with both β-(2,1) and β-(2,6) bonds, are prevalent in cereals. Inulin-type fructans (MW 3-5000 g/mol) are known as prebiotics, while levan-type polymers (MW>10^5 g/mol) exhibit antitumor and immunomodulating effects [1].

Fructooligosaccharides (FOSs) are short-chain fructans with a degree of polymerization (DP) from 3 to 10, which are attributed to numerous benefits, such as prebiotic potential, improved absorption of calcium and magnesium, reduced blood lipid levels, and protection against colon cancer. While inulin-type FOSs are well studied and commercially exploited, the potential of 2,6-type FOSs is still intensively investigated. FOSs could be obtained by microbial or enzymatic synthesis from disaccharides or by hydrolysis of high molecular weight polymers. The presence of glucose and sucrose with a small amount of oligomers are generally considered to be a disadvantage of synthesis processes. On the other hand, using polyfructan as a raw material is expected to obtain the final product in high yield and without glucose and fructose [2].

In this study, microbial levan obtained by fermentation of *B. licheniformis* NS032 was used as the starting material for hydrolysis with the aim to determine the optimum conditions for FOS preparation and examine the composition of the obtained products by MALDI. In parallel, obtained oligomer products were tested for DPPH antioxidant activity to evaluate whether hydrolysis could affect their biological properties adversely (Figure 1).

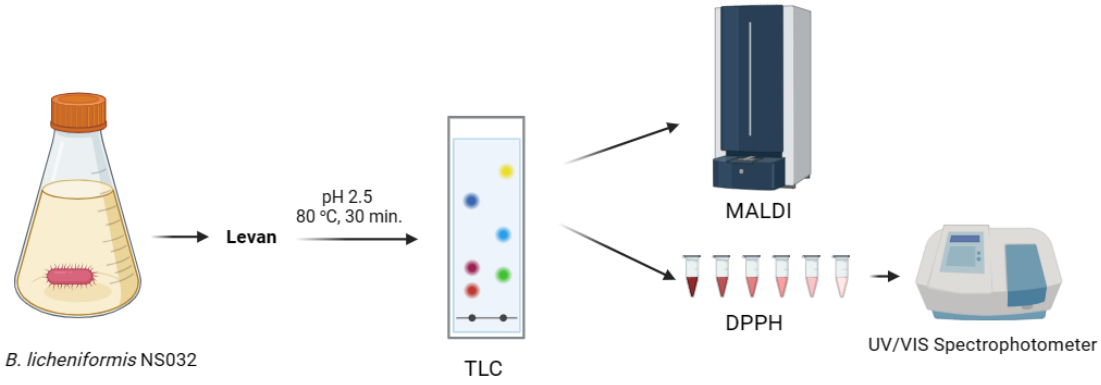


Figure 1. Schematic representation of aim of this work.

METHODS

Polysaccharide levan with molecular weight 10^5 g/mol was obtained by fermentation using *B. licheniformis* NS032 as described previously [3]. Levan solution (20 g/L) was prepared and pH adjusted to 2.5 by 0.1 M hydrochloric acid. Hydrolysis was performed at 80 °C for 30 minutes, and the reaction was stopped by cooling and neutralization with solid Na_2CO_3. During hydrolysis, samples were taken in regular intervals and obtained hydrolysates were analyzed by TLC silica gel 60 plates (Merck) using a solvent system chloroform/methanol/water 30/35/5, V/V/V [4]. Low molecular weight products were separated from polymers by dialysis (molecular weight cut-off 3000). Preparative silica gel chromatography on HTLC silica gel 60 plates (Merck) was used for purification of FOS fractions. DPPH assay was performed according to [5] using FOSs in concentration of 1-5 mg/mL.

Structural characterization of FOSs in the mixtures was performed by MALDI Voyager Biospectrometry DE Pro Workstation (PerSeptive Biosystems, Framingham, MA, USA) using dihydroxybenzoic acid (DHB) as a matrix [6].

RESULTS AND DISCUSSION

Compared to other polysaccharides, fructans are generally more sensitive to acid hydrolysis. Hydrolysis conditions depend on the polymer's molecular weight and branching degree.

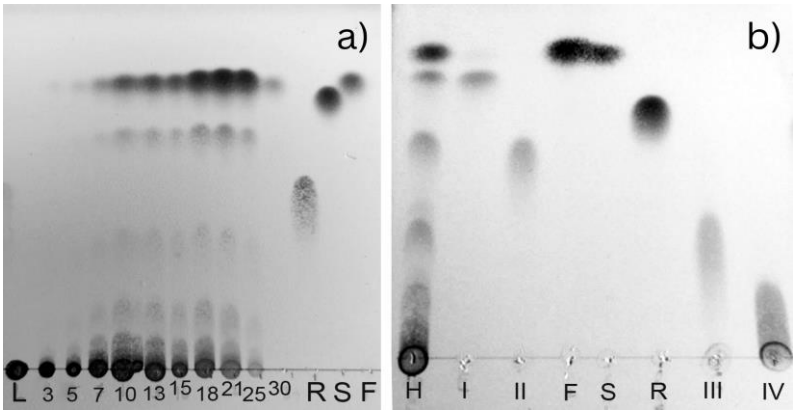


Figure 2. TLC plates showing reference compounds (F -fructose; S-sucrose; R-raffinose, L-levan) and: **a)** the products of hydrolysis as a function of time (3-30 minutes), **b)** H-hydrolisate; I-IV - fractions obtained by preparative chromatography.

Exposure of the polysaccharide solution to an elevated temperature in an acidic environment for too long can lead to the degradation of the molecules and, thus, to the loss of biological activity.

Hydrolysis of high molecular weight levan was performed at 80 °C for 30 minutes, and the hydrolysis products were analyzed by TLC (Figure 2a). Under the tested conditions, hydrolysis started in 3rd minute, which was recorded by the appearance of a fructose spot near the front with Rf 0.85. Complete hydrolysis was achieved after 25 minutes when the polymer from the start completely disappeared. In 15 minutes, products with different degrees of polymerization (DP) (area Rf 0.2-0.7) were obtained. According to the literature data, they are expected to correspond to oligomers with DP 3-9. Based on these results, it is evident that the optimal hydrolysis time for obtaining FOSs was 15 minutes.

The FOS mixture obtained by hydrolysis was refined by preparative chromatography, and the fractions marked with I to IV were obtained (Figure 2b). The composition of the hydrolysate and fractions I to IV was analyzed by mass spectrometry (Figure 3). Signals corresponding to FOS adducts with sodium were observed with the difference in *m/z* 162 Da characteristic of polysaccharide structures.

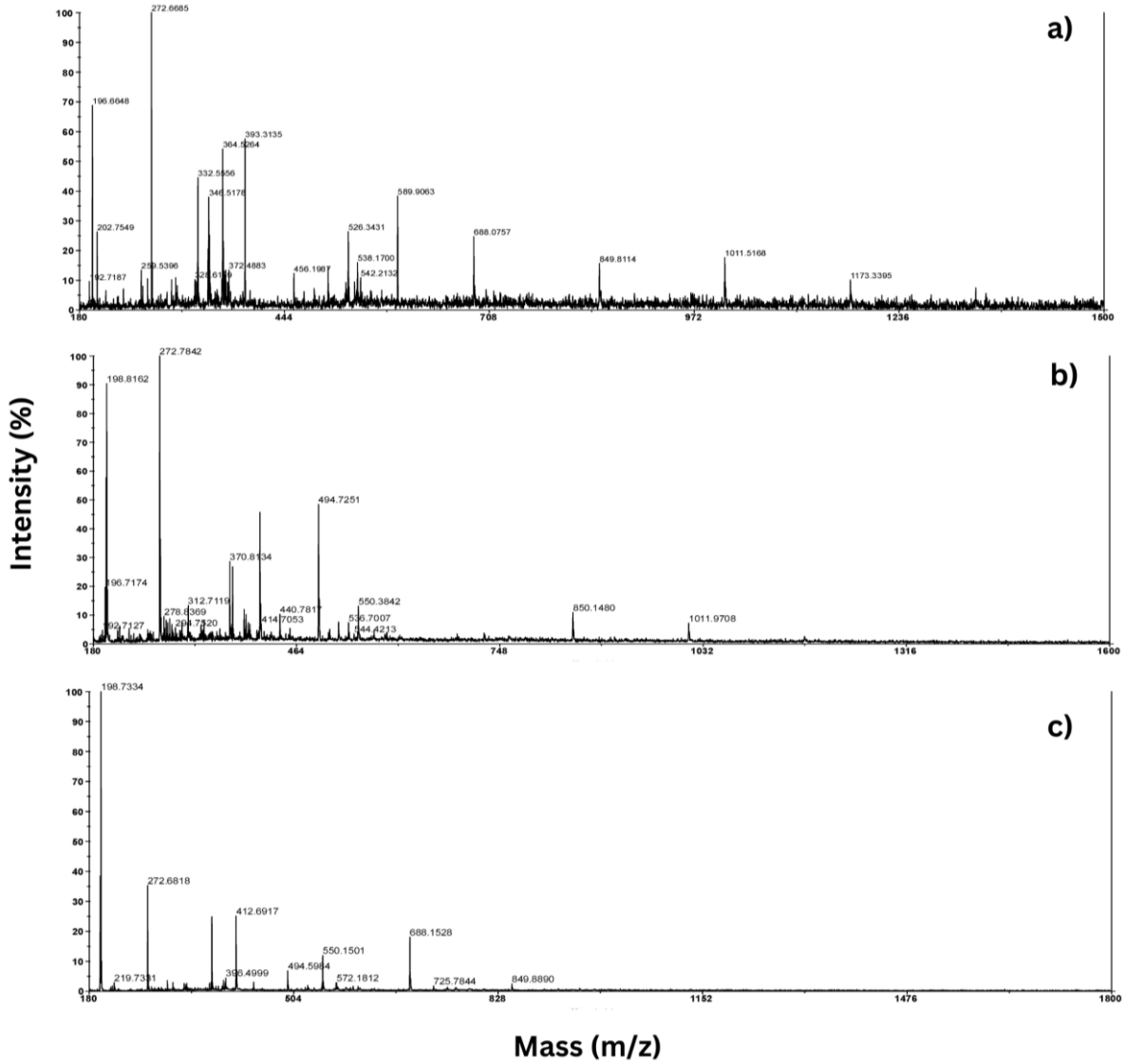


Figure 3. MALDI spectra of a) Hydrolysate; b) Fraction IV and c) Fraction III.

The presence of DP 4-7 (*m/z* 688 -DP4; 849 -DP5; 1011 -DP6; 1173 -DP7) in fractions III and IV was evident and in the hydrolysate, while in fractions I and II, FOSs with lower DP (m/z 364-DP2; 526-DP3) were observed. At *m/z* less than 500, signals originating from the matrix were also observed (*m/z* 272; 346) overlapping with signals from disaccharides.

DPPH assay confirmed that prepared FOSs retained moderate antioxidant activity with IC in the 20-25 % range.

CONCLUSION

The optimum time for the partial hydrolysis of microbial polysaccharide levan at pH 2.5 and 80 °C was found 15 minutes. The experiments showed that FOSs with DP 3-7 was obtained. Prepared oligomers retain antioxidant activity. The applied procedure can be used to obtain β-(2,6) FOSs.

Acknowledgment

This work was supported by the Ministry of Education, Science and Technological Development of the Republic of Serbia (Contract No: 451-03-66/2024-03/200026, 451-03-66/2024-03/200168 and 451-03-66/2024-03/ 200017).

REFERENCES

[1] I. D. Young, D. Latousakis, N. Juge, Nutrients, 13 (2021) 1309.
[2] A. L. Dominguez, L. R, Rodrigues, N. M. Lima, J. A. Teixeira, Food Bioprocess Technol., 7 (2014) 324.
[3] G. D. Gojgic-Cvijovic, D. M. Jakovljevic, B. D. Loncarevic, N. M. Todorovic, M. V. Pergal, J. Ciric, K. Loos,V. P. Beskoski, M. M. Vrvic, Int. J. Biol. Macromol., 121 (2019) 142.
[4] I. Dahech, K.S. Belghith, H. Belghith, H. Mejdoub, Int. J. Biol. Macromol., 51 (2012) 329.
[5] Y. Lim, E. Quah, Food Chem., 103 (2007) 734.
[6] J. Wang, P. Sporns, N. H. Low, J. Agric. Food Chem., 47 (1999) 1549.

COMPETITIVE COPPER, CADMIUM, AND NICKEL IONS REMOVAL FROM AQUEOUS SOLUTION USING AMINO-MODIFIED MAGNETIC POLYMER SORBENT

T. T. Tadić [1], Lj. T. Suručić [2], A. B. Nastasović [1], S. S. Bulatović, N. Ž. Nedić [1], A. E. Onjia [3] and B. M. Marković [1]

[1]*University of Belgrade, Institute of Chemistry, Technology and Metallurgy, Njegoševa 12, 11000 Belgrade, Serbia. (tamara.tadic@ihtm.bg.ac.rs)*
[2]*Faculty of Medicine, University of Banja Luka, Save Mrkalja 14, 78000 Banja Luka, Republic of Srpska, Bosnia and Herzegovina.*
[3]*University of Belgrade, Faculty of Technology and Metallurgy, Karnegijeva 4, Belgrade, Republic of Serbia.*

DOI: https://doi.org/10.46793/Phys.Chem24II.429T

ABSTRACT

In this study, amino-modified magnetic polymer sorbent, *m*PGME-eda, was employed for the sorption of copper (Cu^{2+}), cadmium (Cd^{2+}), and nickel (Ni^{2+}) ions from aqueous solution. The sorption was studied under competitive conditions by varying contact time and initial metal concentration at unadjusted pH (4.2) and 298 K. It was found that sorption capacity increased with the increase of contact time and initial metal concentration. Equilibrium sorption capacities for Cu^{2+} (1.20 mmol/g) and Cd^{2+} (1.15 mmol/g) were attained after 360 min, while for Ni^{2+} (1.01 mmol/g) it was reached after 90 min. It was noticed that metal ions sorption follows a pseudo-second-order kinetic model. The mechanism of sorption was found to be intra-particle diffusion-controlled with an evident influence of liquid film diffusion. Equilibrium sorption data were best fitted with the Langmuir isotherm model.

INTRODUCTION

Water resource contamination with heavy metals as one of the most harmful types of pollutants poses great environmental and human health risks. The major sources of these contaminants are industries such as mining, tanneries, fertilizer industries, metal plating facilities, batteries, and paper and textile industries [1]. The most common toxic heavy metals that occur in contaminated waters are mercury (Hg), cadmium (Cd), lead (Pb), chromium (Cr), copper (Cu), zinc (Zn), nickel (Ni), and arsenic (As). Some heavy metals such as Cu, Ni, and Zn are essential in the human body in limited concentrations, while high concentrations are toxic. Other metals like Hg, Cd, and Pb are toxic even in low concentrations [2].

Since most heavy metals are toxic, cancerogenic, non-biodegradable, and tend to accumulate in the environment, their removal from contaminated waters is important [3]. Today, numerous removal technologies are employed for the treatment of heavy metal-contaminated waters [4]. Considering sorption advantages like high efficiency, economic feasibility, easy operation conditions, low toxicity and renewable sorbents, this technique is the best choice for heavy metal removal from aqueous solutions [5]. Common sorbents such as low-cost biomaterials derived from agricultural waste and plants, fly ash, zeolites, as well as activated carbon have been used in the removal of heavy metals from wastewater [6]. Nevertheless, these types of sorbents have certain disadvantages like low sorption capacity, poor mechanical and thermal properties, and the complexity of regeneration and separation from aqueous solutions [4]. Thus, much attention has been focused on the development of highly efficient, low-cost, and renewable materials as sorbents

for wastewater treatment. The use of magnetic polymer-based sorbents in wastewater treatment has recently become popular due to their exceptional thermal and chemical stability, high specific surface area, chemical versatility, reusability, and easy separation from the aqueous solution in the presence of an external magnetic field. Among the magnetic polymer sorbents, glycidyl methacrylate (GMA)-based sorbents are very attractive since the presence of reactive epoxy groups allows very easy post-functionalization with various amines, thiols, carboxylic acids, azide, etc. [7].

In this study, magnetic GMA-based composite functionalized with ethylenediamine was used as a sorbent for Cu^{2+}, Cd^{2+}, and Ni^{2+} ions removal from aqueous solutions. The effects of contact time and initial metal concentration on sorption capacity were examined. Also, the kinetics and mechanism of the sorption process were investigated.

METHODS

Copper(II) nitrate trihydrate ($Cu(NO_3)_2 \cdot 3H_2O$, ≥99.5 %), cadmium nitrate tetrahydrate ($Cd(NO_3)_2 \cdot 4H_2O$, 98 %), and nickel(II) nitrate hexahydrate ($Ni(NO_3)_2 \cdot 6H_2O$, ≥97 %) were purchased from Sigma Aldrich and used without further purification. Deionized water (Milli-Q Millipore, resistivity of 18 MΩ/cm) was used for the preparation of all solutions.

Magnetic amino-modified GMA-based sorbent (*m*PGME-eda) was prepared by suspension copolymerization in the presence of 10 wt.% magnetic nanoparticles and modified with ethylenediamine as described previously [8], [9]. Sorption of Cu(II), Cd(II), and Ni(II) ions by *m*PGME-eda sorbent was carried out in competitive batch conditions with a dose of sorbent of 10 g/L at an unadjusted pH (4.2) and 298 K. The effect of contact time (0 – 24 h) and initial metal concentration (0.001 – 0.02 mol/dm^3) was investigated. The residual metal ions concentrations were determined by atomic absorption spectrometry, AAS (model Perkin Elmer AAnalyst 400, Waltham, USA). All experiments were repeated in duplicate.

The sorption capacity, q_t (mmol/g) for *m*PGME-eda sorbent was determined using Equation 1 [7]:

$$q_t = \frac{(C_i - C_t) \cdot V}{m} \qquad (1)$$

where C_i (mmol/dm^3) and C_t (mg/dm^3) are the concentrations of metal ions in the initial solution and the aqueous phase at time t, respectively, V (dm^3) is the volume of the aqueous phase, and m (g) is the amount of *m*PGME-eda sorbent.

RESULTS AND DISCUSSION

The results of the influence of contact time and initial metal concentration on the sorption capacity of Cu^{2+}, Cd^{2+}, and Ni^{2+} ions are shown in **Figure 1**.

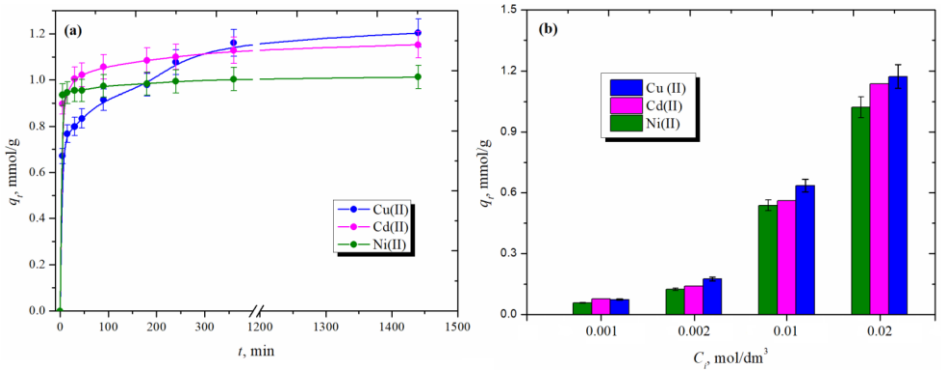


Figure 1. Effect of (a) contact time and (b) initial concentration of metal ions on the sorption capacity of Cu^{2+}, Cd^{2+}, and Ni^{2+} ions by *m*PGME-eda sorbent.

It can be observed that the sorption was very fast in the initial 15 minutes (**Figure 1a**). With a further increase in contact time, the sorption capacity slowly increased and the saturation of the sorbent was attained after 360 minutes for Cu^{2+} and Cd^{2+} ions, while for Ni^{2+} ions sorbent saturation was attained after 90 minutes. As can be seen from **Figure 1b**, the sorption capacity increased with the increase of the initial metal ion concentrations. It can be noticed that the order of the sorption ability was $Cu^{2+} > Cd^{2+} > Ni^{2+}$. These results are a consequence of different hydrated ionic radius of investigated metals. The sorption capacities of 1.20 mmol/g, 1.15 mmol/g and 1.01 mmol/g for Cu^{2+}, Cd^{2+}, and Ni^{2+} ions at $C_i = 0.02$ mol/dm^3 were achieved, respectively.

To analyze the sorption kinetics of Cu^{2+}, Cd^{2+}, and Ni^{2+} by *m*PGME-eda sorbent, the linear forms of pseudo-first-order, pseudo-second-order, liquid film diffusion, and intra-particle diffusion models were applied [7]. The obtained results are given in **Table 1**.

Table 1. Kinetic parameters for Cu^{2+}, Cd^{2+}, and Ni^{2+} sorption by *m*PGME-eda sorbent.

Pseudo-first-order				**Pseudo-second-order**			
	Cu^{2+}	Cd^{2+}	Ni^{2+}		Cu^{2+}	Cd^{2+}	Ni^{2+}
$k_1 \cdot 10^3$, 1/min	6.45	5.99	5.53	k_2, g/mmol min	0.04	0.12	0.34
q_e, mmol/g	0.53	0.20	0.07	q_e, mmol/g	1.22	1.16	1.01
R^2	0.967	0.957	0.990	R^2	0.999	0.999	0.999
Liquid film diffusion				**Intra-particle diffusion**			
	Cu^{2+}	Cd^{2+}	Ni^{2+}		Cu^{2+}	Cd^{2+}	Ni^{2+}
$k_{LFD} \cdot 10^2$, 1/min	0.64	0.59	0.56	$k_{id} \cdot 10^2$, mmol/g min$^{0.5}$	2.65	0.84	0.38
C_{LFD}	0.83	1.75	2.63	C_{id}	0.65	0.97	0.93
R^2	0.967	0.957	0.990	R^2	0.983	0.991	0.967

k_1 – pseudo-first order rate constant, k_2 – pseudo-second order rate constant, q_e– amount of sorbed ions at equilibrium, R^2 – correlation coefficients, k_{LFD} - the liquid film diffusion coefficient, k_{id} – intraparticle diffusion coefficient, C_{LFD} – liquid film diffusion constant, C_{id} – constant, related to the thickness of the boundary layer

As can be seen from **Table 1**, the values of correlation coefficients, R^2, obtained from pseudo-second-order were higher compared with values of R^2 obtained for pseudo-first-order. Also, the values of experimental q_e were almost equal to the calculated q_e values obtained from pseudo-second-order. The results demonstrate that the sorption of Cu^{2+}, Cd^{2+}, and Ni^{2+} on the *m*PGME-eda followed the pseudo-second-order kinetic model indicating the chemisorption nature of the process. The high R^2 values (> 0.950) for liquid film diffusion and intra-particle diffusion models indicated that the sorption of Cu^{2+}, Cd^{2+}, and Ni^{2+} was controlled by both intra-particle diffusion and diffusion through the liquid film.

The equilibrium data obtained for the sorption of Cu^{2+}, Cd^{2+}, and Ni^{2+} ions on the *m*PGME-eda were analyzed using the linear forms of Langmuir and Freundlich isotherm models [7]. The values of the isotherm parameters are summarized in **Table 2**.

Table 2. Isotherm parameters for Cu^{2+}, Cd^{2+}, and Ni^{2+} sorption by *m*PGME-eda sorbent.

Langmuir				**Freundlich**			
	Cu^{2+}	Cd^{2+}	Ni^{2+}		Cu^{2+}	Cd^{2+}	Ni^{2+}
K_L,mmol/g	1.15	0.71	2.79	K_F, L^n mmol^{n-1}/mmol	0.35	0.11	1.06
q_{max}, L/mmol	1.45	1.40	1.31	n	1.55	1.73	1.58
R^2	0.984	0.992	0.991	R^2	0.911	0.979	0.976

K_L – Langmuir isotherm constant, q_{max} – Langmuir maximum adsorption capacity, K_F – Freundlich isotherm constant, n – Freundlich isotherm exponent

According to the high values of R^2 (>0,910) obtained for Cu^{2+} (0.984), Cd^{2+} (0.992), and Ni^{2+} (0.991) sorption on *m*PGME-eda, both models show good fits, however, the Langmuir model provided a better fit than the Freundlich model. These results indicated monolayer sorption of Cu^{2+}, Cd^{2+}, and Ni^{2+} ions at specific homogenous sites on *m*PGME-eda sorbent. The maximum sorption capacity, q_{max}, obtained from Langmuir model increases in the order: Ni^{2+} (1.31 mmol/g) < Cd^{2+} (1.40 mmol/g) < Cu^{2+} (1.45 mmol/g).

CONCLUSION

The sorption behavior of Cu^{2+}, Cd^{2+}, and Ni^{2+} from aqueous solution by magnetic amino-functionalized polymer sorbent under competitive conditions was investigated. The increase in contact time and initial metal concentration resulted in an increase in the sorption capacity of metal ions by *m*PGME-eda sorbent. The sorption of three metal ions followed the pseudo-second-order kinetic model. The intra-particle and liquid film diffusion controlled the Cu^{2+}, Cd^{2+}, and Ni^{2+} sorption onto the tested sorbent. Equilibrium data fitted best with the Langmuir isotherm model. The present study concludes that *m*PGME-eda can be employed as a sorbent for the removal of heavy metal ions from aqueous media under competitive conditions.

Acknowledgment

This research has been financially supported by the Ministry of Science, Technological Development and Innovation of Republic of Serbia (Contract No: 451-03-66/2024-03/200026 and 451-03-65/2024-03/200135).

REFERENCES

[1] N. A. A. Qasem, R. H. Mohammed, D. U. Lawel, Npj Clean Water, 4 (2021) 36.
[2] M. Senila, E. Neag, O. Cadar, E. D. Kovacs, I. Aschilean, M. H. Kovacs, Molecules, 27 (2022) 3938.
[3] Z. Huang, L. Lu, Z. Cai, Z. J. Ren, J. Hazard. Mater., 302 (2016) 323.
[4] Z. M. Ayalew, X. Guo, X. Zhang, J. Hazard. Mater. Adv., 8 (2022) 100158.
[5] Lj. Suručić, T. Tadić, G. Janjić, B. Marković, A. Nastasović, A. Onjia, Metals, 11 (2021) 1777.
[6] K. Moreno-Sader, A. García-Padilla, A. Realpe, M. Acevedo-Morantes, J. B. P. Soares, ACS Omega, 4 (2019) 10834.
[7] A. Nastasović, B. Marković, Lj. Suručić, A. Onjia, Metals, 12 (2022) 814.
[8] B. M. Marković, Z. M. Vuković, V. V. Spasojević, V. B. Kusigerski, V. B. Pavlović, A. E. Onjia, A. B. Nastasović, J. Alloy. Compd., 705 (2017) 38.
[9] T. Tadić, B. Marković, Z. Vuković, P. Stefanov, D. Maksin, A. Nastasović, A. Onjia, Metals, 13 (2023) 1864.

KINETIC STUDY OF CONGO RED DYE SORPTION ON MACROPOROUS GMA-BASED COPOLYMER

B. M. Marković [1], T. T. Tadić [1], Z. P. Sandić [2], S. S. Bulatović [1], N. Ž. Nedić [1], S. P. Petrović [1] and A. B. Nastasović [1]

[1]University of Belgrade, Institute of Chemistry, Technology and Metallurgy, Njegoševa 12, 11000 Belgrade, Serbia. (bojana.markovic@ihtm.bg.ac.rs)
[2]University of Banja Luka, Faculty of Natural Science and Mathematics, Mladena Stojanovića 2, Banja Luka, Republic of Srpska, Bosnia and Herzegovina.

DOI: https://doi.org/10.46793/Phys.Chem24II.433M

ABSTRACT

Diethylenetriamine macroporous crosslinked copolymer of glycidyl methacrylate (GMA) and ethylene glycol dimethacrylate (EGDMA), SGE80-deta, was tested as sorbent of Congo red (CR), in static experiments, from aqueous solutions, at room temperature. The sorption is found to be rapid, with a sorption half-time of 2 min, and a maximum uptake capacity higher than 80% after 30 min. In order to calculate kinetic parameters as well as to determine the rate-limiting step and CR sorption mechanism, obtained kinetic data were fitted to kinetic models. The obtained results suggest a complex mechanism of CR sorption by SGE80-deta, which includes chemisorption and external and internal diffusion.

INTRODUCTION

Discharge of organic compounds especially dyes widely applied in industries such as leather, textile, pharmaceuticals and cosmetics, printing, rubber, and plastic industries, arise serious threats and harmful effects for living organisms and eco-systems [1, 2]. Congo Red (CR) is a benzidine-based anionic azo dye, highly soluble in aqueous solutions. CR undergoes cleavage to yield benzidine, a human mutagen, and carcinogen, causing respiratory issues, blood clotting, and eye and skin irritations [2]. Methods for CR removal from wastewater include ion exchange, coagulation, flocculation, membrane filtration, etc. However, the drawbacks of these methods are numerous, such as incomplete dye removal, low selectivity, high cost, large energy requirements, and secondary pollution [3]. On the other hand, adsorption is characterized by simplicity, low cost, and high efficiency. Various materials, like biochar, clay, chitosan, waste, graphene, and activated carbon were reported as dye sorbents in literature [2].

Macroporous highly cross-linked copolymers based on GMA and EGDMA (SGE) are well-known for their multipurpose applications, as sorbents of heavy and precious metals, radionuclides, and organic compounds [3], [4], [5]. The main advantages of these types of sorbents include simple synthesis and functionalization, adaptable and controllable surface chemistry, and porous structure, combined with chemical and thermal stability. Previously, we evaluated this type of copolymer as a sorbent for Acid Orange 10 and Bezaktiv Rot reactive dye [6]. Based on our extensive previous research lasting more than three decades, macroporous copolymer (SGE80) was synthesized by radical suspension copolymerization, functionalized by ring-opening reaction of the epoxy group with diethylenetriamine (SGE80-deta), and tested as CR sorbent. The effects of contact time on CR sorption by SGE80-deta were investigated in batch experiments. In order to calculate kinetic parameters as well as to determine the rate-limiting step and CR sorption mechanism, obtained kinetic data were fitted to pseudo-first-order (PFO), pseudo-second-order (PSO), Elovich, fractional power (FP), intraparticle diffusion (IPD), Bangham, and liquid film diffusivity (LFD) models.

METHODS

All the chemicals used for copolymer synthesis were analytical grade products and used as received. Dye solutions were prepared using Congo red (Sigma-Aldrich, Darmstadt, Germany) and deionized water (Milli-Q Millipore, 18 MΩ/cm conductivity). Macroporous crosslinked SGE80 was obtained by the suspension copolymerization of GMA and EGDMA in the presence of an inert component, and subsequently amino-functionalized according to a previously published procedure [7]. CR sorption was studied in batch experiments at unadjusted pH (around 5) with a sorbent dose of 10 g/L, at room temperature. An experimental dye solution of the desired concentration (20 mg/dm^3) was obtained by appropriate dilution of the stock solution (1000 mg/dm^3). To determine the sorption rate, the suspension of SGE80-deta and CR was shaken at 400 rpm for 30 min. After predetermined time, SGE80-deta was filtrated and CR concentration in solution was determined by Ultraviolet-visible spectroscopy (NOVEL-102S UV-Vis Double Beam Spectrophotometer, COLO Lab Experts, Slovenia), in 1 cm quartz cuvette within the range of 300–700 nm, at a maximum absorption wavelength, λ_{max}, of 497 nm. The adsorption capacity (Q_t, mg/g) and sorption efficiency (E, %) were calculated using equations 1 and 2 [5]:

$$Q_t = \left(C_i - C_t\right)V / m \tag{1}$$

$$E = \left(\left(C_i - C_t\right) / C_i\right) \times 100 \tag{2}$$

Where: C_i (mg/dm^3) and C_t (mg/dm^3) are the initial concentration and concentration at time t of CR in the solution, V (dm^3) is the volume of the solution, and m (g) is the mass of SGE80-deta.

For understanding the sorption mechanism and the interactions of CR with SGE80-deta, the experimental data were analyzed using well-known surface reaction- and diffusion-based models, such as PFO (equation 3), PSO (equation 4), Elovich (equation 5), FP (equation 6), IPD (equation 7), and LFD (equation 8) [5]:

$$Q_t = Q_e\left(1 - e^{-k_1 t}\right) \tag{3}$$

$$Q_t = Q_e^2 k_2 t / 1 + Q_e^2 k_2 t \tag{4}$$

$$Q_t = \left(1/\beta\right)\ln\left(\alpha\beta t + 1\right) \tag{5}$$

$$Q_t = Kt^{\nu} \tag{6}$$

$$Q_t = k_{id} t^{0.5} + C_{id} \tag{7}$$

$$Q_t = Q_e\left(1 - e^{-k_{LFD} t}\right) \tag{8}$$

Where: k_1 and k_2 are the sorption-rate constants for PFO and PSO, respectively, Q_e is the equilibrium sorption capacity, α is the initial sorption constant, β is the desorption constant, k_{FP} is the fractional power constant, ν is the fractional power rate constant, k_{id} is IPD rate constant, C_{id} is the intercept (proportional to the thickness of the boundary layer), and k_{LFD} is LFD rate constant.

RESULTS AND DISCUSSION

The effect of contact time on CR sorption onto SGE80-deta, was determined in the contact time range of 1 to 30 min (**Figure 1a**). The adsorption of CR increases within 5 min, slows down and gradually attains equilibrium at 20 min, with a maximal capacity of 1.95 mg/g. As can be observed, CR sorption was very fast, with sorption half time of 2 min. UV-Vis spectra (**Figure 1b**) show the

gradual absorbance decrease over time and reduction of CR peaks at 350 and 497 nm intensities, confirming almost complete dye removal after 30 minutes.

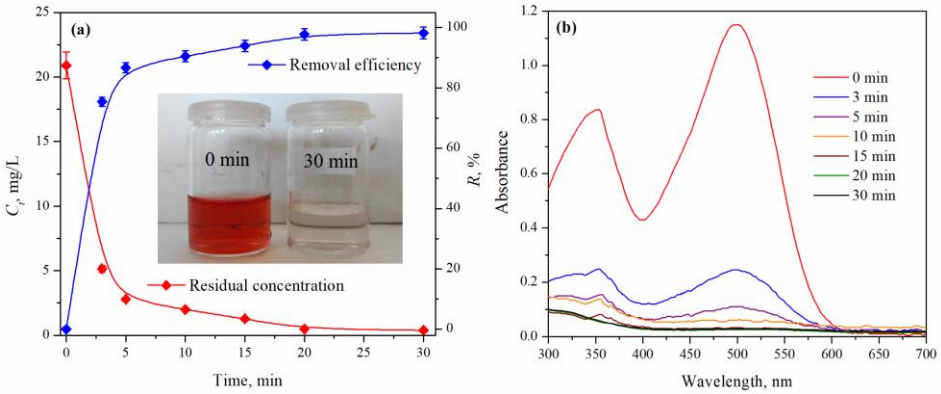


Figure 1. (a) Effect of contact time on CR sorption (inset displays images of the dye solutions at the beginning and after 30 min) and (b) Uv-Vis spectra of CR solution at indicated contact time.

The calculated kinetic parameters and coefficients of determination (R^2) are listed in **Table 1** while fitting curves are displayed in **Figure 2**.

Table 1. Kinetic parameters for CR sorption by SGE80-deta sorbent.

PFO		**PSO**		**Elovich**	
k_1, 1/min)	0.49	k_2, g/mg min	0.49	α	132.57
Q_e^{cal}, mg/g	1.90	Q_e^{cal}, mg/g	2.02	β, g/mg min	4.92
R^2	0.916	R^2	0.972	R^2	0.930
FP		**IPD**		**LFD**	
k_{FP} , mg/g	1.37	k_{id} (mg/g min$^{0.5}$)	0.10	k_{LFD} (1/min)	0.20
v (1/min)	0.12	C_{id} (mg/g)	1.50	C_{LFD}	0.80
R^2	0.917	R^2	0.991	R^2	0.895

The experimental value of sorption capacity at equilibrium, Q_e^{exp}, (1.95 mg/g) is almost the same as the Q_e^{cal} values for PFO (1.90 mg/g) and PSO model (2.02 mg/g). Also, R^2 values for PSO and PFO are both high (R^2>0.9). According to Azizian's theoretical approach, the PSO model is more suitable for fitting the kinetic data for low adsorbate initial concentrations, while the PFO model is better fit for high initial concentrations [8]. It seems to be that the initial concentration (20 mg/dm^3) in the investigated CR/SGE80-deta adsorption system is a borderline case with respect of the initial concentration, which might be the reason that R^2 values for PSO and PFO are both high. Based on R^2 values, the fitting order was as follows: PSO > Elovich > FP > PFO. The highest R^2 value for the PSO model might suggest chemisorption which involves electron transfer among CR and SGE80-deta as the dominant sorption mechanism. However, such a conclusion might be misleading and cannot be made without an analysis of diffusion models (**Figure 2b**). Multi-stage IPD plot is clearly observed, with three CR sorption stages, i.e. external diffusion of CR from the solution to the SGE80-deta particle surface controlled by the boundary layers, internal diffusion from particle surface to the functional groups in the porous particle interior, and finally, the formation of chemical bonds between CR and functional groups of SGE80-deta [2]. The IPD plot passes through the origin in the early adsorption stage, suggesting the IPD control of the CR/SGE80-deta adsorption system. The IPD deviation in later stages indicates that both IPD and LFD take place.

High R^2 values for IPD (0.991) and LFD (0.895), even though LFD plot (inset of **Figure 2b**) deviates from the origin, confirm that CR sorption involves not only interactions of CR molecules with functional groups of SGE80-deta, but suggest definite influence of intraparticle and film diffusion on CR sorption mechanism. The similar C_{id} and C_{LFD} values also suggest almost equal participation of both mechanisms.

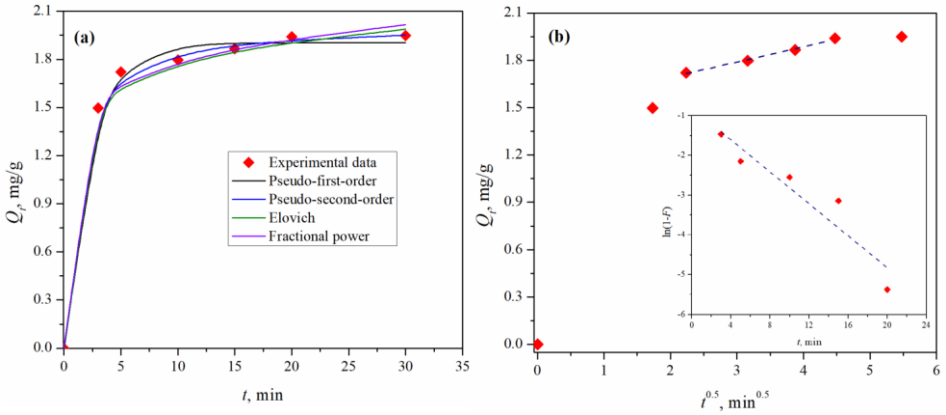


Figure 2. (a) Sorption kinetic plots and (b) multi-stage IPD plot for CR sorption on SGE80-deta. Inset: The LFD plot for CR sorption.

CONCLUSION

In this study, the kinetics of CR sorption onto amino-functionalized macroporous SGE80-deta was investigated. The sorption is found to be rapid, with a sorption half-time of 2 min, and a maximum uptake capacity higher than 80% after 30 min. The experiments were performed at room temperature and at unadjusted pH, to avoid additional heating and secondary pollution. The analysis of kinetic data obtained from applied models suggests a complex controlling mechanism of CR sorption by SGE80-deta, which includes bonding CR molecules with functional groups on the SGE80-deta particle surface, as well as external and internal pore diffusion.

Acknowledgment

This research has been financially supported by the Ministry of Science, Technological Development and Innovation of Republic of Serbia (Contract No: 451-03-66/2024-03/200026).

REFERENCES

[1] N. S. L. Dissanayake, M. A. Pathirana, N. D. Wanasekara, B. Mahltig, G. K. Nandasiri, Nanomaterials, 13 (2023) 1350.
[2] K. Z. Elwakeel, A. M. Elgarahy, G. A. Elshoubaky, S. H. Mohammad, J. Environ. Health Sci. Eng., 18 (2020) 35.
[3] B. M. Marković, D. Lj. Janković, A. A. Vukadinović, D. V. Ranđelović, D. D. Maksin, V. V. Spasojević, A. B. Nastasović, RSC Adv., 7 (2017) 21412.
[4] A. Nastasović, B. Marković, Lj. Suručić, A. Onjia, Metals, 12 (2022) 814.
[5] Lj. Suručić, G. Janjić, B. Marković, T. Tadić, Z. Vuković, A. Nastasović, A. Onjia, Materials, 16 (2023) 2233.
[6] Z. P. Sandić, A. B. Nastasović, N. P. Jović-Jovičić, A. D. Milutinović-Nikolić, D. M. Jovanović, J. Appl. Polym. Sci., 121 (2011) 234.
[7] D. D. Maksin, A. B. Nastasović, A. D. Milutinović-Nikolić, Lj. T. Suručić, Z. P. Sandić, R. V. Hercigonja, A. E. Onjia, J. Hazard. Mater., 209 (2012) 9.
[8] S. Azizian J. Colloid Interface Sci., 276 (2004) 47.

SOME PHYSICOCHEMICAL ASPECTS OF SCALLING APPROACHE TO (TECHNOLOGICAL) UNIT OPERATIONS

M.M. Plavsic [1, 2] and M.B. Plavsic [3, 4]

[1] *The Academy of Applied Studies -Polytechnic, Belgrade-Serbia*
Boulevard of Z. Djindjic 152a, (milankaplav@gmail.com)
[2] *University of Niš- Faculty of Technology- Leskovac, Serbia*
[3] *University of Belgrade -TMF, (plavsic@tmf.bg.ac.rs)*
[4] *Engineering Science Academy of Serbia, Belgrade, Serbia*

DOI: https://doi.org/10.46793/Phys.Chem24II.437P

ABSTRACT

In the paper are compared scaling data at two fundamental levels of structure: cell and sub-cell, both important, for modern engineering and physical chemistry, although the approaches differ. But, they can be used in complementary way, for research and development of nano-technologies development. New methods of subcellular testing confirm the predictions of our Network grow scaling theory of cells and cell systems, so it can be used also for bio-thermodynamics scaling in those new approaches.

INTRODUCTION

It is generally accepted opinion, that Transport Phenomena form the core of Unit Operations and that the Operations are one of the main columns which hold the whole structure of modern chemical technology [1-10]. Mainly for these reasons, have been unit operations (UO) translated as “Tehnološke operacije” (“technological operations”) in Serbian language. That opinion on theory of transport phenomena started with publishing of the book “Transport Phenomena” of Bird and colleagues in 1960. But, the approach had been considered in the long period before, because of obvious needs for creating some theoretical background, in parallel with extraction of common denominators from the huge pool of practical manufacturing experience to define unit operations. But then, so classified practical rules about groups of unified operations, should be again integrated but at much higher level of understanding. At the first site those staring steps seem today simple: the main relations are made in the form: the intensity of operation(I) = driving force (ΔU) / residence of the system (R), what is analogy to Ohm low, but the paradigm was Fourier low of heat transfer, see Eq.1. Later the newton low of force was reformulated in similar way and the Fick first low for mass transfer, as well. Of course, the approach to those phenomena is possible from different aspects In biology the mass transfer into organism (food, oxygen, products) is unavoidable condition to survive. The metabolic rate is measured in most cases just by mass transfer with later recalculations But it has universality scaling character as described in [1], so we face immediately the important relations of UO with scaling phenomena. The interest for extension of UO principles to work with very small systems, as in the areas of the materials science and engineering so in bioengineering and the areas shared in-between, as tissue engineering and bio-medical research in general [4,7,9,10].

The possibilities to use UO tools for bio-medical purposes was recognized very early in 1961, in papers on mass transfer into living cell at the basic structure of all living been. But, at that time, the transfer research, as theoretical integrations so experimental, was focused on the macro scale approaches. The situation can be described, in short, as the numerous efforts to design equipment and experimental conditions at macro level, to mimic transfer into cells at micro level, in parallel

with development of new research techniques in the field. Last years the situation is changing dramatically, with new sophisticated technics, what opens chances for much deeper insight to living systems transfer phenomena, and obtain parameters and relation of much precision, but also to check those been long in use (as only available, but very important, at least to take a peek) and even the existing theories on the subject.

METHODS

Experimental data

Staring from 3 principle structural levels of bio-systems in bio-thermodynamics, and scaling principles developed in [1], we have focused attention here to cell and sub-cell level, scaling data.

For the cell level (i.e. micro-scale), we have analyzed numerous results published and selected here to elaboration the set of 20 experiments on volume rate measurements of hemoglobin moving through Millipore membranes produced with pore size of 0.45±0.02 μm, and of thickness in the range of 150 ±10 to 300±40 μm. Other parts of equipment are of macro level: made simply in the form of two Plexiglas chambers of 50 cm^3 in average, with Millipore filter in-between. The upper chamber is at start with HG solution of the water concentrations presented in Fig.1a what is left to freely move with measurements of time and concentration spectroscopic, in standard way (interesting details will be elaborated later) [1.6].

For the nano-scale are analyzed results obtained by several methods of cell internal reflection fluorescence microscopy developed last years [7, 10, 11]. The total internal reflection florescence microscopy applied with an extra transporting load provides measurement of volume flow into the cell and interactions at that. The single-protein interaction microscopy gives insight into trajectory of the entering protein or test nano-particle, but only driven by thermal fluctuations (Einstein diffusion). In other words, at that scale, several specific limits arises well known optical methods, photo-bleaching with saturation of blinking limit the number of photons collected from the single fluorophore and in that way hamper the temporal resolution as well as localization precision of the testing particle. Numerous efforts have been made last years to overcome such situations. Mainly the dielectric nanoparticles are used. But also some bio-molecules can be used by applying elastic scattering. Even better results gives interferometric scattering microscopy, but for us are of most importance in this analysis, the collected results on volume (in) homogeneity of cytoplasm, due to network produced by cell skeleton, with associated free proteins, and water complement. So we have been looking for results on trajectories and the dynamic of emitter movements along them, all inside a cell.

Theoretical background

The main set of differential equation of transport, formulated at the start, as described in Sect.1 can be presented by [5, 8]

$$\tau = -\mu \frac{dw}{dz}\left[\frac{N}{m^2}\right] \tag{1a}$$

$$q = -\lambda \frac{dT}{dz}\left[\frac{W}{m^2}\right] \tag{1b}$$

$$N_{i,F} = -D_i \frac{dC_i}{dz}\left[\frac{mol}{\sec m^2}\right] \tag{1c}$$

Based on that that is formulated the following system of differential equations to describe transport of oxygen by HG

$$\frac{\partial (nc_{bnd}(x,t)Y_{ef}}{\partial t} = D_{bnd}\frac{\partial^2 (nc_{bnd}(x,t)Y_{ef}}{\partial x^2} \tag{2a}$$

$$\frac{\partial c_{fre}(x,t)}{\partial t} = D_{fre}\frac{\partial^2\left[c_{fre}(x,t)\right]}{\partial x^2} \qquad (2b)$$

Here indexe: *fre* and *bnd* ,indicate free oxygen and the bounded to HG with corresponding efficiency *Y* of number of active sites *n*, down the trajectory x in time t. The system has been solved for the conditions described in Sec.2.1 and for chamber calibration constant β for the transfer coefficient of HG in the form : $D = \left[-\ln(\Delta C_t / \Delta C_0)/\beta t\right]$ [6].

RESULTS AND DISCUSSION

The results of our comparative analysis, that we consider as the most useful for scaling analysis are presented in Fig.1.a,b. They follow from our elaboration of data from two different scaling levels so

a) b)

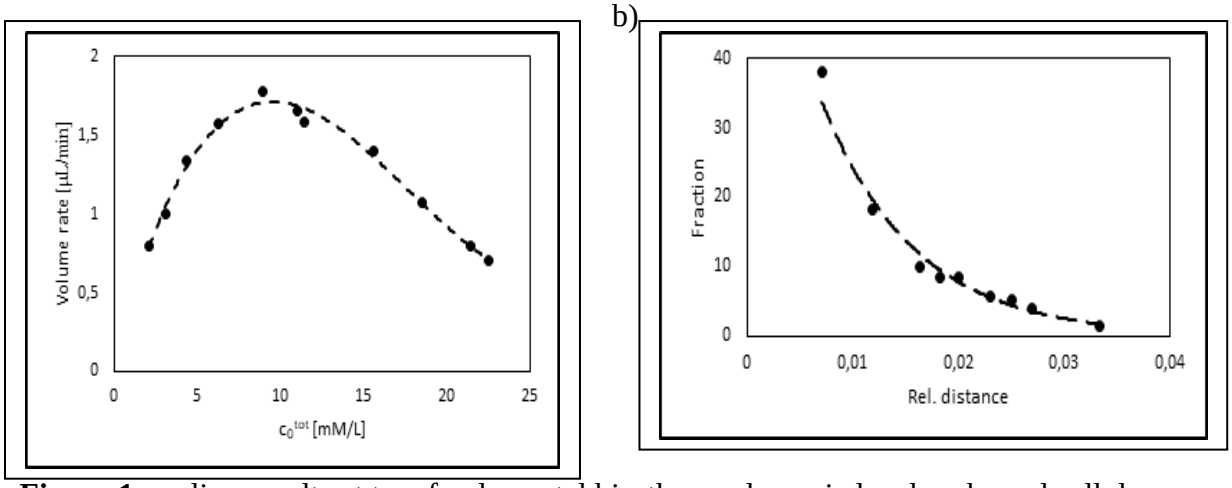


Figure 1. scaling results at two fundamental bio-thermodynamic levels sub- and cellular.

considering possible differences in transfer features , should be first compared transfer coefficient *D* as the parameter most used, especially in bio-medical research with HG. Keeping in mind that at sub-cellular level (SCL), is tested the single particle transport, the data from Fig.1a should be extrapolated to very high dilution (as it is done for intrinsic viscosity calculation of polymer solutions) still the differences of *D* coefficient are very high: 6.6 -7.5x 10^{-11} (m^2 /sec) for HG compared to 1-10x 10^{-15} (m^2 /sec) for SCL. It is important, because it has been used in some papers parity long time for entrance into cell calculations (due to lack of other data). Also the average speed of single particle movements is about thousand times higher than HG under simulated conditions. Indicating much higher dynamics inside cell, compared to flow in blood capillaries, for which such investigations seem more appropriate now. But the most interesting are trajectory size results of the particle on SCL level. In short: the particle moves long time in one restricted area inside cell, with the same size and then jumps over (something) into another such area. It is n perfect agreement with our theory, on gel network structure of cytoplasm: The cell skeleton attracts movable macromolecules to slip down the fibrils are solubilized with the complement of water having low amount of free volume. But the surrounding water areas have much more free volume providing space for the gel network extension, lake apertures in the fiber networks. In those apertures is the particle moving more freely. Translated from UO more to physicochemical terms it can be described by transformation Eq.1 in the form:

$$\tau = \frac{(mw)}{A\cdot t} = -\frac{\mu}{\rho}\frac{(\rho\cdot w)}{dz} = -\nu_K\frac{d(\rho\cdot w)}{dz} \qquad (3a)$$

$$q = \frac{Q}{A \cdot t} = -\frac{\lambda}{\rho \cdot c_P} \frac{d(\rho \cdot c_P \cdot T)}{dz} = -a_D \frac{d(\rho \cdot c_P \cdot T)}{dz} \quad (3b)$$

$$j_D = \frac{N_{Mol.i}}{A \cdot t} = \frac{\frac{m_{gr}}{m_{Mol}}}{A \cdot t} = -D_i \frac{dC_i}{dz} \quad (3c)$$

From Eq.3 we see that all three constitutive equations (containing constitutive parameters of 3 basic transport phenomena) can be transformd in the form having the constitutive parameters with the same dimensions e.g. (m^2 /sec). To understand that help the basic models of physical chemistry on mowing particles (e.g. the gas molecules in the simples case) inside control volume of the system:

$$\mathbf{J}_{z,net} = -\frac{1}{6} l_{avr} \cdot w_{sav} \frac{d\Gamma}{dz} \quad (4)$$

here average velocity w_{av} is the average velocity of and l_{fr} the average distances in function of potential Γ [1.4,8, 12]. The Eq.4 can be understood as supstitution for all 3 forms of transport at macro level equations in form of Eq.1 or Eq.2, (of course with modifications for the appropriate nano-level systems), Such scaling make kind of bridge between UO and physicochemical approaches, much more necessary in modern nano-technologies.

CONCLUSION

The results indicates possibilities and needs for much closer approaches to scaling cell systems at different levels of well-established methods and experience of nowadays UO and physical chemistry.

REFERENCES

[1] M.B. Plavsic, M.M. Plavsic, (paper at this, the same Conf.) this Proceeding.
[2] M.B. Plavsic, M.M. Plavsic at al., int. J. Modern Phys., B 24 (2010) 813.
[3] M.B. Plavsic, M.M. Plavsic at al., Acta Physica Pol. 120 (2011) 266.
[4] M.B. Plavsic, Polymeric Materials Science and Eng. (in Serbian) N.Knj., Belgrade 1996.
[5] R.B. Bird, W.E. Stewart, E.N. Lightfoot, Transport Phenomena, Wiley, New York, 1960.
[6] J.B. Wittenberg, Physiol. Rev. 50 (1970) 539.
[7] A. Kusumi at al, Nature Chem. Biol. Rev. 10 (2014) 524.
[8] A.S. Foust, Principles of Unit Operations, Wiley, N.Y. 1960.
[9] ASTM/ISO 52900 Standard: Additive Manufacturing-General Principles, 2015.
[10] L. Bujak at al., Small Methods (2021) 370.
[11] https://bionumbers.hms.harvard.edu and *references therein (Ref. in).*
[12] P. Atkins, J. de Paula, Physical chemistry 8th Ed Oxford Un Press, NY, 2006.

K *– Environmental Protection,*
Forensic Sciences,
Geophysical Chemistry,
Radiochemistry,
Nuclear Chemistry

THERMODYNAMIC ANALYSIS OF DEUTERIUM-BASED NUCLEAR FUSION REACTIONS

S. Tosti

ENEA, Nuclear Department, Via E. Fermi 45, 00044 Frascati, Italy. (silvano.tosti@enea.it)

DOI: https://doi.org/10.46793/Phys.Chem24II.443T

ABSTRACT

In the nuclear physics approach, the feasibility of D-based nuclear fusion reactions is studied through the evaluation of their reaction rate (reactivity) and their degree of exothermicity expressed by the Q-value, a parameter linked to the amount of the energy released by the process. Under the thermodynamic point of view, these analyses miss the evaluation of the entropy that, indeed, can affect significantly the feasibility of nuclear fusion reaction carried out at very high temperatures. In fusion reactions the temperature acts as a very powerful amplifier of the entropic term (- T ΔS) that, at the temperature of tokamaks (≈ 10^8 K), may reduce significantly the thermodynamic spontaneity of these processes.

The effect of the temperature on both kinetics (nuclear reactivity) and thermodynamics (ΔG) of the D-based reactions of interest for the magnetically confined nuclear fusion has been investigated. The entropy of the reacting D-based plasma is evaluated via the Sakur-Tetrode equation and the results of this study confirm that the DT reaction is the most promising fusion reaction to be realized in tokamak devices. At the temperature of 1.5 ×10^8 K (≈ 13 keV), the DT reaction exhibits a large thermodynamic spontaneity (ΔG = - 16.0 MeV) and its reactivity is of the order of 10^{-22} m^3/s, a value capable of guaranteeing the tritium burning rate needed to operate the nuclear plants under tritium self-sufficiency conditions and with a net energy production.

INTRODUCTION

The exploitation of nuclear fusion as future energy supply is very ambitious and will allow to meet the sustainability goals capable to face the challenges raised by the climate change trend [1]. Furthermore, nuclear fusion is considered inexhaustible and inherently safe energy source [2-4].

Despite of the large research investments carried out since 60's years, the realization of fusion power plants has to face important challenges related to the development of specific technologies and materials and to the control of the instability of the magnetized plasma [5, 6]

The criteria adopted by the nuclear physics to evaluate the feasibility of a nuclear process are based on the assessment of its reaction rate (a parameter linked to the reaction probability) and exothermicity (Q-value). When compared to a classical thermodynamic analysis, this nuclear physics approach misses the evaluation of the entropy, a parameter that could play a key role in establishing the feasibility of the nuclear fusion reactions realized at very high temperatures (10^8 K) in the tokamak machines [7-9].

In this study, the spontaneity of the D-based nuclear fusion reactions is studied through the assessment of the Gibbs free energy change. The effect of the temperature on both the ΔG and the reaction rate is discussed in order to evaluate their application for the exploitation of the fusion energy.

METHODS

The following four D-based fusion reactions have been taken into consideration:

$$D + T = {}^{4}\mathrm{He} + 17.586\ \mathrm{MeV} \quad (1)$$

$$D + D = T + 3.267\ \text{MeV} \quad (2)$$
$$D + D = {}^{3}\text{He} + 4.032\ \text{MeV} \quad (3)$$
$$D + {}^{3}\text{He} = {}^{4}\text{He} + 18.351\ \text{MeV} \quad (4)$$

where the energy released by the reactions corresponds to the Q-value and D and T represent deuterium and tritium, respectively.

The initial state of the processes consists of two monoatomic atoms at very high temperature T and low pressure (≈ 5 Pa), according to both experiments and designs of magnetic fusion devices [10]. The final state of the reactions (1-4) has been chosen under the assumption that their products (atoms of helium and tritium, protons and neutrons) have interacted with the system's walls and changed their energy into heat. Such a condition could be verified in a tokamak surrounded by shielding walls where the energy released by the nuclear reactions is extracted through a cooling system at 700 K, a temperature representative of shielding and blanket systems of the magnetically confined fusion devices [11].

Then the change of the Gibbs free energy has been evaluated through the expression:

$$\Delta G = -Q_{value} - [(700\ S_{700\,K} - T\,S_T)] \quad (5)$$

where T is the temperature and S the entropy calculated via the Sakur-Tetrode equation [12]:

$$S = n \cdot R \cdot \left[ln\left(\frac{M^{\frac{3}{2}} \cdot T^{\frac{5}{2}}}{P} \right) - 1.16 \right] \quad (6)$$

where n is the number of moles, P is the pressure (atm), M the molecular weight and R the gas constant.

The feasibility analysis has been coupled with the assessment of the reaction rate that expresses the number of reactions per unit time and per unit volume. Such a parameter is proportional to the cross section that has the dimension of an area and is a measure of the probability that a nuclear reaction will occur. The reactivities of the reactions (1-4) have been calculated from literature [13, 14].

RESULTS AND DISCUSSION

In principle, the change in entropy of a fusion reaction (ΔS_{FUS}) is estimated to be negative since in these processes more light atoms merge to form a heavier nucleus and thus we can expect an increase in the order of the system. In fission, heavy nuclei split into smaller fragments and, therefore, we assume that the change in entropy (ΔS_{FIS}) is positive. Assumed that, in practice, only strongly exothermic nuclear reactions are considered (Q-value ≈ MeV/part.), it results that fission reactions are always spontaneous while the fusion reactions could become non-spontaneous when the entropic term (T ΔS) balances the Q-value. In other words, for the nuclear fusion reactions it is possible to define a critical temperature (T*) over that the process is thermodynamically unfeasible:

$$T^* = \text{Q-value} / \Delta S_{FUS} \quad (7)$$

This behavior is schematically represented in the Fig. 1 [9].

Then the study has been dedicated to analyze the effect of the temperature of the reacting D-mixture on the reactivity and the change in Gibbs free energy of the reactions (1-4). As a main result, the reaction (1) is the only one exhibiting both a good level of thermodynamic spontaneity (i.e., large negative values of ΔG) and reactivity values enough to realize a feasible burn fraction (i.e. the amount of tritium burned in the plasma before confinement is lost). In particular, the reaction (1) at the tokamak temperature (13 keV ≈ 1.5 ×10^8 K) exhibits a ΔG ≈ - 16 MeV/part., see Fig. 2 [9].

The other results show that at the tokamaks' temperature the two branches of the DD reaction (formulas 2 and 3) exhibit a modest spontaneity (ΔG around - 2 MeV) coupled to very low

reactivity values (10^{-24} m^3/s). The temperature rising aimed to increase the reactivity is however ineffective to improve the reaction feasibility since it would augment the entropic term as well, thus shifting the ΔG towards positive values. The D^3He reaction (4) is soundly spontaneous at the tokamaks' temperature (ΔG values of -17.2 MeV) while its kinetics is close to that of the DD reactions, that is at least two orders of magnitude lower than that of the DT reaction.

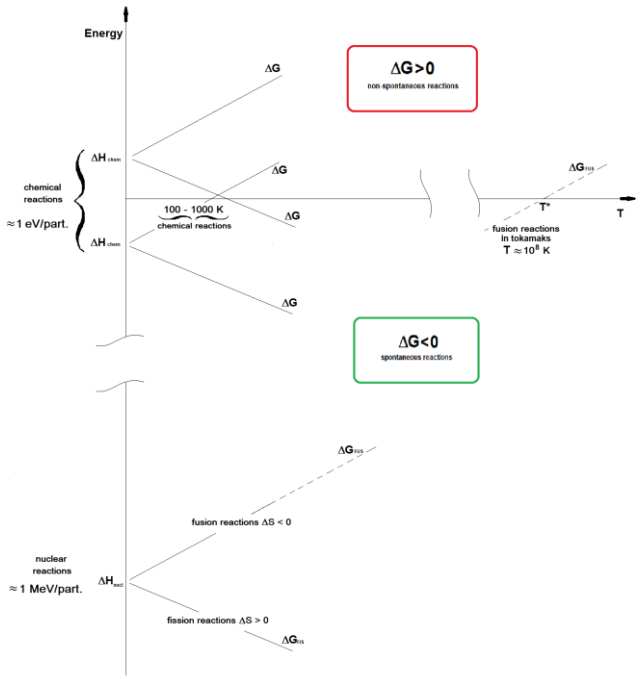


Figure 1. Change in Gibbs free energy vs. the temperature: comparison of the behavior of chemical and nuclear reactions. ΔH_{chem} and ΔH_{nucl} indicate the change in enthalpy of chemical and nuclear reactions, respectively. ΔG_{FIS} and ΔG_{FUS} indicate the change in Gibbs free energy of fission and fusion reactions, respectively [9].

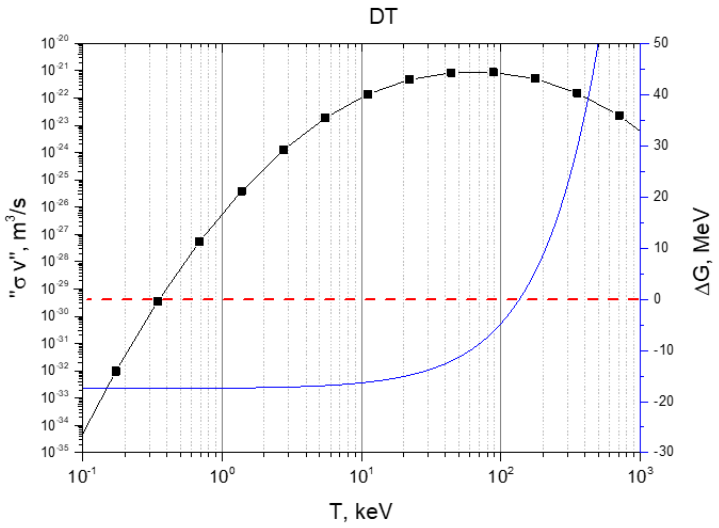


Figure 2. Reactivity and change of Gibbs free energy vs. temperature for the Deuterium-Tritium reaction. [9]

CONCLUSION

The thermodynamic analysis of the nuclear reactions addresses the role of the entropy, an aspect so far neglected by the nuclear physics for evaluating the process spontaneity. Differently from the fission reactions that are always spontaneous, in the fusion reactions the temperature acts as a powerful amplifier of the entropic term ($T\ \Delta S_{FUS}$) that, at very high temperatures, could overcome the energy released by the reaction (Q-value). Accordingly, the nuclear fusion reactions are non-spontaneous when the temperature overcomes a critical value T^* = Q-value / ΔS_{FUS}. Although the Q-value is of the order of MeV/part. and the ΔS_{FUS} is numerically much smaller ($\approx 10^{-2}$ - 10^{-3} eV/part.), the operation of the fusion reactions at the tokamak temperatures ($\approx 1.5 \times 10^{8}$ K) could involve that a significant part of the energy released (Q-value) is spent to make the system more ordered ($T\ \Delta S$) then significantly reducing the amount of the work available (ΔG = Q-value – $T\ \Delta S_{FUS}$). At least, when $T\ \Delta S_{FUS}$ overcomes the term Q-value the process is non-spontaneous.

REFERENCES

[1] Sustainable Development Goals (SDGs), https://unric.org/en/united-nations-sustainable-development-goals/.
[2] L. Artsimovich: Nature. 239 (1972) 18–22.
[3] R Toschi, Fusion Eng Des., 36(1) (1997) 1–8.
[4] J.L. Ongena, EPJ Web of Conferences.,189 (2018) 00015.
[5]W.E. Parkins, Energy. Science., 311 (2006) 1380.
[6]J. Ongena, R. Koch, R. Wolf, et al. Nat Phys. 2012 (2016) 398–410.
[7] S. Tosti, Spontaneity of nuclear fusion: a qualitative analysis via classical thermodynamics, Open Res. Eur. 2021, https://open-research-europe.ec.europa.eu/articles/1-67
[8] S. Tosti, L. Marrelli, Hydrogen 3 (2022) 53–61.
[9] S. Tosti, Energies, 16 (2023) 3996.
[10] T. Giegerich, C. Day, C. Gliss, X. Luo, H. Strobel, A. Wilde, S. Jimenez, Fusion Engineering and Design 146 (2019) 2180–2183.
[11] F. Cismondi, et al., Fusion Engineering and Design 136 (2018) 782-792.
[12] K.G.Denbigh, The Principles of Chemical Equilibrium: With Applications in Chemistry and Chemical Engineering. United Kingdom: Cambridge University Press,1981.
[13] L.M. Hively, Nucl. Fusion 17 (1977) 873.
[14] L.M. Hively, Nuclear Technology/Fusion, 3(2) (1983) 199-200.

CHARACTERIZATION OF BIOCHARS DERIVED FROM *MYRIOPHYLLUM SPICATUM* USING FOURIER TRANSFORM INFRARED SPECTROSCOPY

J. Milojković [1], C. Wurzer [2], Z. Lopičić [1], T. Šoštarić [1], A. Antanasković [1], D. Smiljanić [1] and O. Masek [2]

[1] *Institute for Technology of Nuclear and Other Mineral Raw Materials, Franchet Desperey Blvd 86, 11000 Belgrade, Serbia. (j.milojkovic@itnms.ac.rs)*
[2] *UK Biochar Research Centre, School of GeoSciences, University of Edinburgh, Alexander Crum Brown Road, Edinburgh EH9 3FF, United Kingdom*

DOI: https://doi.org/10.46793/Phys.Chem24II.447M

ABSTRACT
Aaquatic plants are one type of biomass that has been studied lately due to its potential for commercial use, environmental significance, and bioremediation. Invasive aquatic weeds, when introduced and allowed to spread in aquatic ecosystems, can cause significant environmental and economic harm. Producing biochar from aquatic weeds offers a sustainable solution to managing invasive species while providing significant environmental, economic, and practical benefits. Herein, Fourier transform infrared spectroscopy (FTIR) was used as an analytical tool to analyze the characteristics of three biochars made from the aquatic weed *Myriophyllum spicatum*.

INTRODUCTION
The accelerating process of industrialization and urbanization result in increasing environmental pressure, making the balance between environmental protection and economic growth an intriguing area of research. A primary objective is the development of cost-efficient methods for treating pollutants while fulfilling emission regulations. Biomass resources are widely available and inexpensive, making them popular for producing environmental treatment materials [1].

Aquatic plants, particularly when they become invasive, can have significant economic and ecological impacts. Their ability to rapidly colonize and dominate water bodies results in significant biodiversity loss, alteration of habitats, altered ecosystem functioning, habitat degradation, blockage of water flow etc. These environmental changes, in turn, have an impact on various economic sectors, imposing heavy financial burdens on management and control efforts [2].

Aquatic and semi-aquatic invasive plants cost the world economy more than US$ 32 billion between 1975. and 2020. of which submerged plants were responsible for $8.4 billion (25.5 %) [3]. The study of biomass from aquatic plants represents a promising area of research and development with significant potential to contribute to renewable energy production, environmental sustainability, and economic growth [2]. Every year, huge volumes of biomass are produced by aquatic plants which need to be managed in an environmentally sound and economic way.

The carbon-rich, sustainable material known as biochar, which is produced by pyrolysis, can be utilized as a sorbent for both organic and inorganic pollutants, and as a soil amendment [4]. Transformation of biomass from aquatic plants into biochar presents a novel, constructive waste treatment option while providing a solution for environmental contamination [5].

Myriophyllum spicatum L. is a globally distributed submerged aquatic plant. This invasive plant is classified as a Category 1 Weed because of its widespread damaging impacts on the ecosystem worldwide [6]. According to [7], it is classified by its: rapid growth, dense bed formation, water

flow obstruction, potable and industrial water supply systems clogging, blockage of sunlight for native aquatic plants, and mosquito habitat creation.

The primary aim of this study is to characterize three biochars derived from Myriophyllum spicatum (MS), all produced at the same pyrolysis temperature but with different additives, using FTIR.

METHODS

Freshly obtained MS samples were collected from Sava Lake in Belgrade, Serbia. The public firm "Ada Ciganlija" collected the fresh plant used for the study using a mechanized underwater harvester. MS was prepared according to [8]. Producing MS ash-enriched MS pellets (containing 10% ash (w/w)), based on the procedure applied in [9]. Ochre originated from the Fife, Scotland, Coal Authority Minto mine water treatment scheme [10]. Preparing MS ochre-enriched MS (10% ochre (w/w)) by the method being used in [10]. The raw MS was treated similarly with water 2ml before pressing in pellets. The dry pellets were then pyrolysed in a horizontal quartz glass reactor inserted in an electrical furnace and pyrolysed at 600°C for 45min under a flow of N_2 (200ml min^{-1}). Heating rate was 25C°min^{-1}.

Thermo Nicolet 6700 FTIR (International Equipment Trading Ltd., USA) was used to conduct Fourier Transform Infrared Spectroscopy (ATR mode) on all samples to identify their surface functional groups. The spectra were recorded by averaging 32 scans from 4000 to 400 cm^{-1}.

RESULTS AND DISCUSSION

Yield from preparation of three MS biochars is presented in Table 1.

Table 1. Yield from preparation of three MS biochars.

Biochar	feed [d.b.]	Biochar [d.b.]	Yield [%]
MS600	31.73	21.33	67
MS600 Ash	36.66	28.79	79
MS600 Ochre	41.17	31.45	76

FTIR spectra of the MS, biochars: MS600, MS600 Ash and MS600 Ochre samples are presented in **Figure 1**. Chemically active groups found in FTIR spectra of raw MS, have been identified as components of proteins, lignin, cellulose and hemicellulose, polysaccharides, and lignin [11]. Following the pyrolysis of the biomass, changes in the functional groups were detected using the FTIR technique. Bands were observed between 2000 and 4000 cm^{-1} (3298.45 and 2921.52 cm^{-1}), related to C-H and O–H stretching of cellulose [12]. Following pyrolysis, these lignocellulosic bands disappeared, indicating that the material was aromatized. The MS volatile ingredients are removed at greater temperatures during pyrolysis, which produces more porous material with an expanded surface area and increased sorption capacities [13]. The FT-IR spectra of biomass MS showed absorption bands at 1614 cm^{-1} of the carbonyl bond from hemicellulose which was not detected in biochar spectras. During pyrolysis, hemicellulose decomposes into volatile products, losing its characteristic carbonyl absorption band in the FT-IR spectrums of the resultant biochars. The stretching vibration of the benzene ring skeleton (C=C) is responsible for the distinctive absorbance band between 1680 and 1440 cm^{-1} from the aromatics [14]. Absorption band of -C-O and O-CH_3 in lignin was observed at around 1026 cm^{-1} [15]. After pyrolysis that band weakened, making it almost undetectable in FTIR spectras of biochars.

MS has 5% calcium (mainly in the form of carbonate), which originates from the water environment in which this aquatic weed grows [8,11]. The bands around 860 cm^{-1} were assigned to out-of-plane bending mode of carbonates (CO_3^{2-}) [16]. Peaks at 867 cm^{-1} are stronger in the

biochars compared to the MS, it suggests that the pyrolysis process has concentrated the carbonate content which is expected due to negligible carbonate degradation at the used pyrolysis temperature. Pyrolysis removes volatile organic components and concentrates mineral residues, including carbonates, in the resulting biochar.

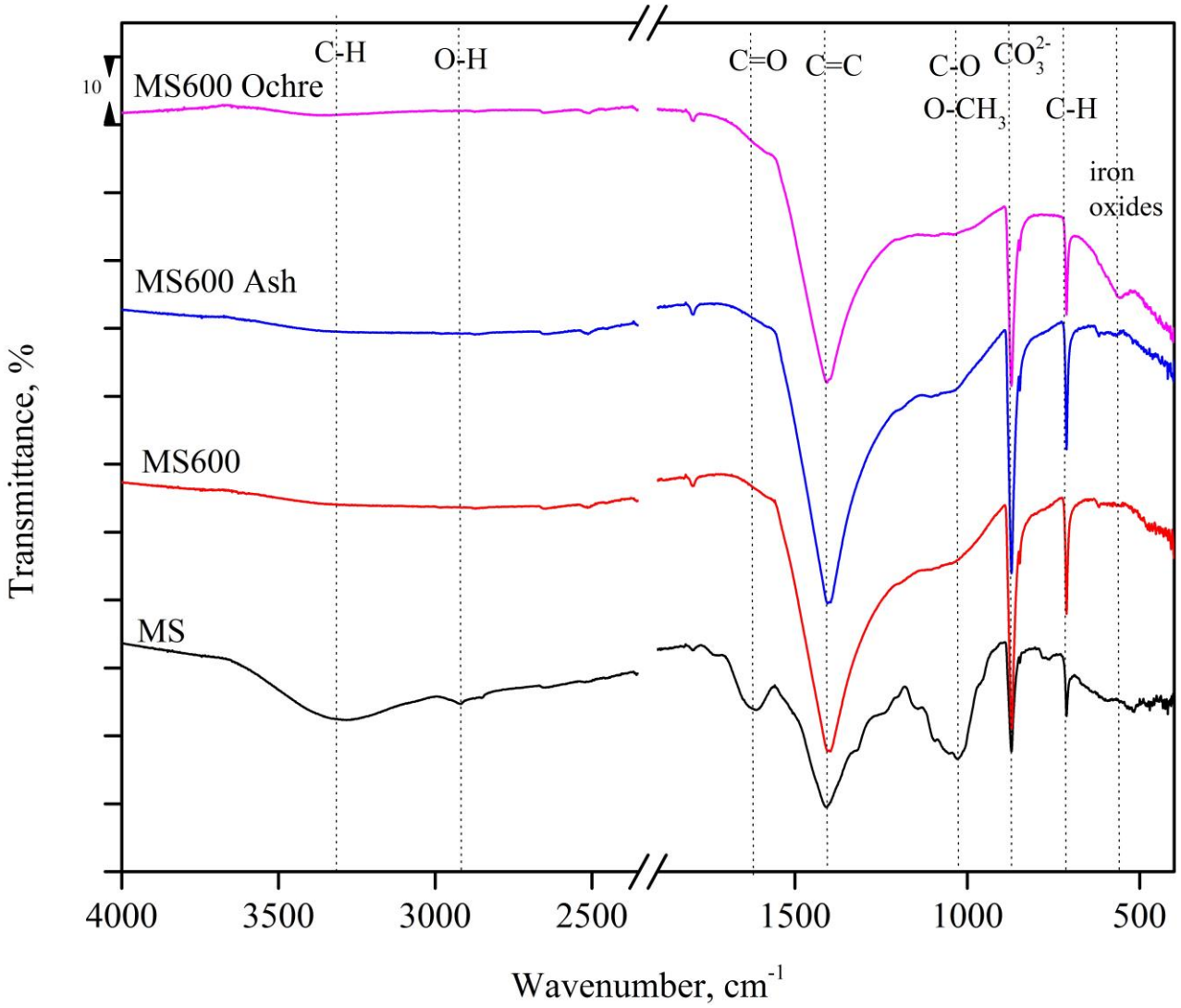


Figure 1. FTIR spectra of dry biomass (MS), biochars: (MS600), (MS600 Ash) and (MS600 Ochre).

The band at 709 cm^{-1} in the FTIR spectra of MS and its biochar represents the out-of-plane bending vibrations of aromatic C-H bonds (700–900 cm^{-1}) [17]. The stronger intensity of these bands in biochars indicates a higher concentration of aromatic compounds, reflecting the effects of pyrolysis on the chemical composition of the aquatic biomass.

Biochar with 10% Ochre (MS600 Ochre) showed a peak at 559.4 cm^{-1} that is not visible in the other FTIR spectras. It is a peak that occurs due to ochre. Band is assigned to iron oxides [18].

CONCLUSION

Production of biochar from biomass of invasive aquatic plants represents a strategic concept for the circular economy, closed-loop technology, and sustainability. Applying a circular economy concept creates many advantages: valorization of waste, zero waste approach, sustainable product lifecycle

biochar, as well as economic benefits. The utilization cycle of invasive plant products can be prolonged by using the biochar for various applications, including soil amendment, water filtration, and carbon sequestration [19].

M. spicatum is a renewable resource that can be sustainably harvested to provide a steady supply of feedstock for biochar production. Also, control of the spreading of this invasive species helps restore and maintain the balance of aquatic ecosystems, which supports biodiversity and the ecosystem.

Acknowledgment

This work was supported by the Ministry of Science, Technological Development and Innovation of the Republic of Serbia (grant no through 451-03-66/2024-03/200023). Jelena Milojković is grateful to the public company "Ada Ciganlija" (Belgrade, Serbia) for providing samples of fresh *M. spicatum.*

REFERENCES

[1] W. Zhang, P. Zhang, H. Wang, J. Li, S.Y. Dai, Trends Biotechnol. 40 (2022) 1519.
[2] M. Kaur, M. Kumar, S. Sachdeva S.K. Puri, Bioresour. Technol. 251 (2018) 390.
[3] R L. Macêdo, P.J. Haubrock, G. Klippel, R.D. Fernandez, B. Leroy, E. Angulo, L. Carneiro, C.L. Musseau, O. Rocha, R.N. Cuthbert, Sci. Total Environ., 908 (2024) 168217.
[4] K.Y. Khan, B. Al, Y. Song, B. Iqbal, X. Cui, W. Ahmed, G. Li, Y. Guo, Pol. J. Environ. Stud. 32 (2023) 1.
[5] X. Cui, J. Wang, X. Wang, M.B. Khan, M. Lu, K.Y. Khan, Y. Song, Z. He, X. Yang, B. Yan, G. Chen, Chemosphere 287 (2022) 132259.
[6] G.D. Martin, J.A. Coetzee, Aquat. Bot. 114 (2014) 1.
[7] S.G. Aiken, R. Newroth, I. Wiles, H. Control, Can. J. Plant Sci. 59 (1979) 201.
[8] J.V. Milojković, Z.R. Lopičić, I.P. Anastopoulos, J.T. Petrović, S.Z. Milićević, M.S. Petrović, M.D. Stojanović, J. Environ. Manage. 232 (2019) 97.
[9] W. Buss, S. Jansson, C. Wurzer, O. Mašek, Acs Sustain. Chem. Eng. 7(2019) 4204.
[10] C. Wurzer, O. Mašek, Bioresour. Technol. 321 (2021) 124473.
[11] J.V. Milojković, M.L. Mihajlović, M.D. Stojanović, Z.R. Lopičić, M.S. Petrović, T.D. Šoštarić, M.Đ. Ristić, J. Chem. Technol. Biotechnol., 89 (2014), 662.
[12] E. Girija, S. Latha, S. Kalkura, C. Subramanian, P. Ramasamy, Mater. Chem. Phys. 52 (1998) 253.
[13] S.S. Suryawanshi, P.P. Kamble, R. Gurav, Biomass Conv. Bioref. 13 (2023) 5353.
[14] L. Luo, C. Xu, Z. Chen, S.Z. Zhang, Bioresour. Technol. 192 (2015) 83.
[15] D. Xu, Z. Li, P. Wang, W. Bai, H. Wang, Sustain. Chem. Pharm. 17 (2020) 100275.
[16] K. Lammers, G. Arbuckle-Keil, J. Dighton, Soil Biol. Biochem. 41 (2009) 340.
[17] P. Fu, S. Hu, L. Sun, J. Xiang, T. Yang, A. Zhang, J. Zhang, Bioresour. Technol. 100 (2009) 4877.
[18] C. Genestar, C. Pons, Anal Bioanal. Chem. 382 (2005) 269.
[19] P. Singh, M. Dhanorkar, S. Sharma, Resour. Conserv. Recycl. 202 (2024) 107385.

AIR QUALITY ASSESSMENT IN BELGRADE: SPATIAL AND TEMPORAL VARIATIONS

J. Obradović [1], M. Obradović [2] and A. Onjia [3]

[1]*College of Applied Studies Aviation Academy,*
Bulevar vojvode Bojovića 2, 11000 Belgrade, Serbia. (obradovic.j@vakademija.edu.rs)
[2]*University of Belgrade, Vinča Institute of Nuclear Sciences,*
Mike Petrovića Alasa 12-14, 11000 Belgrade, Serbia.
[3]*University of Belgrade, Faculty of Technology and Metallurgy*
Karnegijeva 4, 11000 Belgrade, Serbia.

DOI: https://doi.org/10.46793/Phys.Chem24II.451O

ABSTRACT
Urban areas are particularly affected by polluted air. The objective of this research was to evaluate the air quality in Belgrade, focusing on the distinct distribution of pollutants across various locations during different seasons. The air quality was determined by analyzing the spatial and temporal distribution of SO_2, NO_2, PM_{10}, $PM_{2.5}$, CO, benzene, and ground-level O_3 in real-time at eleven locations. Data analysis showed spatial and temporal variations in SO_2, CO, and benzene concentrations, but the limit values were not exceeded. The average monthly concentrations of NO_2, $PM_{2.5}$, and PM_{10} indicate a similar seasonal distribution, with increased concentrations in cold periods of the year and exceeded limit values. In contrast, the concentrations of O_3 surpassed the limit values mostly in the summer months. The analyzed data indicate that the air in Belgrade was excessively polluted during 2021, but there are significant differences in the seasonal and spatial distribution of air pollutants.

INTRODUCTION
Air pollution represents one of the major problems that has a harmful effect on health and the environment [1-2]. Human-made air pollution primarily originates from the combustion of fossil fuels [3-4]. Urban areas are particularly affected by polluted air, considering numerous sources, such as traffic, industry, and heating processes [2]. The major urban air pollutants include sulfur dioxide (SO_2), nitrogen dioxide (NO_2), carbon monoxide (CO), carbon dioxide (CO_2), ozone (O_3), volatile organic compounds, and particulate matter (PM) [2-3]. Reducing the emissions of these pollutants is crucial for improving air quality and mitigating the negative impacts of air pollution. In order to decrease the harmful effects of polluted air, numerous regulations have limited the concentration of pollutants in the air [5]. Air quality monitoring stations are distributed in and around cities and measure the concentrations of various pollutants every hour [7]. The air quality monitoring stations are equipped with reference instruments that provide reliable data on the concentration of pollutants in the air [7-8]. Setting up a larger number of stations and networking the obtained data into a unique system is essential for obtaining detailed information on pollutants, identification of pollution hotspots, and preventive action [9]. The objective of the research was to evaluate the air quality in Belgrade, focusing on the distinct distribution of pollutants across various locations during different seasons within the city.

METHODS
The air quality was determined by analyzing the spatial and temporal distribution of SO_2, NO_2, PM_{10}, $PM_{2.5}$, CO, benzene, and ground-level O_3 in real time at 11 representative locations in

Belgrade during 2021. The concentrations of air pollutants were obtained from the Serbian Environmental Protection Agency (SEPA) (http://www.amskv.sepa.gov.rs/stanicepodaci.php). These data represent an integral network of air pollution data obtained from the SEPA and the City Institute for Public Health, as well as data from automatic monitoring in the local networks of Belgrade. Average annual concentrations, average monthly concentrations, the number of days with exceeding daily upper values, and maximum daily concentrations of pollutants were analyzed at the following eleven locations: Stari grad, Novi Beograd, Mostar, Vračar, Zeleno brdo, Ovča, Zemun, Despota Stefana, Omladinskih brigada, Dragiša Mišović and Vinča. Data are expressed as means ± SD (standard deviation).

RESULTS AND DISCUSSION

Figure 1 shows the temporal distribution of monitored pollutants and is characteristic for the heating and summer seasons. Data analysis showed variations in SO_2, CO, and benzene concentrations at different locations in the city and during different seasons, but the limit values of these pollutants were not exceeded during 2021 (**Figure 1**). The primary source of SO_2, CO, and benzene is incomplete combustion, especially from vehicles, power plants, and biomass burning [2]. All of these pollutants are dangerous to human health and have negative environmental impacts [2-3].

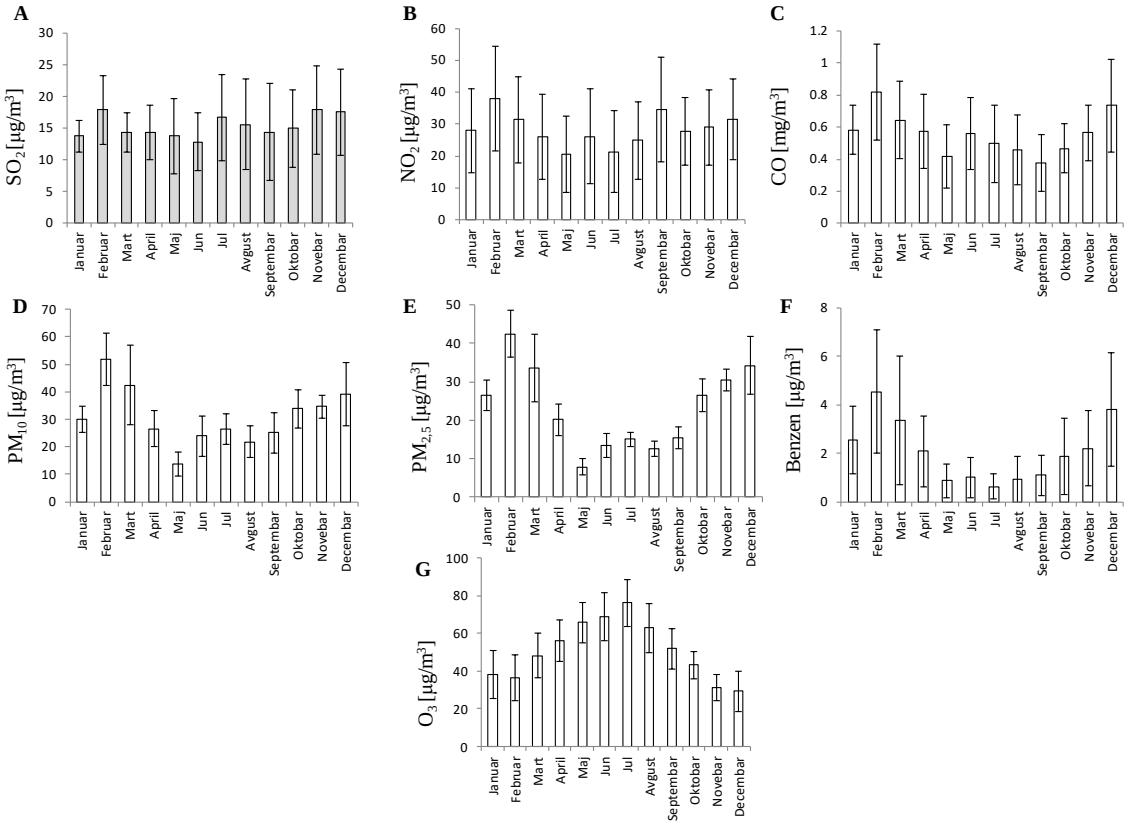


Figure 1. Temporal distribution of pollutants in Belgrade during 2021. Data are presented as the mean ± SD.

Nitrogen oxides come from various combustion sources and contribute to environmental acidification and respiratory issues [10]. Average monthly concentrations of NO_2 show specific temporal distribution in all locations in Belgrade, with increased concentrations in the cold period of the year and decreased concentrations in warm periods, respectively (**Figure 1**). The average annual concentrations of NO_2 exceeded the limit values (>40 μg/m^3) at two of the eleven locations, Mostar and Despota Stefana (**Figure 2**). In addition, the hourly limit value of NO_2 of 150 μg/m^3 was

exceeded (4-183 times) at six locations (Stari grad, Mostar, Vračar, Despota Stefana and Omladinskih brigada). Considering that the concentration of NO_2 was increased in highly trafficked locations such as Mostar and Despota Stefana, it can be assumed that traffic is the main source of this pollutant.

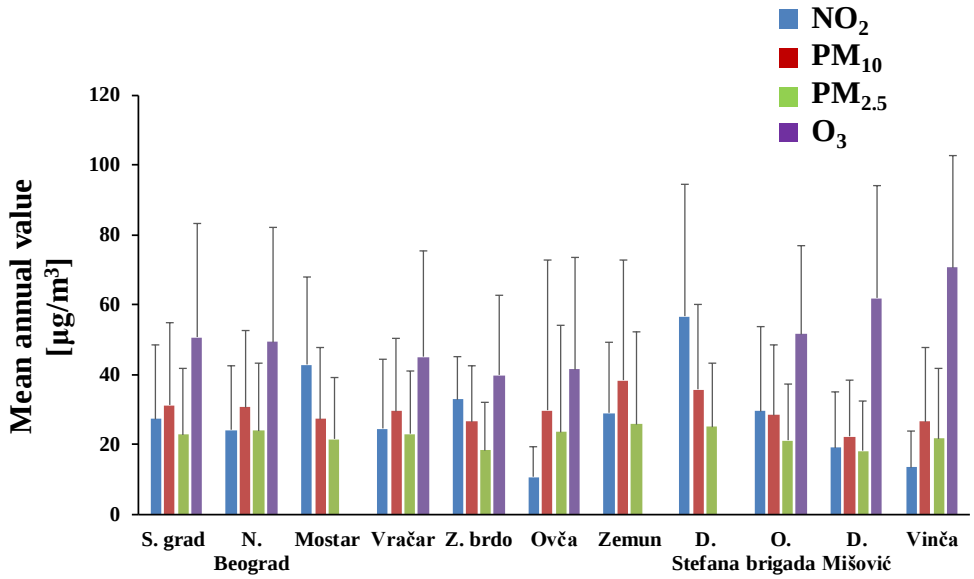


Figure 2. Average annual concentrations of NO_2, PM_{10}, $PM_{2.5}$ and O_3 in Belgrade during 2021. Data are presented as the mean ± SD.

Particles in air are a mixture of solid and liquid aerosols of different sizes, shapes, and chemical compositions. PMs from sources like vehicles, power plants, and construction cause cardiovascular and respiratory diseases due to their size and composition [11-12]. The average monthly concentrations of $PM_{2.5}$ and PM_{10} indicate a similar temporal distribution in all locations in Belgrade, with increased concentrations in the cold periods of the year (**Figure 1**). Although the mean annual value of PM_{10} was not exceeded (**Figure 2**), daily concentrations of PM_{10} exceeded the limit values (>50 μg/m^3) at all measuring sites (16-61 times). Considering $PM_{2.5}$, an exceedance of the average annual value (>25 μg/m^3) was recorded at the two sites, Zemun and Despota Stefana (**Figure 2**). Besides heavy traffic, these results suggest that high concentrations of PMs in heating period probably originate from combustion.

Ground-level O_3, formed by pollutant reactions in sunlight, is suspected to be carcinogenic and harms lung function, affecting both humans and the environment negatively [2-3]. The analyzed data show that O_3 concentrations increased in the summer months in all locations, indicating a specific temporal distribution (**Figure 1**). The 8-h concentrations of O_3 surpassed the limit values 1-37 times (> 120 μg/m^3) at 7 locations (Stari grad, Novi Beograd, Vračar, Ovča, Omladinskih brigada, Dragiša Mišović and Vinča), except at the Zeleno brdo. In addition, the hourly concentrations of O_3 were above the limit values (>180 μg/m^3) at the four measuring sites, such as Stari grad, Omladinskih brigada, Dragiša Mišović, and Vinča. The increased concentration of ground-level O_3 come from increased air pollution, which is especially evident in the summer months, but certain exceptions indicate that the air in some locations is less polluted.

CONCLUSION

The analyzed data indicate that the air in Belgrade was excessively polluted during 2021, but with significant differences in the seasonal and spatial distribution of air pollutants. The average annual concentrations of NO_2 and $PM_{2.5}$ exceeded the limit values at two of the eleven locations, whereas

the average daily concentrations of PM_{10} and eight-hour concentrations of O_3 surpassed the limit values at all locations and ten of the eleven sites in the city. Some specific locations within Belgrade showed fewer instances of exceeding the limit values for air pollutants. Furthermore, seasonal variations in all studied pollutants were recorded. Identification of specific hotspots within the city and seasonal patterns of pollutant distribution represent a good basis for developing a strategy for air pollution reduction.

Acknowledgment
This work was funded by Erasmus+KA220 Ecology and Meteorology project (Contract No#2023-1-RS01-KA220-VET-000155067).

REFERENCES

[1] S. Coelho, J. Ferreira, D. Lopes, D. Carvalho, M. Lopes, Sci Total Environ., 876 (2023) 162767.
[2] I. Manisalidis, E. Stavropoulou, A. Stavropoulos, E. Bezirtzoglou, Front Public Health, 8 (2020) 14.
[3] J. Rentschler N. Leonova, Nat Commun, 14 (2023) 4432.
[4] Ž. Ćirović, M. Ćujić, M. Radenković, J. Obradović, A. Onjia, Thermal Science. 27(3) (2023) 2321-31.
[5] S. Dimitroulopoulou, M.R. Dudzińska, L. Gunnarsen, L. Hägerhed, H. Maula, R. Singh, O. Toyinbo, U. Haverinen-Shaughnessy, Environ Int, 178 (2023) 108127.
[6] Y. Li, K.I. Hoi, K.M. Mok, K.V. Yuen, in: Air Quality Monitoring and Advanced Bayesian Modeling, Li, Y. (Eds.), Elsevier. 2023.
[7] E.M. Wu, S.L. Kuo, Atmosphere, 2013. 4, 349-364.
[8] S. Verghese A.K. Nema, SERRA., 36 (2022) 2963-2978.
[9] W. de Vries, Curr Opin Environ Sci Health., 21 (2021) 100249.
[10] H.H. Zhang, Z. Li, Y. Liu, P. Xinag, X.Y. Cui, H. Ye, B.L. Hu, L.P. Lou, J Zhejiang Univ Sci B, 19 (2018) 317-326.
[11] M. Ćujić, Ž. Ćirović, M. Đolić, Lj. Janković-Mandić, M. Radenković, A. Onjia, Thermal Science, 27(3) (2023) 2265-73.

ENHANCED ADSORPTION OF EMERGING CONTAMINANT DICLOFENAC SODIUM BY ZEOLITE MODIFIED WITH CATONIC SURFACTANT

M. Obradović, A. Daković, D. Smiljanić, M. Marković, and M. Ožegović

Institute for Technology of Nuclear and Other Mineral Raw Materials, Franše d' Eperea 86, 11000 Belgrade, Serbia. (m.obradovic@itnms.ac.rs)

DOI: https://doi.org/10.46793/Phys.Chem24II.455O

ABSTRACT

Octadecyldimethylbenzylammonium (ODMBA) chloride was used as a surfactant to modify the natural zeolite for the preparation of organozeolites. The natural zeolite was modfied with surfactant in amounts equal to 20, 50, 75 and 100% of the zeolite's external cation exchange capacity (ECEC). Obtained organozeolites, denoted as OZ-20, OZ-50, OZ-75 and OZ-100, were tested as adsorbents for non-steroidal anti-inflammatory drug diclofenac sodium (DS), a common contaminant of water systems. Results showed that with the increase of the amounts of surfactant in organozeolite, as well as with the increase of the amounts of solid phase in the suspension, DS adsorption increased. The material with the highest surfactant amount (OZ-100) showed capability to remove 90.7% of DS from buffer solution. Characterization of the organozeolites, before and after DS removal, performed using FTIR method confirmed successful modification of zeolite and presence of DS in organozeolites after adsorption.

INTRODUCTION

Pharmaceuticals are one of the most significant groups of environmental pollutants. Commonly found pharmaceuticals in waters are non-steroidal anti-inflammatory drugs (NSAIDs). NSAIDs are widely used in treating human and animal diseases for their anti-inflammatory, analgesic, and antipyretic properties [1]. Due to their high consumption and persistence in environment, they are found in waters at concentrations ranging from ng/L to μg/L [2]. Various methods have been used for the removal of NSAIDs from waters including photocatalytic degradation, microextraction, oxidation, biodegradation, chlorination, biofiltration, electrocoagulation/flotation, electrochemical oxidation, and adsorption [3]. Among these techniques, adsorption stands out as a simple and cost-effective process with high efficiency in removing pharmaceuticals from water [4].

Commonly used adsorbents for the removal of pharmaceuticals are the natural aluminosilicate minerals (clays and zeolites). In natural forms these minerals are hydrophyllic and posess hydrated exchangeable inorganic cations (Ca^{2+}, Mg^{2+}, Na^{+} and K^{+}), thus they are ineffective in removal of low polar organic mollecules (like NSAIDs) or anions. For these purposes, the modification through cation exchange of inorganic cations with long chain cationic surfactants is necessary. Incorporation of surfactants leads to creation of the hydrophobic envionment which enhance adsorption of organic or anionic molecules.

The objective of this study is to modify the natural zeolite with different quantities of surfactant - octadecyldimethylbenzylammonium (ODMBA) chloride in order to obtain materials that would effectively remove DS (representative of NSAIDs) from aqueous solutions. The effects of the amount of surfactant in organozeolites as well as the amount of each adsorbent in suspension on DS adsorption were followed. FTIR-ATR spectroscopy was used for characterization of organozeolites and to confirm the presence of DS in organozeolites after drug adsorption.

METHODS

A sample of the natural zeolite – clinoptilolite (Z) from Zlatokop deposit in Vranje (Republic of Serbia) was used as starting material. Detailed mineralogical composition of Z was given elsewhere [5]. The total cation exchange capacity (CEC) of Z, determined by the ammonium chloride method, was 139 meq/100 g [5] while the ECEC, determined by the method of Ming and Dixon [6], was 10 meq/100 g.

ODMBA (purity of 75%, Hoechst AG) was used for preparation of organozeolites. To obtain organozeolites with different loadings, the 5 wt% aqueous suspension of the initial zeolite was treated with surfactant amounts equivalent to 20, 50, 75 and 100% of zeolite's ECEC. Suspensions were stirred at 5000 rpm for 10 min at 60°C, then filtered, rinsed with distilled water and dried. Organozeolites were denoted as OZ-20; OZ-50; OZ-75 and OZ-100.

Samples were characterized by Fourier-transform infrared (FTIR) spectroscopy. FTIR spectra were recorded using a Thermo Scientific Nicolet iS50 spectrophotometer using Attenuated Total Reflection (ATR) with a diamond ATR smart accessory. Spectra were obtained in the range of 4000–400 cm^{-1} at 64 scans per spectrum at 2 cm^{-1} resolution.

DS (2-[(2,6-dichlorophenyl)amino]benzeneacetic acid sodium salt) was supplied from Sigma Aldrich. The adsorption of DS on OZ-20, OZ-50, OZ-75 and OZ-100 was investigated by addition of 10, 25, 50 and 100 mg of each adsorbent to the 25 mL of DS solution containing 50 mg/L of the drug. Experiments were conducted in a phosphate buffer at pH 7, at a constant temperature of 298 K using a rotary shaker (250 rpm, Heidolph Unimax 1010 Shaker with incubator). After 60 min, suspensions were filtered, and the concentrations of drug were determined in supernatants. The concentrations of DS before and after adsorption were determined by using UV-Visible Spectrophotometry (UV-VIS 1800, Shimadzu), at a maximum wavelength of 276 nm. After adsorption organozeolites with adsorbed drug were collected and tested by FTIR spectroscopy.

RESULTS AND DISCUSSION

FTIR spectra of Z and organozeolites are shown in Figure 1. FTIR spectroscopy provided information on the structure of Z before and after modification with surfactant molecules. Bands characteristic for Z did not change their shape or position after modification with surfactant confirming that the basic mineral structure remained unchanged. From Figure 1., it can be seen that after modification with ODMBA ions, characteristic peaks originating from ODMBA, at around 2924 and 2854 cm^{-1}, attributed to the asymmetric and symmetric stretching CH_2 vibrations of the surfactant, as well as a band at 1468 cm^{-1} which corresponds to the C–H bending vibration of methyl and methylene groups are observed [7]. The intensity of these bands increased with the increase of the surfactant amount in organozeolites.

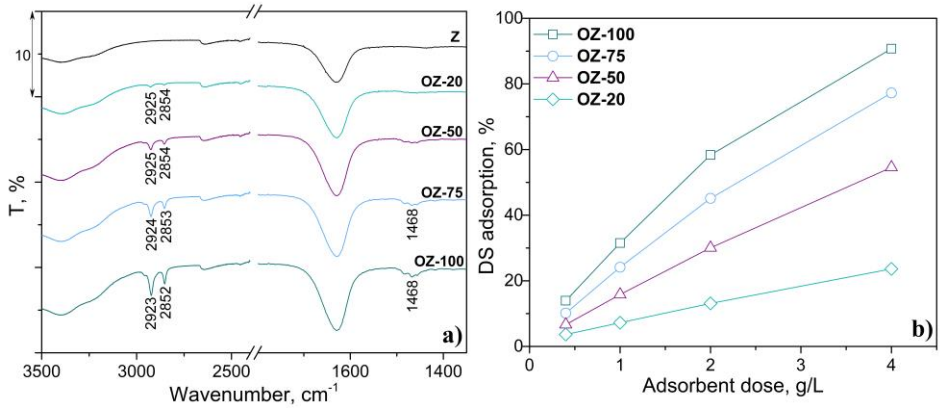


Figure 1. a) FTIR spectra of starting zeolite and organozeolites; **b)** DS adsorption by organozeolites.

DS is hydrophobic molecule ($\log K_{OW}$=3.5), soluble in water. Its dissociation constant (pK_a=4.1) suggests that at pH 7, at which adsorption experiments were performed, it exists in anionic form. In the preliminary experiment, it was demonstrated that initial Z exhibits no affinity for adsorption of DS, while the results presented in Figure 1. b) suggest that the modification of Z with ODMBA ions increased materials affinity for adsorption of DS. It was shown that drug adsorption by organozeolites, OZ-20, OZ-50, OZ-75 and OZ-100, increased with the increase of levels of solid phase in suspension (achieving removal indexes of 23.6; 54.6; 77.3 and 90.7% for the highest amount of solid phase in suspension – 4 g/L)). It was also observed that, at the same concentration of each organozeolite in suspension, DS adsorption increased with the increase of amounts of organic cation in organozeolite. Among organozeolites, OZ-100 containing the highest amount of ODMBA showed the highest efficiency for DS removal from buffer solution. For this sample, adsorption isotherm was previously determined [8]. It was found that adsorption of DS increased with increasing of the initial drug concentration and the experimental data showed good correlation with both Langmuir and Freundlich isotherm model with high values of correlation coefficients (r^2 > 0.8). The DS maximum adsorbed amount (qmax) calculated by Langmuir isotherm model was 23.86 mg/g.

These findings indicated that the hydrophobic surfactant molecules at the surface of organozeolites are the active sites at which the drug was adsorbed. The obtained results indicate that the degree of hydrophobicity plays a role in adsorption process of DS.

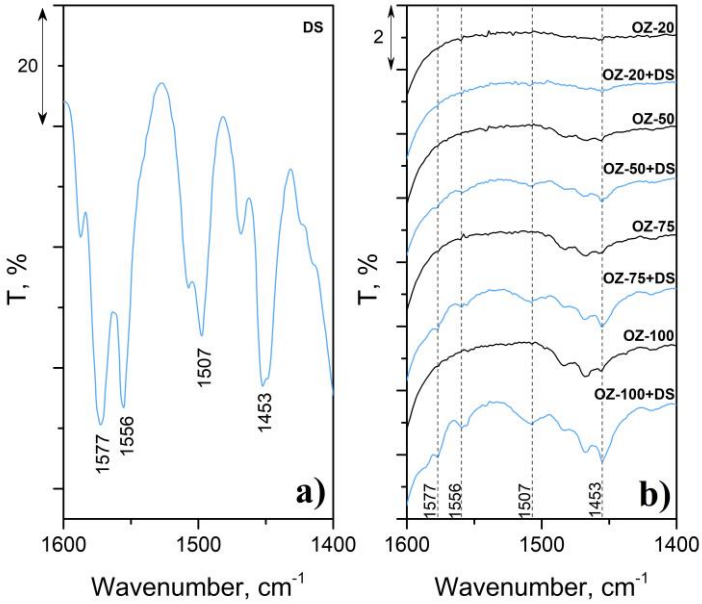


Figure 2. FTIR spectra of: **a)** DS; **b)** organozeolites after DS adsorption.

The incorporation of drug molecules onto adsorbents surfaces was tested using FTIR spectroscopy. FTIR spectra of pure DS and organozeolites before and after adsorption are presented in Figure 2. in the wavenumbers range in which DS showed characteristic bands (1600-1400 cm^{-1}) considering that in this range DS have intensive peaks which were visible in the organozeolites after adsorption of drug and they do not interfere with the peaks originating from the surfactant or Z in organozeolites. In the organozeolites spectra after DS adsorption new peaks originating from the drug appeared: at 1577 cm^{-1} assigned to vibration of carboxylate group (COO^-), at 1556 cm^{-1} assigned to N–H vibration, at 1507 cm^{-1} corresponding to C=C vibration in the aromatic ring and at 1453 cm^{-1} corresponded to the carboxylate group vibration [9]. These peaks observed in the

organozeolites spectra after adsorption, confirmed adsorption of drug at organozeolites surfaces. Also, their intensities increased as the amount of adsorbed drug onto organozeolites increased.

CONCLUSION

This study showed that zeolite modification with four different levels of ODMBA in amounts below or equal to zeolite's ECEC (20, 50, 75 and 100%) was sucessful. DS removal increased with the increase of the organozeolite dose and with the increase of the amounts of organic phase. FTIR characterization of organozeolites after adsorption of DS confirmed drug adsorption and that there were no structural changes in zeolitic framework. Characterization results and high DS removal demonstrated that organozeolites have an affinity for the removal of DS. This highlights organozeolites efficacy as promising adsorbents for the removal of DS from polluted water environments.

Acknowledgment

This work was supported by the Ministry of Education, Science and Technological Development of the Republic of Serbia (grant no 451-03-66/2024-03/200023).

REFERENCES

[1] N.C. Huynh, T.T.T. Nguyen, D.T.C. Nguyen, T. Van Tran, Sci. Total Environ. 898 (2023) 165317.
[2] A. Rastogi, M.K. Tiwari, M.M. Ghangrekar, J. Environ. Manage. 300 (2021) 113694.
[3] M.J. Ahmed, J. Environ. Manage. 190 (2017) 274–282.
[4] A. Vona, F. di Martino, J. Garcia-Ivars, Y. Picó, J.A. Mendoza-Roca, M.I. Iborra-Clar, J. Water Process Eng. 5 (2015) 48–57.
[5] A. Daković, S. Matijašević, G.E. Rottinghaus, V. Dondur, T. Pietrass, C.F.M. Clewett, J. Colloid Interface Sci. 311 (2007) 8–13.
[6] D.W. Ming, J.B. Dixon, Clays Clay Miner. 36 (1988) 224.
[7] M. Marković, A. Daković, G.E. Rottinghaus, A. Petković, M. Kragović, D. Krajišnik, J. Milić, Colloids Surfaces A Physicochem. Eng. Asp. 529 (2017) 7–17.
[8] M. Obradović, A. Daković, D. Smiljanić, M. Ožegović, M. Marković, G.E. Rottinghaus, J. Krstić, Microporous Mesoporous Mater. 335 (2022) 111795.
[9] Y. Zhao, F. Liu, X. Qin, Chemosphere. 180 (2017) 373–378.

PLANT GROWING SITE CHARACTERISTICS – AN IMPORTANT FACTOR FOR BIOMASS SELECTION

T. Šoštarić[1*], Z. Lopičić[1], D. Ranđelović[1], T. Rakić[2], A. Antanasković[1], I. Mikavica[1] and J. Milojković[1]

[1]*Institute for Technology of Nuclear and Other Mineral Raw Materials, Bulevar Franše d'Eperea 86, 11000 Belgrade, Serbia, (t.sostaric@itnms.ac.rs)*
[2]*University of Belgrade, Faculty of Biology, Studentski trg 16, 11000 Belgrade, Serbia*

DOI: https://doi.org/10.46793/Phys.Chem24II.459S

ABSTRACT

The characteristics of leaf biomass of invasive *Acer negundo* L. tree species from three different growing sites were evaluated, and its potential influence for its further usage was considered. Two natural and one mining site were chosen for the sampling of soil and leaves: Mountain Avala (A), Great War Island (B) and the banks of former coal separation pond in Piskanja (C). The results confirmed that soil sample C from the most anthropogenic influenced area, stands out from the other two samples and coresponding biomass differs in terms of physical and chemical characteristics. The amount and proportion of macro elements and surface charge in sample C differes from other two samples. This study confirmed that the growing site characteristics influence the chemical composition of plant biomass, primarily in terms of macro elements composition, important for the further development of specific bio-based materials.

INTRODUCTION

Invasive plant species are introduced species that affect natural habitats causing ecological and environmental harm and their distribution causes great concern. With the increasing global spread of invasive species, collecting their abundant biomass could be a promising source for some biomass valorization technologies. However, the characteristics of the biomass are the important aspect that influences the decision on the most appropriate valorization technology such as direct combustion, thermo-chemical conversion processes (pyrolysis, gasification), bio-chemical (anaerobic digestion, fermentation) and physico-chemical processes (sorption) [1]. For example alkali and alkaline earth metals tend to have a catalytic effect that enhances biomass gasification kinetics [2]. Additionally, high content of certain macro elements in the biomass enables its potential usage as a soil amendment or fertilizer after combustion, pyrolysis or anaerobic digestion [3]. Further, biomass with increased macro elements in exchangeable positions (detected by CEC value) can be a good candidate for development of adsorbents, since their involment in the ion-exchange mechanism throught sorption process.

The invasive species that was chosen for this study is box maple *Acer negundo* L. a tree of little economic value native to North America, but widespread in Europe. In Serbia, it is considered one of the most aggressive invasive tree species in forest ecosystems [4]. As invasive species, its eradication is conducted through different methods of mechanical and chemical control, leaving significant amount of biomass that is considered to be a type of biological waste which is currently unutilized. Abiotic factors, such as climate, soil characteristics and anthropogenic activities influence the yield and chemical composition of plant biomass [5], which can have effects on its future use that are not yet fully recognized. Site characteristics can particularly influence the leaf composition since the plant leaves are the organs that are most sensitive to the influence of environmental factors, which can cause differences in the functional properties, macro- and

microelement content, as well as in presence of different functional groups [6]. Therefore, the *A. negundo* leaves were selected as a biomass of interest for this investigation. In this study, the macroelement content and surface charge of the leaves biomasses taken from different habitat types was investigated in order to reveal if there are notable differences among them. The detected differences could indicate the possibility of further utilization of biomass for different purposes. This should be additional aspect of future investigations before selection of plant material for bio-based products whether it is in sectors such as energy, green chemistry, environmental protection, and particularly for the development of alternative, sustainable, eco-friendly and cheap sorbents.

METHODS

Sampling points

Three different locations selected for the sampling of *A. negundo* leaves were placed at: outstanding natural landscape protected area of Mountain Avala (**A**), area of the natural landscape Great War Island (**B**) and on the banks of a former coal separation pond in Piskanja, which is a part of Ibar coal mining basin in South-Central Serbia (**C**).

Plant biomass

To make representative samples about 100 fully developed leaves were picked from the 3-5 individuals approximately similar age. Leaves were rinsed and air-dried and then ground in a blade grinder (20.000-30.000 rpm) at particle size less than 0.2 mm. Simultaneously soil composite samples were taken at each sampling site. Soil samples were air-dried and sieved through a 2.0 mm stainless steel sieve before analysis. Soil pH and redox potential (Eh) were measured in deionized water in a 1:2.5 soil/solution ratio with pH meter SensION3 (Hach, USA). The content of soil organic carbon (SOC) was determined by oxidation with a solution of $KMnO_4$ according to the method of Kotzman [7]. The leaves samples were dissolved using a standardized microwave-assisted acid dissolution procedure for this type of material [8] in the High-performance Microwave Digestion System ETHOS UP, Milestone. Concentrations of K, Ca and Na were determined by atomic emission spectrometry using PerkinElmer PinAAcle 900T, USA, directly from the prepared solution. Analyses were performed with three replicates, where mean values are presented. The value of the point of zero charge - pH_{pzc} was determined according to the method described by Milonjić et al. [9]. Cation exchange capacity (CEC) was determined by stiring 0.2 g of each sample and 100 mL of 1.0 mol/L ammonium acetate for 2h. The concentrations of exchangeable cations in filtrates were determined by atomic adsorption spectrophotometer.

RESULTS AND DISCUSSION

Measurements of the soil pH, oxido-reduction potential, and content of organic matter in topsoil layers (0-20 cm) of the three sampling sites are presented in **Table 1**, together with the content of macroelements and CEC in leaves. Results of soil parameters revealed that: i) soil pH ranges from neutral (A) and slightly acidic (B), to acidic (C); ii) all samples are moderately reduced according to the results of redox potential and iii) the proportion of organic matter is the lowest in sample C. According to the investigated parameters, soil sample C stands out from the other two samples potentially reflecting on biomass composition and physiology. Therefore, the content of macro elements in the leaves taken at these sites was investigated as well and results are given in Table 1. As can be seen in Table 1, the highest concentration of K is recorded in sample C, while the concentration of Ca and Mg is lowest in this sample. Similar findings were obtained by Liu et al., [6] who compared the content of leaf macro elements in healthy and declining stands of Acer saccharum and found a significantly lower concentration of Ca and Mg in the declining stand compared to the healthy one, and a higher concentration of K in the declining stands compared to

healthy ones. This can be explained by the role of K in the alleviation of increased abiotic stresses by the synthesis of protein and carbohydrate metabolism [10]. Also, the lowest value of total CEC at sample C indicates the lowest content of exchangeable ions, making this biomass sample the least suitable candidate for sorbent formulations.

Table 1. Soil pH, oxido-reduction potential (Eh) and SOC content from the topsoil layer, together with leaves macro elements content and CEC.

	A	**B**	**C**
Soil			
pH_{soil}	6.85 - 7.15	5.90 - 6.27	4.64 - 4.76
Eh_{soil} (mV)	271.0	212.2	370.2
SOC (%)	4.0	3.4	2.6
Leaves (%)			
Mg	0.469	0.441	0.333
K	1.433	1.530	1.742
Na	0.009	0.009	0.009
Ca	5.141	3.991	2.643
CEC (meq/100g)	170	165	145

Additionaly, the point of zero charges was determined and the results are shown in **Figure 1**.

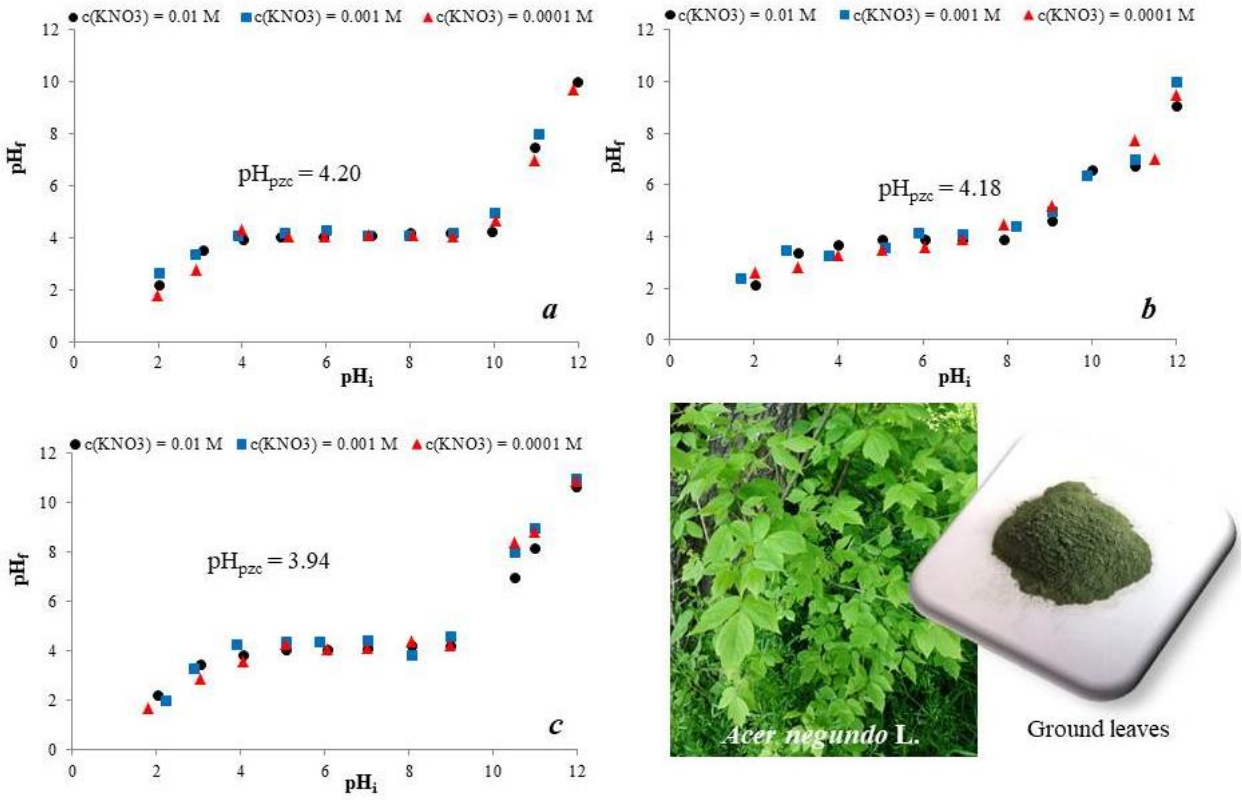


Figure 1. Determination of the point of zero charge (pH_{pzc}) of *A. negundo* samples taken from three different locations.

The point of zero charge (pH_{pzc}) is defined as the pH value at which the surface charge is zero. The surface charge is negative if the pH value of the solution is higher than pH_{pzc}, and it is positive

if the pH value of the solution is lower than pH_{pzc}. As can be seen from Figure 1, the curves of equilibrium pH (pH_f) versus initial pH (pH_i) show the same shape for all samples and at all electrolyte concentrations. The same values for pH_{pzc} obtained for different concentrations of KNO_3 mean that pH_{pzc} does not depend on the ionic strength and that no specific adsorption of K^+ or NO^{3-} occurred occurred [11]. Initially, for all samples causes an increase in pH_f. Changing the pH_i from 4.0, did not affect pH_f and the curves reached plateaus. The plateaus represent the pH range where the samples exhibited buffering properties, meaning that the addition of H^+ or OH^- in this range does not affect the equilibrium pH values (pH_f). However, these ranges are different for investigated samples: for sample C this range is between 4.0 to 8.0, for sample B it is up to 9.0, while for sample A this range goes to 10.0. The obtained pH_{pzc} values are 3.94 for sample C, 4.18 for sample B and 4.20 for sample A. The surface of the samples has a positive charge when the pH_i values are higher than 8.0 (C), 9.0 (B) and from 10.0 (C) the surface has a negative charge. The obtained results confirmed the previous conclusion: **i)** samples A and B have very similar pH_{pzc} values (4.2 and 4.18), while the pH_{pzc} value of sample C is lower (3.94), **ii)** samples A and B have almost the same length of the plateau, while, the length of the plateau in sample C is significantly smaller, and its ability to maintain a buffer environment is significantly lower.

CONCLUSION

The results of this study revealed that the plant growing site could represent an important factor that influences biomass characteristics. The detected differences indicate the direction for further utilization of biomass. Anthropogenically modified soil formed on coal separation pond showed lower pH and SOM values compared to soils from natural sites, followed by differences in macroelement content, CEC and surface charge of biomass from this location. The amount and proportion of macro elements and surface charge in sample C differes from other two samples, whereas the lowest value of total CEC makes this biomass sample the least suitable candidate for sorbent formulations. Although invasive species are not currently used in practice as adsorbents, they represent a material with prominent potential for exploitation.

Acknowledgement

This work was supported by the Ministry of Science, Technological Development and Innovation of the Republic of Serbia (grant no 451-03-66/2024-03/200023 and 451-03-65/2024-03/200178).

REFERENCES

[1] N. C. Joshi, S. Sinha, P. Bhatnagar, Y. Nath, B. Negi, V. Kumar, P. Gururani., Curr Res Microb Sci, 6 (2024) 100237.
[2] T. Dahou, F. Defoort, M. Jeguirim, C. Dupont, Fuel., 282 (2020) 118806.
[3] K. Hjouji, R. Haldhar, A.A. Alobaid, M. Taleb, Z. Rais, Ind Crop Prod., 216 (2024) 118820.
[4] M. Glišić, D. Lakušić, J. Šinžar-Sekulić, S. Jovanovi, Bot Ser., 38 (2014) 131-138.
[5] B. Farwa, B. Saraj, L. Wenxing, Frontiers in Forests and Global Change, 7 (2024)
[6] X. Liu, D. S. Ellsworth, M. T. Tyree, Tree Physiol., 17 (1997) 169-178.
[7] JDPZ, 1966. Chemical methods for soil analysis, Beograd.
[8] I. Anastopoulos, A. Robalds, H. N. Tran, D. Mitrogiannis, D. A. Giannakoudakis, A. Hosseini-Bandegharaei, G. L. Dotto, Environ Chem Lett., 17 (2019) 755-766.
[9] S. K. Milonjić, J. Serbian Chem Soc., 72 (2007) 1363-1367.
[10]M. Hasanuzzaman, M. H. M. Borhannuddin Bhuyan, K. Nahar, Md. S. Hossain, J. Al Mahmud, Md. S. Hossen, A. A. C. Masud, Moumita, M. Fujita. Agronomy., 8 (2018) 31.
[11]J. J. Gulicovski, Lj. S. Čerović, S. K. Milonjić, Mater. Manuf. Processes., 23 (2008) 615-619.

MODIFIED POTATO STARCH INTERCALATED WITH MONTMORILLONITE AS A NATURAL ADSORBENT FOR THE REMOVAL OF HEAVY METALS AND DYES FROM WATER

N. Karić [1], M. Vukčević [2], M. Maletić [1], A. Perić Grujić [2] and K. Trivunac [2]

[1] *Innovation Centre of the Faculty of Technology and Metallurgy, Karnegijeva 4, 11120 Belgrade, Serbia.*
[2] *University of Belgrade, Faculty of Technology and Metallurgy, Karnegijeva 4, 11120 Belgrade, Serbia (marijab@tmf.bg.ac.rs).*

DOI: https://doi.org/10.46793/Phys.Chem24II.463K

ABSTRACT

In this study, we report on the method of preparation, and application of modified potato starch following the principles of sustainable development. Modified starch was tested as an adsorbent for removing heavy metals and dyes from water. The modification method is environmentally friendly, without the use of expensive and toxic chemicals, and economically profitable with low operating costs. The starch modification is based on introducing amino functional groups into the starch structure, followed by the addition of montmorillonite clay, in order to obtain a novel bicomposite, and to investigate the influence of clay on the adsorption properties. It has been found that applied treatments induced the changes in morphological and surface characteristics of the obtained adsorbents consequently increasing the adsorption efficiency of modified samples for the removal of both, heavy metal ions and dyes.

INTRODUCTION

Heavy metal ions and dyes are often found in the environment as a result of their extensive industrial use [1]. There are many types of technologies used to remove heavy metals and dyes from wastewater, but adsorption is the most commonly used because of its efficiency and cost-effectiveness [2].

Biocomposites are materials that are attracting increasing attention for application in environmental remediation, i.e. adsorption of inorganic and organic pollutants from water. They may be created by combining biopolymers, e.g. starch, and inorganic solids, usually layered silicates belonging to the group of clay minerals. These materials exhibit exceptional structural and functional properties similar to conventional composites. What makes biocomposite materials more acceptable than conventional ones is their non-toxicity, biocompatibility and biodegradability, which come from both biopolymers and clay [3–6].

Potato starch was chosen as a biopolymer in order to obtain a green biocomposite because it is low cost, available in nature in large quantities, and easily renewable [3,7]. Also, it has a larg e number of hydroxyl groups that can easily be replaced by other functional groups to improve the adsorption capacity of this biocomposite [7]. The introduction of amino groups into the starch structure creates new active sites for adsorption and facilitates the binding of biopolymers with charged clay minerals to obtain more stable adsorbents, which are more easily separated from the suspension after adsorption compared to the native starch [8]. Montmorillonite clay was chosen for modification due to its high adsorption efficiency of cations from aqueous solutions [9].

Therefore, in this work, two new materials were prepared, modified starch with amino groups, and a biocomposite based on amino starch and montmorillonite clay. The modification method is simple, effective, and completely environmentally safe, without the use of expensive and toxic

organic solvents and the creation of by-products. The characterization of the obtained materials confirmed the success of the modification method. The adsorption efficiency of the prepared materials for the removal of heavy metal ions, Pb^{2+} and Cd^{2+}, as well as organic dyes, crystal violet (CV) and brilliant green (BG), from individual solutions, as well as from a mixture of metals and a mixture of dyes, was tested.

METHODS

Modification of starch (S) with cysteine (SC) was performed by mixing 10 g of native potato starch with 100 mL of distilled water for 30 min at 40 °C to obtain a starch suspension to which cysteine (1.0 g) was then added, and stirring at 400 rpm was continued at 40 °C for another 3 h. The resulting mixture was washed and filtered several times and then dried at 50 °C to constant weight [10]. A biocomposite (SCmm) based on starch modified with cysteine (SC) and montmorillonite clay (mm) (K 10, powder; Sigma Aldrich, CAS: 1318-93-0) was obtained by suspending 10 g of SC in 50 mL of deionized water and kept in a water bath at 70 °C with continuous stirring at 400 rpm for 1 h. Montmorillonite clay (1.0 g) was dispersed in 50 mL of deionized water and the resulting dispersion was added to the gelatinized starch solution. The reaction was continued at 60 °C with constant stirring on a magnetic stirrer at 400 rpm for 3 h. The sample was dried at 50°C in an oven, and finally, the dry sample was ground into a powder.

The morphological and surface properties of obtained materials were determined by scanning electron microscopy and Fourier transform infrared spectroscopy, respectively.

Adsorption experiments were performed in a batch system, with constant mixing (150 rpm) at room temperature for 3 h. The adsorption of heavy metals (Pb^{2+} and Cd^{2+}) and dyes (CV and BG) from a solution of a single component or binary mixture (initial concentration 10 mg dm^{-3} for each component) were examined with a constant dose of adsorbent (0.05 g), and the volume of the solution (25 mL). The concentration of dyes in the aqueous solution was analyzed using a UV-VIS spectrophotometer (Shimadzu 2600) for the visible range at 582 and 630 nm for CV and BG, respectively. The concentration of heavy metal ions in an aqueous solution after microfiltration was determined using atomic absorption spectroscopy (Pye Unicam SP9, Philips) at 283.3 and 228.8 nm for Pb^{2+} and Cd^{2+}, respectively.

RESULTS AND DISCUSSION

The FTIR spectra of native starch and the prepared materials are shown in **Figure 1**. The bond at 3612 cm^{-1} in the spectrum of SCmm is assigned to the –OH stretching vibration of structural hydroxyl groups and water molecules in montmorillonite clay present in the interlayer [11]. The broad band with peaks at around 3329, 3332, and 3334 cm^{-1} are attributed to the vibrations of –OH groups from the starch structure, while the peak at 2932, 2935, and 2941 cm^{-1} originates from $–CH_2$ stretching vibration [12]. The characteristic peak for the cysteine structure appears at 2548 and 2551 cm^{-1} and originates from –S–H stretching vibrations [10, 13]. Bands at 1641 and 1645 cm^{-1} are attributed to –OH bending vibrations originating from adsorbed water molecules in the starch structure [12]. The absorption peak at 1578 and 1583 cm^{-1} may indicate the presence of –C=N groups originating from the cysteine structure [10,

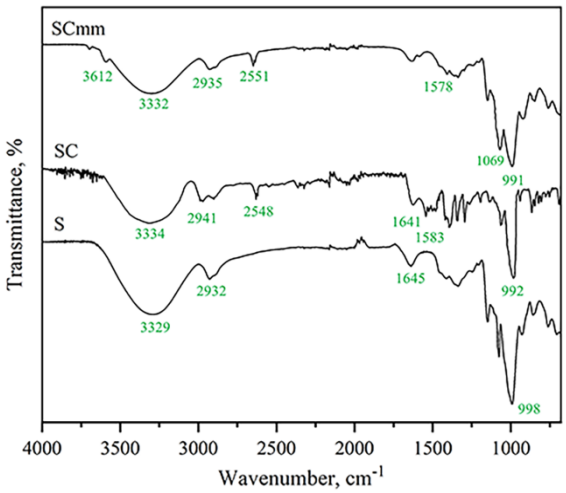


Figure 1. FTIR of examined samples.

13]. The strong band at 1069 cm^{-1} is associated with Si–O stretching vibrations, which indicates that there are a large number of silanol (SiOH) groups on montmorillonite clay surfaces [11]. The high-intensity band appearing at 991, 992, and 998 cm^{-1} reflects the –C–O stretching in the starch structure [12].

SEM micrographs of native potato starch, and modified starch are shown in **Figure 2**. Native potato starch shows a smooth granule surface, a typical elliptical and spherical shape without any cavities or fissures (**Figure 2a**) [14]. In **Figures 2b** and **2c** it can be seen that starch modification did not destroy the original shape of starch granules. Modification of starch with cysteine leads to deposition of cysteine on the surface of starch granules (**Figure 2b**). Additional modification of the starch-cysteine material with clay leads to the creation of an uneven and rough surface of the starch granules, due to the coating of the starch granules with parts of clay (**Figure 2c**).

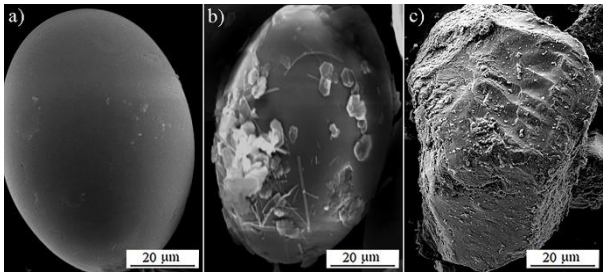


Figure 2. SEM of examined samples.

The results of the adsorption efficiency have shown that starch modification contributed to the increase in the removal efficiency for both heavy metal ions and dyes (**Figure 3**). All materials were slightly more efficient for the removal of heavy metal ions (Pb^{2+}>Cd^{2+}) than dyes (CV>BG). Also, it was determined that the additional modification of amino starch with clay did not increase the adsorption efficiency, which may be a consequence of covering active functional groups from amino-starch with parts of clay.

Examination of the simultaneous removal of heavy metal ions and dyes from binary metal-metal (**Figure 3a**) and dye-dye (**Figure 3b**) mixtures showed that their competition for adsorption sites resulted in a decrease in the removal efficiency of both, metals and dyes, from binary solutions.

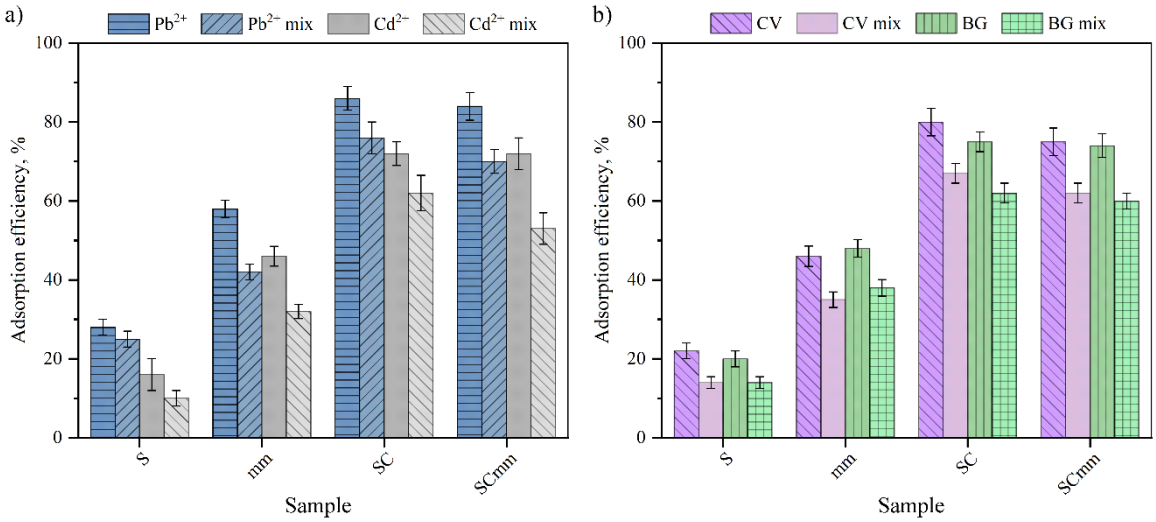


Figure 3. Adsorption efficiency of examined samples for a) heavy metals and b) dyes removal from aqueous solutions.

CONCLUSION

In this study, a new method for obtaining starch-based adsorbents, which meets all the principles of green chemistry and sustainable development, was successfully developed. The accomplishment of the modification was confirmed through the structural-morphological characterization, as well as through the examination of the adsorption properties of modified starch. It has been proven that the amino groups introduced into the starch structure were responsible for the adsorption of pollutants. Additional modification of starch with montmorillonite clay did not significantly affect the adsorption properties of the material, which may be a consequence of covering the surface of the starch with parts of clay and reducing the available sites for adsorption. The obtained adsorbents proved to be somewhat more efficient for the removal of heavy metal ions (>80% for Pb^{2+} and Cd^{2+}) compared to the removal of dyes (75-80% for CV and BG). Also, the adsorption efficiency from the mixture of metals and the mixture of dyes was over 60%, which indicates the possibility of applying the obtained materials for the purification of wastewater in real systems.

Acknowledgment

This work was supported by the Ministry of Education, Science and Technological Development of the Republic of Serbia (Contract No. 451-03-65/2024-03/200135 and 451-03-66/2024-03/200287).

REFERENCES

[1] Z. S. Pour, M. Ghaemy, RSC Adv., 5 (2015) 64106.
[2] P. Daraei, S. S. Madaeni, E. Salehi, N. Ghaemi, H. S. Ghari, M. A. Khadivi, E. Rostami, J. Memb. Sci., 436 (2013) 97108.
[3] M. del M. Orta, J. Martín, J. L. Santos, I. Aparicio, S. Medina-Carrasco, E. Alonso, Appl. Clay Sci., 198 (2015) 105838.
[4] S. Lawchoochaisakul, P. Monvisade, P. Siriphannon, Carbohydr. Polym., 253 (2021) 117230.
[5] A. C. S. Alcântara, M. Darder, P. Aranda, E. Ruiz-Hitzky, Appl. Clay Sci., 96 (2014) 2.
[6] N. E. Kochkina, O. A. Skobeleva, Y. V. Khokhlova, Part. Sci. Technol., 35 (2017) 259.
[7] G. Xie, X. Shang, R. Liu, J. Hu, S. Liao, Carbohydr. Polym., 84 (2011) 430.
[8] F. Chivrac, E. Pollet, M. Schmutz, L. Avérous, Biomacromolecules, 9 (2008) 896.
[9] S. S. Gupta, K. G. Bhattacharyya, Phys. Chem. Chem. Phys., 14 (2012) 6698–6723.
[10] N. Karić, M. Vukčević, M. Maletić, S. Dimitrijević, M. Ristić, A. Perić Grujić, K. Trivunac, Int. J. Biol. Macromol., 241 (2023) 124527.
[11] M. Ouardi, M. Laabd, H. A. Oualid, Y. Brahmi, A. Abaamrane, A. Elouahli, A. A. Addi, A. Laknifli, Environ. Sci. Pollut. Res., 26 (2019) 19615.
[12] I. Dankar, A. Haddarah, F. E. L. Omar, M. Pujolà, F. Sepulcre, Food Chem., 260 (2018) 7.
[13] S. Devi, B. Singh, A. K. Paul, S. Tyagi, Anal. Methods, 8 (2016) 4398.
[14] I. Chakraborty, S. Pallen, Y. Shetty, N. Roy, N. Mazumder, Biophys. Rev., 12 (2020) 105.

ALKALI-ACTIVATED FLY ASH: A SUSTAINABLE ADSORBENT FOR YTTRIUM REMOVAL FROM WATER

T. Radojičić [1], M. Maletić [2], M. Vukčević [1] and K. Trivunac [1]

[1] *Faculty of Technology and Metallurgy, University of Belgrade, Karnegijeva 4, 11120 Belgrade, Serbia. (marijab@tmf.bg.ac.rs)*
[2] *Innovation Centre of the Faculty of Technology and Metallurgy, Karnegijeva 4, 11000 Belgrade, Serbia.*

DOI: https://doi.org/10.46793/Phys.Chem24II.467R

ABSTRACT
Given the substantial waste produced by coal combustion in thermal power plants, including bottom ash and fly ash, it's imperative to explore novel applications for these by-products. In order to improve the adsorption characteristics of fly ash, chemical modification of fly ash was applied. Unmodified and modified materials were used as adsorbents for yttrium removal from water. Obtained samples were characterized using Fourier transform infrared spectroscopy and scanning electron microscopy. The effect of the initial pH value and concentration of the yttrium solution, as well as contact time on adsorption were examined. It was found that the adsorption of yttrium follows a pseudo-second order kinetic model, while the Freundlich adsorption isotherm best describes the adsorption process in equilibrium. Obtained results demonstrated that alkali-activated fly ash can be used as a highly effective adsorbent for the removal of yttrium from aqueous solutions.

INTRODUCTION
Electricity is one of the main requirements for daily human necessities and its demand is getting higher with time. In Serbia, 70% of electricity is produced by thermal power plants, which as by-products make huge amounts of fly ash. This waste is a significant problem for the population as it covers a vast area and harms the environment. In order to decrease the amount of fly ash discharged in landfills, it can be reused in the construction industry, especially in concrete production [1]. Additionally, unmodified and modified fly ash can be utilized as adsorbents to eliminate hazardous contaminants, organic and inorganic chemicals [2], heavy metals, and dyes from wastewater [3,4], as well as selective adsorbent for rare earth elements [5]. The rare earth elements (REEs) are an important part of modern life since they are present in different high-tech applications across industries. As new technologies are developed, the increased demands for REEs bring the extensive exploitation and reduction of REE resources. Therefore, increased attention is paid to recycling as an alternative resource of REE, along with developing the appropriate adsorbent for the separation of REE from the acidic solution with low concentrations of these elements. The aim of this work was to examine the possibility of using fly ash and alkali-activated fly ash as adsorbents for yttrium separation. The influence of the applied modification on the surface and adsorption characteristics of fly ash was examined and the yttrium adsorption process was optimized by choosing the appropriate contact time, the initial pH, and the concentration of yttrium solution.

METHODS
Fly ash (FA) was obtained from a coal-based thermal power plant “Nikola Tesla B”, near Obrenovac, Serbia. Washed FA was homogenized and sifted into small particles before being used for the experiment. The synthesis of alkali-activated fly ash (AAFA) was carried out by mixing 9.77

g of FA and 4.21 g of diatomaceous earth in a plastic mold, after which 9.95 g of sodium silicate was added. Improved mixing and bonding of the reactants were achieved by adding a few drops of 16 mol dm^{-3} NaOH. Afterwards, the material was dried at 105°C for 2 hours and then left in a closed mold at room temperature to age for 30 days. The surface characterization of the unmodified and modified fly ash was performed by scanning electron microscopy (SEM JEOL JSM-6610LV), and Fourier transform infrared spectroscopy (Nicolet iS10, Thermo Scientific). The adsorption experiments were performed in a batch system with constant shaking (150 rpm). As the pH value affects the adsorption process, that parameter was optimized by immersing 0.05 g of material (FA and AAFA) in 20 ml of yttrium solutions (25 mg dm^{-3}) with initial pH adjusted at 2, 4 and 6. The optimal pH value was used in the following adsorption experiments. Yttrium concentrations after adsorption were determined by inductively coupled plasma-optical emission spectrometry (ICP-OES Agilent 5800). The adsorption efficiency of the tested materials was calculated using the following equation (1):

$$Adsorption\,efficiency = \frac{C_0 - C_e}{C_0} \cdot 100,\ \% \quad (1)$$

where C_e and C_0 are the equilibrium and the initial concentration of yttrium in solution, respectively (mg dm^{-3}).

Adsorption kinetic was carried out by soaking 0.25 g of material (FA and AAFA) immersed in 100 ml of an aqueous solution of yttrium with an initial concentration of 15 mg dm^{-3}. Samples were taken at certain time intervals 10, 30, 60, 120 and 180 minutes. Further research included examining the influence of different initial concentrations of yttrium (10, 15, 20, and 25 mg dm^{-3}), utilizing 0.05 g of adsorbents alongside 20 ml of yttrium solution.

Two adsorption kinetic models were applied to predict the yttrium adsorption mechanism, the pseudo-first order model, equation (2), and the pseudo-second order model, equation (3):

$$q_t = q_e \cdot (1 - e^{-k_1 t}) \quad (2)$$

$$q_t = q_e - \left(\frac{1}{q_e} + k_2 \cdot t \right)^{-1} \quad (3)$$

where q_e and q_t (mg g^{-1}) are adsorption capacities at equilibrium and time t and k_1 (min^{-1}), and k_2 (mg g^{-1} min^{-1}) are rate coefficients of pseudo-first and pseudo-second order equations, respectively.

Additionally, the adsorption behavior of yttrium at the equilibrium, and its maximum adsorption capacities on unmodified and modified fly ash were analyzed using the Langmuir (4), and Freundlich (5) equations:

$$q_e = \frac{Q_0 \cdot b \cdot C_e}{1 + b \cdot C_e} \quad (4)$$

$$q_e = K_F \cdot C_e^{\,1/n} \quad (5)$$

where Q_0 is the amount of adsorbed substance per unit mass of adsorbent that is needed for monolayer surface covering (μg g^{-1}), b is a constant connected to the heat of adsorption (dm^3 μg^{-1}), while K_F (μg g^{-1} (μg dm^{-3})$^{-1/n_F}$) is Freundlich constant connected to the adsorption capacity, and 1/n is the heterogeneity factor.

RESULTS AND DISCUSSION

Scanning electron micrograms show the surface morphology of unmodified and modified fly ash (**Figure 1a** and **1b**). The analysis shows that the unmodified fly ash has a porous structure with irregular shapes and sharp edges. Conversely, alkali-activated modification of the fly ash made edges smoother and fluffier, while maintaining a similar overall structure. FTIR spectra of unmodified and modified fly ash are given in **Figure 1c.** The sharp peaks in the FA spectra at 1078,

and around 780 cm^{-1} can be assigned to the asymmetric and symmetric stretching vibration of Si-O-Si bond, respectively [7].

For alkali activated FA, the peak corresponding to asymmetric vibration of Si-O-Si bond is shifted to 1000 cm^{-1}, while intensity of the peak around 780 cm^{-1} is decreased, confirming the successful activation of fly ash. The peak at 1460 cm^{-1} can be assigned to the sodium carbonate, formed on the surface of the AAFA samples in the reaction of excessive sodium silicate or sodium hydroxide with atmospheric CO_2. Additionally, broad bands around 3450 and 1650 cm^{-1} are related to the -OH groups in water molecules.

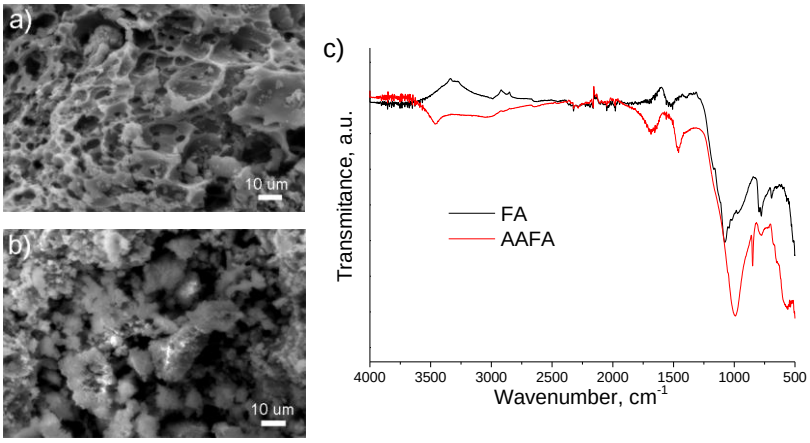


Figure 1. SEM images of a) fly ash and b) alkali-activated fly ash, and c) FTIR spectra of examined samples.

The effect of the initial pH value solution on the equilibrium adsorption of yttrium was examined at the pH range of 2.00-6.00 (**Figure 2**).

With an increase in pH value, there is an increase in adsorption efficiency. However, in attempt to examine the adsorption behavior in more acidic conditions, pH value of 4 was selected as initial pH for further analysis.

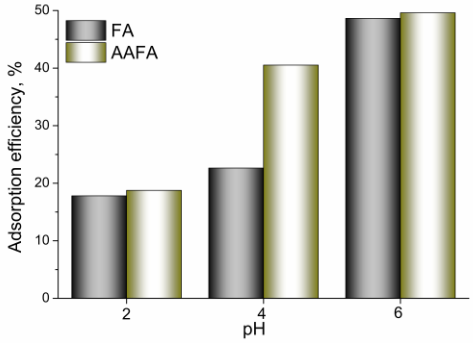


Figure 2. Influence of initial pH of yttrium solution on adsorption efficiency of fly ash and alkali-activated fly ash.

The influence of contact time on the adsorption of yttrium is shown in **Figure 3a**. The obtained results show that sample AAFA has a higher adsorption capacity compared to FA. Sample FA reaches the equilibrium within 90 minutes, while sample AAFA does not reach equilibrium in the examined time interval of 180 minutes (**Figure 3a**). The experimental data was well-fitted by the pseudo-second-order equation, which suggests that chemisorption is the primary mechanism of adsorption. This is supported by the high correlation coefficients (R^2) and adsorption capacities at equilibrium (q_e) presented in **Table 1**.

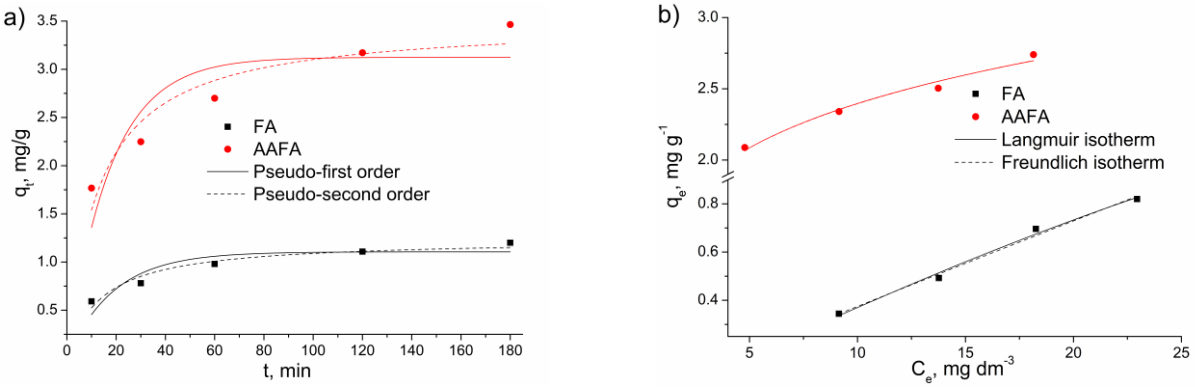


Figure 3. The influence of a) contact time and b) initial yttrium concentration on adsorption and fitting of experimental data with theoretical models.

The influence of the initial concentration, given as the dependence of q_e on C_e, is illustrated with Langmuir and Freundlich adsorption isotherms, as shown in **Figure 3b**. The adsorption capacities of examined samples increase with initial concentration, and a characteristic plot is not established in the range of tested concentrations. Sample AAFA shows a higher capacity compared to FA. The adsorption equilibrium data were fitted with Langmuir and Freundlich isotherm models, and the parameters obtained are summarized in **Table 1**. Freundlich isotherm model better describes the adsorption of yttrium onto the examined samples, as indicated by the correlation coefficients (R^2).

Table 1. Kinetic and isotherm parameters for yttrium adsorption on FA and AAFA.

Material	Pseudo-first order			Pseudo-second order		
	q_e, mg g^{-1}	k_1, min^{-1}	R^2	q_e, mg g^{-1}	k_2, g mg^{-1} min^{-1}	R^2
FA	1.10535	0.05301	0.75868	1.23724	0.05939	0.92906
AAFA	3.12467	0.05705	0.65352	3.49548	0.02249	0.87976
	Langmuir isotherm			**Freundlich isotherm**		
	Q_0	b	R^2	K_F	1/n	R^2
FA	2.73058	0.00925	0.97616	0.0409	0.96519	0.98624
AAFA	32.62319	0.04834	0.93557	1.51341	0.19946	0.96886

CONCLUSION

This study demonstrates the promising potential of alkali-activated fly ash as an effective adsorbent for the removal of yttrium from moderately acidic aqueous solutions. Surface characterization confirmed that modification was successful, leading to improved performance in adsorption experiments. The adsorption process followed a pseudo-second order kinetic model, while equilibrium adsorption was well described by the Freundlich model. These findings underscore the viability of alkali-activated fly ash as a potential candidate for yttrium separation, offering a sustainable and efficient solution for addressing yttrium recycling. Further research can explore optimization strategies to enhance its adsorption capacity and applicability in practical settings.

Acknowledgment

This research was funded by the Science Fund of the Republic of Serbia, Program Ideas, GRANT No 7743343, Serbian Industrial Waste towards Sustainable Environment: Resource of Strategic Elements and Removal Agent for Pollutants - SIW4SE.

REFERENCES

[1] P. K. De Maeijer, B. Craeye, R. Snellings, H. Kazemi-Kamyab, M. Loots, K. Janssens, G. Nuyts, Constr. Build. Mater., 263 (2020) 120493.
[2] M. Medykowska, M. Wiśniewska, K. Szewczuk-Karpisz, R. Panek, M, Franus, Clean. Techn. Environ. Policy., 25 (2023) 1133.
[3] U. O. Aigbe, K. E. Ukhurebor, R. B. Onyancha, O. A. Osibote, H. Darmokoesoemo, H. S. Kusuma, J. Mater. Res. Technol., 14 (2021) 2751.
[4] J.X. Lin, S.L. Zhan, M.H. Fang, X.Q. Qian, H. Yang, J. Environ. Manage., 87 (2008) 193.
[5] J. Cui, Q. Wang, J. Gao, Y. Guo, F. Cheng, Chin. J. Chem. Eng., 47 (2022) 155.
[6] Z. Zhang, H. Wang, J. L. Provis, J. Sustain. Cem.-Based Mater., 1 (2012) 154.

HYDROTHERMAL CARBONS MODIFIED WITH GRAPHENE OXIDE AS ADSORBENTS FOR METHYLENE BLUE

M. Vukčević [1], M. Maletić [2], D. Stojanović [1] and P. Uskoković [1]

[1]*University of Belgrade, Faculty of Technology and Metallurgy, Karnegijeva 4, 11000 Belgrade, Serbia (marijab@tmf.bg.ac.rs)*
[2]*Innovation Center of Faculty of Technology and Metallurgy, Karnegijeva 4, 11000 Belgrade, Serbia.*

DOI: https://doi.org/10.46793/Phys.Chem24II.471V

ABSTRACT
Hydrothermal carbons as adsorbents for methylene blue removal from water, were synthesized starting from glucose and sawdust as carbon precursors. In an attempt to improve surface and adsorption properties, obtained hydrothermal carbons were modified by the addition of graphene oxide in the reaction mixture. Characterization of examined samples was performed by scanning electron microscopy, determination of surface area and porosity, and Fourier transform infrared spectroscopy. Modification with graphene oxide caused differences in the morphology, specific surface area, and porosity, but did not introduce new groups on the surface of hydrothermal carbons. Although modification improved the adsorption properties of glucose-based hydrothermal carbons, samples obtained from sawdust showed the highest adsorption capacities and faster adsorption process that can be described by pseudo-second order kinetic and Langmuir isotherm models.

INTRODUCTION
The global demand for sustainable and efficient methods of water purification has intensified in recent years due to increasing environmental concerns and population growth. Among various contaminants, organic dyes pose a significant threat to aquatic ecosystems and human health. Methylene blue (MB), a common dye utilized in textile industries, is known for its toxic and carcinogenic properties. Thus, the development of cost-effective and eco-friendly strategies for the removal of MB from wastewater is imperative. Hydrothermal carbonization (HTC) has emerged as a promising technique for converting biomass into hydrochar under moderate temperature and pressure conditions. This process offers several advantages, including energy efficiency, simplicity, and environmental friendliness. By subjecting glucose and lignocellulosic biomass to hydrothermal conditions, carbonaceous materials with tailored properties can be obtained, making them suitable candidates for various applications, including adsorption [1,2]. The modification of hydrothermal carbons with graphene oxide (GO) represents a novel approach to enhance their adsorption capabilities. GO, a two-dimensional carbonaceous material derived from graphite possesses abundant functional groups such as hydroxyl, carboxyl, and epoxy, which can interact with organic pollutants via π-π stacking, electrostatic interactions, and hydrogen bonding. Incorporating GO into hydrothermal carbons not only improves their structural integrity but also enhances their surface area, porosity, and surface chemistry, thereby enhancing their adsorption performance towards MB.
The addition of GO during the synthesis of hydrothermal carbons influences their structural, surface, and adsorption properties [3]. The presence of GO nanosheets within the carbon matrix promotes the formation of a hierarchical porous structure, leading to increased surface area and pore volume. Moreover, the functional groups on GO facilitate the adsorption of MB molecules through electrostatic interactions and π-π stacking, thereby enhancing the overall adsorption capacity of the

composite material [4]. Several studies have investigated the synthesis and characterization of hydrothermal carbons modified with GO for the removal of various pollutants from water. For instance, Ai and Jiang [5] used a hydrothermal approach for the production of a cylindrical graphene–carbon nanotube hybrid that showed a good adsorption performance for the removal of methylene blue from an aqueous solution.

The aim of this work was the synthesis, characterization, and application of hydrothermal carbons modified with graphene oxide as efficient adsorbents for methylene blue removal from water. We investigate the influence of starting material, as well as the addition of graphene oxide on the structural, surface, and adsorption properties of hydrothermal carbons. Our findings contribute to the development of sustainable and cost-effective adsorbents for water purification applications, addressing the pressing environmental challenges associated with dye contamination in aquatic environments.

METHODS

Hydrothermal carbons were produced using D(+)-Glucose and beech sawdust as carbon precursors. To produce glucose-based hydrothermal carbon (sample marked as HTC), a precursor solution was prepared by dissolving 6 g of glucose into 45 cm^3 of deionized water. Sawdust-based hydrothermal carbon (sample marked as HTC_p) was produced from a precursor solution containing 5 g of beech sawdust, 0.011 g of citric acid (used as a catalyst), and 40 cm^3 of deionized water. For the preparation of both samples, precursor solution was placed into a 50 cm^3 Teflon-lined stainless-steel autoclave. After sealing, the autoclave was heated in the programmable oven for 15 h at 180°C. The obtained solid powders were abundantly washed with deionized water and alcohol and then dried at 80°C for 24h. Additionally, by adding 0.07 g of graphene oxide into both precursor solutions and using the same production conditions, GO-doped glucose-based hydrothermal carbon (sample marked as HTC/GO) and GO-doped sawdust-based hydrothermal carbon (sample marked as HTC_p/GO) were obtained.

The morphological characteristics of examined samples were assessed by scanning electron microscopy (Mira3, Tescan and SEM JEOL JSM-6610LV). FTIR spectra of the samples, within a range of 400-4000 cm^{-1}, were recorded using a Nicolet™ iS™ 10 FT-IR Spectrometer (Thermo Fisher Scientific). Specific surface area and porous properties were determined using Micromeritics ASAP 2020, Surface and Porosity Analyzer (Micromeritics Instrument Corporation, U.S.). From the data obtained from N_2 adsorption and desorption isotherms, and using manufacturer software, specific surface area (S_{BET}), mean pore diameter (D_m), as well as micropore (V_{micro}), mesopore (V_{meso}) and total (V_{total}) pore volume, were obtained.

The adsorption experiments were conducted in a batch system with constant shaking (150rpm) to examine the influence of contact time and initial adsorbate concentration on adsorption capacities. Adsorption kinetics was examined by soaking 0.1 g of tested samples in 50 cm^3 of MB solution (20 mg/dm^3), and the concentration of MB was measured in defined time (5, 15, 30, 60, 120 and 180 minutes) by UV/Vis spectrophotometer. The influence of initial MB concentration (5, 7.5, 10 and 20 mg/dm^3) was examined using 0.025 g of adsorbents and 12.5 cm^3 of MB solution.

RESULTS AND DISCUSSION

The structure and surface morphology of unmodified, and hydrothermal carbons modified with GO are shown in **Figure 1**. Sample HTC (**Figure 1a**) exhibits the characteristic microspherical structure, and a few of these microspheres are also visible in the sample HTC_p (**Figure 1c**), which retains the precursor structure. The modification with GO has a large impact on the structure of hydrothermal carbons, leading to the formation of a large number of flakes in the structure of HTC/GO (**Figure 1b**), and pores and cavities on the HTC_p/GO surface (**Figure 1d**).

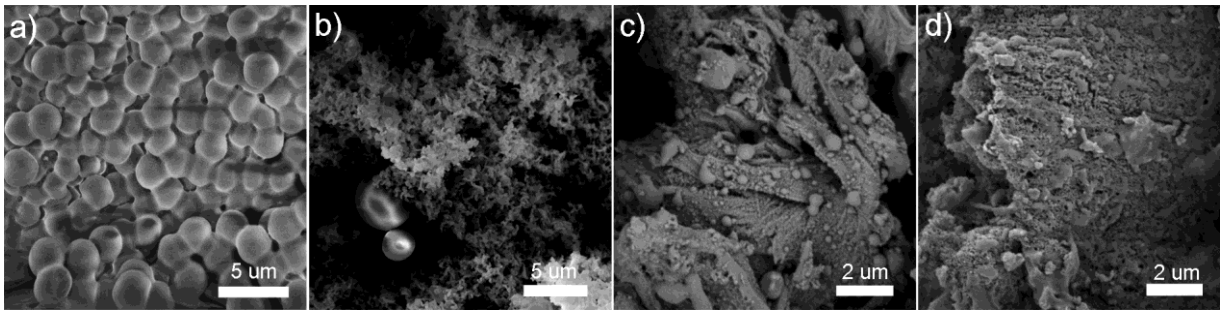


Figure 1. SEM photographs of a) HTC, b) HTC/GO, c) HTC_p and d) HTC_p/GO.

According to the results shown in **Table 1**, all examined samples are mesoporous with the mean diameter ranging from 3.99 to 13.06 nm.

Modification with GO has a different influence on the specific surface area and porosity of hydrothermal carbons, depending on the type of precursor: for the hydrothermal carbon obtained from glucose addition of GO in the reaction mixture leads to the decrease in the specific surface area and porosity, while for sawdust based hydrothermal carbon modification with GO increase the S_{BET} and porosity.

Table 1. Textural properties of unmodified and GO modified hydrothermal carbons.

Sample	S_{BET}, m^2/g	V_{total}, cm^3/g	V_{meso}, cm^3/g	V_{micro}, cm^3/g	D_m, nm
HTC	55.1	0.0739	0.0687	0.0143	4.05
HTC/GO	8.10	0.0208	0.0190	0.0026	13.06
HTC_p	46.4	0.0635	0.0597	0.0119	4.08
HTC_p/GO	54.6	0.0729	0.0681	0.0134	3.99

Unlike hydrothermal carbon obtained from glucose (HTC), hydrothermal carbon obtained from sawdust (HTCp) shows more intense peaks (**Figure 2**) in the areas of 3500-3300 cm^{-1} (stretching vibrations of the O-H bond of hydroxyl and carboxyl groups) and 3000-2800 cm^{-1} (stretching vibrations of the aliphatic C-H bond). For the samples HTC_p and HTC_p/GO the intensity of the peak at 1710 cm^{-1} (C=O vibrations indicating carbonyl, quinone, ester, and carboxyl groups) is lower compared to the peak at 1620 cm^{-1} (vibrations of the aromatic C=C bond), which indicates a higher degree of aromatization than for HTC sample. In the region 1500-1000 cm^{-1} (originating from C-O, C-O-C, C-C vibrations, indicating the presence of different groups: ether, ester, lactone) HTC_p shows a large number of peaks significantly more intense than HTC. These peaks most likely originate from the chemical constituents of sawdust (cellulose, hemicelluloses, and lignin) that are not completely degraded in the hydrothermal carbonization process. Modification with GO does not affect the type of the surface oxygen groups since there is no additional peaks on FTIR spectra of modified samples (HTC/GO, and HTC_p/GO). Accordingly, modification with GO does not bring a significant improvement in adsorption efficiency since surface oxygen groups represent active sites for adsorption. Nevertheless, for a lower initial concentration of MB, the GO modification of HTC increases the adsorption capacity (**Figure 3a**). Kinetic data obtained for all examined samples (**Table 2**) fits well with the pseudo-second order model and adsorption of MB onto HTC_p and HTC_p/GO is a fast process that reaches equilibrium after 5 minutes (**Figure 3a**). Additionally,

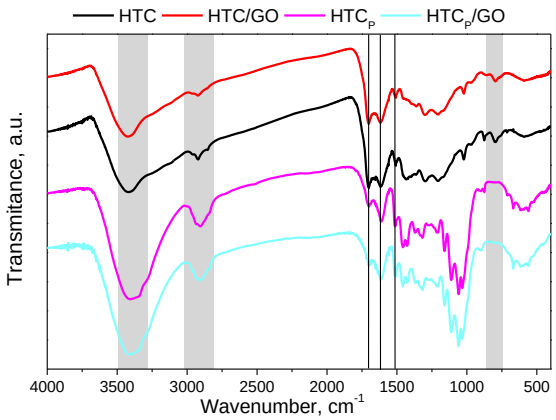


Figure 2. FTIR spectra examined samples.

samples HTC_p and HTC_p/GO show higher adsorption capacities in the examined range of initial MB concentrations, while the adsorption process at equilibrium on all examined samples can be described by the Langmuir isotherm model (**Figure 3b**).

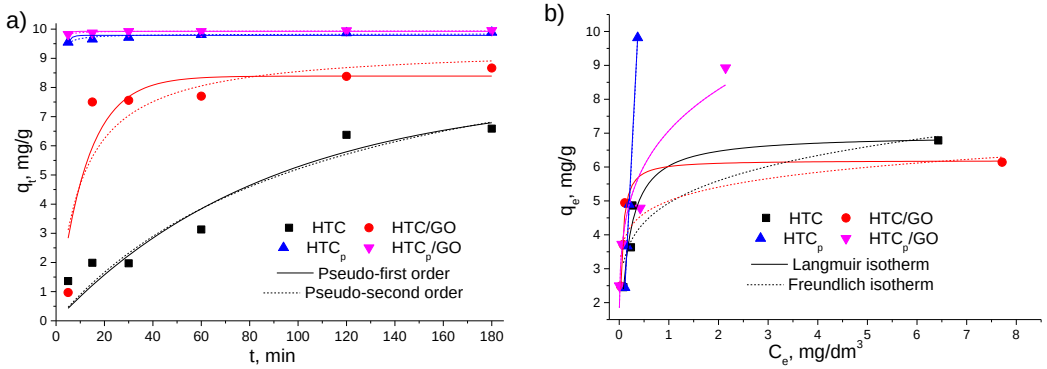


Figure 3. The influence of a) contact time and b) initial MB concentration on adsorption.

Table 2. Kinetic parameters for MB adsorption on unmodified and GO modified hydrothermal carbons.

Sample	Pseudo-first order			Pseudo-second order			$q_{e,exp}$, mg/g
	$q_{e,cal}$, mg/g	k_1, min^{-1}	R^2	$q_{e,cal}$, mg/g	k_2, g/(mg min)	R^2	
HTC	7.82	0.011	0.88817	11.12	0.001	0.88931	6.59
HTC/GO	8.39	0.082	0.81030	9.41	0.010	0.74113	8.67
HTC_p	9.79	0.742	0.43055	9.84	0.601	0.76502	9.89
HTC_p/GO	9.92	0.918	0.58137	9.94	1.534	0.87136	9.95

CONCLUSION

Hydrothermal carbons were obtained using two carbon precursors, glucose and sawdust, while the addition of graphene oxide in the reaction mixture was used for the modification of material characteristics. Applied modification with graphene oxide caused differences in the morphology, specific surface area, and porosity, but did not affect the distribution of surface oxygen groups. These changes slightly improved the adsorption properties of glucose-based hydrothermal carbon, while in the case of more efficient sawdust-based hydrothermal carbon GO modification did not influence methylene blue adsorption. Besides the much higher adsorption capacities, sawdust-based hydrothermal carbons enabled very fast methylene blue adsorption. It was found that the adsorption of methylene blue on all hydrothermal carbons follows the pseudo-second order kinetic, while equilibrium adsorption processes can be described by the Langmuir isotherm model.

Acknowledgment

This work was supported by the Ministry of Science, Technological Development and Innovation of the Republic of Serbia (Contract No. 451-03-65/2024-03/200135 and 451-03-66/2024-03/200287).

REFERENCES

[1] T. Wanga, Y. Zhaia, Y. Zhu, C. Lia, G. Zeng, Renew. Sustain. Energy Rev., 90 (2018) 223.
[2] K. Czerwinska, M. Sliz, M. Wilk, Renew. Sustain. Energy Rev., 154 (2022) 111873.
[3] Y. Wang, L. Jiang, ACS Sustainable Chem. Eng., 5 (2017) 5588.
[4] B. Anegbe, I. H. Ifijen, M. Maliki, I. E. Uwidia, A. I. Aigbodion, Environ. Sci. Eur., 36 (2024) 15.
[5] L. Ai, J. Jiang, Chem. Eng. J. 192 (2012) 156.

IDENTIFICATION AND ALLOCATION OF HEAVY METAL POLLUTION SOURCES IN GROUNDWATER NEAR LADJEVCI AIRPORT USING POSITIVE MATRIX FACTORIZATION RECEPTOR MODEL

J. Vesković, and A. Onjia

University of Belgrade, Faculty of Technology and Metallurgy, Karnegijeva 4, 11120 Belgrade, Serbia. (jveskovic@tmf.bg.ac.rs)

DOI: https://doi.org/10.46793/Phys.Chem24II.475V

ABSTRACT

This study investigated sources of heavy metal pollution in groundwater near Ladjevci airport in Serbia. Groundwater was collected from 42 monitoring wells and analyzed for nine heavy metals (As, Cd, Pb, Cr, Cu, Ni, Sb, Zn, and Hg). Positive matrix factorization (PMF) receptor model was utilized to identify and apportion groundwater pollution sources. The results showed that traffic and road construction-related activities, agricultural practices, and natural/geogenic processes were the three main factors affecting heavy metal concentration in groundwater. The leading cause of groundwater pollution was natural/geogenic processes, contributing 35.0%, while agricultural practices and traffic and road construction activities contributed 33.3% and 31.7%, respectively.

INTRODUCTION

Groundwater is the primary drinking water source for people around the world [1,2]. However, there remains a significant challenge as 884 million people globally do not have adequate access to uncontaminated and safe drinking water [3]. Heavy metals including, but not limited to, antimony (Sb), lead (Pb), nickel (Ni), copper (Cu), zinc (Zn), arsenic (As), chromium (Cr), cadmium (Cd), and mercury (Hg), are one of the most concerning aspects of groundwater pollution [4,5].

These elements are naturally present in in the groundwater, resulting from pedogenic processes of soil. However, anthropogenic activities, such as agricultural practices and industrial activities, also represent their sources [6]. Given their toxic properties and harmful effect on human health [7], it is crucial to identify possible sources of their origin in order to successfully manage heavy metal pollution in groundwater.

METHODS

Study area and chemical analysis

The study area is located near Ladjevci airport in central Serbia, in the valley of the West Morava River. Additionally, beginning 2019, the study area has included a road construction site (Figure 1). Groundwater was sampled from 42 monitoring wells in 1-L polypropylene bottles previously washed with deionized water. To maintain heavy metals in solution, each sample was acidified with nitric acid (pH < 2) after being filtered through a 0.45 μm membrane. Afterwards, samples were brought to the laboratory for heavy metal examination. The samples were analyzed for As, Cd, Pb, Cr, Cu, Ni, Sb, Zn, and Hg. To determine concentration of heavy metals, excluding Hg, ICP-MS (iCAP Qc, Thermo Scientific, USA) was used, while the Hg concentration is measured using a direct mercury analyzer (DMA80, Milestone, Italy).

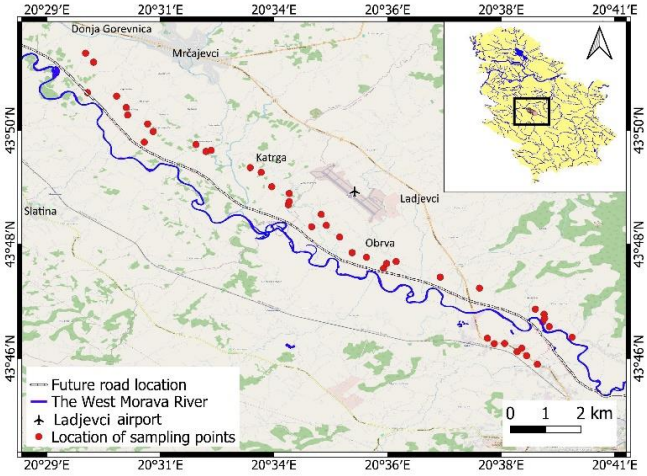


Figure 1. Study area.

Positive matrix factorization model

In this study positive matrix factorization (PMF) receptor model was utilized to examine the origin of heavy metals in groundwater. The model is represented by the following equations [1].

$$X_{ij} = \sum_{k=1}^{p} g_{ik} f_{kj} + e_{ij} \tag{1}$$

$$Q = \sum_{i=1}^{n} \sum_{j=1}^{m} \left(\frac{e_{ij}}{u_{ij}} \right)^2 \tag{2}$$

where X_{ij}, g_{ik}, f_{jk}, e_{ij}, Q, and u_{ij} represent the original data set, source contribution matrix, source profile matrix, residual matrix, objective function, and uncertainty, respectively. The indices i, j, and k refer to each sample, each heavy metal, and each pollution source, respectively, with n being the number of samples, m being the number of heavy metals, and p being the number of pollution sources.

The calculation of u_{ij} involves the concentration of heavy metal (c), method detection limit (MDL), and error fraction (ef). The u_{ij} is computed using equation (3) if the heavy metal concentration is higher than MDL. On the contrary, the equation (4) is used to determine u_{ij}.

$$u_{ij} = \sqrt{(ef \times c)^2 + (0.5 \times MDL)^2} \tag{3}$$

$$u_{ij} = \frac{5}{6} \times MDL \tag{4}$$

The PMF 5.0 software is used to perform the computations [8].

RESULTS AND DISCUSSION

Three major sources of pollution were found by the PMF model: Factor 1, Factor 2, and Factor 3. These sources contributed 31.7%, 33.3%, 35.0% of the total pollution, respectively (Figure 2a).

Factor 1 is characterized by Cd (76.8%), Zn (65.7%), and Pb (47.3%) (Figure 2b). Pb has long been recognized as a major component of traffic-related pollution, with approximately two-thirds of global Pb emissions resulting from vehicle exhaust [9]. Furthermore, Cd is found in tires, while Zn

is linked to tire hardeners and exhaust emissions [7]. The ongoing construction of a new highway in the study area, involving heavy machinery, further contributes to the elevated levels of Cd, Zn, and Pb. Additionally, air traffic significantly impacts environmental pollution, as evidenced by higher concentrations of heavy metals in soil near airports [10]. The existence of Ladjevci airport suggests that air traffic may also be contributing to these metal levels. Therefore, Factor 1 can be interpreted as pollution from traffic and road construction-related activities.

The predominance of Hg (75.9%), Sb (58.2%), and Ni (55.5%) in Factor 2 suggests a link to agricultural activities. Previous research [11] have demonstrated that chemical fertilizers and pesticides contribute to the accumulation of Ni and Sb in soil. Furthermore, Hg is commonly found in pesticides and herbicides [12]. The latest agricultural census in Serbia reveals that artificial fertilizers and pesticides are widely used within the study area, with approximately 70% of agricultural land treated with mineral fertilizers and pesticides [13]. Consequently, Factor 2 could be interpreted as an indicator of agricultural pollution.

Dominated by Cr (71.6%), Cu (70.2%), and As (50.9%), Factor 3 reflects influences from geological and natural processes. It is reported that Cr and As levels are primarily controlled by their widespread presence in the earth's crust [14]. Additionally, the presence of Cu in soil and its development through pedogenic processes indicate its natural origin. Consequently, Factor 3 can be characterized as a natural/geogenic pollution source.

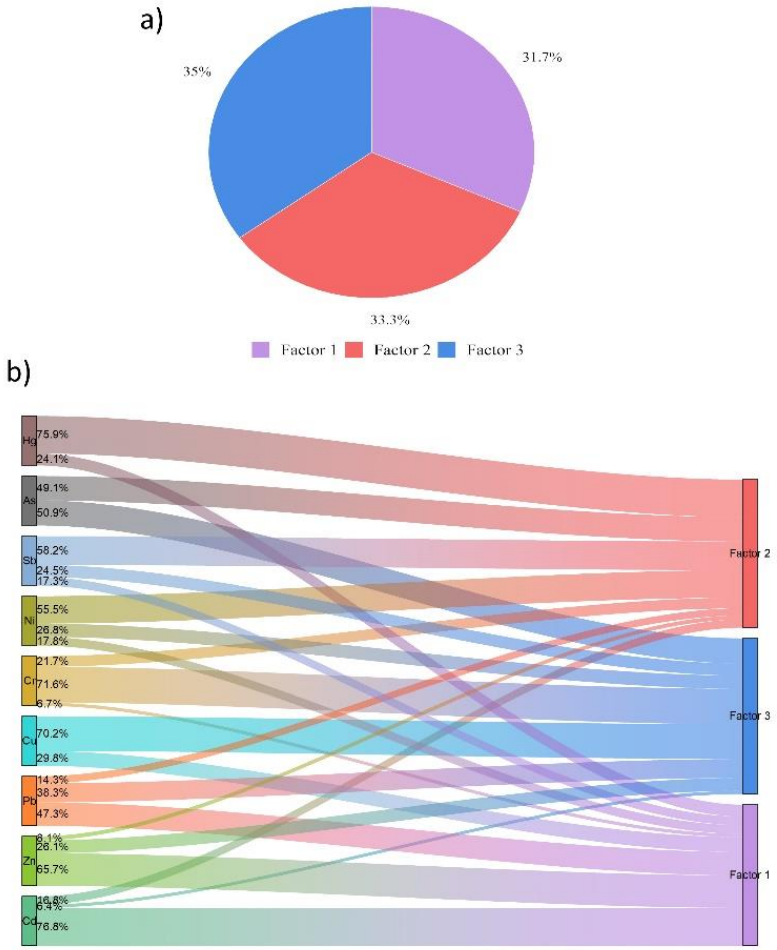


Figure 2. The overall pollution contribution by each factor (a) and contribution of each factor to the concentration of each heavy metal (b).

CONCLUSION

The PMF receptor model was implemented in this study to identify groundwater pollution sources of heavy metals. Results showed that Cd, Zn, and Pb were mostly sourced from traffic and road-construction activities, while Hg, Sb, and Ni mainly originated from agricultural practices. Natural/geogenic processes were mainly responsible for the levels of Cr, Cu, and As in groundwater. Furthermore, natural pollution was identified as the main contributor to the overall pollution, followed by pollution from agricultural practices and traffic and road-construction activities. These findings can serve as important information in managing groundwater pollution in the study area.

Acknowledgment

This work was supported by the Ministry of Education, Science and Technological Development of the Republic of Serbia (grant no 451-03-65/2024-03/200135).

REFERENCES

[1] J. Vesković, I. Deršek-Timotić, M. Lučić, A. Miletić, M. Đolić, S. Ražić, A. Onjia, Mar. Poll. Bul., 201 (2024) 116277.
[2] J. Vesković, M. Lučić, M. Ristić, A. Perić-Grujić, A. Onjia, Toxics, 12 (2024) 62.
[3] W. Han, Y. Pan, E. Welsch, X. Liu, J. Li, S. Xu, H. Peng, F. Wang, X. Li, H. Shi, W. Chen, C. Huang, Ecotoxicol. Environ. Saf., 267 (2023) 115642.
[4] J. Vesković, S. Bulatović, A. Miletić, T. Tadić, B. Marković, A. Nastasović, A. Onjia, Stoch. Environ. Res. Risk Assess., 38 (2024) 1597.
[5] I. Tomašek, H. Mouri, A. Dille, G. Bennett, P. Bhattacharya, N. Brion, M. Elskens, K. Fontijn, Y. Gao, P.K. Gevera, J. Ijumulana, M. Kisaka, M. Leermakers, C. Shemsanga, K. Walraevens, J. Wragg, M. Kervyn, Sci. Total Environ., 807 (2022) 150487.
[6] E.T.W. Nachana'a Timothy, Chemistry, 3 (2019) 72.
[7] J. Huang, Y. Wu, J. Sun, X. Li, X. Geng, M. Zhao, T. Sun, Z. Fan, J. Hazard. Mater., 415 (2021) 125629.
[8] USEPA, Positive Matrix Factorization (PMF) 5.0 Fundamentals and User Guide, (2014).
[9] J.O. Olowoyo, N. Lion, T. Unathi, O.M. Oladeji, IJERPH, 19 (2022) 10238.
[10] M. Brtnický, V. Pecina, T. Baltazár, M. Vašinová Galiová, L. Baláková, A. Bęś, M. Radziemska, Sustainability, 12 (2020) 7224.
[11] L. Liu, X. Xu, J. Han, J.-M. Zhu, S. Li, L. Liang, P. Wu, Q. Wu, G. Qiu, Process Saf. Environ. Prot., 166 (2022) 669–681.
[12] Z. Feng, L. Deng, Y. Guo, G. Guo, L. Wang, G. Zhou, Y. Huan, T. Liang, Environ. Geochem. Health, 45 (2023) 4057–4069.
[13] D. Marković, Republički zavod za statistiku, Beograd, 2013.
[14] S. Pervez, P. Dugga, M.N. Siddiqui, S. Bano, M. Verma, C. Candeias, A. Mishra, S.R. Verma, A. Tamrakar, I. Karbhal, M.K. Deb, K. Shrivas, Y. Pervez, R.K. Jha, Groundw. Sustain. Dev., 14 (2021) 100628.

REMOVAL OF RADIOACTIVE IODINE USING Zr-BASED MOF UiO-66

Đ. Petrović [1], Z. Eraković [2], K.Kumrić[1], S.Ilić-Stojanović[2], K.Stanković[1], R.Vujasin[1] and M.Eregić[1]

[1] Vinča Institute of Nuclear Sciences, Department of Physics, University of Belgrade, Mike Petrovića Alasa 12-14, 11351 Vinča, Belgrade (djpetrovic@vin.bg.ac.rs).
[2] University of Niš, Faculty of Technology, Bulevar Oslobođenja 124, 16000 Leskovac, Serbia.

DOI: https://doi.org/10.46793/Phys.Chem24II.479P

ABSTRACT

Increasing water pollution, such as contamination with heavy metals, has become a pressing issue due to their omnipresence in the environment. In recent times, metal-organic frameworks (MOFs) based adsorbents, micro- and nano-porous materials with crystalline structures with high specific surface areas, adjustable pore sizes, shapes, and easy modifications, have attracted much attention. The present study investigated the potential application of Zr-based MOF UiO-66 for removing radioactive iodine from aqueous solutions. In the batch experiment, 25 cm^3 of aqueous solution containing 10 mg dm^{-3} NaI was brought into contact with 10 mg of UiO-66. The results showed that the highest removal efficiency of radioactive iodine was obtained in the pH range from 4 to 8 and that the removal of 88% of iodine was achieved after 40 min. Complete removal of radioactive iodine from aqueous solutions was achieved after 210 min.

INTRODUCTION

Iodine ion (I^-), as a typical toxic anion contaminant, tends to accumulate in the thyroid gland of the animal body via the food chain, leading to an increase in thyroid cancer, leukemia, and metabolic disorders. Radioactive iodine-131 (^{131}I, I-131) is an important radioisotope of iodine with a radioactive decay half-life of about eight days [1]. ^{131}I is a major fission product of uranium and plutonium, comprising nearly 3%wt of the total fission products. It is a reliable indicator of a nuclear accident because it occurs in all uncontrolled nuclear explosions and is easily detected due to its volatility. In the first weeks of the Chernobyl disaster and the Fukushima nuclear crisis, a large fraction of the contamination hazard was ^{131}I [2]. Also, ^{131}I was a significant contributor to the health hazards from open-air atomic bomb testing in the 1950s. ^{131}I is one of the oldest radiotracers used in nuclear medicine, having been in use for over 50 years. It is used in the diagnosis, treatment, and theranostic approach to thyroid lesions. Small doses (MBq) are used for diagnostic scans, while higher doses (GBq) are used in radionuclide therapy.

The potential impact of this research is significant, as it could lead to the development of a novel adsorption green material that efficiently removes radioactive iodine from wastewater, originating from a patient's urine [3].

To remove I^- from aqueous solution, various trials have been conducted using different methods such as surface adsorption, ion exchange, chemical precipitation, solvent extraction, and membrane separation, among which adsorption stands out because of its efficiency and economic competitiveness. As a new generation of promising adsorbent materials, metal−organic frameworks (MOFs) have gained wide attention [4].

Adsorbents based on the MOFs, a relatively new class of micro- and nano-porous materials with crystalline structures and excellent properties, such as high specific surface areas, adjustable pore sizes, shapes and easy modifications, have attracted much attention for the adsorptive removal of

awide range of pollutants from the environment, including dyes, pesticides, pharmaceutical products, heavy metals, radioactive metals, and toxic gases.

This paper presents the results of radioactive iodine sorption on Zr-based MOF UiO-66.

MATERIALS AND METHODS

Chemicals used in the experiments, NaOH, HNO_3, and NaI, were purchased from Sigma-Aldrich (USA). All the chemicals were analytical reagent grade and used without further purification. Radioactive ^{131}I was purchased from the National Centre for Nuclear Research – Radioisotope Centre POLATOM, Poland.

UiO-66 xerogel was synthesised at room temperature by adding terephthalic acid and zirconium oxychloride octahydrate to methanol, and the mixture was stirred at ambient temperature. The obtained white suspension was centrifuged and heated in an oven at 80 °C to obtain white xerogel product, which was washed with dimethylformamide and methanol and then dried at room temperature. The obtained material had a high porosity. The BET surface area and the total pore volume were 1132 m^2/g and 0.78 cm^3/g. Also, immersing UiO-66 in water results in the release of the OH group, with the Zr node remaining positively charged, which results in a positively charged surface of materials [5].

The study of ^{131}I adsorption onto Zr-based MOF, UiO-66 was performed at room temperature by batch technique in hot cells located in Vinča Institute of Nuclear Sciences, National Institute of the Republic of Serbia, according to the following procedure: 10 mg of UiO-66 was mixed with 25 cm^3 of aqueous solution containing 10 mg dm^{-3} NaI. As a radiotracer, radioactive ^{131}I ($Na^{131}I$) of about 37 kBq was added. pH values were adjusted using 0.01M NaOH and 0.01M HNO_3.

The mixtures in closed Erlenmeyer flasks were shaken for 240 min at a stirring speed of 150 rpm. After that, the liquid phases were separated from the solid phases by filtration through a 0.45 μm membrane filter. The initial and residual $I^-/^{131}I$ radioactive concentrations were measured using a Capintec CRC-15 dose calibrator (Capintec, USA), and their difference was taken into account when recalculating the sorption on MOF. All the experiments were carried out in triplicate and mean values were taken for further calculations.

RESULTS AND DISCUSSION

The obtained experimental data were used for analysis and evaluation of the UiO-66 ability to remove radioactive iodine contaminants from aqueous solutions. All results are given in graphical forms as the mean of three repeated measurements.

Effect of initial pH: The pH of the solution is one of the most important adsorption parameters that may affect the surface properties of the adsorbent. The ionic forms of iodine in the solution depend on pH value too. In order to study the influence of the pH initial solution of iodine removal on MOF sorbent, the experiments were performed in the pH range of 2 to 10. The removal efficiency of iodine, *E* (%), significantly increases from pH 2 to 4, as shown in Fig.1a. The maximum efficiency was achieved in the pH range from 4-8, and the sorption efficiency ranges were from 95-97%. By increasing the pH value to pH 9-10, efficiency falls abruptly. Graphical presentation of results contains bars with added values of standard deviation. Various chemical forms of iodine, which depend on pH and Eh conditions, can be an explanation for such behavior. At lower pH (up to pH 4), the dominant species is molecular iodine (I_2), while at higher pH values, the domination of anion iodine (I^-) has been proven [6]. That is the reason why the positively charged surface of UiO-66 strongly electrostatically attracted negatively charged iodine anions presented in the solution.

Effect of contact time: The effect of contact time on the adsorption of I^- onto UiO-66 was studied at an initial iodine concentration of 10 mg dm^{-3} at pH 6, and the results were exhibited in

Fig. 1b. With increasing contact time up to 40 min, the adsorption efficiency sharply increased up to 88%, then increased at a slower rate and, finally, attained the equilibrium value within 210 min of contact. These results indicated that 97% of the maximum adsorption capacity was reached within the initially rapid stage, suggesting fast kinetics.

a)

b)

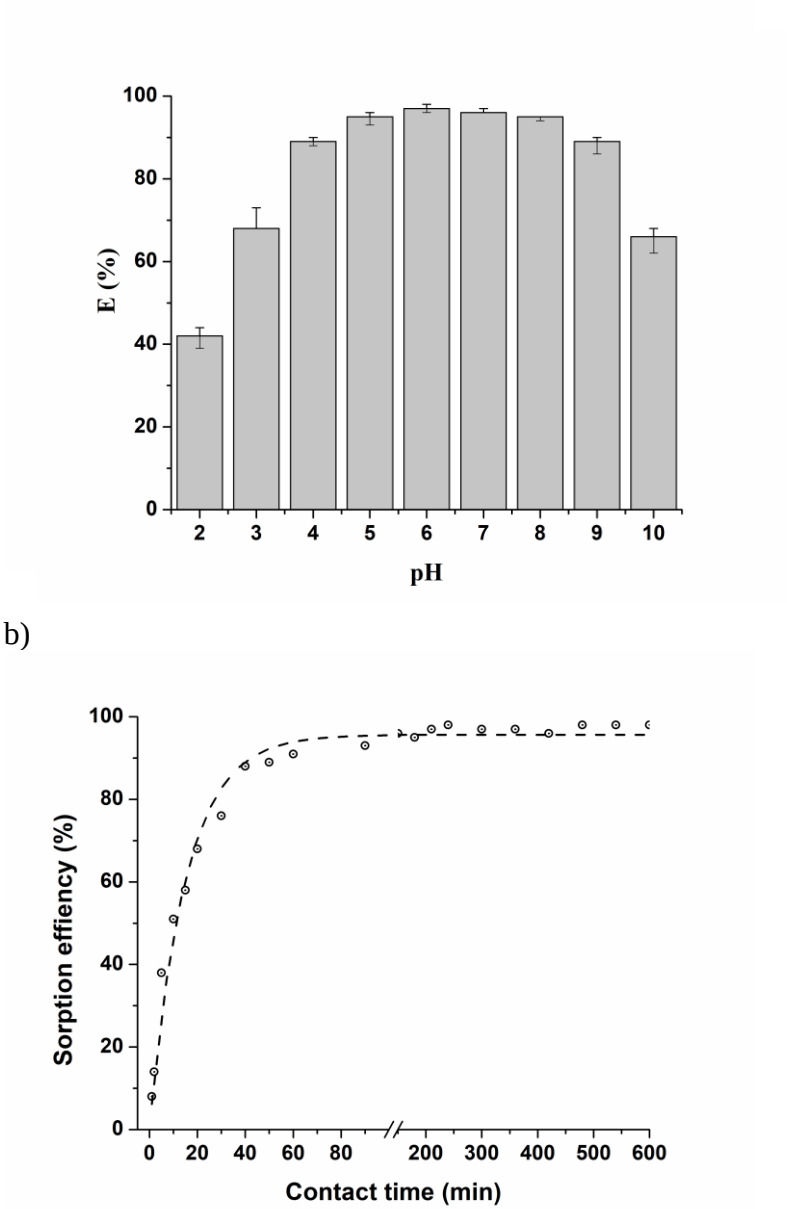


Figure 1. a) Effect of the initial solution pH on the removal of adsorption of I^- onto UiO-66. Conditions: Initial iodine concentration: 10 mg dm^{-3} in 25 cm^3 NaI water solution; UiO-66 xerogel dosage: 10 mg; Contact time: 240 min. b) Effect of contact time on the sorption of ^{131}I. Conditions: Initial iodine concentration: 10 mg dm^{-3} in 25 cm^3 NaI water solution; UiO-66 xerogel dosage: 10 mg; pH = 6.

CONCLUSION

In this paper, the ability of UiO-66 to remove I^- was investigated. The obtained results showed that the maximum removal efficiency of I^- was achieved in the pH range of 4-8. Adsorption reactions of iodine on UiO-66 take place very fast so that in just 40 minutes, sorption of 88% was achieved, while for 210 minutes, sorption was almost complete (97%). The results presented in this study indicate that UiO-66 can be regarded as an efficient adsorbent, which could be potentially applied in the treatment of wastewater containing radioactive iodine. Further experiments will be oriented toward its application in real systems.

Acknowledgment

This work was supported by the Ministry of Education, Science and Technological Development of the Republic of Serbia (grant no 451-03-66/2024-03/200017, 451-03-65/2024-03/200133 and 451-03-66/2024-03/200133).

REFERENCES

[1] T. Kubota, S. Fukutani, T. Ohta, Y. Mahara, J. Radioanal. Nucl. Chem., 296 (2013) 981.
[2] J. Kang, F. Cintron-Colon, Hy. Kim, J. Kim, T. Varga, Y. Du, O. Qafoku, W Um, T. G. Levitskaia, Chem. Eng. J., 430 (2022) 132788.
[3] El-Khatib, A.M., Bondouk, I.I., Omar, K.M. Sci. Rep. 14 (2024) 4242.
[4] Y. Cai-Xia, L. Xue-Jing, Z. Jia-Shu, Y. Dong-Jiang, L. Ai-Ping, Z. Yan-Li, L. Xiao-Qiang, L. Lei-Lei, Inorg. Chem., 61 (2022) 13883.
[5] Li, F. Wu, Y. U.S. Patent 2021, US 11111255B1.
[6] A. Artasensi, S. Mazzotta, L. Fumagalli, Antibiotics 10 (2021) 613.

HUMAN HEALTH RISK ASSESSMENT OF ARTIFICIAL SWEETENERS DETECTED IN WELL WATER

E. Gvozdić [1], I. Matić Bujagić [2], T. Đurkić [3] and S. Grujić [3]

[1]*Innovation Centre of the Faculty of Technology and Metallurgy, Karnegijeva 4, 11000 Belgrade, Serbia*
[2]*Academy of Applied Technical Studies Belgrade, Polytechnic College, Katarine Ambrozić 3, 11000 Belgrade, Serbia*
[3]*University of Belgrade, Faculty of Technology and Metallurgy, Karnegijeva 4, 11000 Belgrade, Serbia (svetlana.grujic@tmf.bg.ac.rs)*

DOI: https://doi.org/10.46793/Phys.Chem24II.483G

ABSTRACT
Artificial sweeteners are emerging contaminants that are widely detected in natural waters as a result of their widespread use in the food industry and continual release into aquatic ecosystems via municipal wastewater. Recent research has shown that frequent consumption of these compounds can cause negative effects on human health. In this paper, human health risk assessment for possible chronic exposure to sweeteners detected in groundwater wells in Belgrade and the surrounding area was performed. The results showed the widespread presence of acesulfame and sucralose in well water, at concentrations up to 80 ng L^{-1} and 25 ng L^{-1}, respectively. According to US EPA risk characterization guidance and calculated hazard quotients, the detected levels of sweeteners do not pose a threat to human health. However, the cumulative effect of all ingested sweeteners and other food additives should be considered, as well as their potential carcinogenicity, in future long-term health risk assessments.

INTRODUCTION
Artificial sweeteners are synthetic sugar substitutes used in sweets, beverages, medicines etc., that do not have caloric value. These compounds are metabolically inert and are excreted mainly in the unchanged form [1]. Although they are widely used in food and pharmaceutical industry, some scientific research has shown that consumption of artificial sweeteners has been increasingly associated with negative health outcomes, such as obesity, type 2 diabetes and metabolic syndrome [2]. Municipal wastewater is the main source of these substances in the environment, with high concentrations recorded in natural waters worldwide [3,4]. Artificial sweeteners belong to a new class of emerging contaminants with high persistence and negative effects on aquatic organisms [4].

Some studies have proven the high mobility of artificial sweeteners through the aquifer and their presence in groundwater, especially at localities with a high wastewater burden [5,6]. This can have a major impact on the quality of drinking water in areas where groundwater is a main source of drinking water production. In addition, it was determined that two persistent sweeteners, acesulfame and sucralose, are not eliminated in the drinking water treatment and consequently are detected in tap water [7]. In this paper, groundwater samples from three wells in Belgrade and its surroundings were analyzed in order to determine the levels of eight artificial sweeteners and to evaluate the chronic health impact of detected sweeteners, using the human health risk assessment (HHRA) model of the United States Environmental Protection Agency (US EPA).

METHODS

Analytical standards (≥ 98%) of seven sweeteners (acesulfame, saccharin, cyclamate, aspartame, NHDC, neotame and stevioside) were obtained from Sigma-Aldrich (Buchs, Switzerland), while sucralose was purchased from TCI Europe (Zwijndrecht, Belgium). Solvent methanol was supplied from J.T. Baker. Groundwater samples were collected from three water wells: two groundwater samples from the Ranney wells constructed on the bank of the Sava River in Belgrade (WELL1 and WELL2) and one groundwater sample from the observation well on the bank of the Danube downstream from Belgrade (WELL3). All water samples were filtered through 1–3 μm glass fiber filter (Whatman GmbH, Dassel, Germany) prior to extraction.

For sample preparation, the previously optimized solid-phase extraction (SPE) method was used [8]. The SPE method consisted of the extraction of 50 ml of water sample (pH adjusted to 3.0) using Oasis HLB cartridge (200 mg/6 mL; Waters, Milford, USA) and the elution of analytes from the cartridge with 10 mL of methanol. After evaporation under a gentle nitrogen stream to a volume of 0.5 mL, the extract was filtered through a 0.45 μm PVDF filter (Roth, Karlsruhe, Germany) into a glass vial and analyzed. The instrumental analysis was performed using liquid chromatography–tandem mass spectrometry (LC-MS/MS) method. LC and MS operating parameters for the analysis of eight sweeteners were optimized in a previous study [8]. Chromatographic separation was carried out using a Dionex UltiMate 3000 HPLC system (Thermo Fisher Scientific, Waltham, USA) with Luna® C8 reverse-phase column, 150 mm × 3.0 mm i.d. and 3 μm particle size (Phenomenex, Torrance, USA). The mobile phase consisted of deionized water, methanol, and 0.1 mol L^{-1} aqueous solution of ammonium acetate. MS/MS analysis was performed using LTQ XL (Thermo Fisher Scientific) linear ion trap mass spectrometer. Electrospray ionization (ESI) in the negative mode was applied as the ionization technique.

The risk of developing adverse health effects due to the exposure to chemical substances that are ingested through drinking water was estimated using hazard quotients (HQs) for noncarcinogenic substances. HQs were determined by dividing the calculated chronic daily intake (CDI) values with the corresponding acceptable daily intake (ADI) values obtained from the published literature [1]. CDI values were calculated based on the equation presented at the Risk Assessment Information System (RAIS) for noncarcinogenic age-adjusted chronic resident exposure through tap water [9]:

$$\text{CDI (mg/kg/day)} = C \times IFW / AT$$

where C is measured concentration of artificial sweetener in the water sample, IFW is age-adjusted drinking water ingestion factor (327.95 L kg^{-1}), and AT is the average time of exposure (365 days/yr × exposure duration (ED) 26 yr). A value of HQ below 1 indicates that the exposed resident is unlikely to experience adverse health effects, and HQ value higher than 1 indicates a potential health risk [10].

RESULTS AND DISCUSSION

In this research, out of eight investigated artificial sweeteners, only acesulfame and sucralose were detected in all well water samples, with the highest concentration of acesulfame (80 ng L^{-1}) found in the observation well on the bank of the Danube downstream from Belgrade (WELL3), and the highest levels of sucralose (25 ng L^{-1}) found in Ranney well on the bank of the Sava River (WELL2) (**Figure 1**). Apparently, the two persistent artificial sweeteners are easily transported through the aquifer to wells located near the river course. The mere presence of artificial sweeteners in groundwater is problematic, as they are well-known markers of sewage pollution. It is evident that the absence of a wastewater treatment plant in Belgrade provides a direct route for many dangerous substances, as well as pathogenic microorganisms, to the drinking water sources.

Compared to a limited number of similar studies from other countries, the recorded concentrations of these artificial sweeteners in well water in the Republic of Serbia were significantly lower. For instance, in well water from Switzerland acesulfame was detected at levels up to 524 ng L^{-1} [11], while in Canada both sweeteners were found at much higher concentrations (up to 1534 ng L^{-1} for acesulfame and up to 541 ng L^{-1} for sucralose) [6]. Moreover, several studies have reported extremely high levels of acesulfame in well water samples from aquifers heavily affected by sewage effluents: up to 4.7 μg L^{-1} in Switzerland [5] and up to 2.9 μg L^{-1} in Germany [12]. The higher levels of sweeteners detected in other studies reflect the larger population and different consumption patterns in the investigated areas.

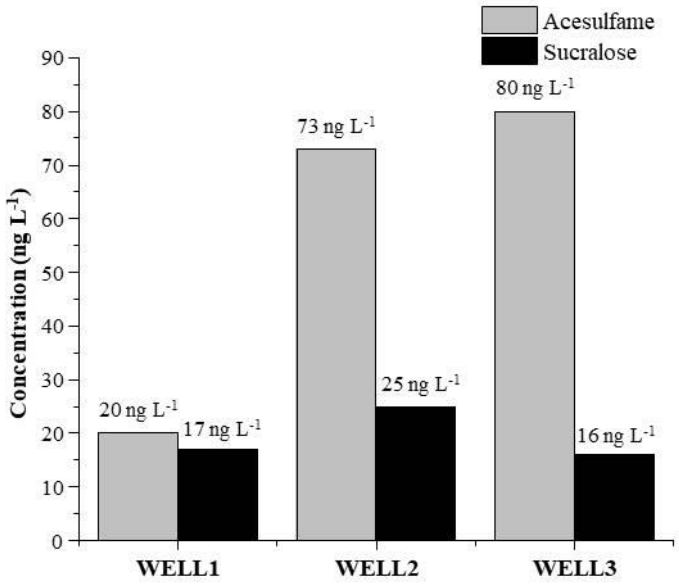


Figure 1. Concentrations of detected artificial sweeteners in well water samples (ng L^{-1}).

The calculated hazard quotients do not indicate a threat to human health based on the detected concentrations of artificial sweeteners in well water (**Table 1**).

Table 1. Human health risk assessment for detected artificial sweeteners in well water with acceptable daily intake (ADI)* values.

Artificial sweeteners	**Hazard quotient (HQ) = CDI/ADI**		
	WELL1	**WELL2**	**WELL3**
Acesulfame (*9 mg kg^{-1})	$7.7 \cdot 10^{-8}$	$2.8 \cdot 10^{-7}$	$3.1 \cdot 10^{-7}$
Sucralose (*5 mg kg^{-1})	$1.2 \cdot 10^{-7}$	$1.7 \cdot 10^{-7}$	$1.1 \cdot 10^{-7}$

Namely, the calculated HQs for all tested water samples were below the value of 1, which indicates that the exposed residents will not have adverse health effects [10]. However, cumulative risk should be considered when evaluating the health outcomes of the combined effects of chemical mixtures. The concentration of sweeteners ingested daily can cause adverse effects on human health if the levels ingested through food are added to the drinking water intake. In addition, recent studies have revealed that some artificial sweeteners show potential carcinogenicity [13], so it would be necessary to consider other approaches in HHRA, such as evaluating possible long-term carcinogenic and mutagenic effects.

CONCLUSION

Out of eight investigated artificial sweeteners, acesulfame and sucralose were detected in all well samples (up to 80 ng L^{-1} and 25 ng L^{-1}, respectively), indicating a high wastewater burden on drinking water sources in Belgrade and its surroundings. The calculated hazard quotients showed that the measured concentrations of sweeteners in well water do not pose a risk to human health. Also, the intake of sweeteners and other additives through food should be considered for the cumulative risk assessment of additive and synergistic effects of chemical mixtures on human health.

Acknowledgment

This work was supported by the Ministry of Science, Technological Development and Innovation of the Republic of Serbia (Contracts No. 451-03-66/2024-03/200287 and 451-03-65/2024-03/200135).

REFERENCES

[1] M. Carocho, P. Morales, I.C.F.R. Ferreira, Food Chem. Toxicol., 107 (2017) 302–317.
[2] S.E. Swithers, Trend Endocrinol. Metab., 24 (2013) 432–441.
[3] S.M. Praveena, M.S. Cheema, H.-R. Guo, Ecotoxicol. Environ. Saf., 170 (2019) 699–707.
[4] J. Luo, Q. Zhang, M. Cao, L. Wu, J. Cao, F. Fang, C. Li, Z. Xue, Q. Feng, Sci. Total Environ., 653 (2019) 1149–1160.
[5] I.J. Buerge, H.-R. Kahle, M.D. Müller, T. Poiger, Environ. Sci. Technol., 43 (2009) 4381–4385.
[6] M. Wu, Y. Qian, J.M. Boyd, S.E. Hrudey, X.C. Le, X.-F. Li, J. Chromatogr. A, 1359 (2014) 156–161.
[7] A. M. Dietrich, Z. Pang, H. Zheng, X. Ma, Chem. Eng. J. Adv., 6 (2021) 100100.
[8] E. Gvozdić, I. Matić Bujagić, T. Đurkić, S. Grujić, Microchem. J., 157 (2020) 105071.
[9] RAIS, 2024. Chemical Risk Calculator User's Guide, Land Use Descriptions, Equations, and Technical Documentation. https://rais.ornl.gov/tools/rais_chemical_risk_guide.html (last accessed: May 26, 2024).
[10] Risk characterization handbook, Science Policy Council, U.S. Environmental Protection Agency, Washington, DC 20460, https://www.epa.gov/sites/default/files/2015-10/documents/osp_risk_characterization_handbook_2000.pdf (last accessed: May 26, 2024).
[11] W. Ens, F. Senner, B. Gygax, G. Schlotterbeck, Anal. Bioanal. Chem., 406 (2014) 2789–2798.
[12] L. Wolf, C. Zwiener, M. Zemann, Sci. Total Environ., 430 (2012) 8–19.
[13] C. Debras, E. Chazelas, B. Srour, N. Druesne-Pecollo et al., Plos Med., 19 (2022) 1003950.

DETERMINATION OF GROWTH PROMOTHER PROGESTERONE IN CHICKEN EGGS

Lj. Tolić Stojadinović [1], K. Pavićević [2] and S. Grujić [2]

[1] *Innovation center of the Faculty of Technology and Metallurgy, Karnegijeva 4, 11000 Belgrade, Serbia.*
[2] *University of Belgrade, Faculty of Technology and Metallurgy, Karnegijeva 4, 11000 Belgrade, Serbia. (svetlana.grujic@tmf.bg.ac.rs)*

DOI: https://doi.org/10.46793/Phys.Chem24II.487TS

ABSTRACT

Animal products are a major source of human exposure to hormones that could be harmful to health if present in elevated concentrations. In this paper, the development and optimization of the liquid chromatography–tandem mass spectrometry (LC–MS/MS) method for the determination of progesterone in chicken eggs were described. Egg samples were prepared using ultrasonic extraction and clean-up with Oasis HLB cartridges. Extracts were analyzed by LC–MS/MS with atmospheric pressure chemical ionization. The developed and optimized method provided high recoveries, with RSDs lower than 4%. The method was applied to the analysis of progesterone in four different chicken egg types. Progesterone was detected in all investigated samples in the concentration range from 123 ng g^{-1} to 206 ng g^{-1}. Compared to the acceptable daily intake values (0–30 μg (kg bw)$^{-1}$), the progesterone levels found in the tested eggs are not of concern.

INTRODUCTION

Steroid hormones are vital to the normal development, maturation and cell aging of the body. However, elevated hormone levels can have a toxic effect on human health [1]. Animal products are a major source of human exposure to steroid hormones. These compounds are naturally-occurring in food of animal origin, but can also be used as growth promoters. Hormonal growth promoters are substances that, by affecting the metabolism, lead to a more complete consumption of food, leading to enhanced animal growth. In some countries (USA, Canada, Australia), the controlled application of hormonal growth stimulators is allowed in animal husbandry, while in the EU and the Republic of Serbia (RS), their use is strictly prohibited [2,3]. However, the illegal use of these substances may lead to high levels in food of animal origin, which may be potentially harmful to consumers. Assessment of the dietary intake of steroid hormones and their impact on human health is very important, especially for susceptible groups such as children, pregnant women, etc.

Eggs are animal products often used in human diet. The presence of steroid hormones in eggs has been previously reported in several studies [4-6]. One of the most frequently detected hormones in eggs is progesterone, primarily known for its role in the female reproductive system. As it can be used as a growth promoter, its presence in eggs needs to be monitored.

The determination of steroid hormones in eggs as a complex matrix is a challenging task. High levels of fat and protein require extensive, time-consuming clean-up of the obtained extract. The analytical technique most commonly used for the detection of steroid hormones in eggs is liquid chromatography coupled to tandem mass spectrometry (LC–MS/MS) [5,6].

The objectives of this study were: (i) to develop a simple, fast and sensitive LC–MS/MS method for the determination of progesterone; (ii) to optimize the sample preparation procedure for the analysis of progesterone in eggs; and (iii) to determine progesterone concentrations in different egg samples.

METHODS

A high purity (99.3%) progesterone analytical standard was purchased from Dr. Ehrenstorfer GmbH (Augsburg, Germany). All solvents used were HPLC grade from Sigma-Aldrich (St. Louis, MO, USA). Anhydrous sodium sulphate was obtained from Sigma-Aldrich. Silica gel (Promochem, LGC Standards GmbH, Germany) had a particle size of 0.063–0.2 mm. Prior to use, anhydrous sodium sulphate and silica gel were baked at 450 ºC for 6 h and stored in a sealed desiccator. Deionized water was obtained by passing the tap water through a GenPure ultrapure water system (TKA, Niederelbert, Germany).

Optimization of the sample preparation procedure was performed on chicken eggs purchased in the local supermarket in Belgrade, RS. The extraction solvents tested were methanol and acetonitrile. The packing type of the clean-up cartridge was also optimized, and Oasis HLB packing (hydrophilic-lipophilic balance, 200 mg/6 mL, Waters, Milford, MA, USA) and silica gel/anhydrous sodium sulphate were tested. The sample preparation procedure was as follows: 2.5 g of a previously homogenized egg sample was extracted with 7.5 mL of the extraction solvent in the ultrasonic bath for 10 min. The sample was then centrifuged for 10 min at 5000 rpm, and the extract was separated. The extraction was repeated one more time. Supernatants were combined, and 1.0 g of $ZnCl_2$ was added to minimize the lipid content extracted from the egg sample. The sample was vortex-mixed for 1 min and then centrifuged for 10 min at 5000 rpm. The supernatant was separated and evaporated to a volume of 0.5 mL. When Oasis HLB cartridges were used, 10 mL of deionized water was added to the extract, vortex-mixed, and transferred onto the clean-up cartridge. In the case of silica gel/anhydrous sodium sulphate packing, 0.5 mL of the extract was passed through the cartridge. An extraction solvent (10 mL) was then used for the elution of the analyte. The collected extract was then evaporated to dryness and reconstituted in 1 mL of methanol. All extracts were filtered through a 0.45 µm polyvinylidene difluoride (PVDF) filter, acquired from Roth (Karlsruhe, Germany), and analyzed. The optimized method was used in real sample analysis of four types of chicken eggs: eggs from cage egg farming (white and brown) purchased from local supermarkets, organic eggs from markets selling organic products, and domestic eggs from countryside farms.

For the LC–MS/MS analysis, Dionex UltiMate 3000 HPLC system (Thermo Fisher Scientific, Waltham, US) coupled to the linear ion trap mass spectrometer LTQ XL (Thermo Fisher Scientific) was used. The reverse-phase Zorbax Eclipse® XDB–C18 column, 75 mm × 4.6 mm ID and 3.5 µm particle size, was used. The mobile phase consisted of deionized water (A) and methanol (B). The mobile-phase gradient was changing as follows: 0 min, B 70%; 6 min, B 100%; 12 min, B 100%. The initial conditions were then re-established and held for 5 min. The flow rate of the mobile phase was 0.5 mL min^{-1}. An aliquot of 20 µL of the final extract was injected into the LC system. The mass spectrometric analysis was performed using the atmospheric pressure chemical ionization (APCI) technique in the positive mode. The optimized APCI parameters were a capillary temperature of 200 ºC and a vaporizer temperature of 400 ºC.

RESULTS AND DISCUSSION

In the optimization of progesterone extraction from egg samples, different extraction solvents and packing types of the clean-up cartridge were tested. The use of methanol as an extraction solvent resulted in cartridge obstruction, making analyte elution impossible. Consequently, the use of methanol as an extraction solvent was discontinued, and acetonitrile was used as an extraction solvent in further experiments. The recoveries obtained with both Oasis HLB and silica gel/anhydrous sodium sulphate packing types as the clean-up cartridges were acceptable (72% and 98%, respectively). However, commercially available Oasis HLB cartridges were selected over cartridges packed with silica gel/anhydrous sodium sulphate due to higher repeatability (RSD < 4% compared to RSD of up to 20%).

Both electrospray (ESI) and APCI were tested as ionization techniques. Although there are studies with the detection of progesterone using ESI [5-7], in this work only APCI was found to be efficient for ionization of progesterone. The recorded mass spectrum showed that the protonated molecule ($[M+H]^+$) of progesterone (*m/z* 315) was dominant, and it was selected as the precursor ion. In Figure 1a, fragmentation of the precursor ion (MS/MS spectrum) is presented. The fragmentation reaction of the precursor ion to the most intensive fragment ion (*m/z* 297) was selected for progesterone identification and quantification (Figure 1b).

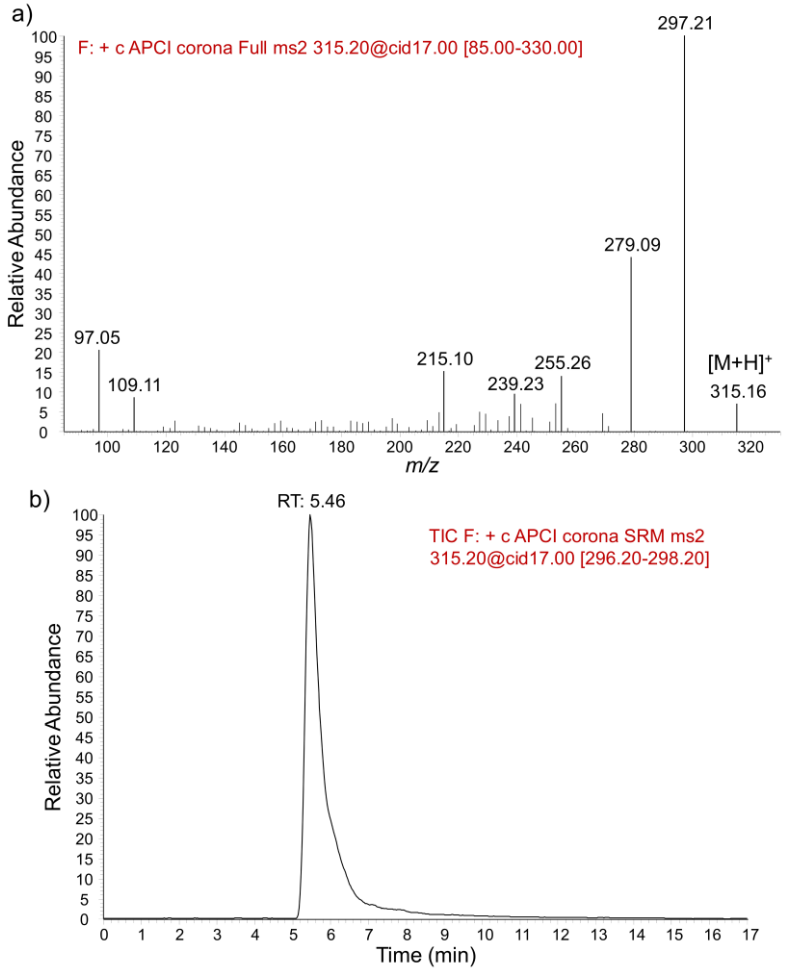


Figure 1. (a) MS/MS spectrum and (b) mass chromatogram of progesterone.

The developed method was applied in real sample analysis of four types of chicken eggs. The results obtained are presented in Table 1. Progesterone was found in all analyzed samples. The levels of progesterone in different samples varied from 123 ng g^{-1} to 206 ng g^{-1}. The detected concentrations were either higher than [4,5] or consistent with [7] those previously reported. This could be explained by the difference in the breeds of egg-laying hens, the chicken diet and the raising environment. The obtained results indicate that a considerable amount of progesterone in the human diet originates from eggs. The Joint FAO/WHO Expert Committee on Food Additives (JECFA) established an acceptable daily intake (ADI) of 0–30 µg (kg bw)$^{-1}$ for progesterone [1]. For a person weighing approximately 60 kg, it is acceptable to intake up to 1.8 mg of this steroid hormone each day. If the person consumes 3 eggs per day (the average mass of the tested eggs is 46.6±2.0 g), he will ingest 29 µg of progesterone. Clearly, compared to the ADI values, the

progesterone levels in the tested eggs are not of concern. However, it is necessary to consider other foods of animal origin, including meat, meat products, milk and dairy products, that could jointly enhance concentration of ingested progesterone to the levels higher than the ADI values.

Table 1. Concentrations of progesterone detected in eggs.

Analyte	Concentration ± SD, ng g^{-1}			
	Cage eggs (white)	Cage eggs (brown)	Organic eggs	Domestic eggs
Progesterone	145 ± 24	123 ± 13	184 ± 13	206 ± 49

CONCLUSION

In this paper, the LC–MS method for identification and quantification of the steroid hormone progesterone in eggs was developed and optimized. The optimized sample preparation consisted of ultrasonic extraction of the egg sample with acetonitrile as the extraction solvent. The extract clean-up was performed using an Oasis HLB cartridge and acetonitrile as the elution solvent. The APCI ionization technique was selected for the analysis. The developed and optimized method provided high recoveries, with RSDs lower than 4%. The applicability of the developed method was confirmed by the analysis of four different egg types. Progesterone was detected in all investigated samples in the concentration range of 123–206 ng g^{-1}. Compared to the ADI values, the progesterone levels in the tested eggs are not of concern. However, joint intake of this steroid hormone through other foods of animal origin should be considered. The obtained results indicate that the developed method can be used for the determination of growth promoter progesterone in eggs.

Acknowledgment

This work was supported by the Ministry of Science, Technological Development and Innovation of the Republic of Serbia (Contracts No. 451-03-66/2024-03/200287 and 451-03-65/2024-03/200135).

REFERENCES

[1] Fifty-second meeting of the Joint FAO/WHO Expert Committee on Food Additives (JECFA), Toxicological Evaluation of Certain Veterinary Drug Residues in Food, No. 43, World Health Organization, Geneva, 2000.
[2] Commission of the European Communities, Council Directive 96/22/EC, Off. J. Eur. Commun. L 125 (1996) 3.
[3] Animal Welfare Law, Off. Gaz. Rep. Srb., No. 41/2009, 2009.
[4] S. Hartman, M. Lacorn, H. Steinhart, Food Chem., 62 (1998) 7.
[5] Y. Yang, B. Shao, J. Zhang, Y. Wu, J. Ying, J. Chrom. B, 870 (2008) 241.
[6] X. Mi, S. Li, Y. Li, K. Wang, D. Zhu, G. Chen, J. Chrom. A, 1356 (2014) 54.
[7] T. Nakajima, Y. Tsuruoka, M. Kanda, H. Hayashi, T. Hashimoto, Y. Matsushima, S. Yoshikawa, C. Nagano, Y. Okutomi, I. Takano, Food Addit. Contam. Part A, 32 (2015) 1833.

CARBAMAZEPINE ADSORPTION BY PROMISSING HYDROPHOBIC SURFACTANT-CLAY COMPOSITES

D. Smiljanić [1], A. Daković [1], M. Obradović [1], M. Marković [1], M. Ožegović [1], I. Dimitrijević [2] and Ž. Mravik [3]

[1] *Institute for Technology of Nuclear and Other Mineral Raw Materials, Franše d' Epere 86, 11000 Belgrade, Serbia. (d.smiljanic@itnms.ac.rs)*
[2] *Faculty of Technology and Metallurgy, University of Belgrade, Karnegijeva 4, 11000 Belgrade, Serbia.*
[3] *Center of Excellence for Hydrogen and Renewable Energy (CONVINCE), Laboratory of Physics, Vinča Institute of Nuclear Sciences, – National Institute of the Republic of Serbia, University of Belgrade, 11000 Belgrade, Serbia.*

DOI: https://doi.org/10.46793/Phys.Chem24II.491S

ABSTRACT

In this study, two surfactants, primary amine dodecylamine (D) and di(hydrogenated tallow)dimethylammonium chloride known under the trade name Arquad®2HT-75 (A) were used to modify bentonite in amounts equivalent to 50% and 100% of bentonite`s cationic exchange capacity. For prepared composites static water contact angle and true density were maeasured. Obtained composites were tested as adsorbents for an anticonvulsant drug – carbamazepine (CARB). The results of the contact angle measurements confirmed that the modification of the starting material changed its surface properties from hydrophilic to hydrophobic. Additionally, the true density decreased as the surfactant content in the bentonite increased, which suggest that the surfactant was intercalated into the interlayers of the bentonite. Adsorption isotherms have shown that CARB adsorption increased with increasing of the initial drug concentration as well as with the increase of the amount of each surfactant in composites.

INTRODUCTION

Pharmaceutical pollutants significantly impact the environment due to their persistence and widespread presence in aquatic systems. Among these, CARB stands out for its extensive use as an anticonvulsant and mood stabilizer, commonly prescribed for epilepsy and bipolar disorder [1]. Consequently, CARB frequently appears in water bodies, posing potential risks to human health and the environment due to its resistance to conventional wastewater treatment processes [1]. The challenge of removing pharmaceuticals like CARB from water has driven the exploration of various advanced treatment technologies. One promising approach for drug removal is adsorption, which is simple, cost-effective, and highly efficient. Natural clays, such as bentonite, and zeolites, are abundant and inexpensive materials studied for their adsorption capabilities for various pollutants. However, their inherent hydrophilicity and exchangeable inorganic cations limit their effectiveness in adsorbing hydrophobic organic molecules such as CARB. To overcome these limitations, clays can be modified with cationic surfactants to enhance their affinity for organic pollutants. Previous studies have demonstrated the potential of surfactant-modified clays in removing pharmaceuticals, specifically NSAIDs [2,3]. However, the specific interactions between CARB and organoclays require further detailed investigation.

This study focuses on modifying bentonite clay using different quantities of surfactants to enhance its affinity for CARB. The aim is to prepare and characterize the composites through

contact angle and true density measurements and to evaluate the adsorption performance of these modified clays for CARB removal.

METHODS

A sample of natural bentonite (S) from the Šipovo deposit (Bosnia and Herzegovina), previously concentrated and characterized [4], was used as starting material. Its total cation exchange capacity (CEC), determined by the ammonium chloride method, was 96.6 meq/100 g [5]. Dodecylamine (Fluka AG, Buchs, Switzerland) and Arquad®2HT-75 (Akzo Chemie, Amersfoort, Netherlands) were used to modify the bentonite surface. To create organoclays with different surfactant loadings, a 5 wt% aqueous suspension of S was treated with surfactant amounts equivalent to 50% and 100% of its CEC. The suspensions were stirred at 5000 rpm for 20 min at 60°C, then filtered, rinsed with distilled water and dried. The organoclays were labeled SD50, SD100, SA50, and SA100.

Contact angles were measured for all prepared composites and the unmodified bentonite. A water droplet with a known volume (5 μl) was carefully deposited onto the horizontal surface of each sample. Using a Moticam350 CCD camera mounted on a Motic SMZ-143 series optical microscope, images of the droplet were captured and subsequently analyzed using ImageJ software [6]. The contact angle was determined based on the assumption that the droplet's profile resembled a portion of a circle with a specified radius. It was calculated as the angle between the substrate surface and the tangent drawn from the droplet's edge to its contour [7]. To determine the true (skeletal) density of the bentonite and composites, a gas pycnometer (Ultrapyc 5000, Anton Paar, Graz, Austria) was used, operating with nitrogen as the displacement gas at a target pressure of 0.690 bar and 20°C. A 9-cycle pulse purge was used to prepare the samples prior to measurement (pressure built to 0.2 bar and then released). At least 5 consecutive measurements were taken per sample, with the process concluding when the variance was below 0.1%.

The ability of composites to adsorb CARB (Serva, Heidelberg, Germany) was tested. Each adsorbent (5 mg) was placed in Erlenmeyer flasks, to which 10 mL of drug buffer solution (5-100 mg/L, pH = 7) was added. Adsorption isotherm experiments were conducted at room temperature using a rotary shaker (250 rpm, Heidolph Unimax 1010, Schwabach, Germany). After 60 min, the solutions were filtered, and the drug concentrations in the filtrates were determined. The concentrations of CARB before and after adsorption were measured using UV-Visible Spectrophotometry (UV-VIS 1800, Shimadzu, Kyoto, Japan), at a maximum wavelength of 285 nm. For the analysis of adsorption isotherms, Langmuir and Freundlich models were applied to fit the experimental results.

RESULTS AND DISCUSSION

Figure 1 a-e) illustrates the contact angles (θ) of the initial material and the prepared composites. According to literature data, when $\theta<90°$, the material surface is considered hydrophilic; when $90°<\theta<150°$, it's classified as hydrophobic, and if $\theta>150°$, the material is labeled as superhydrophobic [8]. The pristine bentonite demonstrated rapid absorption of the water drop, resulting in a contact angle estimated at 22.8°, confirming its hydrophilic nature. The contact angles of all composites fell within the range of 134-141°, indicating that modification with both surfactants produced highly hydrophobic materials that are expected to provide adsorption sites for hydrophobic organic molecules such as CARB.

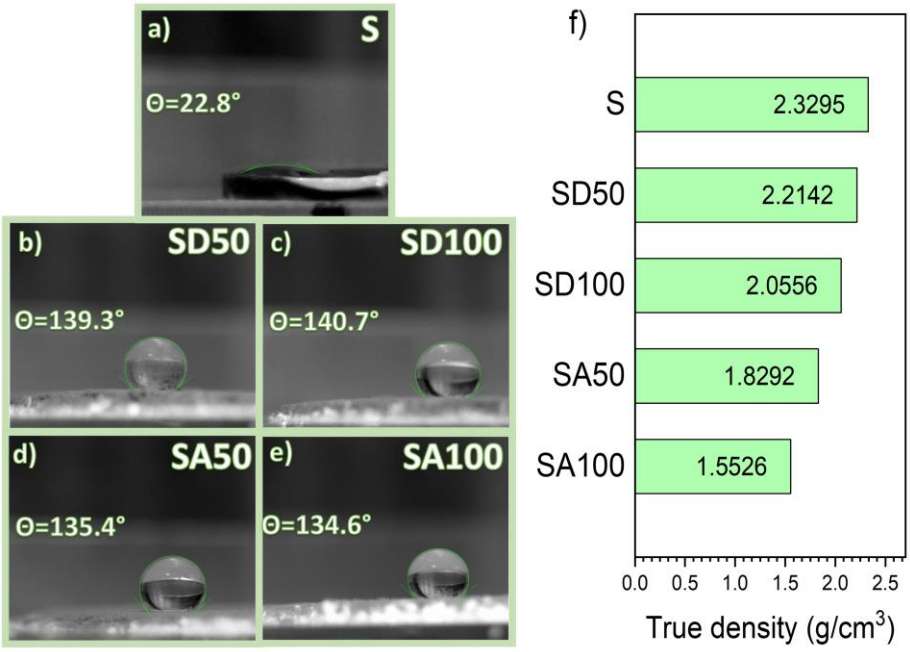


Figure 1. Contact angle measurment of: **a)** starting material S; **b)** SD50, **c)** SD100, **d)** SA50, **e)** SA100; and **f)** True densities of starting material and composites.

Figure 1 f) presents the results of true density measurements. The initial bentonite exhibited a density of 2.3295 g/cm^3, consistent with literature values [9]. For following modifications with surfactants, the density decreased as the percentage of surfactant in the composites increased. According to the literature, the reduction in density of the organoclay is attributed to the expansion of bentonite's basal spacings [10], indicating the intercalation of surfactant molecules between the bentonite layers. Among the composites, those prepared with surfactant A showed lower densities than those with D. This could be explained by different surfactant structures: surfactant A has two hydrophobic chains and probably induced a greater increase in basal spacing compared to composites prepared with D, which has a single hydrophobic chain.

A preliminary experiment demonstrated that unmodified bentonite has low affinity for adsorbing CARB. The results of CARB adsorption onto organoclays are depicted in **Figure 2**.

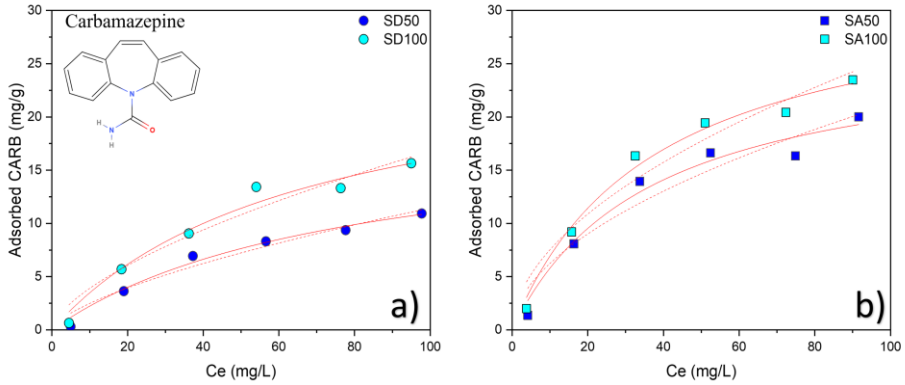


Figure 2. Adsorption isotherms of carbamazepine (CARB) on: **a)** composites prepared with dodecylamine (D); **b)** composites prepared with Arquad®2HT-75 (A). Langmuir isotherm model (solid line) and Freundlich isotherm model (dotted line).

Experimental data were modeled using both the Langmuir and Freundlich isotherm models, with both showing high correlation coefficients ($R^2 > 0.92$). The Langmuir isotherm model predicted the maximum adsorbed amount of the drug (Q_{max}) for the composites. For composites prepared with surfactant A, the Q_{max} values were 27 mg/g for SA50 and 33 mg/g for SA100, while for those prepared with surfactant D, the Q_{max} values were 19 mg/g and 27 mg/g for SD50 and SD100, respectively. It was observed that the adsorption of CARB increased with the increase of surfactant amount, confirming that surfactant molecules act as active sites for drug adsorption. Additionally, adsorption was higher for composites prepared with surfactant A, indicating that its structure, with two hydrophobic chains, enhanced the adsorption of CARB. The dissociation constants of CARB (pKa = 2.3 and 13.9) suggest that at pH 7, the condition under which adsorption experiments were conducted, this molecule remains non-ionized. Therefore, the adsorption mechanism onto organoclays most likely involves hydrophobic interactions between the surfactant chains and the hydrophobic CARB molecules ($\log K_{ow} = 2.45$).

CONCLUSION

Results reported in this paper demonstrated that modification of the bentonite with two surfactants, in amounts corresponding to 50% and 100% of bentonite's CEC, improved adsorption of CARB. Characterization results suggest that surfactant molecules were adsorbed on bentonite creating highly hydrophobic composites. Adsorption isotherms further confirmed the affinity of organoclays for CARB removal. In conclusion, modifying bentonite to create organoclays is a promising strategy for improving the removal of persistent pharmaceuticals like CARB from aqueous environments. While further research is needed to optimize and fully understand the potential of this approach, the use of organoclays as adsorbents represents a viable option for addressing pharmaceutical pollution in water.

Acknowledgment

This work was supported by the Ministry of Education, Science and Technological Development of the Republic of Serbia (grants No. 451-03-66/2024-03/200023 and 451-03-66/2024-03/200017), and from the Science Fund of the Republic of Serbia, grant No. 6706, acronym–ASPIRE.

REFERENCES

[1] F.I. Hai, S. Yang, M.B. Asif, V. Sencadas, S. Shawkat, M. Sanderson-Smith, J. Gorman, Z.Q. Xu, K. Yamamoto, Water 10 (2018) 107.
[2] M. Obradović, A. Daković, D. Smiljanić, M. Ožegović, M. Marković, G.E. Rottinghaus, J. Krstić, Microporous Mesoporous Mater. 335 (2022) 111795.
[3] M. Obradović, A. Daković, D. Smiljanić, M. Marković, M. Ožegović, J. Krstić, N. Vuković, M. Milojević-Rakić, Processes 12 (2023) 96.
[4] A. Daković, S. Matijašević, G.E. Rottinghaus, D.R. Ledoux, P. Butkeraitis, Ž. Sekulić, Colloids Surf. B Biointerfaces 66 (2008) 20–25.
[5] M.A. Marković, A.S. Daković, G.E. Rottinghaus, M.D. Stojanović, V.T. Dondur, M.M. Kragović, Z.P. Gulišija, Hem. Ind. 70 (2016) 519–524.
[6] C.A. Schneider, W.S. Rasband, K.W. Eliceiri, Nat. Methods 9 (2012) 671–675.
[7] Z. Jovanović, A. Kalijadis, D. Vasiljević-Radović, M. Erić, M. Laušević, S. Mentus, Z. Laušević, Carbon 49 (2011) 3737–3746.
[8] K.Y. Law, J. Phys. Chem. Lett. 5 (2014) 686–688.
[9] S. Kaufhold, M. Plötze, M. Klinkenberg, R. Dohrmann, J. Porous Mater. 20 (2013) 191–208.
[10] S. Akbulut, Z.N. Kurt, S. Arasan, Y. Pekdemir, Sadhana 38 (2013) 317–329.

ENGINEERING BIOREMEDIATION - THE TECHNOLOGY OF CHOICE FOR THE TREATMENT OF AQUIFERS CONTAMINATED WITH OIL POLLUTANTS

J. Avdalović, K. Joksimović, S. Spasić, J. Milić, M. Ilić, G. Dević and S. Miletić

University of Belgrade, Institute of Chemistry, Technology and Metallurgy, National Institute of the Republic of Serbia
Njegoševa 12, 11000 Belgrade, Serbia. (kristina.joksimovic@ihtm.bg.ac.rs)

DOI: https://doi.org/10.46793/Phys.Chem24II.495A

ABSTRACT

Increasing environmental pollution and the concept of sustainable development have both caused increased ecological awareness, which altogether have contributed to the development of new effective, ecologically and economically acceptable technologies for decontamination of contaminated spheres of environment, such as engineered bioremediation. This paper presents the engineered bioremediation of aquifers (groundwater and sediments) in the locality of the New Belgrade heating plant. In the process, which lasted for 12 months, aquifer contaminated by various petroleum derivatives was treated by *in situ*. The treatment was carried out by a bipolar model with groundwater recirculation, by combination of extraction and injection wells. During process, the total petroleum hydrocarbon content in groundwater was reduced dramatically (98%). In the same time, the total petroleum hydrocarbon content in the sediment decreased by 93% of the initial level.

INTRODUCTION

Worldwide, petroleum hydrocarbons are contaminating the environment, and are now a major global problem.Once released, these hydrocarbons percolate through the soil due to gravity and eventually reach groundwater, where they disperse laterally. Hydrocarbon droplets with low mobility and high molecular weight are trapped in sediment pores and adsorbed onto clay, known as the residual phase. These contaminated sediments continuously release petroleum hydrocarbons, leading to ongoing groundwater pollution [1]. The use of bioremediation to reduce different organic pollutants from various environmental matrices has been widely promoted in recent decadesal [2]. Engineered bioremediation is preferred for its ability to modify polluted sites at controlled intervals to accelerate contaminant degradation. This process involves biostimulation, which provides nutrients, electron acceptors, and biosurfactants [2,3], and bioaugmentation, which introduces microbial biomass—ideally a consortium—to enhance degradation capacity, synergistic performance, and co-metabolic activities [3,4]. Using microbial consortia from the polluted site itself is particularly advantageous because these native bacteria produce a large, active biomass when reintroduced, speeding up the bioremediation process. The most rapid biodegradation rates are achieved by combining biostimulation and bioaugmentation [4].

During regular analysis of groundwater quality at the location of the New Belgrade heating plant (HP) (Serbia), it was found that the petroleum hydrocarbon concentrations were greater than the remediation value (0.6 mg dm^{-3}, according to national legislation). Groundwater contamination is a reflection of solid-phase contamination, i.e., it originates and is transmitted from the polluted aquifer's sediment-solid phase (in the terminology of environmental forensic chemistry, water provides a fingerprint of what happens in the polluted solid phase, because the pollution is transferred to the water as a solvent). Therefore, sediment analyses were performed in this area to a depth of 15 m. Sediment analyses showed the presence of hydrocarbons at all depths. At greater

depths, measured hydrocarbon concentrations were above the maximum allowed concentrations (for samples that contain less than 2% organic matter, the remediation value is 1000 mg kg^{-1}), which was a consequence of their leakage from the fuel transport pipeline. Since the contaminated site is located near two radial collector wells of the Belgrade water supply system, it was deemed necessary to clean up the contaminants. Based on our own assessment and published data, we concluded *in situ* engineered bioremediation would be the most appropriate technique to improve the quality of aquifer (groundwater and sediments) in the locality of the New Belgrade HP.

This paper provides insight into research and activities of *in situ* bioremediation to remove petroleum hydrocarbon pollutants from contaminated sediment at the New Belgrade HP location.

METHODS

Microbiological analysis

Aquifer samples were analyzed to determine the microbial population density by the serial dilution (10^{-2} to 10^{-6}) method. Suitable dilutions were spread onto agar plates and incubated at 28 °C. The following media were used: nutrient agar (total chemoorganoheterotrophs, TC); mineral salts medium [5] with 2000 ppm diesel fuel (hydrocarbon-degrading microorganisms, HD); Malt agar with streptomycin 50 mg L^{-1} (fungi, F); *Pseudomonas* isolation agar (*Pseudomonas spp*., Ps) [6]; M3 agar (*Nocardia* and *Rhodococcus spp.*, NR) [7]. The incubation durations were 2 (TC), 3 (Ps), 4 (F) or 10 days (HD, NR).

The microbial population from all four media was used to inoculate (approx. 1 vol.%) for bioreactor designed by us [8], producing the biomass for bioaugmentation.

Chemical analyses

Total petroleum hydrocarbons (TPH) from groundwater were extracted as per methods ISO 9377-2 (2000) and determined by gas chromatography. TPH in the composite samples of sediment was extracted as per method ISO 16703 (ISO 16703, 2004) and determined by gas chromatography. The gas chromatographic analyses were conducted on an Agilent 7890A gas chromatograph with a flame ionization detector. The software used for data processing was ChemStation, Agilent Technologies.

RESULTS AND DISCUSSION

In situ remediation treatment

The contaminated area was located at the thermal energy facility, near the city of Belgrade, on the terrace sediments of the Sava River. In the process, which lasted for 12 months, groundwater and sediment in contact with groundwater were treated by *in situ* bioremediation.This remediation treatment was performed by a combination of biostimulation and bioaugmentation within the closed bipolar system. The bioremediation system consisted of 15 bioremediation wells, which could operate both as injection and extraction wells, and 10 filtration/adsorption/bioreactor columns (FABC). The cycle of bioremediation consisted of three phases:

- Injection of nutrients and chemical oxidant—biostimulation
- Injection of the zymogenous consortium of microorganisms—bioaugmentation
- Establishment of recirculation in a closed bipolar system [4].

The bioremediation system was organized into several bioremediation units. Each bioremediation unit consisted of one extraction and one injection well, with a FABC between them. The bioremediation procedure is described below using the example of one unit. The first step was to activate (oxygenate) the aquifer with an oxidizing agent, which was, in our approach, 30% w/v H_2O_2. After that, the biomass of an indigenous consortium of microorganisms was added through an injection well [4,9]. As it was necessary to keep the microbial population in the groundwater

between 10^5 and 10^8 CFU mL^{-1}, reinoculation of biomass was repeated whenever the microbial population fell to around 10^5 CFU mL^{-1}. Groundwater recirculation in this closed system was managed as follows: water was extracted from an extraction well and pumped to the FABC, where it was filtered before being re-injected into the ground via an upstream injection well. The FABC contained sand and commercially available natural, hydrophobic, biodegradable adsorption materials. These materials served a dual purpose: filtering and adsorbing hydrocarbon pollutants from the groundwater, and providing a large specific surface area for biofilm formation by indigenous microorganisms, thus enhancing the biodegradation of hydrocarbon pollutants. After sediment treatment, the adsorption material from the FABC was transported to a biopile for *ex situ* bioremediation (Figure 1).

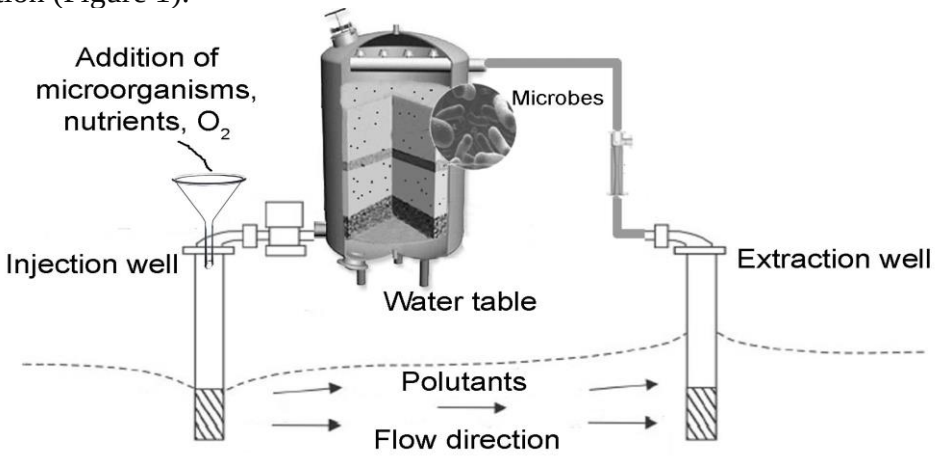


Figure 1. Schematic of the closed recirculation system.

Microorganisms

Microbiological analysis showed that the contaminated aquifers contained a significant number of hydrocarbon-degrading bacteria (10^3-10^4 CFU g^{-1}). Also, bacteria from *Pseudomonas* and *Nocardia-Rhodococcus* groups, well known as hydrocarbon degraders, were present in considerable numbers as shown in Table 1.

Table 1. Total number of chemoorganoheterotrophs (TC), fungi (F), *Pseudomonas* (Ps), hydrocarbon degraders (HD) and *Nocardia-Rhodococcus* (NR) in aquifer.

Locations	**TC, (CFU g^{-1})**	**F, (CFU g^{-1})**	**Ps, (CFU g^{-1})**	**HD, (CFU g^{-1})**	**NR, (CFU g^{-1})**
Aquifer	5.5×10^6	4.2×10^2	2.8×10^4	5.6×10^4	5.6×10^4

The biomass of an indigenous consortium of microorganisms (isolated from the contaminated aquifer) was used to inoculate (approx. 1 vol.%) a bioreactor, producing the biomass for bioaugmentation.

Total petroleum hydrocarbons

A year-long *in situ* bioremediation treatment was performed at the New Belgrade HP location. The bioremediation process included both groundwater and the aquifer's sediment, because both spheres of the environment were in contact and needed to be treated simultaneously. Table 2 shows the concentration of TPH in the aquifer samples during the bioremediation process.

Table 2. Average hydrocarbon concentration in sediment and groundwater collected from contaminated area at the start (a), after 5 months of *in situ* bioremediation (b), and after 12 months of *in situ* bioremediation (c).

	Content of hydrocarbons in the range C10–C40		
	(a) At the start	**(b) After 5 months**	**(c) After 12 months**
Sediment (mg kg^{-1})	3701	1502	340
Groundwater (mg L^{-1})	1,5	0,6	0,02

The twelve months' bioremediation very efficiently removed the petroleum hydrocarbons from the the aquifer. The hydrocarbon content of from the groundwater and the aquifer's sediment decreased by 91%, and 98% of their initial levels, respectively.

The described treatment is more cost-effective in relation to other remediation techniques such as "pump-and-treat". Also, there is no waste production that needs to be further disposed. Additionally, the procedure described may also treat surfaces that are inaccessible to other techniques. Contaminating substances that are adsorbed or trapped in the pores of sediment particles can be effectively removed, as shown in this paper.

CONCLUSION

This study describes *in situ* bioremediation of groundwater and sediment contaminated by petroleum hydrocarbons. The bioremediation technology we used involved exploiting the naturally occurring microorganisms isolated from the contaminated site itself. The efficiency of bioremediation was evaluated on the basis of changes in the content of TPH. During bioremediation, the TPH content in groundwater was reduced dramatically (98%). In the same time, the TPH content in the sediment decreased by 91% of the initial level. These results provide evidence of the high efficiency of the applied method for removing petroleum pollutants from groundwater and sediment in contact with groundwater by an *in situ* bioremediation treatment in a closed bipolar system.

Acknowledgment

This work was supported by the Ministry of Education, Science and Technological Development of the Republic of Serbia (grant no 451-03-66/2024-03/200026).

REFERENCES

[1] P. Logeshwaran, M. Megharaj, S. Chadalavada, M. Bowman, R. Naidu, Environ Technol Innov 10 (2018) 175.
[2] T. Sayara, A. Sánchez, Appl Sci 10 (2020) 3684.
[3] I. C. Ossai, A. Ahmed, A. Hassan, F. S. Hamid, Environ Technol Innov 17 (2020) 100526.
[4] N. Marić, M. Ilić, S. Miletić, G. Gojgić-Cvijović, V. Beškoski, M. M Vrvić, P. Papić, Environ Earth Sci 74 (2015) 5211.
[5] C. Löser, H. Seidel, A. Zehnsdorf, U. Stottmeister, Appl Microbiol Biotechnol 49 (1998) 631.
[6] C. H. Collins, P. M. Lyne, J. M. Grange, J. O. Falkinham, Collins and Lyne's Microbiological Methods, 8th ed. Arnold, London, 2004.
[7] R. M. Atlas, Handbook of Microbiological Media, 4th ed. CRC Press, Taylor & Francis Group, Washington, 2010.
[8] J. Avdalović, A. Đurić, S. Miletić, M. Ilić, J. Milić, M. M. Vrvić, Waste Manag Res 34 (2016) 734.
[9] S. Bulatović, N. Marić, T. Šolević-Knudsen, J. Avdalović, M. Ilić, B. Jovančićević, M. M. Vrvić, J Serbian Chem Soc 85 (2020) 1067.

DOPED CARBON CRYOGELS AS ADSORBENTS FOR PHARMACEUTICAL REMOVAL FROM WATER: A KINETIC STUDY

A. Krstić[1*], I. Bracanović[2], D. Vasić Anićijević[1] and A. Kalijadis[2]

[1]*„VINČA" Institute of Nuclear Sciences - National Institute of the Republic of Serbia, University of Belgrade, Department of Physical Chemistry Belgrade, Serbia (aleksandar.krstic@vin.bg.ac.rs)*
[2]*„VINČA" Institute of Nuclear Sciences - National Institute of the Republic of Serbia, University of Belgrade[2], Department of Materials, Belgrade, Serbia*

DOI: https://doi.org/10.46793/Phys.Chem24II.499K

ABSTRACT
The aim of this work was a kinetic study of ibuprofen adsorption from water using carbon cryogel, nitrogen-doped, and nitrogen and sulfur co-doped carbon cryogel. Nitrogen and sulfur were incorporated into the carbon structure to improve textural, surface, and electronic properties. Ibuprofen is most commonly used with occurrence in the water systems. A kinetic study was performed to optimize the adsorption condition for ibuprofen removal. Obtained experimental data was fitted with four models: pseudo-first and pseudo-second order, Elovich and Intraparticle diffusion model. The obtained results suggested better adsorption kinetic properties for doped and co-doped samples compared to pristine carbon cryogel, which is a consequence of heteroatom incorporation and improving their surface properties.

INTRODUCTION
The rapid increase of human activities and industrialization in the past decade has led to pharmaceuticals emerging as significant pollutants in water ecosystem [1]. As non-steroidal, anti-pyritic, analgesic and anti-inflammatory drugs, ibuprofen is most commonly used with occurrence in water systems and his presence posses to danger to flora and fauna. Other methods for pharmaceutical removal are ozonization, photolysis, electrochemical degradation. The adsorption method was recognized as an economical and high-efficiency method for trace level pharmaceutical removal [2]. Different materials were used as sorbent for the adsorption of pharmaceutical: activated walnut shell biochar, magnetic biochar prepared from chrysanthemum waste, polymeric resin . In the past decade, carbon aero/xero and cryogels are recognized as novel carbonaceous materials for adsorption of different types of organic compounds. The advantages of these materials are low density, high-developed porosity and high surface area [3]. In order to improve surface, electronic and textural properties of carbon materials, chemical functionalization and heteroatom doping are commonly used. The aim of this study is the application of pristine carbon cryogel, N-doped and N, S co-doped carbon cryogels, which are synthesized in the previous studies [4-5] for adsorption ibuprofen from water. The samples with the best textural and surface properties are selected.

METHODS
Synthesis of carbon cryogel was previously described [4-5]. For nitrogen doping, melamine was used as a nitrogen source, which was added in a nominal concentration of 6 wt% nominal concentration. For nitrogen and sulfur co-doping, thiourea was used as an N, S source, in nominal concentration of 10 wt%. These samples were marked as CC, CCN_2 and $CCNS_3$. All kinetics experiments were performed using a batch adsorption kinetics. For pharmaceutical contamination of

water, ibuprofen was used as a model analyte. The kinetics experiments were performed in the 5–1440-time interval, at 25°C in duplicate and in the same adsorption vessel.

The initial adsorbate concentration was 20 mg/l. For the ibuprofen quantification after adsorption, the LLG-uniSPEC 2 Spectrophotometer (LLG Labware) was used, at wavelength 195 nm. Obtained experimental data were fitted and analyzed using the following models: pseudo-first and pseudo-second order model, Elovich and Intraparticle diffusion model. According to the literature, these models are the most common used for describe adsorption kinetic behavior of organic compounds.

RESULTS AND DISCUSSION

The adsorption kinetics results are shown in Figure 1. As can be seen for all samples, in the first-hour, adsorption was fastest and slowed down after two hours until a steady state was reached; for CC samples after 5 hours, for the CCN_2 sample after 3 hours, and for the $CCNS_3$ samples steady state was reached after two hours of adsorption. After 24 h, the CC sample adsorbed 94% of ibuprofen, the CCN_2 sample adsorbed 96%, and the $CCNS_3$ sample adsorbed 98%. The kinetics parameters for applied kinetic models are presented in Table 1. The constant rate obtained from the slope and intercept ln (q_e-q_t) versus t from the plots for linear PFO and t/q_t versus t from the plots, for linear PSO. Based on R^2 parameter, it can be concluded that the non linear and linear pseudo-first order doesn't fit well for all samples. For all samples, the linear PSO model has shown the best fit (R^2>0,99). Also, Elovich model fits well for CCN_2 samples. Similar results were obtained in our previous research for the adsorption of carbamazepine, naproxen, diazepam and diclofenac [4]. The constant rate value, k_2, is highest for the CCN_2 sample, which means that the ibuprofen has first adsorbed on the CCN_2 sample surface. The lower constant rate for CC sample, obtained from liner PSO indicates slower ibuprofen adsorption, probably due to the lower volume of micropore and lower specific surface area compared to CCN_2 sample. [3]. The higher values of Elovich constant α, describing the adsorption rate, were obtained for the CCN_2 and $CCNS_3$ samples, in comparison to pristine CC, indicating faster adsorption and higher adsorption rate for these samples. Figure 2 shows the plots of multilinear fitting for the intraparticle diffusion model (Q_t versus $t^{1/2}$). This model describes and determines the rate-controlling step of the adsorption process. The intercept constant C is obtained from the intercept, and rate constants (k_{i1}, k_{i2}) are obtained from the slope. The equations for all applied kinetic models are shown below [3-6]:

$q_t = q_e \times (1 - e^{-k_1 \times t})$ non linear PFO $\quad \ln(q_e - t) = \ln q_e - k_1 t$ linear PFO

$q_t = q_e \times \left(\frac{1}{q_e} + k_2 + t\right)^{-1}$ non linear PSO $\quad \frac{1}{q_t} = \frac{1}{k_2 q_2^{\,2}} + \frac{1}{q_2} t$ (4) linear PSO

$$q_t = \frac{1}{\beta} ln(\alpha * \beta) + \frac{1}{\beta} lnt \quad \text{Elovich model}$$

$$q_t = k_{id} * t^{\frac{1}{2}} + C \quad \text{Intraparticle diffusion model}$$

The value of this parameter is given in Table 2. Figure 2 shows that the adsorption process has two stages: first, the fast initial process, which represents the external surface adsorption, and the second step is moderate intraparticle diffusion adsorption. The higher k_{i1} values and lower k_{i2} values indicate that initially very fast adsorption and the slow down intraparticle diffusion due to extremely low ibuprofen concentration in the solution, respectively [7]. Also, it can be seen that obtained curves do not pass through the origin, which indicates that

intraparticle diffusion is not the only rate-controlling step in the adsorption process. Considering that external mass transport is faster than diffusion, the adsorption of ibuprofen depends on the diffusion through the pore and adsorption at interior active sites [7].

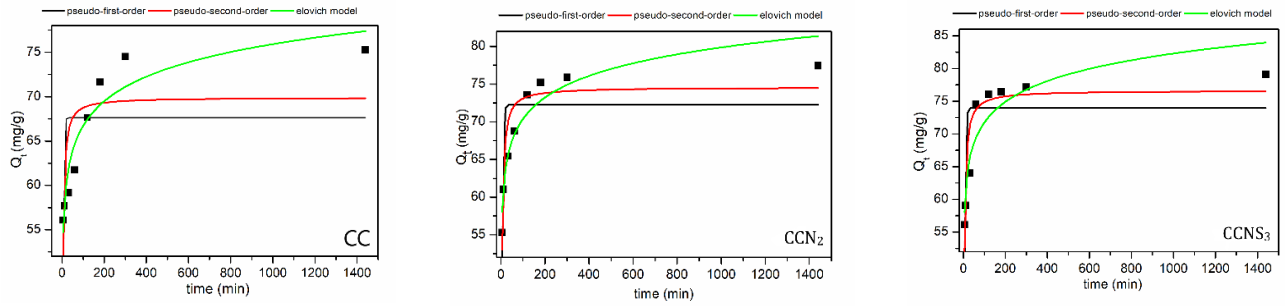


Figure 1. Kinetic model for ibuprofen adsorption onto CC, CCN_2 and $CCNS_3$ sample.

Table 1. Obtained kinetic parameters for applied kinetic models.

Sample	PFO - non-linear PFO - linear			PSO – non-linear PSO - linear			Elovich model		
	R^2	k_1, *g/mg min*	q_e *calc, mg/g*	R^2	k_2, *g/mg min*	q_e *calc, mg/g*	R^2	*α, mg/g min*	*β, g/mg*
CC	0.2182	0.308	67.63	0.5331	0.588	69.90	0.8889	70.28	0.25
	0.7383	0.0028	10.83	0.9999	0.0019	75.19			
CCN_2	0.6046	0.255	72.26	0.8659	0.493	74.57	0.9055	106.25	0.24
	0,6891	0.0023	8.66	0.9999	0.0029	76.92			
$CCNS_3$	0.5349	0.234	73.97	0.8303	0.425	76.62	0.8392	289.74	0.22
	0.8463	0.0034	9.43	0.9999	0.0027	79.37			

*****PFO – Pseudo-first-order; PSO- Pseudo-second-order

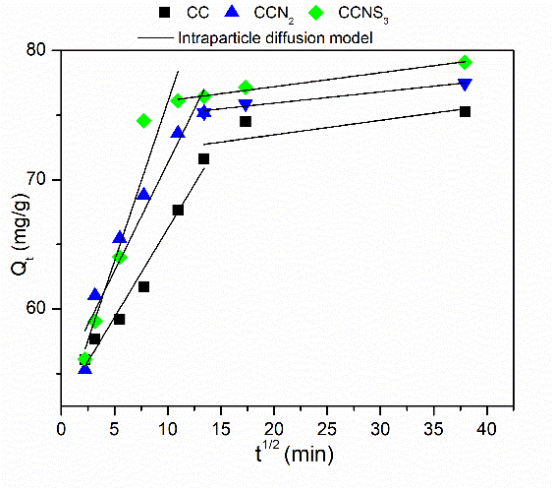


Figure 2. Intraparticle diffusion model for ibuprofen adsorption onto investigated samples.

Table 2. Obtained Intraparticle diffusion model parameters for ibuprofen adsorption.

Samples	R_1	ki_1 (mg/gmin$^{1/2}$)	C_1 (mg/g)	R_2	ki_2 (mg/gmin$^{1/2}$)	C_2 (mg/g)
CC	0.9888	1.368	52.51	0.9723	0.112	54.63
CCN_2	0.9667	1.665	54.63	0.9892	0.089	74.18
$CCNS_3$	0.9633	2.458	51.41	0.9927	0.108	75.04

CONCLUSION

This work investigated a kinetic study for the possible application of pristine carbon cryogel, N-doped and N, S, co-doped carbon cryogel for ibuprofen adsorption from water solution. The obtained results showed satisfactory adsorption ability for all three samples, experimental data fits well with linear pseudo-second-order and Elovich kinetic model, and adsorption of ibuprofen depends on the diffusion through the pore and adsorption at interior active sites. The CCN_2 and $CCNS_3$ samples showed faster and better adsorption properties compared to pristine CC samples, which is a consequence of better surface and textural properties occurring doping of nitrogen and sulfur. The future investigation will provide more detailed information about the adsorption capacity of the samples and also the influence of the interference on ibuprofen adsorption.

Acknowledgment

This work was supported by the Ministry of Education, Science and Technological Development of the Republic of Serbia (grant no 451-03-66/2024-03/ 200017, topic number 1702407).

REFERENCES

[1] A.Osman, A.Ayati, M. Farghali, P. Krivoshapkin, B. Tanhaei, H. Karimi-maleh, E. Krivohapkina, P. Taheri, C. Tracey, A. Al-Fatesh, I. Ihara, D. Rooney, M. Sillanpaa Environmental Chemistry Letters , 22 (2024). 373-418.
[2] S. Kollarahithlu and R. M. Balakrishnan, J Clean Prod, 294 (2021) 126155.
[3] A. Krstić, A. Lolić, M. Mirković, J. Kovač, T. Minović Arsić, B. Babić, A. Kalijadis, J Environ Chem Eng, 10 (6) (2022) 108998.
[4] B. Babić, B. Kaluderović, L. Vračar, N. Krstajić, Carbon 42 (12–13) (2004) 2617-2624.
.[5] A. Kalijadis, N. Gavrilov, B. Jokić, M. Gilić, A. Krstić, I. Pašti, B. Babić, Mater Chem Phys, 239 (2020) 122120.
[6] D. Đukić, A. Krstić, K. Jakovljević, S. Butulija, Lj. Anđelković, V. Pavlović, M. Mirković, Sustainability, 14 (7) (2022) 4003.
[7] M. Vukčević, B. Pejić, A. Kalijadis, I. Pajić-Lijaković, M. Kostić, Z. Laušević, M. Laušević, Chemical Engineering Journal, 235 (2014) 284.

THE NICKEL SORPTION CAPACITY OF THE ARAGONITE-BASED SHELLS OF *ARCA NOAE*

I. Smičiklas, M. Jović, A. Mraković and S. Dragović

University of Belgrade, "VINČA" Institute of Nuclear Sciences - National Institute of the Republic of Serbia, Mike Petrovića Alasa 12-14, 11351 Beograd, Srbija. (ivanat@vin.bg.ac.rs)

DOI: https://doi.org/10.46793/Phys.Chem24II.503S

ABSTRACT

Assessing the sorption capacity and mechanisms of calcium carbonate interaction with nickel (Ni(II)) ions helps evaluate the potential risks associated with heavy metal contamination in natural systems and designing mitigation approaches for contaminated environments. In this study, the sorption of Ni^{2+} was investigated using shells of *Arca noae* (AN) species as a source of biogenic carbonate, mainly aragonite. The sorption of Ni^{2+} decreased significantly with an increase in the size of AN particles. The interaction of AN with Ni^{2+} solutions led to the rise in pH and the release of Ca^{2+} ions. X-ray diffraction analysis of the Ni-saturated AN sample revealed the absence of newly precipitated crystalline phases. The results suggest that the sorption of Ni^{2+} occurs via several surface reactions, including inner-sphere complexes formation, coprecipitation, or re-crystallization. The 0.045-0.125 mm AN fraction showed a maximum sorption capacity of 18.3 mg/g.

INTRODUCTION

Due to its versatility and effectiveness as a sorbent and remarkable buffering capacity, calcium carbonate holds immense potential to contribute to protecting and restoring ecosystems and human health. It is widely used for the sorption of heavy metals [1] and organic pollutants [2] from contaminated water and soil, thereby reducing their toxicity. Additionally, it aids in the adjustment of acidic soils or wastewater pH, enhancing the effectiveness of remediation processes [3].

Investigating the interaction between metal cations and calcium carbonate provides insights into the surface chemistry and properties of calcium carbonate-based materials, which can be useful in water treatment, catalysis, and material synthesis. Industries releasing increasing amounts of effluents with elevated Ni(II) concentrations, such as oil refining, mining, electroplating, mineral processing, and battery production, caused this metal to become one of the priority pollutants and a serious environmental issue [4]. Recent reviews on Ni(II) sorption studies highlight the relevance of studying natural and waste-derived materials as affordable and locally available sorbents [4, 5].

This study aimed to investigate the Ni^{2+} sorption capacity of seashells, which contain biogenic calcium carbonate, and to gain a better understanding of the interactions between Ni^{2+} and the seashell surface.

METHODS

Approximately 1 kg of bivalve mollusk *Arca noae* (AN) shells were collected in the southeast Adriatic Sea (Njivice, Montenegro). The shells, free of flesh, were washed with deionized water, oven-dried at 50°C for 24 h, pulverized in a planetary mono mill, and sieved into different particle size fractions.

The solutions of Ni^{2+} were prepared from $Ni(NO_3)_2$ (Carlo Erba, p.a.). The sorption of Ni^{2+} was first studied by varying the AN particle size fraction (from 0.045-0.125 mm to 1-2 mm range), using an initial Ni^{2+} concentration of 10^{-2} mol/L. The solid-to-solution ratio was 5 g/L (0.100 g/20 mL), the initial pH was adjusted to pH 5.0±0.1, and the shaking time was set to 24 h to ensure

equilibrium conditions. For comparison, commercial-grade synthetic $CaCO_3$ (Merck, p.a., particle size d_{50}= 0.014 mm) was included in the sorption study. The second batch experiment set involved determining the AN sample's maximum sorption capacity using the 0.045-0.125 mm particle fraction, solutions with increasing Ni^{2+} concentration (10^{-4} mol/l – 10^{-2} mol/L) and maintaining other conditions from the previous experiment. The experiments were conducted in duplicate.

After centrifugation and filtering through syringe micro filters (pore size 0.45 μm), the residual Ni^{2+} concentrations and concentrations of released Ca^{2+} ions were measured using Inductively Coupled Plasma Optical Emission Spectroscopy (ICP-OES, Perkin Elmer Avio 200). The amounts of sorbed Ni^{2+} were calculated based on the difference between the initial and residual Ni^{2+} concentrations in the solution. Solution pH at equilibrium was measured by WTW InoLab pH Level 1 pH meter. The crystalline phases in the pristine AN sample and the solid phase recovered after AN (0.045 - 0.125 mm) contact with 10^{-2} mol/L of Ni^{2+} (AN-Ni sample) were analyzed by X-Ray Diffraction (XRD) analysis on the Rigaku Smartlab SAXS diffractometer. The AN's loss of ignition (LOI) was determined by heating at 500 °C for 4 h.

RESULTS AND DISCUSSION

The pristine AN sample lost 6.15 % of its mass at 500 °C, which can be attributed to the content of water and organic matter [6]. The shells' inorganic phase was a rich calcium carbonate source (**Figure 1**). Semiquantitative analysis by the MATCH! Program confirmed the prevalence of aragonite (84.0 %) compared to calcite polymorph (6.0%), with the addition of the magnesium calcium carbonate ($Ca_{0.9}Mg_{0.1}CO_3$) phase (8.4 %) and traces of quartz (1.6 %).

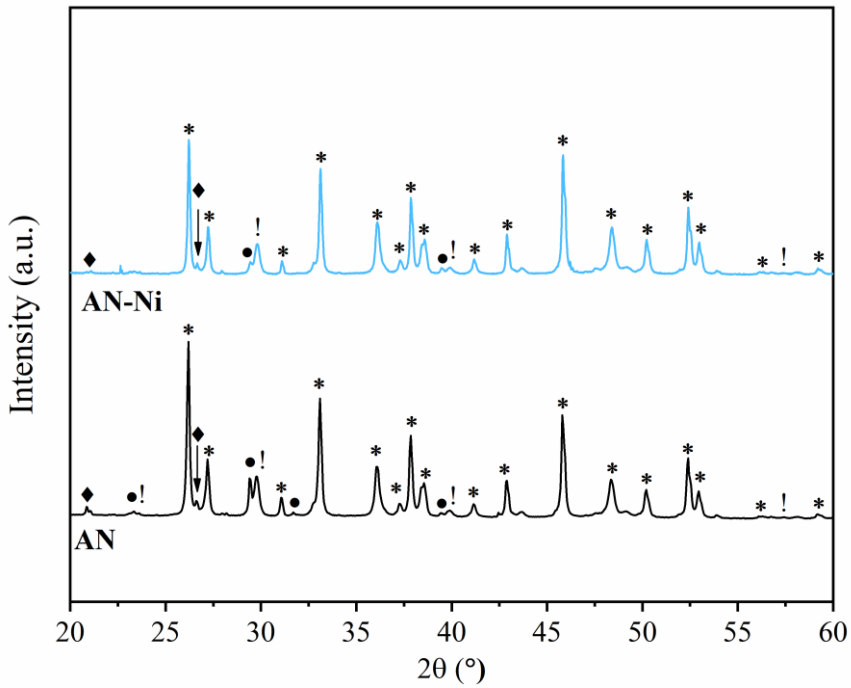


Figure 1. X-ray diffraction patterns of native (AN) and Ni-saturated (AN-Ni) shells with identified phases denoted as aragonite (✱), calcite (●), quartz, SiO_2 (♦), magnesium calcium carbonate $Ca_{0.9}Mg_{0.1}CO_3$ (!).

A substantial decrease in the sorbed amount of Ni^{2+} with increased size of AN particles was revealed (**Figure 2**). The capacity of 0.274 mmol/g, characteristic for 0.045-0.125 mm fraction, decreased to 0.204 mmol/g and 0.127 mmol/g for 0.125-0.2 mm and 0.2-1 mm fractions,

respectively, while particles with 1-2 mm size displayed minor Ni^{2+} sorption capacity (0.003 mmol/g). This trend implies that Ni^{2+} ions accumulate at the AN surface, which progressively decreases with increasing particle size.

In relation to the initial pH 5, the equilibrium pH values (**Figure 2**) shifted to 7.6-7.7 due to the partial dissolution of carbonates in AN. Results support the sorption of Ni^{2+} ions, as these soluble species are dominant below pH 8 [4], while a pH range optimal for $Ni(OH)_2$ precipitation is pH 9-10 [7]. Importantly, the synthetic $CaCO_3$ powder exhibited negligible Ni^{2+} sorption capacity under equivalent conditions and attained the lowest equilibrium pH of 7.2. This underscores the biogenic AN composite's unique structure and surface properties, which contribute to its enhanced sorption performance compared to pure inorganic $CaCO_3$ with 100% calcite polymorph [8].

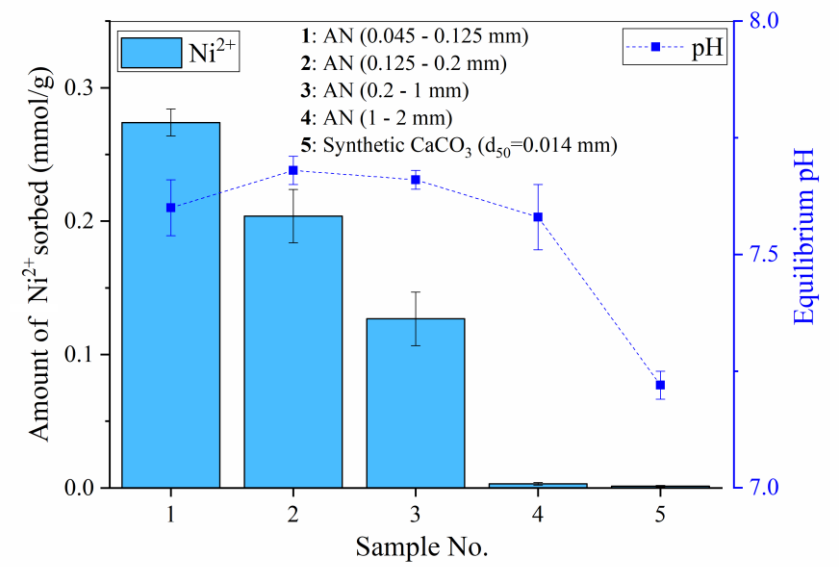


Figure 2. The equilibrium pH values and the amounts of sorbed Ni^{2+} ions using different particle size fractions of AN and synthetic $CaCO_3$.

The sorption isotherm of Ni^{2+} on 0.045-0.125 mm AN fraction is presented in **Figure 3a**. The shape of the isotherm indicates an increase in sorption with the increase in the initial concentration of Ni^{2+}, leading to the gradual saturation of the AN surface. The results were fitted using the Langmuir equation [9]:

$$Q_e = Q_m K_L C_e/(1+K_L C_e)$$

Where Q_e (mg/g) and C_e (mg/L) denote equilibrium Ni^{2+} concentrations in the solid and liquid phase, Q_m (mg/g) is the maximum sorption capacity, and K_L (L/mg) is the Langmuir constant. The coefficient of determination (R^2=0.987) indicated a good fit, with a calculated Q_m of 18.3±1.2 mg/g. This value is within the range of capacities published for numerous natural materials, composites, waste, and modified materials [4].

With increasing initial Ni^{2+} concentration, sorbed Ni^{2+} amounts and the amounts of Ca^{2+} ions released into the solution increased in parallel (**Figure 3b**). Due to the AN buffering capacity, the equilibrium pH values also increased compared to the initial pH 5 (**Figure 3b**). However, the more Ni^{2+} was sorbed, the lower the pH of the system was (ranging from 9.1 to 7.6). The results signify the complexity of the Ni^{2+} sorption mechanism which may take place in several steps including complexation with the AN surface groups forming inner-sphere complexes, and coprecipitation or

re-crystallization. In support, no newly formed crystalline phases were found in the X-ray diffractogram of a Ni-saturated sample (AN-Ni, **Figure 1**).

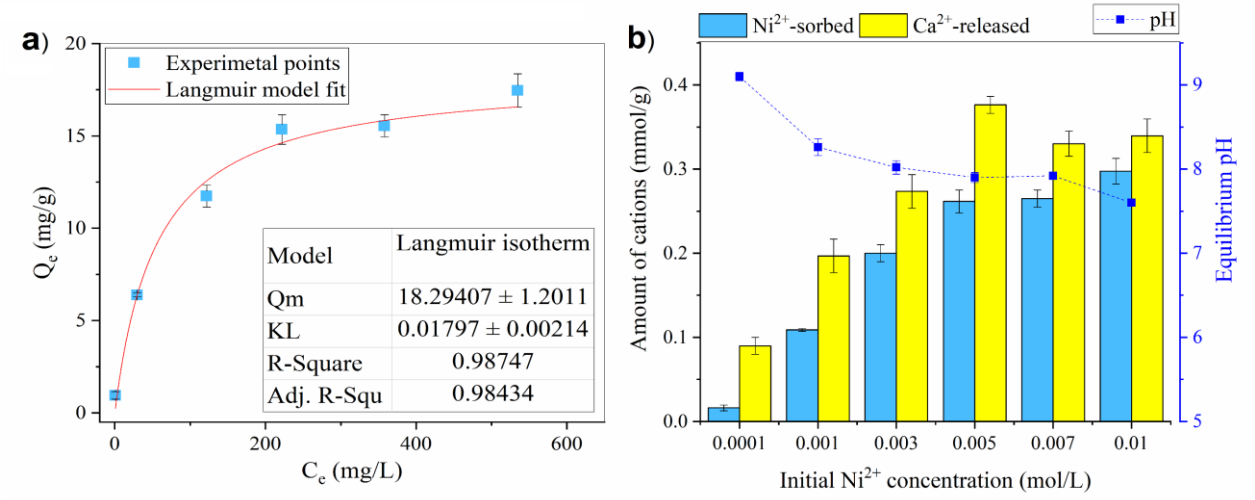


Figure 3. a) Ni^{2+} sorption isotherm by AN with Langmuir model fit, and b) comparison of the equilibrium amounts of sorbed Ni^{2+}, released Ca^{2+} ions, and equilibrium pH at different initial Ni^{2+} concentrations.

CONCLUSIONS

Using waste shells from marine mollusks, such as AN, can help remove soluble Ni^{2+} ions and contribute to environmental cleanup and remediation efforts. Biogenic AN, primarily composed of aragonite, performs better than synthetic calcite. Given that the origin and properties of carbonate-based sorbent play a crucial role in Ni sorption, it would be valuable to conduct a future study comparing the Ni sorption capacities of shells with different mineral phase compositions and surface properties.

Acknowledgment

This work was supported by the Ministry of Science, Technological Development and Innovation of the Republic of Serbia (grant no 451-03-66/2024-03/200017).

REFERENCES

[1] J.M. Zachara, C.E. Cowan, C.T. Resch, Geochim. Cosmochim. Acta, 55 (1991) 1549.
[2] I. Zielińska, D. Polak, A. Jurkiewicz, J. Osełkowska, A. Lorek, M. Stor, A. Krasiński, P. Gierycz, M. Szwast, Sustainability, 16 (2024) 3794.
[3] E. J. Kellaway, M. C. Eimers, S. A. Watmough, Sci. Total Environ., 805 (2022) 150321.
[4] A. Islam, R. Awual, M. J. Angove, J. Environ. Chem. Eng., 7 (2019) 103305.
[5] S. Charazińska, E. Burszta-Adamiak, P. Lochyński, Rev. Environ. Sci. Biotechnol., 21 (2022) 105.
[6] B. Janković, I. Smičiklas, N. Manić, A. Mraković, M. Mandić, Đ. Veljović, M. Jović, Thermochim. Acta, 686 (2020) 178568.
[7] N. A. Zainuddin, T. A. R. Mamat, H. I. Maarof, S. W. Puasa, S. R. M. Yatim, IOP Conference Series: Materials Science and Engineering, 551 (2019) 012122.
[8] R. Ismail, T. Cionita, W. L. Shing, D. F. Fitriyana, J. P. Siregar, A. P. Bayuseno, F. W. Nugraha, R. C. Muhamadin, R. Junid, N. A. Endot, Materials (Basel), 15 (2022) 5712.
[9] I. Langmuir, J. Am. Chem. Soc., 40 (1918) 1361.

SMALL-SCALE VARIABILITY OF GULLY EROSION RATES AND SOIL PROPERTIES IN THE CRVENI POTOK CATCHMENT

A. Čupić [1], I. Smičiklas [1], M. Jović [1], M. Đorđević [2], M. Đokić [2], R. Dragović [2], M. Manić [3], B. Gajić [4] and S. Dragović [1]

[1]*University of Belgrade, "VINČA" Institute of Nuclear Sciences, National Institute of the Republic of Serbia, Mike Petrovića Alasa 12-14, 11351, Belgrade, Serbia. (aleksandar.cupic@vin.bg.ac.rs)*
[2]*University of Niš, Faculty of Sciences and Mathematics, Department of Geography, Višegradska 33, 18000, Niš, Serbia.*
[3]*University of Belgrade, Faculty of Geography, Studentski Trg 3, 11000, Belgrade, Serbia.*
[4]*University of Belgrade, Faculty of Agriculture, Nemanjina 6, 11080, Beograd, Serbia.*

DOI: https://doi.org/10.46793/Phys.Chem24II.507C

ABSTRACT

Contemporary research has given much attention to explaining and managing gully erosion processes, which significantly compromise environmental quality. The need to reliably quantify soil redistribution has led to the development of the (nuclear) ^{137}Cs technique, herein applied to obtain such estimates within the gully in the Crveni potok catchment, an erosion-prone area of Eastern Serbia. The study also aimed to find relations among the erosion rates and soil physicochemical properties. The erosion rate was significantly correlated ($p<0.05$) only with the particle size distribution, specifically being negatively correlated with silt and positively correlated with the fine sand fraction. The loss of silt fraction could lead to erosion expansion and sedimentation outside the gully, implying that remediation measures (e.g., reestablishing a vegetation cover) must be taken to prevent the advancement of soil redistribution issues.

INTRODUCTION

Gully erosion is a geomorphic process that poses a substantial challenge to land management and environmental conservation in many regions around the world, particularly in hilly terrains [1]. This phenomenon results from accelerated soil erosion and is responsible for severe soil loss [2]. The flow of surface water may transport soil particles of different sizes through the gully channels, from fine clay and silt to coarser sand and gravel. Understanding the transportation of these diverse particles is vital for comprehending the mechanisms driving gully erosion and its implications on soil quality.

The study focuses on the northern part of the Crveni potok catchment in Eastern Serbia. The hilly, erosion-prone area spans about 8 km², with altitudes up to 729 m. Geology includes sandstone, conglomerate, and siltstone, leading to loamy, well-drained, and erosion-susceptible *Haplic Cambisol*. Steep slopes (frequently over 20°) and intense rainfall (over 800 mm in the highest area) contribute to significant gully erosion. Vegetation comprises deciduous forests and transitional woodland/shrubs [3]. The main objectives were (i) to assess the extent of erosion at different locations within the gully found in the study area using the nuclear technique based on fallout radionuclide ^{137}Cs redistribution, and (ii) to analyze the associations between the erosion rates and physicochemical soil properties. Such studies are lacking for at-risk areas of Serbia to assess the impact of erosion on soil conditions and help design site-specific protection measures.

METHODS

The sampling points were located in a sector of a gully with a depth ranging from 4 to 6 m (43°22'37.13"N, 22°0'34.68"E). Ten samples were collected at the bottom and one (sample point 11) at the sidewall of the gully. The distance between the first and the last sampling point was about 140 m, with the distances between the individual points varying between 5 and 30 m. The gully was covered with fallen leaves and sparse, undeveloped vegetation, mainly oaks. Topsoil samples (0-20 cm) were collected, dried at room temperature, and sieved to a < 2 mm fraction for soil physicochemical analysis. Standard procedures were applied to determine the particle size distribution (ISO 11277:1998(E)), soil pH (ISO 10390:2021), and electrical conductivity (ISO 11265:1994(E)). After soil samples digestion in aqua regia (EN 16174:2012), the concentration of selected elements (Ca, Mg, K, Na, Al, Fe, Mn, and P) was measured using Inductively Coupled Plasma - Optical Emission Spectrometry (ICP-OES, Perkin Elmer Avio 200). The ^{137}Cs activity concentrations in soil samples were measured on an HPGe gamma-ray spectrometer (Baltic Scientific Instruments, 65% relative efficiency and 1.74 keV energy resolution for ^{60}Co at 1.33 MeV). The estimate of the measurement methods error was up to 5%. The ^{137}Cs inventories (Bq m^{-2}) were derived using its activity concentrations (Bq kg^{-1}) and the bulk density values for each soil profile. Profile distribution (PD) model was used to derive estimates of soil erosion and deposition rates from the ^{137}Cs inventories [4]. The methodology was based on comparing the total ^{137}Cs inventories for the sampling point with the reference inventory, i.e., nearby site where no soil redistribution processes (erosion and deposition) have occurred since the primary ^{137}Cs deposition. Details on applied methodology can be found in our previous work [5]. Although the PD model does not take into account the time-dependent nature of ^{137}Cs fallout input and the post-fallout redistribution of ^{137}Cs in the soil profile, the reliability of the ^{137}Cs technique in estimating gully erosion in forested areas [3, 6, 7] was previously tested and validated.

RESULTS AND DISCUSSION

While taken from a relatively small area, soil samples were characterized by notable differences in erosion rates and particle size distribution (**Table 1**), as indicated by coefficients of variation (CV).

Table 1. Soil erosion rates and particle size distribution at different gully points.

No	Erosion rate (t ha^{-1} y^{-1})	Coarse sand (%)	Fine sand (%)	Silt (%)	Clay (%)
1	8.7	7.8	17.4	46.9	27.9
2	23.4	10.7	20.8	41.6	26.9
3	20.5	8.2	19.7	45.0	27.1
4	13.6	13.7	21.5	43.3	21.5
5	5.7	11.5	16.4	47.1	25.0
6	6.5	13.3	18.0	46.1	22.6
7	6.2	12.5	11.9	49.0	26.6
8	7.2	9.3	19.2	48.6	22.9
9	35.3	13.3	24.4	39.8	22.5
10	8.9	7.9	16.0	56.8	19.3
11	9.5	4.3	16.4	58.9	20.4
CV	71.10	29.23	18.16	12.27	12.38

The mean erosion rates obtained in this study are typical for similar landscapes [7, 8]. Considering Lazarević's erosion scale [9], weak erosion was detected at 7 locations, moderate

erosion at 1 location, and severe erosion at 3 locations. The high variability of erosion rates in a relatively small area could be explained by variations in microrelief (length and steepness of slope), vegetation cover (grass, moss, shrubs, trees, etc.), debris and underneath root system at sampling points, which are all factors governing the intensity of erosion. The results of elemental analysis, pH measurements, electrical conductivity (EC) measurements, and variations expressed through CV values are portrayed in **Table 2**.

Table 2. Soil pH, EC, and pseudo-total concentration of elements at different gully points.

No	pH	EC (µS/cm)	Ca	Mg	K	Na	Al	Fe	Mn	P
			(mg/kg)							
1	7.7	101	3342	5560	2284	150.8	20310	34560	962.4	136.3
2	7.8	92.7	4790	5244	2391	158.9	18740	32580	962.3	172.0
3	7.8	115	4088	5214	3389	201.6	20030	28120	947.1	191.8
4	7.6	95.8	2974	4450	2467	166.7	13700	26510	702.0	196.3
5	7.4	81.6	3684	5945	2132	141.4	16470	36710	757.5	241.7
6	7.6	85.8	3906	6766	2721	172.9	18460	40380	1206	261.2
7	7.2	139	4971	8337	4264	199.4	22960	43230	743.8	359.5
8	7.4	60.7	3311	6318	3073	189.9	20480	35970	838.8	188.5
9	7.9	80.1	3343	5997	2576	198.4	17900	37590	539.1	201.5
10	7.9	129	6340	5284	1904	185.4	15230	30410	288.2	250.4
11	6.0	39.7	1823	6863	3455	199.8	18930	32220	715.6	189.5
CV	7.06	30.93	30.68	17.64	24.97	12.13	14.11	14.76	30.86	27.39

The comparison of the linear relationships between investigated soil properties is presented in **Figure 1**. The pH was positively correlated with the soil EC (r=0.625, p=0.040) and Ca content (r=0.632, p=0.037), indicating the role of calcium carbonate in controlling soil pH and EC. In addition, an inverse relationship between the pH and silt fraction was found (r=-0.610, p=0.046).

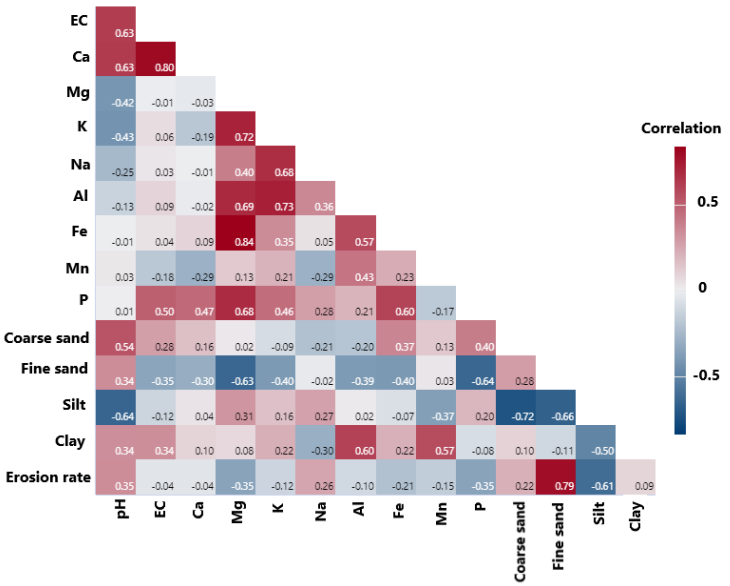


Figure 1. Pearson's correlogram of soil physicochemical properties and erosion rates.

Significant correlations regarding the elements were found between K and Na (r=0.677, p=0.022), Al (0.731, p=0.011), and Mg (0.718, p=0.013), as well as between Mg and Fe (r=0.839, p=0.001), Al (r=0.693, p=0.018), and P (r=0.683, p=0.020). These correlations imply a relationship between these elements, indicating their co-occurrence in the soil. The study also observed a significant positive correlation between the pseudo-total content of Al and clay fraction (r=0.605, p=0.049). Meanwhile, the fine sand fraction had a negative correlation with the content of Mg (r=-0.635, p=0.036) and P (r=-0.636, p=0.036).

However, the rate of erosion in the gully was not statistically significant in terms of the pseudo-total content of examined elements, soil pH, and EC values. On the other hand, the erosion rate was significantly correlated with the soil particle size distribution. Specifically, it was negatively correlated with silt (r=-0.610, p=0.046) and positively correlated with fine sand fraction (r=0.793, p=0.004). Further, the silt fraction negatively correlated with both coarse (r=-0.724, p=0.012) and fine sand (r=-0.663, p=0.026) fractions, indicating that they are mostly separated from each other during the erosion process. These results suggest that the gully erosion process preferentially transports particles of the silt fraction, leading to an increase in the fraction of fine sand particles in the soil. The findings are in correspondence with correlations obtained in our recent study, indicating that the silt-size particles in studied gullies of the Crveni potok catchment are preferentially transported due to erosion [6].

CONCLUSION

The implications of gully erosion leading to enrichment in fine sand and depletion in silt fraction can include reduced fertility, decreased water retention, loss of soil structure, and increased erosion risk. Furthermore, sediment-laden runoff from the gully affects the environmental stability beyond the immediate gully area by deposition of silt-sized particles in downstream regions. Addressing gully erosion and restoring soil health through erosion control measures and soil conservation practices is crucial to mitigate these impacts and maintain overall soil quality. The restoration of vegetative cover in gully-prone areas of the Crveni potok catchment would assist in stabilizing the soil and enhancing nutrient cycling.

Acknowledgment

This research was supported by the Science Fund of the Republic of Serbia, #GRANT No 7047, *Development of erosion prediction tool for sustainable soil management* – Predict-Er.

REFERENCES

[1] J. Poesen, J. Nachtergaele, G. Verstraeten, C. Valentin, Catena 50 (2003) 91.
[2] C. Valentin, J. Poesen, Y. Li, Catena 63 (2005) 132.
[3] M. Manić, M. Đorđević, M. Đokić, R. Dragović, D. Kićović, D. Đorđević, M. Jović, I. Smičiklas, S. Dragović, Front. Environ. Sci., 10 (2022) 897248.
[4] D. E. Walling, Q. He, J. Environ. Qual., 28 (1999) 611.
[5] J. Petrović, S. Dragović, R. Dragović, M. Đorđević, M. Đokić, B. Zlatković, D. Walling, J. Environ. Radioact., 158–159 (2016) 71.
[6] M. Đokić, M. Manić, M. Đorđević, M. Gocić, A. Čupić, M. Jović, R. Dragović, B. Gajić, I. Smičiklas, S. Dragović, Environ. Res. 235 (2023) 116679.
[7] P. Porto, D.E. Walling, A. Capra, Soil Till. Res., 135 (2014) 18.
[8] P. Porto, G. Callegari, J. Soils. Sedim. 23 (2023) 3689.
[9] R. Lazarević, Erosion Map of SR Serbia 1:500,000, Institute of forestry and wood industry of Serbia, Department of erosion and melioration, Belgrade, 1983 [In Serbian].

Ambrosia artemisiifolia BIOSORBENT FOR REMOVAL OF SYNTHETIC ORGANIC DYES FROM AQUATIC SOLUTION

S. Bulatović, N. Nedić, T. Tadić, B. Marković and A. Nastasović

University of Belgrade, Institute of Chemistry, Technology and Metallurgy, Njegoševa 12, 11000 Belgrade, Serbia. (sandra.bulatovic@ihtm.bg.ac.rs)

DOI: https://doi.org/10.46793/Phys.Chem24II.511B

ABSTRACT

The main causes of water pollution in the environment are industries which wastewaters contain many pollutants, including synthetic organic dyes. These compounds can be toxic to organisms, and it is important to eliminate them from wastewaters. Biosorption is a sorption method in which the sorbent is of biological origin, the so-called biosorbent. This method is cheap, simple and eco-friendly. In this investigation the biomass of *Ambrosia artemisiifolia* was used as a biosorbent of synthetic dyes: Malachite Green (MG), Congo Red (CR), and Rhodamine B (RB). The effectiveness of the analyzed biosorbent was monitored by UV-Vis spectroscopy. The biosorbents were characterized before and after sorption with Fourier Transform Infrared Spectroscopy (FTIR). After 24 h of biosorption, removal efficiency was more than 80 % for all synthetic organic dyes.

INTRODUCTION

Due to the intensive development of the chemical, pharmaceutical and agricultural industries, many chemical compounds, such as synthetic organic dyes, can easily reach the aquatic environment. These compounds are considered as environmental micropollutants, due to their low concentration (ng/l to µg/l) in aquatic ecosystems. They are widely used in textile, paper, pharmaceutical, and cosmetics industries, medicine etc. Some of them are toxic to organisms and may pose a threat to environmental balance, and it is important to eliminate them from the wastewater and prevent their presence into the environment [1, 2, 3]. Biosorption is an economic, simple and effective method for removing pollutants from wastewater, using biosorbent [5]. Biosorbent is a natural product of biological origin (microorganisms), plants, or waste biomass from industry, for sorption of pollutants. Several biosorbents have been examined for dyes removal from water [6]. Therefore, it was important to develop low-cost approach for dyes removing from wastewaters to enable safe waste disposal and environmental protection. The aim of this investigation was to evaluate the use of *Ambrosia artemisiifolia* biomass, as a biosorbent, for removal of synthetic organic dyes: Congo Red (CR; anionic), Malachite Green (MG, cationic), and Rhodamine B (RB; cationic), from aquatic solution by batch systems. *A. artemisiifolia* is a weedy plant with allergenic pollen [7]. The usage of this plant as a biosorbent is additionally significant, because in this way organic dyes with toxic potential [8-10], including this invasive plant, could be eliminated from the environment.

METHODS

The plant samples were collected from the periphery area of Belgrade, capital of Serbia, by cutting whole plant above the ground. After washing with distilled water, plant samples were dried at room temperature, for seven days. The samples were then crushed into small particles using electric mill, and sifted through a sieve to obtain the biosorbent fraction < 300 µm. The obtained biosorbent was washed with distilled water to remove possible impurities. Washed biopolymer was dried for 48 h / 50 °C, and prepared for experimental work. The batch biosorption experiments were carried out at a constant room temperature, for 24 h. Biosorption studies were carried out with 5 ml of dye solutions

(50 ppm) in contact with 0,1 g of biosorbent. After sorption tests, the biosorbent was separated by centrifugation at 4000 rpm for 5 min. Dyes concentrations in the pre- and post-sorption solutions were estimated using a UV-Vis spectrophotometer (NOVEL-102S UV-Vis Double Beam Spectrophotometer, COLO Lab Experts, Slovenia) at maximum wavelengths of 618 (MG), 498 (CR), and 553,6 nm (RB). The experimental dyes removal efficiency was obtained by applying the equation [8]:

$$R\ (\%) = \frac{C_0 - C}{C_0}\ x\ 100\%$$

where: C_0 (ppm) and C (ppm) are dye concentration before and after biosorption.

Fourier Transform Infrared (FTIR) spectroscopy analysis (Nicolet 380 spectrometer) was performed to determine the presence and changes in functional groups on the biosorbent surface before and after synthetic organic dyes sorption**.**

RESULTS AND DISCUSSION

Results of UV-Vis showed that the efficiency of the analyzed biosorbent, in removing synthetic organic dyes from the water solution, was very successful: for MG – 97.6 %, for CR – 85.8 %, and for RB – 81.6 % (**Figure 1**).

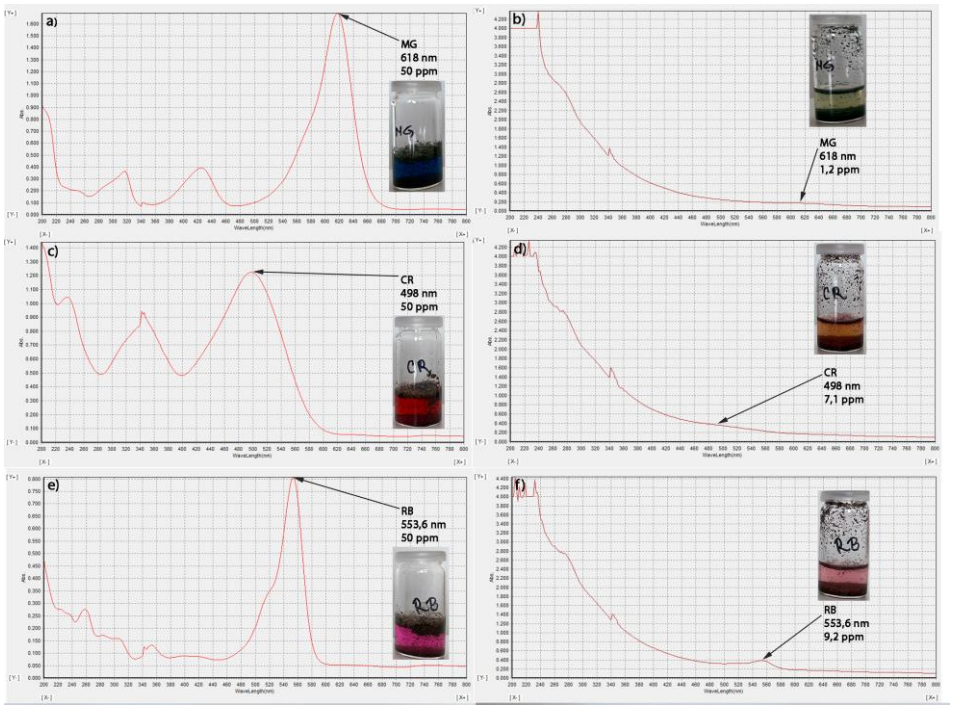


Figure 1. Biosorption of synthetic organic dyes: a) MG before biosorption, b) MG after biosorption, c) CR before biosorption, d) CR after biosorption, e) RB before biosorption, f) RB after biosorption.

FTIR spectra before and after dyes biosorption were monitored in the range of 400 - 4000 cm^{-1} (**Figure 2**). The band around 3300 cm^{-1} corresponds to the stretching vibration of the O–H groups in lignin, cellulose, and hemicellulose. The bands around 2918 and 2850 cm^{-1} can be attributed to the C–H stretching of methoxy groups in lignin, cellulose, and hemicellulose. The bands around 1733 cm^{-1} indicated C=O stretching in carbonyl or carboxyl groups. The peaks from 1600 to 1300 cm^{-1} are assigned to C=C/C–H bonds of CH_2 groups. The bands around 1320 cm^{-1} correspond to the phenols' angular C–O–H deformations and the C–O stretching vibrations in carboxylate (alkanes and alkyl groups). The peak obtained at 1250 cm^{-1} was attributed to stretching frequency of amine (C–N) group. The band between 600 and 540 cm^{-1} indicated the existence of –C–N–C scissoring, characteristic only for protein structure. Comparing the FTIR spectra before (spectrum A-*Ambrosia* biosorbent) and after dyes biosorption (spectra of *Ambrosia* biosorbent with MG (A-MG), CR (A-CR) and RB (A-RB); **Figure 2**), indicated that the functional groups (–C=O, –C–O, –OH) on the biosorbent surface could be the potential adsorption sites for synthetic dyes biosorption, with almost the same binding trend for anion and cationic dyes.

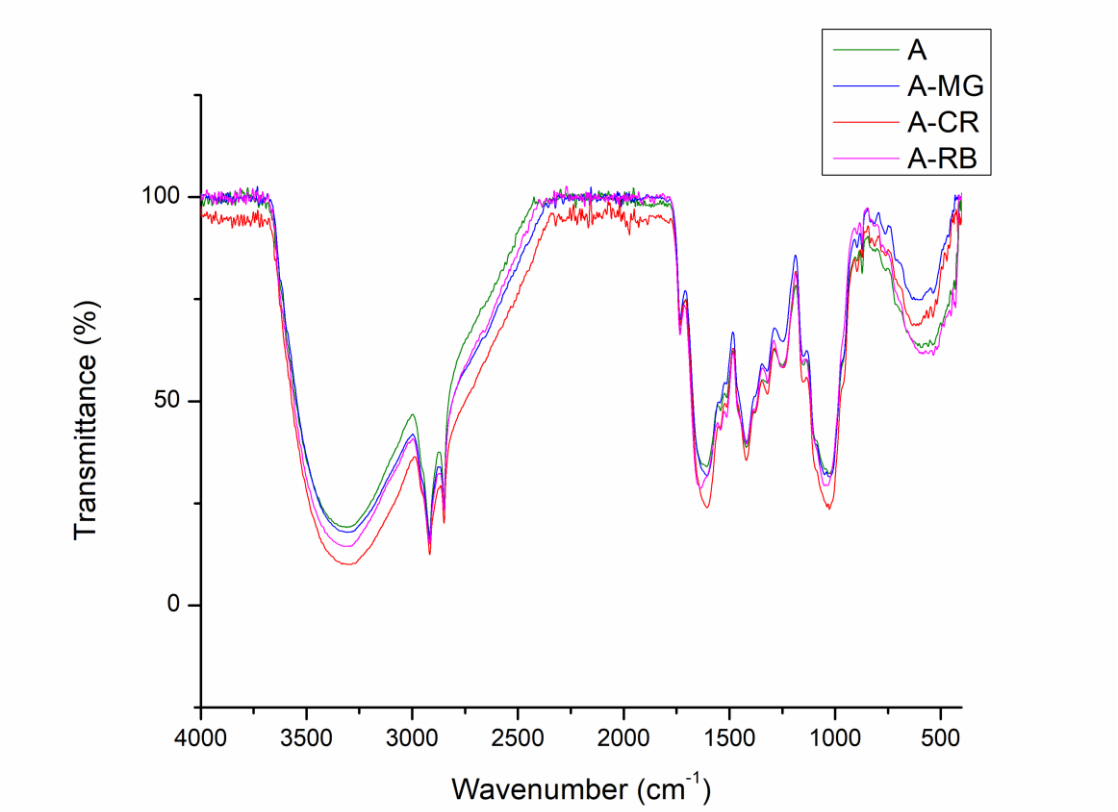


Figure 2. FTIR spectra of *Ambrosia* biosorbent before and after dyes biosorption.

CONCLUSION

The biosorption of synthetic organic dyes from water solution, onto the biosorbent of *A. artemisiifolia* biomass investigated in this study, was very successful, with dyes removal efficiency > 80 %. Biosorbent showed the highest sorption efficiency for MG, then for CR, and the lowest for RB. FTIR analysis also confirmed dyes biosorption.

Acknowledgement
This research has been financially supported by the Ministry of Science, Technological Development and Innovation of Republic of Serbia (Contract No: 451-03-66/2024-03/200026).

REFERENCES

[1] M. Gebrezgiher, Z. Kiflie, J. Environ. Public Health, 2020 (2020) 5383842.
[2] P. Saravanan, J. Josephraj, B. P. Thillainayagam, Environ. Nanotechnol. Monit. Manag., 16 (2021)100560.
[3] A. Tkaczyk, K. Mitrowska, A. Posyniak, Sci.Total Environ., 17 (2020) 137222.
[4] G. Bayazıt, B. E. Tastan, U. D. Gül, Global NEST J., 22 (2020) 1-7.
[5] S. Lazarova, R. Tonev, S. Dimitrova, G. Dimova, I. Mihailova, Processes, 11 (2023) 2291.
[6] H. Tounsadi, Y. Metarfi, N. Barka, M. Taleb, Z. R. Jegede, J. Chem., 2020 **(**2021)7234218.
[7] S.-H Liu, S. Kazemi, G. Karrer, A. Bellaire, W. Weckwerth, J. Damkjaer, O. Hoffmann, M. M. Epstein, Front. Allergy, 3 (2022) 854038.
[8] M. M. Jegede, O. S. Durowoju, J. N. Edokpayi, Adsorpt. Sci. Technol., 2021 (2021) 6297451.
[9] L. Soldatkina, M. Yanar, Chem. Engineering, 7 (2023).
[10] Z. M. Şenol, N. El Messaoudi, Y. Fernine, Z. S. Keskin, Biomass Convers. Bioref., 2023.

REMOVAL OF ^{101}Rh FROM MIXED HNO_3/HCl MATRIX

Đ.Cvjetinović, J.Petrović, Z.Talip and D.Schumann

Paul Scherrer Institut, Forschungsstrasse 111, 5232 Villigen, Switzerland
(djorde.cvjetinovic@psi.ch)

DOI: https://doi.org/10.46793/Phys.Chem24II.515C

ABSTRACT

Proton irradiation of vanadium leads to the production of many rare radionuclides such as ^{32}Si, ^{26}Al, ^{41}Ca, and ^{44}Ti/^{44}Sc. The ^{32}Si is a particularly interesting radionuclide that can be used as a radiometric geochronometer. However, due to the high half-life uncertainty it is first needed to precisely measure the ^{32}Si half-life which is the aim of the SINCHRON project. The first step in this endeavor has been to produce and radiochemicaly separate large amounts of ^{32}Si from other radionuclides produced during proton irradiation. One of the more elusive radionuclidic impurities encountered during the radiochemical separation was ^{101}Rh. It is well known that Rh forms different stable complexes in acidic media, ranging from cationic, anionic to neutral making it difficult to remove in a single step. We report that we have successfully implemented ion-exchange chromatography to remove trace amounts of ^{101}Rh from an acidic (pH = 2) HNO_3/HCl mixed matrix.

INTRODUCTION

Radiometric dating is very important in assessing long past geological changes and monitoring relatively recent human activities. For this purpose, various radionuclides are used, the best-known being radiocarbon – ^{14}C. Unfortunately, one of the more interesting age periods (100 – 1000 years) hasn't been properly covered and this period is extremely important in monitoring the impact of human activities and industrialization on the environment. Therefore, it would be of great importance to fill in this missing radiometric gap using a suitable radionuclide. The best candidate for this purpose would be naturally occurring cosmogenic radionuclide ^{32}Si, with a half-life of 153 ± 19 years [1–3]. However, the existing half-life value for ^{32}Si has an unfavorably large uncertainty and also presents a mean value of several vastly different measurements performed in the past. All of these measurements suffered from the same problem which was the lack of high activities of ^{32}Si used for activity measurement.

Aim of the SINCHRON project was to produce and purify large amounts of ^{32}Si (> 10 MBq) that could then be used for various measurements by different international institutions in order to establish a new, precise and (cross)verified value for the ^{32}Si half-life. By redetermining the ^{32}Si half-life we expect to introduce a new geochronometer that can be used for geological and environmental studies. For this purpose, 150 vanadium discs were proton (590 MeV) irradiated at Paul Scherrer Institut (PSI) for 2 years in order to produce large amounts of ^{32}Si [1]. Over the course of the SINCHRON project different multi-step separation procedures have been developed in order to extract the wanted ^{32}Si as well as other valuable radionuclides (^{26}Al, ^{41}Ca, and ^{44}Ti/^{44}Sc) [1,4,5]. Additionally, worldwide unique activities of ^{32}Si (> 40 MBq) have been recovered, purified and shipped to various institutions for the purpose of ^{32}Si half-life redetermination.

From the 150 vanadium discs that were irradiated approximately 110 have been found to contain radionuclide ^{101}Rh and to smaller extent radionuclides ^{102m}Rh/^{102}Rh. Since we aim to produce ^{32}Si samples completely free of other radionuclide impurities it was very important to find a way to remove ^{101}Rh from the mix. Unfortunately, Rh is an element that makes different complexes in HCl

or HNO_3 media, with pronounced aging effects [6]. After applying previously developed radiochemical separation scheme we found ^{101}Rh to be present in various amounts (0.1-100 Bq) in pre-final ^{32}Si fractions. It is unfortunate that these fractions contain a mix of 0.05M HCl and 0.05M HNO_3 allowing Rh to make a multitude of different cationic, anionic, and neutral species. We needed to find a way to remove all of these complexes from the ^{32}Si samples, and for this purpose we used ion-exchange chromatography.

METHODS

Preliminary investigation on the removal of Rh from acidic media was conducted using inactive batch studies. For these studies a pre-weighed amount of a resin is mixed and equilibrated with a standard solution of Rh and Si, in the corresponding acidic mix. Following the equilibration process the solution is centrifuged and supernatant is analyzed using ICP-OES to determine the content of Si and Rh that has not been adsorbed. This procedure, in brief, is performed in the following steps: 50 ± 2 mg of resin is weighed into 2 mL plastic vials; addition of 0.5 mL of the appropriate acidic mix into the vial; vial shaking for 30 min; addition of 1 mL of a standard solution (contains 50 ppm of both Si and Rh) in the same acidic mix; shaking for 16 h; vial centrifugation at 15000 rpm for 5 minutes; supernatant collection (0.5 mL); supernatant dilution with 4.5 mL of 2% HNO3. Finaly the samples prepared in this way are measured using ICP-OES. By quantifying the elemental composition post-adsorption, we can define the mass distribution coefficient (D, mL/g) for each element as shown in equation (1):

$$D = (C_{max} - C_{mes})/C_{mes} * V_{mL}/M_g \quad (1)$$

where C_{max} is the maximum element concentration prior to adsorption, C_{mes} is the element concentration post adsorption and V_{mL} and M_g are solution volume (1.5 mL) and resin mass (g).

Based on these screening adsorption tests as well as the literature data [6] it was possible to determine the best resin candidates (Purolite S985 and Monophos) that could be used to remove ^{101}Rh from the mix. Following the separation scheme published previously [4,7], at our disposal we had samples containing ^{101}Rh and ^{32}Si in 0.05M HCl/ 0.05M HNO_3. One of these fractions, containing approximately 20 Bq of ^{101}Rh and 30 kBq of ^{32}Si was diluted to the desired pH ≈ 2 (with 0.01M HCl) and divided into aliquots (40 mL). These active samples were used to perform dynamic column adsorption studies. Column studies were performed utilizing custom made PMMA (length 100 mm, inner diameter 10 mm) columns that were packed with resins to the height of 4 cm and immobilized between two 50 μm porous frits. Peristaltic pumps (REGLO Digital MS-2/8, Cole-Parmer Instrument Company, LLC., U.S.A.) were used for the column separations at flow rate of 1 mL/min, with the same squeeze tubes (Ismaprene PharMed®, SC0307, Cole-Parmer Instrument Company, LLC., U.S.A.) Columns were pre-washed with the appropriate acidic mix, until reaching the desired pH, and then loaded with 40 ml of the active load solution and washed with 10 ml of the same acidic matrix. Load and the wash phase were collected together and measured using γ-spectroscopy for ^{101}Rh (127 keV, 198 keV) while ^{32}Si was quantified using liquid scintillation counting.

RESULTS AND DISCUSSION

Results of our cold batch investigation indicated that the best combo for the removal of ^{101}Rh would be the combination of chelating anion exchange resin Purolite S985 (Purolite, US) and chelating cation exchange resin Monophos (100-200 mesh, TrisKem SAS, Bruz, France). As can be seen in Fig. 1 and Fig. 2 no ^{101}Rh is detectable in the load + wash phase when Purolite S985 and Monophos resins are used together in succession. In the case of using just Purolite S985 we can conclude that

most (≈ 90%), but not all of the ^{101}Rh is removed while in the case of Monophos only a small amount of ^{101}Rh (≈ 10%) is removed. As is expected, Rh makes predominantly anionic complexes under these conditions therefore making Purolite S985 efficient in removing most of the present ^{101}Rh.

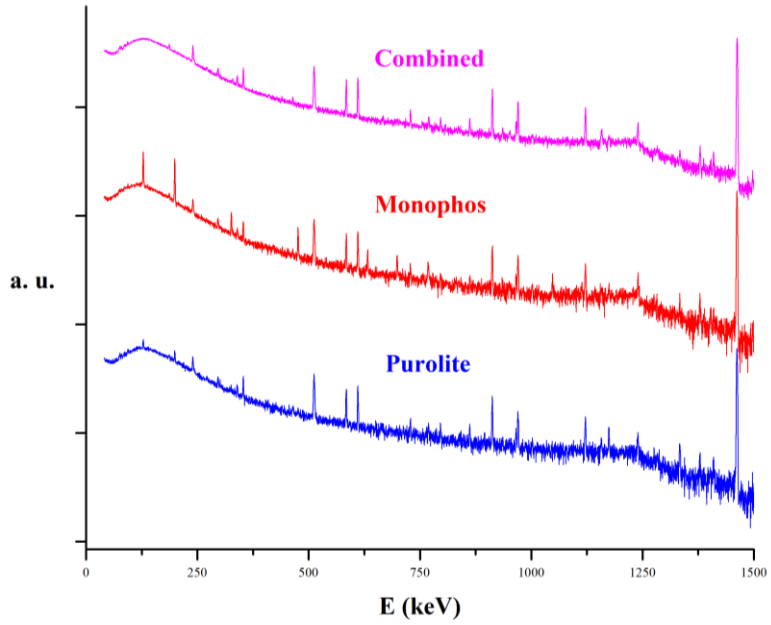


Figure 1. Full gamma spectra of the load+wash phase following Purolite S985 (*bottom*), Monophos (*middle*) and combined Purolite S985 + Monophos (*bottom*) separation. Acquisition time for Purolite S985 and Monophos gamma spectra was 16h and 60h for the combined separation.

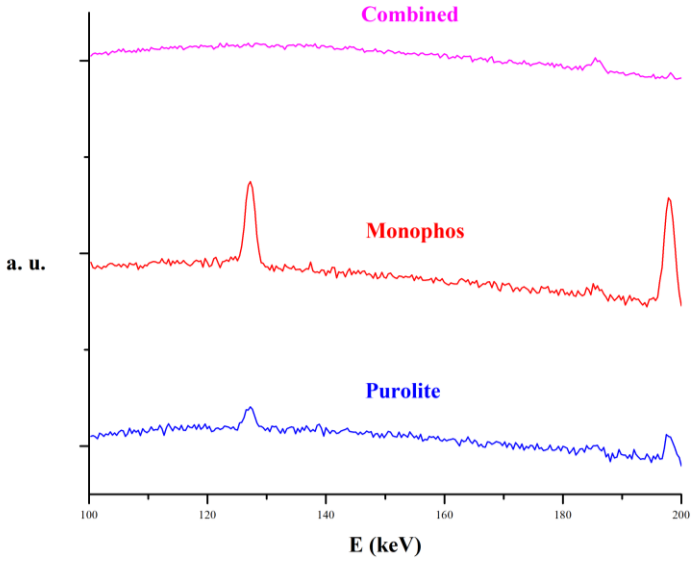


Figure 2. Partial gamma spectra (100 – 200 keV) of the load+wash phase following Purolite S985 (*bottom*), Monophos (*middle*) and combined Purolite S985 + Monophos (*bottom*) separation. Acquisition time for Purolite S985 and Monophos gamma spectra was 16h and 60h for the combined separation. Gamma lines of ^{101}Rh are visible at 127 keV and 198 keV for Monophos/Purolite S985 and absent for the combined separation.

However, due to the aging effects of the solution as well as the presence of HNO_3 in the acidic mix it is presumed that ^{101}Rh exists in cationic and possibly neutral complexes which can be adsorbed by Monophos resin. As for the ^{32}Si activity, it seems that only smaller activity losses occur since all of the load + wash fractions show high ^{32}Si activity (98 ± 4 %), compared to pre-column run.

CONCLUSION

By combining two chelating ion-exchange resins, Purolite S985 and Monophos we have succeeded in removing trace amounts of ^{101}Rh activity (< 0.01 Bq/mL) from an acidic mix of HCl and HNO_3. Since Rh is able to form different stable complexes in acidic media with pronounced aging effects, it is very difficult to remove it completely making this separation scheme a valuable tool in radiochemical separation and purification processes.

Acknowledgment

This project is funded by the Swiss National Science Foundation (SNSF) as part of SINERGIA (No. 177229) and receives additional financial support from the European Union's Horizon 2020 research and innovation program under the Marie Skłodowska-Curie grant agreement No. 884104 (PSI FELLOW-III-3i).

The authors are grateful to the UK representative office of the Purolite Corporation for providing the Purolite S 985 resin.

REFERENCES

[1] M. Veicht, I. Mihalcea, Đ. Cvjetinovic, D. Schumann, Radiochim. Acta. 109 (2021) 735–741.
[2] Z.S. Finch, B.N. Seiner, L.M. Arrigo, J.E. Strivens, M.E. Keillor, T.W. Hossbach, A.W. Myers, G.A. Gill, J. Radioanal. Nucl. Chem. 307 (2016) 2451–2458.
[3] L.K. Fifield, U. Morgenstern, Quat. Geochronol. 4 (2009) 400–405.
[4] J.M. Wilson, I. Mihalcea, M. Veicht, Đ. Cvjetinović, D. Schumann, Radiochim. Acta. 111 (2023) 265–271.
[5] Đ. Cvjetinović, X. Pan, J. Petrović, D. Schumann, Microchem. J. 200 (2024) 110477.
[6] Đ. Cvjetinovic, M. Veicht, D. Schumann, 5232 Villigen PSI Switzerland, 2022.
[7] O.N. Kononova, A.M. Melnikov, T.V. Borisova, A.S. Krylov, Hydrometallurgy. 105 (2011) 341–349.

BIOWASTE-DERIVED CARBON MATERIAL AS AN EFFECTIVE ADSORBENT FOR REMOVING ANTIBIOTICS FROM WASTEWATER

V. Milanković, T. Tasić, J. Mušović, D. Tekić, S. Marić, A. Jocić, A. Dimitrijević and T. Lazarević-Pašti

University of Belgrade, Institute of nuclear sciences Vinča,
Mike Petrovića Alasa 12-14 11000 Vinča, Belgrade, Serbia. (sladjana.maric@vin.bg.ac.rs)

DOI: https://doi.org/10.46793/Phys.Chem24II.519M

ABSTRACT

Environmental contamination is a significant global concern, demanding effective remediation strategies. This study investigates the efficacy of biowaste-derived carbon material in removing antibiotics amoxicillin and ceftriaxone. Adsorption experiments were conducted at 25°C, and the adsorption behavior was analyzed using various adsorption isotherm models. Our findings reveal a complex process involving both monolayer and multilayer adsorption on the material's heterogeneous surface. At a concentration of 0.1 mg mL^{-1}, the carbon material exhibited high adsorption capacities of 82 mg g^{-1} for amoxicillin and 181 mg g^{-1} for ceftriaxone. The adsorbent was successfully regenerated and reused for at least 10 cycles without significantly impacting its adsorption capacity. These results highlight the potential of biowaste-derived carbon material as an efficient adsorbent for antibiotics, underscoring its promising role in environmental remediation.

INTRODUCTION

Discharging effluents containing pollutants from various industrial processes has significantly contributed to environmental degradation. Pharmaceutical residues from drug manufacturing and healthcare facilities are major contributors to the prevailing pollution crisis [1]. Antibiotics such as amoxicillin (AMX) and ceftriaxone (CFX) in environmental matrices have raised concerns due to their potential impact on microbial communities and the emergence of antibiotic-resistant strains [2, 3].

AMX, widely used in human medicine and livestock farming, poses a significant threat when found in water bodies due to incomplete metabolism and excretion, potentially fostering antibiotic resistance in bacteria [4]. Chronic exposure to AMX in aquatic environments can lead to the emergence of antibiotic-resistant bacterial strains, making infections in humans and animals more challenging to manage [5]. Similarly, CFX, a broad-spectrum antibiotic, exhibits environmental persistence and contributes to the proliferation of antibiotic resistance. Its presence in water sources can spur the development of antibiotic-resistant bacteria, compromising the efficacy of critical antibiotics in medical treatments and exacerbating the management of infectious diseases [6].

Biowaste-derived carbon materials have emerged as highly effective adsorbents, offering a sustainable solution for environmental remediation. These materials are produced from organic waste sources such as agricultural residues, food waste, and forestry byproducts, which are converted into carbon-rich adsorbents through processes like pyrolysis. The resulting carbon materials possess unique properties, including high surface area, porous structure, and diverse functional groups, which enhance their adsorption capabilities.

One of the key advantages of biowaste-derived carbon materials is their ability to remove a wide range of contaminants from water and air. These adsorbents are particularly effective in capturing pollutants such as heavy metals, dyes, and pharmaceutical residues, including antibiotics. The

adsorption process often involves complex interactions, including physical adsorption and chemical bonding, facilitated by the heterogeneous surface of the carbon material.

Moreover, biowaste-derived carbon materials are not only cost-effective but also environmentally friendly, as they promote the recycling of waste and reduce the need for conventional, non-renewable adsorbents. Their regeneration and reuse capabilities further enhance their practicality for large-scale applications. Typically, these materials can be regenerated using simple techniques like solvent washing or thermal treatment, maintaining their adsorption efficiency over multiple cycles.

METHODS

The adsorbent was obtained from spent coffee grounds. Coffee was treated with boiling water, left for 2 h to cool to the ambient temperature, filtered, and left to dry. The carbonization was carried out in a tube furnace (Protherm Electrical Tube Furnace, Protherm Furnaces, Turkey) under a nitrogen flow atmosphere of 100 L h^{-1}. The sample was heated to 900 °C with a heat rate of 5 °C min^{-1} and held isothermal for 60 min. The carbonized sample was then treated with H_3PO_4, heated to 900 °C, and held isothermal for 60 min under a CO_2 flow of 100 L h^{-1}. The material was washed with 0.1 M NaOH, 0.1 M HCl, deionized water, and finally suspended in 50 % ethanol to obtain a stock suspension with a mass concentration of 2 mg mL^{-1}.

A mixture of 1 mL adsorbent stock dispersion (2 mg mL^{-1}) and the designated amounts of antibiotics stock solutions were made to deliver the targeted concentration of adsorbent and contaminants. After that, the mixtures were put in a laboratory shaker and left for the specified period. Subsequently, they underwent centrifugation at 14,500 rpm, and the supernatant was analyzed. Antibiotics were analyzed using a UV–Vis spectrophotometer (Perkin Elmer Lambda 35). The maximal absorption wavelengths were determined as 199 and 240 nm for AMX and CFX, respectively. All experiments were done in three replicates, and the mean values were further used with standard deviation as error limits. Control experiments were performed identically but without the adsorbent.

RESULTS AND DISCUSSION

In order to determine equilibrium time and investigate the kinetics of adsorption, the material and antibiotics were mixed to obtain final concentration 1 mg mL^{-1} for the material and 5×10^{-5} mol dm^{-3} for the antibiotics. The mixtures were incubated for 1-120 min, and the obtained experimental data were examined using pseudo-first-order, pseudo-second-order, and Elovich kinetic models (Figure 1). The equilibrium time for both antibiotic was determined to be 60 min, and all investigated kinetic models describe the adsorption very well, implying its complexity.

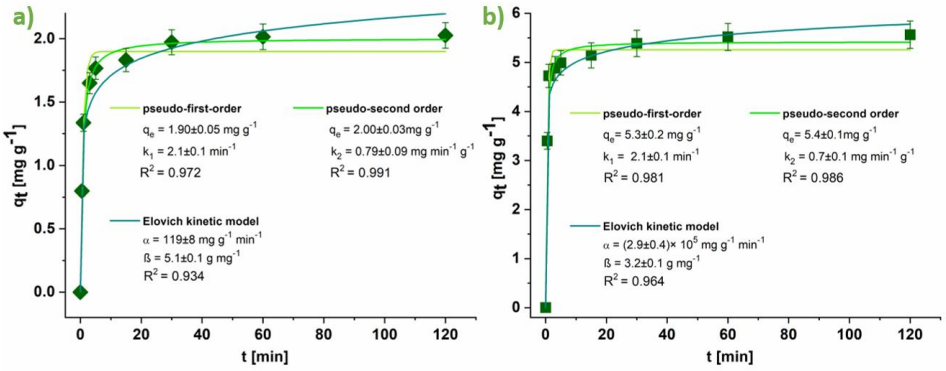


Figure 1. Graphical representations of kinetic models' fittings the experimental data with corresponding parameters for the adsorption of a) AMX and b) CFX.

To obtain experimental data for isotherm studies of antibiotics adsorption onto biowaste-derived carbon material, different concentrations of the adsorbent (1, 0.5, and 0.1 mg mL^{-1}) were incubated for 60 min (previously determined time for equilibration of the system reaching) with AMX and CFX in the concentration range 5×10^{-6} - 5×10^{-5} mol dm^{-3} at 25 °C. The experimental data were analyzed using non-linear Freundlich, Langmuir, Temkin, and Dubinin-Radushkevich isotherm models. The obtained results are provided in Figure 2.

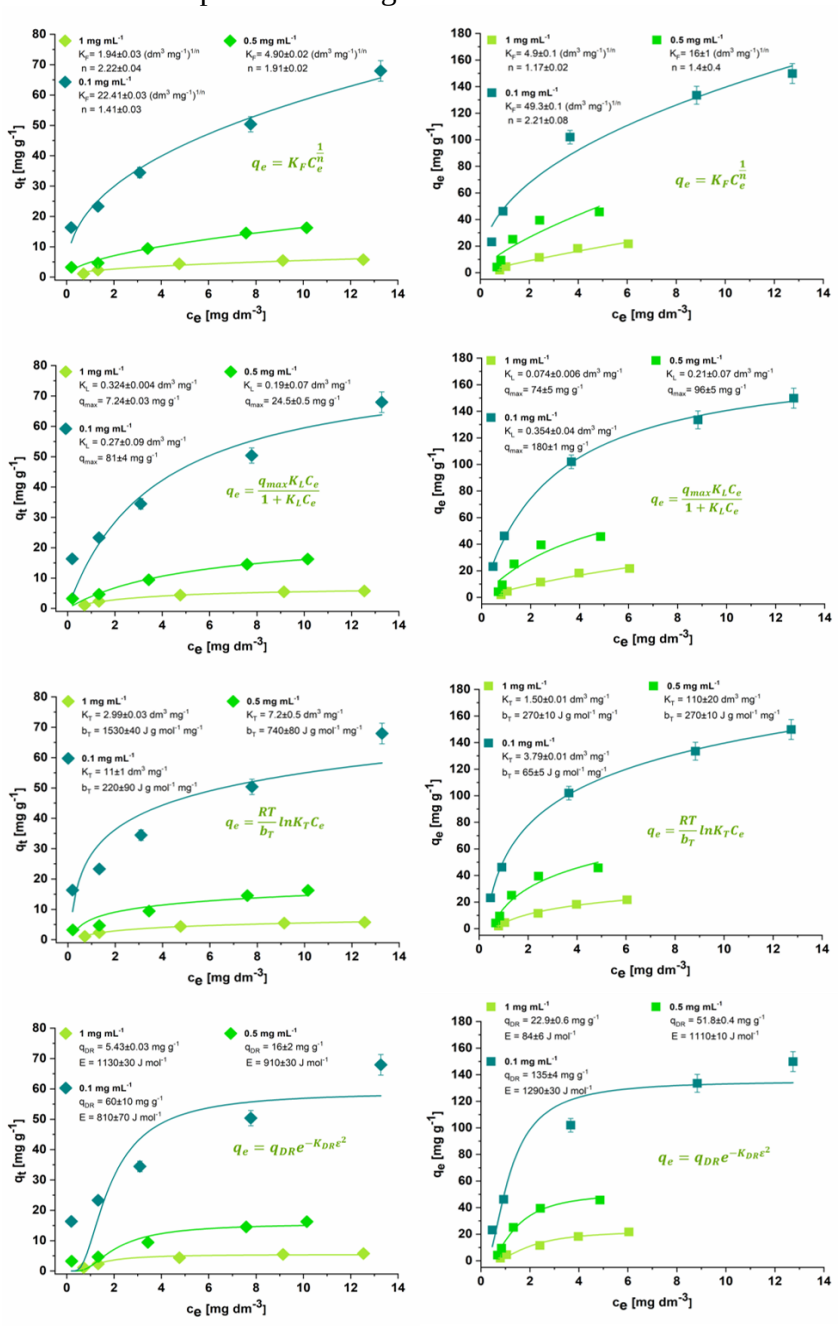


Figure 2. Graphical representations of isotherm models' fittings the experimental data with corresponding parameters for the adsorption of AMX (left) and CFX (left).

It can be concluded that all isotherm models describe the adsorption of AMX and CFX on adsorbent well by analyzing the results presented in Figure 2. As all values of the parameter n in the Freundlich isotherm are greater than 1, it is concluded that the adsorption of AMX and CFX onto

the investigated material is a favorable process. At 25 °C, the q_{max} value for CFX adsorption is 10 times higher than the AMX when the adsorbent concentration is 1 mg mL^{-1}. For lower adsorbent concentrations, the difference in q_{max} value for CFX and AMX is decreasing. These conclusions are in agreement with Temkin isotherm parameters, indicating stronger interactions between adsorbent and AMX than CFX (higher b_T values). The mean free energy of adsorption values obtained from the KDR of the Dubinin-Radushkevich isotherm is, in all cases, less than 8000 J mol^{-1}, indicating that the AMX and CFX adsorption process on the investigated material is predominantly physisorption.

To evaluate the regeneration and reusability of the adsorbent, the nylon filter (0.22 μm) was filled with 1 mg of the material, and 1 mL of antibiotics (5×10^{-5} mol dm^{-3}) was injected. The adsorbed concentrations of contaminants were determined as previously described. Subsequently, the filter was washed using 5 mL of 25 % ethanol solution and reused as the adsorbent for the same contaminant. The process was repeated in 10 cycles. The obtained results are shown in Table 1. By observing the presented results, it can be concluded that the material can be successfully regenerated using 5 mL of 25 % ethanol solution and reused for at least 10 cycles without significant impact on the adsorption capacity.

Table 1. Regeneration and reuse of the adsorbent for AMX and CFX adsorption in 10 cycles.

	% of adsorbed antibiotic									
Cycle	**1**	**2**	**3**	**4**	**5**	**6**	**7**	**8**	**9**	**10**
AMX	23±4	20±4	21±2	20±4	20±4	20±4	20±4	20±3	20±4	20±4
CFX	78±8	74±4	75±4	74±5	75±4	76±4	74±5	74±4	73±4	72±3

CONCLUSION

This study confirms the effectiveness of biowaste-derived carbon material in removing antibiotics amoxicillin and ceftriaxone from water. Adsorption experiments at 25°C, analyzed using Freundlich, Langmuir, Temkin, and Dubinin-Radushkevich isotherm models, show that both AMX and CFX adsorption is favorable and involves both monolayer and multilayer adsorption. The material achieved high adsorption capacities of 82 mg g^{-1} for AMX and 181 mg g^{-1} for CFX at 0.1 mg mL^{-1}. The process is primarily physisorption, with the adsorbent maintaining its performance over at least 10 regeneration cycles. Thus, biowaste-derived carbon material presents a promising, sustainable solution for environmental remediation of antibiotic contamination.

Acknowledgment

This work was supported by the Serbian Ministry of Science, Technological Development, and Innovation (grant no 451-03-66/2024-03/200017).

REFERENCES

[1] T. Lazarević-Pašti, T. Tasić, V. Milanković, N. Potkonjak, Chemosensors, 11 (2023) 35.
[2] S.A. Kraemer, A. Ramachandran, G.G. Perron, Microorganisms, 7 (2019) 180.
[3] S.I. Polianciuc, A.E. Gurzău, B. Kiss, M.G. Ştefan, F. Loghin, Med. Pharm. Rep., 93 (2020) 231.
[4] R. Andreozzi, M. Canterino, R. Marotta, N. Paxeus, J. Hazard. Mater., 122 (2005) 243.
[5] S.S. Mosavi, E.N. Zare, H. Behniafar, M. Tajbakhsh, Water, 15 (2023) 202.
[6] M. Abdullah, J. Iqbal, M.S. Ur Rehman, U. Khalid, F. Mateen, S.N. Arshad, A.G. Al-Sehemi, H. Algarni, O.A. Al-Hartomy, T. Fazal, Chemosphere, 317 (2023) 137834.

INNOVATIVE APPROACH TO REGENERATE ACTIVATED CARBON ADSORBING CHLORPYRIFOS USING SALICYLATE IONIC LIQUID AQUEOUS SOLUTIONS

D. Tekić, S. Marić, A. Jocić, J. Mušović, T. Lazarević. Pašti, T. Tasić, V. Milanković and A. Dimitrijević

University of Belgrade, Institute of nuclear sciences Vinča,
Mike Petrovića Alasa 12-14 11000 Vinča, Belgrade, Serbia. (sladjana.maric@vin.bg.ac.rs)

DOI: https://doi.org/10.46793/Phys.Chem24II.523T

ABSTRACT

In this study, the regeneration of activated carbon used for the adsorption of the organophosphate pesticide chlorpyrifos was performed using aqueous solutions of synthesized ionic liquids based on the salicylate anion. The regeneration efficiency was influenced by various factors, including the concentration of the ionic liquid, temperature, mixing method and addition of salts. Optimal conditions achieved 60% adsorbent regeneration in one cycle. This approach offered a more efficient, environmentally friendly and biocompatible alternative to conventional adsorbent regeneration techniques, highlighting its potential for applications in waste management.

INTRODUCTION

Pesticides pose a significant threat to both the environment and human health, with organophosphates (OPs) being particularly notable for their acute toxicity. OPs enter water sources primarily through agricultural runoff, improper disposal, and leaching from treated soils. Among OPs, chlorpyrifos (CHP) stands out having been banned in various regions due to its long-term environmental and health impacts [1]. Therefore, it is crucial to find a method for its removal from water sources. Adsorption using activated carbon is a commonly studied method for removing CHP from water, due to its cost-effectiveness and efficiency [2]. However, the main drawback is the saturation of the adsorbent material, making its regeneration necessary to ensure effective and economical application. Regeneration of adsorbents is often done through thermal degradation or the use of inorganic acids, which can pose significant environmental risks. Thermal degradation typically requires high energy input, contributing to increased carbon emissions, while the use of inorganic acids can lead to the generation of hazardous waste and potential contamination of water sources [3].

Ionic liquids (ILs) are emerging as green and sustainable options for regenerating adsorbents. ILs, composed of organic cations and organic or inorganic anions, have melting points below 100°C and are known for their non-volatility and low toxicity. Their unique properties, such as high thermal stability, wide liquid temperature range, and tunable solubility, make them highly effective in various applications. In addition to their environmental benefits, ILs can be customized for specific tasks by selecting different combinations of cations and anions, allowing for precise control over their chemical and physical properties. This adaptability positions ILs as a versatile and eco-friendly solution in the field of adsorbent regeneration, offering a sustainable alternative to traditional methods that often involve harsh chemicals and high energy consumption. [4].

This study investigated the use of aqueous solutions of synthesized salicylate-based ILs for regenerating CHP-adsorbed activated carbon. Salicylate-based ILs have proven to be nontoxic and effective in sustainable extraction and concentration process of CHP from water, using water as antisolvent to clean the CHP-saturated IL [5]. Using aqueous solutions of these ILs for CHP-

adsorbed activated carbon regenerating could offer biocompatible and sustainable approach, unlike other regeneration methods found in the literature [6], with adsorbent and regeneration solution recycling. Additionally, this method would minimize environmental impact, making it an environmentally friendly alternative to traditional regeneration techniques. Therefore, tested ILs included tetrabutylphosphonium salicylate (TBPSal), tetrabutylammonium salicylate (TBASal), cholinium salicylate (ChSal), and 1,3-dibutylimidazolium salicylate (bbimSal). Optimization of parameters affecting the regeneration process was also performed, including IL concentration, temperature, mixing method and addition of salts, demonstrating the potential of ILs to achieve efficient and economically feasible regeneration.

METHODS

Materials

Activated carbon was purchased from Centrohem (Serbia), while chlorpyrifos (purity ≥ 99 wt%), sodium citrate dihydrate (purity ≥ 99 wt%), potassium chloride (purity ≥ 99 wt%), tetrabutylphosphonium hydroxide (40 wt% in water), tetrabutylammonium hydroxide (40 wt% in water) and cholinium hydroxide (45 wt% in water) were purchased from Sigma-Aldrich (USA). Sodium salicylate (purity ≥ 98 wt%) was supplied by ThermoFisher (Germany).

IL synthesis

TBASal, TBPSal and ChSal were synthesized through a neutralization reaction. A solution of tetrabutylphosphonium, tetrabutylammonium or cholinium hydroxide was added dropwise to a solution of salicylic acid in acetone and stirred for 2 hours at room temperature. The solvent was then evaporated, and the resulting viscous liquid was dried at 0.1 mbar with stirring for 24 hours to obtain IL. Also, bbimSal was synthesized through a metathesis reaction, by measuring equimolar amounts of bbimBr and sodium salicylate which were dissolved in acetone. The precipitated sodium bromide was removed by centrifugation, and the acetone was evaporated at 70 °C under reduced pressure.

Adsorbent material preparation

Activated carbon (AC) with adsorbed CHP was prepared by mixing a 2 mg/ml ethanol suspension of AC with a 10^{-3} M pesticide solution in equal parts. The mixture was incubated on an orbital shaker for 60 minutes at room temperature and then centrifuged for 20 minutes. After centrifugation, 0.95 ml of the supernatant was extracted and filtered and analyzed using Waters ACQUITY UPLC system with a tunable UV detector, controlled by the Empower software, with BEH C18 column and mobile phases: 10% acetonitrile and 100% acetonitrile using gradient method. The remaining AC and 0.05 ml of supernatant were subjected for regeneration.

IL screening studies

To determine the most efficient IL for regeneration, regeneration solutions of tested ILs were prepared by measuring ILs and water to achieve a total mass of 1 g and 25 wt% of IL in each solution. Solutions were introduced to the CHP-adsorbed material and gently agitated on a thermal shaker for 30 minutes at the adsorption temperature. After agitation, the systems were centrifuged and the supernatant was and analyzed in the same manner as described in the previous section.

Optimization studies

Optimization was performed by varying IL concentration (from 5 to 25 wt%), temperature (from 20-30 °C), the mixing method (presence and absence of ultrasound) and regeneration solution composition (presence and absence of salts). In the case of salt addition, the salt concentration (around 3 wt%) was selected from monophasic region of phase diagrams to ensure the regeneration solution remained monophasic. Phase diagrams were previously determined using cloud point titration method. Regeneration percentage was then determined as previously described.

RESULTS AND DISCUSSION

The adsorption percentage of CHP on the tested AC material reaches up to 90 %, demonstrating the material's suitability for removing this pesticide from water. The regeneration percentages achieved in IL screening in a single cycle is decreasing in the order: TBP > bbim > TBA > Ch (**Figure 1a**). CHP is a highly hydrophobic molecule, with a $\log K_{ow}$ of approximately 5, and is non-ionizable [7]. The hydrophobicity of the ILs corresponded with higher regeneration percentages, suggesting that the regeneration process is potentially driven by hydrophobic interactions.

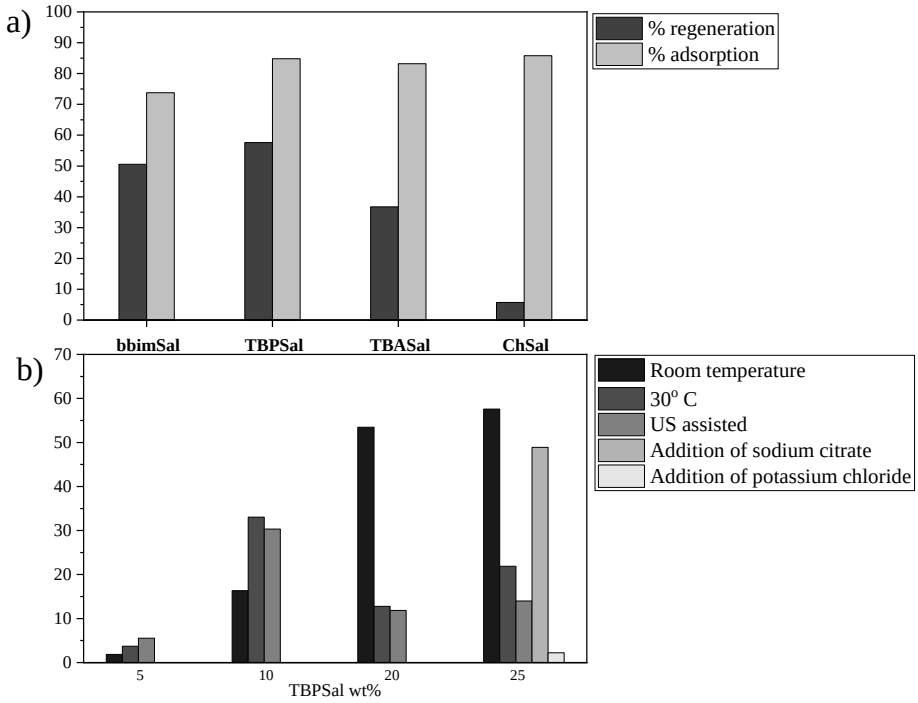


Figure 1. a) Regeneration percentage compared to percentage of adsorption achieved; b) Regeneration percentage during optimization studies.

Due to its highest regeneration efficiency, TBPSal was selected for further optimization. Regeneration percentages obtained during the following optimization are shown in **Figure 1b**. With reduced IL concentration, regeneration percentage significantly dropped, so 25 wt% of TBPSal was chosen as optimal concentration. Ultrasound mixing and increased temperature, which are commonly used to achieve regeneration, were also tested. These methods showed slight improvements in regeneration only at lower TBPSal concentrations, while having an inhibitory effect at higher concentrations, which could be explained due to potential pesticide degradation [8]. Additionally, the addition of sodium citrate to 25 wt% TBPSal aqueous solution slightly decreased the regeneration percentage, whereas the addition of potassium chloride caused a complete drop in regeneration efficiency. This can be attributed to the increased hydrophilicity of the regeneration solution due to the salt addition. The study found that the highest regeneration percentages in a single cycle (around 60 %) of the adsorbent material were obtained using 25 wt% TBPSal at room temperature, without the use of ultrasonic mixing nor the addition of salts.

In the existing literature, there are no studies specifically focused on the regeneration of materials saturated with CHP, except for the study by Maliyekkal et al. [6] that achieved 90% regeneration using hexane. While this study demonstrated high regeneration efficiency, it utilized

hexane, which is not biocompatible, and the study did not address the development of a sustainable regeneration process.

CONCLUSION

This study investigated a series of salicylate-based ILs for the regeneration of CHP-adsorbed activated carbon. The results demonstrated that the regeneration process is potentially driven by hydrophobic interactions, with TBPSal achieving the highest regeneration percentages (around 60%). The optimal conditions were determined to be a 25 wt% aqueous solution of TBPSal at room temperature. Furthermore, it was shown that neither ultrasonic mixing nor the addition of salts were necessary to achieve high regeneration efficiency.

This research highlights the significant potential of using ILs for adsorbent regeneration, offering a greener and more sustainable alternative to conventional methods, which often involve environmentally harmful processes. By utilizing ILs, the economic feasibility of the regeneration process is also enhanced, as these compounds can be tailored for low volatility and low toxicity.

The findings suggest that multiple regeneration cycles could further improve the efficiency and effectiveness of the process, making it even more viable for practical applications and for more sustainable and eco-friendly practices in the management of pesticide-contaminated water.

Acknowledgement

This work was supported by the Ministry of Science, Technological Development and Innovation of the Republic of Serbia (Contract number: 451-03-66/2024-03/200017)

REFERENCES

[1] W.J. Lee, M.C.R. Alavanja, J.A. Hoppin, J.A. Rusiecki, F. Kamel, A. Blair, D.P. Sandler, Environ. Health Perspect., 115 (4) (2007) 528.
[2] O.A. Hussain, A.S. Hathout, Y.E. Abdel-Mobdy, M.M. Rashed, E.A. Abdel Rahim, A.S.M. Fouzy, Toxicol. Reports, 10 (2023) 146.
[3] A. Larasati, G.D. Fowler, N.J.D. Graham, J. Environ. Chem. Eng., 9 (4) (2021) 105555.
[4] M.G. Freire, Introduction to Ionic-Liquid-Based Aqueous Biphasic Systems (ABS), Springer, Berlin, Heidelberg, 2016.
[5] A. Jocić, S. Marić, D. Tekić, T. Lazarević-Pašti, J. Mušović, J. Filipović Tričković, A., J. Water Process Eng., 64 (2024) 105621.
[6] S.M. Maliyekkal, T.S. Sreeprasad, D. Krishnan, S. Kouser, A.K. Mishra, U. V. Waghmare, T. Pradeep, Small, 9 (2) (2013) 273.
[7] Developed by ChemAxon. Available online: http://www.chemaxon.com (accessed on 15 May 2024).
[8] S. Yuan, F. Yang, H. Yu, Y. Xie, Y. Guo, W. Yao, Food Chem., 383 (2022) 132550.

INVESTIGATION OF POLYPHENOLS PARTITION IN AQUEOUS TWO-PHASE SYSTEMS WITH COPOLYMER AND IONIC LIQUID

S. Marić, D. Tekić [1], A. Jocić, J. Mušović, T. Lazarević Pašti, T. Tasić, V. Milanković and A. Dimitrijević

University of Belgrade, Institute of nuclear sciences Vinča,
Mike Petrovića Alasa 12-14 11000 Vinča, Belgrade, Serbia. (sladjana.maric@vin.bg.ac.rs)

DOI: https://doi.org/10.46793/Phys.Chem24II.527M

ABSTRACT

In this study, an aqueous two-phase system utilizing the copolymer Pluronic and the ionic liquid cholinium acetate was employed for the extraction of polyphenolic compounds (gallic acid, vanillic acid and resveratrol) from the aqueous solution. The logarithmic value of the partition coefficient of -1.22 and extraction efficiency of approximately 8% indicated that resveratrol preferentially partitions into the copolymer phase. In contrast, approximately 75% of the phenolic acids were extracted into the ionic liquid phase. Vanillic and gallic acids were successfully separated from resveratrol with selectivity factors of 34.58 and 41.90, respectively. This study demonstrates that the proposed biocompatible copolymer-based aqueous two-phase system has substantial potential as a platform for separating resveratrol from gallic and vanillic acids in real samples, such as food waste.

INTRODUCTION

Polyphenols are valuable natural compounds primarily due to their antioxidant properties and are present in relatively high concentrations in food waste, from where they could be extracted. The most commonly used commercial technique for polyphenol extraction is solvent extraction. However, due to the extensive use of organic solvents, long extraction time, and often lower extraction efficiency [1], aqueous two-phase systems offer a promising alternative extraction platform.

Aqueous two-phase system (ATPS) can be formed by mixing aqueous solutions of two water-soluble components at appropriate concentrations. Cholinium-based ATPS, composed of cholinium ionic liquids (ILs) and salts or polymers, have been investigated for the extraction of various molecules. However, only a limited number of studies have examined cholinium-based ATPS for the extraction of polyphenols [2]. A recent study demonstrated that ATPS based on cholinium dihydrogen phosphate ([Ch][DHP]) and propylene glycol 400 (PPG400) is effective for the selective separation of gallic acid and resveratrol [3]. Given that cholinium ionic liquids, salts with melting temperatures below 100 °C, paired with cholinium cations and suitable anions, present outstanding biodegradable and low-toxicity properties [4], in this study cholinium acetate is utilized as one component of the ATPS. On the other hand, Pluronics have recently begun to be studied as a potential alternative component in ATPS. The diversity of chemical structures among Pluronic which includes variations in the number of monomer units and their molecular weight, allows precise control over the characteristics of each Pluronic, making them promising candidates in extraction and separation processes. Additionally, the use of Pluronics in ATPS can enhance the system's biocompatibility and reduce environmental impact, further promoting sustainable extraction methods. It has been shown that the Pluronic PE6200-based system has the potential for separating various molecules in combination with ionic liquids [5,6]. To our knowledge, no study investigates the extraction of polyphenolic compounds in Pluronic PE6200-based ATPSs.

Therefore, this study aims to evaluate the partitioning of polyphenols with different polarities (gallic acid, vanillic acid, and resveratrol) in an ATPS composed of cholinium acetate ionic liquid, copolymer Pluronic PE6200, and water.

METHODS

Materials. Gallic acid (HGal, purity ≥ 98 wt%) and vanillic acid (HVan, purity ≥ 98 wt%) standards were acquired from Thermo Scientific (Germany), while trans-Resveratrol (RSV, purity ≥ 98 wt%) was purchased from LGC (England). Pluronic PE6200 was acquired from BASF (Germany), cholinium acetate ([Ch][Ac]) from Iolitec (Germany) and ethanol (CH_3CH_2OH, purity ≥ 99.8 wt%) was purchased from Honeywell (Germany).

Partition study. The ternary mixture composition was chosen based on the phase diagram earlier reported [6]. To investigate the partitioning of polyphenols, ATPSs were prepared by sequentially adding 20 wt% [Ch][Ac] + 30 wt% PE6200 + 50 wt% water + 20 µL phenol stock standard solutions into 1.5 mL microtubes (total system mass of 1g). Stock standard solutions of individual phenols were prepared in 80% ethanol with the following concentrations: 4860 mg/L of gallic acid, 5010 mg/L of vanillic acid, and 1350 mg/L of resveratrol. These mixtures were vigorously stirred using a vortex agitator (Reax Top, Heidolph) and incubated in a thermoshaker incubator (ALEMADR-MSC, COLO) for 1 h at (25.0 ± 0.1) °C to ensure equilibration. ATPSs were then centrifuged for 5 min at 10000 rpm to achieve complete phase separation. After careful separation, the phases were weighed, diluted, and the polyphenol content quantified by UV spectroscopy using an LLG-uniSPEC2 spectrophotometer at wavelengths of 272 nm for gallic acid, 261 nm for vanillic acid, and 305 nm for resveratrol, using calibration curves. Working solutions required for calibration curves were prepared by dilution in 80% ethanol over a concentration range of 2.5 – 50 mg/L. The partition coefficients (K) of HGal, HVan, and RSV were determined as the ratio of the concentration of polyphenol in the IL- and copolymer-phase, denoted as $[\text{Phenol}]_{\text{IL-phase}}/[\text{Phenol}]_{\text{copolymer-phase}}$. The selectivities (S) of HGal and HVan with respect to RSV were calculated as the ratio of the partition coefficients, while the extraction efficiencies of each phenol (EE, %) were calculated toward IL-phase using the following equation (1):

$$\text{EE}\ (\%) = \frac{[\text{Phenol}]_{\text{IL-phase}} \cdot V_{\text{IL-phase}}}{[\text{Phenol}]_{\text{copolymer-phase}} \cdot V_{\text{copolymer-phase}} + [\text{Phenol}]_{\text{IL-phase}} \cdot V_{\text{IL-phase}}} \cdot 100 \qquad (1)$$

where $V_{\text{copolymer-phase}}$ and $V_{\text{IL-phase}}$ are the volumes of copolymer- and IL-phase, respectively.

RESULTS AND DISCUSSION

Based on the previously determined phase diagram of Pluronic PE6200, cholinium acetate, and water, a composition for the extraction of polyphenols was selected (Figure 1. a). The composition was chosen well within the biphasic region to ensure rapid phase separation and to reduce cross-contamination between phases enriched with opposite components. In this case, the upper phase is enriched in the IL (IL-phase) and the bottom phase is majorly constituted by PE6200 (copolymer-phase). At a composition of 20% [Ch][Ac] and 30% PE6200, the volume ratio of the phases ($V_{IL}/V_{copolymer}$) 1.5, the obtained logarithmic partition coefficients of polyphenols in the ATPS at 25 °C are presented in Figure 1. b. The logarithmic partition coefficients, logK(HGall)=0.31 and logK(HVan)=0.40, indicate that both gallic and vanillic acids migrate toward the more hydrophilic IL-phase, which is consistent with their hydrophobicity (at pH=7.48 $\log K_{ow}$(HGal) =-2.48 and $\log K_{ow}$(HVan) =-1.89). Value logK=-1.22 suggest that RSV tends to migrate to the copolymer-phase in accordance to octanol-water partition coefficient value ($\log K_{ow}$(RSV)=3.37).

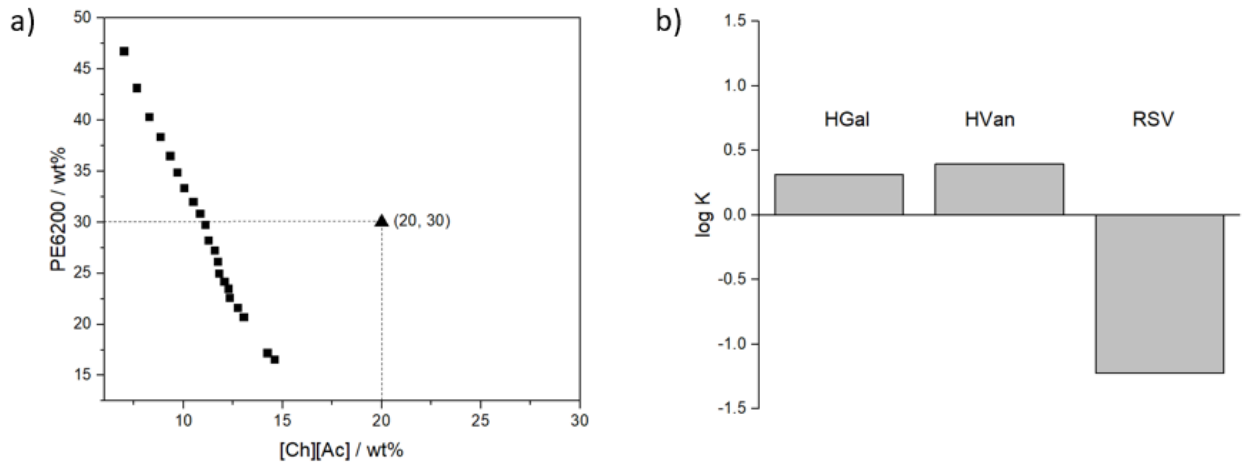


Figure 1. a) Ternary phase diagram composed of [Ch][Ac] + PE6200 + H_2O at 25°C; ▲composition of ATPS mixture selected for partition study and b) partition coefficients of polyphenols in ATPS composed of 20 wt% [Ch][Ac] + 30 wt% PE6200 + 50 wt% H_2O at 25 °C.

The selectivities of HGal and HVan with respect to RSV and the extraction efficiencies of polyphenols in IL-phase are presented in Table 1. It can be seen that EE of gallic and vanillic acid are higher than 75%, while RSV is extracted to IL-phase at only 8%.

The obtained logK value of 0.31 for gallic acid using the PE6200/[Ch][Ac] ATPS system is lower than the values reported in the study for various cholinium ionic liquids (cholinium acetate was not investigated) and PPG400 (0.84 < logD(HGal) < 1.2) [3]. The lowest partition coefficient for resveratrol, -0.49 with cholinium dihydrogen phosphate, is close to the value obtained in this work. The achieved resveratrol extraction efficiency of 70-92% for the cholinium-based IL ATPS, with the highest efficiency of 92% using cholinium dihydrogen phosphate [3], is comparable to the results obtained using the copolymer and IL system, where only 8% of resveratrol was extracted into the ionic liquid phase. However, this system shows a much lower extraction efficiency for gallic acid (75%) compared to the system with cholinium dihydrogen phosphate (EE_{HGal} ~93%). This suggests that the system has significant potential for application in the extraction of resveratrol and other polyphenols from various types of food waste.

Table 1. The extraction efficiencies (EE, %) and selevtivities (S) of gallic acid, vanillic acid and resveratrol for 20 wt% [Ch][Ac] + 30 wt% PE6200 + 50 wt% H_2O ATPS, at 25 °C.

Polyphenol	**EE / %**	**S**
HGal	75.57	34.58
HVan	78.94	41.90
RSV	8.21	/

CONCLUSION

In this study, the partitioning of the polyphenols gallic acid, vanillic acid and resveratrol, in an aqueous two-phase system based on the copolymer Pluronic PE6200 and the ionic liquid cholinium acetate was investigated. The separation process resulted in gallic and vanillic acids partitioning into the ionic liquid-phase (logK(HGall)=0.31 and logK(HVan)=0.40), while resveratrol remained in the copolymer-phase (logK(RSV)=-1.22). This system of a biocompatible copolymer and non-toxic IL extracted polyphenols with efficiencies exceeding 75 % for gallic and vanillic acids into

the IL phase and only ~8% of resveratrol was extracted into the IL phase, indicating an extraction efficiency of 92% for resveratrol into the copolymer phase. Further optimization of extraction conditions and ATPS composition is essential to maximize efficiency and minimize the consumption of ATPS constituents for the extraction and separation of polyphenolic compounds from food waste.

Acknowledgment
This work was supported by the Ministry of Science, Technological Development and Innovation of the Republic of Serbia (Contract number: 451-03-66/2024-03/200017).

REFERENCES

[1] A. Sridhar, M. Ponnuchamy, P.S. Kumar, A. Kapoor, D.V.N. Vo, S. Prabhakar, Environ Chem Lett 19, (2021) 3409.
[2] H. Tian, P. Berton, R.D. Rogers, Fluid Phase Equilib., 502 (2019) 112258.
[3] A. Dimitrijević, S. Marić, A. Jocić, D. Tekić, J. Mušović, J.S. Amaral, Foods, 13 (6) (2024).
[4] S.P.M. Ventura, F.A. e Silva, A.M.M. Gonçalves, J.L. Pereira, F. Gonçalves, J.A.P. Coutinho, Ecotoxicol. Environ. Saf., 102 (1) (2014) 48.
[5] S. Marić, A. Jocić, A. Krstić, M. Momčilović, L. Ignjatović, A. Dimitrijević, Sep. Purif. Technol., 275 (2021) 119101.
[6] A. Dimitrijević, A.P.M. Tavares, A. Jocić, S. Marić, T. Trtić-Petrović, S. Gadžurić, M.G. Freire, Sep. Purif. Technol., 248 (2020) 117050.

FTIR ANALYSIS OF MODIFIED BIOCHAR PRODUCED FROM THE PLUM STONE BIOWASTE

Z. Lopičić, M. Đošić, T. Šoštarić, A. Antanasković, V. Adamović, D. Smiljanić and J. Milojković

Institute for Technology of Nuclear and Other Mineral Raw Materials, Franchet Desperey Blvd 86, 11000 Belgrade, Serbia. (z.lopicic@itnms.ac.rs)

DOI: https://doi.org/10.46793/Phys.Chem24II.531L

ABSTRACT

Fruit processing generates huge amounts of waste biomass, which can serve as potential renewable resource for many value-added products. Unfortunately, these reserves are often dumped or incinerated inducing environmental and health risk issues. Thermochemical conversions might transform this waste into a variety of carbon rich products (e.g. biochar). In the same time, tremendous efforts in phosphate release control are done in order to minimize ecosystems eutrophication. In this paper, waste plum stones (PS) were converted into the biochar (PS-B) by slow pyrolysis. Before pyrolysis, PS samples were modified by magnesium salt in order to increase its capacity toward phosphates. The characteristic functional groups of the PS, Mg-modified and phosphate-enriched samples were investigated using FTIR analysis. These analyses confirmed significant aromaticity increase, existence of periclase at modified PS-B surface and additional present of groups related to successful phosphate binding.

INTRODUCTION

Huge amounts of solid biomass waste are generated worldwide. Proper management of these wastes is faced with economic and environmental challenges, including a limited number of landfills, environmental threats, and public awareness [1]. In the same time, the world is faced with rapid depletion of non-renewable resources, either in the material, or energy form. The application of thermochemical conversion techniques in converting biomass waste to energy and multiple functional products is gaining wide acceptance due to the many benefits resulting from this conversion. The composition of the cheap and abundant waste biomass, allows its conversion into high energy containing materials and various products such as sorbents, fertilizers, green chemicals, recyclable nutrients, pharmaceuticals etc. [2]. Therefore, the thermochemical conversion of waste biomass represents a promising technique which might support the sustainability concept and allow the circular economy to be employed more efficiently. Among the others, pyrolysis represents one of the simplest methods, in which the biomass is treated at high temperatures in the absence of oxygen, which results in carbon capture and storage [3]. The quality of the pyrolysis products depends not only on the feed (raw material) composition but also on parameters applied during the pyrolysis process (e.g. heating rate, pyrolytic temperature, holding time etc.).

In the same time, tremendous efforts have been made by wastewater treatment plants in order to remove contained phosphorus before the final discharge. Strict low limit concentration in the effluents (for example 1.0 mg/L in Europe (Council Directive 91/271/EEC)), have induced necessity of developing efficient and cost-effective phosphorous removal technologies. Sorption by various sorbents has been recognized as a suitable technology for such purposes, because of the simple system design, easy operation and cost-effectiveness [4].

Biochar represents a solid, carbon-dense material produced through thermal treatment of biomass in an oxygen-deficient environment. It is recognized for its large specific surface area, significant porosity, high pH value and diversity of functional groups that can serve as binding

places for many contaminants [5, 6]. The phosphate loaded biochar can further be reused as soil amendment but also as slow-release fertilizer which enables simultaneous phosphate recovery and waste biomass reuse [4].

In 2021, the global production of plums exceeded 12 million tons, as reported by the Food and Agriculture Organization of the United Nations, where approximately 10% of the fruit's total weight consists of the plum stone (kernels) that are commonly used to manufacture pellets worldwide [7]. Plums are one of the most often fruits raised in Serbia, with official production data of 330,582 tons in 2017, which ranks Serbia at the top of the world's plum producers [8]. The plum processing/production results in huge amounts of lignocellulosic waste in the form of plum stones, which are, unfortunately, either burned out or deposited at open landfills.

In order to contribute to waste minimisation and support environment protection, the plum stones (PS) were used as a starting material and converted into the biochar (PS-B) by slow pyrolysis. For the purpose of increase of binding capacities toward phosphates, PS samples were firstly modified with Mg and then pyrolysed. In order to observe changes in surface functional groups that have been occurred (after modification, pyrolysis and phosphate sorption process), samples have been subjected to FTIR analysis.

METHODS

The waste plum (*Prunus domestica* L) stones samples were taken from the local fruit processing company "Fruvita", Serbia. After receiving, samples were dried at room temperature and used for further experiments. Samples grinding was performed in "Siebtechnik – TS250" vibrating mill (Siebtechnik GmbH, Germany) and sieved to desired particle sizes. Grinded plum stone samples (PS) were first modified according to the procedure described in [9], obtaining modified sample (PS-M). In brief, 10 g of PS was mixed with 200 mL of 2M $MgCl_2$ solution in respective flasks, shaken at a constant temperature oscillator at 180 rpm for 24 h; after this, suspension was heated at 80 ^oC until the supernatant evaporated, and dried at 105 ^oC for 6 h. After this, both PS and PS-M were pyrolysed at 500 °C within argon atmosphere (100 mL/min, 10 °C/min) in a Nabertherm 1300 muffle furnace (Nabertherm, Germany) for 90 min. The obtained biochar samples were labelled as PS-B and PS-M-B. Phosphates binding was performed using batch sorption technique under following operation parameters: $C_i(PO_4^{3-})$ = 400 mg/L, m/V = 2 g/L, 180 rpm, 24 h, 25 ^oC, pH_i = 5.10. Modified biochar sample after phosphate binding was marked as PS-M-B-P. Surface functional groups in all samples were determined by Fourier Transform Infrared Spectroscopy (ATR mode) using a Thermo Nicolet 6700 FTIR device (International Equipment Trading Ltd., USA). The spectra were recorded by averaging 32 scans from 4000 to 400 cm^{-1}.

RESULTS AND DISCUSSION

FTIR spectra of the PS, PS-M-B and PS-M-B-P samples are presented in **Figure 1.** Spectra recorded for PS-M and PS-B are omitted from the figure, since these samples couldn't bind phosphates. As can be seen from **Figure 1**, for the PS sample, in the region between 3700 and 3000 cm^{-1}, two bands can be distinguished: one at 3290 cm^{-1} attribute to stretching vibrations of OH groups, originated from the raws' material moisture content, phenolic or acidic groups, and band at 3006 cm^{-1} attributed to C–H stretching in celullose structure [10]. Very strong bands detected at 2923 and 2853 cm^{-1}, can be assigned to the asymmetric and symmetric stretching of C–H bonds in alkyl groups, in the aliphatic and olefinic structure, respectively in hemicellulose, cellulose and lignin structure [10, 11]. Band at 1744 cm^{-1} represent the stretching vibration of carbonyl groups (C=O) originated from hemicellulose, while the presence of lignin can be confirmed through the existence of band at 1641 cm^{-1}, corresponding to C=C vibration in aromatic structure [10, 12]. Five bands, detected in the range from 1600 to 1100 cm^{-1}, denoted with arrows in FTIR spectra for PS,

can be: bands at 1456 cm^{-1} and 1544 cm^{-1} can be assigned to C=O stretching and the aromatic skeletal vibration in lignin stucture; band detected between 1470 and 1430 cm^{-1} correspond to the methoxyl–O–CH_3 group in lignin; band at 1377 cm^{-1} denote C–H bending in cellulose and hemicellulose; bands at 1236 cm^{-1} represent C–O vibration in lignin and at 1157 cm^{-1} C–O–C asymmetric stretching vibration of the pyranose ring in hemicellulose and cellulose structure [10, 12]. Prominent peak at 1027 cm^{-1}, correspond to C–O stretching can be assigned to hemycelullose, lignin, and cellulose [13].

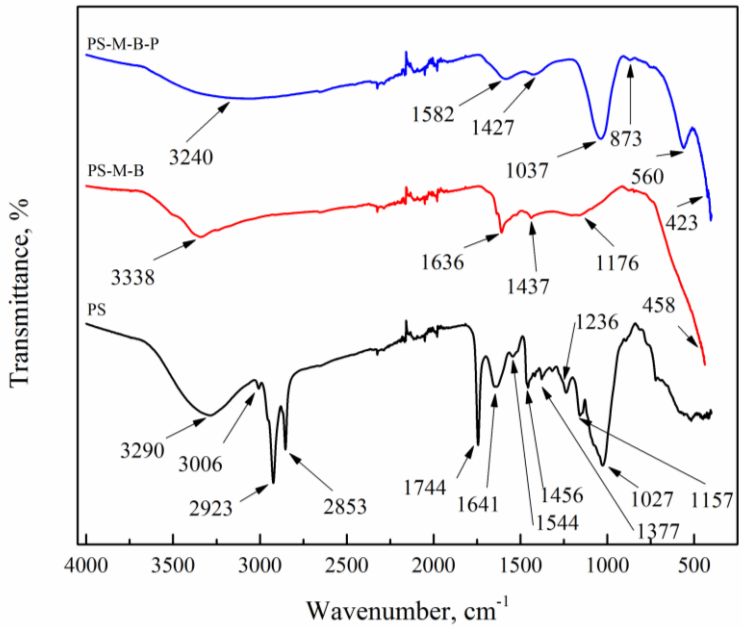


Figure 1. FTIR spectra of the raw material (PS), modified biochar (PS-M-B) and modified biochar after phosphate sorption (PS-M-B-P).

Modification of the PS sample introduced magnesium in the form MgO, while the thermochemical conversion at 500 ^oC induced changes in the starting material structure. It can be seen that in the PS-M-B sample (**Figure 1.**), only one absorption band at 3338 cm^{-1} can be distinguished, most probably from the presence of O–H groups [14], while the other bands (present in PS) in the region between 3700 and 3000 cm^{-1} interval, disappeared, as a consequence of pyrolysis process. The degradation of hemicellulose was also confirmed by the absence of band in the region from 1800 to 1700 cm^{-1} [15]. Increase in aromaticity might be confirmed by the presence of bands detected at 1636 and 1437 cm^{-1} which can be assigned to the aromatic skeletal vibration in lignin structure [10]. At 458 cm^{-1} detected small peak might correspond to formation of the periclase (MgO) at the sample surface. The existence of mineral periclase was also confirmed by XRD analysis (results not shown). Other researchers also found that the bands in the range 512–422 cm^{-1} are assigned to the bonds of the metals (in this case Mg) with oxygen [4], indicating metal-oxygen bonds related to the incorporation of metals in the biochar matrices.

FTIR spectra of modified biochar after phosphate sorption (PS-M-B-P), also presented in **Figure 1.**, indicates following: band detected at 3240 cm^{-1} can be attributed to stretching vibrations of OH groups, originated from the materials moisture content while the bands detected at 1582 and 1427 cm^{-1} can be assigned to the biochar, e.g. lignin presence [10]. Band at 1037 cm^{-1} can be assigned to the antisymmetric stretching mode of PO_4^{3-} group, while bands between 900-400 cm^{-1} can be assigned to bending and symmetric and asymmetric deformation of O–P–O group, confirming sucesful phosphate binding [16].

CONCLUSION

Biochar, a cost-effective and environmental friendly material, represents a promising solution with great application potential in many environmental concerning issues. However, the pristine biochar usually has low binding capacity toward specific pollutants (phosphates), so it is necessary to impregnate biomass with metal salts before pyrolysis, which results in modified metal-oxides-loaded biochar. During the pyrolysis, $MgCl_2x6H_2O$ underwent dehydration process to form MgO; the hermochemical conversion at 500 ^oC induced thermally cleaving of less temperature resistant hemicellulose and cellulose (forming mainly volatile products), while contained lignin mainly forms aromacic char structure due to its stability to thermal degradation. The change in structure and Mg presence increases the phosphate sorption capacity of the biochar, resulting in material which can be safely disposed on the soil, in order to improve soil quality and support plant growth.

Acknowledgment

This research was supported by the Science Fund of the Republic of Serbia #7439, "From Waste to Food and Soil Enrichment - minimizing waste by applying circular economy in fruits/vegetables processing industry" - WasteBridge. Part of this research was supported by the Ministry of Science, Technological Development and Innovation of the Republic of Serbia, through the grant numbers 451-03-66/2024-03/200023.

REFERENCES

[1] S. Elkhalifa, P. Parthasarathy, H.R. Mackey, T. Al-Ansari, O. Elhassan, S. Mansour, G. McKay, Biomass Conv. Bioref., (2022).
[2] L. Zhang, C. Xu, P. Champagne, Energy Convers. Manag., 51 (2010) 969.
[3] N. Rajendiran, S. Ganesan, D. Weichgrebe, S. S. Venkatachalam, Clean Techn. Environ. Policy, 25 (2023) 3189.
[4] P. Wang, M. Zhi, G. Cui, Z. Chu, S. Wang, R. Soc. Open Sci., 8 (2021) 201789.
[5] B. Zhao, D. O'Connor, J. Zhang, T. Peng, Z. Shen, D. C.W. Tsang, D. Hou, J. Clean. Prod., 174 (2018) 977.
[6] B. A. Oni, O. Oziegbe, O. O. Olawole, Ann. Agric. Sci., 64 (2019) 222.
[7] P. B. Aurtherson, B. T. Nalla, K. Srinivasan, K. Mehar, Y. Devarajan, Biomass Conv. Bioref., 13 (2023) 6249.
[8] Statistical Office of the Republic of Serbia. Available Online: Https://Data.Stat.Gov.Rs/ (Accessed on 20th January 2024).
[9] L. Ronghua, J. W. Jim, Z. Baoyue, Z. Zengqiang, L. Shuai, L. Shuang, X. Ran, J. Clean. Prod., 147 (2017) 96.
[10] E. Pehlivan, Processes, 11 (2023) 2536.
[11] Đ. Katnić, M. Marinović-Cincović, S. J. Porobić, I. Vujčić, A. Šaponjić, B. Sikirić, D. Živojinović, J. Clean. Prod., 352 (2022) 131637.
[12] Y. Hao, Y. Pan, R. Du, Y. Wang, Z. Chen, X. Zhang, X. Wang, Adv. Mater. Sci. Eng., (2018) ID 8461407.
[13] H. Yang, R. Yan, H. Chen, D.H. Lee, C. Zheng, Fuel., 86 (2007) 1781–1788.
[14] M. Đošić, S. Eraković, A. Janković, M. Vukašinović-Sekulić, I. Z. Matić, J. Stojanović, K. Y. Rhee, V. Mišković-Stanković, S.J. Park, J. Ind. Eng. Chem., 47 (2017) 336.
[15] Z. Lopičić, J. Avdalović, J. Milojković, A. Antanasković, M. Lješević, N. Lugonja, T. Šoštarić, Hem. Ind., 75 (2021) 329.
[16] C. Raptopoulou, K. Kalaitzidou, A. Tolkou, P. A. Palasantza, M. Mitrakas, A. Zouboulis, Waste and Biomass Valorization, 7 (2016) 851.

A NOVEL METHODOLOGY FOR DESIGN OF QSAR MODEL: MUTAGENICITY OF NITROAROMATIC COMPOUNDS

B. Stanković [1] and F. Marinković [2]

[1] *University of Belgrade, Vinča Institute of Nuclear Sciences –National Institute of the Republic of Serbia, Mike Petrovića Alasa 12-14, Belgrade, Serbia. (branislav.stankovic@vin.bg.ac.rs)*
[2] *University of Belgrade, Faculty of Physics, Studentski trg 12-16, Belgrade, Serbia.*

DOI: https://doi.org/10.46793/Phys.Chem24II.535S

ABSTRACT

Nitroaromatic compounds (NACs) are omnipresent and pervasive organic pollutants. Here, we aim to design transparent, interpretable, reproducible, and publicly available methodologies for deriving quantitative structure-activity relationship models and testing them by modeling the mutagenicity of NACs against the *Salmonella typhimurium* TA100 strain.

Selection of molecular descriptors are performed using a genetic, Boruta, Featurewiz, and ForwardSelector algorithm. Modelling utilizes the multiple linear regression method. The models are ranked by the Multi-Criteria Decision Making procedure. Our findings reveal that Featurewiz showing a slight advantage over Boruta and ForwardSelector and significantly outperforms genetic algorithm. Constructed models can serve as valuable tools for the quick and reliable prediction of NACs mutagenicity.

INTRODUCTION

NACs are aromatic molecules containing at least one nitro group attached to the benzene ring. Their degradation is not efficacious enough, leading to accumulation in the environment [1]. The primary source of NACs in the environment is emission, mainly by industry and vehicles. Notably, NACs are not only omnipresent in the environment but have been detected in food [2]. NACs exhibit a myriad of toxic effects. They are reported to be mutagenic and carcinogenic, as well as, to cause gastrointestinal, neurological, and reproductive disorders, respiratory and skin irritation, allergic reactions, immunotoxicity, methemoglobinemia, endocrine system impairment, etc [3].

Experimental testing of mutagenicity has a few drawbacks: it requires significant time, costs, and manpower. Since millions of organic chemicals are used in industry, it is impossible to evaluate all of them experimentally. To address these challenges, several *in silico* approaches have been developed, with quantitative structure-activity relationship (QSAR) standing out.

The focus of this research is on enhancing feature selection techniques, which the literature has not explored extensively. The developed methodologies are applied to estimate the mutagenicity of NACs against the *Salmonella typhimurium* TA100 strain.

METHODS

The investigation focused on a set of 48 nitroaromatic compounds sourced from Benigni's report for the OECD [4]. Mutagenicity values are given as the logarithm of the number of revertants per nanomole (logTA100).

Modeling was performed in Python programming language. Splitting of data in the training and the test set followed the stratified sampling approach. The molecules were sorted based on their mutagenic activity, organized into groups of four, and one molecule was selected from each group for inclusion in the test set. The remaining NACs were assigned to the training set. Additionally, both the least and most mutagenic compounds were intentionally included in the training set to

ensure that the molecules selected for the test set fall within the applicability domain of the subsequently developed QSAR model.

Molecular descriptors were calculated by Mordred and RDKit packages. Modeling was performed using the multiple linear regression method incorporating up to 7 descriptors. Before the selection process, descriptors with missing values for at least one molecule or containing non-numerical values were discarded. Following this step, the dataset was split into training and test sets and normalized so that each descriptor was in the range of 0–1. As the initial step of the feature selection, both constant and nearly constant descriptors were omitted. For the selection process, we employed the genetic algorithm (GA) along with three algorithms that, to our knowledge, have not been previously utilized in the QSAR literature, namely Boruta, Featurewiz, and the ForwardSelector algorithm. A two-step procedure was implemented. First, a set of descriptors was narrowed to ensure that no pair of descriptors had a pair-wise correlation higher than 0.95. In the second step, the above-mentioned algorithms were employed.

The leverage approach was utilized to define the applicability domain (AD), representing the region of chemical space where the model's predictions are expected to be reliable. AD is estimated from the Williams plot, which depicts standard residuals versus leverage (*h*).

To thoroughly evaluate the derived model, we employ a range of commonly used statistics. These include measures for goodness-of-fit and robustness, such as the root mean square error in both the training set, $RMSE_{tr}$, and cross-validation, $RMSE_{cv}$, coefficients of determination in training set, R^2, as well as in leave-one-out, Q^2_{LOO}, and leave-many-out, Q^2_{LMO}, cross-validation. Additionally, we assess the adjusted coefficients of determination, R^2_{adj}, concordance correlation coefficient in the training set CCC_{tr}, and internal validation, CCC_{cv}, along with *F*-value. Predictive performance is estimated using mean square error in the test set, $RMSE_{ext}$, mean absolute error in the test set, MAE_{ext}, alongside three metrics derived from coefficients of determination: Q^2_{F1}, Q^2_{F2}, and Q^2_{F3}. Furthermore, we consider correlation coefficient in test set, CCC_{ext}, slopes of regression lines of predicted vs. experimental values, *k*, and experimental vs. predicted values, *k*', (both through the origin), along with $\langle r_m^2 \rangle$, Δr_m^2, and R^2_{ext}.

To mitigate multicollinearity and chance correlation, a three-fold selection process was employed. Initially, the QUIK (Q Under Influence of K) rule was applied. Only models exhibiting a difference of more than 0.05 between two K indexes were retained for further assessment. Subsequently, the Variance Inflation Factor (VIF) was calculated, and models where each descriptor had a VIF value lower than 5 passed to the final test. Y-Scrambling was then applied to ensure the robustness of the selected models.

The process of selecting the optimal model involved the application of the Multi-Criteria Decision Making (MCDM) procedure. This approach summarizes all the measures of goodness-of-fit, robustness, and predictivity from the previous section to rank various models. In addition to the MCDM value, we also considered the number of descriptors as a factor in determining the most suitable model. This dual consideration ensures a comprehensive assessment, incorporating both the model's overall performance according to MCDM and the simplicity reflected in the number of descriptors utilized.

RESULTS AND DISCUSSION

Derived models are given by **equations 1-4** (corresponding to models 1-4), while calculated statistics parameters are presented in **Table 1** and **Table 2**. Models 1, 2, 3, and 4 are the best models obtained with Featurewiz, Boruta, ForwardSelector, and GA algorithm, respectively.

$$\text{logTA100} = 2.27\ \text{AATS1v} - 5.38\ \text{VE2\_Dzse} - 2.59\ \text{GATS1are} - \\ -1.60\ \text{ATS8dv} - 0.858\ \text{GATS4i} - 0.453\ \text{CIC4} + 3.45 \quad (1)$$

$$\text{logTA100} = -2.18\ \text{Vabc} - 6.45\ \text{FpDensityMorgan1} - 3.44\ \text{GATS2p} + \\ + 0.658\ \text{EState\_VSA3} - 0.820\ \text{GATS1pe} + 6.08 \quad (2)$$

$$\text{logTA100} = -0.983\ \text{Xc-3d} - 5.95\ \text{FpDensityMorgan1} - 1.87\ \text{C3SP2} - 1.63\ \text{fr\_bicyclic} - \\ -1.51\ \text{CIC4} + 0.743\ \text{NumAliphaticCarbocycles} + 3.79 \quad (3)$$

$$-1.71\ \text{ATSC0m} + 3.97\ \text{ATSC2p} - 5.42\ \text{ZMIC3} - 10.1\ \text{FpDensityMorgan1} - \\ -1.17\ \text{NumRotatableBonds} + 7.09 \quad (4)$$

Table 1. Internal fitting parameters of the models.

No	Descriptors	R^2	adjR^2	$RMSE_{tr}$	CCC_{tr}	F	Q^2_{LOO}	$RMSE_{cv}$	CCC_{cv}	Q^2_{LMO}	R^2_{Yscr}	Q^2_{Yscr}
1	AATS1v, VE2_Dzse, GATS1are, ATS8dv, GATS4i, CIC4	0.926	0.910	0.473	0.961	60	0.879	0.604	0.938	0.864	0.155	-0.413
2	Vabc, FpDensityMorgan1, GATS2p, EState_VSA3, GATS1pe	0.929	0.918	0.461	0.963	79	0.896	0.558	0.947	0.889	0.141	-0.296
3	Xc-3d, FpDensityMorgan1, C3SP2, fr_bicyclic, CIC4, NumAliphaticCarbocycles	0.951	0.941	0.384	0.975	94	0.921	0.487	0.960	0.903	0.166	-0.344
4	ATSC0m, ATSC2p, ZMIC3, FpDensityMorgan1, NumRotatableBonds	0.957	0.950	0.358	0.978	135	0.943	0.414	0.971	0.919	0.136	-0.290

Table 2. External validation parameters of the models.

No	R^2_{ext}	$RMSE_{ext}$	Q^2_{F1}	Q^2_{F2}	Q^2_{F3}	CCC_{ext}	MAE_{ext}	r^2_m	Δr^2_m	k	k'	$\frac{R^2_{ext} - R^2_0}{R^2_{ext}}$	$\frac{R^2_{ext} - R^2_0}{R^2_{ext}}$
1	0.835	0.670	0.836	0.835	0.851	0.911	0.544	0.798	0.058	0.999	0.877	0.000	0.008
2	0.819	0.757	0.790	0.790	0.810	0.902	0.592	0.780	0.001	0.867	0.995	0.003	0.003
3	0.785	0.787	0.774	0.773	0.794	0.884	0.608	0.737	0.095	0.907	0.925	0.000	0.019
4	0.783	0.807	0.762	0.761	0.784	0.883	0.675	0.739	0.086	0.916	0.904	0.016	0.000

All models have great fitting ability and external predictive performance, while model 4 slightly overfit data. Model 1 was selected as the best model among models 1–4. A scatter plot depicting the experimental vs. predicted mutagenicity values for the training and test sets (**Figure 1**) confirms the excellent fitness and predictability.

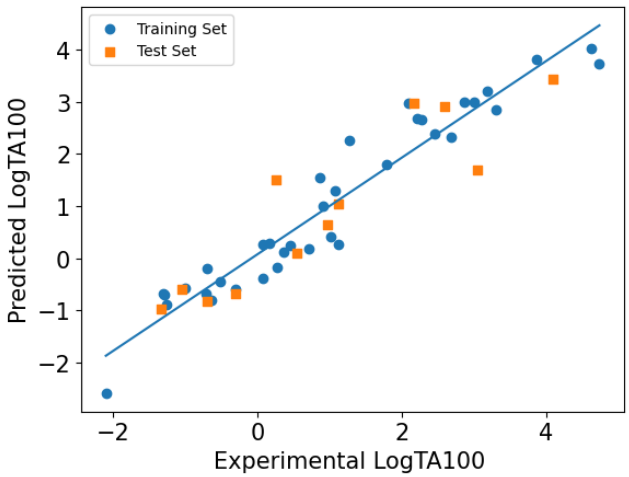


Figure 1 Scatter plot of predicted versus experimental mutagenicity.

Leverage of each compound in both training and test sets falls below the threshold (h^* = 0.58). Therefore, it can be concluded that no response outlier is present. Moreover, no structural outliers were identified. In essence, all molecules are within AD and there is a stable basis to assert that the proposed model is suitable for predicting mutagenicity across a broad spectrum of NACs.

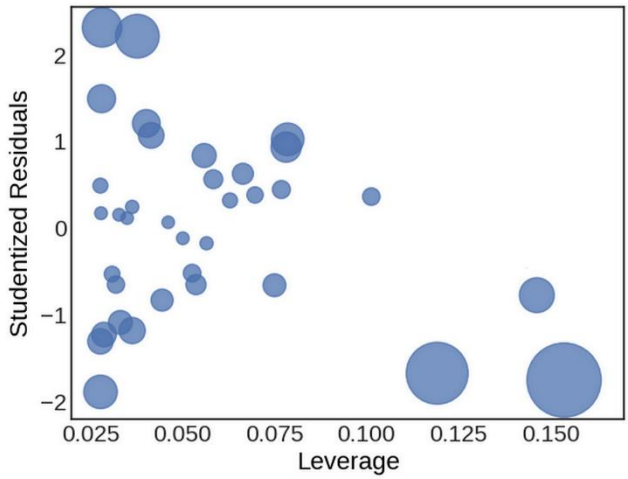


Figure 2. The Williams plot for the model 1.

CONCLUSION

The QSAR models developed in this study aimed to predict the mutagenicity of NACs against *Salmonella typhimurium* TA100. The approach involved the utilization of Mordred and RDKit descriptors and used innovative, transparent, interpretable, reproducible, and publicly available feature selection methodologies. Constructed models showcase excellent fitting ability and external predictive performance. QSAR models prove their reliability for practical use, thereby potentially reducing the necessity for experimental procedures. The best results were obtained using Featurewiz algorithm.

Acknowledgment

This work was supported by the Ministry of Education, Science and Technological Development of the Republic of Serbia (grants no No. 451-03-66/2024-03/200017 and 451-03-66/2024-03/ 200162).

REFERENCES

[1] C. L. Zhang, Y. Y. Yu, Z. Fang, S. Naraginti, Y. H. Zhang, Y. C. Yong, Process. Biochem., 70 (2018) 129.
[2] J. Tiwari, P. Tarale, S. Sivanesan, A. Bafana, Environ. Sci. Pollut. Res., 26 (2019) 28650.
[3] P. Kovacic, R. Somanathan, J. Appl. Toxicol., 34 (2014) 810.
[4] Organization for Economic Co-Operation and Development - Guidance Document on the Validation of (Q)SAR Models (2007).

EFFECTS OF HYDROCHLORIC, HYDROFLUORIC, AND ACETIC ACID ON PIG BONE ESTIMATED BY FTIR, RAMAN, LIBS, AND SEM-EDX

M. Marković, M . Kuzmanović, I. Pašti, D. Bajuk-Bogdanović , D. Ranković and D. Dimić

University of Belgrade, Faculty of Physical Chemistry, Studentski trg 12-16, 11000 Belgrade, Serbia
(milica.markovic@ffh.bg.ac.rs)

DOI: https://doi.org/10.46793/Phys.Chem24II.539M

ABSTRACT

ATR-FTIR, Raman spectroscopy, LIBS, and SEM-EDX methods were used for analyzing the demineralization effect of hydrochloric, hydrofluoric, and acetic acid on pig shoulder bone after an immersion period of 14 days. Chemical changes were accessed through Fourier deconvolution applied in the amide I (1700-1600 cm^{-1}), phosphate (900-1200 cm^{-1}), and carbonate (500-650 cm^{-1}) FTIR regions. Different components in the bone samples, depending on the environment and acids′ concentration, were identified and provided insight into the mineral and collagen matrix composition. SEM-EDX analysis indicated a significant alteration in the chemical composition of the bone upon acid treatment with a generally preserved morphology of the bone. The results suggested that an increase in acid concentration primarily affected the intensity and the structure of the phosphate band as the phosphate content was more susceptible to demineralization.

INTRODUCTION

In forensic practice there are several ways of destroying the human remains after a homicide, burial, dismemberment, treatment with chemicals, and burning. Although chemicals can cause significant modifications of human skeletal remains, some investigations have implicated that bone samples can preserve DNA even after being treated with strong chemicals like acids [1,2].

Bone is a composite tissue. The bone matrix that forms the bone lamellae is partly organic and partly inorganic. Bone strength is determined by the ratio of inorganic and organic substances as well as their structure. The dominance of organic substances ensures significant bone elasticity, which decreases with age (or under the influence of various diseases) as the amount of inorganic compounds increases, making the bones brittle. Bone consists of approximately 45% water, 30% protein, 15% salt and 10% lipid. Organic compounds make up 30 to 40% of bone mass. The organic matrix, the steroid matrix, and bones consist of fibers of collagen and non-collagen proteins embedded in a mucopolysaccharide protein complex [2-4].

Mineral matrix is made of mineral hydroxyapatite (an analog of natural crystalline calcium phosphate (85%), $Ca_{10}(PO_4)_6(OH)_2$), calcium carbonate (10%), and traces of calcium hydroxide, calcium fluoride, magnesium chloride. Bones contain structurally changed hydroxyapatite, non-stoichiometric apatite, which has a significant amount of anionic (e.g., HPO_4^{2-}, CO_3^{2-}, Cl^-) and cationic (e.g., Na^+, Mg^{2+}) species, water and ionic vacancies in the crystal lattice. Also, the bones contain elements like aluminum, zinc, silicon, iron, sodium, potassium, and copper. Within the crystal lattice of hydroxyapatite CO_3^{2-} ions, whose weight share can reach ∼5–9% of bone mineral composition, can take the place of PO_4^{3-} ions (B-type substitution, the main type of substitution) and/or OH^- ions (A-type substitution, a less common type of substitution) [4,5].

This paper summarizes the effect of different concentrations of hydrochloric, hydrofluoric, and acetic acid on pig shoulder bone after the immersion period of 14 days.

METHODS

Chemicals and bone samples

Hydrochloric, hydrofluoric, and acetic acid were purchased from Merck, Germany. All substances were of p.a. grade purity and used without any change. The demineralization of pig bone was monitored in 0.1 and 1.0 M aqueous acid solutions. Pig shoulder bone was obtained from a butcher shop. The bone was first degreased through immersion in ethanol at 70%, v/v, and, washed with distilled water. The sample was stored at 4°C. Before immersion in investigated solutions, the bone was fragmented into samples to nearly 5 g. Each sample was placed in approximately 50 cm^3 of acid solutions and left for 14 days.

SEM-EDX analysis

Scanning electron microscopy and Energy-Dispersive X-ray analysis were done using a Phenom ProX microscope (Phenom, The Netherlands). EDX analysis was done using 15 kV acceleration voltage and at low magnification to sample the chemical composition of the bone samples properly. No conductive layer was deposited on the samples, and the charge reduction holder was used for all the experiments. For SEM-EDX analysis powdered bone samples were used.

FTIR spectra

FTIR spectra of pig shoulder bone treated under different chemical conditions were recorded in the mid-IR region (4000-525 cm^{-1}) using a Nicolet iS 20 FT-IR Spectrometer operating in the ATR mode using a monolithic diamond crystal and a measuring resolution of 4 cm^{-1} with 16 scans. The samples were powdered to improve the contact with the crystal and its coverage. Samples were recorded multiple times and the averaged spectra were discussed. The absorption bands characteristic to vibration modes of specific chemical groups were analyzed by curve fitting analysis using PeakFit program 4.12 and Voigt spectral line profile. Band positions were acquired from the second derivative spectra.

Raman spectra

Raman spectra of powdered bone samples were recorded on a Raman spectrometer with a microscope (DXR Raman microscope, Thermo Scientific). Recording conditions were as follows: exposure time: 10 s; the number of exposures 10; laser wavelength 532 nm; laser power 10mW; grating: 900 lines/mm; spectrograph aperture: 50 μm pinhole. The spectra were recorded in the range of wave numbers from 3500-50 cm^{-1}. Samples were recorded multiple times and the averaged spectra were discussed.

LIBS spectra

LIBS spectra of compact bone samples were recorded using the Transversely Excited Atmospheric pressure carbon dioxide (TEA CO_2) laser, developed at the VINCA Institute of Nuclear Sciences. The operating laser wavelengths were 10.5709 and 10.5909 μm and the pulse repetition rate was up to 2 Hz, when in a multimode regime. The initial laser peak which lasted around ~100 ns carried approximately 35% of total pulse energy. The initial peak was followed by a decaying tail which lasted around ~ 2 μs. The optimized measurement parameters were: laser pulse energy of 155 mJ, laser beam focused at the sample surface, and 1 mm distance of plasma slice that focused on spectrograph slite. ZnSe lens was used for laser beam focusing. A plasma image was projected on the entrance slit of a Carl Zeiss PGS2 spectrograph by an achromatic quartz lens. U2C-16H11850 CCD camera with enhanced sensitivity in the UV range was used to capture plasma emission spectra. To reduce dark current and noise, the CCD camera was triggered at a minimal exposure time of 10 ms.

RESULTS AND DISCUSSION

SEM-EDX analysis suggests that the treatment with acids has the primary effect on the chemical composition and the chemical structure but does not affect the overall morphology, although the

samples treated in more concentrated acids look more eroded. After treatment with acids calcium and phosphorus content are reduced, compared to the reference sample (kept in water). Generally speaking, the carbon content increases upon the treatment with acids, being the most prominent in the case of the treatment with HCl.

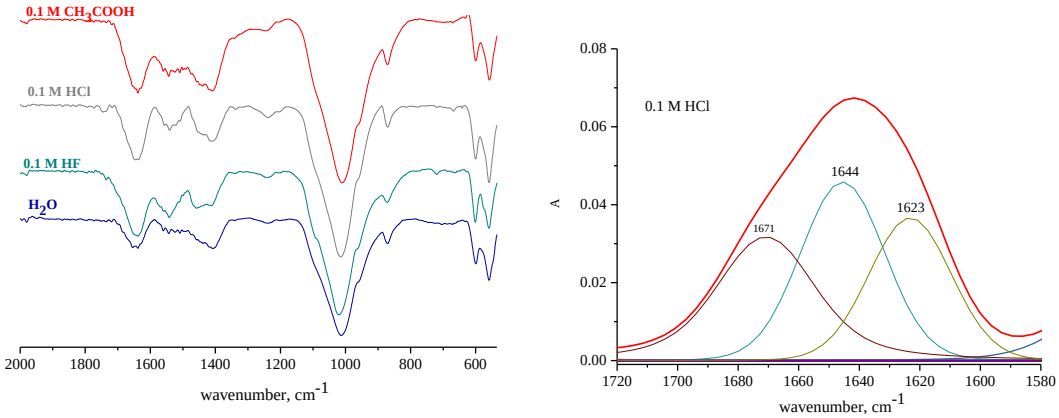


Figure 1. Comparative display of ATR-FTIR spectra of pig shoulder bone in different acids (0.1 M) (left panel) and the results of curve fitting analysis in the amide I FTIR region (0.1 M) (right panel).

The intensity of the amide I band in all spectra is generally low and significantly lower than the intensity of the phosphate band (Figure 1, left panel). After deconvolution, multiple peak positions were identified based on traditional protein band assignments (β-sheet; unordered, random collagen; β-structure; α-helix; β-turn) (Figure 1, right panel). The analysis of the complex band in the 1200-900 cm^{-1} region, assigned to the vibrations of the crystalline and non-crystalline phosphate structure, and the bands in the 650-500 cm^{-1} region, assigned to the $\nu_4(PO_4^{3-})$ vibrations, show that acidic dissolution of phosphate with different acids has a different effect on the intensity and structure of the phosphate band. The results of curve fitting analysis in carbonate,$\nu_2(CO_3^{2-})$ band, region indicate that the dominant substitution pattern of the sample in reference medium, hydrochloric, and acetic acid is carbonate B type except for hydrofluoric acid, where B and A_2 type substitutions are present. In Raman spectra, the band assigned to $\nu_1(PO_4^{3-})$ mode is almost the same intensity in the sample spectra recorded in water and 0.1 M solutions of all acids. In 1 M sample solution of acetic acid $\nu_1(PO_4^{3-})$ band significantly decreases in intensity and shifts to higher wavenumbers, indicating the change in vibrational mode, now assigned, most probably, to $\nu_3(HPO_4^{2-})$ (986 cm^{-1}) of brushite form of acidic calcium phosphate, sometimes seen in acidic solutions. Laser-induced plasma spectroscopy is used to assess the bone's relative surface hardness after the treatment with selected chemicals. The measurements are based on the fact that the ionic-to-atomic line ratio (Figure 2) is a function of the material's hardness [6].
Quantitative relationships, based on FTIR data, used to describe the alternations in the chemical composition

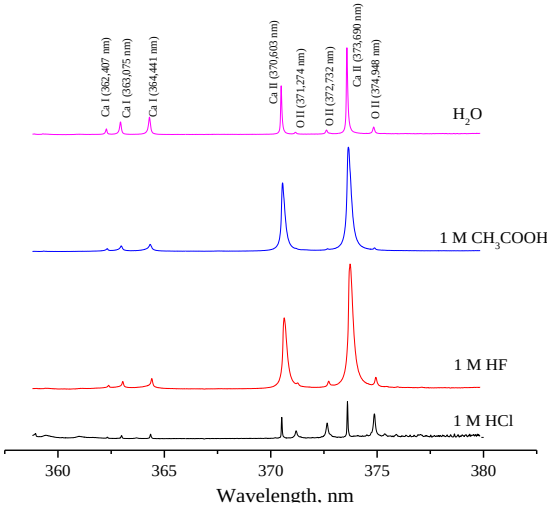


Figure 2. LIBS spectra of pig shoulder bone in 360-380 nm region(1 M solutions).

of pig shoulder bone are mineral-to-matrix ratio (MM), crystallinity index (CI), and carbonate-to-phosphate ratio (Figure 3).

Mineral-to-matrix ratio reflects the ratio of phosphate to organic matrix content and is assumed to be a good measure of bone bending stiffness. The carbonate-to-phosphate ratio gives information about carbonate content while CI reflects a degree of crystal order in the lattice, higher CI implies larger and/or more ordered crystals, while the lower values indicate lattice strain and smaller apatite crystals.

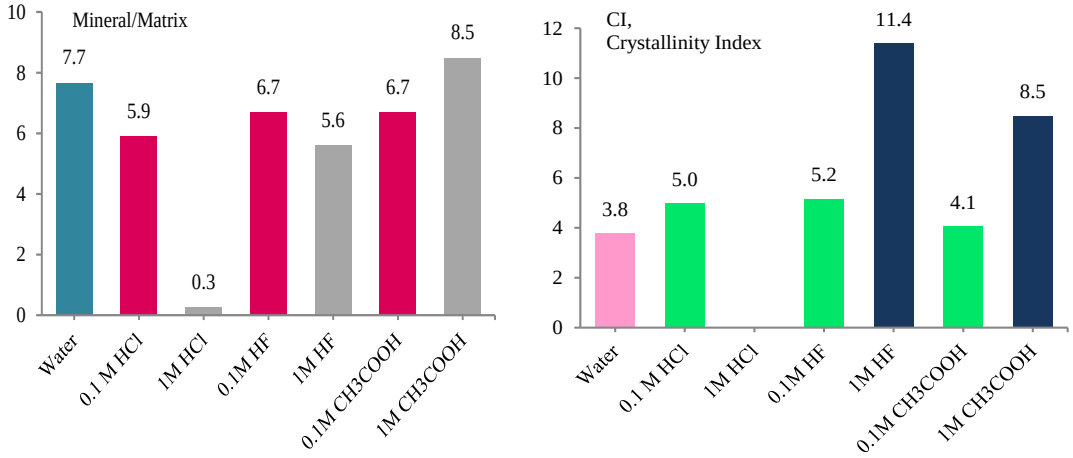


Figure 3. Characteristic parameters of pig shoulder bone obtained from ATR-FTIR spectra

$$(\mathrm{MM}=\frac{A\ (\nu_1(\mathrm{PO}_4^3))}{A\ (\text{Amide I})}\ ;\ \mathrm{CI}=\frac{Abs(604\ cm^{-1})+Abs(565\ cm^{-1})}{Abs(595\ cm^{-1})}).$$

CONCLUSION

Valuable data and new insights obtained on structural/morphological changes in pig shoulder bone, caused by the action of different acids, were obtained by applying complementary methods of molecular spectroscopy (FTIR-ATR, Raman), *in situ*, atomic emission spectroscopy (LIBS), and high-resolution techniques for analysis of sample surfaces (SEM-EDX). Overall, the characteristic compositional parameters calculated from the ATR-FTIR data could be correlated with analogous parameters calculated from the Raman spectra, and at the same time, both data obtained from vibrational spectra could be correlated with spectral line intensities obtained from LIBS spectra and data from SEM-EDX analysis. Characteristic parameters of pig bone, mineral-to-matrix content, crystallinity index, and carbonate content changed in concentration-dependent manner.

Acknowledgment

The authors acknowledge the financial support of the Ministry of Science, Technological Development and Innovation, Serbia, Grant No 451-03-65/2024-03/200146**.**

REFERENCES

[1] D. Congram, A. Gill Green, P. Perouz Seferian, Deposition and Dispersal of Human Remains as a Result of Criminal Acts, in J. T. Pokines, E. N. L'Abbe, S. A. Symes (Eds.), Manual of Forensic Taphonomy, 2nd Edition, CRC Press, 2021.
[2] J.K. Pringle, J.P. Cassella, J.R. Jervis, Forensic Sci. Int. 198 (2010) 126–133.
[3] S. Y. Smith, A. Varela, R. Samadfam, Bone Toxicology, Springer 2018.
[4] S. Von Euw, Y. Wang, G. Laurent, C. Drouet, F. Babonneau, N. Nassif, T. Azaïs, Sci. Rep. 9 (2019) 8456-8466.
[5] S. Y. Smith, A. Varela, R. Samadfam, Bone Toxicology, Springer 2018.
[6] Z. A. Abdel-Salam, A. H. Galmed, E. Tognoni, M. A. Harith, Spectrochim. Acta Part B At. Spectrosc. 62 (2007) 1343–1347.

L *– Phase Boundaries, Colloids, Liquid Crystals, Surface-Active Substances*

LIQUID-LIQUID PHASE EQUILIBRIA IN WATER-AMPHIPHILE-OIL TERNARY SYSTEMS: EXPERIMENT AND MOLECULAR SIMULATION

A. Novikov, A. Kuchierskaya, D. Kopitsyn, and A. Semenov

Gubkin University, Physical and Colloid Chemistry Department, Leninsky prospect 65/1, 119991 Moscow, Russia. (novikov.a@gubkin.ru)

DOI: https://doi.org/10.46793/Phys.Chem24II.545N

ABSTRACT

We have studied the ternary systems 'water–methanol–trichloromethane' and 'water–methanol–dichloromethane'. We obtained the dependences of the interfacial tension on the fraction of methanol in the oil phase, which were approximated by the crossover isotherm, combining the adsorption-induced rapid decrease of the interfacial tension (Langmuir–von Szyszkowski behavior) and the gradual vanishing of the interfacial tension near the critical point. The experimental values were used to refine the simulation parameters and a good agreement between molecular dynamics and experiment was obtained.

INTRODUCTION

Classical laboratory methods for lipid extraction are often based on the use of the ternary systems 'water–methanol–trichloromethane' and 'water–methanol–dichloromethane' [1,2]. Surprisingly, these popular ternary systems have not yet been studied in detail. In particular, tabulated data on equilibrated phase density and interfacial tension are lacking. Furthermore, these systems are the simplest among those including water, amphiphile and oil components in terms of molecular size and can be readily simulated by techniques such as molecular dynamics and Monte Carlo. In this work, we show that phase behavior and interfacial tension in these ternary systems can be reproduced by molecular dynamics methods and confirm the generic behavior of nonionic hydrotropes in 'water–hydrotrope–oil' ternary systems.

METHODS

Chloroform (TCM; ≥99.8%), dichloromethane (DCM; ≥99.8%), methanol (MeOH; ≥99.7%), and freshly prepared distilled water (specific conductivity less than 5 μS/cm) were used to study the phase behavior. The position of the phase boundary in the ternary systems was determined by volumetric titration. Two-phase samples of the system were prepared by the gravimetric method using laboratory balances Ohaus Pioneer PA413C (Ohaus, USA) in specially made glass cells with a jacket and a reverse slit to prevent evaporation of volatile components [3]. The titration was carried out as previously described [4], at pressure p = 0.100 MPa and temperatures of 277.15 and 293.15 K, the temperature was maintained using a cryothermostat F25ME (Julabo, Germany). The density of the equilibrated phases was measured using a DMA4500 instrument (Anton Paar, Austria). The position of the tielines was determined by correlating the measured density with a three-dimensional piecewise continuous calibration function showing the change in density (from the apex of water to the critical point) and refractive index (from the critical point to the apex of oil) along the binodal. The interfacial tension was measured using the rotating drop method on an SDT tensiometer (Kruss, Germany). Molecular dynamics (MD) simulations were performed using the CGenFF parameters for TCM, DCM, and MeOH [5] with point charges additionally optimized by IFT values, and the TIP3P rigid model for water. The model systems were assembled in a 6×6×12 nm cell using the Packmol program [6]. The simulations were performed using the NAMD3

program [7] in the NPT ensemble with a step of 2 fs and a simulation time of at least 60 ns. The measurement and simulation results were processed and compared in the Python environment using NumPy, SciPy, Pandas, Matplotlib, MDAnalysis [8] and Pytim packages. The systems were visualized using the VMD program [9].

RESULTS AND DISCUSSION

Phase diagrams of the TCM–MeOH–H_2O and DCM–MeOH–H_2O systems are shown in **Figure 1**. The phase diagrams are in good agreement with classical published data [10].

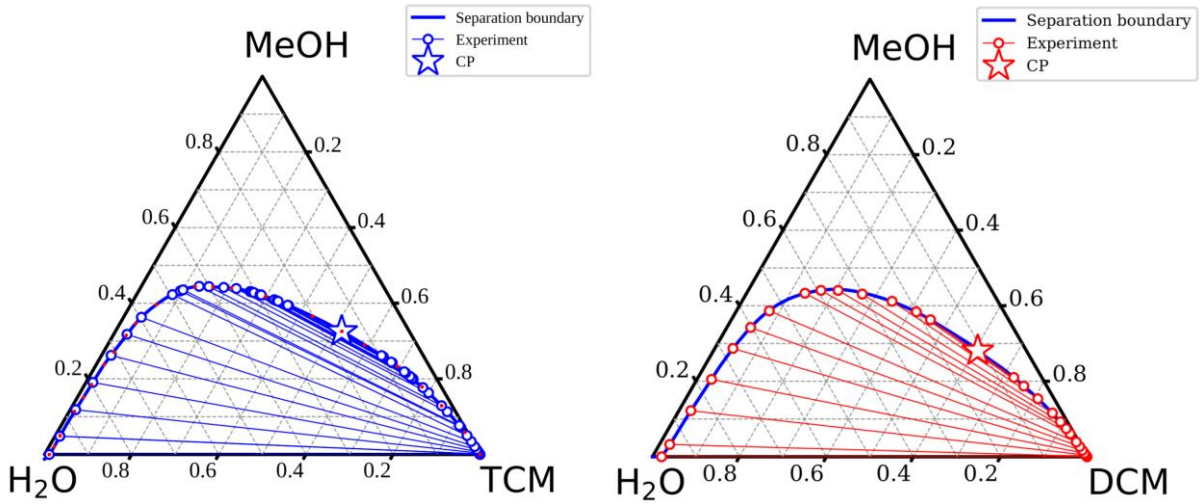


Figure 1. Phase diagrams of ternary systems ‘water–methanol–trichloromethane’ and ‘water–methanol–dichloromethane’ (in weight percent).

The critical points are shifted toward the oil vertex in both systems. This fact facilitates the use of these ternary systems for lipid extraction because the mass fraction of methanol is higher in the aqueous phase and the oil phase is enriched in TCM and DCM and consequently in the extracted lipids. However, if we had plotted the phase diagrams in molar fractions, the critical points would have been close to the maximum methanol content of the two-phase regions. The distribution of methanol between the aqueous and oil phases can be visualized by molecular dynamics simulation.

The density profiles of the components were calculated, averaging the atom trajectories after the equilibrating 40-ns MD runs. The MD snapshot of the TCM–MeOH–H_2O ternary system is shown in **Figure 2 (up)**, while the calculated density profiles along the Z axis are shown in **Figure 2 (down)**. Apparently, the calculated density profiles agree well with the MD snapshot, showing the non-polar TCM molecules concentrated in the central part of the simulation box, and more polar MeOH and H_2O molecules in the border regions. The density profiles were normalized to [0;1] range and approximated by the hyperbolic tangent functions. Thus, the bulk phases were identified as the regions where normalized TCM and H_2O density was more than 0.99. The regions with lower TCM and H_2O density were identified as oil/water interface and were shown as grey-filled areas in **Figure 2**.

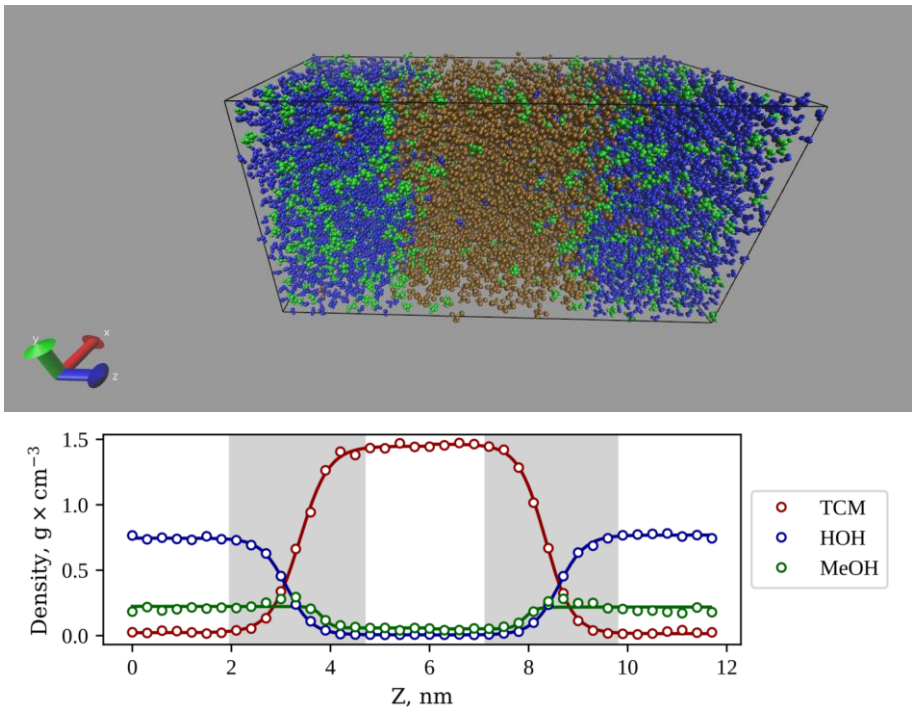


Figure 2. MD snapshot (up) and one-dimensional density profiles (down) of the system assembled from 1380 TCM + 1376 MeOH + 6160 H_2O molecules after the equilibrating MD run.

The MD simulations can also provide the direct estimate of the interfacial tension calculated as the pressure difference at the box sides. This estimate can be compared with the experimental values and could be approximated by the same crossover IFT isotherm proposed earlier [11]. The measured and simulated IFT values are shown in **Figure 3**.

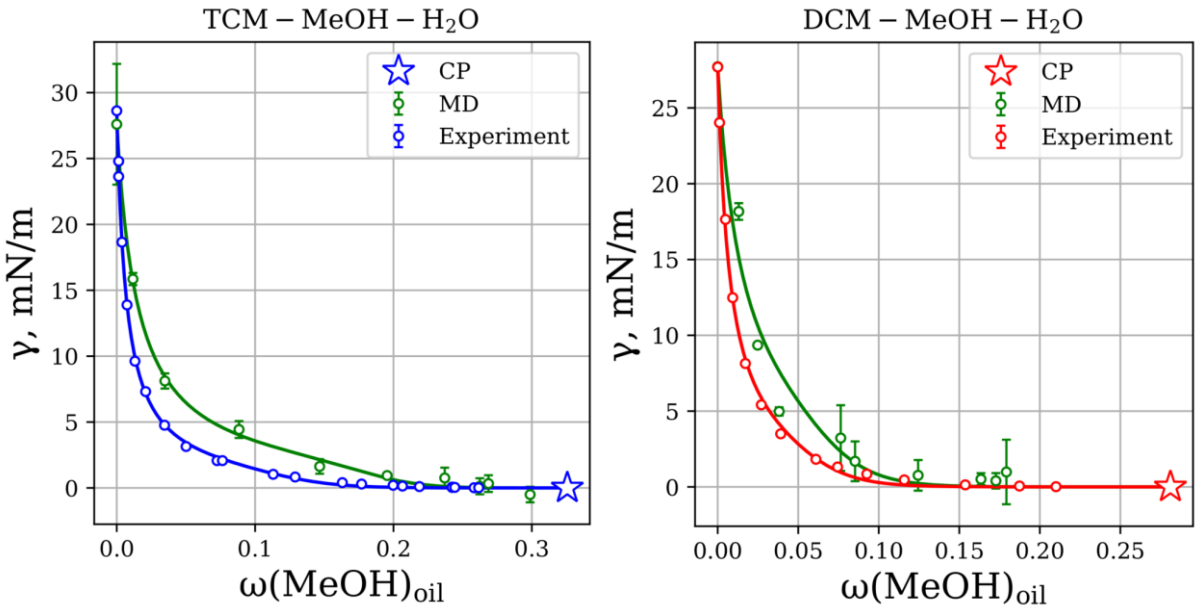


Figure 3. Interfacial tension isotherms for TCM–MeOH–H_2O and DCM–MeOH–H_2O systems as functions of MeOH mass fraction in the oil phase along the binodal curve (error bars are two standard sample deviations).

The experimental and simulated IFT isotherms agree well with each other. However, one would notice that simulated isotherms are shifted to the right, which means larger enrichment of oil phase with methanol compared with the experiment. The simulations can be further improved by refining the applied force fields and point charges, as well as increasing the simulation box size and number of simulated molecules.

CONCLUSION

The experimental results presented demonstrate the dual role of hydrotropes in aqueous solutions. At low concentrations, methanol acts as a typical surfactant, lowering the interfacial tension by adsorption. After saturation of the interface, methanol acts as a cosolvent, gradually eliminating the compositional difference and the interfacial tension between the oil and aqueous phases. The detailed study and simulation of the ternary systems with methanol and halogenated hydrocarbons will help to understand the distribution of the components and to refine the lipid extraction protocols.

Acknowledgment

This work is supported by the Russian Science Foundation (Grant No. 20-79-10388).

REFERENCES

[1] Q. Phan, E. Tomasino, Food Chem. 355 (2021) 129409.
[2] A. C. R. Silva, C. C. da Silva, R. Garrett, C. M. Rezende, Food Res. Int. 137 (2020) 109727.
[3] A. A. Novikov, A. P. Semenov, A. A. Kuchierskaya, D. S. Kopitsyn, V. A. Vinokurov, M. A. Anisimov, Langmuir 35 (2019) 13480.
[4] A. A. Novikov, A. A. Kuchierskaya, D. G. Karpov, A. P. Semenov, Chem. Technol. Fuels Oils 59 (2023) 967.
[5] I. Vorobyov, V. M. Anisimov, S. Greene, R. M. Venable, A. Moser, R. W. Pastor, A. D. MacKerell, J. Chem. Theory Comput. 3 (2007) 1120.
[6] L. Martinez, R. Andrade, E. G. Birgin, J. M. Martínez, J. Comput. Chem. 30 (2009) 2157.
[7] J. C. Phillips et al., J. Chem. Phys. 153 (2020) 044130.
[8] N. Michaud-Agrawal, E. J. Denning, T. B. Woolf, O. Beckstein, J. Comput. Chem. 32 (2011) 2319.
[9] W. Humphrey, A. Dalke, K. Schulten, J. Mol. Graph. 14 (1996) 33.
[10] E. G. Bligh, W. J. Dyer, Can. J. Biochem. Physiol. 37 (1959) 911.
[11] A. A. Novikov, A. P. Semenov, V. Monje-Galvan, V. N. Kuryakov, J. B. Klauda, M. A. Anisimov, J. Phys. Chem. C 121 (2017) 16423.

ENZYMATIC REACTIONS IN GIANT VESICLES TO APPROACH ARTIFICIAL CELLS

M. Itatani,[1] G. Holló,[2] P.Albanese,[3] N. Valletti,[3] S. Kurunczi,[4] R. Horvath,[4] F. Rossi,[3] and I. Lagzi[1,5]

[1] *Department of Physics, Institute of Physics, Budapest University of Technology and Economics, Hungary.*

[2] *Department of Fundamental Microbiology, University of Lausanne, Switzerland.*

[3] *Department of Physics, Earth and Environmental Sciences, University of Siena, Italy. (federico.rossi2@unisi.it)*

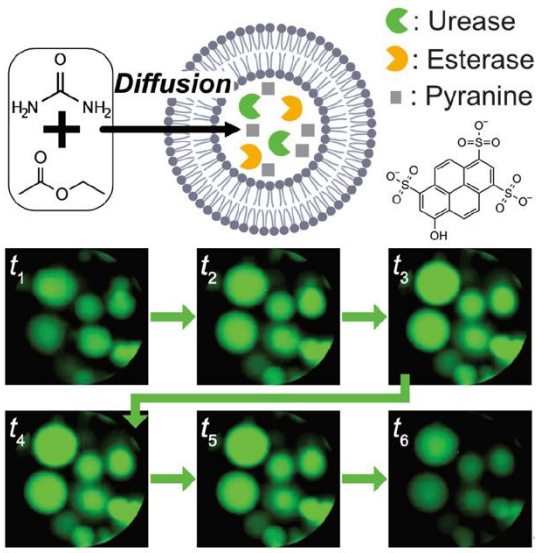
[4] *Nanobiosensorics Group, Institute of Technical Physics and Materials Science, Centre for Energy Research, Hungary.*

[5] *ELKH-BME Condensed Matter Research Group, Budapest University of Technology and Economics, Hungary.*

DOI: https://doi.org/10.46793/Phys.Chem24II.549I

ABSTRACT

We present the synthesis and multifaceted applications of Giant Unilamellar Vesicles (GUVs) in cellular modeling and the development of advanced materials. GUVs, known for their capacity to mimic cell membranes, are synthesized through a phase transfer method using self-assembling amphiphilic molecules that form bilayers, creating isolated environments ideal for both biological and material science experiments. In the realm of cellular modeling, GUVs are utilized to replicate complex cellular behaviors, such as enzymatic reaction networks, signal transduction, and self-division, offering a simplified yet dynamic model to explore fundamental biological processes and the mechanisms underlying cellular communication.



Here we investigate the transient pH changes in batch or semi-batch reactors orchestrated by the interplay of two antagonistic enzymatic reactions: urea hydrolysis by urease (production of OH^-) and ethyl acetate hydrolysis by esterase (production of H^+). The delicate balance between urease and esterase results in complex and transient pH variations within the reaction environment.

We explored the underlying mechanisms governing the antagonistic nature of urease and esterase, emphasizing their reciprocal impact on pH dynamics. In particular, substrate-specific kinetics, pH dependencies, and feedback loops characterizing these enzymatic reactions were investigated.

The enzymes, either alone or conjunction, were encapsulated in GUVs to produce emerging phenomena such as membrane self-division or transient pH variations.

THE INFLUENCE OF SURFACTANT TYPE ON DEGREASING EFFICIECY OF LIQUID DETERGENTS

S. M. Blagojević [1], N. Pejić [1] and S. N. Blagojević [2]

[1] *University of Belgrade – Faculty of Pharmacy, Vojvode Stepe 450, 11221 Belgrade, Serbia*
[2]*Institute of general and physical chemistry, Studentski Trg 12/V, 11158 Belgrade, Serbia*
(stevan.blagojevic@gmail.com)

DOI: https://doi.org/10.46793/Phys.Chem24II.551B

ABSTRACT
Evaluation of surface properties in liquid detergent formulations containing binary mixture of anionic/amphoteric surfactants as well as ternary mixtures of anionic/amphoteric/nonionic surfactants, is discussed. To examine the degreasing ability, five surfactant mixtures with different surfactant type and concentration were used to determine wetting angle, surface tension and emulsification power on oily ceramic plate. These tests assess the ability of detergents to remove grease, food residues, and other impurities from dishes.

INTRODUCTION

In contemporary world, the efficacy of dishwashing detergents plays a crucial role in maintaining hygiene in households and commercial establishments. Surfactants are fundamental ingredients in dishwashing formulations and play a key role in removing grease and dirt from dishes. Within dishwashing formulations, surfactants can exhibit various properties such as the surface tension, emulsification power and wettability property, and which depends on their chemical structure.

Wettability property of surfactants is estimated by the wetting angle, θ (the angle formed between the tangent to the liquid surface at the wetting point and the solid surface). This is important parameter that can influence the cleaning efficacy and grease removal from dishes, and consequently can also lead to the improvement of dishwashing formulations as well as enhance their effectiveness. Thus, the aim of this research is to investigate the impact of surfactants mixture on wetting properties as well as surface tension (γ) and emulsification power (EP), on the performance of dishwashing formulations, with a specific focus on grease removal efficiency. Through systematic analysis and experimental investigations, we aim to provide deeper insights into this topic and contribute to the development of more efficient dishwashing detergents [1].

Modern cleaning liquid formulation has a mixture of surfactants, mainly anionic, amphoteric and nonionic. Because of its dual affinity, these amphiphilic compounds in water-based solvents show tendency to the spontaneous adsorbed at phase boundary surfaces, thus resulting in the water surface tension lowering and enhancing surface wetting properties. In this paper evaluation of degreasing efficiency of dishwashing formulations containing both binary and ternary mixtures of anionic/amphoteric and anionic/amphoteric/nonionic surfactants, is discussed. Surfactants used include: Sodium Laureth Sulfate, SLES (anionic surfactant commonly used in cleaning product), Cocoamidopropyl Betaine, CAPB (amphoteric surfactant derived from coconut oil and dimethylaminopropylamine; used as a mild surfactant and foam booster, as well as skin irritation reducer), Lauramidopropylamine Oxide, LAO (a nonionic surfactant used as a cleaning agent, foam stabilizer and to improve cleaning performance) as well as Alkylpolyglucosides, APG (nonionic surfactants derived from glucose and fatty alcohols; biodegradable and used in environmentally friendly cleaning products, but also to improve wetting and cleaning performances). As we known, when applied to dirty surfaces, surfactants work by reducing the interfacial tension between water

and the greasy/oily residues, allowing them to be easily lifted off the surface and dispersed in the cleaning solution [2]. The wetting angle of surfactants plays a crucial role in this process, as it determines how effectively the cleaning solution spreads on the surface and interacts with the contaminants [3]. Previous studies have shown that the wetting angle, surface tension and emulsification power of surfactants can vary significantly depending on their chemical structure, molecular weight, the wetting angle. It is possible to tailor the cleaning performance of dishwashing formulations to specific needs, such as improved grease removal, reduced water consumption, or enhanced surface compatibility [4]. Thus, the primary objective of this study is to investigate how the mixture of surfactants can affect the wetting angle and other properties that influence the cleaning efficacy of dishwashing formulations. Specific research objectives include both determination and comparison the wetting angles of different mixture of surfactants commonly used in dishwashing detergent and assess the impact of wetting angle on the spreading behavior of cleaning solutions on greasy surfaces, as well as optimization of the wetting properties of surfactants in dishwashing formulations to enhance cleaning performance.

METHODS

To examine the influence of different types of commercial dishwashing detergents on the degreasing efficiency, five formulations (mixtures of surfactants denoted as I, II, III IV and V, Table 1) were prepared. These formulations (I, II, III IV and V) with different composition and concentration of surfactants (Table 1), were used commercially surfactants SLES (Texapon N 70-BASF, Germany), CAPB (Dehyton K-BASF, Germany), LAO (Dehyton PL-BASF, Germany) and APG (Glucopon 215 UP-BASF, Germany). Demineralized water (specific conductivity $\leq$ 5 μS cm^{-1}) was used as sample I (Table 1). In all experiments, the concentrations of surfactants were the same as in a real product on the market. The surfactant mixture solutions were prepared in a 100-mL volumetric flask and then diluted with demineralized deionized water to the desired concentration. Total surfactant concentration was 10 % for all samples (mixtures of surfactants).

Table 1. Samples of surfactants mixture.

Sample	Mixture of surfactants	Surfactant concentration in mixture (%)*
0	Demineralized water	–
I	SLES/CAPB	8 (SLES)/2 (CAPB)
II	SLES/CAPB/LAO	7 (SLES)/1 (CAPB)/2 (LAO)
III	SLES/CAPB/LAO	6 (SLES)/1 (CAPB)/3 (LAO)
IV	SLES/CAPB/APG	7 (SLES)/1 (CAPB)/2 (APG)
V	SLES/CAPB/APG	6 (SLES)/1 (CAPB)/3 (APG)

*Total concentration of all mixtures 10%

There are certain standard ISO methods, such as drawing up liquid films [5] and wetting tension [6] for measuring the wetting angle, surface tension and emulsification power of detergents. To measure wetting angle, the contact angle measurements were conducted, and according to standard practice [7], for characterizing the wettability of surfaces, water (test liquid) contact angle has been used to establish weather a surface is superhydrophilic (wetting angle < 10º), hydrophilic (wetting angle range 10 – 90º), hydrophobic (wetting angle range 90 – 150º) and superhydrophobic (wetting angle range 150 – 180º). For wetting angle measurement, the ceramic plates with olive and sunflower oil mixture (1:1) on surface in amount of 1 g/plate (Ø 20 cm) have been used. For surface

tension measurement the pendant drop method [8] was used. To measure the wetting angle between a ceramic plate (solid surface) and a drop of investigated sample, as well as surface tension at 25º C, DSA30S drop shape analyzer (KRÜSS, Germany), was used. The instrument provides angular resolution and accuracy of 0.01° and 0.3°, respectively, as well as surface tension measurement range 0.01 – 2000 mN with resolution of 0.01 mN m^{-1}. The DSA30S instrument used Young–Laplace (YL) model for determining the wetting angle in drop shape analysis. Emulsification powers (EP) were determined by electrical conductivity measurements of various surfactant solutions in a mixture with oil.

RESULTS AND DISCUSSION

In this study, we examined five surfactant mixtures (sample I – V) for wettability. The values of wetting angle (θ), surface tension (γ) and emulsification power (EP) of 1.0 % water solutions of examined surfactant mixtures, are all summarized in Table 2. According to standard procedure [5,8], demineralized water wetting angle and surface tension was firstly measured, then the sample is fouled with olive and sunflower oil, measured again for its demineralized water wetting angle and then measured five different samples. A smaller wetting angle indicates that the liquid wets the surface well (hydrophilic), while a larger wetting angle suggests poor wetting (hydrophobic). Smaller surface tension indicates better washing performances.

Table 2. Measured wetting angle*, surface tension and emulsification power of 1% solution in demineralized water at 25º C.

Sample	**θ (º)**	**γ (mN m^{-1})**	**EP (mg g^{-1})**
0	55	72.8	–
I	85	32.1	14.5
II	40	20.2	25.5
III	8	14.1	32.1
IV	42	20.5	25.3
V	10	14.5	32.0

* of ceramic oily plate/water/surfactants mixture

From the obtained results (Table 2), it is obvious that the surfactants type and concentration have a great impact on wetting angle, and the surface condition is changed from superhydrofobic to superhydrophilic. Also, the difference in surface tension and emulsification power is strongly dependent on concentration of nonionic surfactants. Sample III (SLES/CAPB/LAO) has the lowest wetting angle of 8º, indicating excellent wetting properties. This sample shows the best ability to spread on the surface, also sample III has the lowest surface tension at 14.1 mN m^{-1}, indicating good spreading properties. Lower surface tension values suggest better wetting ability and finally sample III has the highest emulsification power at 32.1 mg g^{-1}, indicating strong emulsification capabilities. This sample is effective at forming stable emulsions. Overall, sample III performs the best in terms of wetting angle, surface tension, as well as emulsification power. The reason for these properties of sample III is synergism of anionic and nonionic surfactants refers to the enhanced performance achieved when these two types of surfactants are used together in a formulation. This synergistic effect is commonly observed in various applications such as detergents, cleaning products, emulsions, and personal care items. The combination of these surfactants often leads to synergistic effects, where the total surface activity, detergency, and emulsifying properties of the formulation are greater than the sum of the individual effects of each surfactant. Anionic surfactants can be negatively affected by hard water ions (Ca^{2+} and Mg^{2+}), resulting in reduced effectiveness.

Nonionic surfactants are less affected by water hardness. Combining anionic and nonionic surfactants can mitigate the negative impact of hard water, maintaining cleaning efficiency even under challenging water conditions. Indicated synergism, as presented in this paper and also shown previously [9] leads to unique application properties and improved performance in terms of grade removal and foam volume in the formulation of liquid detergents.

CONCLUSION

The results provide valuable insights into the impact of surfactants on wetting angle measurements of ceramic plates when exposed to water and various substances. Both, the wetting angle (θ) and surface tension (γ), serves as an indicator of the surface's interaction with liquids, varying from hydrophobic to hydrophilic properties. For the clean sample, the wetting (initial) angle is 55º which suggests a moderate hydrophilic nature of the ceramic surface. When fouled with olive and sunflower oil, θ significantly increases, indicating a transition towards a more hydrophobic state due to the presence of the oils. Subsequent measurements on five different samples (I to V) treated with surfactants reveal varying wetting angles. For Sample I (SLES/CAPB), θ = 85º, indicating a moderate hydrophilic behavior. In contrast, for samples with the same composition, but different concentration of surfactants, such as samples II and III (SLES/CAPB/LAO) as well as IV and V (SLES/CAPB/APG), wetting angles are 40º, 8º, 42º, and 10º respectively, which reflecting a progression towards enhanced hydrophilicity. These findings underscore the critical role of surfactants in altering the wetting properties of ceramic surfaces, influencing the wetting angle with water. The shift from superhydrophobic to superhydrophilic states highlights the tunable nature of surface interactions through the manipulation of both surfactant type and concentration. Measurements of surface tension and emulsification power indicates that presence of nonionic surfactants, have a large impact on both properties and a large impact of performances of final products, because it is well known that products with lower γ and higher EP have better performance to remove grease and other impurities from ceramic surface of dishes.

Acknowledgment

This research was funded by the Ministry of Science, Technological Development and Innovation, Republic of Serbia through Grant Agreement with Institute of general and physical chemistry No 451-03-66/2024-03/200051 and University of Belgrade – Faculty of Pharmacy No 451-03-65/2024-03/200161.

REFERENCES

[1] N. Shardt, M. B. Bigdeli, J A. W. Elliott, P. A. Tsai, J. Phys. Chem. Lett., 10(23) **(**2019**)** 7510.
[2] G. Popescu, G. Nechifor, M. Olteanu, Colloids Surf. A: Physicochem. Eng. Asp., 90(1) (1994) 1.
[3] B. Bera, O. Carrier, E. H. G. Backus, M. Bonn, N. Shahidzadeh, D. Bonn, Langmuir 34(41) (2018) 12344.
[4] K. Saxena, Y. Chen, Proceedings of the ASME 2023 International Mechanical Engineering Congress and Exposition. Volume 9: Fluids Engineering. New Orleans, Louisiana, USA. October 29 – November 2, (2023).
[5] SPRS ISO 304:2011, Surface active agents – Determination of surface tension by drawing up liquid films.
[6] ISO 8296:2003 Plastics – Film and sheeting – Determination of wetting tension.
[7] ASTM D7334-08(2022) Standard Practice for Surface Wettability of Coatings, Substrates and Pigments by Advancing Contact Angle Measurement.
[8] SRPS EN ISO 19403-2:2003, Determination of the surface tension using the pendant drop method.
[9] S. M. Blagojevic, N. D. Pejic, S. N. Blagojevic, Russ. J. Phys. Chem. A, 91(13) (2017) 2690.

M *– Complex Compounds*

INVESTIGATION OF CATALYTIC AND ELECTROCHEMICAL PROPERTIES OF PEROVSKITE $Ca_{0.9}Er_{0.1}MnO_3$

T. B. Vlašković [1], B. B. Petković[1], B. Laban[1], M. Čebela[2] and M. Rosić[2]

[1] *Faculty of Sciences and Mathematics, University of Priština in Kosovska Mitrovica, Lole Ribara 29, 38220 Kosovska Mitrovica, Serbia. (branka.petkovic@pr.ac.rs)*
[2] *Laboratory for Material Science, Institute of Nuclear Science„Vinča“, National Institute of the Republic of Serbia, University of Belgrade, P.O. Box 522, 11001 Belgrade, Serbia*

DOI: https://doi.org/10.46793/Phys.Chem24II.557V

ABSTRACT

The nanomaterial with perovskite structure of the formula $Ca_{0.9}Er_{0.1}MnO_3$ was synthesized by the sucrose-nitrite process (SNP). In this synthesis process, nitrate salts were combined in the appropriate stoichiometric ratio, and sucrose $C_{12}H_{22}O_{11}$ was used as fuel. The obtained nanopowder was annealed at temperatures of 800, 900 and 1000 ºC. The obtained nanostructured powders were characterized by XRD. The catalytic reduction of Methylene blue dye (MB) in the presence of perovskite $Ca_{0.9}Er_{0.1}MnO_3$ was studied by UV/Vis spectrophotometry. Electrochemical properties of the studied material were investigated by cyclic voltammetry (CV) at the $Ca_{0.9}Er_{0.1}MnO_3$ modified carbon paste electrodes (CPEs) in $[Fe(CN)_6]^{3-/4-}$ redox system. CV profiles and EIS measurements confirm better electrochemical activity of perovskite $Ca_{0.9}Er_{0.1}MnO_3$ modified CPE over bare CPE, which makes them a promising material for further application as an electrochemical sensor.

INTRODUCTION

The perovskite structured materials, or only perovskites, are compounds well known by generic formula ABX_3, where A and B are two different cations, and X is mainly oxygen but can be some different anions such as halides, nitrides, or sulfides [1]. Numerous studies have focused on perovskites with structure ABO_3 due to their important role in various fields such as material science, heterogeneous catalysis, etc. [1]. When synthesizing different nanopowders, a big challenge is controlling the nanoparticle size, size distribution, morphology, crystallinity, shape, and properties in order to obtain materials for different applications. There are several methods for synthesizing perovskite structured materials, and the choice of method influences the physico chemical characteristics of perovskite [2]. Various forms of perovskite can be obtained, such as bulk, nanocrystalline, nanowires, etc. Due to large surface area to volume ratio of perovskite nanomaterials leads to their use as catalysts. Perovskite oxides are of interest as catalysts because of their stability, high design flexibility, and tunable surface properties [3]. These nanomaterials possess controllable defects to create ionic or electronic conductivities. The redox property of perovskite oxide is mainly due to multiple oxidation states of B-site [1, 3].

The electrochemical behavior of perovskite has been widely investigated [4]. Perovskites have potential applications as an electrode material for supercapacitors as well as for optical and electrochemical sensors [5].

This work is a continuation of our recent research based on newly synthesized perovskite oxide $Ca_{0.9}Er_{0.1}MnO_3$ [6], further as a study of catalytic reduction of Methylene blue dye (MB) and electrochemical study of this material incorporated in CPE as potential efficient electrode modifier.

METHODS

The starting chemicals used for the synthesis of nanostructured perovskite are nitrate salts: Ca-nitrate ($Ca(NO_3)_2{\cdot}4H_2O$), Mn-nitrate ($Mn(NO_3)_2{\cdot}H_2O$), Er-nitrate ($Er(NO_3)_3{\cdot}5H_2O$), in combination with sucrose ($C_{12}H_{22}O_{11}$), which was used as a fuel. The composition of the mixture was calculated according to the principle of propellant chemistry.

At the beginning of the synthesis, sucrose was added to the mixed metal nitrate solution in a molar ratio of 1:1 (fuel/oxidant). After the synthesis, an amorphous, voluminous powder was obtained. Then obtained powders were calcined in an annealing furnace at temperatures of 800, 900, and 1000 ºC in a time interval of 15 minutes. The following methods were used to characterize the obtained powder.

Sample characterization

Powder XRD patterns of all the powders were performed by using an Ultima IV Rigaku diffractometer (XRPD, Rigaku Ultima IV, Tokyo, Japan), equipped with CuKα1,2 radiations, using a generator voltage of 40.0 kV and a generator current of 40.0 mA. The range of 10–80º 2θ was used for all powders in a continuous scan mode with a scanning step size of 0.02º and at a scan rate of 10º/min, using a D/TeX Ultra-high-speed detector. A glass sample carrier was used to prepare the sample. The PDXL2 (Ver. 2.8.4.0) software was used to evaluate the phase composition and identification [7]. All the structural models for refinement, i.e., cif files, were taken from the ICSD database [8]. The absorption spectra of MB, and reaction mixture were measured using LLG – uniSPEC 2 UV–Vis spectrophotometer in a quartz cuvette with a path length of 1cm.

Electrochemical measurements

Cyclic voltammetry measurements were performed on PalmSens 3 potentiostat/galvanostat/impedance analyzer with PSTrace software (PalmSens BV, Netherland), Three-electrode system in the electrochemical cell consisting of Ag/AgCl (1M KCl) reference electrode and platinum wire counter electrode (CH Instruments, USA) while working electrode was carbon paste electrode doped with 10% of $Ca_{0.9}Er_{0.1}MnO_3$ (each electrode doped with material annealed at different temperatures from 800, 900 and 1000 ºC). CV measurements were performed in the presence of a stationary 5 mM $K_3[Fe(CN)]_6/K_4[Fe(CN)]_6$ (1:1) mixture as a redox probe in 0.1 M KCl solution.

RESULTS AND DISCUSSION

XRD analysis

The phase composition of the examined samples was determined using the X-ray powder diffraction method (the completion of the reaction and the single phase of the samples were confirmed). Based on the results of X-ray analysis of samples with the chemical formula $Ca_{0.9}Er_{0.1}MnO_3$ obtained after the combustion reaction (not shown), it was determined that the phases present are amorphous, which is probably a consequence of insufficient heat during spontaneous combustion. After the calcination of the samples in an experimentally determined interval, it was determined that the perovskite phase of the chemical formula $Ca_{0.9}Er_{0.1}MnO_3$ was present in the samples. The representative diffractograms for $Ca_{0.9}Er_{0.1}MnO_3$ samples after different calcination temperatures are given in **Figure 1a**. All broad peaks of weak intensity indicate the nanocrystalline nature of the powders, Fig. 1a. A good agreement was obtained (based on data from the database, card numbers 03-0830, 24-0508, 24-0430) by comparing the experimental and calculated diffractograms.

Catalytic and electrochemical study

MB dye is a blue-colored dye, and the reduction/degradation of the MB molecules can be easily followed by a change in MB absorption spectra. When MB dye molecules are reduced, the color changes from blue to transparent. The reduction of MB in aqueous solution over $Ca_{0.9}Er_{0.1}MnO_3$ is shown in **Figure 1b**. From **Figure 1b**, it can be seen that the intensity of MB absorption band in the presence of $Ca_{0.9}Er_{0.1}MnO_3$ decreased. Observing the MB absorption spectra for a few days (not shown in Figures), the MB absorption band's intensity increased, indicating that the reduction of MB molecules was reversible and that MB molecules are not adsorbed on perovskite surfaces. We found that all samples of perovskite oxide $Ca_{0.9}Er_{0.1}MnO_3$, calcined at 800, 900, and 1000 ºC, can degrade MB molecules after 10 minutes. This result suggests that $Ca_{0.9}Er_{0.1}MnO_3$ has a strong catalytic oxidation ability for MB dye molecules at room temperature without adding additional oxidants or light irradiation.

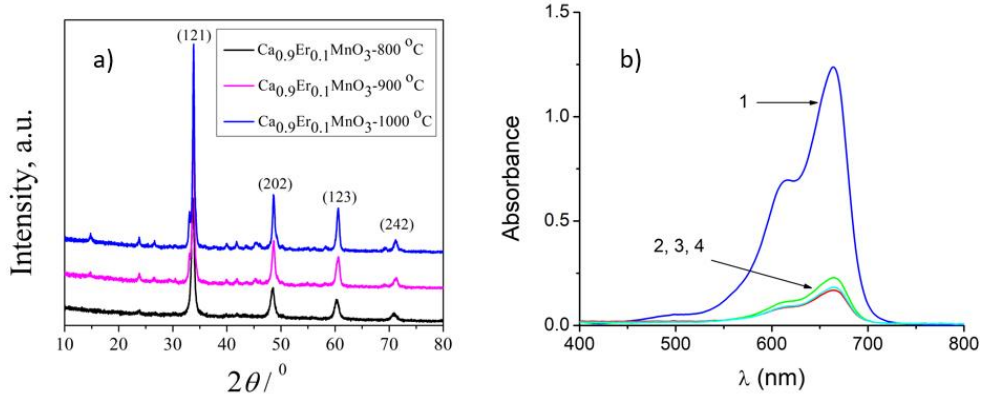


Figure 1. a) XRD pattern of $Ca_{0.9}Er_{0.1}MnO_3$ samples after different temperatures of calcination; b) Absorption spectra of MB line 1 (blue), MB in the presence of perovskite calcined at different temperature lines 2, 3, and 4 (800 ºC -red, 900 ºC -green, 1000 ºC -light blue).

Cyclic voltammetry profiles in **Figure 2a** shows that $Ca_{0.9}Er_{0.1}MnO_3$ used as electrode modifiers highly improved electron transfer property and promoted electrochemical reaction in $[Fe(CN)_6]^{3-/4-}$ redox system due to higher peak current compared to signal obtained at bare CPE. It can be noticed that peak current increases with increasing temperature. The cathodic and anodic peak currents increased with an increase in scan rate from 10 to 125 mV/s (**Figure 2b**), and the linear relationship between anodic/cathodic peak current *vs* square root of scan rate (**Figure 2c**) is observed. It is also observed that log peak current *vs* log scan rate (**Figure 2d**) also resulted with straight line with slope of 0.62, which is close to the theoretical value of 0.5 for diffusion-controlled process [9]. That means that the electrode reaction is controlled by diffusion as a rate-determining step while the adsorption and/or other specific interactions on the $Ca_{0.9}Er_{0.1}MnO_3$ modified CPE surface are negligible.

The equations which express the linear dependence are:

$I\ (\mu A) = -1.52 + 9.95 \times v^{1/2}\ (mV/s)^{1/2}$; (R = 0.988)

$\log I\ (\mu A) = -5.37 + 0.62 \times \log v\ (mV/s)$; (R = 0.998)

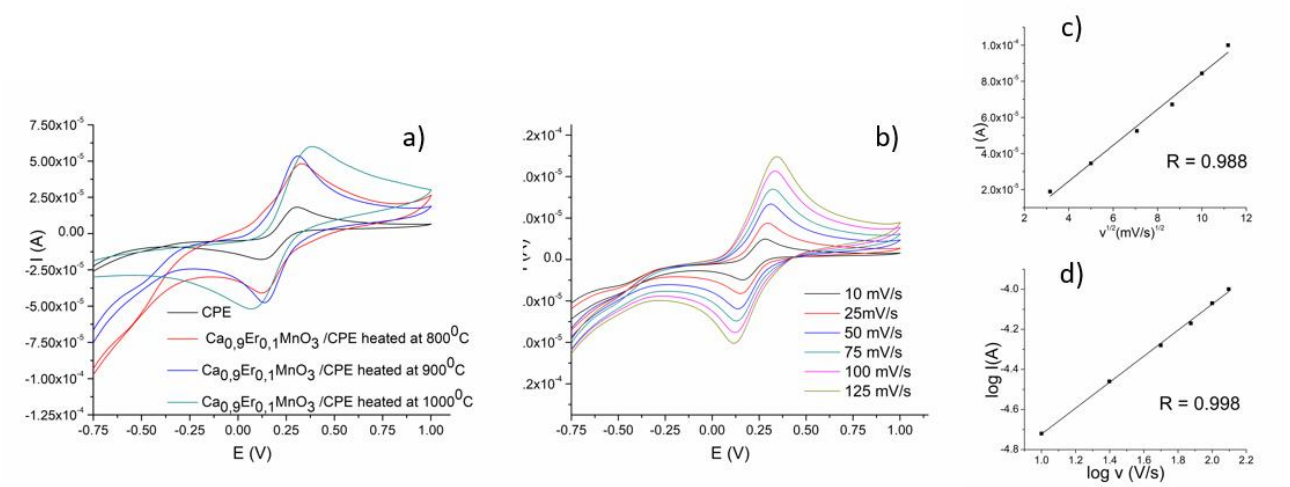


Figure 2. a) CV profiles of bare and modified CPEs with different perovskite materials; b) Effect of scan rate on $Ca_{0.9}Er_{0.1}MnO_3$ – 900 ºC modified CPE; c) The peak current *vs* scan rate derived from graph b; d) The logarithm of peak current *vs* the logarithm of scan rate derived from b.

CONCLUSION

The perovskite oxide, with the structure $Ca_{0.9}Er_{0.1}MnO_3$, can be successfully synthesized by the sucrose-nitrite process. The XRD analysis confirmed that all samples, which are calcined at three different temperatures 800, 900, and 1000 ºC, have the nanocrystalline nature of the powders. All three samples of perovskite oxide showed good catalytic activity of MB dye molecule reduction without adding additional oxidants or light irradiation. Electrochemical study indicates possible successful utilization of this material as an electrode modifier for sensor applications.

Acknowledgment

This work was funded by the Ministry of Education, Science and Technological Development of the Republic of Serbia Grant No. 451-03-65/2024-03/ 200123 and Faculty of Sciences and Mathematics University of Priština in Kosovska Mitrovica, Project Number IJ-2301.

REFERENCES

[1] P. K. Pankaj and V. R. Anil in: Recent Advances in Multifunctional Perovskite Materials, S. Poorva and K. Ashwini (Eds.), IntechOpen 2022.
[2] S. A. Kulkarni, S. G. Mhaisalkar, N. Mathews, P. P. Boix, Small Methods, 3 (2019) 1800231.
[3] K. Wang, C. Han, Z. Shao, J. Qiu, S. Wang, S. Liu, Adv. Funct. Mater., 31 (2021) 2102089.
[4] Q. Hu, B. Yue, F. Yang, H. Shao, J. Wang, L. Ji, Y. Jia, Y. Wang, J. Liu, ChemistrySelect, 4 (2019) 11903.
[5] G. K. Jesna, V. V. Halali, C. G. Sanjayan, V. Suvina, M. Sakar, R. G. Balakrishna, Inorg. Chem. Front., 7 (2020) 2702.
[6] T. B. Vlašković, B. Laban, M. Milošević, M. Čebela, V. Dodevski, M. Rosić, CYSC-2023: 15th EcerS Conference for Young Scientists in Ceramics, programme and book of abstracts; Oct 11-14, Novi Sad, (2023) 65.
[7] Rigaku, PDXL Integrated X-Ray Powder Diffraction Software. 2011, Rigaku, Tokyo: Japan.
[8] International Crystallographical Database (ICDD), N.S. 12 Campus Blvd, PA 19073, USA, Editor. 2012: USA.
[9] H. S. Ali, A. A. Abdullah, P. T. Pınar, Y. Yardım, Z. Şentürk, Talanta, 170 (2017) 384.

ELECTROCHEMICAL AND ENZYME-LIKE ACTIVITY OF SELECTED BTC MOF-DERIVED METAL OXIDE NANOPARTICLES

M. Marković [1], M. Ognjanović [2]and B. B. Petković [1]

[1] *University of Priština in Kosovska Mitrovica, Faculty of Sciences and Mathematics, Lole Ribara 29, 38220 Kosovska Mitrovica, Serbia (milenatasic4@gmail.com)*
[2] *VINČA Institute of Nuclear Sciences, National Institute of the Republic of Serbia, University of Belgrade, Belgrade, Serbia*

DOI: https://doi.org/10.46793/Phys.Chem24II.561M

ABSTRACT

The goal of this work was to investigate and compare cerium, copper and iron oxide nanoparticles (NPs) obtained from trimesic acid (designated as BTC) metal-organic frameworks (MOFs) in terms of their electrochemical and enzyme-like catalytic properties. Thermal decomposition of MOFs was used for producing high-performance porous materials. The structural characterization was verified using powder X-ray diffraction (PXRD). Selected metal oxide nanoparticles were incorporated in carbon paste electrodes (CPEs) and electrochemical characterization of those modified CPEs was performed by electrochemical impedance spectroscopy and cyclic voltammetry in $[Fe(CN)_6]^{3-/4-}$ redox system. Reaction of oxidation of TMB by hydrogen peroxide was used for studying the catalytic properties of selected BTC MOF-derived metal oxide nanoparticles. It was found that MOF-derived CuO/C NPs showed the highest electrochemical signal while BTC MOF-derived CeO_2 NPs showed the highest catalytic activity.

INTRODUCTION

Among the classes of highly porous materials, metalorganic frameworks (MOFs) are unparalleled in their degree of tunability and structural diversity as well as their range of chemical and physical properties. Furthermore, the possibility for postsynthetic modification and thermal production of other materials adds dimension to these materials [1].

Metal oxide nanoparticles are prepared by traditional synthesis methods such as the most commonly used sol-gel and solvothermal/hydrothermal synthesis, followed by microwave synthesis, electroless deposition and chemical vapor deposition. A new approach through template-assisted nanomaterials offers promising protocols for obtaining nanoparticles with improved performance [2]. Producing of metal oxide nanoparticles and carbon material/metal oxide nanoparticles by controlled thermal decomposition of MOFs is one of the possible ways of obtaining porous and high-performance materials for diverse applications [3].

Metal and metal oxide nanoparticles attract the great attention of researchers due to their unique optical and electrical properties. Nanoparticles catalytic activity and intrinsic ability in generating or scavenging reactive oxygen species, in general, can be used to mimic the catalytic activity of natural enzymes. Many nanoparticles with enzyme-like activities have been found, potentially capable of being applied for commercial uses, such as in biosensors, pharmaceutical processes, and the food industry. To date, a variety of nanoparticles, especially those formed from noble metals, have been determined to possess oxidase-like, peroxidase-like, catalase-like, and/or superoxide dismutase-like activity [4].

Various nanomaterials have been used for electrode modification, due to an increase in their surface area and improvement of electrochemical properties. Electrode modified by nanoparticles has a variety of potential applications including catalysis, chemical and biological sensing, as

energy-conversion devices, etc. The goal of this work is to produce in simple and reliable way, then characterize and compare ceria, copper and iron oxide NPs with significant electrochemical properties for further application in electrochemical sensing.

EXPERIMENTAL

Synthesis of MIL-100($FeSO_4$), HKUST-1, Ce-BTC

Trimesic acid, benzene-1,3,5-tricarboxylic acid (BTC) was used as a linker for the synthesis of all MOFs which are made according to the previously described procedures [5-7].

Fabrication of MOF-derived NPs (α-Fe_2O_3, CuO/C, and CeO_2)

The as-prepared MOFs were calcinated in air and appropriate NPs were produced according to the references [5, 8, 9].

Electrochemical measurements

Cyclic voltammetric (CV) and *electrochemical* impedance spectroscopy (EIS) measurements were performed in the presence of a stationary 5 mM $K_3[Fe(CN)]_6/K_4[Fe(CN)]_6$ (1:1) mixture as a redox probe in 0.1 M KCl solution. An electrochemical system Autolab 302 N with corresponding software NOVA 2.0.2 was used for measurements. The electrochemical working cell consisted of a three-electrode system: an Ag/AgCl (saturated KCl) was the reference electrode, a Pt-wire used counter electrode and carbon paste type of electrode loaded with NPs (10%), carbon powder, and paraffin oil. EIS measurements were performed with the frequency changed from $1 \cdot 10^5$ Hz to $1 \cdot 10^2$ Hz with a signal amplitude of 5 mV at the potential of 0.05 V.

PXRD characterization

The crystal structure of synthesized MOFs and their respective oxides was determined by analyzing powder X-ray diffraction (PXRD) data. The measurements were performed on dried powders using a high-resolution Smart Lab® diffractometer (Rigaku, Japan), equipped with Cu Kα radiation source (λ = 1.5406 Å) under a voltage of 40 kV and a 30-mA current. The data collection for the patterns was performed in the 5-70° 2θ range.

Study of enzyme-like activity

The catalytic activity of MOF-derived metal oxide nanoparticles for the H_2O_2 reduction reaction was investigated using the oxidization reaction of 3,3′ -5,5′ - tetramethylbenzidine (TMB) dissolved in phosphate buffer solution (PBS) pH=4. The degree of catalytic activity for the reduction reaction of H_2O_2 was quantified by the absorbance of oxidized TMB [10]. Measurement determinations were performed on Thermo Scientific Spectrophotometer Genesis 10S UV-Vis, on 400-800 nm.

RESULTS AND DISCUSSION

The crystal structures of the samples were examined using X-ray powder diffraction data. In the obtained diffraction patterns, all reflections were successfully matched with the desired metal-organic frameworks: MIL-100($FeSO_4$) in which iron is linked by BTC, HKUST-1 in which copper is linked by BTC, and Ce-MOF based on cerium linked with BTC (see **Fig. 1a-c**). After the calcination procedures, the respective metal oxides were also analyzed using PXRD. In Fig. 1d, a pure hematite phase (α-Fe_2O_3) was identified in the space group R $\bar{3}$c, No. 167. The crystalline size, estimated by Scherrer analysis from the peak broadening of the diffraction pattern due to the finite size of crystallites, was found to be about 20 nm. After the calcination of HKUST-1, pure copper oxide diffraction peaks were identified in space group C 1 *c* 1, No. 9, with an average crystallite size of about 37 nm. Additionally, a (002) reflection of graphite was observed at 28.3° 2θ

(**Fig. 1e**). In Fig. 1f, a pure cubic CeO_2 (indexed in F*m*-3*m*, No. 225 crystal phase) was obtained after the calcination of Ce-MOF, with an average crystallite size of about 7 nm.

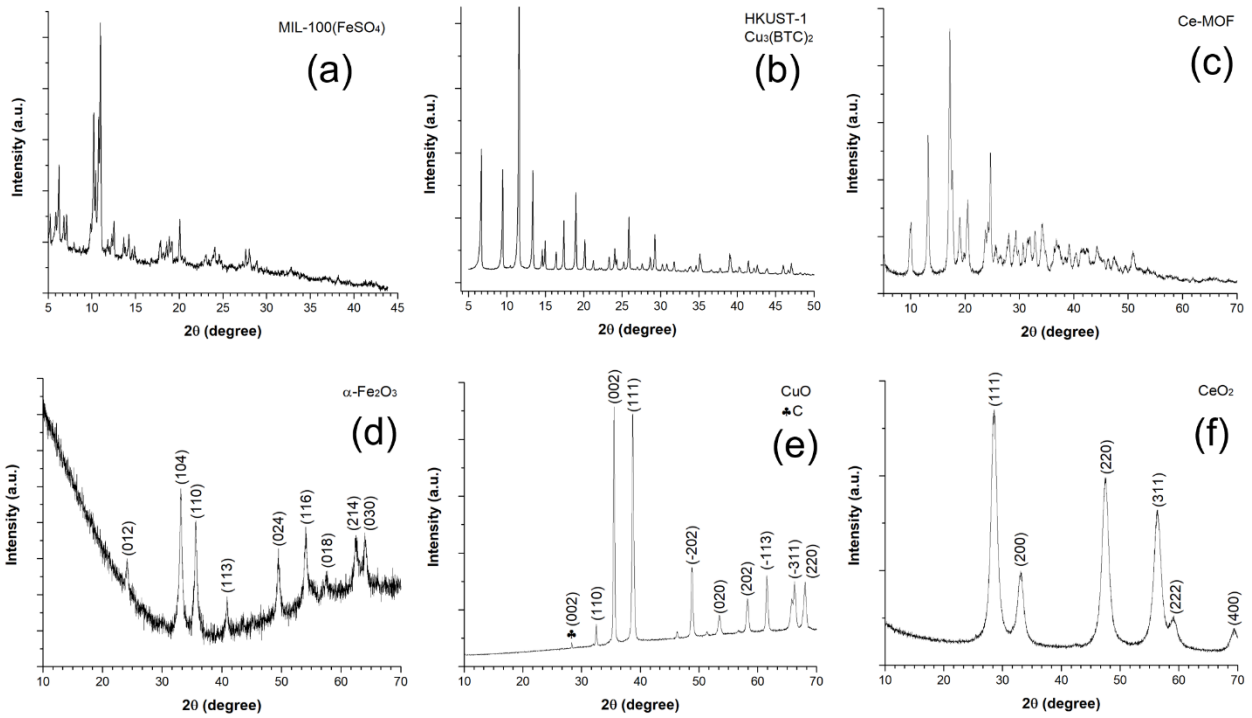


Figure 1. XRPD diffraction patterns of prepared MOFs: (a) MIL-100($FeSO_4$), (b) HKUST-1, (c) Ce-MOF; and their respective oxides after calcination: (d) α-Fe_2O_3, (e) CuO/C and (f) CeO_2.

Figure 2a shows the CVs recorded at bare CPE and CPE loaded with MOF-derived α-Fe_2O_3, CuO/C CeO_2 NPs. CV profiles of modified CPE showed a higher peak current for iron complex solution compared to bare CPE and the highest peak current was recorded for MOF-derived CuO/C NPs. An additional wave in the area from 0 to 0.1 V can also be seen for this material, which originated from copper in the electrode material. Iron in α-Fe_2O_3 CPE modifier also can increase peak current in CV profile and that can be an explanation for better conductivity of MOF-derived CeO_2 modified CPE recorded by EIS measurement (**Fig. 2b**). EIS spectra of all electrodes were recorded in the $[Fe(CN)_6]^{3-/4-}$ same solution and the diameter of the obtained semicircle correspond to charge transfer resistance. The smaller semicircle refers to promoted electron transfer at the electrode surface.

The TMB solution became blue in the presence of all investigated metal oxide NPs. According to **Fig. 2c**, the TMB solution with CeO_2 NPs showed the most significant color change and the highest absorbance at 652 nm among the samples measured by UV–VIS spectroscopy. This means that the enzyme-like catalytic activity of CeO_2 NPs is highest among the metal oxide NPs tested for H_2O_2 reduction.

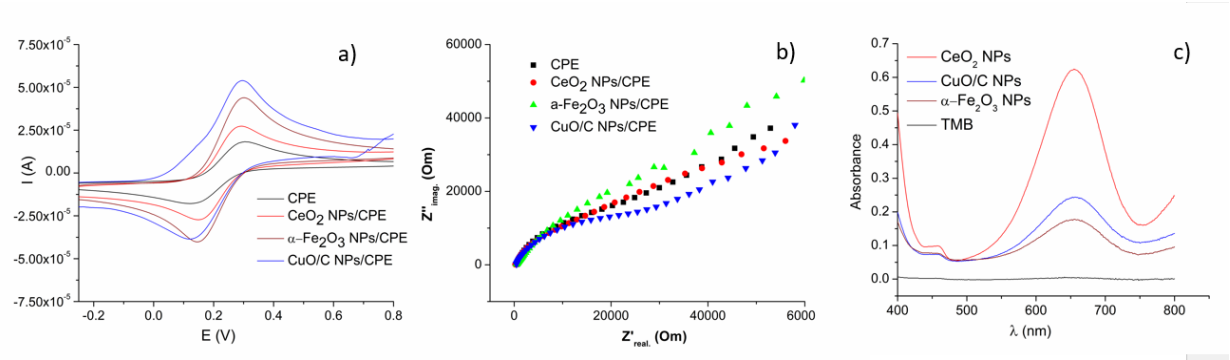


Figure 2. CV profiles (a) and EIS responses (b) of bare CPE and CPE modified with different NPs recorded in 0.1M KCl solution containing 5 mM $[Fe(CN)_6]^{3-/4-}$ redox couple; c) UV–Vis profile showing the oxidation reaction of TMB in the presence of studied metal oxide NPs and H_2O_2.

CONCLUSION

α-Fe_2O_3, CuO/C, and CeO_2 NPs were easily prepared by simple calcination of appropriate BTC MOFs in air condition. The structure of synthesized BTC MOFs and metal oxide NPs obtained from them were verified by comparing obtained PXRD and previously recorded data. MOF-derived metal oxide NPs have shown promising electrochemical and catalytic activity when they are incorporated in CPE. Based on these results, BTC MOF-derived NPs were selected for further investigations as potentially active materials for electrochemical sensors.

Acknowledgment

Financial support for this study was granted by the Ministry of Education, Science and Technological Development of the Republic of Serbia Grant No. 451-03-65/2024-03/ 200123 and the Faculty of Sciences and Mathematics, University of Priština in Kosovska Mitrovica, Project Number IJ-2301.

REFERENCES

[1] L. E. Kreno, K. Leong, O. K. Farha, M. Allendorf, R. P. Van Duyne, J. T. Hupp, Chem. Rev. 112 (2012) 1105–1125.
[2] Z. Alhalili, Molecules 28 (2023) 3086.
[3] P. Behera, S. Subudhi, S.P. Tripathy, K. Parida, Chem. Rev. 456, 1 (2022) 214392.
[4] W. He, W. Wamer, Q. Xia, J. Yin and P. P. Fu, J. Environ. Sci. Health C, 32 (2014) 186–211.
[5] J. He, Y. Xu, W. Wang, B. Hu, Z. Wang, X. Yang, Y. Wang, L. Yang, J. Chem. Eng. 379 (2020) 122431.
[6] K.L. Tan, K.Y. Foo, Arab. J. Chem. 14 (2021) 103359.
[7] J. Zhao, W.T. Nunn, P.C. Lemaire, Y. Lin, M.D. Dickey, C.J. Oldham, H.J. Walls, G.W. Peterson, M.D. Losego, G.N. Parsons, J. Am. Chem. Soc. 137, 43 (2015) 13756–13759.
[8] R. Liang, Z. He, C. Zhou, G. Yan, L.Wu, Nanomaterials 10 (2020) 1701.
[9] C. Zhao, X. Tang, J. Zhao, J. Cao, Z. Jiang, J. Qin, J. Nanobiotechnology 20 (2022) 507.
[10] J. Ji, S. Y. Ko, K. M. Choi, Y. Kwon, Appl. Surf. Sci. 554 (2021) 148786.

HYDROLYTIC AND THERMAL STABILITY OF UREA-FORMALDEHYDE COMPOSITES BASED ON CHITOSAN AND ZEOLITE ZSM-5

M. Ristić[1], S. Samaržija- Jovanović[1], T. Jovanović[2], M. Krstić[3], B. B. Petković[1], V. Jovanović[1] and M. Marinović-Cincović[4]

[1]*Faculty of Sciences, University of Priština-Kosovska Mitrovica, Lole Ribara 29, 38000 Kosovska Mitrovica, Serbia. (branka.petkovic@pr.ac.rs)*
[2] *Faculty of Sciences and Mathematics, University of Niš, Višegradska 33, 18000 Niš, Serbia.*
[3]*Faculty of Technology Novi Sad, University of Novi Sad, Bulevar cara Lazara 1, 21000 Novi Sad, Serbia.*
[4] *Vinča Institute of Nuclear Sciences - National Institute of the Republic of Serbia, University of Belgrade, Mike Petrovića Alasa 12-14, 11351 Vinča, Belgrade, Serbia.*

DOI: https://doi.org/10.46793/Phys.Chem24II.565R

ABSTRACT
In this work, a comparative investigation of the hydrolytic and thermal stability of urea-formaldehyde (UF) resins modified with chitosan (UF/H) and zeolite (UF/Z) was performed. Zeolite ZSM-5 and chitosan were used to modify the *in situ* synthesized UF resin with a low formaldehyde/urea (FA/U) molar ratio (0.8), to reduce the free FA content in the UF resin. The disulfite method determined free and released FA from the synthesized composites. The modified UF composites were characterized using TG/DTG, and SEM. The results showed that chitosan and zeolite are good scavengers of FA from cross-linked modified UF composites. Both tested composites have the same content of free FA (0.06%). The UF/H composite is hydrolytically more stable because it has a lower content of released FA (2.52%), after acid hydrolysis, compared to the UF/Z composite (4.08%). On the other hand, the UF/Z composite proved to be thermally more stable ($T_{5\%}$= 205.4^{o}C) than the UF/Z composite ($T_{5\%}$= 91.9^{o}C).

INTRODUCTION
The wood industry is the main consumer of adhesives based on UF resins, which are produced in the polycondensation reaction of urea and formaldehyde (FA) [1]. In addition to many advantages [1-3], there is a serious drawback of UF adhesives which is the emission of FA into the environment. One way to reduce FA is to add compounds known as "scavengers" of free FA from UF adhesives. Some of the studies show that tree bark [4], tannins [5], cellulose [6], and betaine [5] are good FA scavengers because there is successful chemical bonding of FA with functional groups in organic scavengers. Inorganic materials used as adsorbents for various harmful substances are aluminosilicates (clay, montmorillonite, zeolite, bentonite). The use of montmorillonite as a FA scavenger has already been confirmed in several papers [7], and now the focus is on zeolite as a structurally more complex aluminosilicate.

The work aims to examine the influence of chitosan and zeolite on the hydrolytic and thermal stability of modified UF composites.

METHODS
Materials: Urea is supplied from Alkaloid (Skopje, Republic of North Macedonia) and 35% formaldehyde supplied from Unis (Goražde, Bosnia and Herzegovina) was used for the synthesis of

UF resins. Chitosan (Thermo Fisher Scientific, USA) with molecular weight: 600.000–800.000, and zeoliteZSM-5 (Thermo Scientific Chemicals) were used as fillers.

Synthesis of UF composites: UF composites with chitosan and zeolite (UF/H and UF/Z) were synthesized according to the procedure [8].

Determination of free FA: The percentage of free FA was determined by the sulfite method which was explained in more detail in our previous work [8].

Hydrolytic stability: The samples were exposed to acid hydrolysis, according to the procedure described in Jovanović et al., [8].

SEM micrographs: Micrographs of the modified UF resin were taken with a Tescan FESEM Mira 3 XMU scanning electron microscope at 20 kV acceleration voltage. Before recording, the samples were steamed with gold on a Polaron SC503, Fisons Instruments.

Thermal analysis: The Setaram Setsis Evolution 1750 instrument was used to test thermal stability. The samples were heated in an argon atmosphere, with a flow rate of 20 cm^3/min, in the temperature range of 30-500 ^oC, with a heating rate of 10 ^oC/min.

RESULTS AND DISCUSSION

Based on the same value for the percentage of free FA in Table 1, it can be concluded that both fillers are excellent scavengers of free FA, regardless of their different nature. After acid hydrolysis, UF/H resin shows a significantly lower percentage of released FA (2.52%) compared to UF/Z resin (4.08%) (**Table 1**), based on which it can be said that UF/H resin is hydrolytically much more stable.

Table 1. Free and liberated FA in modified UF resins.

Composites	Free FA (%)	Liberated FA (%)
UF/H	0.06	2.52
UF/Z	0.06	4.08

Confirmation of the ability of these fillers to bind FA also depends on their morphology (**Figures 1 and 2**). As can be seen from Figures 1 and 2, both modified resins have spherical structures that are connected like a cluster. UF resin molecules can lead to insolubility, crystallinity, and globular structure, especially when the molar ratio of FA to U is small. Many spherical particles can be seen on the SEM micrograph of the UF/Z composite (**Figure 1**), some of which are grouped into agglomerates. In addition, a linear arrangement in the clusters is noticeable, which speaks in favor of a high degree of crystallinity of the sample. The adsorption capacity of chitosan in the resin is also explained by the porous structure, more precisely by the porous layer of spheres composed of a network of pores, often grouped into clusters (**Figure 2**). Since a network of voids has developed on the surface of UF/H due to the presence of chitosan, it is not surprising that the liberated FA content is lower in that sample.

The first stage up to 200℃ is associated with the evaporation of water and small organic molecules such as FA. Mass losses in that phase are 1.5% for UF/Z and 5.95% for UF/H, respectively (**Table 3**). The second phase above 200℃ was identified as the main phase where the maximum mass loss occurs. For the UF/H composite, the second phase is at 174.5–368.5 ℃. The degradation of chitosan begins with amino groups forming unsaturated structures.

During the pyrolysis of polysaccharides, glycosidic bonds are randomly split, followed by decomposition, whereby acetic and butyric acids and several lower fatty acids are formed, dominated by C2, C3, and C6. In the same temperature interval, the UF resin degrades. The second phase is divided into two subintervals. Two simultaneous processes occur at the same time,

resulting in a peak that has two peaks, one shoulder at 255°C and the other at 277.9°C. The peak at 255°C corresponds to the breaking of the methylene ether bond while the peak at 277.9°C corresponds to the breaking of the unstable methylene bond. The mass loss in the second phase amounts to 53.44%. The total mass loss was 65.7%.



Figure 1. SEM micrographs of UF/Z with different magnifications at 10.000 x and 20.000 x.



Figure 2. SEM micrographs of UF/H with different magnifications at 10.000 x and 20.000 x.

Figure 3 and **Table 3** show the TG/DTG curves of UF/Z and UF/H composites and their DTG data on peak values, temperature intervals, values of $T_{5\%}$, and mass loss.

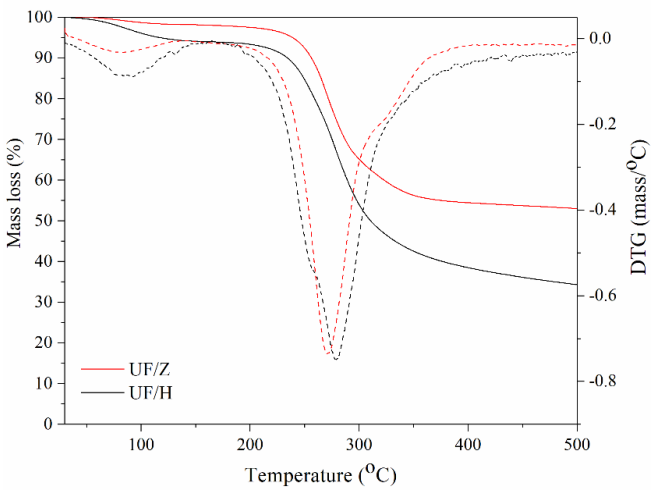


Figure 3. TGA and DTG curves of modified UF resins.

The second phase of decomposition of the UF/Z sample is in the interval 186.7-393.2°C, in which one shoulder is at 270.5°C and the other at 332.4°C. The mass loss maxima at 270.7°C and

325.6 °C on the DTG curve of the UF/Z composites correspond to the breaking of the methylene ether bond and the unstable methylene bond, respectively. The mass loss in the second phase is 43.8%, and the total mass loss is 46.5%.

Based on the results for the $T_{5\%}$ value (the temperature at which the initial mass of the sample decreased by 5%) as a criterion of thermal stability, which is 91.9°C for the UF/H composite, and for the UF/Z composite it is 205.4 °C, we can say that the modified UF resin with zeolite ZSM-5 is thermally more stable and the degradation starts at higher temperatures.

Table 3. DTG data on peak values, temperature intervals, T5%, and mass loss from modified UF composites.

Composite	Temperature interval (ºC)	DTG peak values (ºC)	Mass loss (%)	$T_{5\%}$ (ºC)	Total mass loss (%)
UF/Z	30.0-142.0 186.7-393.2*	80.7 270.5* 332.4*	1.5 43.8*	205.4	46.5
UF/H	30-158.3 174.5-368.5*	88.1 255.0* 277.9*	5.95 53.44*	91.9	65.6

*Overlapping peaks and the corresponding total mass loss.

CONCLUSION

This research demonstrated the effectiveness of available, inexpensive natural materials in reducing the percentage of FA from UF adhesives and improving their hydrolytic and thermal stability. We have shown that chitosan and zeolite, as materials of a completely different nature, have one common feature: the same ability to bind FA with UF composites. The resin modified with an organic modifier proved to be more hydrolytically stable, while the resin modified with an inorganic filler was more thermally stable, which is by the nature of the filler.

Acknowledgment

This work was supported by the Ministry of Science, Technological Development and Innovation of the Republic of Serbia (contract number 451-03-65/2024-03/200123, 451-03-66/2024-03/200017, 451-03-66/2024-03/200124 and 451-03-66/2024-03/ 200134), and Faculty of Sciences and Mathematics, University of Priština in Kosovska Mitrovica, Serbia (contract number IJ-2301).

REFERENCES

[1] B. Park, V. Causin, Eur Polym J. 49 (2013) 532.
[2] A. Singh, V. Causin, A. Nuryawan, B. Park, Eur Polym J. 56 (2014) 185.
[3] T. Ahamad, S. Alshehri, Arab J Chem. 7 (2014) 1140.
[4] J. Walkiewicz, J. Kawalerczyk, R. Mirski, D. Dziurka, M. Wieruszewski, Dent Mater. 15 (2022) 7201.
[5] M. Ristić, S. Samaržija-Jovanović, V. Jovanović, M. Kostić, T. Erceg, T. Jovanović, G. Marković, M. Marinović Cincović, J. Vinyl Addit Technol. 29 (2023) 1082.
[6] G. Nemli, S. Yildiz, E. Gezer, Bioresour Technol. 99 (2008) 6054.
[7] M. Ristić, S. S. Samaržija-Jovanović, T. Jovanović, V. Jovanović, M. Kostić, G. Marković, M. Marinović-Cincović, J. of Environmental Chem. Engineering 12 (1) (2024) 111828.
[8] V. Jovanović, S. Samaržija-Jovanović, B. Petković, Z. Milićević, G. Marković, M. Marinović-Cincović, Polym Compos. 40 (2019) 1287.

DEVELOPMENT OF Cu(II)-MESO-HMPAO COMPLEX AS A MODEL FOR POTENTIAL ^{64}Cu RADIOPHARMACEUTICALS

M. Mirković[1*], F. Belaj[2], M. Perić[1], D. Stanković[1,3], M. Radović[1], Z. Milanović[1], S. Vranješ-Đurić[1], D. Janković[1] and Lj.E. Mihajlović-Lalić[4]

[1]*„VINČA" Institute of Nuclear Sciences - National Institute of the Republic of Serbia, University of Belgrade, 11001 Belgrade, Serbia (mmarija@vin.bg.ac.rs)*
[2]*Institute of Chemistry, University of Graz, Schubertstrasse 1, 8010 Graz, Austria*
[3]*Faculty of Chemistry, University of Belgrade, Belgrade, Serbia*
[4]*Innovative Centre Faculty of Chemistry Belgrade, Studentskitrg 12-16, Belgrade, Serbia*

DOI: https://doi.org/10.46793/Phys.Chem24II.569M

ABSTRACT

Cu(II) complexes with meso-HMPAO and d,l-HMPAO were synthesized and characterized using single-crystal X-ray diffraction analysis, FTIR spectroscopy, cyclic voltammetry, and mass spectrometry. The electrochemical data indicated that the complexes bind to DNA molecules, specifically through guanine. These findings suggest that the new compounds have significant potential for further investigation, particularly for their anticancer activity and as models for the development of radiopharmaceuticals with ^{64}Cu.

INTRODUCTION

Copper complexes are a promising group of metal-containing drugs that are being proposed as a substitute for platinum complexes in cancer treatment. Due to their biologically accessible redox potentials and relatively high affinity for nucleobases, copper coordination compounds are widely investigated as DNA cleavage agents. Diimine-dioximes and diamine-dioxime class compounds easily form complexes with metals. HMPAO (hexamethylpropylene amine oxime) is an effective tetradentate chelating agent, owing to its possession of four nitrogen atoms that bind ^{99m}Tc(V) in aqueous solutions. Although both (meso and d,l) HMPAO isomers are deposited in the brain and used in medicine, the accumulation of the ^{99m}Tc complex with meso-HMPAO is less due to the lower lipophilicity. ^{99m}Tc-d,l-HMPAO is extensively employed for brain imaging [1]. Furthermore, the formation of a complex with the radioactive copper isotope (Cu-64) can be advantageous for PET/CT imaging and targeted radiotherapy. Numerous studies explored the potential use of copper(II) complexes as possible positron emission tomography (PET) radiopharmaceuticals [2]. DNA interactions with Cu metal complexes have been widely examined using different spectroscopic, calorimetric and electrochemical techniques.

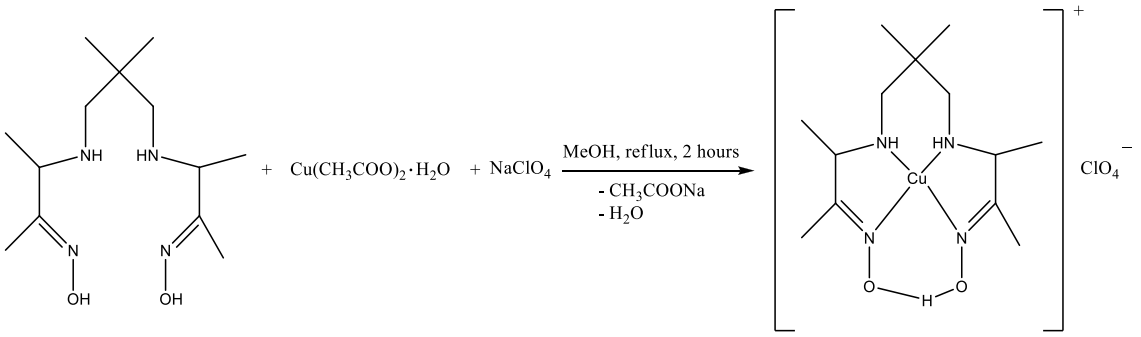
In this study, we synthesized Cu(II) complexes with meso-HMPAO (C1) and d,l-HMPAO (C2) as models for developing potential ^{64}Cu radiopharmaceuticals. The structures of these complexes were characterized using FTIR spectroscopy, mass spectrometry, cyclic voltammetry, and X-ray crystallography. Interactions with DNA were also examined. However, a significant structural disorder in the [Cu(II)-d,l-HMPAO]$^+$ complex domains precluded the refinement of X-ray data for this complex, leading this paper to primarily focus on the [Cu(II)-meso-HMPAO]$^+$ complex.

METHODS

Material and methods. The synthesis and characterization of HMPAO ligands are previously described [3]. The infrared spectrum was recorded on Bruker Optics ALPHA FTIR Spectrometer equipped with an ATR diamond probe head, using the ATR technique in the range from 4000 cm^{-1}

to 400 cm^{-1}. Obtained spectra were assigned following the abbreviations for very strong (vs), strong (s), medium (m), and weak (w) bonds. Mass spectra were recorded using an Agilent 5973 MSD – Direct Probe using the EI ionization technique.

Synthesis of complexes. The general procedure for the synthesis of complexes (**Scheme 1.**) involves the reaction of metal precursor, copper(II) acetate monohydrate (136 mg, 0.5 mmol) primarily dissolved in MeOH, and hot MeOH ligand suspension (99.8 mg, 0.5 mmol, 10 mL) in a molar ratio 1:1. After the addition of a counterion (61.6 mg, 0.5 mmol) the purple product was precipitated and the reaction mixture was allowed to stand at room temperature for 3 days. Finally, purple crystals were formed from MeOH mother liquor and suitable ones were collected for single-crystal XRD. Yield (**C1**): 61%. IR (ATR, cm^{-1}) (**C1**): 3542.5 (w), 3494.5 (w), 3237.9 (w), 3202.5 (w), 2959.6 (w), 1622.9 (w), 1604.5 (w), 1468.7 (w), 1432.2 (w), 1373.7 (w), 1078.4 (vs), 1025.1 (s), 982.6 (s), 621.1 (s), 449.9 (w), 422,1 (w). EI-MS (**C1**): (m/z, positive mode): 334.1 [M^+– ClO_4], 705.1 [M^+]. Yield (**C2**): 55%. IR (ATR, cm^{-1}) (**C2**): 3545.1 (w), 3489.9 (w), 3236.3 (w), 3202.8 (w), 2959.7 (w), 1624.3 (w), 1559.2 (w), 1428.7 (w), 1078.5 (vs), 1026.5 (s), 982.2 (s), 621.1 (s), 448.4 (w), 416,4 (w). EI-MS (**C2**) (m/z, positive mode): 334.1 [M^+– ClO_4], 705.1 [M^+].



Scheme 1. Reaction scheme for the synthesis of the complexes.

Crystal Structure Determination. All the measurements were performed using monochromatized Mo K_a radiation at 100K: $2(C_{13}H_{29}CuN_4O_3^+ClO_4^-) \cdot H_2O$, M_r 922.80, monoclinic, space group P $2_1/c$, a = 7.5260(4)Å, b = 21.0213(12)Å, c = 24.8715(14)Å, b = 91.564(3)°, V = 3933.4(4)$Å^3$, Z = 4, d_{calc} = 1.558g cm^{-3}, m = 1.291mm^{-1}. A total of 162316 reflections were collected (Q_{max} = 30.0°), from which 11477 were unique (R_{int} = 0.0615), with 8082 having I >2s(I). The structure was solved by direct methods (SHELXS-97) and refined by full-matrix least-squares techniques against F^2 (SHELXL-2014/6).

Electrochemical behaviour and interactions with DNA. The electrochemical behaviour was examined using a standard three-electrode cell. The cell setup included a glassy carbon working electrode with a diameter of 3 mm, a reference Ag/AgCl electrode, and a counter electrode made of platinum wire with a large surface area. The solutions of all the tested compounds were prepared at a concentration of 1 mg mL^{-1} in DMSO. The DNA concentration was maintained at 20 mg L^{-1}, while the complex was added at concentrations of 5, 15, and 20 mg L^{-1}. As a supporting electrolyte PBS at pH 7.4 was used.

RESULTS AND DISCUSSION

Synthesis and characterization. New copper complexes (C1 and C2) with meso-HMPAO and d,l-HMPAO ligands were synthesized via a reaction of methanolic solutions of the metal precursor and ligand refluxed for 2 h. The crystalline purple product was precipitated by adding a proper amount of counterion. Isolated crystalline precipitates were air-stable, partially soluble in water and EtOH,

soluble in polar (DMSO, MeOH, and CH_3CN) but insoluble in nonpolar solvents (toluene and benzene). The IR spectrum of C1 showed when the complex is formed, two C=N bonds are distinguishable. Two C=N are noted at lower frequencies than that in the free ligand. The peak was observed at 3494 cm^{-1}. The shape and intensity of the band indicate the formation of anintramolecular hydrogen bond. At last, in the area below 550 cm^{-1}, three bands were observed for complex, attributed to M–N and M–O vibrations. Thus, the assigned IR spectrum suggests the coordination of the metal center via four nitrogen atoms of the ligand. The IR spectrum of C2 showed negligible differences in comparison to C1. Additional structural conformation obtained by MS spectra indicates two ionic species for both complexes in acetonitrile, [M+ – ClO4] and [M+].
Crystal Structure. The crystal structure analysis of C1 showed the compound to be aqua-(3,6,6,9-tetramethyl-4,8-diazaundecane-2,10-dione-dioximato-N,N',N'',N''')-copper(II) perchlorate hydrate (2:1). All atoms lie on general positions. The asymmetric unit consists of two complex cations A and B (**Figure 1.**), two disordered perchlorate anions, and a water molecule between the anions and the aqua ligand of complex A. The two complex cations have the same conformation and show very similar bonding parameters. The Cu atoms have square-pyramidal coordination geometries with the 4 N atoms as bases [Cu–N 1.954(2)-2.003(2)Å] and aqua ligands as apices [Cu1–O11 2.2410(18)Å, Cu2–O21 2.2720(18)Å]. This geometry has been observed also for complexes with similar diimine-dioximes and diamine-dioxime ligands. Trigonal-bipyramidal type of coordination is not possible with those classes of ligands. Due to the presence of conjugated bonds ligator atoms can coordinate the metal only in one plane. Each cation shows a presumably strong intermolecular hydrogen bond [O2•••O10 2.507(3)Å, O2–H2•••O10 165.8(9)°; O22•••O30 2.506(3)Å, O22–H22•••O30 170.0(7)°]. Two cations are held together by four weaker N–H•••O hydrogen bonds [N•••O 3.073(3)-3.156(3)Å, N–H•••O 138.9(13)-149.5(12)°]. The refinement of collected X-ray data for C2 was impossible due to high structural disorder of domains.

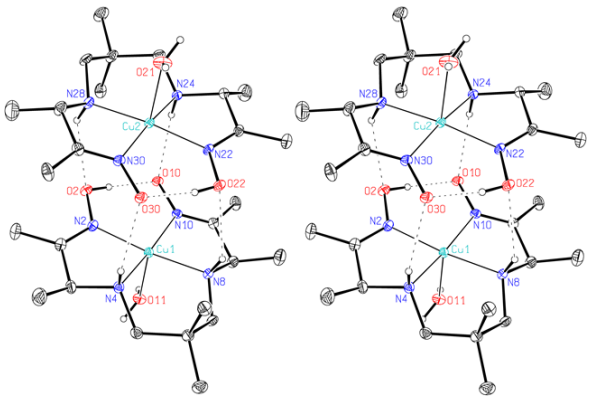


Figure 1. Stereoscopic ORTEP plot of complex cations A and B of C1 showing the hydrogen bonds indicated by dotted lines. The probability ellipsoids are drawn at the 30% probability level. The H atoms bonded to C atoms were omitted for clarity, the other H atoms are drawn with arbitrary radii.

The electrochemical response of copper(II) acetate monohydrate, meso-HMPAO, and C1 was investigated using cyclic voltammetry. Corresponding voltammograms are shown in **Figure 2A**. **Figure 2A** represents the electrochemical profile of the supporting electrolyte showing its electrochemical behaviour (baseline) and the electrochemic al profiles of the components from which the complex is built. Cyclic voltammograms of copper(II) acetate monohydrate, meso-HMPAO, and C1 show that the formation of the complex strongly affects the redox behaviour of the electroactive groups.

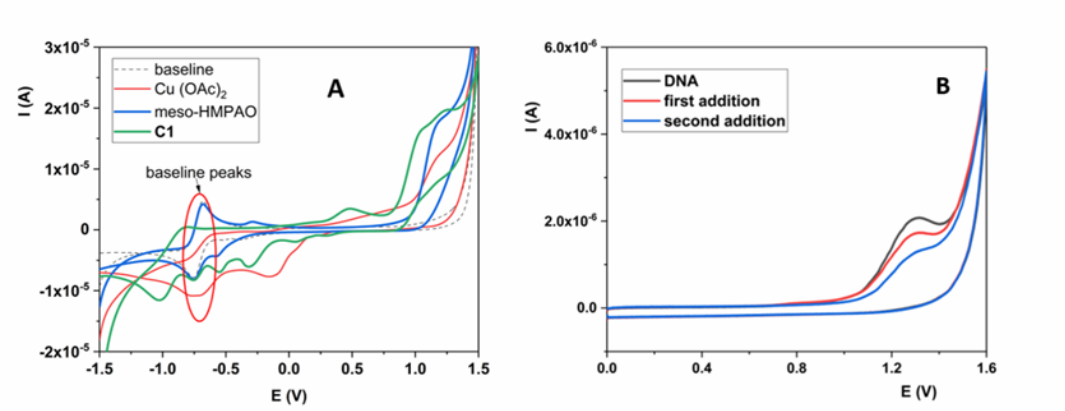


Figure 2. A) Electrochemical profiling of copper(II) acetate monohydrate, meso-HMPAO, and C1 (glassy carbon working electrode at a scan rate of 50 mV s^{-1}). B) Changes in guanine from DNA oxidation current after addition of complex.

Cyclic voltammetry, a method used to examine changes in the electrochemical response of DNA, was employed. The results of this experiment are illustrated in **Figure 2B**. At approximately 1.31 V (vs Ag/AgCl (3M KCl) reference electrode), the DNA molecule produces a distinct signal originating from the oxidation of guanine on a glassy carbon electrode. The introduction of C1 into the solution resulted in a reduction in the intensity of the guanine oxidation current, indicating that the complex molecules are efficiently penetrating the DNA structure.

CONCLUSION

Copper complexes with the biocompatible ligand hexamethylpropylene amine oxime (HMPAO) were designed, synthesized, and characterized. The characterization methods demonstrated that HMPAO functions as a tetradentate ligand, coordinating through the nitrogen atoms of its oxime and amine groups. Electrochemical analyses confirmed the binding interaction between the copper complex and DNA molecules. These experimental findings support the potential of these complexes for further exploration as anticancer agents or in nuclear medicine as ^{64}Cu radiopharmaceuticals.

Acknowledgment

The research was supported by the Ministry of Education, Science and Technological Development of the Republic of Serbia, contract numbers: 451-03-66/2024-03/200017, 451-03-47/2023-01/200288; VINCENT Center of Excellence; and Science fund of the Republic of Serbia, Program PRIZMA, GRANT No 4961/2023, Project title RADIOMAG.

REFERENCES

[1] J.P. Leonard, D.P. Nowotnik, R.D. Neirinckx, J. Nucl. Med. 27 (1986) 1819.
[2] B. Gutfilen, S.A.L. Souza, G. Valentini, Drug Des. Devel. Ther. 12 (2018) 3235.
[3] N. Nikolić, D. Veselinović, J. Vučina, H. Lingeman, K. Karljiković-Rajić, J. Pharm. Biomed. Anal. 32 (2003) 1159.

DFT STUDY OF HYPERFINE COUPLINGS IN *D* METAL COMPLEXES WITH TETRAHYDRO BORATE LIGANDS

M. Perić*, M. Radović, M. Mirković, Z. Milanović, D. Janković, A. Vukadinović, S. Vranješ-Đurić and D. Stanković

„VINČA" Institute of Nuclear Sciences - National Institute of the Republic of Serbia, University of Belgrade, Belgrade, Serbia (markoperic1983@gmail.com)

DOI: https://doi.org/10.46793/Phys.Chem24II.573P

ABSTRACT

Metal complexes with BH_4^- ligands show peculiar structural and dynamic properties, and possess many important and applicable qualities (potent reducing agents and catalysts, materials for hydrogen storage). Electron paramagnetic resonance (EPR) is very important for the characterization of complex compounds, determination of their electronic configuration and geometry. Also, Density Functional Theory (DFT) can predict EPR parameters and explain them more profoundly. Hence, in this paper hyperfine coupling constants of *d* metal complexes with BH_4^- ligands have been determined by DFT calculations, and analyzed in detail.

INTRODUCTION

Numerous efforts have been made to clarify the unusual properties of tetrahydroborate complexes, which is to a great extent enabled by the development of the diverse methods of characterization. The complex compounds are characterized by various spectroscopic techniques including the ^{1}H NMR, ^{13}C NMR, ^{31}P NMR, ^{59}Co NMR, UV-VIS and IR spectroscopies and the X-ray and the neutron diffraction studies, and magnetic measurements. Electron paramagnetic resonance spectroscopy (EPR) is a method applied to investigate chemical structures with unpaired electrons. EPR spectroscopy has a significant role in explaining of inorganic and organic radicals, transition metal complexes, and metalloenzymes with paramagnetic centers [1]. The determination of different EPR parameters in species with unpaired electrons is crucial task for EPR spectroscopy, and can help in analysis of electronic configuration and geometry of investigated systems. For transition metal complexes, theoretical calculations, especially Density Functional Theory (DFT), afford significant source of data allowing to attain both, the molecular geometry and the hyperfine coupling constants (hfcc) [2]. Since the energy difference of the various coordination modes of BH_4^- ligands are almost negligible, it is very difficult to determine the best geometry of the complex based on theoretical calculations. Bearing in mind aforementioned, a detailed DFT analysis of EPR hyperfine coupling constants was carried out on series of *d* transition metal complexes with BH_4^- ligands.

METHODS

Unrestricted Kohn-Sham (UKS) calculations of hyperfine coupling constants of *d* metal complexes (**Figure 1**) have been carried out using CP basis set [3] for central metal ions, and IGLO-II basis set [4] for all other atoms. In all calculations BP86 functional [5,6] has been used. The coordinates for complexes **1-3** have been extracted directly from X-ray structures [7,8]. The structures of complexes **4-7** have been obtained by replacing vanadium in complex 2 with Cr^{3+}, Mn^{3+}, Fe^{3+} and Mn^{2+} respectively, and by subsequent optimization at LDA level of theory [9], along with TZVP basis set [10] for metal ions, and SVP basis set for other atoms [11]. In all calculations ORCA software package has been used [12].

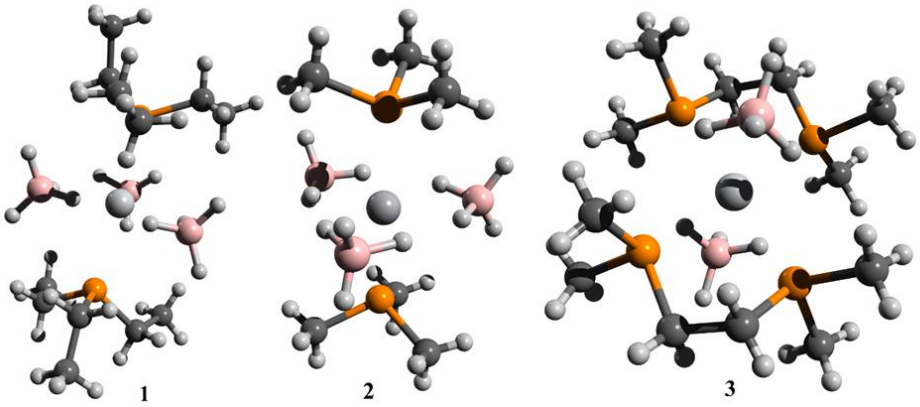


Figure 1. Structures of investigated complexes. Coordinates of complexes with numbers 1-3 are extracted directly from X-ray structures. Complexes designated with numbers 4-7 in the main text have been obtained by replacing vanadium in complex 2 with Cr^{3+}, Mn^{3+}, Fe^{3+} and Mn^{2+} respectively, and by subsequent optimization at LDA level of theory. All complexes 4-7 posses three BH_4^- ligands and two threemethyl phosphine ligands in axial position.

RESULTS AND DISCUSSION

Concerning complexes **1** and **2** hydrogen atoms that form bridge between central metal ion and boron atoms have large negative isotropic values. In contrast terminal hydrogen atoms exhibit large positive isotropic values. Exception is one terminal hydrogen atom of Ti^{3+} complex belonging to η^3 coordinated BH_4^- unit. The Fermi contact interaction **(FC)** represents the magnetic interaction between atomic nucleus and electron and is responsible for the emergence of isotropic hyperfine coupling (a_{iso}).

In order to gain better insight, the analysis of singly occupied molecular orbitals (SOMOs) should be performed. Starting from Ti^{3+} complex with d^1 configuration the only SOMO is antibonding with respect to H_t of two η^2-coordinated BH_4^- units (**Figure 2**). Hence the unpaired electron is delocalized directly into s orbitals of H_t atoms, leading to significant positive values of a_{iso}. The s orbitals of bridging hydrogen atoms do not contribute to SOMO, and FC can manifest only through polarization mechanism, giving rise to large negative a_{iso}. In addition, η^3-coordinated BH_4^- unit is non-bonding with respect to SOMO, and negative spin density on hydrogen atoms can be expected.

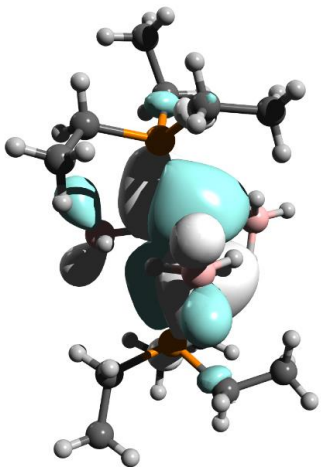


Figure 2. Singly occupied molecular orbital (SOMO) of complex 1.

With increasing number of unpaired electrons (d^2 configuration) lowering of a_{iso} values at terminal hydrogens has been observed. This effect is caused by the action of opposite contributions (**Figure 3).**

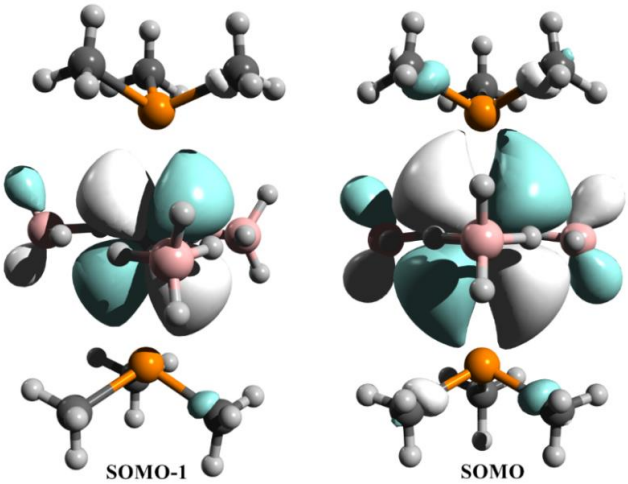


Figure 3. SOMO and SOMO-1 of complex 2.

SOMO orbital of complex **2** is antibonding with respect to H_t of two BH_4^- units, and some amount of positive spin density is delocalized on s orbitals of those hydrogen atoms. Third BH_4^- unit is non-bonding to SOMO, hence the negative spin density at hydrogen s orbitals arises due to polarization mechanism. However, SOMO-1 is antibonding with respect to third BH_4^- unit, and there is no contribution of hydrogen s orbitals from first two BH_4^- ligands. As a consequence, the unpaired electron from SOMO-1 is delocalized on H_t of one BH_4^- ligand, and negative spin density is placed at H_t of other two ligands. Similar behavior has been observed in complex **3** (d^2 configuration). Two BH_4^- ligands, arranged in trans position contribute with s orbitals of H_t to SOMO orbital, while SOMO-1 orbital is totally non-bonding. The net a_{iso} values at H_t are something lower in comparison to complex **1**. The situation is complicated with a further increase in the number of unpaired electrons. Concerning Cr^{3+} complex with S=3/2 it can be observed that two bridging hydrogen atoms have large positive a_{iso} values. This is due to an additional unpaired electron, placed in an orbital with very large contribution of H_b *s* orbitals (**Figure 4**). At the same time a_{iso} values of terminal hydrogens are decreased. In Mn^{3+} complex (S=2) all terminal and bridging hydrogen atoms have positive a_{iso} values, since all hydrogen atoms contribute to SOMO orbitals. Those values are comparably smaller with respect to complexes with d^1 and d^2 electronic configuration as a result of competition between opposite effects; delocalization of positive spin density on to BH_4^- units, and placing of negative spin density through polarization mechanism, which is more pronounced with an increase in the number of unpaired electrons.

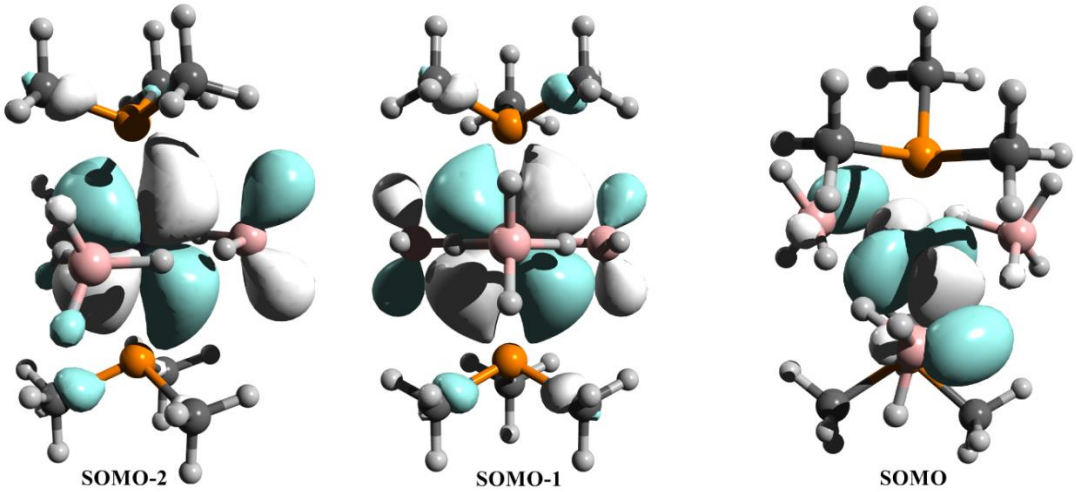


Figure 4. SOMOs of complex 4.

CONCLUSION

Concerning *d*-metal complexes **1-3**, as the number of unpaired electrons increases, the a_{iso} hyperfine coupling constants decrease due to the interaction of the opposite effects of delocalization and polarization. It is noted that positive constants occur at terminal hydrogen atoms, while negative constants occur at bridging hydrogen atoms, but both sets are significant in magnitude. A change in this trend occurs in *d* metal complexes with d^3 electronic configuration, i.e. the bridging hydrogen atoms also have positive constants. With further filling, there is a decrease in the value of the constants of all hydrogen atoms.

Acknowledgment

The research was supported by the Ministry of Education, Science and Technological Development of the Republic of Serbia, contract numbers: 451-03-66/2024-03/200017; VINCENT Center of Excellence; and Science fund of the Republic of Serbia, Program PRIZMA, GRANT No 4961/2023, Project title RADIOMAG.

REFERENCES

[1] K.E. Prosser, C.J. Walsby Eur. J. Inorg. Chem. 2017 (2017) 1573–1585,
[2] A.C. Saladino, S.C. Larsen, Catal. Today 105 (2005) 122–133.
[3] F. Neese, Inorganica Chim. Acta. 337 (2002) 181–192.
[4] M. Kutzelnigg, W. Fleischer, U. Schindler, Springer-Verlag, Berlin, 1991.
[5] A.D. Becke, Phys. Rev. A 38(6) (1988) 3098–3100.
[6] J.P. Perdew Phys. Rev. B 33(12) (1986) 8822–8824.
[7] J.A. Jensen, S.R. Wilson, G.S. Girolami, J. Am. Chem. Soc. 110 (1988) 4977–4982,
[8] J.A. Jensen, S.R. Wilson, A.J. Schultz, G.S. Girolami, J. Am. Chem. Soc. 109 (1987) 8094–8096.
[9]] M.N.S.H. Vosko, L. Wilk, Can. J. Phys. 58 (1980) 80–159.
[10] A. Schafer, H. Horn, R. Ahlrichs, J. Chem. Phys. 97(4) (1992) 2571–2577.
[11] A. Schafer, C. Huber, R. Ahlrichs, J. Chem. Phys. 100(8) (1994) 5829–5835.
[12] F. Neese, ORCA an ab initio, density functional and semiempirical program package, Version 2.6-3 (Institute for physical and theoretical chemistry, Bonn, Germany, 2006).

CYTOTOXIC ACTIVITY OF AMINOCARBOXYLATEMACROCYCLIC Cu(II) COMPLEXES

B. Dražić[1], M. Antonijević Nikolić[2], V. Stanić [3], V. Stojiljković[3] and S. Tanasković[1]

[1] *Faculty of Pharmacy, University of Belgrade, Belgrade, Serbia, (bdrazic@pharmacy.bg.ac.rs)*
[2]*Academy of Applied Studies Šabac, Department for Medical, Business and Technological Studies, Šabac, Serbia*
[3]*Vinča Institute of Nuclear Sciences - National Institute of the Republic of Serbia, University of Belgrade, 11000 Belgrade, Serbia*

DOI: https://doi.org/10.46793/Phys.Chem24II.577D

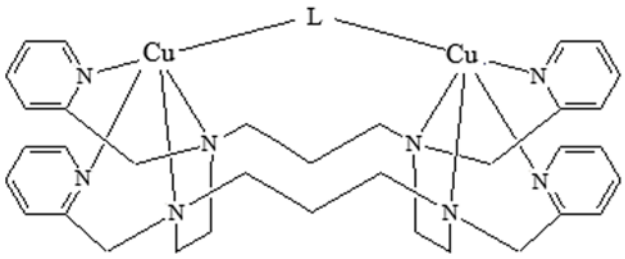
ABSTRACT

Five binuclear complexes with general formula $[Cu_2(L)tpmc](ClO_4)_4$, L= valine (**1**), norvaline (**2**) leucine (**3**), norleucine (**4**) and isoleucine (**5**) were tested *in vitro* against human tumor cell lines: THP-1 (human acute monocytic leukemic cell line), Jurkat (human acute T cell leukemia) and Ramos (B cells, Burkitt's lymphoma cell line). The values of IC_{50} were calculated. All tested complexes showed significant activity against the tested lines. Complex **2** has promoted significant decreases in the metabolic activity of all three cell lines, especially according to Ramos (IC_{50} value is 40.21 ± 1.45 μM) and complex **3** of the Jurkat cells (IC_{50} value is 41.01 ± 1.71 μM). Results were compared with the analogous complexes with glycine and alanine as additional ligands.

INTRODUCTION

Different coordination modes for transition metal cations of tetraazamacrocyclic ligands and their arm derivatives allow their use as antitumor, antiviral (including HIV activity), antibacterial, antifungal, or antimalarial agents [1]. This makes them very attractive and intensively studied during the last decades. Copper is a biologically important metal. It plays an important role in endogenous processes like oxidative DNA damage and has been used in the preparation of numerous complexes with potentially cytotoxic roles. It is an essential trace mineral and plays a key role in such functions within the body as red blood cell production, iron absorption, the regulation of heart rate and blood pressure, and the development and maintenance of connective tissue, bones and organs. Another reason why copper is especially important for human health in pandemic conditions like the present is the part it plays in immune system maintenance and activation. Copper helps to ensure a healthy supply of white blood cells, many of which are phagocytes that protect the body by engulfing bacteria, foreign particles and dying cells. Copper enzymes usually contain metal ions bound to a specific amino acid residue or directly to the amide group in the peptide backbone, offering different coordination environments for their application as antitumor, antiviral, antibacterial, antifungal or antimalarial agents.

The goal of the article was screening the *in vitro* cytotoxicity of the mixed macrocycle Cu(II) complexes with amino acids, valine, norvaline, leucine, norleucine and isoleucine, as additional ligand compared to the effect of commonly used drugs, *cis*-platin against human tumor cell lines. The structures of the investigated complexes are shown in Figure 1.



L = valine (**1**), norvaline (**2**), leucine (**3**), norleucine (**4**) and isoleucine (**5**)

Figure 1. Structures of the complex cation $[Cu_2(L)tpmc]^{4+}$.

MATERIALS AND METHODS

Cell Culture

THP-1, Jurkat and Ramos cells were maintained in an RPMI medium (Sigma-Aldrich) supplemented with 10% fetal bovine serum (Gibco, Grand Island, NY, USA), 2 mM *L*-glutamine, 100 U/ml penicillin, 100 mg/ml streptomycin and 50 μM 2-mercaptoethanol (all purchased from Sigma-Aldrich). Cells were cultured in a humidified chamber (37°C, 5% CO_2).

Metabolic activity assay

The metabolic activity of cells was assessed with tetrazolium MTS assay using CellTiter 96® Aqueous One Solution Cell Proliferation Assay (Promega, Madison, WI, USA) according to manufacturer's instructions. In brief, THP-1 (human acute monocytic leukemic cell line), Jurkat (human acute T cell leukemia) and Ramos (B cells, Burkitt's lymphoma cell line) cells were treated with different concentrations (200, 100, 50, 25 or 12,5 μM) of the compounds (**1**–**5** and free ligands) or corresponding vehicle (control cells). Cells were then seeded in 96 well plates. After 48 h, 10 μL of MTS solution was added to each 100 μL of cell suspension [2, 3]. Following 3 h of incubation, the absorbance was measured at the Tecan Safire automated microplate reader (Tecan, Mannedorf /Zürich, Switzerland). Cell viability was calculated by subtracting the negative control, which contained no cells, and normalizing to vehicle-treated controls. For each of the three cell lines, experiments were performed in triplicate and in three biological settings. The data are presented as the average ± RSD (relative standard deviation).

RESULTS AND DISCUSSION

Copper complexes are emerging as an alternative to the development of cancer drugs [4]. Many copper (II) complexes are active despite the fact that their ligands do not have significant antiproliferative activity. As a continuation of our research, to study how the structure of ligands is related to the cytotoxic activity of the complexes [5], we analyzed the antiproliferative properties of five binuclear complexes with the general formula $[Cu_2(L)tpmc](ClO_4)_4$, L= valine (**1**), norvaline (**2**), leucine (**3**), norleucine (**4**) and isoleucine (**5**). All complexes were tested against human tumor cell lines: THP-1 (human acute monocytic leukemic cell line), Jurkat (human acute T cell leukemia), and Ramos (B cells, Burkitt's lymphoma cell line). Cells were incubated with various concentrations of the test substances. After 48 h of incubation, MTS reagent was added. The cytotoxic activity was determined according to the dose values of the complex, required to reduce the cell survival by 50% (IC_{50}) compared with vehicle-treated control cells. In vitro cytotoxicity of

the complexes **1**–**5**, $Cu(ClO_4)_4 \cdot 6H_2O$ and ligands (valine, norvaline, leucine, norleucine and isoleucine) was evaluated using *cis*-platin as referent cytostatic drug. The antiproliferative properties of target compounds are presented in Table **1**.

Table 1. $IC_{50} \pm SD$ values (μM) after 48 h of action of the investigated complexes **1-5**, free ligands, and cisplatin on the tested cell lines, determined by the MTS test.

Compound		Cell line		
		Jurkat	THP 1	Ramos
$[Cu_2(val)tpmc](ClO_4)_4$	(**1**)	58.62 ± 1.52	44.18 ± 2.06	53.31 ± 1.10
$[Cu_2(nval)tpmc](ClO_4)_4$	(**2**)	47.86 ± 2.14	44.77 ± 1.78	40.21 ± 1.45
$[Cu_2(leu)tpmc](ClO_4)_4$	(**3**)	41.00 ± 1.71	50.73 ± 0.45	55.15 ± 1.63
$[Cu_2(nleu)tpmc](ClO_4)_4$	(**4**)	55.19 ± 2.56	50.61 ± 1.51	54.64 ± 0.85
$[Cu_2(ileu)tpmc](ClO_4)_4$	(**5**)	60.41 ± 2.08	59.92 ± 2.08	49.11 ± 0.05
tpmc, val, nval, leu, nleu, ileu, $Cu(ClO_4)_2 \cdot 6H_2O$		>200	>200	>200
cis-platin		7.1 ± 0.2	3.2 ± 0.4	2.1 ± 0.3

According to the data in Table **1**, the cytotoxic effects of all complexes are lower than those of *cis*-platin. The IC_{50} values of the complexes were in the range of 40.21- 60.41 μM against the three tested cell lines, while for *cis*-platin (*cis*- -diamminedichloridoplatinum (II)), they were in the range 2.1–7.1 μM. The tpmc, the aminocarboxylate co-ligands, and $Cu(ClO_4)_4 \bullet 6H_2O$ showed significantly lower activity (IC_{50} > 200 μM) for all tested cell lines under the same conditions indicating that moderate activity originates from complexes **1-5**. Nevertheless, the inhibition of cell proliferation by these Cu(II) carboxylate complexes is notable. All tested Cu (II) carboxylate complexes showed significant activity against all tested lines. Complex **2** has promoted significant decreases in the metabolic activity of all three cell lines, especially Ramos cells (IC_{50} value is 40.21 ± 1.45 μM) while complex **3** showed activity against Jurkat cells (IC_{50} value is 41.01 ± 1.71 μM).

Since the additional ligands in complexes **1-5** are structurally similar, the complexes have similar lipophilicity, so the antiproliferative effect against the tested human cancer cell lines is very similar. Also, results were compared with the analogous Cu(II) complexes with glycine and alanine as additional ligands and previously published results [6] are very similar to the values obtained in this study.

CONCLUSION

The results of the *in vitro* cytotoxicity of the Cu(II) complexes showed significant cytotoxic activity against the tested human malignant cell lines. The determined IC_{50} values for the investigated Cu (II) complexes **1-5** against all investigated human tumor cell lines (Jurkat, THP-1, and Ramos) have very similar values ranging from 40.21 - 60.41 μM. Finally, complex **2** has promoted significant decreases in the metabolic activity of all three cell lines, especially towards Ramos (IC_{50} value is 40.21 ± 1.45 μM).

Acknowledgment

This work was supported by the Ministry of Science, Technological Development and Innovation, Republic of Serbia (Grant No. 451-03-66/2024-03/200161).

REFERENCES

[1] P. M. Reddy, R. Rohini, E. Ravi Krishna, A. Hu, V. Ravinder, Int. J. Mol. Sci., 13 (2012) 4982-4992.
[2] T. Mosmann, J. Immunol. Methods, 65 (1e2) (1983) 55-63.
[3] G. Malich, B. Markovic, C. Winder, Toxicology, 124(3) (1997) 179-92.
[4] I. Iakovidis, I. Delimaris, S. M. Piperakis, Molecular Biology International, 2011 (2011) 594-529.
[5] M. Antonijević-Nikolić, J. Antić-Stanković, S. B. Tanasković, M. J. Korabik, G. Gojgić-Cvijović, G. Vučković, Preparation, J. Mol. Struct., 1054–1055 (2013) 297–306.
[6] M Antonijević Nikolić, B. Dražić, B. Cristóvão, A. Bartyzel, B. Miroslaw, S. Tanasković, J. Mol. Struct., 1252 (2022) 131969.

CRYSTALLOGRAPHIC AND HIRSHFELD SURFACE ANALYSIS OF TWO COPPER(II) PYRIDOXAL-AMINOGUANIDINE COMPLEXES CONTAINING DIFFERENT COUNTERIONS (NO_3^- and SO_4^{2-})

L. Golubović [1], V. Jevtović [2], A. Rakić [1], D. Dimić [1] and J. Dimitrić Marković [1]

[1] *University of Belgrade, Faculty of Physical Chemistry, Studentski trg 12-16, 11000 Belgrade, Serbia. (markovich@ffh.bg.ac.rs)*
[2] *Chemistry Department, College of Science, University Ha'il, 81451Ha'il, Saudi Arabia*

DOI: https://doi.org/10.46793/Phys.Chem24II.581G

ABSTRACT

Pyridoxal-aminoguanidine (PLAG) is a tridentate ligand known for its complexation with different transition metals. These complexes possess promising anticancer, antioxidant, and catalytic activities. In this contribution, two novel Cu(II)-PLAG complexes with different counterions (NO_3^- and SO_4^{2-}) were synthesized, and their crystal structures were solved. The structural differences resulted from the size and charge of counterions leading to the square-pyramidal geometry of the first and square-planar geometry of the second. The Hirshfeld surface analysis was employed to obtain quantitative parameters for the stabilization interactions between various atoms. The overall geometry significantly influenced the relative percentages of these interactions.

INTRODUCTION

Organometallic chemistry is an important field contributing to the quest for novel anticancer agents. This area developed tremendously upon the introduction of cisplatin, and different metal and ligand systems were later included. The most active complexes include iron, copper, ruthenium, and palladium central metal ions.

Pyridoxal-aminoguanidine (PLAG) ligand is obtained by condensation between pyridoxal and aminoguanidine, which results in a tridentate ONN system [2]. The complexation mode of this ligand depends on the protonation of present groups, and neutral, monoanionic, and dianionic forms are possible (Figure 1). Several complexes of PLAG with different metal ions, such as copper, cobalt, vanadium, zinc, and iron, are known in the literature. These compounds showed interesting anticancer, antioxidant, and catalytic behavior [3].

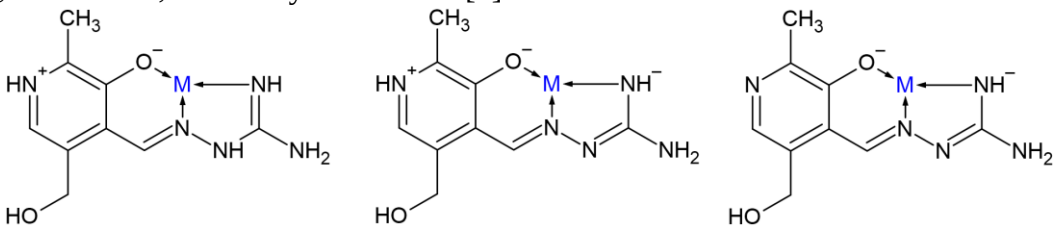


Figure 1. Different complexation modes of PLAG ligand.

This contribution presents results on the synthesis and crystal structure determination of two novel copper(II)-PLAG complexes with different counterions, namely NO_3^- and SO_4^{2-}. Special emphasis was placed on differences in geometry that are a consequence of the counterion size and charge. The Hirshfeld surface analysis was applied to investigate the counterion effects further and quantify the contribution of specific interactions.

METHODS

Synthesis of ligand Pyridoxal-aminoguanidine (PLAG)

Aminoguanidine-hydrocarbonate (AG·H_2CO_3) 0.70 g (5 mmol) was dissolved in 15 cm^3 of H_2O. The dissolution was done by heating up to the boiling point when a warm solution of 1.0 g (5 mmol) pyridoxal-hydrochloride (PL·HCl) in 5 cm^3 H_2O was added to this solution. The amount of 0.75 g (2.5 mmol) of $Na_2CO_3 \cdot 10H_2O$ previously dissolved in 10 cm^3 H_2O and heated was added to the mixture prepared above. The mixture was left at room temperature and, after two hours, the yellow crystals were filtered and washed with EtOH and Et_2O. Yield: 1.15 g (92%).

*Synthesis of [Cu(PLAG)(NO_3)(H_2O)]NO_3 (**1**)*

Ligand PLAG (0.15 g - 0.5 mmol) was dissolved in 15 cm^3 of EtOH with gradual heating. When the ligand was completely dissolved and the temperature was close to boiling, $Cu(NO_3)_2 \cdot 3H_2O$ (0.12 g - 0.5 mmol) was added to the hot, heated solution. The mixture was heated for about a few minutes. After a week, large dark green crystals were formed. The crystals were washed with EtOH and Et_2O. Yield: 0.15 g (82%).

*Synthesis of [Cu(PLAG)(H_2O)]SO_4 (**2**)*

The ligand PLAG (0.15 g -0.5 mmol) was dissolved in 15 cm^3 of EtOH with gradual heating. When the ligand was completely dissolved, and the temperature was close to boiling, $CuSO_4 \cdot 5H_2O$ (0.09 g - 0.5 mmol) was added to the very hot, heated solution. Heating was continued until the salt and ligand were completely dissolved. The mixture was left at room temperature to crystallize. After three days, large dark green crystals were formed. The crystals were washed with EtOH and Et_2O. Yield: 0.20 g (89%).

X-Ray structural analysis

A representative pale green thin plate crystals with dimensions 0.072×0.047×0.010 mm (complex **1**) and 0.144×0.072×0.011 mm (complex **2**) were selected and mounted on a nylon cryoloop. Diffraction data w×ere collected at 123 K using CuKa radiation (l = 1.54184 Å) on a Rigaku Synergy S diffractometer fitted with a HYPIX 6000 hybrid photon counting detector. Data were collected and processed, including an empirical (multi-scan) absorption correction, with the CrysAlisPro software [1]. The structure was solved and refined by standard methods using the SHELX software suite in conjunction with the Olex2 graphical interface [2,3]. Non-hydrogen atoms were refined with anisotropic displacement ellipsoids, and hydrogen atoms attached to carbon were placed in calculated positions using a riding model. The positions of hydrogen atoms attached to oxygen and nitrogen were apparent in the difference Fourier map and were refined with restrained d(O-H) = 0.88(2)Å or d(N-H) = 0.91(2)Å (DFIX). Two complexes were deposited in the Cambridge Crystallographic Data Centre (CCDC, 12 Union Road, Cambridge CB2 IEZ, UK; e-mail: depos-it@ccdc.cam.ac.uk) with the following numbers: 2344024 (**1**) and 2344013 (**2**).

Hirshfeld surface analysis

The crystallographic structure of the investigated compound is stabilized by various intermolecular interactions, examined by the Hirshfeld surface analysis. These interactions were accessed by the CrystalExplorer program [4] based on the experimental structure. Within this approach, surface analysis is presented in a graph connecting two distances, one between the two nearest nuclei (de) and the other connecting nuclei with the external surface (di). The distances are normalized and colored depending on the van der Waals separations between atoms. The distances are colored in red, white, and blue if the separation is shorter, equal, or longer than the sum of the van der Waals radii between connecting atoms. In this contribution, the normalized distances are between -0.7428

(red) and 1.1252 (blue). The specific interactions between atoms are also represented by the fingerprint plots that determine the relative percentages of these contacts to the total number.

RESULTS AND DISCUSSION

Two copper(II) complexes with PLAG ligand were obtained from two initial salts (nitrate and sulfate). The crystal structures of the complexes were solved, and they are presented in Figure 2. The first complex crystallized in the monoclinic $P2_1/c$ group, while the second crystallized in the orthorhombic $Pna2_1$ group.

Although different anions were present, the complex backbone consisting of one central metal ion, PLAG in neutral form, and water molecule is almost identical in both compounds. The PLAG is in neutral form, as proven by the protonation of pyridine and hydrazine nitrogen atoms. Three bonds were formed between donor atoms of PLAG (ONN ligand system) and central metal ion, while the fourth position was occupied by water molecules originating from the starting complex salts. These four donor atoms led to the square-planar geometry of the complex. The shortest bonds were found between phenolic oxygen and central metal ion (1.875 (**1**) and 1.886 Å (**2**)). The distance between amino nitrogen and copper(II) was shorter than between hydrazine nitrogen and copper(II). The coordination of water molecules led to Cu−O distances of 1.942 (**1**) and 1.937 Å (**2**). The angles within the coordination sphere additionally prove that square-planar geometry was formed.

The most important difference in these two structures is an additional coordination bond between nitrate ion and copper(II) ion, which changes the overall geometry of the complex to square-pyramidal. The axially coordinated nitrate ion is weakly bound, with a very long Cu-O distance of 2.8248 Å. In the analogous copper-Schiff base compounds, these distances are between 2.530 and 2.551 [4]. Additionally, the presence of nitrate ions in the coordination sphere influences the formation of other interactions between units in crystal cells, especially hydrogen bonds.

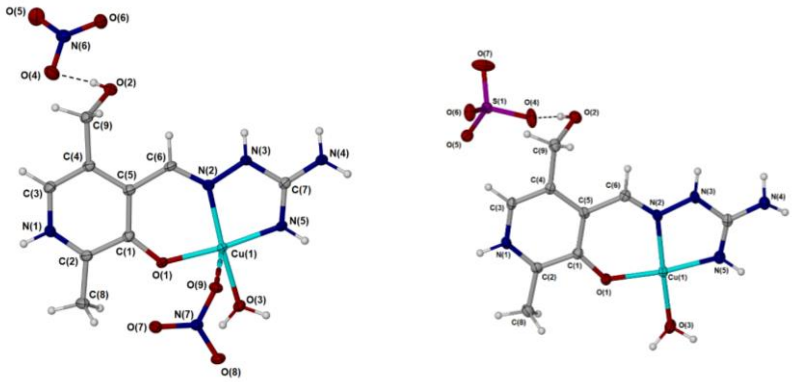


Figure 2. Molecular diagram of $[Cu(PLAG)(NO_3)(H_2O)]NO_3$ (left) and $[Cu(PLAG)(H_2O)]SO_4$ (right) with non-hydrogen atoms represented by 50% displacement ellipsoids and hydrogen atoms as spheres of arbitrary size.

The effects of the counterions on the overall stabilization of the crystallographic structure were examined by the Hirshfeld surface analysis, starting from the experimental structure. The Hirshfeld surfaces of both complexes are presented in Figure 3. The planar geometry of complex **2** allows the formation of interactions between two central metal ions, denoted as Cu···Cu (0.1%), that were not found in **1**. Other interactions, including copper, are Cu···H (0.9%) and Cu···C (1.3%) in the crystal structure of 1, and Cu···O (4.4%) and Cu···C (0.7%) in the crystal structure of **2**. The overall geometry around central metal ions profoundly affects the relative abundance of different

interactions. The most numerous interactions are formed between oxygen and hydrogen atoms in a structure of **1** (52.1%). This result is expected due to the presence of oxygen-rich nitrate ions and relative hydrogen abundance in the structure of PLAG. The Hirshfeld surface of **1** (Figure 3) shows that protonated nitrogen atoms of the pyridine ring, hydrazine, and amino moieties behave as hydrogen atom donors towards neighboring species. The oxygen atoms in the structure are hydrogen-atom acceptors. A similar can be found in the structure of **2**, although the relative contribution of these interactions is lowered to 34.8%, which is the most important difference between these stabilization interactions in **1** and **2**. Weak H···H interactions account for 23.6% (**1**) and 34.9% (**2**), similar to previously described complex compounds with this type of ligand [2]. These percentages are a consequence of the protonation of nitrogen-containing groups. It is important to notice that interactions involving hydrogen atoms and nitrogen/carbon atoms are almost the same in the case of both compounds, around 5.0% (H···N) and 4.0% (H···C). Other types of interactions contribute much less.

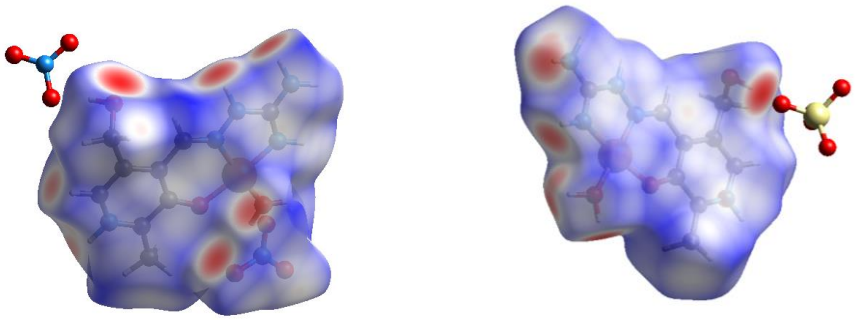


Figure 3. Hirshfeld surfaces of complexes 1 (left) and 2 (right) (normalized distances between -0.7428 (red) and 1.1252 (blue).

CONCLUSION

Two novel copper(II)-PLAG complexes with nitrate and sulfate counterions were obtained, and their crystal structures were solved. The structural parameters of the central metal ion surrounded by tridentate PLAG ligand and water molecule were almost the same for both complexes. The important difference was the coordination of one nitrate ion to Cu(II), leading to the change in geometry from square-planar to square-pyramidal. Due to its planar geometry, the Cu(II)-PLAG complex with sulfate ions was characterized by a higher percentage of interactions, including central metal ions. The existence of nitrate ions in the coordination sphere led to a higher percentage of O···H interaction in the case of the first complex (52.1%) than in the second (34.8%). Further experimental and theoretical studies are advised to investigate the effect of counterions on reactivity and stability.

Acknowledgment

This work was supported by the Ministry of Education, Science and Technological Development of the Republic of Serbia (grant no 451-03-65/2024-03/200146).

REFERENCES

[1] F.A. Al-Saif, M.S. Refat, J. Mol. Struct., 1021 (2021) 40–52.
[2] V. Jevtovic, M.S.O. Alhar, D. Milenković, Z. Marković, J. Dimitrić Marković, D. Dimić, Synthesis, Int. J. Mol. Sci., 24 (2023) 14745.
[3] V. Jevtovic, A.K. Alshamari, D. Milenković, J. Dimitrić Marković, Z. Marković, D. Dimić, Int. J. Mol. Sci., 24 (2023) 11910.
[4] H.-Y. Zhang, W. Wang, H. Chen, S.-H. Zhang, Y. Li, Inorg. Chim. Acta., 453 (2016) 507–515.

N – General Physical Chemistry

SALTING-OUT AND SYNERGISM IN THE EXTRACTION OF ACETYLSALICYLIC ACID FROM AQUEOUS SOLUTIONS

G.M. Nikolić [1], M.V. Grigorov [2] and M.G. Nikolić [3]

[1] *University of Niš, Faculty of Medicine, Department of Chemistry, Bulevar dr Zorana Đinđića 81, 18000 Niš, Serbia. (e-mail: goranhem@yahoo.com)*
[2] *University of Niš, Faculty of Medicine, Department of Pharmacy, Bulevar dr Zorana Đinđića 81, 18000 Niš, Serbia.*
[3] *University of Niš, Faculty of Sciences and Mathematics, Department of Chemisty. Višegradska 33, 18000 Niš, Serbia.*

DOI: https://doi.org/10.46793/Phys.Chem24II.587N

ABSTRACT

Salting-out and synergic effects in the extraction of acetylsalicylic acid from aqueous solutions were investigated. The presence of NaCl in aqueous phase improved extraction efficacy of acetylsalicylic acid by diethyl ether and Setschenow salting-out constant was determined to be 0.2178 which is close to the value obtained from the solubility measurements. Higher distribution ratio values for the extraction of acetylsalicylic acid were also obtained when extraction was performed with diethyl ether/1-butanol binary solvent mixtures instead of pure solvents for the whole range of binary mixture compositions. Synergic coefficients obtained for acetylsalicylic acid are similar to the ones obtained for paracetamol extraction with the same binary mixtures. However, for acetylsalicylic acid the synergic effect was highest when binary mixture with slight excess of diethyl ether was used for extraction while in the case of paracetamol the synergic effect was highest when binary mixture with an excess of 1-butanol was used.

INTRODUCTION

Acetylsalicylic acid (aspirin) is one of the most widely used drugs in the world and its quantitative analysis in various biological and environmental samples is often performed [1, 2]. Various analytical methods may be used for such purpose but usually a sample pretreatment is applied in order to obtain more accurate and precise results, especially when very low concentrations of acetylsalicylic acid are to be determined. Liquid-liquid extraction is a common procedure for sample preconcentration and salting-out is frequently applied in order to increase extraction efficacy when high performance liquid chromatography (HPLC) is applied for the quantitative analysis of acetylsalicylic acid and its metabolites in various samples [1, 3]. Beside the practical importance of salting-out effect, determination of salting-out constant (known also as Setschenow constant) is significant for the physicochemical characterization of various substances [4, 5].

Another useful method for increasing extraction efficacy is the application of binary solvent mixtures when synergic effect is achieved. This approach has been already demonstrated to be very useful in many cases including pharmacologically active compounds and drugs [6, 7].

Here we investigated salting-out and synergic effects in the extraction of acetylsalicylic acid from aqueous solutions.

MATERIALS AND METHODS

All the chemicals used in this study were of analytical grade (*p.a.*) quality, obtained from commercial suppliers (Merck (Germany) and Centrohem (Serbia)) and used without further purification. Stock solutions of acetylsalicylic acid (5 mmol/L) and NaCl (4 mol/L) were prepared

by dissolving exactly weighted amounts of pure substances in doubly distilled water. Working solutions for extractions were prepared from the stock solution of acetylsalicylic acid by dilution with doubly distilled water or 4 mol/L NaCl solution so that final acetylsalicylic acid concentration was 2.5 mmol/L. All extractions were performed from working solutions by the shake-flask method in a uniform manner and in duplicate for each sample. For salting-out determination extractions of acetylsalicylic acid from aqueous phases with different NaCl concentrations were performed with diethyl ether, and for synergism determination extractions of acetylsalicylic acid from aqueous phases containing 2 mol/L of NaCl were performed with diethyl ether, 1-butanol, and their binary mixtures of various compositions.

Absorbances of aqueous phases were measured by using an Evolution 60 UV/Vis scanning spectrophotometer (Thermo Scientic, USA) at the λ_{max} of acetylsalicylic acid which was 274 nm. By using absorbance values measured for aqueous phases before (A_0) and after extraction (A) the distribution ratio values (D) were calculated by the following equation

$$D = \frac{R \times A_0 - A}{A} \times \frac{V_{aq}}{V_{org}}$$

where R was the dilution ratio of acetylsalicylic acid stock solution used for obtaining the value of A_0, and V_{aq} and V_{org} were the volumes of aqueous and organic phase, respectively.

Salting-out effect can be quantified by measuring the solubility of nonelectrolytes in salt solutions with different salt concentrations [4] but here we used the distribution ratios obtained by the extraction of acetylsalicylic acid with diethyl ether from aqueous solutions with various NaCl concentrations [5] by applying the following equation

$$\log D = K_s C_s + \log D_0$$

where D and D_0 are distribution ratios of acetylsalicylic acid between diethyl ether and acetylsalicylic acid aqueous solutions containing NaCl or without NaCl, respectively, C_s is the salt concentration in aqueous phase, and K_s is Setschenow salting-out constant which is the quantitative measure of salting-out effect. This expression enables the calculation of D_0 by extrapolation based on D values measured for different salt concentrations.

Synergic effect in the extraction with binary solvent mixtures can be quantified by calculating synergic coefficient, K_c [6], according to the equation

$$K_c = \log(D_{mix}/D_{add})$$

where D_{mix} represents experimentally measured and D_{add} theoretically predicted additive distribution ratio values, respectively. Theoretically predicted additive distribution ratio is calculated as

$$D_{add} = D_1 x_1 + D_2(1\text{-}x_1)$$

where D_1 and D_2 are distribution ratios obtained with pure solvents and x_1 is the mole fraction of one of the solvents in the mixture.

RESULTS AND DISCUSSION

As expected, the presence of NaCl in aqueous phase increased the distribution ratio of acetylsalicylic acid between diethyl ether and aqueous phase (salting-out effect). The dependence of log$D$ values obtained for diethyl ether extraction of acetylsalicylic acid from aqueous solutions containing different NaCl concentrations on salt concentration is shown in Figure 1.

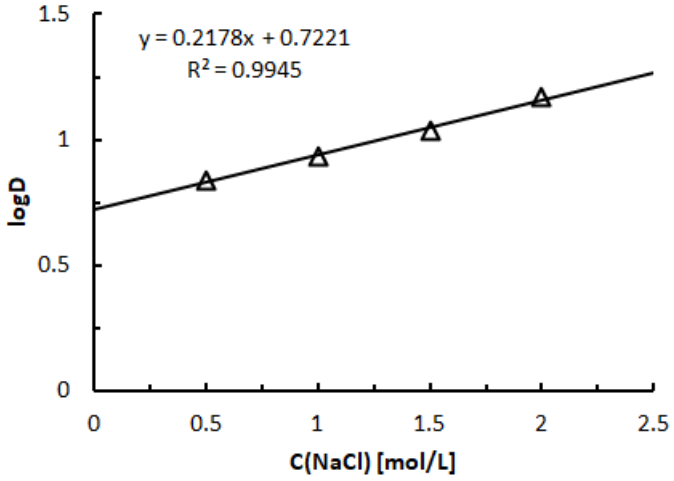


Figure 1. The dependence of log*D* values obtained for diethyl ether extraction of acetylsalicylic acid from aqueous solutions containing different NaCl concentrations on salt concentration.

Obtained K_s value was 0.2178 and this is close to the Setschenow constant value obtained by the measurements of acetylsalicylic acid solubility in aqueous NaCl solutions (0.202) [8]. Extrapolation of data shown in Figure 1. allowed us to calculate D_0 value as 5.274. However, experimentally obtained D_0 value was 5.539 but it should be considered as less accurate due to the partial miscibility of diethyl ether and water in the absence of salt in aqueous phase.

Data obtained for the extraction of acetylsalicylic acid from aqueous solutions containing 2 mol/L NaCl with diethyl ether, 1-butanol, and their binary mixtures are given in Table 1.

Table 1. Data used for the determination of synergic effect in the extraction of acetylsalicylic acid from aqueous solutions by the diethyl ether/1-butanol binary mixtures.

x(1-butanol)	D_{mix}	D_{add}	D_{mix}/D_{add}	K_c
0	14.709	14.709	1.000	-
0.222	26.532	15.279	1.737	0.240
0.433	29.391	15.821	1.858	0.269
0.632	25.012	16.331	1.532	0.185
0.821	18.361	16.817	1.092	0.038
1	17.276	17.276	1.000	-

Distribution ratio values for acetylsalicylic acid are higher than theoretically calculated additive values, D_{add}, in the whole composition range of the diethyl ether/1-butanol binary mixtures (synergic effect). The synergic coefficient values for the extraction of acetylsalicylic acid obtained in this work are similar to the values obtained for paracetamol extraction with the same binary solvent mixtures [7]. However, maximum synergic effect in the extraction of acetylsalicylic acid was achieved with a binary mixture containing 0.567 mole fraction of diethyl ether, while maximum synergic effect in the extraction of paracetamol was achieved with a binary mixture containing an excess of 1-butanol. Graphical presentation of data given in Table 1. is shown in Figure 2.

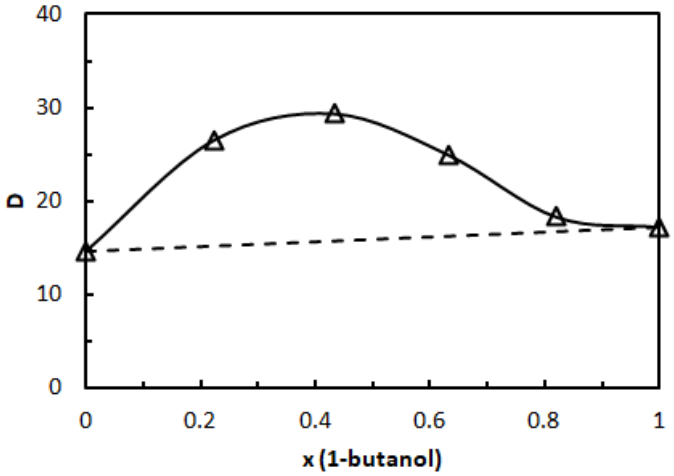


Figure 2. Graphical presentation of the synergic effect in the extraction of acetylsalicylic acid by the diethyl ether/1-butanol binary solvent mixtures (experimental D_{mix} values - triangles; theoretically predicted D_{add} values - dashed line).

CONCLUSION

Salting-out effect on the extraction of acetylsalicylic acid from aqueous solutions was determined by measuring its distribution ratios between diethyl ether and aqueous solutions containing different concentrations of NaCl. Setschenow salting-out constant was determined to be 0.2178 and this value is close to the value reported in the literature which was obtained by solubility measurements. Extractions with binary diethyl ether/1-butanol solvent mixtures were performed for the assessment of synergic effect. For the whole range of binary solvent mixture compositions higher distribution ratios were obtained in comparison to the acetylsalicylic acid extraction with pure solvents. According to the values of synergic coefficients, the highest synergic effect was achieved when extraction of acetylsalicylic acid from aqueous solution was performed with a binary mixture containing slight excess of diethyl ether.

Acknowledgment

This work was supported by the Ministry of Education, Science and Technological Development of the Republic of Serbia (grants no 451-03-65/2024-03/200113 and 451-03-65/2024-03/200124).

REFERENCES

[1] R. Mullangi, K. Sharma, N. R. Srinivas, Biomed. Chromatogr., 26 (2012) 906.
[2] R. C. Assis, A. B. Mageste, L. R. de Lemos, R. M. Orlando, G. D. Rodrigues, Talanta, 223 (2021) 121697.
[3] V. Yu. Belov, S. V. Kursakov, V. I. Sevast'yanov, E. N. Antonov, S. É. Bogorodskii, V. K. Popov, Pharm. Chem. J., 52 (2018) 151.
[4] N. Ni, S. H. Yalkowsky, Int. J. Pharm., 254 (2003) 167.
[5] K. Pešić, J. Momčilović, J. Živković, G. Nikolić, Med. Podmladak, 71 (2020) 39.
[6] N. Ya. Mokoshina, O. V. Erina, O. A. Pakhomova, R. V. Savushkin, Russ. J. Phys. Chem. A, 81 (2007) 1964.
[7] G. M. Nikolić, J. V. Živković, D. S. Atanasković, M. G. Nikolić, Russ. J. Phys. Chem. A, 87 (2013) 2191.
[8] R. Castro-Varela, C. Rey-Castro, T. Vilariño, M. E. Sastre de Vicente, J. Chem. Eng. Data, 47 (2002) 1432.

O *– Pharmaceutical Physical Chemistry*

DEVELOPMENT OF AN INTEGRATIVE PLATFORM FOR DESIGN OF NOVEL SIRT2 INHIBITORS

N. Djokovic [1], M. Rahnasto-Rilla [2], A. Djuric [3], D. Ruzic [1], M. Petkovic [4], T. Srdic-Rajic [3] and M. Lahtela-Kakkonen [2]

[1] University of Belgrade, Faculty of Pharmacy, Department of Pharmaceutical Chemistry, Vojvode Stepe 450, 11221 Belgrade, Serbia. (nemanja.djokovic@pharmacy.bg.ac.rs)
[2] School of Pharmacy, University of Eastern Finland, P.O. Box 1627, 70210 Kuopio, Finland.
[3] Department of Experimental Oncology, Institute for Oncology and Radiology of Serbia, Pasterova 14, 11000 Belgrade, Serbia.
[4] Department of Organic Chemistry, Faculty of Pharmacy – University of Belgrade. Vojvode Stepe 450, 11000, Belgrade, Serbia.

DOI: https://doi.org/10.46793/Phys.Chem24II.593DJ

ABSTRACT

Sirtuin 2 inhibitors (SIRT2i) represent a promising avenue in pharmaceutical research particularly for their potential in addressing neurodegenerative and malignant diseases. However, despite preclinical success, no SIRT2 inhibitors have reached clinical trials, highlighting the need for further development. Key challenges include understanding the complex conformational dynamics of SIRT2, lack of structure-activity correlation, and limited exploration of pharmacological contexts. This study aims to establish a platform integrating molecular modelling, cheminformatics, and bioinformatics approaches to aid in rational design of SIRT2 inhibitors.

The platform's development involved exploration of conformational dynamics of SIRT2 and creating a structure-based virtual screening (SBVS) pipeline. By devising a protocol for enhanced sampling of the conformational space of SIRT2, previously unknown alternative conformational states of SIRT2 were identified and utilized to explore distant regions of the SIRT2i chemical space through SBVS. Furthermore, cheminformatics quantitative structure-activity models were developed to predict compound activity and selectivity, culminating in the creation of SIRT2i_Predictor, a machine learning-based application for rational design of novel SIRT2i. A bioinformatics protocol was also devised to predict synergistic small-molecule combinations, leading to the identification of biological targets for the future design of novel classes of dual SIRT2i as more effective antineoplastic agents. Experimental validation confirmed the platform's effectiveness in virtual screening and led to the discovery of novel chemical species of SIRT2 inhibitors and novel synergistic combinations. Additionally, data generated through the platform contributed to the discovery of novel binding sites on sirtuins, which were further validated through co-solvent molecular dynamics simulations and funnel metadynamics. In summary, the platform integrates biomolecular simulations, cheminformatics, and bioinformatics to facilitate the design and validation of new SIRT2 inhibitors. It serves as a bridge between complex SIRT2 conformational considerations, structural and biological data on inhibitors.

Acknowledgment

This research was funded by the Ministry of Science, Technological Development and Innovation, Republic of Serbia through two Grant Agreements with University of Belgrade-Faculty of Pharmacy No 451-03-65/2024-03/200161 and No 451-03-66/2024-03/200161. The authors thank the COST Actions CA18240, CA18133 and CA22125 of the European Community for support.

INVESTIGATING TEMPERATURE-INDUCED PHASE TRANSITIONS IN ATORVASTATIN USING RAMAN SPECTROSCOPY

J.J. Lazarević, S. Uskoković-Marković, J. Mitrić and N. Lazarević

Center for Solid State Physics and New Materials, Institute of Physics Belgrade, University of Belgrade, Pregrevica 118, 11080 Belgrade, Serbia (jasminal@ipb.ac.rs)
[2] Faculty of Pharmacy, University of Belgrade, 11221 Belgrade, Serbia

DOI: https://doi.org/10.46793/Phys.Chem24II.595L

ABSTRACT

The Raman spectra of atorvastatin calcium trihydrate (ATC) were systematically investigated across a temperature range from 100 K to 460 K, revealing intricate vibrational and structural dynamics. Key observations included temperature-induced changes in spectral features, with significant transformations at 420 K, where intermolecular vibrations were strongly suppressed, indicating a collapse in crystal structure and potential formation of a liquid crystalline phase. This phase transition was evidenced by the disappearance of well-defined peaks and the appearance of broad hump-like structures, suggesting residual order before complete isotropic melting at 460 K. The study focused on both intramolecular and intermolecular vibrations, with the latter being prominent below 175 cm^{-1}. Temperature variations affected Raman modes, notably around 420 cm^{-1}, 490 cm^{-1}, and 635 cm^{-1}, reflecting structural and electronic changes. The investigation highlighted the stepwise dehydration of ATC, especially between 320 K and 380 K, supporting prior findings. These raveled changes provide extremely usable insights into the thermal adaptability and structural responsiveness of ATC, offering implications for its stability and performance in pharmaceutical applications.

TWISTED AMIDES: FROM SUPRAMOLECULAR ASPECT TO PHARMACOLOGICAL APPLICATION

I. Đorđević

University of Belgrade, Institute of Chemistry, Technology and Metallurgy
National Institute of the Republic of Serbia,
Njegoševa 12, 11000 Belgrade, Serbia (ivana.djordjevic@ihtm.bg.ac.rs)

DOI: https://doi.org/10.46793/Phys.Chem24II.597DJ

ABSTRACT

The amide bond is a fundamental and arguably one of chemistry and biochemistry's most important functional groups. Furthermore, the peptide bond is one of nature's most ubiquitous amide bond examples. It links amino acids in peptides and proteins, determining the secondary structures formation of proteins and their biological activities. It is well known that typical amides are planar due to the resonance effect, a concept introduced by Pauling nearly a century ago. The vast majority of amides contain planar bonds of approximately 40% partial double bond character as a consequence of the n_N to $\pi^*_{C=O}$ conjugation and resonance energy of 15−20 kcal mol^{-1}.

The amide group can be represented by two resonance structures: apolar (R′RN–C(=O)R) and dipolar (RRN^+=C(–O^-)R), differing in the location of the double bond. In reality, the electrons are delocalized across the amide group, as a hybrid of these two theoretical structures and the electron distributions. The contribution of dipolar form is only possible if the chemical bonds around the amide lie in the same plane to meet the geometrical requirements of the carbon-nitrogen double bond. When coplanarity cannot be achieved without structural distortion, electron delocalization is hindered, destabilizing the amide bond. Such non-planar amides exhibit unusual amide bond distortions, which can be characterized using the Winkler-Dunitz parameters. According to these parameters, three types of non-planar amides can be distinguished as amides featuring:

1. Perpendicularly twisted C(O)–N amide bonds and non-pyramidalized trigonal N atoms (twisted amides),
2. Pyramidalized nitrogen atoms and planar C(O)–N bonds (pyramidalized amides), and
3. A combination of twisted C(O)–N bonds and pyramidalized N atoms (twisted pyramidalized, and twisted-pyramidalized amides).

The early examples of twisted amide bond properties were reported in conformationally locked bridged *β*-lactam antibiotics. Recently, there has been growing interest in acyclic non-planar (twisted) amides. Geometrically distortion of the amide bond in non-planar amide arises from either: 1) steric (e.g., classic bridged lactams), 2) electronic (e.g., classic anomeric amides) or 3) combined steric and electronic reasons (e.g., classic acyclic twisted amides).

Distortions of the amide bond from planarity have profound consequences on all major chemical properties of amides. Therefore, non-planar amides are an essential design feature for peptide *cis*−*trans* isomerization, peptide cleavage (enzymatic processes) change of the thermodynamic protonation site from oxygen to nitrogen, increased propensity to hydrolysis, nucleophilic acyl substitution, cleavage of σ_{N-C} bonds, and oxidative addition of the N−C(O) bond to transition metals.

Acknowledgment

This work was supported by the Ministry of Science, Innovation and Technological Development of the Republic of Serbia (grant no 451-03-66/2024-03/200026).

2D QSAR MODEL FOR SARS-COV-2 MAIN PROTEASE INHIBITORS

B. Stanković

University of Belgrade, Vinča Institute of Nuclear Sciences –National Institute of the Republic of Serbia, Mike Petrovića Alasa 12-14, Belgrade, Serbia. (branislav.stankovic@vin.bg.ac.rs)

DOI: https://doi.org/10.46793/Phys.Chem24II.599S

ABSTRACT

A novel procedure for descriptor selection was tested on a quantitative structure–activity relationship (QSAR) model for SARS-CoV-2 main protease inhibitors, aimed at developing transparent, interpretable, reproducible, and publicly available methodologies applicable in drug development and other QSAR-related fields. The model was trained and tested using molecules collected from the CHEMBL database. Descriptors were selected from a set of Mordred molecular descriptors. The models were constructed using multiple linear regression algorithms, followed by scrutiny of fitting and predictive performance, reliability, and robustness through various statistical validation criteria. Among the models, those trained with ordinary least squares linear regression exhibited the best performances. Due to their good predictive performances the constructed models can serve as valuable tools for the quick and reliable prediction of inhibitory activity toward SARS-CoV-2 main protease.

INTRODUCTION

The SARS-CoV 2 (severe acute respiratory syndrome-related coronavirus 2) is a positive-strand RNA virus with the largest genome of all known RNA viruses with a length of about 28–30 kilobases in length. The SARS-CoV 2 shares ~80% genome similarity with the SARS-CoV first reported in 2002 [1]. The SARS-CoV-2 pandemic affected over 600 million people and caused the death of nearly 7 million till May 2024 [2].

There is currently no highly effective drug available on the market. While vaccines have helped control pandemics, concerns persist over their safety for individuals with allergies, immune disorders, and during pregnancy. Additionally, vaccine efficacy against new coronavirus variants remains uncertain, highlighting the ongoing need for effective treatments [3].

The coronavirus 3-chymotrypsin-like protease (M^{pro} or $3CL^{pro}$) is a key protease involved in viral replication and transcription, making it a prime target for pharmaceutical interventions to control virus multiplication and proliferation [4]. Notably, $3CL^{pro}$ possesses a substrate-recognition pocket that is highly conserved across all coronaviruses. Therefore, the aim of this study is to develop a quantitative structure-activity relationship (QSAR) model capable of predicting inhibitory activity toward 3CLpro, with the goal of proposing novel drug candidates.

METHODS

In this study, chemical structures exhibiting inhibitory activity against $3CL^{pro}$ were sourced from the CHEMBL database. The half maximal inhibitory concentration (IC_{50}) values were converted to pIC_{50} values using the **equation 1** and utilized as target values.

$$pIC_{50} = (9 - \log IC_{50}) \quad (1)$$

The research is performed with Python program package. The Mordered 2D molecular descriptors were calculated. Modelling was conducted using up to 14 descriptors. Various linear regression models were employed.

Descriptors containing missing values or non-numerical entries were omitted from the dataset. The data were then divided into training (80%) and test sets (20%) using the Kennard-Stone algorithm and normalized using the MinMaxScaler. Additionally, descriptors with a standard deviation less than 0.05 in the training set were excluded from the analysis.

In the initial step of the descriptor selection process, we filtered the set of descriptors to exclude any pairs exhibiting a pairwise correlation higher than 0.95. After that, we applied the Featurewiz algorithm using Q^2_{LOO} as the fitness function.

Model evaluation entails a comprehensive examination, employing a diverse array of commonly utilized statistical metrics as outlined in literature. These encompass various indicators for assessing goodness-of-fit and robustness, including root mean square error (*RMSE*) for both the training set ($RMSE_{\text{tr}}$) and cross-validation ($RMSE_{\text{cv}}$,), coefficients of determination for the training set (R^2), leave-one-out (Q^2_{LOO},), and leave-many-out (Q^2_{LMO}) cross-validation methods. Additionally, adjusted coefficients of determination (R^2_{adj}), concordance correlation coefficient in the training set (CCC_{tr}), and internal validation (CCC_{cv}) are considered, along with the *F*-value. Predictive performance is gauged through mean square error ($RMSE_{\text{ext}}$) and mean absolute error (MAE_{ext}) in the test set, along with three metrics derived from coefficients of determination: Q^2_{F1}, Q^2_{F2}, and Q^2_{F3}. Moreover, correlation coefficients in the test set (CCC_{ext}), slopes of regression lines through the origin of predicted vs. experimental values (*k*), and experimental vs. predicted values (*k'*) are evaluated, along with $\langle r^{2}_{\text{m}} \rangle$, Δr^2_{m}, and R^2_{ext}. To delineate applicability domain (AD), we employ the leverage approach, utilizing the Williams plot, which juxtaposes standard residuals against leverage (*h*).

To address multicollinearity and chance correlation, a three-fold selection process was implemented. Initially, the QUIK (Q Under Influence of K) rule was utilized. Subsequently, the Variance Inflation Factor (VIF) was computed, and models with each descriptor having a VIF value below 5 passed to the final test. Y-Scrambling was then employed to ensure the robustness of the selected models.

The optimal model selection process utilized Multi-Criteria Decision Making (MCDM), integrating all measures of goodness-of-fit, robustness, and predictivity from the previous section to rank models. We also factored in the number of descriptors, ensuring a balanced assessment of model performance and simplicity. This dual approach ensures comprehensive evaluation, capturing both overall model performance via MCDM and the model's complexity based on descriptor count.

RESULTS AND DISCUSSION

The best model originating from this study is given by **equation 1**, while calculated statistics parameters for various linear regression models are presented in **Table 1** and **Table 2**.

$$\begin{aligned} \text{pIC}_{50} = {} & 2.22 \cdot 10^{-2}\ \text{AATS7Z} + 1.47\ \text{GATS5c} + -1.85\ \text{GATS2are} - 2.72 \cdot 10^{-2}\ \text{SMR\_VSA6} + \\ & + 1.18\ \text{n10FaRing} + 3.35 \cdot 10^{-2}\ \text{EState\_VSA9} + 0.31\ \text{naHRing} - 3.57 \cdot 10^{-2}\ \text{PEOE\_VSA10} + \\ & + 0.30\ \text{NaaaC} + 0.11\ \text{StsC} + 0.24\ \text{NssssC} - 4.13 \cdot 10^{-2}\ \text{SssNH} - \\ & - 4.34 \cdot 10^{-3}\ \text{EState\_VSA4} - 1.57 \cdot 10^{-3}\ \text{PEOE\_VSA6} + 1.36 \end{aligned} \quad (1)$$

Table 1. Internal fitting parameters of the models.

No	Descriptors	R^2	adjR^2	$RMSE_{tr}$	CCC_{tr}	F	Q^2_{LOO}	$RMSE_{cv}$	CCC_{cv}	Q^2_{LMO}	R^2_{Yscr}	Q^2_{Yscr}
1	Linear Regression	0.829	0.783	0.377	0.906	18	0.706	0.494	0.846	0.651	0.196	-0.366
2	Ridge Regression	0.827	0.781	0.379	0.903	17	0.706	0.494	0.846	0.651	0.198	-0.364
3	LassoLars	0.829	0.783	0.377	0.906	18	0.706	0.494	0.846	0.651	0.198	-0.364
4	Bayesian Ridge Regression	0.823	0.777	0.383	0.899	15	0.706	0.494	0.846	0.651	0.198	-0.364
5	ARDRegression	0.821	0.774	0.385	0.898	16	0.706	0.494	0.846	0.651	0.198	-0.364
6	Lasso	0.824	0.777	0.382	0.899	15	0.706	0.494	0.846	0.651	0.198	-0.364
7	Linear SVR	0.780	0.722	0.428	0.870	11	0.706	0.494	0.846	0.456	0.198	-0.364

Table 2. External validation parameters of the models.

No	R^2_{ext}	$RMSE_{ext}$	Q^2_{F1}	Q^2_{F2}	Q^2_{F3}	CCC_{ext}	MAE_{ext}	r_m^2	Δr_m^2	k	k'	$\frac{R^2_{ext} - R^2_0}{R^2_{ext}}$	$\frac{R^2_{ext} - R'^2_0}{R^2_{ext}}$
1	0.845	0.461	0.84	0.84	0.744	0.916	0.394	0.778	0.051	1.014	0.976	0.003	0.014
2	0.841	0.465	0.838	0.838	0.740	0.912	0.402	0.772	0.108	1.016	0.974	0.000	0.025
3	0.845	0.461	0.84	0.84	0.744	0.916	0.394	0.778	0.051	1.014	0.976	0.003	0.014
4	0.838	0.469	0.835	0.835	0.735	0.908	0.407	0.764	0.143	1.017	0.972	0.000	0.036
5	0.842	0.466	0.837	0.837	0.739	0.911	0.403	0.773	0.120	1.02	0.97	0.000	0.028
6	0.840	0.468	0.836	0.835	0.736	0.909	0.406	0.769	0.141	1.019	0.971	0.000	0.034
7	0.807	0.557	0.767	0.766	0.626	0.878	0.434	0.728	0.008	1.05	0.939	0.011	0.013

To thoroughly investigate the performances of our model, we analyzed scatter plots comparing experimental and predicted activity values for the training and test sets (**Figure 1**) and the Williams plot (**Figure 2**). It is evident that model demonstrate strong fitness and predictability. No Y-outliers are detected. Moreover, all compounds in both the training and test set fall below the threshold of *h**, indicating the absence of response outliers and suggesting that predictions of inhibitory activity against the SARS-CoV-2 main protease could be extrapolated.

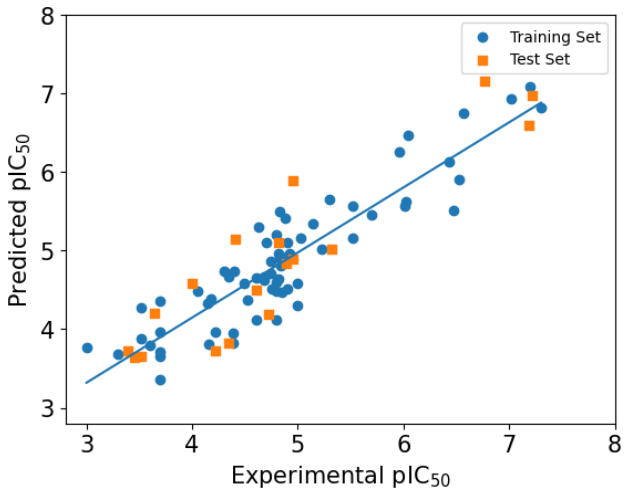


Figure 1 Scatter plot of predicted versus experimental mutagenicity.

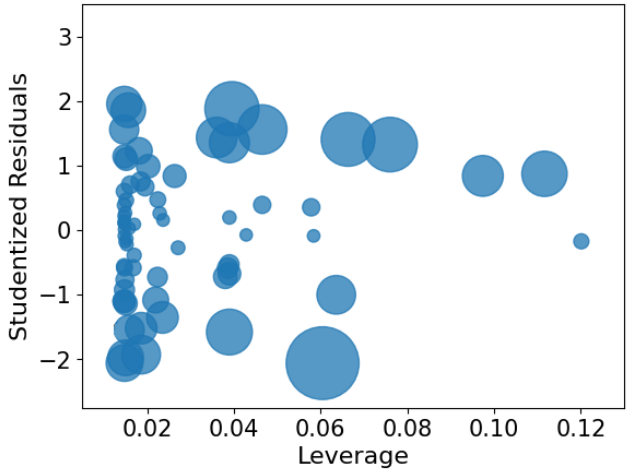


Figure 2. The Williams plot.

Derived model shows that pIC_{50} value increases with hydrophobicity and existence of heteroatomic rings with single heteroatom, while decreases with branching. Secondary amides, aromatic ketones, and molecules containing pyrimidine, thiazole, and pyrazole rings or cyano groups have low pIC_{50} values. On the other side, best inhibitors should have localized change distribution

CONCLUSION

Using a novel procedure for descriptor selection, QSAR models, that estimate inhibitory activity toward the SARS-CoV-2 main protease with excellent fitting ability and external predictive performance, were constructed. These models accurately predicted activities for molecules outside the chemical space in which they were trained, representing an advancement in QSAR modeling and enabling reliable and quick identification of potential drug candidates targeting the main protease of SARS-CoV-2. Given that the proposed methodology is simple, robust, transparent, interpretable, reproducible, and publicly available, we are confident that it can, not only contribute to developing effective drug candidates against SARS-CoV-2, but also be widely applicable in similar studies.

Acknowledgment

This work was supported by the Ministry of Education, Science and Technological Development of the Republic of Serbia (grant no No. 451-03-66/2024-03/200017).

REFERENCES

[1] P. Zhou, X. L. Yang, X. G. Wang, B. Hu, L. Zhang, W. Zhang, H. R. Si, Y. Zhu, B. Li, C. L. Huang, Nature, 579 (2020) 270.
[2] https://data.who.int/dashboards/covid19.
[3] T. Zhai, F. Zhang, S. Haider, D. Kraut, Z. Huang, Protease. Front. Mol. Biosci., 8 (2021) 661424.
[4] Z. Jin, X. Du, Y. Xu, et al.., Nature. 582 (2020) 289.

THE INFLUENCE OF ASCORBATE ON ANTI-HUMAN MELANOMA ACTION OF A MONOLACUNARY WELLS-DAWSON NANOCLUSTER

M. B. Čolović [1], J. J. Žakula [2], L. B. Korićanac [2], N. Savić [3], T. Parac-Vogt [3] and D. Z. Krstić [4]

[1]*Department of Physical Chemistry, "Vinča" Institute of Nuclear Sciences-National Institute of the Republic of Serbia, University of Belgrade, Serbia.* (colovicm@vin.bg.ac.rs)
[2] *Department of Molecular Biology and Endocrinology, "Vinča" Institute of Nuclear Sciences-National Institute of the Republic of Serbia, University of Belgrade, Serbia.*
[3]*Department of Chemistry, KU Leuven, Leuven, Belgium.*
[4]*Institute of Medical Chemistry, Faculty of Medicine, University of Belgrade, Serbia.*

DOI: https://doi.org/10.46793/Phys.Chem24II.603C

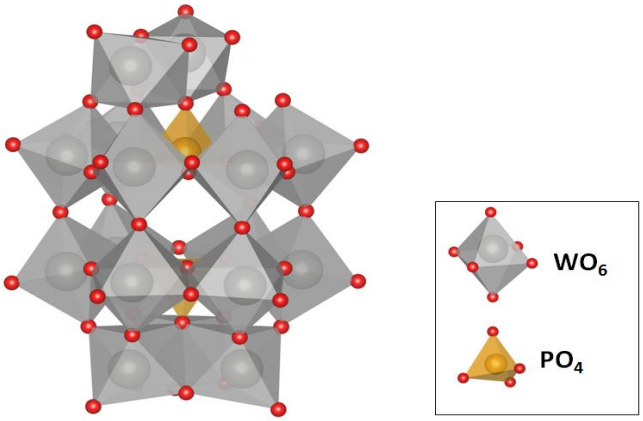
ABSTRACT

The influence of L(+)-ascorbic acid sodium salt (ascorbate), as a widely used antioxidant, on the anti-human melanoma A375 activity of a monolacunary Wells-Dawson polyoxometalate (mono-WD), α_2-$K_{10}P_2W_{17}O_{61}{\cdot}20H_2O$ was assessed in this study. A375 cells were *in vitro* exposed to the selected concentrations of mono-WD (the concentration range of 0.001 - 1 mM), ascorbate (0.040 – 40 mM), and the mixtures of mono-WD and ascorbate in the ratio of 1:40, for 24 and 48 hours. Both mono-WD and ascorbate induced concentration- dependent cytotoxic effects on A375 tumour cells, for both exposure times. The cell viability inhibiting potential of ascorbate was higher after 24-hour exposure, whereas similar cytotoxic effects of the studied compounds were obtained for 48-hour treatment. In summary, the results of the simultaneous exposure of A375 cells to mono-WD and ascorbate (mixed in the ratio of 1:40) showed that the presence of ascorbate does not affect remarkably the observed antitumour potency of the studied polyoxotungstate as a potential metallo-therapeutic.

INTRODUCTION

Polyoxometalates (POMs) are discrete, negatively-charged metal-oxo clusters comprising early *d*-block metal ions in high oxidation states (*e.g.* W^{6+}, V^{5+}). Apart from materials science and catalysis, POMs have also attracted significant interest in biomedicine due to their reported biological activities such as anti-cancer, - viral, -Alzheimer, and –diabetic actions [1, 2]. In this context, our recent study [3] found palladium-based POMs as promising, selective, and safe antitumour next-generation therapeutics, which demonstrated cytotoxic effects against neuroblastoma and leukemia cells comparable to cisplatin as the gold-standard chemotherapeutic.

Our preliminary studies revealed significant cytotoxic effects of Wells-Dawson (WD) POMs against human melanoma A375 cells, similar to cisplatin. Thus, this study aimed to evaluate the effect of L(+)-ascorbic acid sodium salt (ascorbate), as a widely used antioxidant, on the anti-A375 action of a monolacunary WD POM (mono-WD), α_2-$K_{10}P_2W_{17}O_{61}{\cdot}20H_2O$ (**Scheme 1.**). For this purpose, different concentrations of mono-WD and ascorbate and their mixtures in the concentration ratio of 1:40 were exposed to A375 cells and resulting cytotoxicity was monitored.



Scheme 1. Structure of monolacunary Wells–Dawson polyoxotungstate (mono-WD), α_2-$K_{10}P_2W_{17}O_{61}{\cdot}20H_2O$ (red balls–oxygen).

METHODS

All chemicals used in this study were purchased from Sigma-Aldrich Chemical Co. (Steinheim, Germany) and employed without further purification, except monolacunary Wells–Dawson polyoxometalate, α_2-$K_{10}P_2W_{17}O_{61}{\cdot}20H_2O$ (mono-WD) that was synthesized according to a procedure available in literature [4]. A stock aqueous solution of mono-WD (20 mM) was prepared by vigorous mixing and heating at 30-40 °C, whereas ascorbate stock solution (1 M) was mixed at room temperature. The stock solutions were diluted with water up to desired concentrations (working solutions). To obtain final concentrations, 10 μL of the stock/working solutions were added to 90 μL of cell culture samples.

Human melanoma A375 cell line was purchased from the American Tissue Culture Collection (ATCC, Manassas, VA, USA) and cultured in penicillin/streptomycin and high-glucose DMEM medium supplemented with 10% fetal bovine serum, in a humidified atmosphere of 5% CO_2 at 37 °C.

A375 cells were seeded into flat-bottom 96-well plates, at a density of 2×10^3 cells/well and allowed to adhere overnight. Then, cells were exposed to the studied compounds for 24 and 48 hours. Cytotoxicity was evaluated using sulforhodamine B (SRB) assay measuring cellular protein content [5]. Shortly, the cell monolayers were fixed with 10% trichloroacetic acid (TCA) at 4 °C, for 1 hour and stained with 0.4% SRB. After unbound color was removed, the plates were washed with 1% acetic acid before air-drying and protein-bound dye was dissolved in 10 mM Tris buffer solution. Absorbance was monitored at 550 nm and a reference wavelength of 690 nm using a microplate reader (Wallac, VICTOR2 1420 Multilabel counter, PerkinElmer, Finland). Obtained results were expressed as cell viability related to control. Statistical significance was analyzed using Student *t*-test.

RESULTS AND DISCUSSION

The effect of ascorbate on the antitumor activity *in vitro* of mono-WD towards human melanoma A375 cells was assessed by monitoring cell viability, as an indicator of cytotoxicity, in the presence of mono-WD, ascorbate, and their mixture (ratio 1:40) (**Figure 1.**). Previously, the investigated cells were *in vitro* exposed to the selected concentrations of mono-WD (the concentration range of 0.001 - 1 mM), ascorbate (0.040 – 40 mM), and mono-WD-ascorbate mixture (corresponding concentrations) for 24 and 48 h.

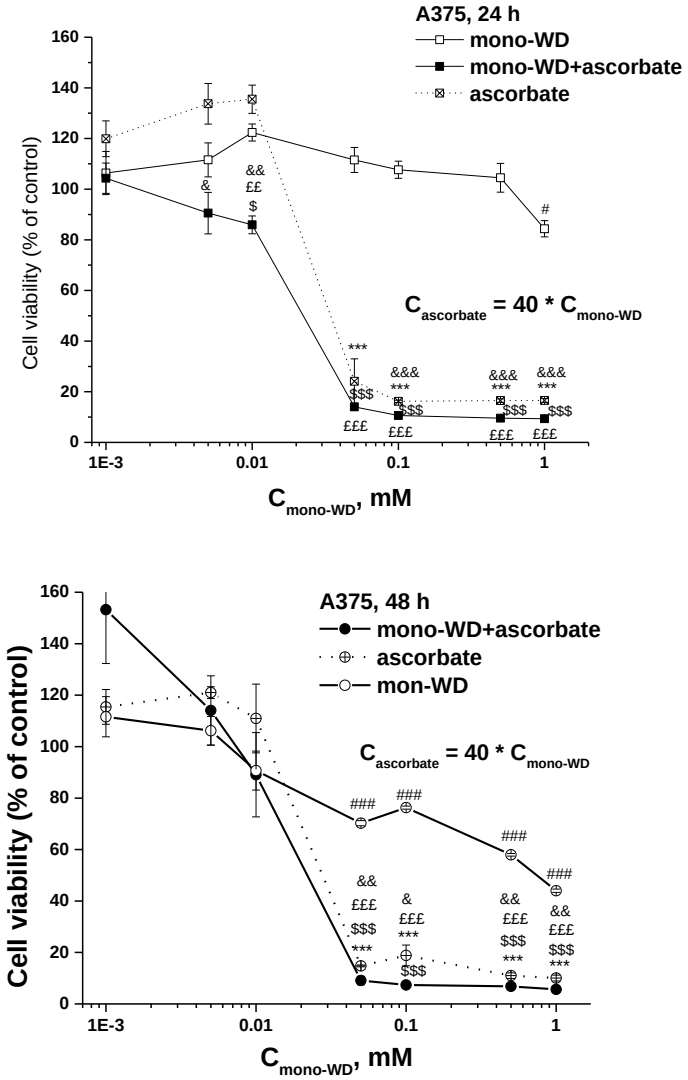


Figure 1. The effect of mono-WD, ascorbate, and the mixture of mono-WD and ascorbate (ratio 1: 40) on the viability of human melanoma A375 cells, after 24 and 48 hours exposure. Cell viability was presented as % of untreated (control) cells (100%). Results are expressed as mean ± S.D. from at least 2 independent experiments done in triplicates. * -statistical significance of ascorbate treated cells compared to control, # -statistical significance of mono-WD treated cells compared to control, $ -statistical significance of mono-WD + ascorbate treated cells compared to control, £ -statistical significance of mono-WD + ascorbate treated cells compared to mono-WD, £ -statistical significance of mono-WD + ascorbate treated cells compared to ascorbate; *, #, $, £, & - 0.05 > p > 0.01, **, ##, $$, ££, && - 0.01 > p > 0.001, ***, ###, $$$, £££, &&& - p < 0.001.

Mono-WD and ascorbate demonstrated concentration-dependent cytotoxic effects on A375 tumour cells, but the cell viability inhibiting potency of ascorbate was considerably higher for 24-hour exposure. EC_{50} values after 24 h were 1.4 and > 1 mM for ascorbate and mono-WD, respectively.

For 24-hour treatment, the mono-WD concentration of 1 mM induced a 15% decrease ($p < 0.05$) in cell viability, whereas lower concentrations did not result in significant effects. Forty times higher ascorbate concentration (40 mM) inhibited cell viability by 85% ($p < 0.001$) and their mixture (ratio 1:40) decreased A375 viability more than 90% ($p < 0.001$), compared to the control.

In accordance, the simultaneous effect of the mono-WD-ascorbate mixture was equal to approximately the sum of cytotoxic effects induced by the single exposures of the investigated compounds.

After 48-hour exposure, mono-WD induced A375 cytotoxicity in the concentration range of 0.05-1 mM resulting in the concentration-dependent decrease in the cell viability ranging 25-55% ($p < 0.001$), whereas forty times higher ascorbate concentrations (2-40 mM) induced cell viability inhibition higher than 80% ($p < 0.001$). The mixtures of the corresponding mono-WD-ascorbate concentrations reduced cell viability almost completely (> 90%) ($p < 0.001$).

CONCLUSION

The results showed similar cytotoxicity potencies of mono-WD and ascorbate against human melanoma A375 cells after 48-hour treatment ($EC_{50} \approx 1$ mM). The simultaneous exposure of A375 cells to mono-WD and ascorbate (mixed in the ratio of 1:40) demonstrated that the presence of ascorbate does not affect remarkably the observed antitumour potency of the studied polyoxotungstate as a potential metallo-therapeutic.

Acknowledgement

This study was financially supported by the Ministry of Science, Technological Development, and Innovation of the Republic of Serbia (contracts no. 451-03-66/2024-03/200017 and 451-03-9/2023-14/200110). The authors are also thankful to the Science Fund of the Republic of Serbia (POMCACT project no. 6526393).

REFERENCES

[1] M. B. Čolović, M. Lacković, J. Lalatović, A. S. Mougharbel, U. Kortz, D. Krstić, Curr. Med. Chem., 27 (2020) 362.
[2] J. Iqbal, M. Barsukova-Stuckart, M. Ibrahim, S. Usman Ali, A. Ahmed Khan, U. Kortz, Med. Chem. Res., 22 (2013) 1224.
[3] A. M. Isakovic, M. B. Čolović, T. Ma, X. Ma, M. Jeremić, M. Gerić, G. Gajski, S. Misirlic-Dencic, U. Kortz, Z. Krstić, J. Biol. Inorg. Chem., 26 (2021) 957.
[4] A. P. Ginsberg, Inorganic Syntheses, John Wiley and Sons, New York, USA, 1990.
[5] P. Skehan, R. Storeng, D. Scudiero, A. Monks, J. McMahon, D. Vistica, J. T. Warren, H. Bokesch, S. Kenney, M. R. Boyd, JNCI-J. Natl. Cancer I., 82 (1990) 1107.

ANTI-HUMAN MELANOMA ACTIVITY OF Fe(III)-CONTAINING WELLS-DAWSON POLYANION: THE EFFECT OF ASCORBATE

D. Z. Krstić [1], J. J. Žakula [2], L. B. Korićanac [2], N. Savić [3], T. Parac-Vogt [3] and M. B. Čolović [4]

[1]*Institute of Medical Chemistry, Faculty of Medicine, University of Belgrade, Serbia.*
[2]*Department of Molecular Biology and Endocrinology, "Vinča" Institute of Nuclear Sciences-National Institute of the Republic of Serbia, University of Belgrade, Serbia.*
[3]*Department of Chemistry, KU Leuven, Leuven, Belgium.*
[4]*Department of Physical Chemistry, "Vinča" Institute of Nuclear Sciences-National Institute of the Republic of Serbia, University of Belgrade, Serbia.* (colovicm@vin.bg.ac.rs)

DOI: https://doi.org/10.46793/Phys.Chem24II.607K

ABSTRACT

This study aimed to investigate the simultaneous effect of Fe(III)-substituted monolacunary Wells-Dawson polyoxometalate (Fe-WD), $K_7[Fe^{III}(\alpha_2\text{-}P_2W_{17}O_{61})(H_2O)]$ and L(+)-ascorbic acid sodium salt (ascorbate) on cell viability of human melanoma A375 cells. A375 cells were exposed *in vitro* to Fe-WD (0.001 - 1 mM), ascorbate (0.040 – 40 mM), and Fe-WD/ascorbate mixtures (concentration ratio 1:40) for 24, 48, and 72 h. Fe-WD and ascorbate inhibited cell viability in a concentration-dependent manner for three treatment durations. Obtained EC_{50} values were 1, 0.58, and 0.52 mM (for 24-, 48-, and 72-hour exposure, respectively) for Fe-WD and 1.32, 1.12, and 0.80 mM (for 24, 48, and 72 hours, respectively) for ascorbate. The simultaneous exposure to Fe-WD/ascorbate mixtures resulted in cytotoxic effects weaker than the mathematical sum of effects induced by single Fe-WD and ascorbate treatments, indicating an antagonistic inhibitory effect of the studied compounds on A375 cell viability. Conclusively, Fe-WD seems to reduce the cytotoxic effect of sodium ascorbate due to the possible autoxidation of ascorbate by oxygen in the presence of ferric (Fe(III)) ions.

INTRODUCTION

Nowadays, metal-based chemotherapeutics such as cisplatin have been used as the gold standard in cancer therapy [1]. Nevertheless, novel potential antitumor drug candidates have been synthesized to overcome particular side effects and disadvantages of current drugs approved for anticancer treatment in clinical practice [2]. In this context, polyoxometalates (POMs) are a class of metal-oxo polyanions containing transition metals (W, V, Mo, and Pd) in high oxidation states, which have been explored as considerable cytotoxic agents against a variety of tumour cells and thus promising next-generation chemotherapeutics [3, 4].

Remarkable cytotoxic effects of Fe(III)-substituted monolacunary Wells-Dawson POM (Fe-WD), $K_7[Fe^{III}(\alpha_2\text{-}P_2W_{17}O_{61})(H_2O)]$ against human melanoma A375 cell line were found in our preliminary studies. Accordingly, the purpose of this study was to assess the combined effect (concentrtion ratio 1:40) of Fe-WD and L(+)-ascorbic acid sodium salt (ascorbate) on the viability of A375 cell line as resistant tumour cells. The ratio of 1:40 was found to produce the most optimal amount of reactive oxygen species (ROS) resulting in cell structure damage and consequently cytotoxicity [5].

METHODS

Fe(III)-substituted monolacunary Wells-Dawson polyoxotungstate (Fe-WD), $K_7[Fe^{III}(\alpha_2\text{-}P_2W_{17}O_{61})(H_2O)]$ was synthesized according to a previously reported method [6]. All other

chemicals used for this research were purchased from Sigma-Aldrich Chemical Co. (Steinheim, Germany). Stock aqueous solutions of Fe-WD (20 mM) and ascorbate (1 M) were made and kept frozen. Working solutions of selected Fe-WD and ascorbate concentrations were prepared by diluting the stock solutions with water immediately before use.

Human melanoma A375 cell line was purchased from the American Tissue Culture Collection (ATCC, Manassas, USA) and cultured in high-glucose DMEM medium (Sigma-Aldrich, Steinheim, Germany) supplemented with 10% fetal bovine serum (Sigma-Aldrich, Steinheim, Germany), and penicillin/streptomycin (Sigma-Aldrich, Steinheim, Germany) at 37 °C, in a humidified atmosphere of 5% CO_2, (Heraeus, Hanau, Germany).

First, human melanoma A375 cells were seeded into flat-bottom 96-well plates, at a density of 2 × 10^3 cells/well. After adhering overnight, the cells were treated with Fe-WD/ascorbate for 24, 48, and 72 hours. Cell viability was determined by sulforhodamine B (SRB) assay based on measuring cellular protein levels, which was performed by following the published method [7]. Shortly, the cell monolayers were fixed with 10% trichloroacetic acid (TCA) (Carlo Erba, Italy) at 4 °C, for 1 hour and stained with 0.4% SRB (Sigma-Aldrich, Germany). After the unbound colour was removed, the plates were washed with 1% acetic acid before air-drying. Then, the protein-bound dye was dissolved in 10 mM Tris buffer. Absorbance was measured at 550 nm and a reference wavelength of 690 nm using a microplate reader (Wallac, VICTOR2 1420 Multilabel counter, PerkinElmer, Finland). Results were expressed as relative cell viability compared to control (a percentage of control). Statistical significance was analyzed using the Student *t*-test.

RESULTS AND DISCUSSION

First, exponentially growing A375 cells were exposed *in vitro* to Fe-WD (0.001 - 1 mM), forty times higher concentrations of ascorbate (0.040 – 40 mM), and Fe-WD/ascorbate mixtures (concentration ratio 1:40) for 24, 48, and 72 h, at 37 °C. Induced cytotoxicity was followed by determining cell viability and expressed as relative cell viability related to control (a percentage of control) (**Figure 1**.).

The results (**Figure 1**.) showed that Fe-WD and ascorbate inhibited cell viability in a concentration-dependent manner for three treatment durations, but with different potencies. Obtained EC_{50} values were 1, 0.58, and 0.52 mM (for 24-, 48-, and 72-hour exposure, respectively) for Fe-WD and 1.32, 1.12, and 0.80 mM (for 24, 48, and 72 hours, respectively) for ascorbate.

After 24 hours, Fe-WD concentrations of 0.05 and 0.1 mM did not significantly decrease A375 viability, whereas forty times higher ascorbate concentrations (2 and 4 mM) resulted in 77 and 84% inhibition ($p < 0.001$), respectively. The simultaneous exposure of A375 cells to mixtures containing the same Fe-WD/ascorbate concentrations induced significantly lower values of viability inhibition (15 and 21%, respectively) compared to ascorbate. The results obtained for higher Fe-WD and ascorbate concentrations and their corresponding mixtures demonstrated that the mixtures-induced cytotoxic effects were less potent than the mathematical sum of effects induced by single Fe-WD and ascorbate treatments at the corresponding concentrations. Similar effects were observed for 48- and 72-hour exposures as well. Moreover, it can be seen (**Figure 1**.) that inhibition curves obtained for Fe-WD/ascorbate mixtures are placed between the experimental plots obtained for single Fe-WD and ascorbate-induced cell viabilities, for all three studied exposure times.

The results obtained for single and simultaneous exposures indicate an antagonist effect of Fe-WD and ascorbate at the concentration ratio of 1:40. This effect might be explained by the autoxidation of ascorbate by oxygen in the presence of Fe(III) ions, resulting in ascorbate and Fe-WD consumption.

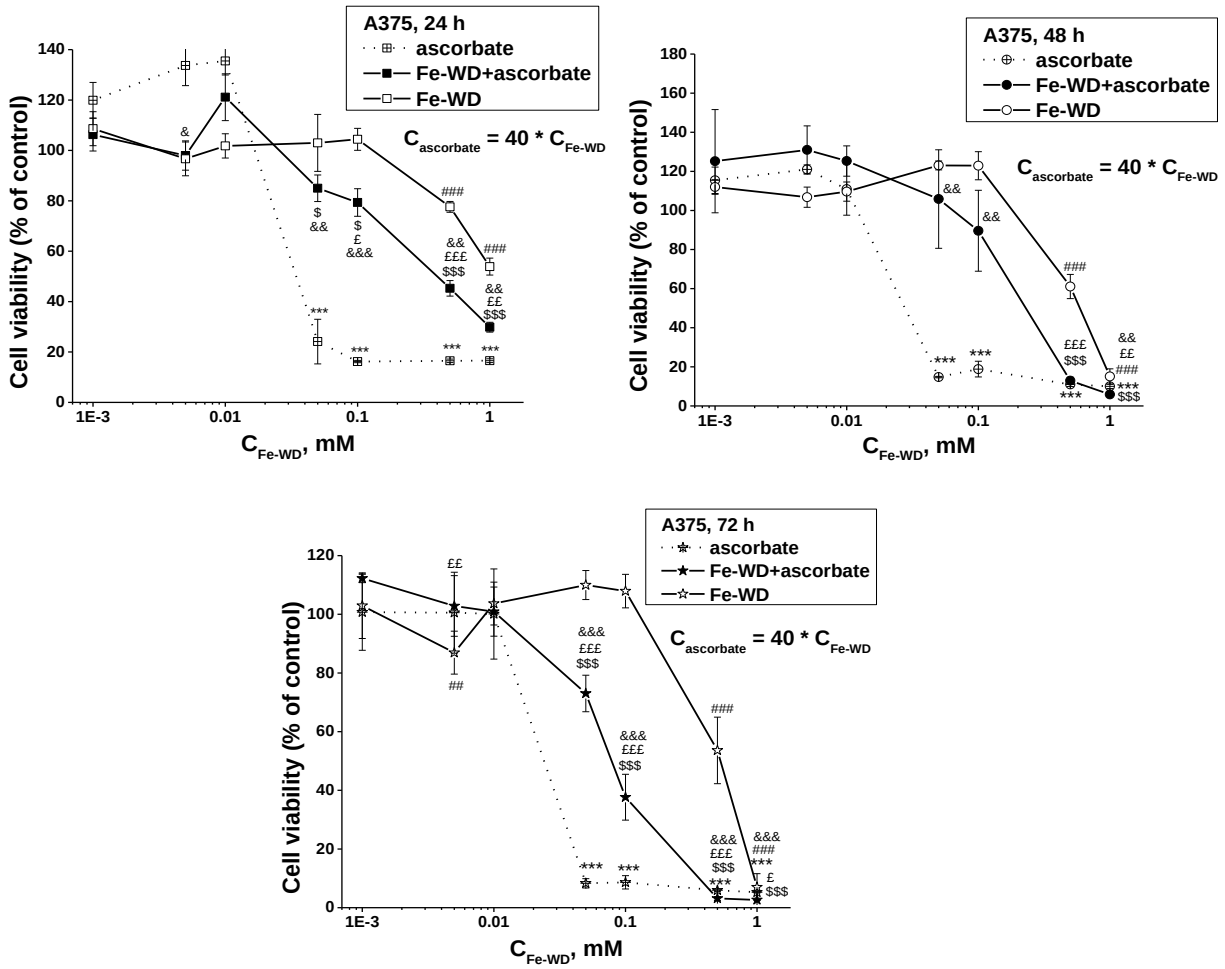


Figure 1. The influence of Fe-WD, ascorbate, and the mixture of Fe-WD/ascorbate (concentration ratio 1:40) on human melanoma A375 cell viability, after 24-, 48-, and 72-hour exposure. Cell viability was presented as % of untreated (control) cells (100%). Results are expressed as mean ± S.D. from at least 2 independent experiments done in triplicates. * -statistical significance of ascorbate treated cells compared to control, # -statistical significance of Fe-WD treated cells compared to control, $ -statistical significance of Fe-WD + ascorbate treated cells compared to control, £ -statistical significance of Fe-WD + ascorbate treated cells compared to Fe-WD, & - statistical significance of Fe-WD + ascorbate treated cells compared to ascorbate; *, #, $, £, & - 0.05 > p > 0.01, **, ##, $$, ££, && - 0.01 > p > 0.001, ***, ###, $$$, £££, &&& - p < 0.001.

CONCLUSION

In summary, the studied Fe(III)-containing monolacunary WD POM, ascorbate, and their mixture (concentration ratio 1:40) induced concentration-dependent cytotoxic effects against human melanoma A375 cell line. The most pronounced cytotoxicity was observed for Fe-WD with EC_{50} values of 1, 0.58, and 0.52 mM for 24-, 48-, and 72-hour exposure, respectively. The simultaneous exposure of Fe-WD/ascorbate mixture (1:40) indicated an antagonistic inhibitory effect of the studied compounds on A375 cell viability. Fe-WD seems to reduce the cytotoxic effect of sodium ascorbate due to the possible autoxidation of ascorbate by oxygen in the presence of ferric (Fe(III)) ions.

Acknowledgement
This study was funded by the Ministry of Science, Technological Development, and Innovation of the Republic of Serbia (contracts no. 451-03-66/2024-03/200017 and 451-03-9/2023-14/200110). The authors would also like to thank the Science Fund of the Republic of Serbia (POMCACT project no. 6526393).

REFERENCES

[1] V. Brabec, O. Hrabina, J. Kasparkova, Coordin. Chem. Rev., 351 (2017) 2.
[2] N. P. Farrell, Chem. Soc. Rev., 44 (2015) 8773.
[3] M. B. Čolović, M. Lacković, J. Lalatović, A. S. Mougharbel, U. Kortz, D. Krstić, Curr. Med. Chem., 27 (2020) 362.
[4] A. M. Isakovic, M. B. Čolović, T. Ma, X. Ma, M. Jeremić, M. Gerić, G. Gajski, S. Misirlic-Dencic, U. Kortz, Z. Krstić, J. Biol. Inorg. Chem., 26 (2021) 957.
[5] S. A. M. Abdelhameed, F. de Azambuja, T. Vasović, N. D. Savić, T. Ćirković Veličković, T. N. Parac-Vogt, Nat. Commun., 14 (2023) 486.
[6] A. P. Ginsberg, Inorganic Syntheses, John Wiley and Sons, New York, USA, 1990.
[7] P. Skehan, R. Storeng, D. Scudiero, A. Monks, J. McMahon, D. Vistica, J. T. Warren, H. Bokesch, S. Kenney, M. R. Boyd, JNCI-J. Natl. Cancer I., 82 (1990) 1107.

SIMULTANEOUS EFFECT OF A WELLS-DAWSON POLYOXOTUNGSTATE AND ASCORBATE ON CERVICAL CARCINOMA HELA CELLS

J. J. Žakula [1], M. B. Čolović [2], L. B. Korićanac [1], N. Savić [3], T. Parac-Vogt [3] and D. Z. Krstić [4]

[1] *Department of Molecular Biology and Endocrinology,"Vinča" Institute of Nuclear Sciences-National Institute of the Republic of Serbia, University of Belgrade, Serbia.*
[2] *Department of Physical Chemistry, "Vinča" Institute of Nuclear Sciences-National Institute of the Republic of Serbia, University of Belgrade, Serbia.* (colovicm@vin.bg.ac.rs)
[3]*Department of Chemistry, KU Leuven, Leuven, Belgium.*
[4]*Institute of Medical Chemistry, Faculty of Medicine, University of Belgrade, Serbia.*

DOI: https://doi.org/10.46793/Phys.Chem24II.611Z

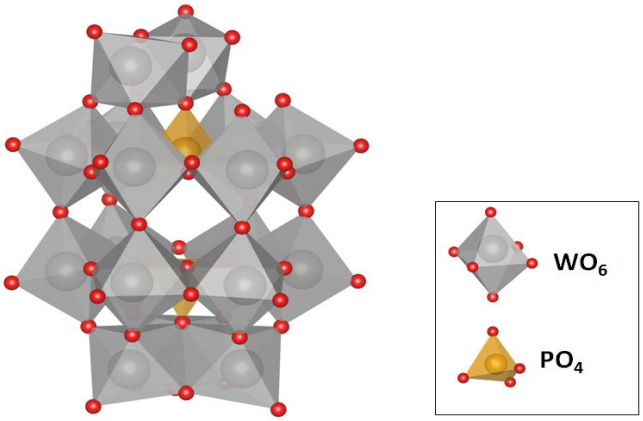
ABSTRACT

The objective of this study was to investigate the simultaneous effect of a monolacunary Wells-Dawson polyoxometalate (mono-WD), α_2-$K_{10}P_2W_{17}O_{61}{\cdot}20H_2O$, which exhibited remarkable cytotoxicity against HeLa cells, and L(+)-ascorbic acid sodium salt (ascorbate), as a strong antioxidant, against HeLa cells as a commonly used model system for research purposes. HeLa cells were treated *in vitro* (single exposure) with different concentrations of mono-WD (0.001 - 1 mM) and ascorbate (0.040 – 40 mM) for 24 and 48 hours. In addition, the tumor cells were simultaneously exposed to mixtures containing the same concentrations of mono-WD and ascorbate (ratio 1:40). Mono-WD and ascorbate induced concentration-dependent cytotoxic effects against HeLa cells, with EC_{50} values of 0.042 and 0.017 mM (for 24 and 48 hours, respectively) for mono-WD and 0.88 and 0.36 mM (for 24 and 48 hours, respectively) for ascorbate. The results of mono-WD/ascorbate mixtures (concentration ratio 1:40) indicated an additive/synergistic cytotoxic effect of the studied compounds against HeLa cell viability. Conclusively, ascorbate improves the antitumour properties of mono-WD as a potential chemotherapeutic candidate.

INTRODUCTION

Polyoxotungstates are polyoxometalates (POMs) containing tungsten ions in their high oxidation states (W^{6+}) surrounded by oxygen. In recent decades, these negatively charged metal-oxo nanoclusters have been reported as promising antitumor agents against a variety of malignant cells and consequently a good base for developing next-generation chemotherapeutics [1-3].

The aim of this study was to evaluate *in vitro* the antitumor potential of a mixture of monolacunary Wells-Dawson polyoxotungstate, α_2-$K_{10}P_2W_{17}O_{61}{\cdot}20H_2O$ (mono-WD) (**Scheme 1**.) and L(+)-ascorbic acid sodium salt (ascorbate), using cervical carcinoma HeLa cells as a model system that has been commonly employed for research purposes. Mono-WD exhibited in our preliminary experiments remarkable cytotoxic effects on HeLa cells (comparable with cisplatin), whereas ascorbate has been widely applied as a strong antioxidant in clinical practice.



Scheme 1. Structure of monolacunary Wells–Dawson polyoxotungstate (mono-WD), α_2-$K_{10}P_2W_{17}O_{61}{\cdot}20H_2O$ (red balls–oxygen).

METHODS

Monolacunary WD POM (mono-WD), α_2-$K_{10}P_2W_{17}O_{61}{\cdot}20H_2O$ was prepared by following a published procedure [4]. All chemicals were purchased from Sigma-Aldrich Chemical Co. (Steinheim, Germany) and used without further processing. A stock aqueous solution of ascorbate (1 M) was prepared by intensive mixing at room temperature. Mono-WD stock solution (20 mM) was made by vigorous mixing and heating at 30-40 °C. Working solutions were prepared by diluting the stock solutions with water up to desired concentrations.

Cervical carcinoma HeLa cells were obtained from the American Tissue Culture Collection (ATCC, Manassas, VA, USA) and cultured in high-glucose DMEM medium (Sigma-Aldrich, Steinheim, Germany) supplemented with 10% fetal bovine serum (Sigma-Aldrich, Steinheim, Germany) and penicillin/streptomycin (Sigma-Aldrich, Steinheim, Germany), in a humidified atmosphere of 5% CO_2 at 37 °C.

HeLa cells were seeded into flat-bottom 96-well plates at a density of 2×10^3 cells per well and allowed to adhere overnight. Then cells were exposed to the selected concentrations of the studied compounds. Cytotoxicity was monitored using a sulforhodamine B (SRB) assay based on the measurement of cellular protein content. The assay was carried out according to the method of Skehan *et al*. [5], 24 and 48 h after the treatment. Cell monolayers were fixed with 10% trichloroacetic acid (TCA) for 1 h at 4 °C and stained with 0.4% SRB. The unbound color was removed, and the plates were washed with 1% acetic acid before air-drying. Protein-bound dye was dissolved in 10 mM Tris buffer. Absorbance was measured at 550 nm and a reference wavelength of 690 nm using a microplate reader (Wallac, VICTOR2 1420 Multilabel counter, PerkinElmer, Turku, Finland). Results were presented as relative cell viability (a percentage of control). Statistical significance was analyzed using Student *t*-test.

RESULTS AND DISCUSSION

HeLa cells were treated *in vitro* (single exposure) with different concentrations of mono-WD (0.001 - 1 mM) and forty times higher concentrations of ascorbate (0.040 – 40 mM) for 24 and 48 hours. Furthermore, the tumor cells were simultaneously exposed to mixtures containing the same concentrations of mono-WD and ascorbate (ratio 1:40). Cytotoxicity was monitored by measuring cell viability and expressed as a percentage of control (cell viability obtained without the studied compounds). The obtained results are presented in **Figure 1**.

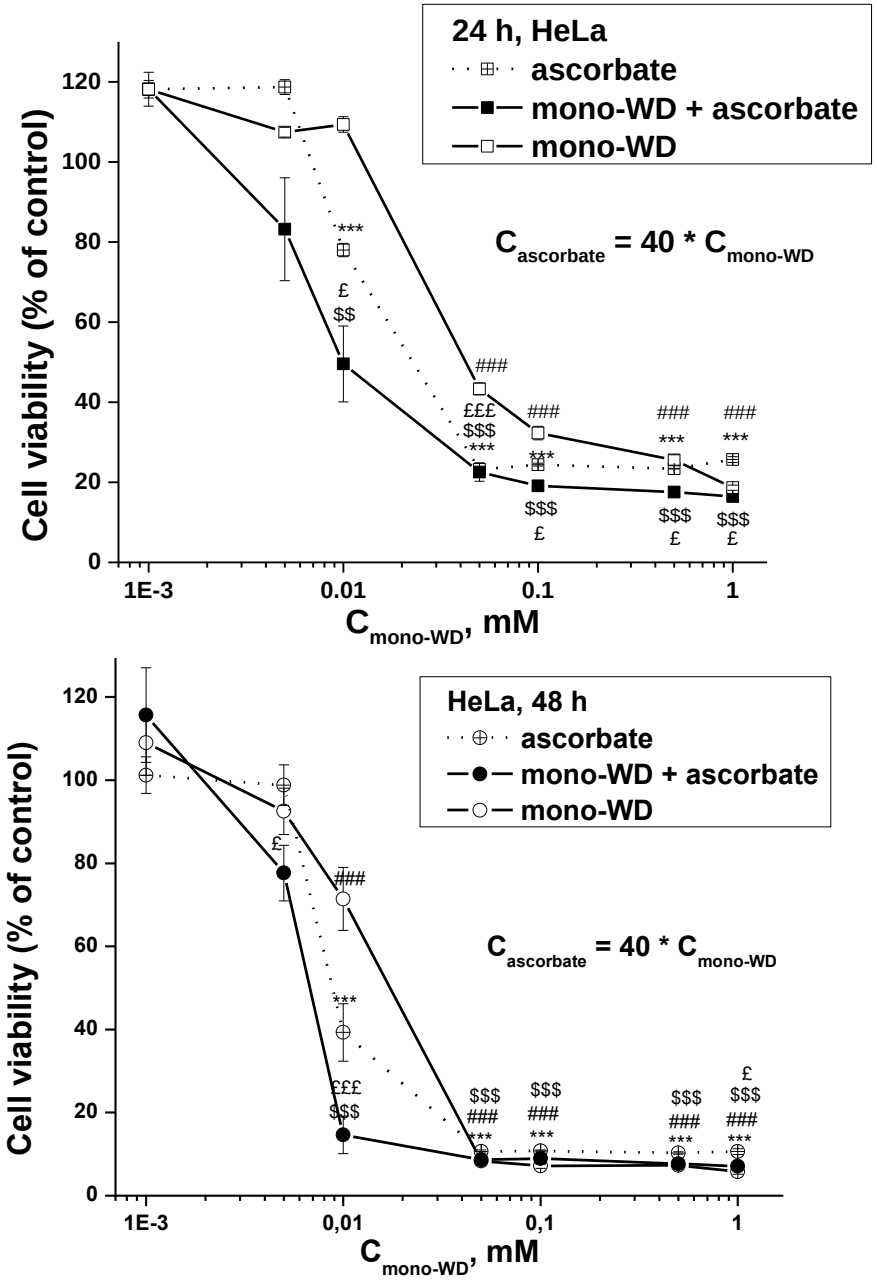


Figure 1. HeLa cell viability induced by mono-WD, ascorbate, and the mixture of mono-WD and ascorbate (ratio 1 : 40), after 24- and 48-hour exposure. Cell viability was presented as % of untreated (control) cells (100%). Results are expressed as mean ± S.D. from at least 2 independent experiments done in triplicates. * -statistical significance of ascorbate treated cells compared to control, # -statistical significance of mono-WD treated cells compared to control, $ -statistical significance of mono-WD + ascorbate treated cells compared to control, £ -statistical significance of mono-WD + ascorbate treated cells compared to mono-WD; *, #, $, £ - 0.05 > p > 0.01, **, ##, $$, ££ - 0.01 > p > 0.001, ***, ###, $$$, £££ - p < 0.001.

Mono-WD and ascorbate (single exposure) inhibited HeLa cell viability in a concentration-dependent manner. Obtained EC_{50} values for mono-WD were 0.042 and 0.017 mM (for 24 and 48 hours, respectively) and 0.88 and 0.36 mM (24 and 48 hours, respectively) for ascorbate. Then, the

simultaneous exposure of HeLa cells to the mixtures of mono-WD and ascorbate (the concentration ratio of 1:40) resulted in significantly more potent cytotoxic effects (**Figure 1**. solid squares and circles). The inhibition curves obtained for mono-WD/ascorbate mixture were shifted to lower concentrations compared to single mono-WD and ascorbate exposures, for both 24 and 48 hours.
For 24-hour treatment, 0.005 mM mono-WD and 0.2 mM ascorbate (single exposures) did not induce a significant cytotoxic effect, whereas a simultaneous exposure to the same concentrations (corresponding mixture) inhibited cell viability by 17%, but no statistical significance compared to control ($p > 0.05$). The mixture containing 0.01 mM mono-WD and 0.4 mM ascorbate induced a 52% decrease in cell viability ($p < 0.01$), whereas single exposures to the same concentrations induced no significant effect for mono-WD ($p > 0.05$) and a 23% decrease for ascorbate ($p < 0.001$). Higher investigated mono-WD and ascorbate concentrations resulted in the values of viability inhibition higher than 50% for single exposures and higher than 80% for the corresponding mixtures. The mixtures containing mono-WD and ascorbate (ratio 1:40) induced a significant cell inhibition compared to mono-WD for mono-WD concentrations ≥ 0.01 mM. A similar trend was observed for 48-hour exposure, just lower cell viability levels were obtained for the same concentrations of the studied compounds (alone or in the mixtures). A significant cell inhibiton was observed for the combined treatments compared to mono-WD, for 0.005, 0.01, and 1 mM mono-WD. Since the obtained effects induced by the mixtures were approximately equal or higher than the mathematical sums of the corresponding single effects, the influence of ascorbate on the anti-HeLa effect of mono-WD might be considered additive or synergistic.

CONCLUSION

In summary, mono-WD and ascorbate induced concentration-dependent cytotoxic effects against tumour HeLa cells, with EC_{50} values of 0.042 and 0.017 mM (for 24 and 48 hours, respectively) for mono-WD and 0.88 and 0.36 mM (for 24 and 48 hours, respectively) for ascorbate. The results of mono-WD/ascorbate mixtures (concentration ratio 1:40) indicated an additive/synergistic cytotoxic effect of the studied compounds against HeLa cell viability. Thus, it seems that ascorbate improves the antitumour properties of mono-WD as a potential chemotherapeutic candidate.

Acknowledgement

This research was funded by the Ministry of Science, Technological Development, and Innovation of the Republic of Serbia (contracts no. 451-03-66/2024-03/200017 and 451-03-9/2023-14/200110) and the Science Fund of the Republic of Serbia (POMCACT project no. 6526393).

REFERENCES

[1] M. B. Čolović, B. Medić, M. Ćetković, T. Kravić Stevović, M. Stojanović, W. W. Ayass, A. S. Mougharbel, M. Radenković, M. Prostran, U. Kortz, Z. Krstić, Toxicol. Appl. Pharm., 333 (2017) 68.
[2] M. B. Čolović, M. Lacković, J. Lalatović, A. S. Mougharbel, U. Kortz, D. Krstić, Curr. Med. Chem., 27 (2020) 362.
[3] A. M. Isakovic, M. B. Čolović, T. Ma, X. Ma, M. Jeremić, M. Gerić, G. Gajski, S. Misirlic-Dencic, U. Kortz, Z. Krstić, J. Biol. Inorg. Chem., 26 (2021) 957.
[4] A. P. Ginsberg, Inorganic Syntheses, John Wiley and Sons, New York, USA, 1990.
[5] P. Skehan, R. Storeng, D. Scudiero, A. Monks, J. McMahon, D. Vistica, J. T. Warren, H. Bokesch, S. Kenney, M. R. Boyd, JNCI-J. Natl. Cancer I., 82 (1990) 1107.

THE EFFECT OF NONIONIC BRIJ 35 MICELLES ON THE IONIZATION OF SOME DRUGS USED IN THE TREATMENT OF ALERGIC REACTIONS

M. Popović-Nikolić [1], S. Oljačić [1] and G. Popović [2]

[1] *University of Belgrade, Faculty of Pharmacy, Department of Pharmaceutical Chemistry, Vojvode Stepe 450, 11221 Belgrade, Serbia. (majap@pharmacy.bg.ac.rs)*
[2] *University of Belgrade, Faculty of Pharmacy, Department of General and Inorganic Chemistry, Vojvode Stepe 450, 11221 Belgrade, Serbia.*

DOI: https://doi.org/10.46793/Phys.Chem24II.615PN

ABSTRACT

The pK_a values of four compounds used in the treatment of allergic reactions, bilastine, cetirizine, montelukast and rupatadine have been potentiometrically determined in micellar solutions of nonionic surfactant Brij 35. Nonionic micelles affected the ionization of investigated compounds from -1.97 to +2.51 pK_a units comparing to "pure" water. The most significant changes in distribution of the equilibrium forms are observed at pH values of biopharmaceutical importance which may indicate on potential interactions with noncharged but polar molecules under the physiological conditions.

INTRODUCTION

The prevalence of asthma and allergy, defined as immunologically mediated hypersensitivity, is increasing. It is estimated that over 20% of the world population suffers from allergic deceases, such as allergic asthma, allergic rhinitis and allergic conjunctivitis, atopic eczema, atopic dermatitis, and anaphylaxis [1]. In this study, we investigated four drugs used in the treatment of allergic disorders, bilastine, cetirizine, rupatadine and montelukast (**Figure 1.**).

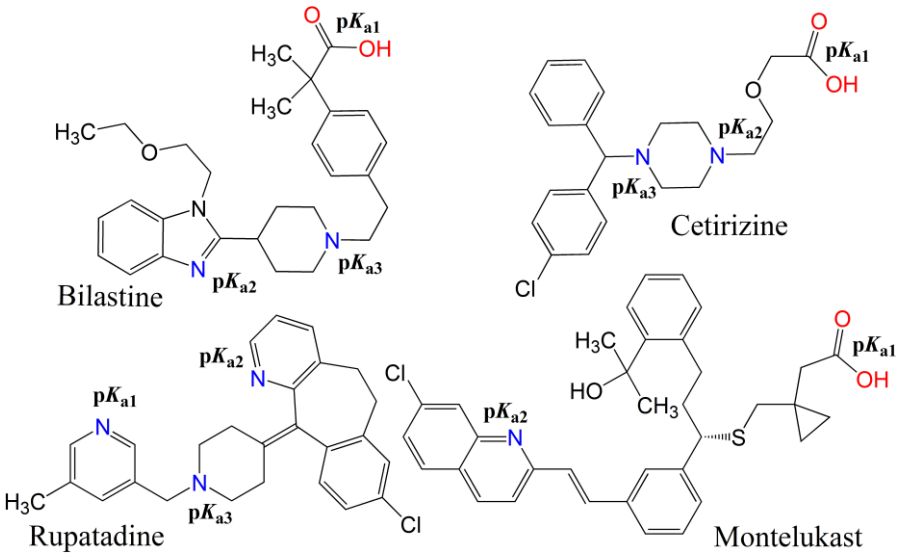


Figure 1. Chemical structures of investigated compounds and their ionization centers.

Bilastine, cetirizine and rupatadine belong to a second generation of histamine H_1 receptor antagonists applied in the therapy of allergic rhinitis and chronic urticaria [2]. Montelukast is a

selective leukotriene receptor antagonist that inhibits the cysteinyl leukotriene CysLT1 receptor, approved for the symptoms of asthma and asthma associated allergic rhinitis. It was shown that a combination therapy against both types of these receptors may provide additive benefit [3]. Taking into account side effects of these drugs due to a blood brain penetration, it is important to consider their phyisco-chemical properties under conditions more similar to physiological, such as micellar solutions of surfactants [4]. Aiming to get better insight into pharmacological behavior and pharmacokinetic properties of bilastine, cetirizine, rupatadine and monetlukast, the protolytic equilibria of these compounds have been investigated in micellar solutions of nonionic surfactant polyoxyethylene (23) lauryl ether (Brij 35), as simplified membrane mimetic system.

METHODS

The examined compounds (bilastine, 2-[4-[2-[4-[1-(2-ethoxyethyl)benzimidazol-2-yl]piperidin-1-yl]ethyl]phenyl]-2-methylpropanoic acid; cetirizine hydrochloride, 2-[2-[4-[(4-chlorophenyl)-phenylmethyl]piperazin-1-yl]ethoxy]acetic acid; montelukast sodium, 2-[1-[[(1*R*)-1-[3-[(*E*)-2-(7-chloroquinolin-2-yl)ethenyl]phenyl]-3-[2-(2-hydroxypropan-2yl)phenyl]propyl]sulfanylmethyl]cyclopropyl]acetate, sodium; rupatadine fumarate, 8-chloro-6,11-di hydro-11-[1-[(5-methyl-3-pyridyl)methyl]-4-piperidylidene]-5H-benzo[5,6]-cyclohepta[1,2-b]pyridine fumarate) were kindly donated from the Medicines and Medical Devices Agency of Serbia (Belgrade, Serbia). Sodium chloride was purchased from Merck (Darmstadt, Germany). Polyoxyethylene (23) lauryl ether (Brij 35) (Sigma-Aldric) was used to prepare micellar solutions. All solutions were prepared with double distilled water. Standard solutions of HCl and CO_2-free NaOH were standardized by potentiometry.

Potentiometric titrations were performed with a titration system 798 MPT Titrino with a combined electrode (LL unitrode Pt1000; Metrohm, Switzerland). Constant temperature of the titrated solutions was maintained using a Huber Polystat CC2 thermostat. Prior to the titration, the electrode was regularly calibrated with standard buffer solutions (pH 4.01, 7.00, and 9.21). All measurements were carried out at 25°C with a continuous magnetic stirring. Constant ionic strength was adjusted to 0.1 M with NaCl. To 40 mL solutions of investigated compounds (5×10^{-4} M), with and without the presence of 10^{-2} M Brij 35, 1.0 mL of standard HCl solution (0.1017 M) was added and titrated with the 0.02 mL aliquots of standard NaOH solution (0.09905 M).

The measured pH values are expressed as pcH values (pcH = -log $[H^+]$), according to the relation pcH = pH - A. The correction factor A was determined experimentally by titrating the standard hydrochloric acid solution at the ionic strength of 0.1 M (NaCl) with the standard NaOH solution for surfactant free and the surfactant supplied solutions [5]. Based on the data obtained by potentiometric titrations, the ionization constants were calculated using a computer program Hyperquad, which enables determination of ionization constants in complex systems containing the overlapped acid-base equilibria [6].

RESULTS AND DISCUSSION

Among investigated compounds, bilastine, cetirizine and rupatadine posses three, while montelukast possess two ionizable centers (**Figure 1.**). From the chemical point of view, bilastine and cetirizine are ampholites, with one acidic (carboxylic group) and two basic groups (aromatic and cyclic aliphatic amines). Montelukast is an ampholite with one acidic (carboxylic group) and one basic group (aromatic amine). Rupatadine represents a triprotic base with two aromatic amines and one cyclic aliphatic amine. By investigating the interactions of drugs with biomembrane mymetic systems, such as micelles, a better insight into the behavior of drugs under physiological conditions could be provided [4]. We have previously shown that the presence of nonionic Brij 35 micelles can significantly shift the protolytic equilbria of pharmacologically active compounds

comparing to "pure" water solutions [7,8]. The pK_a values of bilastine, cetirizine, montelukast and rupatadine determined in 10^{-2} Brij 35 micellar solutions, as well as the difference in a relation to pK_a values obtained in "pure" water (ΔpK_a) under the same conditions, are listed in (**Table 1**).

Table 1. The p*K*a values of investigated compounds potentiometrically obtained with and without the presence of 10^{-2} M Brij 35. ΔpK_a – differences between micelles supplied and micelles free media.

Compound	**Water**			**Brij 35**			**ΔpK_a**		
	pK_{a1}	pK_{a2}	pK_{a3}	pK_{a1}	pK_{a2}	pK_{a3}	pK_{a1}	pK_{a2}	pK_{a3}
Bilastine	5.72	7.86	9.68	4.13	5.89	7.80	-1.59	-1.97	-1.93
Cetirizine	2.48	4.11	6.99	2.38	5.67	9.50	-0.10	+1.56	+2.51
Montelukast	4.07	5.49	-	4.17	5.56	-	+0.10	+0.07	-
Rupatadine	3.45[9]	4.72[9]	6.75[9]	2.53	5.43	5.50	-0.92	+0.71	-1.28

The presence of micelles contributed to the shift in ionization of all investigated ionizable groups, from -1.97 (aromatic amine of bilastine) to +2.51 (cyclic aliphatic amine of cetirizine).

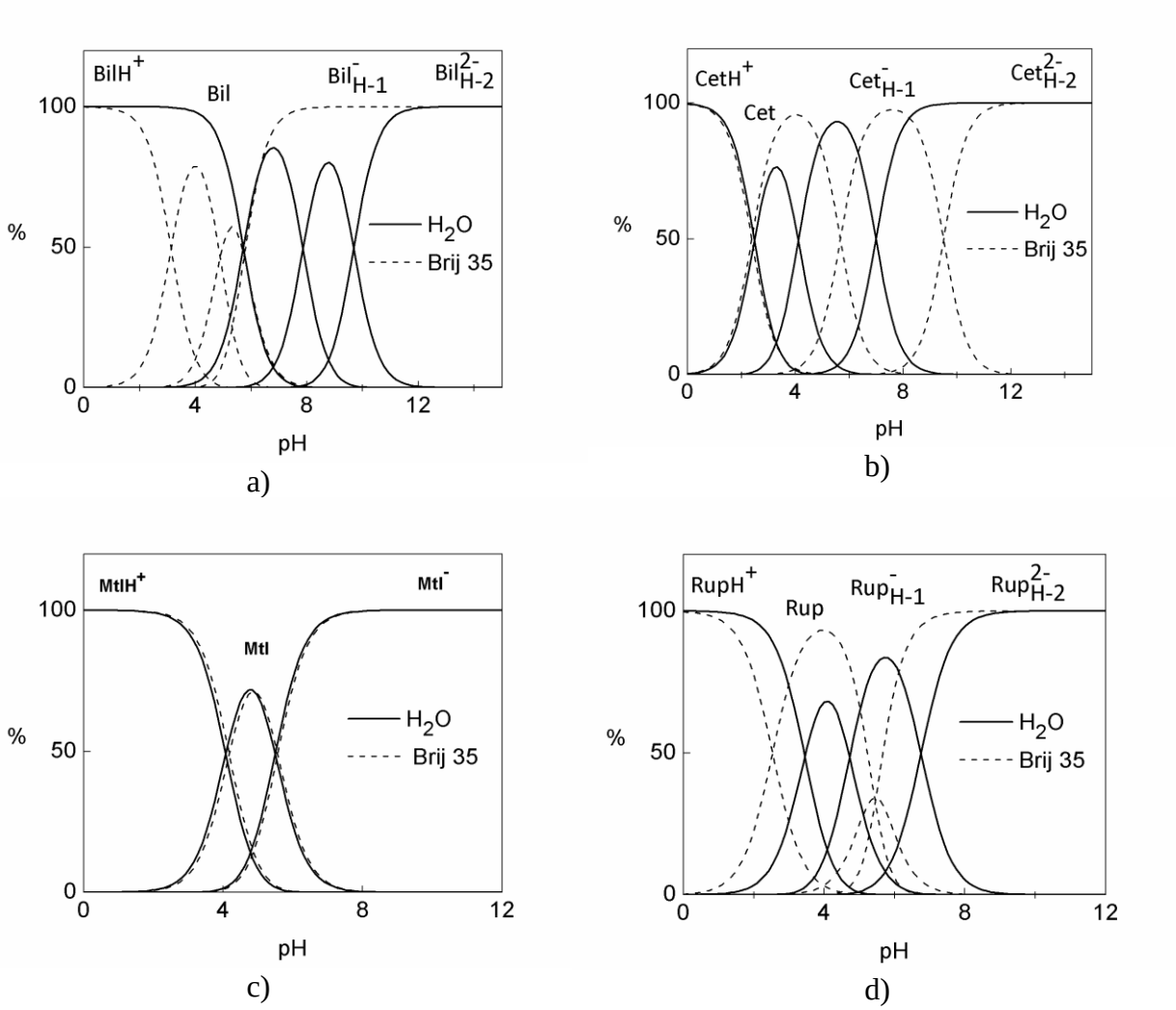


Figure 2. Distribution of the equilibrium forms in water and in the presence of Brij 35 micelles as a function of pH for a) bilastine, b) cetirizine, c) montelukast, d) rupatadine.

The pK_a values of bilastine were the most affected by the presence of nonionic micelles, while the changes are the least pronounced in the case of montelukast. Observed shift in protolytic equilibria in a relation to "pure" water can be mainly explained in terms of properties of Brij 35 micelles. The nonionic micelles do not have a charge and counterions but Brij 35 micelles are characterized by a higher degree of hydration in the palisade layer and allow high water penetration [10]. Changes in ionization mode suggest that the ionizable functional groups of investigated compounds are involved in the interactions with polar oxygen groups and molecules of water in palisade layer of Brij 35 micelles, which include hydrogen bond formation and dipole interactions. Distribution diagrams of investigated compounds indicate on significant shift in ionization in a wide range of pH values including the pH values of biopharmaceutical importance (**Figure 2**). This finding could be considered for potential interactions of investigated compounds with noncharged but polar molecules in physiological conditions which may alter the ionization pattern expected exclusively on the basis of the pK_a values determined in "pure" water.

CONCLUSION

The shift in protolytic equilibria of four drugs applied in the treatment of allergic reactions, bilastine, cetirizine, montelukast and rupatadine (ΔpK_a from -1.97 to +2.51) have been observed in the presence of Brij 35 micelles as a simplified membrane mimicking system. Obtained results indicate that the ionizable groups of invested compounds are involved in interactions with palisade layer of nonionic micelles which can be considered for interactions with biomolecules present in physiological conditions.

Acknowledgment

This research was funded by the Ministry of Science, Technological Development and Innovation, Republic of Serbia through two Grant Agreements with University of Belgrade-Faculty of Pharmacy No 451-03-65/2024-03/200161 and No 451-03-66/2024-03/ 200161. The authors thank the COST Actions CA18240, CA18133 and CA22125 of the European Community for support.

REFERENCES

[1] M. I. Asher, L. García-Marcos, N. E. Pearce, D. P. Strachan, Eur. Resp. J., 56 (2020) 6.
[2] F. E. R. Simons, N. Engl. J. Med., 351 (2004) 2203.
[3] F. Lavorini, A. Matucci, O. Rossi, M. Pistolesi, SKY study investigators, Allergy, 75 (2020) 675.
[4] Fendler, J. H. Chem. Rev., 1987, 87, 877−899.
[5] H. M. Irving, M. G. Miles, L. D. Anal. Chim. Acta, 38 (1967) 475.
[6] P. Gans, A. Sabatini, A. Vacca, Talanta, 43 (1996) 1739.
[7] M. R. Popović-Nikolić, G. V. Popović, D. D. Agbaba, J. Chem. Eng. Data, 62 (2017) 1776.
[8] M. R. Popović-Nikolić, K. M. Nikolić, G. V. Popović, Monatsh. Chem., 154 (2023) 615.
[9] M. R. Popović-Nikolić, G. V. Popović, K. Stojilković, M. Dobrosavljević, D. D. Agbaba, J. Chem. Eng. Data, 63 (2018) 3150.
[10] A. A. Dar, O. A. Chat, J. Phys. Chem. B, 119 (2015) 11632.

UNDERSTANDING THE EFFECT OF DIFFERENTLY CHARGED MICELLES ON THE IONIZATION OF RALOXIFENE

M. Popović-Nikolić [1], and G. Popović [2]

[1] *University of Belgrade, Faculty of Pharmacy, Department of Pharmaceutical Chemistry, Vojvode Stepe 450, 11221 Belgrade, Serbia. (majap@pharmacy.bg.ac.rs)*
[2] *University of Belgrade, Faculty of Pharmacy, Department of General and Inorganic Chemistry, Vojvode Stepe 450, 11221 Belgrade, Serbia.*

DOI: https://doi.org/10.46793/Phys.Chem24II.619PN

ABSTRACT

The protolytic equilibria of raloxifene were investigated in the presence of differently charged and/or polar micelles (CTAB, TX-100, Brij 35). The ionization constants were determined potentiometrically at a constant ionic strength (0.1 M NaCl) and temperature 25°C. In a relation to the pK_a values previously determined in surfactant-free media, the presence of micelles caused a shift from -3.03 pK_a to +3.12 pK_a units. Significant changes in distribution of equilibrium forms at biopharmaceutically important pH values suggest on potential consideration of interactions between raloxifene and molecules present under the physiological conditions.

INTRODUCTION

Raloxifene (**Figure 1.**) is a selective estrogen receptor modulator (SERM) that has been FDA approved for use in the treatment of osteoporosis according to its antiresorptive properties [1]. It is considered as an underutilized treatment option in women with advanced chronic kidney disease and high bone turnover [2]. Considering raloxifene poor aqueous solubility which affects it bioavailability [3], of utmost importance for design and improvement of pharmaceutical formulations is to investigate factors that influence raloxifene solubility and ionization. Applying micellar solutions as simplified biomembrane mimetic systems [4], we have shown that micelles can significantly affect the ionization of pharmacologically active compounds [5,6], which cannot be predicted without experimental investigation for every single compound. After previous determination of the raloxifene protolytic equilibria in "pure" water [7], the aim of this study was to investigate the effects of differently charged surfactants: cationic, (cetyltrimethylammonium bromide, CTAB) and nonionic, (4-octylphenol polyethoxylate, TX-100 and polyoxyethylene (23) lauryl ether, Brij 35) on ionization of raloxifene.

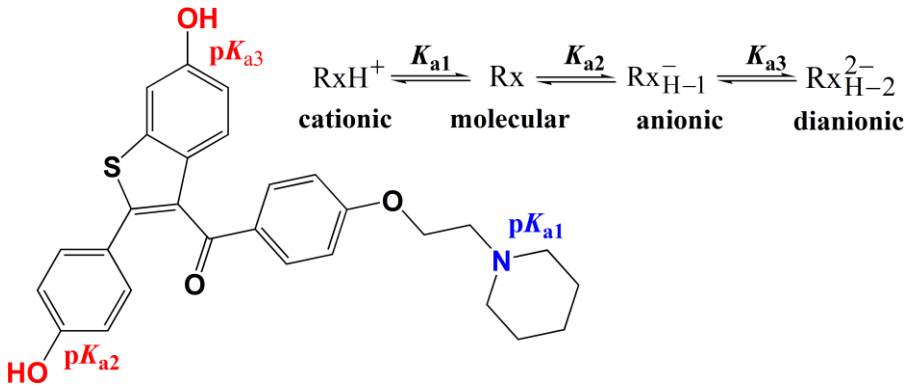


Figure 1. Chemical structure of raloxifene and its ionization profile.

METHODS

For potentiometric determinations Automatic titrator 798 MPT Titrino (Metrohm, Switzerland) with a combined electrode LL unitrode Pt 1000 (Metrohm, Switzerland) was employed. Prior to the titration, the electrode was regularly calibrated with standard buffer solutions (pH 4.01, 7.00, and 9.21). Raloxifene hydrochloride, [6-hydroxy-2-(4-hydroxyphenyl)benzo-[b]thien-3-yl][4-[2-(1-piperidinyl)ethoxy]-phenyl]ethanone hydrochloride, was kindly donated from Hemofarm AD. Polyoxyethylene (23) lauryl ether (Brij 35) (Sigma-Aldrich), CTAB (Acros Organic), and Triton TX-100 (Acros Organic) were used to prepare the micellar solutions. All solutions were prepared with the use of double distilled water. Standard carbonate-free NaOH and HCl solutions were potentiometrically standardized. The constant temperature of the titrated solutions was maintained at 25°C using a Huber Polystat CC2 thermostat.

The ionization constants of raloxifene were determined in the presence of the 10^{-2} M surfactants (Brij 35, CTAB, and TX-100). Constant ionic strength was adjusted to 0.1 M with KNO_3. Solutions of raloxifene hydrochloride in the surfactant-containing media were titrated with the 0.02 mL aliquots of the standard NaOH solution (0.09905 M). In order to prevent dissociation of the phenolic groups and to achieve total protonation of piperidine nitrogen, 0.5 mL of HCl solution (0.1017 M) was added to 40 mL solutions of raloxifene hydrochloride (5×10^{-4} M), and titrated with the 0.02 mL aliquots of standard NaOH solution (0.09905 M).

The measured pH values are expressed as pcH values (pcH = -log $[H^+]$), according to the relation pcH = pH - A. The correction factor A was experimentally determined by titration of the standard HCl solution at the ionic strength of 0.1 M (KNO_3) with the standard NaOH solution. On the basis of the data obtained by potentiometric titrations, the p*K*a values were calculated applying a computer program Hyperquad, which enables determination of equilibrium constants in complex systems containing the overlapped acid-base equilibria.

RESULTS AND DISCUSSION

Chemical structure of raloxifene contains three functional groups that can ionize (**Figure 1.**), one basic group (piperidine nitrogen) and two acidic groups (phenolic hydroxyl group and hydroxyl group attached to benzo-[b]thienyl moiety), which classifying it as an ampholyte.

Table 1. The p*K*a values of raloxifene potentiometrically obtained in the presence of 10^{-2} M surfactants. Δp*K*a - differences in a relation to the p*K*a values obtained in surfactant-free media.

pK_a	**CTAB**	**ΔpK_a**	**TX-100**	**ΔpK_a**	**Brij 35**	**ΔpK_a**
pK_{a1}	5.65±0.02	-1.56	6.48±0.05	-0.73	4.18±0.05	-3.03
pK_{a2}	8.46±0.02	+0.60	10.98±0.05	+3.12	6.59±0.05	-1.27
pK_{a3}	10.69±0.02	+0.72	11.05±0.05	+1.08	9.68±0.05	-0.29

Due to its very low aqueous solubility, in our previous study [7] the apparent pK_a^* values of raloxifene were determined by titration of methanol–water mixtures, (45% - 55% w/w). The pK_a values (pK_{a1} = 7.21 ± 0.02, pK_{a2} = 7.86 ± 0.02, pK_{a3} = 9.97 ± 0.04) which define the ionization in "pure" aqueous media were obtained by extrapolation of the pK_a * values to 0% of methanol. In continuation of research, protolytic equilibria of raloxifene were investigated in the presence of the 3 surfactants, CTAB, TX-100, and Brij 35. Determinations were performed without the use of cosolvent because the surfactants contributed to the increase in raloxifene solubility with their solubilizing effect. The p*K*a values of raloxifene potentiometrically obtained in the presence of 10^{-2} M surfactants, and differences in a relation to the p*K*a values previously determined [7] in surfactant-free media (Δp*K*a) are listed in **Table 1**. The presence of micelles contributed to the shift

in the protolitic equilibria of raloxifene from -3.03 pK_a (the effect of Brij 35 on piperidine nitrogen ionization) to +3.12 pK_a units (the effect of TX-100 on phenolic hydroxyl group ionization), indicating that the ionizable groups of raloxifene are directly involved in the interactions with micelles during solubilization. The shifts in distribution of the equilibrium forms of the raloxifene in the presence of micelles can be clearly seen from the distribution diagrams (**Figure 2**).

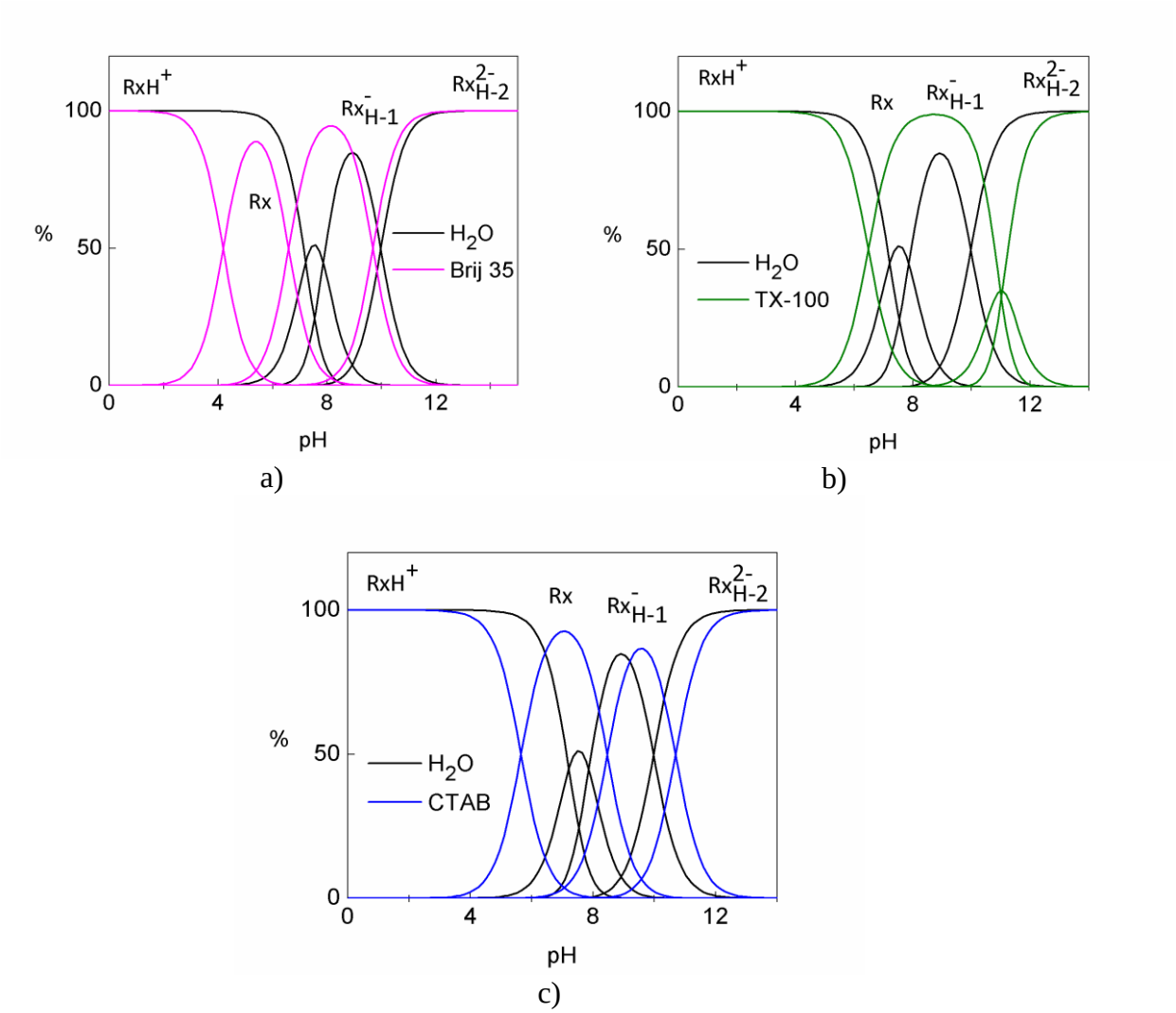


Figure 2. Distribution of the raloxifene equilibrium forms in water and in the presence of a) Brij 35, b) TX-100, c) CTAB micelles as a function of pH.

Based on the equations that describe the ionization of molecules with three ionizable centers, as well as on the basis of the pK_a values experimentally determined with and without the presence of micelles, the percentages of each equilibrium form of raloxifene present in the solution were calculated, at pH values of biopharmaceutical importance, and the values are shown in **Table 2**. The most significant changes in distribution in a relation to "pure" water can be observed at pH values 4.5 and 6.8 which can be found physiologically in different parts of intestinal system. Obtained interactions and the effects of micelles on raloxifene protolytic equilibria suggest on potential interactions, between raloxifene and differently charged and/or polar molecules present in the physiological conditions which could affect its pharmacokinetic properties.

Table 2. Percentage of the equilibrium forms of raloxifene at pH values of biopharmaceutical importance in the surfactant-free and the surfactant-containing media. DA – dianionic, A – anionic, M – molecular, C – cationic.

pH	Water				CTAB				TX-100				Brij 35			
	DA	A	M	C	DA	A	M	C	DA	A	M	C	DA	A	M	C
1.2	0	0	0	100	0	0	0	100	0	0	0	100	0	0	0	100
4.5	0	0	0	100	0	0	7	93	0	0	1	99	0	1	67	32
6.8	0	2	27	70	0	2	92	6	0	0	68	32	0	62	38	0
7.4	0	17	50	32	0	8	91	2	0	0	89	11	0	86	13	0

CONCLUSION

The ionization of raloxifene has been investigated in the presence of differently charged micelles (CTAB, TX-100, Brij 35). Obtained results showed significant shift in protolytic equilibria, from -3.03 to +3.12 pK_a units, suggesting that the ionizable functional groups of raloxifene are directly involved in interactions with surface of micelles. The most pronounce changes in percentage of the equilibrium forms at pH values of biopharmaceutical importance are expressed at pH conditions related to intestinal system indicating that interaction of raloxifene with molecules present in physiological conditions could potentially affect its pharmacokinetic properties.

Acknowledgment

This research was funded by the Ministry of Science, Technological Development and Innovation, Republic of Serbia through two Grant Agreements with University of Belgrade-Faculty of Pharmacy No 451-03-65/2024-03/200161 and No 451-03-66/2024-03/200161. The authors thank the COST Actions CA18240, CA18133 and CA22125 of the European Community for support.

REFERENCES

[1] C. Ginsberg, J. H. Ix, Am. J. Kidney Dis., 79 (2022) 427.
[2] A. Ishani, T. Blackwell, S. A. Jamal, S. R. Cummings, K. E. Ensrud, J. Am. Soc. Nephrol., 19 (2008) 1430.
[3] N. M. Ağardan, Z. Değim, Ş. Yılmaz, L. Altıntaş, T. Topal, J. Drug Deliv. Sci. Technol., 57 (2020) 101612.
[4] J. H. Fendler, Chem. Rev., 87 (1987) 877.
[5] M. R. Popović-Nikolić, G. V. Popović, D. D. Agbaba, J. Chem. Eng. Data, 62 (2017) 1776.
[6] M. R. Popović-Nikolić, G. V. Popović, K. Stojilković, M.Dobrosavljević, D. D. Agbaba, J. Chem. Eng. Data, 63 (2018) 3150.
[7] M. R. Popović-Nikolić, M. Čakar, N. Todorović, K.Nikolić, G. Popović, Chem. Pap., 78 (2024) 4401.

ACID BASE EQUILIBRIA OF OLOPATADINE IN AQUEOUS MEDIA

M. Popović-Nikolić [1], S. Oljačić [1] and G. Popović [2]

[1] *University of Belgrade, Faculty of Pharmacy, Department of Pharmaceutical Chemistry, Vojvode Stepe 450, 11221 Belgrade, Serbia. (majap@pharmacy.bg.ac.rs)*
[2] *University of Belgrade, Faculty of Pharmacy, Department of General and Inorganic Chemistry, Vojvode Stepe 450, 11221 Belgrade, Serbia.*

DOI: https://doi.org/10.46793/Phys.Chem24II.623PN

ABSTRACT

The pK_a values of olopatadine were potentiometrically determined in the presence and in the absence of differently charged micelles, anionic, cationic and nonionic. The ionization of olopatadine has been significantly affected by the interactions of ionizable groups with micelles (ΔpK_a -2.21 to +2.75). All types of micelles caused an increase in the pK_a of carboxylic group (ΔpK_a up to +2.75). Anionic and nonionic micelles contributed to the decrease (ΔpK_a up to -2.21), while cationic micelles caused the increase of the pK_a value of tertiary amino group (ΔpK_a = +0.95). The most significant shift in distribution of equilibrium forms was observed in pH range 4 – 8.

INTRODUCTION

Olopatadine is a selective H_1-receptor antagonist and inhibitor of mast cell degranulation that prevents the release of histamine and other mediators, available for oral, ocular and nasal route of administration. It is used in the treatment of allergic rhinitis and conjunctivitis mainly via intranasal and ocular routes. Comparing to other drugs with the same pharmacological effects, such as desloratadine, clemastine, azelastine, ketotifen and epinastine, by examining surface pressures, activity and interaction with membrane phospholipids, olopatadine showed limited membrane perturbation and limited release of histamine [1]. It is believed that the lack of nonspecific effects of olopatadine on cell membrane integrity contribute to the ocular comfort, which making olopatadine viable alternative to intranasal steroids and oral antihistamines [2]. Olopatadine is generally considered as well tolerated, but some adverse effects may occur especially in the case of nasal application. Examining the physico-chemical properties of drugs contributes to a better insight into their pharmacological and pharmacokinetic behavior, as well as their side effects. However, pharmacokinetic properties may differ from those expected exclusively on the basis of the values of physico-chemical parameters defined in "pure" water. A more reliable assessment may be obtained in determinations under conditions which simulate physiological ones in a simplified manner, such as micellar solutions of surfactants [3].

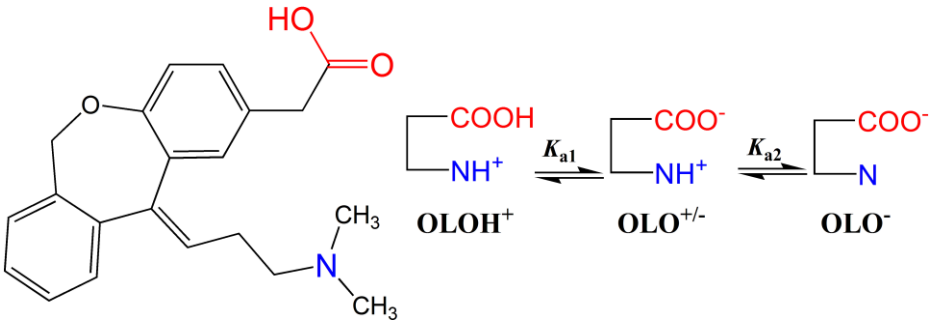


Figure 1. Chemical structure of olopatadine and its ionization profile.

We have previously shown that in micellar solutions, as simplified biomembrane mimicking systems, the ionization of drugs can be significantly changed compared to that of "pure" water [4-6]. Literature survey suggests that there are no data on experimental determination of olopatadine pK_a values. Thus, the aim of this study was to define the ionization of olopatadine in the "pure" water, as well as to determine its pK_a values in micellar solutions of differently charged surfactants: anionic, sodium dodecyl sulfate (SDS); cationic, cetyltrimethylammonium bromide (CTAB); and nonionic, 4-octylphenyl polyethoxylate (TX-100). The pK_a values obtained with and without the micelles, under the same conditions, contributed to evaluation of the effect of surfactants on protolytic equilibria of olopatadine, indicating on potential interactions with molecules in physiological conditions.

METHODS

Automatic titrator 798 MPT Titrino (Metrohm, Switzerland) with a combined electrode LL unitrode Pt 1000 (Metrohm, Switzerland) was used for potentiometric determinations. The electrode was regularly calibrated with standard buffer solutions (pH 4.01, 7.00, and 9.21, Hamilton Duracal, Switzerland). For the interpretation of the measured pH values (pH = − log pH) in terms of the pcH values (pcH = − log c_H), the correction factor A was used. Factor A was determined experimentally by titrating the standard HCl solution at the ionic strength of 0.1 M (NaCl) with the standard NaOH solution, and it was used in the relation pcH = pH − A. The constant temperature of the titrated solutions was maintained at 25°C using a Huber Polystat CC2 thermostat.

Olopatadine hydrochloride, (2-[(11Z)-11-[3-(dimethylamino)propylidene]-6H-benzo[c][1]benzoxepin-2-yl]acetic acid; hydrochloride),was kindly donated from the Medicines and Medical Devices Agency of Serbia (Belgrade, Serbia). SDS (J.T. Baker), CTAB (Acros Organic), and Triton TX-100 (Acros Organic) were used to prepare the micellar solutions. All solutions were prepared with the use of double distilled water. Standard carbonate-free NaOH and HCl solutions were potentiometrically standardized.

To obtain comparable data the ionization constants of olopatadine were determined with and without the presence of the 10^{-2} M surfactants (SDS, CTAB, and TX-100), under the same conditions. Constant ionic strength was adjusted to 0.1 M with NaCl. An addition of the surfactants in the above concentration had no significant effect on the pH of the buffers (under ±0.02 pH units). All surfactants were used at concentrations significantly above their critical micellar concentration (CMC), thus, the influence of the other molecules present in the solution at CMC can be neglected. Solutions of olopatadine hydrochloride in the surfactant-free and surfactant-containing media were titrated with the 0.02 mL aliquots of the standard NaOH solution (0.09905 M). In order to prevent dissociation of the carboxylic group and to achieve total protonation of tertiary amino group, 1 mL of standard HCl solution (0.1017 M) was added to 40 mL solutions of olopatadine hydrochloride (5×10^{-4} M), and titrated with the 0.02 mL aliquots of standard NaOH solution (0.09905 M).

The experimental data obtained by potentiometric titration were evaluated with use of the computer program Hyperquad [7].

RESULTS AND DISCUSSION

Olopatadine can be chemically considered as an ampholite with carboxylic group as an acidic ionizable center, and tertiary amino group as a basic ionizable center (**Figure 1.**) The pK_a values determined in "pure" water for carboxylic group (pK_{a1} = 4.01±0.06), and for tertiary amine (pK_{a2} = 9.61±0.06) are in a relatively good agreement with the values reported in the literature [8,9].

However, there are no sufficient data referred on experimental conditions of determinations, or only one value was reported [10,11] which does not provide insight real into the ionization profile

of the compound and all the equilibrium forms present in the solution, reflecting only some average ionization of the olopatadine.

Table 1. The pK_a values of olopatadine potentiometrically obtained in the presence of 10^{-2} M surfactants. ΔpK_a - differences in a relation to the pK_a values obtained in surfactant-free media.

pK_a	**Water**	**SDS**	**ΔpK_a**	**CTAB**	**ΔpK_a**	**TX-100**	**ΔpK_a**
pK_{a1}	4.01±0.06	4.46±0.06	+0.45	6.76±0.05	+2.75	6.02±0.05	+2.01
pK_{a2}	9.61±0.06	7.40±0.06	-2.21	10.56±0.05	+0.95	9.10±0.05	-0.51

After defining the ionization in the "pure" water, the values were also determined in micellar solutions of differently charged surfactants, anionic SDS, cationic CTAB, and nonionic TX-100. The results are listed in **Table 1** together with the ΔpK_a values which represent differences in a relation to the pK_a values determined in "pure" water. All applied surfactants caused a shift in the protolytic equilibria of olopatadine, from -2.21 to +2.75 pK_a units. Cationic micelles CTAB expressed the stronges effect on olopatadine ionization. The presence of all used micelles contributed to the decreased acidity of the carboxyl group (ΔpK_a +0.45 to +2.75). Anionic and nonionic micelles contributed to the decrease of basicity (ΔpK_a -0.51 to -2.21), while cationic micelles caused the increase of basicity (ΔpK_a +0.95) of the tertiary amino group.

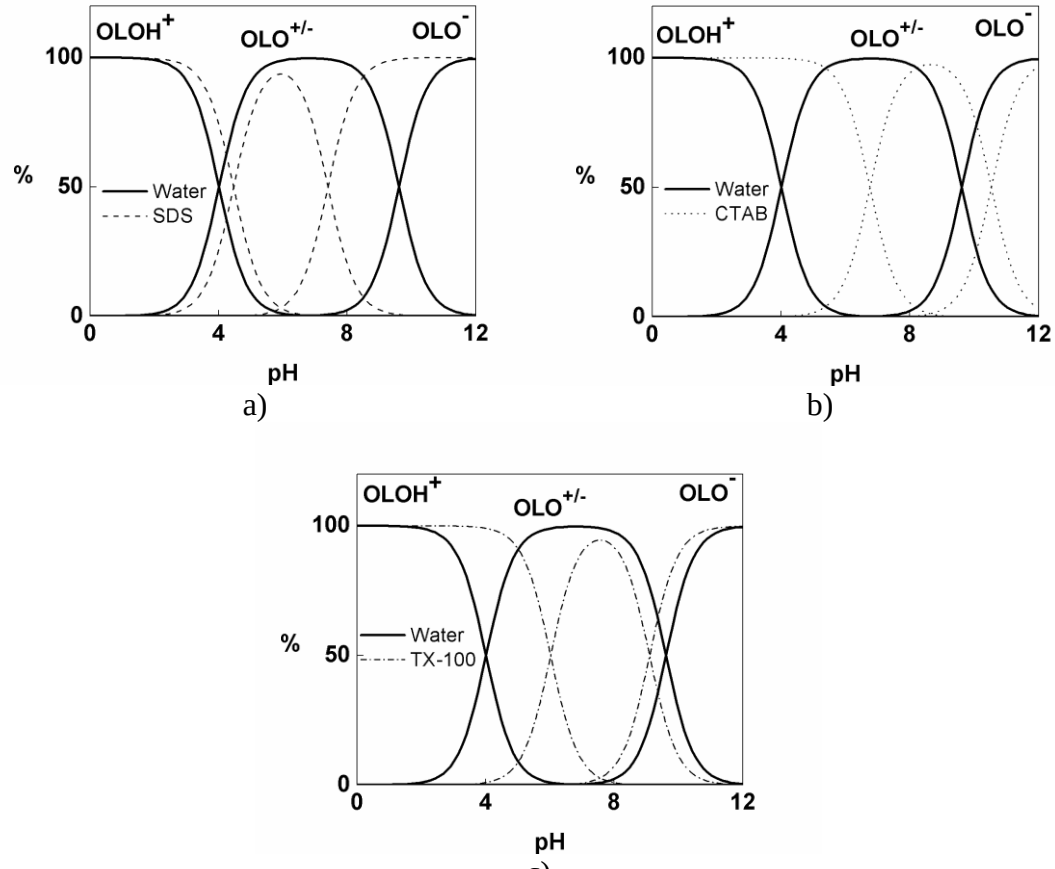


Figure 2. Distribution of the olopatadine equilibrium forms in water and in the presence of a) SDS, b) CTAB, c) TX-100 micelles as a function of pH.

The shift in protolytic equilibria indicate on different type of interactions between olopatadine ionizable groups and polar or charged surface of micelles [6]. In the case of ionic micelles (SDS and CTAB), electrostatic forces are predominant, while in the case of nonionic micelles (TX-100), hydrogen bonds forming in the outer, palisade layer may contribute to ionization changes. The influence of micelles can be clearly seen from the distribution diagrams of equilibrium forms as a function of pH (**Figure 2.**). The most significant changes in a relation to distribution profile in "pure" water are observed in a pH range 4 – 8 which includes pH values considered as biopharmaceutically important. Olopatadine in pharmaceutical formulations is mainly used in the form of eye drops, which need to meet certain pH requirements to maintain compatibility with the eye. Thus, the changes in the ionization of olopatadine caused by interactions with micelles may be potentially considered for physiological conditions, in the terms of side effects at the site of application.

CONCLUSION

Significant shift in protolytic equilibria of olopatadine (ΔpK_a -2.21 to +2.75) was observed in the presence of micelles. All types of micelles caused an increase in the pK_a value of carboxylic group, while the shift of protolytic equilibria in different directions was observed in the case of tertiary amino group. Anionic and nonionic micelles contributed to the decrease, while cationic micelles caused the increase of the pK_a value of tertiary amino group. Obtain results suggest that potential interactions of olopatadine with biomolecules at the site of application, can significantly change its ionization pattern, expected exclusively on the basis of the pK_a values determined in "pure" water.

Acknowledgment

This research was funded by the Ministry of Science, Technological Development and Innovation, Republic of Serbia through two Grant Agreements with University of Belgrade-Faculty of Pharmacy No 451-03-65/2024-03/200161 and No 451-03-66/2024-03/ 200161. The authors thank the COST Actions CA18240, CA18133 and CA22125 of the European Community for support.

REFERENCES

[1] M. B. Abelson, Expert Opin. Pharmacother., 5 (2004) 1979.
[2] A. S.Nickels, V. Dimov, R. Wolf, Expert Opin. Drug Metab. Toxicol. 7 (2011) 1593.
[3] J. H. Fendler, Chem. Rev., 87 (1987) 877.
[4] M. R. Popović-Nikolić, G. V. Popović, D. D. Agbaba, J. Chem. Eng. Data, 62 (2017) 1776.
[5] M. R. Popović-Nikolić, G. V. Popović, K. Stojilković, M.Dobrosavljević, D. D. Agbaba, Acid–base equilibria of rupatadine fumarate in aqueous media. J. Chem. Eng. Data, 63 (2018) 3150.
[6] M. R. Popović, G. V. Popović, D. D. Agbaba, J. Chem. Eng. Data, 58 (2013) 2567.
[7] P. Gans, A. Sabatini, A. Vacca, Talanta, 43, (1996) 1739.
[8] A. A.Mahajan, K. Mohanraj, S. Kale, A. K. Thaker, J. Liq. Chromatogr. Relat. Technol., 36 (2013) 1881.
[9] S. F. Hammad, M. M. Rady, S. F. El-Malla, Sci. Rep., 13 (2023) 18143.
[10] T. Güray, T. Turan, M. Tunçel, U. D. Uysal, J. AOAC Int., 100 (2017) 206.
[11] P. K. Basniwal, J. Deepti, Turk. J. Pharm. Sci., 16 (2019) 392.

INVESTIGATION OF THE SUBSTITUTION EFFECT ON THE LOGP$_{O/W}$ OF BIOLOGICALLY ACTIVE *N*-ARYL-TETRAHYDROISOQUINOLINE DERIVATIVES USING RP-UPLC METHOD

D. Jovanović [1], A. Filipović [2], Z. Džambaski[2], B. P. Bondžić [2] and A.M. Bondžić* [1]

[1] University of Belgrade, VINČA Institute of Nuclear Sciences, Mike Petrovića Alasa 12-14, Chemistry, Technology and Metallurgy,11351 Belgrade, Serbia. (aleksandrab@vin.bg.ac.rs)
[2] University of Belgrade-Institute of Chemistry, Technology and Metallurgy, National Institute of the Republic of Serbia, Njegoševa 12, 11000 Belgrade, Serbia.

DOI: https://doi.org/10.46793/Phys.Chem24II.627J

ABSTRACT
Lipophilicity expressed by the n-octanol/water partition coefficient, logP$_{o/w}$, is one of the physicochemical properties of the drug that determines its solubility, the ability to penetrate through cell barriers, and the probability of transport to the molecular target. It also affects pharmacokinetic processes such as adsorption, distribution, metabolism and excretion of a drug. The aim of this study was to evaluate the influence of substitution with different functional groups of biologically active *N*-aryl-tetrahydroisoquinoline derivatives (THIQs) on the logP$_{o/w}$. The logP$_{o/w}$ for a set of six *N*-aryl-tetrahydroisoquinoline derivatives was estimated using reversed-phase ultra performance liquid chromatography (RP-UPLC) technique using a C18 column as a stationary phase and water/acetonitrile mixtures as mobile phases.

INTRODUCTION
Tetrahydroisoquinoline derivatives (THIQs) have been widely used in medicinal chemistry due to their various biological functions, including anti-inflammatory, sedative, and anticancer properties. Recent publications indicate that these compounds might be considered as promising candidate drugs in the treatment of Alzheimer's disease, if they fulfill two important criteria: appropriate values of lipophilicity and ability to pass the blood-brain barrier [1]. Lipophilicity is an important feature of the molecules in the pharmaceutical, biochemical, and medical chemistry fields. Therefore, lipophilicity is regarded as the reference parameter for predicting the biological activity of potential drugs and it has to be evaluated during the early stage of drug discovery. Physico-chemically, lipophilicity is described as the logarithmic n-octanol-water partition coefficient (logP$_{o/w}$) that is characteristic of a given chemical. This parameter has been used in structure–activity relationship studies. To overcome the limitations of traditional methods like the shake-flask technique, which are time-consuming and labor-intensive as well as given the large number of compounds being investigated, high-throughput strategies with greater accuracy have been developed. For this purpose, chromatographic approaches, based on the correlation between partition coefficients (logP$_{o/w}$) and retention factors (logk), gained traction in pharmaceutical research, as they offer speed and low sample consumption [2].

In this work, logP$_{o/w}$ values of six *N*-aryl-THIQ compounds were determined using RP-UPLC combined with UV/Vis detector. RP-UPLC is a method of choice because of its high accuracy, low sample consumption and its ability to provide reliable measurements even of a complex mixture of compounds.

METHODS

The partition coefficient, $logP_{o/w}$, of the selected THIQs compounds were determined using a Waters ACQUITY UPLC system equipped with a tunable UV detector (from 200 to 500 nm) controlled by the Empower 3 software. The column used for $logP_{o/w}$ determinations was the ACQUITY UPLC BEH C18 column with the dimensions 1.7 µm × 100 mm × 2.1 mm (Waters). The measurements were performed in the isocratic mode. The mobile phase composition was a different percentage of acetonitrile (in the range 64–91%, v/v) and H_2O. The wavelength of the optical detection was 254 nm, and the retention times for every examined compound under certain experimental conditions were determined.

RESULTS AND DISCUSSION

As an indirect measurement of lipophilicity, RP-UPLC does not directly provide a partition coefficient but rather a lipophilicity index which is correlated with the partition coefficient. Here, the lipophilicity index is obtained based on the assumption that compounds are retained in proportion to their nonaqueous-aqueous partition coefficient. Therefore, hydrophilic compounds will be eluted first and lipophilic compounds last, so the lipophilicity index could be expressed by the retention factor k [2]. In order to experimentally evaluate $logP_{o/w}$ values of selected THIQs, the UPLC method was applied using acetonitrile ACN as an organic modifier in isocratic mode (general structure of investigated THIQs is presented in **Fig. 1**). First, the retention factor of selected standards compounds, k, was determined for different percentages of ACN in the mobile phases using equation $k = {(t_r - t_0)}/{t_0}$, where t_r is the retention time of the compound and t_0 is the column dead time (the retention time of an unretained solute). The chosen standard compounds are those with similar structures as the investigated one's and their structures and known $logP_{o/w}$ values are presented in **Table 1**. t_0 is assessed by injecting a NaBr (20 mg/L), which is unretained by the column and recording its retention time using mobile phase composition with different percentage of ACN. The column dead time, t_0, represents the average value of the retention times for NaBr, that were obtained for different percentage of ACN in the mobile phase. The chromatograms obtained for NaBr using different mobile phase compositions (different ratios H_2O/ACN) are presented in **Fig. 2a**. The calculated t_0 was 0.808 min. The retention factors of selected standard compounds were measured at four different mobile phase compositions differing by percentages of acetonitrile (optimized according to the lipophilicity of the investigated compound) and $logK_w$ values (the retention factor for a pure aqueous eluent) are obtained by linear extrapolation of graph logk = f (% of ACN in mobile phase). The obtained K_w values for selected standard compounds are presented in **Table 1.** To determine $logP_{o/w}$ values of investigated compounds, experimentally obtained $logK_w$ for standard compounds are correlated with their known $logP_{o/w}$ (**Fig. 2b**).
Obtained linear plot obeys the equation:

$$logP_{o/w} = 1.065+0.770logK_w$$

where $logK_w$ is the retention factor for a pure aqueous eluent of the investigated compound. This equation is further used for the determination of $logP_{o/w}$ values of investigated THIQs.

Before the determination of $logP_{o/w}$ values of selected THIQs, their $logK_w$ values were determined in the same way as for standard compounds, using different compositions of ACN-water mixture in the mobile phase, and then extrapolated to 0% of ACN. The plot of logk at different ACN percentages in the mobile phase for biologically active THIQs is presented in **Fig. 3** Obtained logP values are presented in **Table 1**. As we can observe from the results presented in **Table 1**, compound **1** has a logP value of 3.68 while the introduction of a methyl group in the *para* position of the phenyl ring (compound **2**) does not significantly change the lipophilicity of the compound.

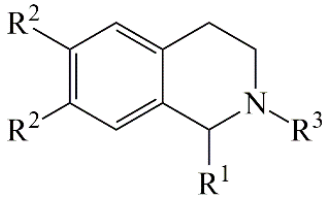
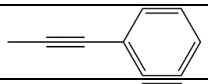
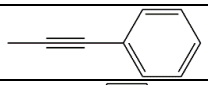
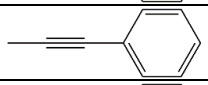
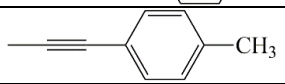
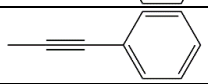
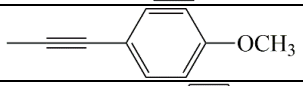
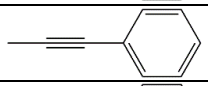
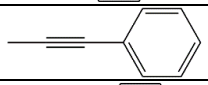
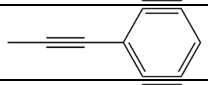
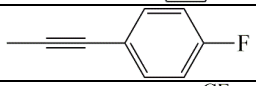
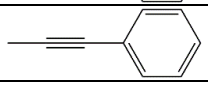
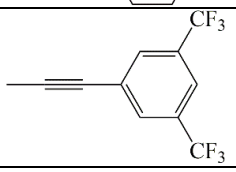
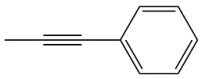


Figure 1. General structure of investigated compounds.

Table 1. The structures of selected standard and investigated compounds, their previously known/experimentally determined $logP_{o/w}$ values and determined $logK_w$ using the RP-UPLC. method.

Compound	R^1	R^2	R^3	$logK_w$	$logP_{o/w}$
S1	-H	-OCH_3	-H	0.097	1.14
S2	-H	-H	-H	0.435	1.40
S3	-H	-H		2.915	3.31
1		-H		3.39	3.68
2		-H		3.30	3.61
3		-H		2.93	3.32
4		-OCH_3		2.42	2.93
5		-OCH_3		2.53	3.02
6		-H		4.63	4.63

On the other hand, the methoxy group (compound **3**) in the same position of the phenyl ring led to a slight decrease in the compound's lipophilicity. By comparing logP values of compound **1** and compound **4,** it is evident that two methoxy groups at the C6 and C7 positions of the THIQ scaffold (compound **4**), significantly decrease the compound's lipophilicity. If we compare the logP values of compounds **1**, **3**, and **4**, it is evident that each of the methoxy groups can decrease the logP value for an average of 0.3 units (**Table 1**). Therefore, *N*-aryl-THIQs derivates with appropriate lipophilicity can be designed by varying the number of methoxy groups present in the structure. Similar results are obtained for the substitution of *para* hydrogen by fluoro atom. The results indicate that the introduction of one fluoro atom, compound **5**, to the *para* position of the phenyl ring of compound **4** does not significantly affect its lipophilicity, while the substitution with two trifluoromethyl groups in the *meta* position of the phenyl ring, (compound **6**) significantly increases lipophilicity.

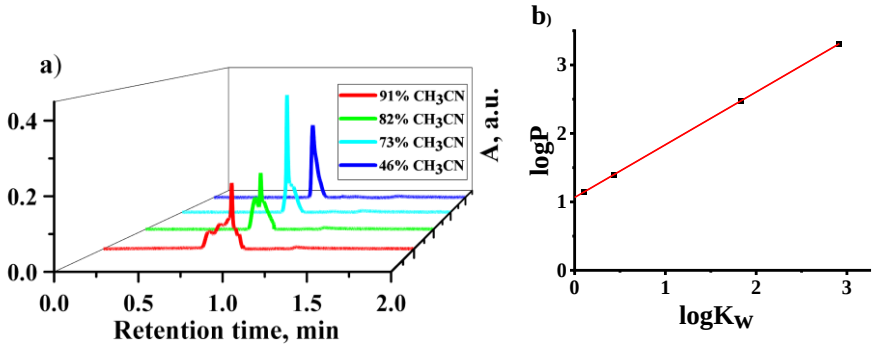


Figure 2. a) UPLC-DAD chromatogram of the 20 mg/L NaBr, obtained for different ACN-water mixtures (as mobile phase) containing a volume fraction of ACN in the range 64–91% volume fraction; **b)** Plot of $logP_{o/w}$ *vs.* $logK_w$ obtained for chosen standard compounds.

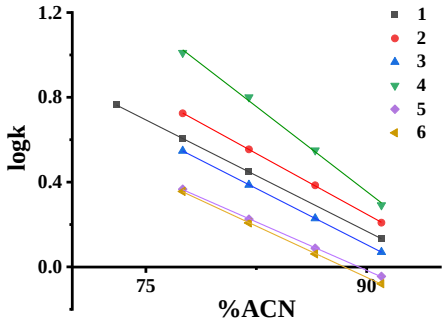


Figure 3. Plot of logk *vs*. the percentage of ACN (% ACN).

CONCLUSION

In summary, the RP-UPLC method proved to be a fast and efficient means of determining the $logP_{o/w}$ value. Obtained results indicate that by varying the number and type of substituents, *N*-aryl-THIQs derivates with appropriate lipophilicity can be designed. The introduction of methoxy group leads to a decrease in the logP values of investigated THIQs, and this decrease does not depend on the position of the substituent, but only on the number of introduced methoxy groups. On the other hand, the introduction of a trifluoromethyl group significantly increased lipophilicity. These findings emphasize the importance of types of substituents in modulating lipophilic properties, a property that is crucial for drug development.

Acknowledgment

This work was supported by the Ministry of Science, Technological Development, and Innovation of the Republic of Serbia (Agreement No. 451-03-66/2024-03/200017 and 451-03-66/2024-03/200026).

REFERENCES

[1] D. Jovanović, A. Filipović, G. Janjić, T. Lazarević-Pašti, Z. Džambaski, B. P. Bondžić, A. M. Bondžić, Int J Mol Sci, 25 (2024) 1033.
[2] J. X. Soares, Á. Santos, C. Fernandes, M. M. M. Pinto, Chemosensors, 10 (2022) 340.

INVESTIGATION OF THE CHELATING ABILITY OF TETRAHYDROISOQUINOLINE-DERIVATIZED QUERCETIN TOWARDS BIOMETALS RELATED TO ALZHEIMER'S DISEASE

M. Vučkovski [1], A. Filipović [2], Z. Džambaski[2], B. Bondžić [2] and A. M. Bondžić*[1]

[1]Vinča Institute of Nuclear Sciences, National Institute of the Republic of Serbia, University of Belgrade, P.O. Box 522, 11000 Belgrade, Serbia. (aleksandrab@vin.bg.ac.rs)
[2] University of Belgrade-Institute of Chemistry, Technology and Metallurgy, National Institute of the Republic of Serbia, Njegoševa 12, 11000 Belgrade, Serbia.

DOI: https://doi.org/10.46793/Phys.Chem24II.631V

ABSTRACT

The potential therapeutic applications of metal chelation in the treatment of Alzheimer's disease have attracted significant attention due to the involvement of metal ion dysregulation in the pathology of the disease. This study investigates the chelation properties of a novel compound, tetrahydroisoquinoline-derivatized quercetin, THIQ-Q, with Cu^{2+}, Zn^{2+}, and Fe^{2+} ions, aiming to evaluate its efficacy as a potential treatment for Alzheimer's disease. Using UV/Vis spectroscopy we analysed the binding interactions and stoichiometry of the compound with these metal ions. Obtained results indicate that the newly synthesized compound, THIQ-Q, forms 2:1 complex with Cu^{2+} and Zn^{2+} while 1:1 complex is formed with Fe^{2+}, which indicate its potential as a therapeutic agent in managing metal ion dysregulation in Alzheimer's disease.

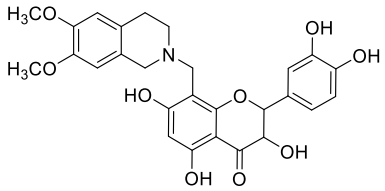
INTRODUCTION

Despite extensive research efforts last several decades, effective drugs for treating Alzheimer's disease (AD) have not yet been discovered. Post-mortem analyses of amyloid plaques have demonstrated a significant link between AD and redox metal dysregulation, showing that levels of copper, iron, and zinc are elevated by 5.7, 2.8, and 3.1 times, respectively, compared to normal brains. Using metal chelators to normalize metal ion homeostasis has been considered a promising strategy to reduce the redox stress lethal to neurons. However, only a few chelators have been developed through rational design to create drugs with a safe profile that can cross the blood-brain barrier after oral administration. [1]

Flavonoids are a diverse group of secondary metabolites found in various natural compounds, known for their wide range of biological effects. Quercetin (Q) is one of the most well-known and widely available flavonoids. Experimental studies have shown that it offers a variety of health benefits, such as cardiovascular protection, anticancer activity, antiulcer effects, as well as antiallergic, antiviral, and anti-inflammatory properties. Many of these effects are linked to its antioxidant capacity, which involves scavenging free radical species and synergistic interactions with enzymes and natural antioxidants in the body. Antioxidant mechanism involves certain compounds' capacity to chelate transition metal ions, particularly iron and copper. This forms stable complexes that, by trapping metals, hinder their involvement in the generation of free radicals. Metal-chelating compounds eliminate metals and can modify their redox potentials, making them inactive. [2] However, despite the promising therapeutic potential of quercetin, its application in treating central nervous system (CNS) disorders faces challenges such as low water solubility, limited bioavailability, rapid metabolism, instability, and difficulty crossing the blood-brain barrier (BBB). Tetrahydroisoquinolines (THIQs) are a versatile class of compounds with a wide range of medical applications. Compounds with this scaffold exhibit anti-inflammatory activity, can act as

ligands for CNS receptors, and possess antitumor properties. Additionally, hybrid compounds containing a tetrahydroisoquinoline moiety demonstrate strong neuroprotective and anti-Alzheimer effects. [3]

In this study, we evaluated chelating ability of compound obtained by modifying quercetin at position 8 (resorcinol ring) with 6,7-dimethoxy-tetrahydroisoquinoline, through the Mannich reaction of quercetin with the iminium ion derived from formaldehyde and the 6,7-dimethoxy-1,2,3,4-tetrahydroisoquinolines structure.[4] The newly obtained compound (**Scheme 1**) possesses improved lipophilicity and therefore improved potential for therapy in AD compared to Q (unpublished results). With this in mind, the chelation ability of this THIQ-Q compound towards biometal ions crucial in AD (Cu^{2+}, Fe^{2+}, and Zn^{2+}) was evaluated.



Scheme 1. The structure of the synthesized compound, THIQ-Q.

METHODS

The absorption spectra were recorded on UV/Vis spectrophotometer (Lambda 35, Perkin Elmer) in the wavelength range 230-550 nm, at room temperature. Quartz cuvettes of 10 mm optical path length were used. Quercetin, $ZnCl_2$, $CuCl_2$ x $2H_2O$, $FeSO_4$, dimethyl sulfoxide (DMSO), ethanol and methanol were obtained from Sigma-Aldrich, Germany. Tetrahydroisoquinoline modified quercetin (THIQ-Q) was synthesized following previously published procedure [4]. The stock solution of THIQ-Q was prepared in DMSO; concentration 1×10^{-2} M. Quercetin stock solution 2×10^{-2} M was prepared in methanol. $ZnCl_2$, $CuCl_2$ and $FeSO_4$ stock solutions were prepared in deionized water, in final concentration of 1×10^{-2} M. The chelation effect of THIQ-Q was evaluated by following changes in its absorption spectrum immediately and 30 minutes after the addition of metal ion, at room temperature. The stoichiometric binding of metals ions was determined using the molar ratio method. [5] To prepare all solutions, THIQ-Q was initially dissolved in ethanol to ensure that the final concentration of THIQ-Q, after the addition of the metal ion, would be 5×10^{-5} M in each solution.

RESULTS AND DISCUSSION

Biometal ions are believed to have significant implications in AD. It was also shown that Fe^{2+}, Zn^{2+} and particularly Cu^{2+} ion, enhance the aggregation of Aβ contributing to neurotoxicity in individuals with AD. Keeping this in the mind as well as neuroprotective ability of Q, the aim of this study was to evaluate the ability of newly synthesized compound THIQ-Q to chelate biometal ions, Cu^{2+}, Fe^{2+}, and Zn^{2+}. The UV/Vis spectrum of 5×10^{-5} M THIQ-Q in ethanol possesses absorption maximum at 378 nm (graph 1, Fig. 1). Appearance of new absorption maxima were observed after addition of 1×10^{-4} M of metal ion at 436nm, 433nm, and 439nm for Cu^{2+}, Zn^{2+} and Fe^{2+} respectively, confirming formation of complexes of THIQ-Q with these metal ions (Fig. 1). To determine binding stoichiometry, molar ratio method was applied. The absorption spectra of THIQ-Q in the presence of increasing concentration of metal ions (from 0 to 1.5×10^{-4} M). are presented in Fig. 2. All the presented spectra were collected 30 minutes after mixing to guarantee that the reaction is complete.

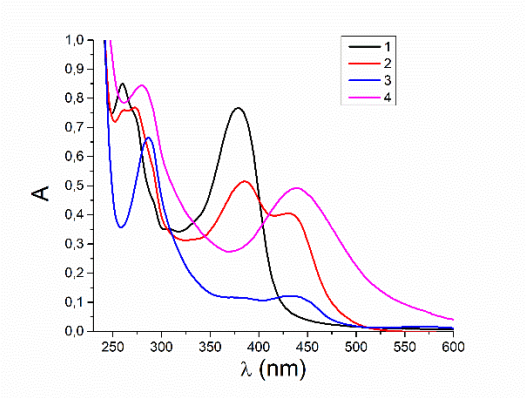


Figure 1. UV/Vis spectra of 5×10^{-5} M THIQ-Q (**1**) and THIQ-Q in the presence of different metal ions: Zn^{2+} (**2**), Cu^{2+} (**3**) and Fe^{2+} (**4**) recorded immediately after ions addition (t = 0 min) in 1:2 THIQ-Q:M ratio.

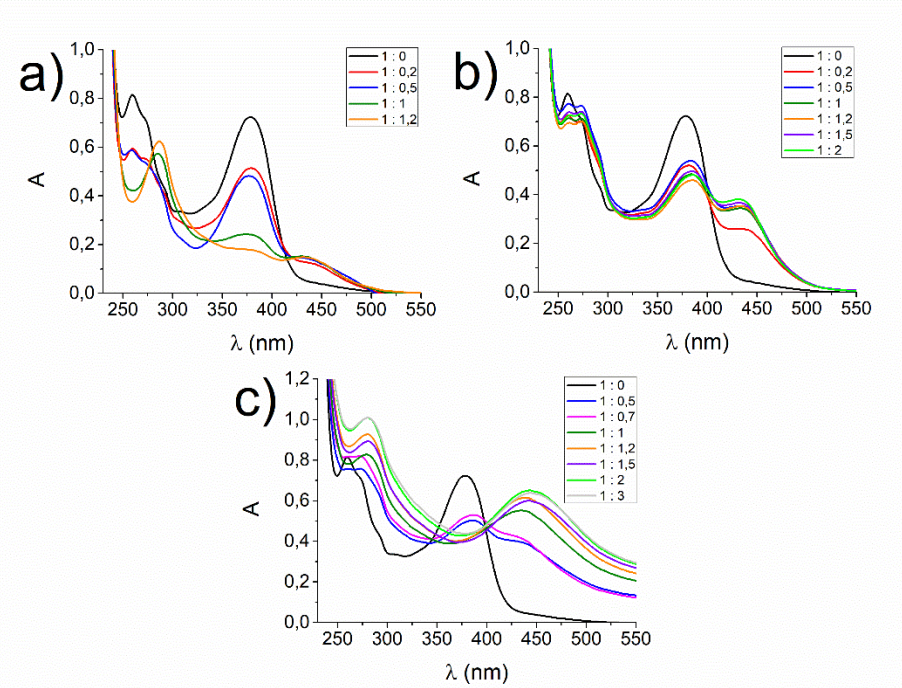


Figure 2. The UV/Vis spectra of 5×10^{-5} M THIQ-Q in the presence of different metal ions **a)** Cu^{2+}, **b)** Zn^{2+}, **c)** Fe^{2+} recorded 30 minutes after mixing THIQ-Q and metal ion solutions. The THIQ-Q to metal ion ratios were varied from 1:0 to 1:3 corresponding to metal ion concentrations ranging from 0 to 1.5×10^{-4} M.

The change in absorption $\left(\Delta A = A_{THIQ\text{-}Q\text{-}M^{2+}} - A_{THIQ\text{-}Q}\right)$ at absorption maxima of formed complex as the function of the $C_{M^{2+}}/C_{THIQ\text{-}Q}$ ratio for each metal ion, is presented in the Fig. 3. This graph enables determination of the binding ratio between THIQ-Q and metal ions. Based on the intersection of the curves on the graph at certain ration, the binding stoichiometry was determined. Analysis of these intersections indicates that the binding stoichiometry for both Cu^{2+} and Zn^{2+} is 2, indicating that one Cu^{2+} or Zn^{2+} coordinates two THIQ-Q. On the other hand, obtained results for Fe^{2+} indicate that only one Fe^{2+} ion could be bound to THIQ-Q. Obtained results are in accordance

with literature data where quercetin is able to form a 1:1 complex with Fe^{2+} [2], and to form a 1:2 complex with Cu^{2+} and Zn^{2+} [6].

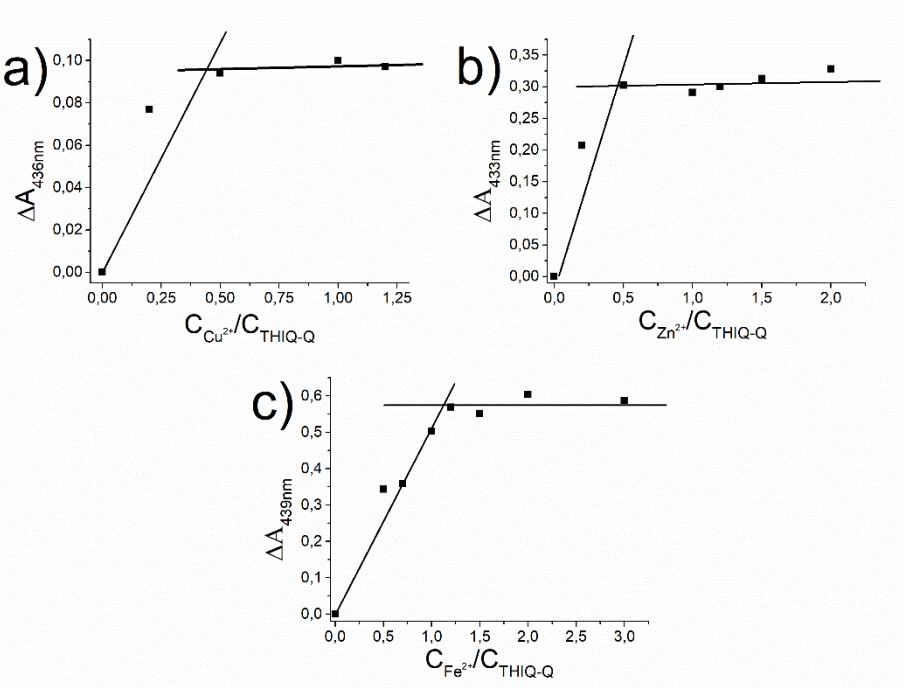


Figure 3. $\Delta A=f(C_{M^{2+}}/C_{THIQ\text{-}Q})$ at absorption maxima of complexes for different metal ions: **a)** Cu^{2+}, **b)** Zn^{2+} and **c)** Fe^{2+}.

CONCLUSION

Based on the above presented results it can be concluded that tetrahydroisoquinoline derivatized quercetin, THIQ-Q, kept its chelating ability towards biometal ions, Cu^{2+}, Zn^{2+}, and Fe^{2+}. These metal ions are associated with accumulation of β-amyloid plaques in AD, indicating that this compound could be promising candidates for the treatment of AD. Obtained results indicate that the binding stoichiometry of selected derivate is the same as for the quercetin where metal ions bind dominantly to the oxygen atoms associated with the 3-hydroxy and 4-oxo groups, or for those linked to the 5-hydroxy and 4-oxo groups.

Acknowledgment

This work was supported by the Ministry of Science, Technological Development, and Innovation of the Republic of Serbia (Agreement No. 451-03-66/2024-03/200017 and 451-03-66/2024-03/200026).

REFERENCES

[1] Y. Liu, M. Nguyen, A. Robert, B. Meunier, Acc. Chem. Res., 52 (2019) 2026–2035.
[2] M. Leopoldini, N. Russo, S. Chiodo, M. Toscano, J. Agric. Food Chem., 54 (2006) 6343–6351.
[3] D. Jovanović, A. Filipović, G. Janjić, T. Lazarević-Pašti, Z. Džambaski, B. P. Bondžić, A. M. Bondžić, Int. J. Mol. Sci., 25 (2024) 1033.
[4] Sh. N. Zhurakulov, D. A. Narbutaeva, A. M. Karakulova, F. M. Tursunkhodzhaeva, V. I. Vinogradova, Chem. Nat. Compd., 59 (2023) 655–661.
[5] A. Moncomble, C. Falantin, J. P. Cornard, J. Phys. Chem. B, 122 (2018) 8943–8951
[6] Y. Liu and M. Guo, Molecules, 20 (2015) 8583–8594**.**

SYNTHESIS, CHARACTERIZATION AND *IN VIVO* BEHAVIOR OF ^{177}Lu-DMSA-SPIONs

D. Stanković[1*], M. Radović[1], M. Mirković[1], Z. Milanović[1], A. Stanković [2], M. Mijović[3], M. Ognjanović[1], D. Janković[1], A. Vukadinović[1], B. Antić[1], S. Vranješ-Đurić[1], M. Savić[4] and Ž. Prijović[1]

[1] *„VINČA" Institute of Nuclear Sciences - National Institute of the Republic of Serbia, University of Belgrade, Belgrade, Serbia (dragana.s@vin.bg.ac.rs)*
[2]*University Clinical Centre of the Republic of Srpska, Banja Luka, Bosnia and Herzegovina.*
[3] *Faculty of Medicine, University of Priština, Kosovska Mitrovica, Serbia.*
[4] *Faculty of Pharmacy, University of Belgrade, Belgrade, Serbia.*

DOI: https://doi.org/10.46793/Phys.Chem24II.635S

ABSTRACT
Combined radionuclide therapy with magnetic nanoparticles has been a research focus as a promising approach for tumor therapy. In this study, superparamagnetic iron oxide nanoparticles (SPIONs) were synthesized using the co-precipitation method and coated with meso-1,2-dimercaptosuccinic acid (DMSA). Structural investigations showed that DMSA-coated SPIONs had a particle size of 140.3±6.5 nm in diameter with a spherical morphology. With a zeta potential of −35.1 mV, functionalization with DMSA led to increase the stability of the nanoparticles in solution. DMSA-SPIONs were radiolabeled with ^{177}Lu in high radiolabeling yield (86.6 ± 2.1%, and after separation by magnetic decantation >99%), showing high *in vitro* stability in saline and human serum up to 96 h. After intratumoral injection into mouse colorectal CT-26 or breast 4T1 subcutaneous tumors, the radiolabeled nanoparticles remained well localized at the injection site over a 14-day period, with limited leakage.

INTRODUCTION
Cancer is a generic term for a large group of diseases characterized by the uncontrolled growth and spread of abnormal cells. Certain types of cancer, along with stroke, ischemic heart disease, and respiratory diseases, are classified by the World Health Organization (WHO) among the top five leading causes of morbidity and mortality worldwide for the year 2023 [1]. In recent decades, a considerable number of scientific disciplines, especially nanomedicine, have flourished due to the emergence of advanced novel nanomaterials. Therapeutic and diagnostic tools based on nanotechnology have revolutionized current medical practice and provided solutions to problems that remain unsolved. Due to the need to address medical issues such as cancer, nanoparticles have gained tremendous interest [2]. The main role of a nanocarrier is the targeted delivery of a drug directly to the affected area, preventing the undesired side effects of conventional medicines and their uncontrolled biodistribution. Radiolabeled nanomaterials have emerged in recent years as a very promising tool for therapeutic applications, especially iron oxide nanoparticles, which have shown no toxicity. In this paper, the formation and physicochemical characterization of these nanoparticles were studied, aiming to develop a potential radioactive agent for nanobrachytherapy.

METHODS
The synthesis of bare SPIONs was performed by the co-precipitation method developed by Massart [3]. For physicochemical characterization, transmission electron microscopy (JEOL-TEM 1010, JEOL, Tokyo, Japan), XRD powder method, DLS measurement (Nano ZS90, Malvern, UK) and

FT-IR (Nicolet iS50, Thermo Fisher Scientific spectrophotometer) were used. For the radiolabeling, DMSA@SPIONs (10 mg/mL) were incubated for 1 hour with $^{177}LuCl_3$ (~370 MBq) with stirring at room temperature. The pH of solution was adjusted to 6.5. Radiochemical purity of ^{177}Lu-DMSA@SPIONs was done with ITLC/SG (Agilent, US) using saline as the mobile phase. The *in vitro* stability of ^{177}Lu-DMSA@SPIONs was determined in normal saline or human serum (HS, National Blood Transfusion Institute, Serbia) over a 144-hour incubation period at 37°C. The in vivo behavior of ^{177}Lu-DMSA@SPIONs was investigated in a mouse xenograft model (against CT-26 and 4T1 tumors) for 14 days. For the radioactivity measurement of samples, a dose calibrator (CRC-15 beta radioisotope, Capintec, Florham Park, NJ, USA) and NaI (Tl) gamma counter (Wizard 2480, Perkin Elmer, Waltham, MA, USA) were used. Results were analyzed using IBM® SPSS® Statistics version 25 software (IBM, Armonk, NY, USA) and were presented as mean ± standard deviation (SD). Statistical significance was examined using one-way ANOVA with a post hoc least significant difference (LSD) test. Differences were considered significant at $p < 0.05$.

RESULTS AND DISCUSSION

The size and morphology of uncoated SPIONs were examined by transmission electron microscopy (TEM). The TEM micrograph shows that the nanoparticles are spherical ("pseudo sphere") with an average diameter of 11.4 ±3.2 nm and a PDI of 28.3% (**Figure 1**). The PDI was used as an indicator for nanoparticle stability and uniformity of formation. This higher value of PDI indicates lower particle stability and the tendency towards the aggregation of SPIONs.

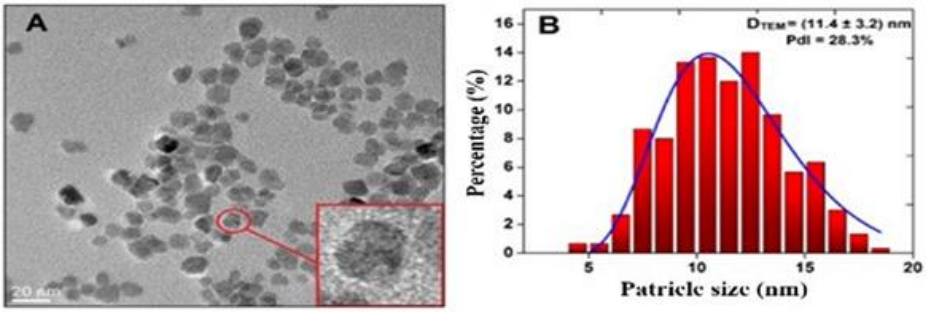


Figure 1. A) TEM images of uncoated SPIONs prepared by co-precipitation method, B) particle size distribution.

The XRD patterns of the uncoated SPIONs and DMSA@SPIONs show well-defined peaks, clearly indicating that the samples are crystalline (**Figure 2**). The hydrodynamic diameter value for SPIONs obtained from DLS measurements was 46.1±3.8 nm. The sizes of particles based on TEM measurement were significantly smaller in comparison with those achieved by the DLS method ($p < 0.05$). This discrepancy can likely be attributed to the presence of SPION aggregates in the suspension due to their lower stability. The mean value of 140.3 ± 6.5 nm showed that the hydrodynamic diameter of nanoparticles increased during SPION coating ($p < 0.05$), as expected. The zeta potential of bare SPIONs was +12.5 mV, which changed to -35.1 mV for DMSA@SPIONs due to the presence of numerous surface carboxyl and thiol functional groups. This change in zeta potential also indicates their increased stability in suspension compared to uncoated SPIONs.

The presence of DMSA on the surface of SPIONs was confirmed by FT-IR analysis (**Figure 2**). The DMSA@SPIONs clearly shows band patterns corresponding to all constituents. The characteristic peaks originating from the stretching of the C-O-Fe bond present in the DMSA@SPIONs spectrum at 1050 cm^{-1} confirm that DMSA molecules bind to the SPIONs surface. Additionally, the peaks at 1632 and 1350 cm^{-1}, related to the symmetric and asymmetric

stretching of carboxyl groups (-COO^-) on the DMSA@SPIONs surface, further confirm the coating of SPIONs with DMSA. The broad band at 2532 cm^{-1} in the DMSA spectrum belongs to the stretching vibration of the S-H bond in the thiol group.

The peak at 540 cm^{-1} observed in both the bare SPIONs and DMSA@SPIONs spectra is attributed to the Fe-O stretching vibration. Based on these results, it can be assumed that during the coating of SPIONs with DMSA, polar Fe-O-C bonds are formed with the separation of water molecules. Additionally, the free -SH groups of DMSA react with each other to form disulfide -S-S- bonds in the envelope (**Figure 2**).

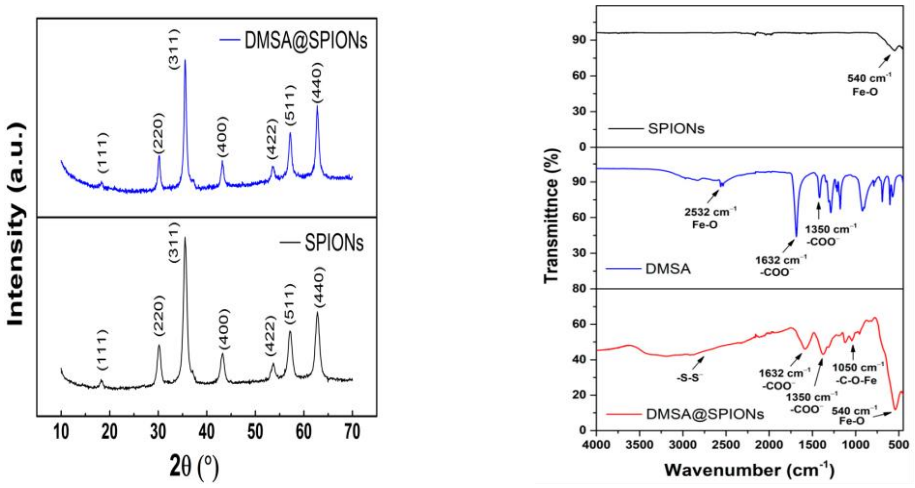


Figure 2. XRD curves of uncoated SPIONs and DMSA@SPIONs (left); FT-IR spectra of uncoated SPIONs, DMSA and DMSA@SPIONs (right).

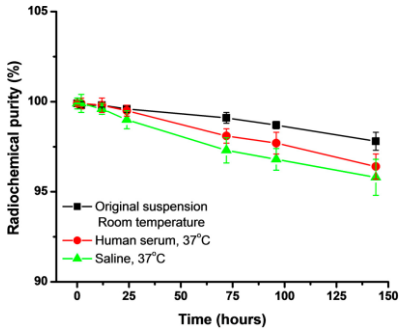


Figure 3. *In vitro* stability of 177Lu-DMSA@SPIONs stored in the original suspension at ambient temperature, incubated in human serum at 37 °C, and saline solution at 37 °C. The values represent mean ±SD, n = 3.

Radiolabeling studies found that ^{177}Lu-DMSA@SPIONs can be obtained with radiolabeling yield 86.6 ± 2.1%, and after separation by magnetic decantation, was >99%. The *in vitro* stability of the ^{177}Lu-DMSA@SPIONs was assessed at ambient temperature (RT) and at 37 °C in human serum and saline, as shown in **Figure 3**. The radiochemical purity determined by ITLC showed that less than 2.2 ±0.5%, 3.6 ± 0.7%, and 4.2 ± 1.0% of $^{177}Lu^{3+}$ was released up to 144 h after keeping the sample at room temperature, and after their incubation in human serum at 37 °C, and saline solution at 37 °C, respectively. It is clear from this study that ^{177}Lu-DMSA@SPIONs showed high in vitro stability up to 144 h. Efficient radiolabeling of DMSA-SPIONS with ^{177}Lu resulted in a stable bond with minimal leakage *in vitro*.

Following intratumoral injection into mouse colorectal CT-26 or breast 4T1 subcutaneous tumors, these radiolaled nanoparticles exhibited prolonged retention at the injection site over a 14-day period (**Figure 4**).

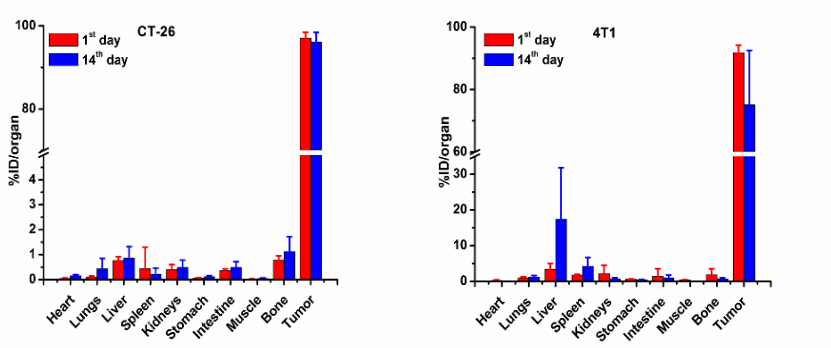


Figure 4. Biodistribution results of ^{177}Lu-DMSA-SPIONs after: a) *i.t.* administration to CT-26 tumors, b) *i.t.* administration to 4T1 tumors. Values shown represent mean ±SD (n=6).

CONCLUSION

Due to the high *in vivo* stability, excellent retention in the tumor, we believe that the synthesized ^{177}Lu-DMSA-SPIONs represent a promising agent for localized tumor radionuclide therapy that should be the subject of further research.

Acknowledgment

This work was supported by Centre of Excellence "VINCENT" funded by Ministry of Education, Science and Technological Development of the Republic of Serbia; the Ministry of Education, Science and Technological Development of Republic of Serbia (contract number: 451-03-47/2023-01/200017); EU funded project FP7-EraChairs-MagBioVin (Grant agreement #621375) and COST Action CA 19114.

REFERENCES

[1] R. Siegel, K. Miller, N. Wagle, A. Jemal, CA Cancer J. Clin. 73(1) (2023) 17-48.

[2] Q. Liu,J. Zou, Z. Chen,W. He, W. Wu, Acta Pharmaceutica Sinica B, 13(11) (2023) 4391-4416.

[3] R. Massart, IEEE Trans. Magn. 17 (1981) 1247–1248.

MOLECULAR DYNAMICS EXAMINATION OF THE CRYPTIC SUBPOCKET OF SIRTUIN 2

N. Đoković, V. Marković and K. Nikolić

University of Belgrade, Faculty of Pharmacy, Department of Pharmaceutical Chemistry, Vojvode Stepe 450, 11221 Belgrade, Serbia. (nemanja.djokovic@pharmacy.bg.ac.rs)

DOI: https://doi.org/10.46793/Phys.Chem24II.639DJ

ABSTRACT

Recently described alternative conformational state of sirtuin 2 (SIRT2) characterized by a cryptic subpocket paved the way for this study which investigates the significance of the newly identified cryptic subpocket in designing a group of SIRT2 inhibitors, derivatives of 4-(4-pyridylmethyl)aniline. With this aim, molecular dynamics simulations were conducted, initiating from two distinct conformational states of SIRT2 defined by the absence, or presence of the cryptic subpocket. Based on the analysis of the generated trajectories and estimated free energies of binding for reference and designed inhibitor, it has been shown that studied ligands were able to stabilize protein in both conformational states. Furthermore, the results suggest that the further design of novel 4-(4-pyridylmethyl)anilines could be focused on finding optimal substitution pattern to facilitate interactions with residue Phe132 within the cryptic subpocket.

INTRODUCTION

The sirtuins represent NAD^+ lysine deacylases highly conserved across different species, with humans possessing seven isoforms known as SIRT1–7. While these enzymes share a common NAD^+-binding pocket and catalytic core, they exhibit variations in their cellular expression patterns, subcellular localization, and substrate specificities [1]. Initially identified as ε-N-acetyllysine (Kac) hydrolases, recent research has demonstrated that sirtuins can remove various ε-N-acyllysine posttranslational modifications (PTMs). Sirtuin 2 (SIRT2) is primarily found in the cytoplasm and nucleus, where it plays a crucial role in regulating PTMs of various proteins involved in cellular metabolism, the cell cycle, chromatin structure and genomic stability [1,2]. The association of SIRT2 dysregulation with neurodegenerative diseases, cancer, and metabolic syndrome underscores its therapeutic potential, yet the ongoing challenges in developing effective inhibitors has hindered their entrance to clinical studies, emphasizing the need for further research in this domain [1]. The recent molecular modeling study revealed an alternative SIRT2 conformation characterized by previously unknown cryptic subpocket within the inhibitors binding site [3]. However, the implications of this hidden pocket to the drug discovery efforts remain unexplored. The description of the dynamics of the SIRT2 binding site through molecular dynamics (MD) simulations could provide a more detailed insight into the behavior of the system and thus enable a more thorough understanding of the design challenges of more selective and potent inhibitors. The aim of this research was to examine the significance of the alternative SIRT2 conformational state with an open cryptic subpocket in the rational design of novel SIRT2 inhibitors, derivatives of 4-(4-pyridylmethyl)aniline.

METHODS

All MD simulations were performed in the GROMACS (Groningen Machine for Chemical Simulations package version 2022.6) software [4] using CHARMM36 force field [5]. For each of the studied SIRT2 inhibitors, topologies and parameters were initially generated using the CGenFF

(CHARMM General Force Field) program version 2.4.0 accessed through a webserver (cgenff.umaryland.edu) [6]. Each system was simulated in an octahedral periodic box. The charge of the protein−ligand complexes was neutralized using 0.15M NaCl. Cutoff value of 12 Å was used when calculating Coulomb and van der Waals interactions. Water molecules were approximated by the TIP3P model. Equilibrations were performed in NVT ensemble (310 K, V-rescale thermostat) and then in NPT ensemble (1 atm, Parinello-Rahman barostat) using position restraints on protein and ligands.

Two groups of systems were set up: systems based on the initial conformation of SIRT2 obtained using X-ray crystallography (hereinafter X-ray) and systems based on the starting alternative conformation of SIRT2 with an open cryptic subpocket previously observed in metadynamics simulations (hereinafter MetaD) [3]. Both systems were studied in the ligand-free state (*apo* state) and in complex with two SIRT2 inhibitors (*holo* state). The alternative conformational state of SIRT2 (MetaD) was sourced from literature [3] while the X-ray was obtained from the Protein Data Bank (PDB ID: 5yqo). For simulations of the *apo* system, initial coordinates were set by manually removing ligand coordinates from the original files. *Holo* system coordinates were prepared using molecular docking with GOLD 2022.3 [7]. The binding site was defined based on ligand coordinates in the two SIRT2 conformational states, with a cutoff distance of 8 Å. Inhibitors 3D structures were optimized using MarvinSketch 24.1.0 with the MMFF94 force field. Ligand poses within the binding site were generated using a genetic search algorithm, yielding 30 optimal solutions while considering ligand flexibility. Pose scoring was performed using the ChemPLP scoring function [8].

Trajectory analyses (root-mean-square deviation (RMSD), root-mean-square deviation of atomic positions (RMSF), principal component analysis (PCA)) were performed using GROMACS built-in tools. Binding free energy calculations were performed using the MM/PBSA (The Molecular Mechanics Poisson-Boltzmann Surface Area) method as implemented in the gmx_MMPBSA software [9] using the last 20 ns of obtained trajectories to ensure sampling from the equilibrium state.

RESULTS AND DISCUSSION

To unravel the dynamics of the cryptic subpocket, we chose the previously identified SIRT2 inhibitor ND18 (3-phenyl-N-(4-(pyridin-4-ylmethyl)phenyl)propanamide) [3] as the primary structure for examining the mechanism of protein-ligand interaction. It’s worth noting that ND18 is a potent and selective inhibitor of SIRT2 with simple chemical structure which makes it perfect candidate for further optimizations. Despite ND18 was discovered through structure-based virtual screening, structural data on its interaction with SIRT2 remains elusive. According to the initial molecular docking calculations and preliminary MD runs performed on MetaD state of SIRT2, ND18 was predicted to only partially occupy the cryptic subpocket. These findings prompted us to design p-trifluormethyl analogue of the ND18 (N-(4-(pyridin-4-ylmethyl)phenyl)-3-(4trifluoromethyl)phenyl)propanamide) (hereinafter CF3 ligand) which could further extend into the cryptic subpocket and achieve additional interactions. Given that molecular docking calculations don't incorporate the conformational flexibility of SIRT2, MD simulations were employed to confirm predicted binding modes and investigate the dynamical behavior of the systems under study. Total of 600 ns of MD simulations were performed for two groups of systems (MetaD and X-ray) in both *apo* and *holo* states starting from initial poses obtained from molecular docking.

Results of the RMSD analysis revealed convergence of the simulations and sampling from equilibrium states (**Figure 1.**). Additional RMSF analysis revealed SIRT2 specific insertion and the cofactor-binding loop as the most fluctuating parts of the protein. This finding was in alignment with literature data [3].

Principal component analysis (PCA) was performed on a data set consisting of atomic positions of the polypeptide backbone during 100 ns of simulations. The projection of coordinates along first principal component (PC1) indicated clear separation of conformational behavior of two groups of studied systems – X-ray and MetaD (**Figure 1.)**. It is worth noting that the simulations starting from X-ray conformational state showed higher mutual similarity of conformational behavior, relative to the simulations starting from conformational state with open cryptic subpocket (MetaD). This could indicate that opening of the cryptic subpocket is highly dependent on the structure of the bound ligand and suggests possible induced-fit phenomena. This hypothesis was in alignment with visual inspection of obtained trajectories which revealed that designed CF3 ligand, relative to ND18, could stabilize cryptic subpocket through extended interactions introduced by CF3 moiety. Furthermore, cryptic subpocket closure was observed during the simulations in which SIRT2 was in alternative conformational state and without ligand (*apo* MetaD). Likewise, comparing ligand binding modes between MetaD and X-ray simulations revealed significant conformational differences in the phenylpropionic fragment due to lack of cryptic subpocket in X-ray simulations (**Figure 1.)**.

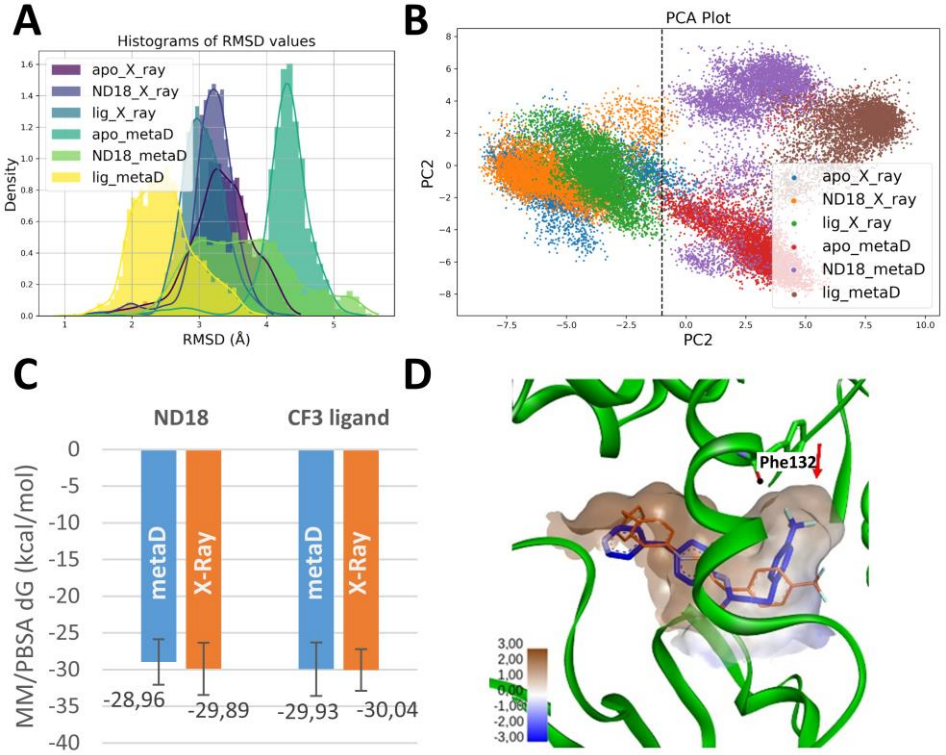


Figure 1. A – Histograms of RMSD fluctuations for simulated systems; B – Projections of obtained trajectories on first two principal components (PCs). Dashed line indicates value of PC1 which separates two studied conformational states of SIRT2; C – Results of MM/PBSA calculations; D – Visualization of the binding mode predicted for designed CF3 ligand in X-ray (orange sticks) and MetaD (blue sticks) conformational states of SIRT2. Red arrow marks the position of the cryptic subpocket, while surface color corresponds to the pocket hydrophobicity.

The relationship between binding affinity (K_a) and the change in Gibbs free energy ($\Delta G = -RT\ln K_a$) implies that higher absolute ΔG values correspond to stronger ligand interactions with the binding pocket. Comparable calculated MM/PBSA ΔG values for SIRT2:ND18 (X-ray: -29.89 kcal/mol, MetaD: -28.96 kcal/mol) and SIRT2:CF3 ligand (X-ray: -30.04 kcal/mol, MetaD: -29.93 kcal/mol) (**Figure 1.**) in both X-ray and MetaD simulations indicated ability of ligands to stabilize

the protein in both conformations. Analyzing the contribution of non-covalent interactions to total enthalpy change, van der Waals interactions emerged as dominant in all systems. This aligns with expectations, given the non-polar nature of SIRT2 binding site and the absence of ionization centers in the ligands (**Figure 1.**).

It has been observed that ND18 and CF3 ligand interacted with amino acid residues within a cryptic subpocket via shared 3-phenylpropionic fragment. However, only CF3 ligand consistently interacted with Phe132 at the subpocket's base, owing to an additional trifluoromethyl substituent which could be related to the increase of absolute MM/PBSA ΔG value for MetaD state (**Figure 1.**).

CONCLUSION

The results of this study shed light on the mechanisms of interaction between SIRT2 inhibitors, derivatives of 4-(4-pyridylmethyl)aniline, and the cryptic subpocket observed in the putative conformational state of SIRT2. To investigate the potential significance of the cryptic subpocket in the rational design of SIRT2 inhibitors, molecular dynamics simulations were conducted, initiating from two distinct conformational states of SIRT2 – one with an open cryptic subpocket and another with a closed one. Guided by observed dynamical behavior of reference SIRT2 inhibitor (ND18), novel inhibitor which could form more pronounced interactions within cryptic subpocket was designed. Studied SIRT2 inhibitors were able to stabilize protein in both conformational states which was further corroborated by MM/PBSA ΔG calculations. Interactions of inhibitors with residue Phe132 positioned at the bottom of the cryptic subpocket were recognized as significant for further design of 4-(4-pyridylmethyl)anilines.

Acknowledgment

This research was funded by the Ministry of Science, Technological Development and Innovation, Republic of Serbia through two Grant Agreements with University of Belgrade-Faculty of Pharmacy No 451-03-65/2024-03/200161 and No 451-03-66/2024-03/200161. The authors thank the COST Actions CA18240, CA18133 and CA22125 of the European Community for support.

REFERENCES

[1] H. Dai, D. A. Sinclair, J. L. Ellis, C. Steegborn, Pharmacol. Ther., 188 (2018) 140.
[2] Ri. Machado de Oliveira, J. Sarkander, A. Kazantsev, T. Outeiro, Front. Pharmacol. 2012, 3.
[3] N. Djokovic, D. Ruzic, M. Rahnasto-Rilla, T. Srdic-Rajic, M. Lahtela-Kakkonen, K. Nikolic, J. Chem. Inf. Model., 62 (2022) 2571.
[4] M. J. Abraham, T. Murtola, R. Schulz, S. Páll, J. C. Smith, B. Hess, E. Lindahl, SoftwareX, 1–2 (2015) 19.
[5] J. Huang, A. D. MacKerell, J. Comput. Chem., 34 (2013) 2135.
[6] K. Vanommeslaeghe, A. D. MacKerell, J. Chem. Inf. Model., 52 (2012) 3144.
[7] G. Jones, P. Willett, R. C. Glen, A. R. Leach, R. Taylor, J. Mol. Biol., 267 (1997) 727.
[8] O. Korb, T. Stützle, T. E. Exner, J. Chem. Inf. Model., 49 (2009) 84.
[9] M. S. Valdés-Tresanco, M. E. Valdés-Tresanco, P. A. Valiente, E. Moreno, J. Chem. Theory Comput., 17 (2021) 6281.

DESIGN AND ADMET PREDICTION OF NOVEL DUAL INHIBITORS FROM THE HISTONE DEACETYLASE FAMILY

A. Ilić, A. Čebzan, B. Radović, N. Đoković and K. Nikolić

University of Belgrade, Faculty of Pharmacy, Vojvode Stepe 450, 11221 Belgrade, Serbia. (nemanja.djokovic@pharmacy.bg.ac.rs)

DOI: https://doi.org/10.46793/Phys.Chem24II.643I

ABSTRACT

The family of histone deacetylases (HDAC) has been associated with various processes in the development and growth of many cancers. Selective inhibition improves the tolerability of HDAC inhibitors, while dual targeting of synergistic targets improves the efficacy of cancer therapy. In this article, we report the design, molecular docking studies and ADMET predictions of nine novel HDAC6/WEE1, HDAC6/GLS1 and SIRT2/AURKA dual inhibitors. The developed compounds show comparable or better docking results and ADMET properties than reference co-crystal ligands.

INTRODUCTION

Histone deacetylases (HDACs) are a family of enzymes that primarily hydrolyze acetyl-lysine residues of histones, but also deacetylate various other targets [1]. Most HDAC isoenzymes have been found to be overexpressed in multiple cancer models, and there are non-selective HDAC inhibitors approved for cancer therapy [1]. The main problem with non-selective HDAC inhibition in humans is the various side effects that occur during treatment [1]. Our previous study of synergism between HDAC inhibitors and other drugs, based on analysis of basal gene expression, has shown the potential of synergy between HDAC6/WEE1, HDAC6/GLS1 and SIRT2/AURKA, for which no dual inhibitors have been described yet, to the best of our knowledge [2]. HDAC6 is a zinc-dependent deacetylase that is involved in tubulin deacetylation and cell motility, among other functions [1]. WEE1 kinase is a regulatory enzyme involved in the regulation of the G2/M checkpoint and the S phase of the cell cycle [3]. WEE1 and HDAC6 signaling pathways have been implicated in the pathology of several cancers, including squamous cell carcinomas of the head and neck [4], pancreatic cancer [2], and acute myeloid leukemia [5]. Glutaminases (GLS) are enzymes that play an important role in the metabolism of glutamine by deamidating it to glutamate [6]. GLS1 has been found to be upregulated and associated with various types of cancer [6]. Some *in vitro* studies have found synergy between GLS1 and HDAC6 inhibitors in lymphoid tumor cell lines [7].

Sirtuin 2 (SIRT2) belongs to the family of sirtuin enzymes, a class III of histone deacetylases found mainly in the cytoplasm. Sirtuins play a key role in the regulation of post-translational protein modifications and influence the cell cycle, autophagy and genome stability [8]. Aurora kinase (AURKA) is a serine/threonine kinase that is crucial for cell division and affects mitotic and meiotic processes [9]. Simultaneous inhibition of SIRT2 and Aurora kinase has the potential to influence cell proliferation, stop division and induce apoptosis. This approach could be particularly beneficial in aggressive tumor types such as small cell lung cancer, pancreatic cancer and hematological tumors [2,8,9].

In this study, molecular docking and ADMET-*in-silico* studies were performed to develop potential dual inhibitors for HDAC6/WEE1, HDAC6/GLS1 and SIRT2/AURKA.

METHODS

Novel dual HDAC6/WEE1 inhibitors (**Figure 1**) were designed by fusing the key structural parts of the WEE1 inhibitor AZD1775 with specific zinc binding groups as the pharmacophore of HDAC6 inhibitors. Two series of dual HDAC6/GLS1 inhibitors were derived from the allosteric GLS1 inhibitor BPTES and its derivatives by fusion with aromatic and aliphatic hydroxamic acids (**Figure 2**). Novel dual SIRT2/AURKA inhibitors (**Figure 3**) were designed using the Sirt2i_Predictor [10] for virtual screening of AURKA inhibitors from the ChEMBL database.

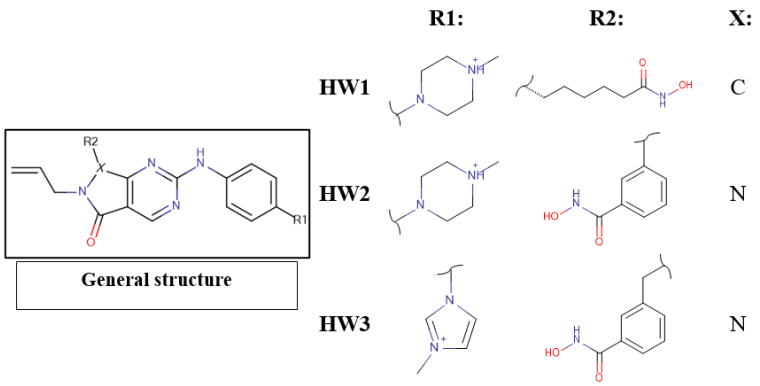


Figure 1. 2D structures of the designed dual WEE1/HDAC6 dual inhibitors HW1, HW2 and HW3.

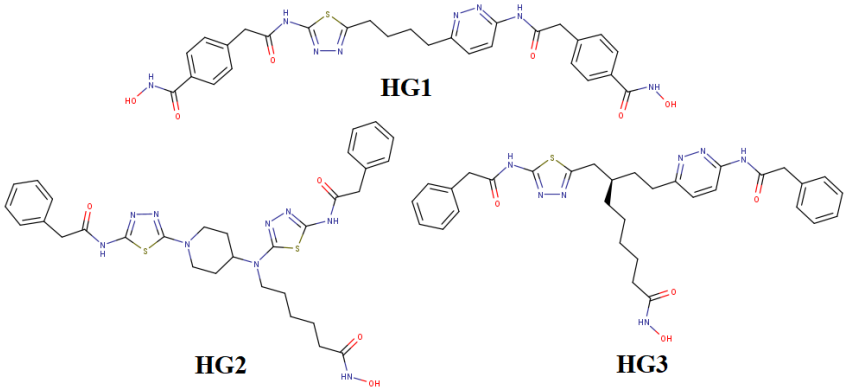


Figure 2. 2D structures of the designed dual HDAC6/GLS1 inhibitors HG1, HG2 and HG3.

The *in silico* affinity of the designed compounds was determined by molecular docking studies using GOLD v.2021 software. The molecular docking studies were performed on WEE1 (PDB: 5V5Y), HDAC6 (PDB: 5G0I) and HDAC1 (PDB: 4BKX) for HDAC6/WEE1 inhibitors; GLS1 (PDB: 7REN), HDAC6 (PDB: 5WGL and 5G0I) and HDAC1 (PDB: 5ICN) for HDAC6/GLS1 inhibitors; AURKA (PDB: 4DHF) and SIRT2 (PDB: 5D7P) for SIRT2/AURKA inhibitors. HDAC1 was included in molecular docking studies to investigate the selectivity of HDAC6/WEE1 and HDAC6/GLS1 inhibitors. In addition, ADMET Predictor 11.0.0.3 software was used to predict the ADMET properties and synthetic difficulty of the novel dual inhibitors of HDAC6/WEE1, HDAC6/GLS1 and SIRT2/AURKA.

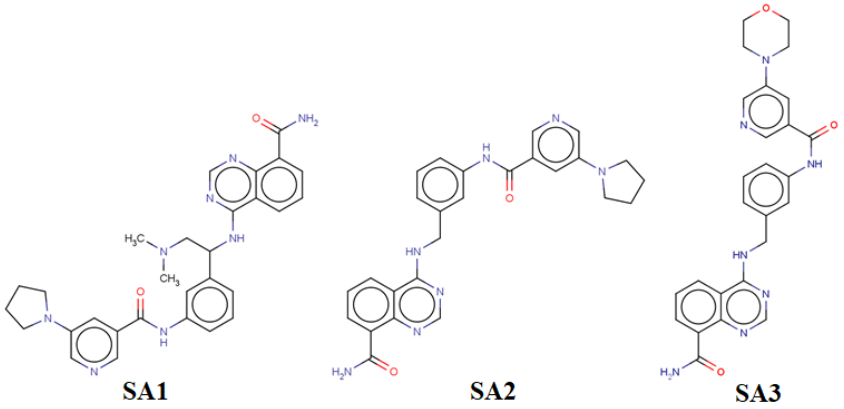


Figure 3. 2D structures of the designed dual SIRT2/AURKA dual inhibitors SA1, SA2 and SA3.

RESULTS AND DISCUSSION

The docking results for all novel designed compounds are listed in **Table 1**. The docking values of the designed HDAC6/WEE1 inhibitors were higher than the values of the reference co-crystal ligands in the case of HDAC6 and WEE1 complexes, while they were lower or similar to the scores of the reference ligands in the case of HDAC1. The three HDAC6/GLS1 inhibitors with the best results are shown, with better or comparable results to the co-crystalline ligands, while none of them bound correctly to HDAC1, with HG3 showing the most balanced scores. All SIRT2/AURKA inhibitors have shown comparable or better docking scores than the reference ligands, with SA1 having overall the best scores in the group.

The predicted ADMET properties and synthetic difficulties of the designed dual inhibitors and some co-crystalline ligands are shown in **Table 2**. The predicted ADMET properties for HDAC6/WEE1 inhibitors were similar or in some cases better than those of the co-crystalline ligands, with HW2 being the best candidate for synthesis. Among the HDAC6/GLS1 inhibitors, HG2 showed the best predicted ADMET properties comparable to those of the reference co-crystalline ligand. The SIRT2/AURKA inhibitors showed the best predicted ADMET properties of all three groups, with SA1 being the best candidate for synthesis.

Table 1. Docking scores of designed compounds.

Targets	HW1	HW2	HW3	Targets	HG1	HG2	HG3	Targets	SA1	SA2	SA3
WEE1[a]	36.59	39.22	37.22	**GLS1**[d]	125.45	108.95	126.12	**AURKA**[g]	85.43	80.00	78.89
HDAC6[b]	18.40	27.19	30.39	**HDAC6**	33.21[e]	28.63[f]	26.61[f]	**SIRT2**[h]	105.01	102.13	105.13
HDAC1[c]	24.02	20.27	20.62								

[a] Reference Gold.Chemscore.Fitness 36.39; [b] Reference Gold.Chemscore.Fitness 24.02; [c] Reference Gold. Chemscore.Fitness 20.45; [d] Reference Plp.Fitness 117.85; [e] Reference Gold.Chemscore.Fitness 45.29; [f] Reference Gold.Chemscore.Fitness 27.83; [g] Reference Gold.Chemscore.Fitness 78.59; [h] Reference Gold.Chemscore.Fitness 67.58.

CONCLUSION

In this study, HDAC6/WEE1, HDAC6/GLS1 and SIRT2/AURKA have been identified as combinations for novel dual-targeting inhibitors, based on previous results. Structure-based drug design methods (molecular docking) and ADMET-*in-silico* studies were used to design and

evaluate potential selective dual inhibitors. The docking scores of the designed inhibitors showed remarkable affinity to the specific targets. They exhibited acceptable ADMET properties, so they will be synthesized for in vitro testing. However, further *in silico* studies are required to fully determine the selectivity of the designed compounds.

Table 2. Predicted ADMET properties and synthetic difficulty of designed compounds and some reference ligands.

	S+logP	RuleOf5	hERG_Filter	TOX_Risk	CYP_Risk	SynthDiff
HW1	1.559	0	No	1	1	3.548
HW2	1.138	2	No	1	0	2.999
HW3	-4.878	1	No	1.5	1.5	3.52
Nexturastat A[a]	2.539	0	No	0	1.125	1.492
AZD1775[b]	2.235	1	No	1	0	3.172
HG1	1.996	3	No	1.5	0.5	2.81
HG2	3.042	2	No	2	1	2.84
HG3	3.238	2	No	2	1.76	3.20
UPGL-00004[c]	3.234	1	No	1	0.22	2.42
SA1	3.304	1	No	1	0.166	3.581
SA2	3.102	0	Yes	1	1.069	2.888
SA3	2.434	0	Yes	1	1	2.939

Legend: S+logP - Simulations Plus model of log P; RuleOf5 - Lipinski's "Rule of Five"; SynthDiff - difficulty of chemical synthesis; hERG_Filter – qualitative estimation of the likelihood of the hERG channel inhibition; Tox_Risk – toxicity liability score; CYP_Risk – CYP450 liability score; [a] co-crystal ligand for 5G0I; [b] co-crystal ligand for 5V5Y; [c] co-crystal ligand for 7REN.

Acknowledgment

This research was funded by the Ministry of Science, Technological Development and Innovation, Republic of Serbia through two Grant Agreements with University of Belgrade-Faculty of Pharmacy No 451-03-65/2024-03/200161 and No 451-03-66/2024-03/ 200161. The authors thank the COST Actions CA18240, CA18133 and CA22125 of the European Community for support.

REFERENCES

[1] Y. Li, E. Seto, Cold Spring Harb Perspect Med., 6(10) (2016) a026831.

[2] N. Djokovic, A. Djuric, D. Ruzic, T. Srdic-Rajic, K. Nikolic, Pharmaceuticals (Basel)., 16(2) (2023) 294.

[3] X. Du, J. Li, X. Luo, R. Li, F. Li, Y. Zhang, J. Shi, J. He, Eur J Med Chem., 203 (2020) 112524.

[4] K. Miyake, N. Takano, H. Kazama, H. Kikuchi, M. Hiramoto, K. Tsukahara, K. Miyazawa, Int J Oncol., 60(5) (2022) 54.

[5] L. Zhou, Y. Zhang, S. Chen, M. Kmieciak, Y. Leng, H. Lin, K. A. Rizzo, C. I. Dumur, A. Ferreira-Gonzalez, Y. Dai, S. Grant, Leukemia, 29(4) (2015) 807.

[6] Y. Chen, L. Tan, J. Gao, C. Lin, F. Wu, Y. Li, J. Zhang, Eur J Med Chem., 252 (2023) 115306.

[7] Q. Qiu et al., Bioact Mater., 21 (2022) 483.

[8] L. Zhang, S. Kim, X. Ren, Front Oncol., 10 (2020) 1721.

[9] R. Du, C. Huang, K. Liu, X. Li, Z. Dong, Mol Cancer, 20(1) (2021) 15.

[10] N. Djokovic, M. Rahnasto-Rilla, N. Lougiakis, M. Lahtela-Kakkonen, K. Nikolic, Pharmaceuticals (Basel), 16(1) (2023) 127.

MOLECULAR MODELING AND DESIGN OF NEW PI3K/HDAC DUAL INHIBITORS

M. Beljkaš, E. Kukić, N. Đoković, and S. Oljačić

University of Belgrade, Faculty of Pharmacy, Department of Pharmaceutical Chemistry, Vojvode Stepe 450, 11000 Belgrade, Serbia. (nemanja.djokovic@pharmacy.bg.ac.rs)

DOI: https://doi.org/10.46793/Phys.Chem24II.647B

ABSTRACT

Phosphatidylinositol 3-kinases (PI3K) are enzymes that play a crucial role in the regulation of cellular processes, and elevated PI3K levels are associated with the pathogenesis of various tumors. Histone deacetylase 6 (HDAC6) plays an important role in tumorigenesis and is therefore an important target for tumor therapy. Previous studies have shown that PI3K and HDAC inhibitors act synergistically against cancer. For this reason, our study focused on the development of dual PI3K/HDAC inhibitors as a new type of anticancer agent. Novel PI3K/HDAC inhibitors were designed by modifying the structure of the pan-PI3K inhibitor copanlisib, using molecular docking to identify moieties that are not involved in essential interactions to inhibit the PI3Kα isoform. These moieties were used to introduce structural features required for inhibition of HDAC6 to achieve a dual PI3K/HDAC inhibitory activity. Based on the identified key interactions with the PI3K and HDAC enzymes, docking scoring values and calculated ADMET properties, compound 4 emerged as the best candidate for further synthesis and evaluation.

INTRODUCTION

Previous studies have shown a positive correlation between PI3K overexpression and various types of cancer [1]. Mutations in the PIK3CA gene, inactivation of tumor suppressor genes, overexpression of oncogenes (Ras) and growth factor receptors lead to overactivity of PI3K signaling pathways. This contributes to the survival of cancer cells, their metastasis, but also to the increase in tumor resistance to various drugs. Four PI3K inhibitors have already been approved by the FDA (U.S. Food and Drug Administration), primarily for the treatment of hematologic malignancies: copanlisib (pan-PI3K), idelalisib (PI3Kδ), duvelisib (dual PI3Kδ/γ) and alpelisib (PI3Kα). Despite high expectations, PI3K inhibitors have shown limited efficacy as monotherapy, most likely due to the activation of alternative signaling pathways [2]. To overcome the shortcomings of monotherapy, various strategies have been employed, such as the multi-target approach, i.e. the design and synthesis of a single molecule that effectively modulates the activity of two or more targets [3]. Based on the multi-target approach, numerous dual- and multi-target PI3K inhibitors have been developed. In view of the structural and functional uniqueness of the isoform of histone deacetylases 6 (HDAC6) and the disadvantages of non-selective HDAC inhibitors, which are primarily reflected in an unfavorable safety profile, intensive research is currently being conducted into the development and synthesis of selective HDAC6 inhibitors for tumor treatment [4]. Unfortunately, selective HDAC6 inhibitors face similar obstacles as PI3K inhibitors, such as resistance and the need for high doses of the inhibitor to achieve a therapeutic effect, with a concomitant loss of selectivity for this enzyme isoform [5]. Considering the drawbacks of monotherapy as well as the results of previous studies showing significant synergistic effects between PI3K inhibitors and HDAC inhibitors, in this work we focus on the design and development of dual PI3K/HDAC inhibitors by combining the pharmacophores required for the inhibition of these two enzymes.

METHODS

The preparation of the *in silico* designed compounds for virtual docking was performed with the following programs: ChemDraw Ultra 7.0, Chem3D Ultra 7.0, Marvin Sketch (https://chemaxon.com/). Gaussian 09, part of Chem3D Ultra 7.0, was used to optimize the developed compounds using the ab initio Hartree-Fock/3-21G basis set [6]. The crystal structures of the enzymes were downloaded from the Protein Data Bank website (https://www.rcsb.org/) - human PI3Kα (PDB: 6PYS) and PI3Kγ (PDB: 5G2N), while the second catalytic domain of the human HDAC6 enzyme corresponds to the PDB code: 5EDU. The crystal structures of the enzymes were prepared for docking simulations using the free platform Play Molecule (https://www.playmolecule.org/proteinPrepare/). Molecular docking studies were performed with GOLD v.5.8.1 [7]. The docking method is considered valid and reliable for further predictions if the RMSD value is below 2 Å.

RESULTS AND DISCUSSION

The development of new dual PI3K/HDAC inhibitors in this study was based on structural modifications of the already known pan-PI3K inhibitor copanlisib. A molecular docking study identified a solvent-exposed part of this molecule that does not form significant interactions essential for inhibition of the PI3Kα isoform, specifically positions C-8, C-9 and C-10 (Figure 1). This part of the molecule was used for the introduction of structural elements essential for the inhibition of histone deacetylases 6, with the aim of achieving a dual inhibitory effect.

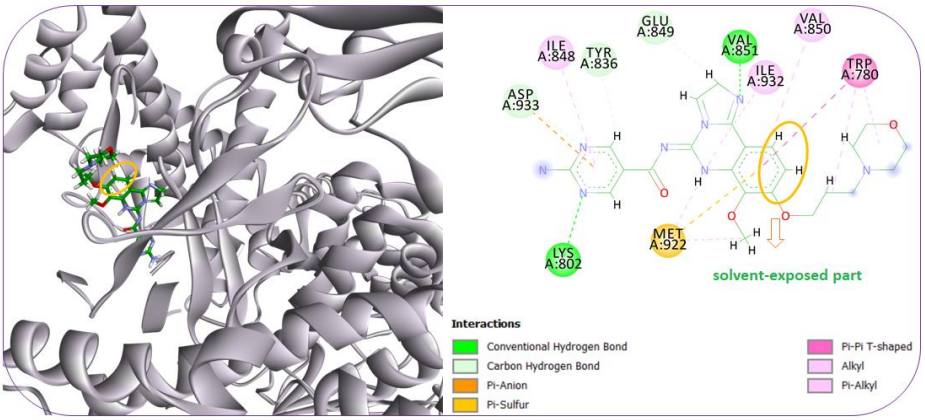


Figure 1. The binding conformation of copanlisib in the binding site of PI3Kα (left) and 2-D depiction of PI3Kα-copanlisib interactions (right).

Of the 35 compounds designed, 4 compounds were selected for further docking analysis based on the scoring results. The RMSD values for all three enzymes were below 2Å, so the docking methods can be used for reliable prediction of binding modes and key interactions between the designed molecules and enzymes.

The zinc-binding group of **compound 1**, hydroxamic acid, forms a complex with zinc in catalytic domain 2 of HDAC6, which is additionally stabilized by hydrogen interactions with His610 and Gly619. **Compound 1** forms a hydrogen bond with Val851 in the hinge region of the PI3Kα isoform as well as a key interaction with the hinge region of PI3Kγ (Val882). Based on these interactions, the inhibitory effect of the given compound on both PI3K isoforms can be expected.

Compounds 2 and **3** formed key interactions with HDAC6. However, **compound 2** does not form a hydrogen bond with the hinge region of PI3Kγ, which may indicate a potential lack of activity of this compound, while **compound 3** does not form the most important interactions with

the hinge regions of PI3Kα (Val851) and PI3Kγ (Val882). Thus, it can be concluded that the **compound 3** would be a potential HDAC6, but not PI3K/HDAC6 dual inhibitor.

Compound 4 coordinates zinc in catalytic domain 2 of HDAC6. This complex is additionally stabilized by hydrogen bonds between hydroxamic acid and the following residues: Gly619 and Tyr782. The linker and CAP group also formed numerous π-alkyl and π-π interactions with Phe620, Phe680, Leu749 and His651 (**Figure 2-A**). **Compound 4**, in contrast to **compound 3**, formed hydrogen bonds with the amino acids of the hinge region of PI3Kα (Val851 - **Figure 2-B**) and PI3Kγ (Val882 - **Figure 2-C**) isoforms. Similar to PI3Kγ, compound 4 achieves additional interactions with PI3Kα that may contribute to its inhibitory effect on the respective isoform, including π-π interactions with Trp780 and hydrogen bonds with Lys802 (**Figure 2-C**).

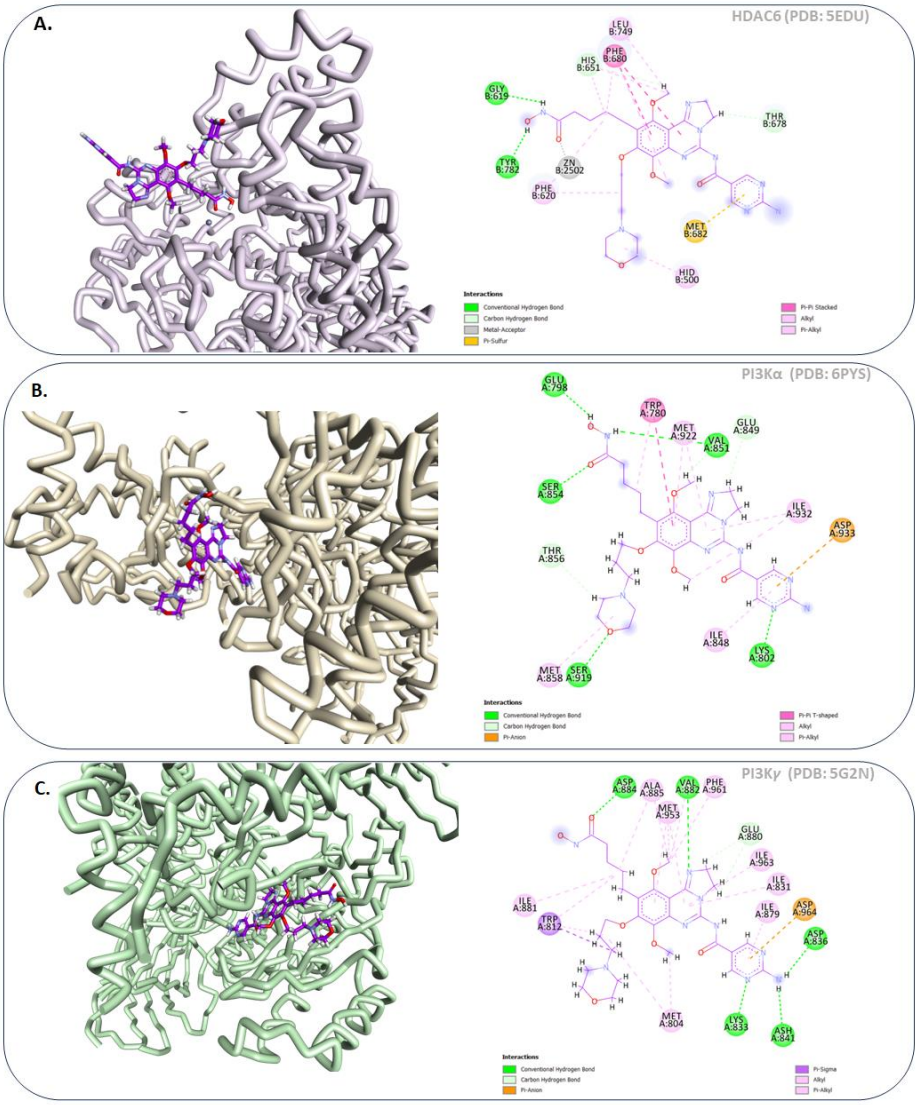


Figure 2: **A-** Position of compound **4 (purple)** inside the HDAC6 (left) and 2D diagram of the most important **4** – HDAC6 interactions (right); **B** - Position of compound **4** (purple) inside the PI3Kα (left) and 2D diagram of the most important **4** – PI3Kα interactions; **C** - Position of compound **4** (purple) inside the PI3Kγ (left) and 2D diagram of the most important **4** – PI3Kγ interactions.

The ADMET predictor [8] was used for the *in silico* calculation of the ADMET properties of newly developed PI3K/HDAC inhibitors and already known inhibitors (ricolinostat, copanlisib).

The predicted ADMET properties of **compound 4** were better than those of **compound 1** – there is no CYP risk (better also compared to already known inhibitors). On the basis of all the results obtained so far, it can be concluded that **compound 4** is the best candidate for further synthesis, testing and evaluation.

CONCLUSION

Using structure-based drug design, this paper proposes the structure of four PI3K/HDAC6 dual inhibitors that could potentially act on one of the key epigenetic regulators - histone deacetylase 6 (HDAC6) - as well as one of the components of many signaling pathways: Phosphatidylinositol 3-kinases (PI3K). Based on the results of molecular docking, where the key interactions between the designed compounds and the target enzymes HDAC6, PI3Kα and PI3Kγ were analyzed, as well as the calculation of ADMET properties, **compound 4** emerged as the best candidate for further synthesis, optimization and evaluation.

Acknowledgment

This research was funded by the Ministry of Science, Technological Development and Innovation, Republic of Serbia, through Grant Agreement with University of Belgrade (Faculty of Pharmacy), No 451-03-65/2024-03/ 200161 and No 451-03-66/2024-03/ 200161.

REFERENCES

[1] Y. ZHe, M. M. Sun, G. G. Zhang, J. Yang, K. S. Chen, W. W. Xu, B. Li, Sig Transduct Target Ther, 6 (2021) 1–17.
[2] P. M. LoRusso, J Clin Oncol, 34 (2016) 3803–3815.
[3] S. Alcaro, M. L. Bolognesi, A. T. García-Sosa, S. Rapposelli, S. Frontiers in Chemistry (2019**)**, 7.
[4] S. Pulya, Sk. A. Amin,N. Adhikari, S. Biswas, T. Jha, B. Ghosh, Pharmacological Research, 163 (2021) 105274.
[5] Y. Depetter, S. Geurs, R. De Vreese, S. Goethals, E. Vandoorn, A. Laevens, J. Steenbrugge, E. Meyer, P. de Tullio, M. Bracke, et al. International Journal of Cancer, 145 (2019) 735–747.
[6] p. J. Hehre, Ab Initio Molecular Orbital Theory Available online: https://pubs.acs.org/doi/pdf/10.1021/ar50107a003 (accessed on 13 November 2023).
[7] G. Jones, P. Willett, R. C. Glen, A. R. Leach, R. Taylor, Journal of Molecular Biology, 267 (1997) 727–748.
[8] ADMET Property Prediction | Machine Learning | AI-Driven Drug Design Available online: https://www.simulations-plus.com/software/admetpredictor/ (accessed on 21 May 2024).

EVALUATING POTENTIAL OF COUMARINS AS PPARα AGONISTS: MOLECULAR DYNAMICS STUDY

K. Stevanović, D. Radošević, S. Glišić and M. Senćanski

University of Belgrade, Institute of Nuclear Sciences Vinča, Department for Bioinformatics and Computational Chemistry, Mike Petrovića Alasa 12-14, 11351 Vinča, Belgrade, Serbia. (kristina.stevanovic@vin.bg.ac.rs)

DOI: https://doi.org/10.46793/Phys.Chem24II.651S

ABSTRACT

Metabolic syndrome encompasses several chronic, severe disorders like dyslipidemia, hypertension, stroke, and type 2 diabetes mellitus. Concerns about its prevalence in global public health are growing. The ligand-activated transcription factor peroxisome proliferator-activated receptor alpha (PPARα) is an essential regulator of lipid metabolism and, therefore, a potential therapeutic target for treating metabolic syndrome. Several studies suggest that various natural compounds activate PPARα. Coumarins have been recognized as a promising class of PPARα activators. In our previous work, we have identified coumarin molecule (E)-3-[(2-oxo-chromen-3-yl)-methyleneamino]-acrylaldehyde as a potential ligand for human PPARα. Here, we attempted to discover more about the stability of the obtained protein-ligand complex using molecular dynamics simulations. Valuable new understandings of the complex's dynamic behavior have been achieved.

INTRODUCTION

The prevalence of metabolic syndrome is rising continuously on a global scale. It includes the development of many conditions that increase the risk of insulin resistance, type II diabetes mellitus, and atherosclerotic cardiovascular disease. PPARα is a key mediator in the control of gene expression related to fatty acid beta-oxidation and glucose homeostasis [1]. Targeting PPARα proved to be a promising approach to treating dyslipidemia and atherosclerosis linked to metabolic syndrome [1]. Studies have demonstrated that a broad range of lipophilic chemicals and synthetic ligands can activate PPARα [2]. The usage of coumarin compounds in medicinal chemistry has been particularly prominent in the last ten years of drug research due to their advantages of having various targets and fewer severe side effects. They have also been identified as PPARα agonists, and in experimental models, several of them have demonstrated the ability to activate PPARα [2]. In our earlier research, we developed a new theoretical criterion for the virtual screening of coumarins as PPARα agonists. Based on constructed QSAR model and molecular docking, we identified (E)-3-[(2-oxo-chromen-3-yl)-methyleneamino]-acrylaldehyde as the most promising candidate [3]. Molecular docking studies, however, only provide the molecule's stationary conformations in the binding site without information about its dynamics and the stability of the resulting complex. Therefore, to demonstrate how protein and ligand conformations alter over time, a molecular dynamics simulation was performed here. The consistency of specific hydrogen (previously found to be critical for activation) was particularly examined.

METHODS

After obtaining the protein-ligand complexes from previously reported favorable docking pose [3], preparation for MD simulation considered adding 20 Å water layers from the positive and negative sides of all three x, y and z-axis. The established water box dimensions were 105×104×105 Å. To

achieve the physiological conditions of 0.15 M ionic strength, NaCl ions were introduced, yielding a system with approximately 103,000 atoms.

The system was energy minimized after 10000 steps and subjected to 250 ps NVT equilibration and 100 ns NPT production. The Langevin thermostat and the Berendsen barostat were used in the simulations to regulate the temperature and pressure to 300 K and 1 bar, respectively. The long-range electrostatics were handled by the Particle Mesh Ewald, and periodic boundary conditions were implemented. The cut-off was set to 12 Å. To restrict all bond lengths involving hydrogen atoms, the SHAKE method was used. The applied integration step was 1 fs. For protein, water and ions a CHARMM36 force field [4] was used. The topology and parameter files for the ligand were generated using CGenFF [5].

MD calculations were carried in NAMD 3.0 alpha [6] and the obtained results were analyzed in VMD 1.9.3.[7].

RESULTS AND DISCUSSION

Molecular docking studies are limited to predicting the target-ligand complex's static binding pose. Consequently, to learn more about the dynamic behavior and characteristics of a bound molecule that direct molecular recognition, molecular dynamics (MD) simulations must be applied. Since our docking study revealed that the (E)-3-[(2-oxo-chromen-3-yl)-methyleneamino]-acrylaldehyde binds to the ligand binding domain on human PPARα [3], we have further initiated MD simulations utilizing the docking binding mode that we got.

An MD simulation was performed once the solved PPRα ligand system had been equilibrated. The receptor demonstrated general stability, with a root-mean-square deviation (RMSD) value of approximately 2 Å reached in 10 ns (Figure 1a). In addition, the stability of the ligand's conformation in the binding site (Figure 1b) and the hydrogen bond between Ser280 of the receptor and the oxygen from the ligand's aldehyde head are also examined (Figure 2). This hydrogen bond was found to be a crucial interaction underlying the potential activity of a candidate compound, in line with the results of the prior docking investigation [3].

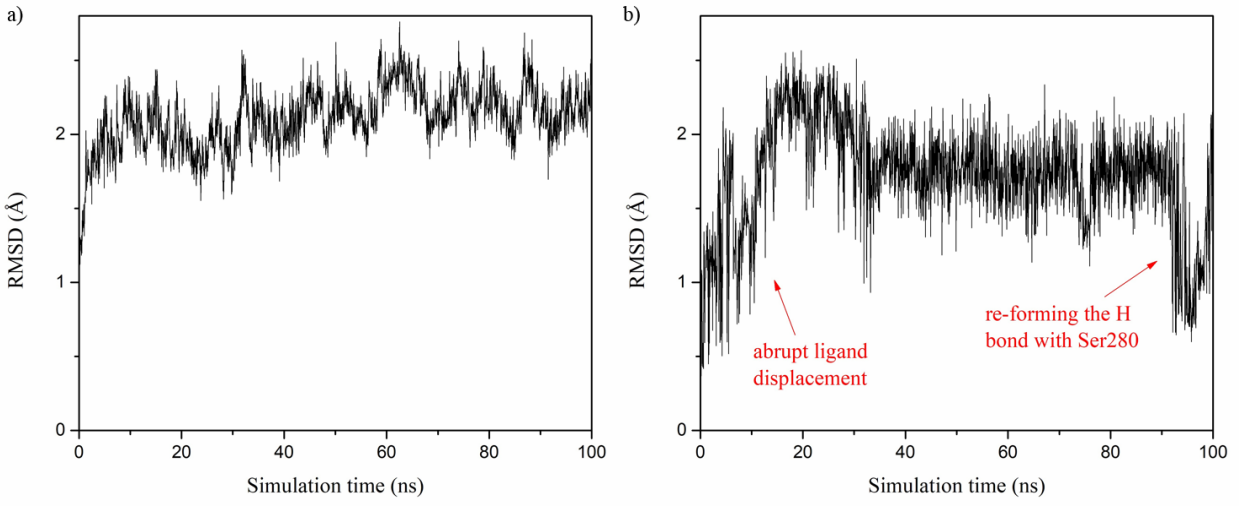


Figure 1. RMSD plot of the: a) PPARα backbone atoms and b) candidate molecule in the protein-ligand complex during the production phase of MD simulation.

Regardless of the stability of the receptor (Figure 1a) during the simulation, the ligand exhibited a propensity to migrate along the ligand binding domain, demonstrating the instability of the observed conformation (Figure 1b). Nonetheless, it was noticed that the ligand occasionally

reverted to its original conformation during the course of the simulation. Monitoring the length of some of the critical hydrogen bonds can also reveal the described effect, depending on how the associated hydrogen bonds are generated or broken at that particular time. Here, the tracking of the length of the hydrogen bond with Ser180 clearly demonstrated the given assumption. Simulation parts where these phenomena can be seen are displayed in Figure 2.

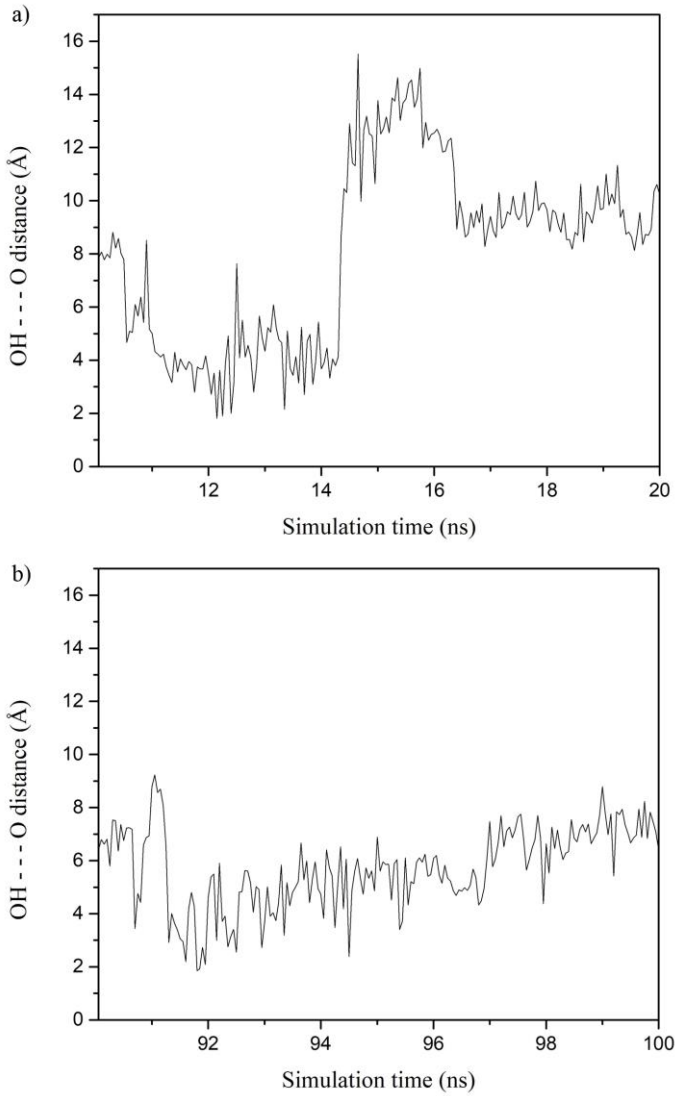


Figure 2. The distance between the oxygen of the ligand COO^- group and the OH group from Ser280 (presenting hydrogen bond of interest) in PPARα – ligand complex during: a) second and b) tenth 10 ns of the production phase of the MD simulation.

According to the obtained results, it can be concluded that the candidate compound, although it has the potential to act as a PPARα agonist, is most likely only a partial activator. However, natural compounds can describe a chemical space and produce new molecular patterns that are rarely found in synthetic libraries. Compounds discovered using the methodology outlined above can act as scaffolds for molecular optimization, which will improve their initial characteristics. In addition, natural partial agonists have been shown to be quite beneficial in the prevention of cardiovascular illnesses [2].

CONCLUSION

Natural compounds are an essential source of novel treatment possibilities for many disorders linked to metabolic syndrome and cardiovascular diseases. The findings of this study confirmed that a coumarin molecule(E)-3-[(2-oxo-chromen-3-yl)-methyleneamino]-acrylaldehyde, which was previously identified as a PPAR agonist, has the ability to activate this receptor, but most likely only partially. However, the selected candidate can be beneficial in the prevention of atherosclerosis and dyslipidemia. Additionally, it can serve as a viable scaffold for further molecular optimizations.

Acknowledgment

This work was supported by the Ministry of Education, Science and Technological Development of the Republic of Serbia (grant no 451-03-66/2024-03/200017).

REFERENCES

[1] A.V. Contreras, N. Torres, A.R. Tovar, Adv. Nutr., 4 (2013).
[2] D. Rigano, C. Sirignano, O. Taglialatela-Scafati, Acta Pharmacol. Sin., 7 (2017) 427.
[3] D. Radošević, K. Stevanović, V. Perović, S. Glišić, 2nd International Conference on Chemo and Bioinformatics ICCBIKG 2023 (597-600).
[4] J. Huang, A. D. J. MacKerell, J. Comput. Chem., 34 (2013) 2135.
[5] K. Vanommeslaeghe, E. Hatcher, C. Acharya, S. Kundu, S. Zhong, J. Shim, E. Darian, O. Guvench, P. Lopes, I. Vorobyov, A. D. Mackerell Jr, J. Comput. Chem., 31 (2010) 671.
[6] J. C. Phillips, D. J. Hardy, J. D. C. Maja, J. E. Stone, J. V. Ribeiro, R. C. Bernardi, R. Buch, G. Fiorin, J. Henin, W. Jiang, R. McGreevy, M. C. R. Melo, B. K. Radak, R. D. Skeel, A. Singharoy, Y. Wang, B. Roux, A. Aksimentiev, Z. Luthey-Schulten, L. V. Kale, K. Schulten, C. Chipot, E. Tajkhorshid, J. Chem. Phys., 153 (2020) 044130.
[7] W. Humphrey, A. Dalke, K. Schulten, J. Mol. Graph., 14 (1996) 33.

IDENTIFYING NATURAL COMPOUNDS AS A PROMISING INHIBITOR OF GABA REUPTAKE

K.Stevanović, S. Glišić and M. Senćanski

University of Belgrade, Institute of Nuclear Sciences Vinča, Department for Bioinformatics and Computational Chemistry, Mike Petrovića Alasa 12-14, 11351 Vinča, Belgrade, Serbia.
(kristina.stevanovic@vin.bg.ac.rs)

DOI: https://doi.org/10.46793/Phys.Chem24II.655S

ABSTRACT
γ-Aminobutyric acid (GABA) targets are relevant in drug discovery because modulation of its levels can be used in the treatment of various diseases, such as epilepsy, anxiety and depression. Using a combined in silico approach, we focused on GABA transporter 1 to select new inhibitors from the ZINC database. A set of known inhibitors was used as a reference. Our results propose several compounds as potential new ligands.

INTRODUCTION

γ-Aminobutyric acid (GABA) is the most important inhibitory neurotransmitter in the central nervous system, targeting $GABA_A$, $GABA_B$ and $GABA_C$ receptors. After being released to the synaptic cleft, it is reabsorbed by four types of GABA transporters (GAT). [1] Maintenance of GABA levels is crucial for excitatory and inhibitory neurotransmitter balance. [2] Inhibition of GABA reuptake leads to higher GABAergic activity, which can be effective in the treatment of many diseases, such as epilepsy, anxiety, depression and pain. There is also evidence for possible use in insomnia, stroke and Alzheimer's disease therapy. [3] Despite the large possibility of using GABA transporter inhibitors in the therapy, there is only one drug, tiagabine, a selective GAT-1 inhibitor, used in the treatment of epilepsy and panic disorder. [4]. Here we focus on the GAT-1 transporter, to propose new compounds from the ZINC natural compounds database, as possible inhibitors. We use combined molecular filtering, including long-range and short-range intermolecular interaction approaches.

METHODS

To identify potential candidates for GABA transporter 1 inhibitor, the ZINC database (https://zinc12.docking.org/) of natural products was screened. A learning set consisting of 44 literature inhibitors, downloaded from the BindingDB database (https://www.bindingdb.org/), was generated to identify good predicting criteria. The initial set of candidates was selected using the ISM-SM (informational spectrum method for small molecules) method [5], as a long range molecular interaction based approach. Then, (by the chemical structure of the existing inhibitors) only those that were electroneutral and had amino and carboxyl groups were isolated. Following the application of Lipinski's rule of five [6] to filter selected compounds, the virtual screening protocol further considered the building of a 3D QSAR model and molecular docking into the receptor binding site (short range interactions approach).

In the ISM-SM algorithm, each amino acid /atomic group is represented by the value of the electron-ion interaction potential (EIIP), corresponding to the average energy states of all valence electrons in a particular amino acid/atomic group [5, 7]:

$$EIIP = 0.25\ Z^* \sin(1.04\ \pi\ Z^*)\ /2\pi, \quad Z^* = \Sigma\ m(ni\ Zi\ /\ N) \qquad (1)$$

where Zi is the valence number of the i-th atomic component, ni is the number of atoms of the i-th component, m is the number of atomic components in the molecule, and N is the total number of atoms. The obtained numerical sequence is transformed into informational spectrum by Fourier transformation, where each frequency corresponds to specific information encoded in the amino acid/atomic groups sequence. Through cross-spectral analysis, information shared by a protein and a related small molecule can be distinguished.

Following the previously indicated stepwise filtering 34 chosen compounds were submitted to QSAR modeling. All compounds were protonated at pH 7.4, optimized using MMFF94 force field [8], and orientated by the principal moments of inertia to prepare them for the QSAR. After calculating standard GRIND descriptors [9] using Pentacle software (version for Linux) [10], the principal component analysis (PCA) model was constructed. When the number of PCA components was set to five, the resulting model's explained variance was 76.31%.

We used AutoDock Vina (version 1.2.5) with AutoDock 4 force filed for the molecular docking [11]. The Cryo-EM crystal structure of human GABA reuptake transporter 1, code 7Y7Z [12], was retrieved from the RCSB Protein Data Bank and preprocessed to compute protonation states and add hydrogen atoms. All ions, cofactors, and crystallographic water were absent from the structure. Energy minimization for the chosen ligands from the PCA model was achieved. A 60 × 60 × 60 Å grid box containing all of the amino acid residues involved in binding was positioned in the center of the ligand binding site based on the coordinates of the co-crystallized ligand.

The ADMET (Absorption, Distribution, Metabolism, Elimination, and Toxicity) parameters of the candidate compounds were calculated using QikProp software in normal mode [13].

RESULTS AND DISCUSSION

Figure 1 illustrates the PCA model that was constructed. Candidates are indicated with black squares, whereas molecules from the learning set are indicated with red circles. Eight compounds were chosen for additional structure-based screening because they most closely matched known inhibitors (Figure 2). We also computed significant ADMET parameters for them, which demonstrated good pharmacokinetic profiles.

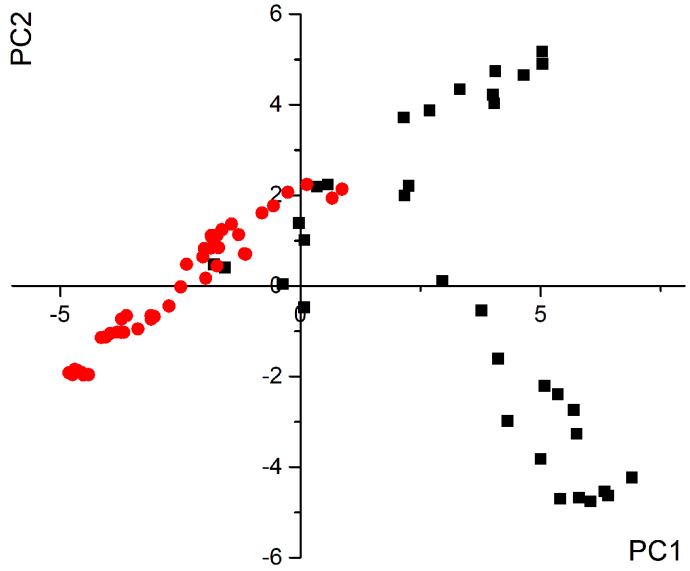


Figure 1. PCA plot of the first two components scores (black squares: candidate molecules, red circles: learning set).

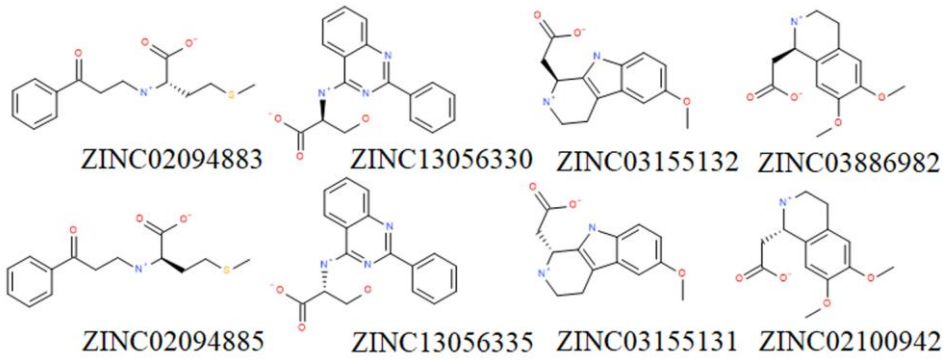


Figure 2. Selected candidates (from PCA model) for structure-based screening.

The docking results indicated that the candidate compounds resembled the positioning of the co-crystallized inhibitor, regardless of the potential of the potentially weak interaction with the receptor (binding energies of about -6 to -7.5 kcal/mol). Particularly significant is the formation of a hydrogen bond with Glu65 via the carboxyl group, which is a crucial interaction for the tiagabine activity (Figure 3) [12]. We found that the candidate ZINC13056330 (IUPAC name: (2S)-3-hydroxy-2-[(2-phenylquinazolin-4-yl)azaniumyl]propanoate) is most effectively positioned after reflecting on all of the obtained docking poses. The position of the designated molecule within the binding site, as determined by our docking methodology, is displayed in Figure 3. It forms hydrogen bonds with Phe294 and Ser295 in addition to the one it already has with Glu65. A π-cation interaction is also established with Phe294 as well. Additionally, amide-π interactions with Tyr296 and π-alkyl interactions with Ala61, Leu300, and Leu303 stabilize it.

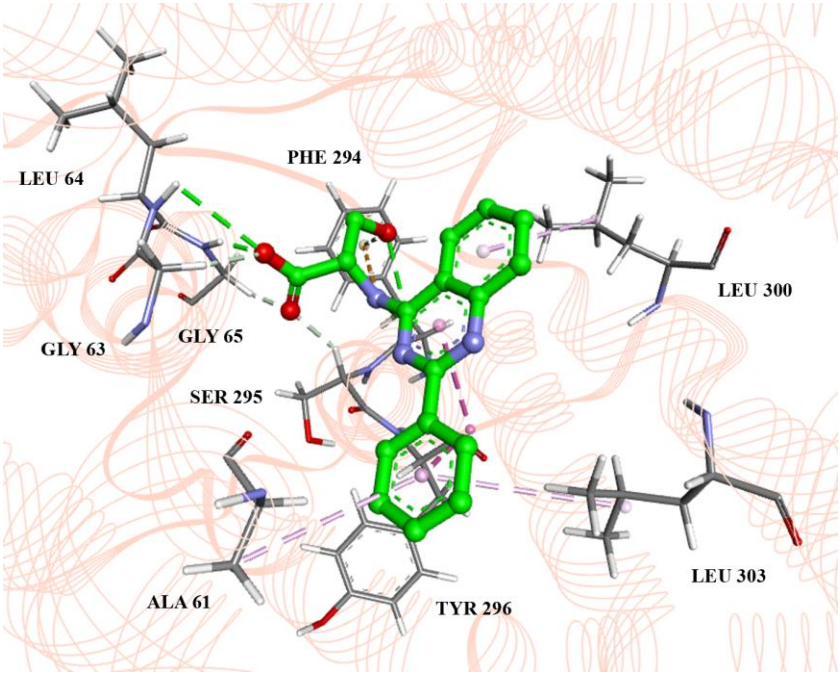


Figure 3. ZINC13056330 ((2S)-3-hydroxy-2-[(2-phenylquinazolin-4-yl)azaniumyl]propanoate) in the human GABA transporter GAT1 inhibitor binding pocket, with marked interacting amino acid residues. Green lines: hydrogen bonds, pink: alkyl-π interactions, magenta: π-amide interactions, yellow: π-cation interactions.

According to molecular docking, the chosen candidates also fit into the binding pocket of GAT1, in addition to the high molecular similarity discovered in the QSAR model. While our *in silico* screening approach showed promise, further experimental testing is necessary. Certainly, this finding creates fresh prospects for finding natural GAT1 inhibitors.

CONCLUSION

Using a combined *in silico* approach, we filtered the ZINC database through several steps, including methods based on long-range and short-range intermolecular interactions. The ISM-SM approach has the advantage of rapidly scanning large compound libraries, and in conjunction with short-range based methods has the significant potential to propose selective inhibitors for a target.

Acknowledgment

This work was supported by the Ministry of Education, Science and Technological Development of the Republic of Serbia (grant no 451-03-66/2024-03/200017).

REFERENCES

[1] J. Bormann, Trends Pharmacol. Sci., 21 (2000) 16.
[2] A. Schousboe, K.K. Madsen, M. L. Barker-Haliski, H.S. White, Neurochem. Res., 39 (2014) 1980.
[3] K.Łątka, J. Jończyk, M.Bajda, Int. J. Biol. Macromol., 158 (2020) 750.
[4] P. Zwanzger, D. Eser, C. Nothdurfter, T. C. Baghai, H.-J. Möller, F. Padberg, R. Rupprecht, Pharmacopsychiatry, 42 (2009) 266.
[5] M. Sencanski, N. Sumonja, V. Perovic, S. Glisic, N. Veljkovic, V. Veljkovic, 2020, arXiv:1907.02713.
[6] C. A. Lipinski, F. Lombardo, B. W. Dominy, P. J. Feeney, Adv. Drug Deliv. Rev., 23 (1997) 3.
[7] V. Veljkovic, A Theoretical Approach to Preselection of Carcinogens and Chemical Carcinogenesis, Gordon & Breach, New York, 1980.
[8] T. A. Halgren, J. Comput. Chem., 17 (1996) 490.
[9] Á. Durán, I. Zamora, M. Pastor, J. Chem. Inf. Model., 49 (2009) 2129.
[10] M. Pastor, G. Cruciani, I. McLay, S. Pickett, S. Clementi, J. Med. Chem., 43 (2000) 3233.
[11] J. Eberhardt, D. Santos-Martins, A. F. Tillack, S. Forli, J. Chem. Inf. Model., 61 (2021) 3891.
[12] A. Zhu, J. Huang, F. Kong, J. Tan, J. Lei, Y. Yuan, C. Yan, Nat. Struct. Mol. Biol., 30 (2023) 1012.
[13] Schrödinger Release 2021-2: QikProp, Schrödinger, LLC, New York, NY, 2021.

CHITOSAN–CLAY COMPOSITES AS POTENTIAL CARRIERS FOR TETRACYCLINE: INFLUENCE OF POLYMER–CLAY MASS RATIO

D. Krajišnik[1], S. Uskoković-Marković[2], A. Daković[3] and M. Marković[3]

[1]*Department of Pharmaceutical Technology and Cosmetology, University of Belgrade – Faculty of Pharmacy, Serbia. (danina.krajisnik@pharmacy.bg.ac.rs)*
[2]*Department of Analytical Chemistry, University of Belgrade – Faculty of Pharmacy, Serbia.*
[3]*Institute for Technology of Nuclear and Other Mineral Raw Materials (ITNMS), Belgrade, Serbia.*

DOI: https://doi.org/10.46793/Phys.Chem24II.659K

ABSTRACT
In this study, the preparation and characterization of chitosan–clay composites prepared at different polymer–clay mass ratios, were performed as potential carriers for tetracycline hydrochloride. The composites based on bentonite (from Beretnica deposit, Republic of Serbia) and low molecular weight chitosan were prepared. Adsorption of tetracycline was investigated at the different initial concentrations (0.5 – 1 mg/mL) at pH 3.4. Characterization of the chitosan–clay composites before and after adsorption of tetracycline was performed by determination of the zeta potential and by FTIR spectroscopy. The characterization results confirmed the presence of polymer and tetracycline on the clay surface. The amounts of adsorbed antibiotic were influenced by the polymer–clay mass ratio, i.e. the presence of chitosan in the composites.

INTRODUCTION
Clay minerals are abundant, low-cost and non-toxic class of materials with unique properties such as intercalation, swelling, ion exchange and adsorption properties that have never lost scientific interest due to their diverse biomedical applications [1]. The incorporation of drug molecules into clay minerals represents a great opportunity, as the obtained clay-drug composites/hybrids are different from simple physical mixtures of the individual components [2]. Furthermore, the modification of the clay surface with polymeric materials enables the preparation of polymer-clay composites as novel materials with improved functional properties. Chitosan, a natural cationic polysaccharide known for its remarkable properties such as good biocompatibility, biodegradability, and renewability as well as its biological activities is very interesting for the preparation of chitosan-clay composites for drug delivery application [3].

In this study, chitosan-clay composites at different clay/chitosan mass ratio were prepared and the adsorption of tetracycline hydrochloride by the obtained composites was further investigated. The adsorption process of the drug by the prepared chitosan-clay composites was followed by determining the adsorption isotherms (Langmuir and Freundlich), while the characterization of the composites before and after the adsorption of tetracycline was carried out by measuring the zeta potential and FTIR spectroscopy.

METHODS
A Ca-bentonite (Beretnica deposit, the Republic of Serbia (BB)) and commercially available low molecular weight chitosan (Sigma-Aldrich, USA) (LMW CS) were used as starting materials for the preparation of chitosan-clay composites. The clay-chitosan composites with two clay/chitosan ratios were prepared. In brief, a 0.5% (m/m) LMW CS solution was prepared in a 1% acetic acid solution. The appropriate amounts of BB were gradually added to 25 mL of the prepared LMW CS solution

to obtain a suitable clay/chitosan ratio. The suspensions were stirred for 10 min at a speed of 1200 rpm. The prepared chitosan-clay composites were separated from the polymer solution by centrifugation at 15000 rpm for 10 min and washed with purified water to remove unbound chitosan. The washing process was carried out until the pH of the supernatant reached the pH of the purified water. Thereafter, the prepared composites were air-dried overnight and ground to obtain particles below 125 μm. The prepared chitosan-clay composites were compared with clay:chitosan prepared clay/chitosan at mass ratio 400 : 1 as described previously [4].

Table 1 shows the clay/chitosan ratio during the preparation and the labels of the obtained composites.

Table 1. The initial clay/chitosan ratio and the labels of the prepared composites.

Clay : chitosan ratio	Sample label
400 :1	BLMW
10 : 1	BLW(10:1)C
4 : 1	BLW(4:1)C

The adsorption of tetracycline hydrochloride (Sigma-Aldrich, USA) (TCH) on the mineral starting material and the prepared composites was carried out in batch experiments at room temperature. Aqueous stock solutions of the active substance (pH 3.4) with different initial concentrations (0.05 – 1 mg/mL) were prepared in purified water. Batch experiments were performed by shaking the mixture containing 40 mg of each composite and 10 mL of each drug solution for 1 hour at room temperature on a laboratory shaker at 250 rpm and then separated after centrifugation at 3000 rpm for 30 minutes. The supernatants were used to determine the non-adsorbed drug concentrations. The non-adsorbed drug concentrations were determined spectrophotometrically at λ=276 nm (Evolution 300 spectrophotometer, Thermo Fisher Scientific, UK). The amounts of adsorbed antibiotic were calculated from the difference between the initial concentrations of TCH and the amounts remaining in the aqueous medium after dynamic equilibrium.

Characterization of the chitosan-clay composites and chitosan-clay-TCH composites was performed using a Zetasizer NanoZS90 instrument (Malvern Instruments, UK) and by Fourier transform infrared (FTIR) spectroscopy using a Nicolet iS50 spectrophotometer (Thermo Fisher Scientific, USA). FTIR spectra were recorded using Attenuated Total Reflection (ATR) with a diamond ATR smart accessory in the range of 4000-400 cm^{-1} at 64 scans per spectrum at 2 cm^{-1} resolution. A background scan was acquired before scanning the samples.

RESULTS AND DISCUSSION

The infrared spectra BB and composites with LMW CS before (a) and after adsorption of TCH (b) are shown in **Figure 1**. In BB, the band at 3620 cm^{-1} is associated with vibrations of the structural OH groups. The broad band around 3400 cm^{-1} represents the OH groups coordinated by hydrogen bonding, while the bending vibration of water is noticed at 1631 cm^{-1}.

After modifying BB with different amounts of LMW CS, a small decrease in the intensities of bands at 3400 cm^{-1} and 1631 cm^{-1} is observed, suggesting the presence of the polymer in composites. Interactions of BB and the composites with TCH are evidenced by the appearance of small intensity bands characteristic of the drug in the wavenumber range 1600-1280 $cm^{-1.}$

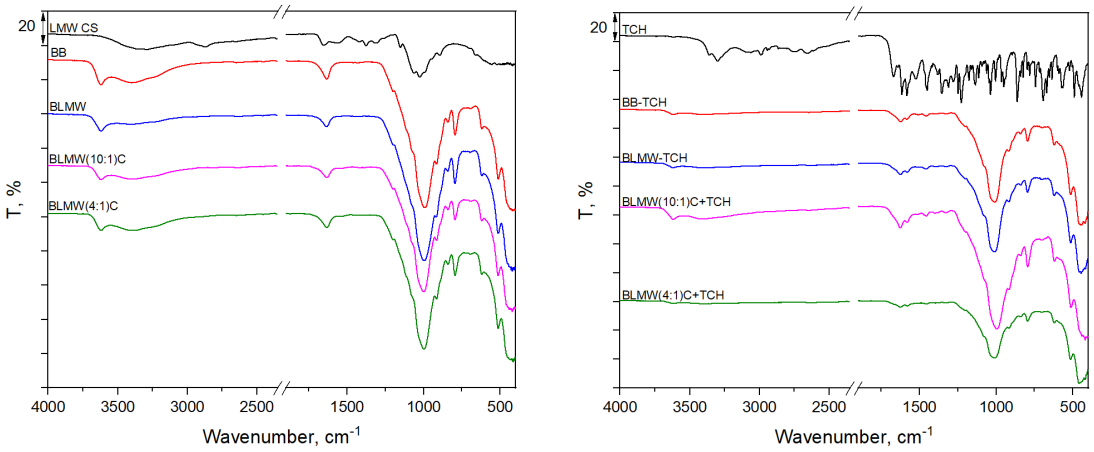


Figure 1. a) FTIR spectra of LMW CS, BB, BLMW, BLMW(10:1)C and BLMW(4:1)C, b) FTIR spectra of TCH, BB-TCH, BLMW-TCH, BLMW(10:1)C+TCH and BLMW(4:1)C + TCH.

The isotherms of TCH adsorption on BLMW(10:1)C and BLMW(4:1)C composites are shown in **Figure 2.** The adsorption of TCH followed a nonlinear adsorption isotherm, and the experimental data were analyzed using the Langmuir and Freundlich models. The Langmuir equation showed a better fit ($R^2 > 0.9$) of the equilibrium adsorption data over the entire concentration range, as previously reported for BB and BLMW [4].

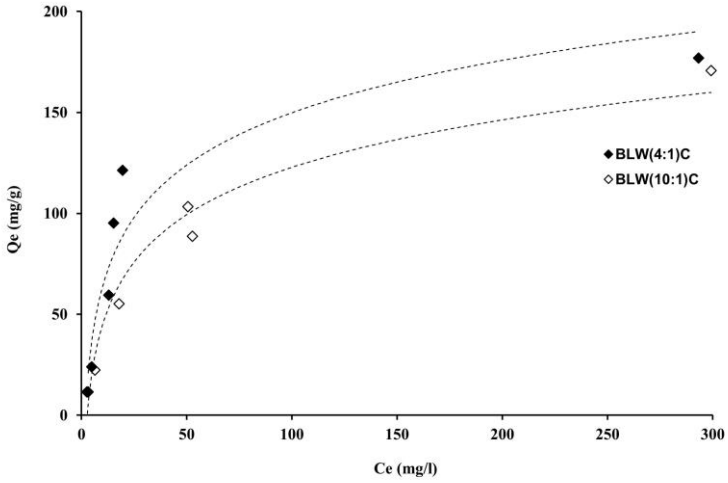


Figure 2. Adsorption of TCH by BLMW(10:1)C and BLMW(4:1)C composites.

The maximum adsorbed amounts of drug at the maximum initial drug concentrations were 170.8 mg/g for BLMW(10:1)C+TCH and 176.9 mg/g for BLMW(4:1)C+TCH. The results showed that both the natural clay and all prepared chitosan-clay composites have a high affinity for adsorption of TCH. The slightly lower amounts of adsorbed TCH by the composites prepared at the lower clay : chitosan ratio could be explained by chitosan binding on the clay surface and occupation of active sites for adsorption.

The interactions of TCH with the starting clay and the prepared clay:chitosan composites were also analyzed by measuring the zeta potential (**Figure 3**). The negative zeta potential value (-29.3 mV) of BB is characteristic of bentonite, while after its modification with LMW CS, the potential

becomes less negative for all clay/chitosan ratios (up to -22.5 mV). After adsorption of TCH, the increased negative value of the zeta potential for all tested samples indicates the interactions between TCH and active sites in the natural clay and the chitosan-clay composites.

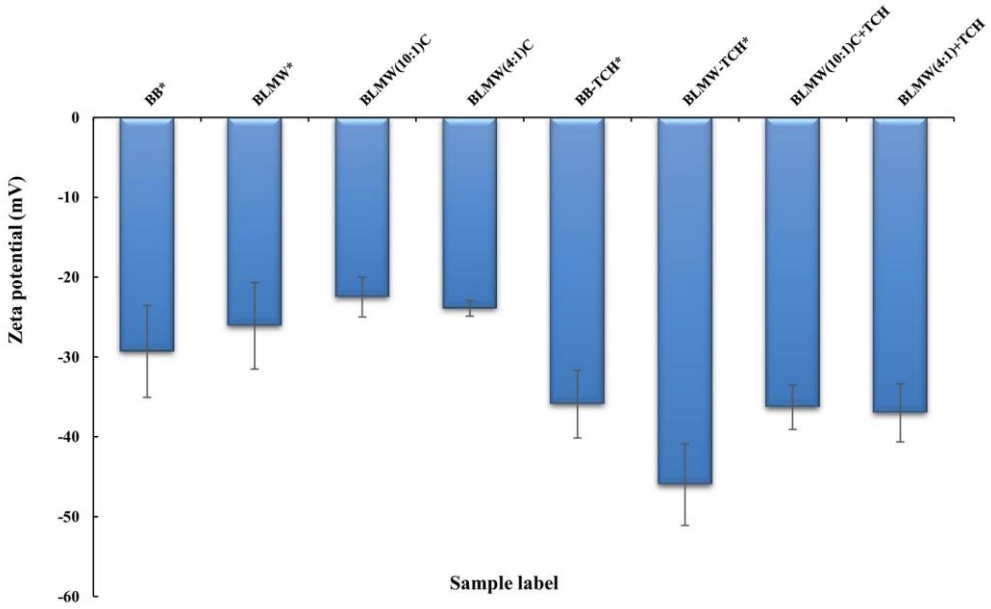


Figure 3. Zeta potentials of: natural BB, BLMW, BLMW(10:1)C and BLMW(4:1)C), and clay-chitosan-drug composites after TCH adsorption: B-TCH, BLMW-TCH, BLMW(10:1)C+TCH and BLMW(4:1)C+TCH (* from the published data [4]).

CONCLUSION

In this study, the adsorption of tetracycline hydrochloride on chitosan–clay composites was influenced by the polymer:clay mass ratio at which they were prepared. Further investigations of the functional properties of the prepared chitosan-clay drug composites, such as drug release, mucoadhesivity, and antibacterial activity, will reveal their potential use as drug carriers for topical application.

Acknowledgment

This research was funded by the Science Fund of the Republic of Serbia, #GRANT No 7748088, Project title: Composite clays as advanced materials in animal nutrition and biomedicine - AniNutBiomedCLAYs.the Ministry of Science, Technological Development and Innovation, and by the Republic of Serbia through the following Grant Agreements: 451-03-65/2024-03/200161 and 451-03-66/2024-03/200161 (University of Belgrade-Faculty of Pharmacy).

REFERENCES

[1] L. Giuseppe, S. Riela, R.F. Fakhrullin, Ther. Deliv., 8(8) 2017 633.
[2] M. H. Kim, G. Choi, A. Elzatahry, A. Vinu, Y. B. Choy, J. H. Choy, Clays Clay Miner., 64(2) (2016) 115.
[3] Y. Wang, Z. Wang, W. Lu, Y. Hu, Int. J. Biol. Macromol., (2023) 128080.
[4] D. Krajišnik, S. Uskoković-Marković, A. Daković, D. Smiljanić, M. Kozarski, V. Lazić in: 5th Metallurgical & Materials Engineering Congress of South-East Europe, Trebinje, BIH (2023) 123.

ELEMENTAL COMPOSITION OF INFUSIONS OF STINGING NETTLE COLLECTED FROM DIFFERENT LOCALITIES IN SERBIA

M. Antonijević-Nikolić[1], K. Popović[1], J. Đuričić-Milanković[1], D. Ranković[2], B. Dražić[3] and S. Tanasković[3]

[1] *Academy of Applied Studies Šabac, Department of Medical and Business-Technological Studies, Hajduk Veljkova 10, Šabac, Serbia. (kosanal@gmail.com)*
[2] *Faculty of Physical Chemistry, University of Belgrade, Studentski trg 12-16, 11000 Belgrade, Serbia*
[3] *Faculty of Pharmacy, University of Belgrade, Vojvode Stepe 450, 11000 Belgrade, Serbia*

DOI: https://doi.org/10.46793/Phys.Chem24II.663AN

ABSTRACT

Medicinal plants can contain various beneficial but potentially toxic trace elements. Traditional preparation and consumption of herbal tea can provide many valuable elements, as well as those harmful to health. In this study, the content of five elements (Cu, Fe, Mn, Ni, and Zn) in infusions prepared from *Urtica dioica* L. leaf samples collected from five different locations in the Republic of Serbia was determined. The infusions were prepared with boiling redistilled water, with an extraction time of 10 minutes. The content of the analyzed elements in the infusions was determined using inductively coupled plasma optical emission spectroscopy (ICP-OES). Mn and Zn were present in higher concentrations in the infusions, while Ni was below the detection limit of the method. Cu had the highest extraction coefficient values (65.8-24.8%), while Fe had the lowest values (1.11-2.84%). The content of elements obtained in the infusions was used to calculate the daily intake (EDI).

INTRODUCTION

Medicinal plants are defined as plants that are used as medicines to prevent diseases, maintain health, or cure diseases [1]. They have a long history of therapeutic use throughout the world and still represent an important part of traditional medicine. The demand for medicinal plants is increasing, and with this, quality control and standardization become crucial requirements [2]. Medical plants are a rich source of minerals and trace elements that are essential to human health, and drinking infusions of herbal teas can be an important source of some essential minerals [3].

Tea infusions can provide many valuable elements, but also those that are harmful to health. Among the most commonly used plants is the stinging nettle (*Urtica dioica L.).* The stinging nettle belongs to the *Urticaceae* family and represents a perennial plant. Stinging nettle is an abundant species occurring in various types of forests, road verges, and grassland sites. In many countries, it is used as both medicine and food since stinging nettle is not aggressive and does not have severe side effects [4].

The components of herbal teas include essential or non-essential minerals/metals such as As, Ba, Cd, Co, Cu, Cr, Ni, Pb, Se, V, and Zn [1]. Since the plant can grow in different areas, they can be contaminated with non-essential elements [5]. Herbs absorb these elements through their roots. The ability of element accumulation of herbs and the geochemical nature of the soil are responsible for the level of presence of the elements in the plants [2].

The aim of this work is to determine the concentration of tested elements in stinging nettle herbal tea and determine the extraction coefficient of tested elements during the preparation of herbal tea by cooking and dry digestion of nettle leaves using ICP-OES.

METHODS

Sampling and Sample Preparation

Stinging nettle (*Urtica dioica* L.) leaves were collected from five localities in the Republic of Serbia during spring (**Figure 1.**). Running tap water was employed to remove the dust and adhered particles, and finally, deionized water. Leaves were dried naturally in the shade on draft for one month. Dried plant material was grounded using a grinder (A 11 BASIC IKA) and passed through a 0.5 mm sieve (laboratory vibrating screen, WQS, Gramma Libero). The powdered samples were stored in paper bags at ambient temperature and used for the analysis.



Figure 1. Location of the sampling points for leaves collection.

Infusions were prepared in the traditional manner. Samples of stinging nettle leaves (1 g each) were weighed on an analytical balance, transferred into a glass beaker, poured over with 50 mL of boiled redistilled water, and left at room temperature for 10 minutes. The infusions were filtered before measurements. The content of elements (Cu, Fe, Ni, Mn, Zn) in infusions was measured by ICP-OES by the Thermo Scientific iCAP 7000 Series model. Three replicates from each sample were analyzed.

RESULTS AND DISCUSSION

Infusions, such as herbal tea beverages, contain various bioactive compounds and minerals that can have a significant impact on human health. Consumption of herbal tea beverages can be an important source of essential minerals, as well as toxic ones. In this work, the content of essential (Cu, Fe, Mn, and Zn) and probably essential in trace (Ni) was determined in infusions using ICP-OES. The content of elements in stinging nettle leaf infusions obtained using boiling redistilled water as an extraction solvent is shown in **Table 1.** The transfer ratio of elements from the stinging nettle to the infusion, i.e., the transference rate of the examined metals, is expressed as the ratio of the metal content in the infusion to the total metal content in the stinging nettle. As shown in **Table 1.**, the transference rates for Cu, Fe, Mn, and Zn differ from each other. For the same element, variations in the transference rate are observed depending on the sampling location. In general, in infusions, the range of concentration in which iron was found in all samples varied from 2.22±0.24 mg/kg to 4.75 ±0.13 mg/kg dry weight, copper 1.30±0.25 mg/kg to 4.44±0.39mg/kg dry weight, manganese 3.49±0.37 mg/kg to 7.82±0.44 mg/kg dry weight and zinc 8.55±0.68 mg/kg to 14.99±0.89 mg/kg dry weight. The content of Ni has been below the detection limit.

In samples, the total content of Fe was the highest (109.75±4.01 - 244.41±13.50 mg/kg dry weight). Manganese was the second highest element found in all tea samples (30.63±1.45 - 68.44±5.11 mg/kg). The concentrations of Ni, Cu, and Zn in the analyzed samples were in the range of 0.54±0.00 to 1.87±0.10 < 2.12±0.69 to 12.79±0.53 < 18.18±0.46 to 28.48±1.37 mg/kg respectively [6]. However, these elements were present at low concentrations in tea infusion (Table 1), and it could be hypothesized that they do not pose a threat to human health. In the case of Ni, the

content of the element in the infusion was below the detection limit; thus, the amount of element released from tea leaves to beverages was treated as zero.

Table 1. The contents of elements (mg/kg dry weight) in infusions, total contents in leaves of stinging nettle (mg/kg dry weight), and the transference rate of the elements from stinging nettle into the infusion (%).

No.	Content of elements in infusions (total content [6]), (mg/kg dry weight)					Transference rate of the elements from stinging nettle into the infusion (%)			
	Cu	Fe	Ni	Mn	Zn	Cu	Fe	Mn	Zn
1	3.22±0.35 (4.89±0.31)	2.24±0.49 (109.75±4.01)	N.D. (0.54±0.00)	3.70±0.26 (30.63±1.45)	10.47±0.53 (18.18±0.46)	65.80	2.04	12.10	57.60
2	4.44±0.39 (12.79±0.53)	2.22±0.24 (181.28±25.12)	N.D. (1.87±0.10)	3.49±0.37 (53.90±7.45)	10.95±0.67 (23.07±2.95)	34.70	1.22	6.50	47.50
3	2.06±0.32 (8.39±0.73)	4.75±0.13 (166.96±12.63)	N.D. (1.27±0.00)	5.54±0.39 (32.16±2.89)	8.55±0.68 (28.48±1.37)	24.55	2.84	17.20	30.00
4	2.23±0.27 (3.97±0.28)	2.72±0.37 (244.41±13.50)	N.D. (0.92±0.00)	7.82±0.44 (66.66±2.21)	14.99±0.89 (25.66±0.91)	56.20	1.11	11.70	58.40
5	1.30±0.25 (2.12±0.69)	2.42±0.48 (120.36±3.70)	N.D. (0.97±0.10)	7.62±0.39 (68.44±5.11)	11.67±0.55 (20.51±0.48)	61.30	2.01	11.10	56.90

ND-not detected

The results in **Table 1.** showed that the highest content in the infusions was obtained for Zn (8.55±0.68-14.99±0.89 mg/kg). The contents of Cu, Zn, Mn, and Fe in the infusions grow in the following order: Cu < Fe < Mn < Zn. However, high levels of extraction (**Table 1.**) of elements copper (24.8–65.8 %) and zinc (30.0–58.4 %) were obtained.

It is noticeable that the Fe level in infusions ranges from 1.11 % of total iron in sample 4 to 2.84 % of total iron in sample 3 (**Table 1.**). Obtained values are extremely low in all plant samples. These data indicate that the preparation of water extracts of medicinal plants (infusions) may deliver to a human digestive system a rather low bioavailable fraction of total iron present in plant material. Additionally, the literature states that at water temperatures above 60 ℃, there will be a decrease in the rate of extraction of elements such as Fe into the solution [7]. This may be the reason for the extremely low concentration of Fe in the infusions compared to the very high total content in nettle leaves. The efficiency of extraction depends on the chemical form of the element, i.e., also on the solubility of the compound, the brewing time, solvent, degree of water mineralization, heterogeneity of raw materials, and the differences in conditions preparing the infusions [8].

The total content of elements in the stinging nettle and the transference rate of the elements from the plant into the infusion were used to evaluate the estimated daily intake (*EDI*) [9] (**Table 2.**). The procedure for determining *EDI* is described in the paper [6].

The *EDI* of the examined elements in all samples was less than the recommended daily intakes expressed by body weight (**Table 2.**). This indicates that the daily intakes of the analyzed elements, provided by drinking five cups of stinging nettle leaf infusions, are significantly lower than the human body's requirements.

Table 2. Estimated daily intake (EDI) (mg/kg bw/day) of elements for adults due to consumption of infusion of stinging nettle, recommended daily intake (RDI) values for investigated elements, and the recommended daily intake (RDI*) expressed for bodyweight (mg/kg body weight/day).

No.	EDI (mg/kg body weight/day) for adults			
	Cu	Fe	Mn	Zn
1	$4.60 \cdot 10^{-4}$	$3.20 \cdot 10^{-4}$	$5.29 \cdot 10^{-4}$	$1.50 \cdot 10^{-3}$
2	$6.34 \cdot 10^{-4}$	$3.16 \cdot 10^{-4}$	$5.01 \cdot 10^{-4}$	$1.57 \cdot 10^{-3}$
3	$2.94 \cdot 10^{-4}$	$6.77 \cdot 10^{-4}$	$7.90 \cdot 10^{-4}$	$1.22 \cdot 10^{-3}$
4	$3.19 \cdot 10^{-4}$	$3.88 \cdot 10^{-4}$	$1.11 \cdot 10^{-3}$	$2.14 \cdot 10^{-3}$
5	$1.86 \cdot 10^{-4}$	$3.46 \cdot 10^{-4}$	$1.09 \cdot 10^{-3}$	$1.67 \cdot 10^{-3}$
RDI (mg/day/person) for men (women) [10]	0.9	8 (18)	2.3 (1.8)	11 (8)
RDI* (mg/kg body weigth/day) for men (women) weighing 70 kg	$1.29 \cdot 10^{-2}$	$1.14 \cdot 10^{-1}$ ($2.57 \cdot 10^{-1}$)	$3.29 \cdot 10^{-2}$ ($2.57 \cdot 10^{-2}$)	$1.57 \cdot 10^{-1}$ ($1.14 \cdot 10^{-1}$)

CONCLUSION

In this paper, ICP-OES was applied to analyze five elements (Cu, Fe, Ni, Mn, Zn) in different infusions prepared for stinging nettle leaves. Analysis of infusions showed different contents of the elements. The metal bioavailabilities were significantly different from 1.11% to 65.80%. The highest percentages of releases from the leaves to their infusions were noticed for Zn and Cu (up to 58.40% for Zn and 65.80% for Cu), while the lowest were devoted to Fe (up to 2.84 %). The content of Ni in the infusion has been below the detection limit. The estimated daily intake of all elements from the analyzed infusions was less than the recommended daily intakes expressed by body weight.

Acknowledgment

This work was supported by the Ministry of Education, Science and Technological Development of the Republic of Serbia (grant no 451-03-47/2023-01/ 200161).

REFERENCES

[1] S. Kilić, M. Soylak, J Food Sci Technol. 57(3) (2020) 927.
[2] A. Balekundri, V. Mannur, Future J. of Pharm. Sci., 6 (2020) 67.
[3] S. Raiæ, V. Kuntiæ, Int. J. Food Prop., 16(1) (2013) 1-8
[4] S. Jarić, Z. Popović, M. Mačukanović-Jocić, L. Djurdjević, M. Mijatović, B. Karadžić, M. Mitrović, P. Pavlović, J. of Ethnopharmacol, 111(1) (2007) 160.
[5] T. Karak T, O. Abollino, P. Bhattacharyya, K. Das, R. Paul, Chemosphere, 85 (2011) 948.
[6] K. Popović K, M. Antonijević Nikolić, J. Đuričić Milanković, D. Ranković, B. Milutinović, B. Dražić, S. Tanasković, Proceed. of EEM 2023, (2023) 419.
[7] S. Tascioglu, E. Kök, J. Sci. Food Agric. 76 (1998) 200.
[8] M. Długaszek, J. Mierczyk, Eur. Food Res. Technol., 250 (2024) 301.
[9] J. Zhang, R. Yang, R. Chen, Y. Peng, X. Wen, L. Gao, Int. J. of Environ. Res. Public Health, 15(1) (2018) 133.
[10] M. Harmanescu, L. M. Alda, D. M. Bordean, I. Gogoasa, I. Gergen, Chem. Cent. J., 5 (2011) 64.

PHENOLIC COMPOSITION, TOTAL PHENOLIC CONTENT AND ANTIOXIDANT ACTIVITY OF PARSLEY POST-DISTILLATION RESIDUES

M. Petrović [1], U. Gašić [2], M. Natić [3] and S. Veljović [4]

[1] *Institute of General and Physical Chemistry, Belgrade, Serbia (mpetrovic@iofh.bg.ac.rs)*
[2] *Institute for Biological Research "Siniša Stanković", Belgrade, Serbia*
[3] *Faculty of Chemistry - University of Belgrade, Belgrade, Serbia*
[3]*Faculty of Hotel Managament and Tourism in Vrnjacka Banja, University of Kragujevac, Vrnjacka Banja, Serbia*

DOI: https://doi.org/10.46793/Phys.Chem24II.667P

ABSTRACT

Essential oil of parsley can be extracted from the leaves and seeds and it is used in pharmaceutical, cosmetics as well as in the food industry as a natural food additive. However, the large amount of solid plant residues remaining after essential oil production represents a valuable source of polyphenols and other bioactive phytochemicals. This study aimed to investigate the valorization potential of underutilized and unexplored solid plant residues as left-over after distillation of parsley essential oil. In that regard, 70 % and 96 % ethanolic extracts of post-distillation residues of parsley have been characterized and compared in terms of phenolic composition measured by ultra-high performance liquid chromatography (UHPLC), as well as total phenolic content and antioxidant activity determined by Folin-Ciocalteu (FC), DPPH and FRAP method, respectively. The obtained results indicate the promising potential of parsley post-distillation residues for application in the food, pharmaceutical and cosmetics industries.

INTRODUCTION

Parsley (*Petroselinum crispum*) is an aromatic, culinary, and medicinal plant used in the cosmetic, food, and pharmaceutical industries. Its leaves have been traditionally used in the treatment of hemorrhoids, and gastrointestinal disorders, as a diuretic, as well as a food-flavoring agent. Parsley has been found to exhibit many bioactivities such as antioxidant, antibacterial, antifungal, hepatoprotective, antidiabetic, analgesic, spasmolytic, immunosuppressant, and gastroprotective properties [1]. Essential oils are a mixture of a wide variety of volatile compounds, including mono- and sesquiterpenes, as well as aromatic and aliphatic components derived from phenols. Essential oils are besides their traditional roles as natural food additives and fragrances recognized for a variety of bioactive properties including antibacterial, antifungal, and anti-inflammatory activities, and many other beneficial properties. Furthermore, numerous essential oils have been reported to possess antioxidant activity [2].

There are different procedures for obtaining essential oil, among them hydrodistillation where the aromatic plant material and an adequate amount of water are placed in a closed chamber, afterwhat the mixture is boiled, followed by condensation and decantation [3]. One of the main focuses of the medicinal and aromatic plant processing industry is the production of essential oils, which is an important area in agriculture and the agri-food industry. However, the ratio between the initial and processed plant biomass after production of EOs is very low, which generates large amounts of by-products, such as solid plant residues, whose management must be taken into account.

Some studies have dealt with the valorization of the solid residues obtained after medicinal plant distillation [4], but solid waste remaining after the production of parsley essential oil has remained unexplored. However, the widening of the application of this high-value and low-cost material plant material could contribute to an increasingly popular and increasingly needed circular economy concept.

Therefore, this is the first study aiming to investigate the phenolic composition, total phenolic content, and antioxidant activity of ethanolic extracts obtained from parsley post-distillation residues.

METHODS

Ethanol-water mixtures in the concentrations of 96% (v/v) and 70% (v/v) were used to obtain extracts from dried parsley leaves as post-distillation residues (P96 and P70). The plant material to solvent ratio was 1:10 (w/v). After maceration for 24 h using an orbital laboratory shaker (Edmund Buhler GmbH SM-30, Bodelshausen, Germany) at 200 rpm, at room temperature (20±2°C) and separation of the remaining soaked plant material, the obtained extracts were centrifuged at 3600 rpm for 5 min.

For the separation and quantification of phenolic compounds, ultra-high performance liquid chromatography (Dionex Ultimate 3000 UHPLC with a diode array detector (DAD)) with a mass spectrometer (TSQ Quantum Access Max triple-quadrupole with heated electrospray ionization (HESI) (ThermoFisher Scientific, Basel, Switzerland) was used. The analytical separation was achieved on column Syncronis C18 (ThermoFisher Scientific, Bremen, Germany), with aqueous formic acid solution 0.1% (A) and acetonitrile (B) as components of the mobile phase. Each polyphenol was quantitated by direct comparison with commercially available standards and the results were expressed as mg/L.

Total phenolic content (TPC) was determined by the Folin-Ciocalteu (FC) method described by Singleton et al. [5]. The DPPH antiradical scavenging activity was evaluated following the modified procedure described by Blois [6]. The FRAP assay was conducted according to the procedure described by Benzie and Strain [7]. The results were expressed as mg gallic acid equivalents (GAE) per liter of extract (TPC), and mmol Trolox equivalents (TE) per liter of extract for antioxidant activity measured (DPPH and FRAP). All measurements were performed in triplicates.

Data are expressed in mg/L of extract and presented as the means of triplicate measurements ± standard deviation.

RESULTS AND DISCUSSION

In total, 12 phenolics were detected and quantified in extracts of parsley post-distillation residues by liquid chromatography (Table 1). Detected phenolic compounds can be classified into phenolic acids (chlorogenic acid, *p*-hydroxybenzoic acid, caffeic acid, and *p*-coumaric acid) and flavonoids (rutin, quercetin 3-O-glucoside, isorhamnetin 3-O-glucoside, luteolin, quercetin, kaempferol, naringenin and apigenin).

It can be observed that the ethanol content significantly influences the amount of extracted phenolic compounds. Since sample P70 has significantly higher amounts of extracted phenolic compounds when compared to P96, it seems that the ethanol-water mixture is a more efficient solvent for phenolic compounds. The most abundant phenolics in P70 were rutin, chlorogenic acid and apigenin, whereas apigenin and rutin were present in P96 in the highest concentration.

Table 1. The content of phenolic compounds in ethanolic extracts obtained from parsley post-distillation residues.

mg/L	P70	P96
Rutin	1.662±0.045	0.470±0.008
Chlorogenic acid	1.334±0.056	0.141±0.007
Apigenin	1.320±0.028	0.895±0.005
Isorhamnetin 3-O-glucoside	0.473±0.006	0.302±0.003
Caffeic acid	0.425±0.007	0.220±0.001
Kaempferol	0.277±0.002	0.176±0.001
Quercetin	0.176±0.001	0.194±0.003
Quercetin 3-O-glucoside	0.163±0.002	0.106±0.000
Luteolin	0.114±0.001	0.077±0.000
p-Coumaric acid	0.047±0.001	0.034±0.000
p-Hydroxybenzoic acid	0.011±0.000	0.012±0.000
Naringenin	0.009±0.000	0.007±0.000
Total amount	6.011±0.049	2.633±0.032

The total phenolic content and antioxidant potential of samples are presented in Table 2. An evident difference in TPC values obtained for two ethanol concentrations can be observed. Aqueous ethanol has been already reported as the best solvent agent for the extraction of polyphenols and other antioxidant compounds from complex biological materials. This can be attributed to the role of water as the plant swelling agent, whereas ethanol, on the other side, may disrupt the bonding between the solutes and plant matrices [8].

To our knowledge, parsley post-distillation residues have not been studied yet. However, few data on unprocessed *Petroselinum crispum* chemical composition can be found. For instance, *Petroselinum crispum* water extracts contained 29 phenolic compounds, identified as flavonoid glycosides, which are the predominant compounds of this plant, including aglycones such as apigenin, luteolin, chrysoeriol, quercetin and isorhamnetin [9].

Table 2. Total phenolic compounds (TPC) and antioxidant potential of ethanolic extracts obtained from parsley post-distillation residues evaluated by FC, FRAP, and DPPH methods.

	TPC (mg GAE/L)	**FRAP (mM TE)**	**DPPH (mM TE)**
P70	412.46±4.24	3.43±0.20	0.64±0.00
P96	179.96±1.07	1.67±0.11	0.38±0.01

Chlorogenic acid, one of the most abundant compounds detected in the P70, is among the most powerful antioxidants, which is related to its special molecular structure containing five active hydroxyl groups and one carboxyl group. Its strong antioxidant potential is, namely, based on the reaction of the phenolic hydroxyl group with free radicals, thus forming hydrogen radicals being

able to eliminate the activity of hydroxyl radicals and superoxide anions [10]. Similarly, the B ring hydroxyl configuration of the flavonoids, such as apigenin and rutin, also present in significant amounts in extracts of parsley post-distillation residue, is the most significant determinant of scavenging free radicals because it donates hydrogen and an electron to radicals, stabilizing them and forming a relatively stable flavonoid radical [11].

The identification and quantification of phenolic compounds, as well as the determination of total phenolic content, have been increasingly applied in the pharmaceutical industry with the aim of standardization of the final product and bringing to focus the bioactive properties of selected phenolics. Flavonoids apigenin and rutin have been recognized to have a high potential for prevention and cancer treatment [10]. Also, chlorogenic acid has been associated with many health benefits such as antioxidant, anti-inflammatory, anti-diabetic, anti-carcinogenic, and anti-obesity impacts [11].

CONCLUSION

The investigation conducted on extracts obtained from parsley post-distillation residues collected after the production of essential oil confirmed the presence of various phenolic compounds, especially rutin, chlorogenic acid and apigenin. All methods applied in the study, such as identification and quantification of phenolic compounds, determination of total phenolic content and antioxidant activity, showed that 70% (v/v) ethanol-water mixture provides better extraction of phenolic compounds from the plant material in comparison to 96 % (v/v) ethanol. Based on the results obtained, parsley post-distillation residues represent high-value plant material that should be more extensively studied and encouraged for exploitation in the food, pharmaceutical, and cosmetics industries. Consequently, besides satisfying the concept of circular economy, it would contribute to the lessening of environmental pollution.

Acknowledgment

This work was supported by the Ministry of Education, Science and Technological Development of the Republic of Serbia (grant no 451-03-47/2023-01/200051).

REFERENCES

[1] C. Agyare, T. Appiah, Y. D. Boakye, J. A. Apenteng in: Petroselinum crispum: a review, V. Kuete (Ed), Academic Press (2017).
[2] G. Nouioura, N. El Hachlafi, H. A. Abuelizz, A. E. Elidrissi, M. Ferioun, N. Soulo, E. Derwich. Heliyon, 10 (2024) e29520.
[3] S. Khan, A. Sahar, T. Tariq, A. Sameen, F. Tariq in: Essential Oils, G. A. Nayik, M. J. Ansari (Eds.), Academic Press, (2023).
[4] C. Moisa, L. Copolovici, S. Bungau, G. Pop, I. Imbrea, A. Lupitu, S. Nemeth, D. Copolovici, Farmacia 66 (2018) 289.
[5] V.L. Singleton, R. Orthofer, R.M. Lamuela-Ravetós in: Methods in Enzymology, Packer L. (eds.), Academic Press, Cambridge, Massachusetts (1999).
[6] M.S. Blois, Nature, 181 (1985) 1199.
[7] I.F.F. Benzie, J.J. Strain, Anal. Biochem. 239 (1966) 70.
[8] K. D. P. P. Gunathilake, K. K. D. S. Ranaweera, H. P. V. Rupasinghe, Food Sci. Nutr. 7 (2019) 528.
[9]. D.M. Epifanio, N. Mara, L. R. I. Cavalcanti, K. F. D. Santos, P. S. C. Duarte, P. Kachlicki, M. Ożarowski, C. J. Riger, D. S. D. A. Chaves, Food Funct. 11 (2020) 5346.
[10] M. Miao, L. Xiang, Adv. Pharmacol. 87 (2020) 71.
[11] S. Kumar, A. K. Pandey, Sci. World J. (2013) 162750.

P *– Food Physical Chemistry*

THERMAL DEGRADATION KINETIC OF DRIED RED CABBAGE PULP

S. Ostojić, D. Micić and S. Zlatanović

University of Belgrade, Institute of General and Physical Chemistry, Studentski trg 12/V, 11000 Belgrade, Serbia. (sostojic@iofh.bg.ac.rs)

DOI: https://doi.org/10.46793/Phys.Chem24II.673O

ABSTRACT

Thermal degradation kinetics of dried red cabbage pulp (*Brassica oleracea var. capitata F. rubra*) has been studied using thermogravimetric analysis. Four stages of degradation were observed in the TGA curves within the temperature range from 25 to 700 °C. The first mass loss corresponds to the evaporation of water, the second and third to the thermal degradation of mono- and disaccharides (fructose, glucose, sucrose) and to the thermal degradation of proteins and fourth weight loss represents the thermal degradation of the cellulose. The kinetic parameters of the thermal degradation process of dried red cabbage, obtained using the Friedman method, were as follows: E_a—activation energy at a conversion degree (α) from 0.1 to 0.9 ranged between 126.5 and 144.6 kJ/mol; lnA—the natural logarithm of the pre-exponential factor ranged from 25.8 to 36.1; $k_{0.5}$—thermal degradation rate constant at a conversion extent (α) value of 0.5 ranged from 0.293 to 0.725 min^{-1}.

The results were discussed in relation to those obtained for the samples' proximate chemical composition.

INTRODUCTION

Red cabbage (*Brassica oleracea var. capitata F. rubra*), also known as purple cabbage, offers numerous health benefits backed by scientific research [1]. Rich in nutrients and bioactive compounds, it is an excellent addition to a healthy diet [1]. Red cabbage is primarily known for its high concentration of anthocyanins [2], which present many nutritional health benefits, including antioxidant, anti-inflammatory, and liver-protective properties [3,4], as well as atherosclerosis prevention [1,5].

Recently, interest in the use of red cabbage has increased, making it one of the best sources of food colorants [6]. De Marchi, et al. [6] investigated the thermal stability of red cabbage anthocyanins. However, data on the overall thermal stability and kinetics of thermal degradation of dried red cabbage pulp obtained after juicing have not been found in the literature. Residual pulp is reach of the fibers, remaining anthocyanins, minerals [1] and can be used as a rich nutritional health promoting supplement. Knowledge about thermal stability and thermal decomposition of the obtained food products can be crucial for tailoring the food technological processing, as thermal treatments can significantly affect the nutritional values during processing.

The aim of this work was to thermally characterize dried red cabbage pulp, and to obtain the kinetic parameters of its thermal decomposition in the N_2 atmosphere, to better understand and characterize the thermal degradation process of the pulp produced under the given conditions.

METHODS

Materials: The red cabbage (*Brassica oleracea L. var. capitata f, rubra*) was purchased from agricultural market known as “Maxi pijaca” in Belgrade.

Drying: The red cabbage was cut into pieces and subjected to juicing using the “Zepter More Juice Press Frozen” for home use. The pulp obtained after squeezing was subjected to drying, Drying was

conducted in the convection way by "Excalibur "food dehydrator, (Sacramento, California USA) at the 40 °C, for the 12 h.

Chemical composition: Chemical composition of dried red cabbage was analyzed in terms of total carbohydrate, diet fibers, fats and proteins, mono and disaccharides (glucose, fructose and sucrose), cellulose, and water content. Total content of carbohydrates as well as the content of glucose, fructose and sucrose, were determined by high performance liquid chromatography on the HPLC Alliance Waters 1515 device (Waters Corporation Milford, MA 01757 USA) with Waters 2414 RI detector carbohydrate analysis column 3.9x300mm. Mobile phase was acetonitrile/water (80/20), f low rate 1.5 ml/min. Total dietary fiber was determined by standard enzymatic-gravimetric AOAC method 985.29. Cellulose content was determined by gravimetry according to [7].

Thermal degradation kinetic

Thermal degradation was studied by thermogravimetric analysis (TGA). Measurements were performed on TA Instruments TGA Q500, Thermogravimetric Analyzer (Delaware, USA), under nitrogen flow of 60 ml/min. Samples were scanned from room temperature to 700 °C, with heating rate (Hr) of 5, 10, 15, 20 and 25 °C/min. All scans were performed in triplicate.

To ascertain the kinetic parameters of the thermal degradation of dried red cabbage pulp, samples were subjected to heating at five distinct rates, β_i (5, 10, 15, 20, and 25 °C/min), within a temperature range from 25 to 700 °C. Three specific peaks on the DTG curve, indicative of the thermal degradation of the dried red cabbage, were selected for the determination of kinetic parameters. The E_a values were computed across an α range from 0.05 to 0.95, with increments of 0.05. The logarithmic values of the pre-exponential factors at each extent of conversion α ($\ln(A_\alpha)$) were calculated using the compensation effect, as detailed by Vyazovkin [8]. Using the values of E, A, and T at the conversion extent α = 0.5, the rate constants ($k_{0.5}$) for the thermal degradation of dried red cabbage were derived through the Arrhenius equation. The methodology for the kinetic studies adhered to the guidelines for collecting kinetic data [9] and performing kinetic computations [8] as recommended by the ICTAC Kinetics Committee.

The activation energy (E_a) for the thermal degradation of dried red cabbage samples was determined using the differential isoconversional non-isothermal method developed by Friedman [8] (Equation (1)).

$$ln\left[\beta_i \left(\frac{d\alpha}{dT}\right)_{\alpha,i}\right] = const - \frac{E_\alpha}{RT_{\alpha,i}} \quad (1)$$

where β is the heating rate (K/min), α is extent of conversion, R is the universal gas constant (8.314 J(molK) $^{-1}$) and T is temperature (K). The indexes *i* and α correspond to a specific heating rate and the extent of conversion, respectively. The value of E_α is calculated from the slope of a linear regression of the left side of Equation (1) against $1/T_{\alpha,i}$ (where $T_{\alpha,i}$ represents the temperature at which the extent of conversion α is achieved under the *i*-th heating rate).

RESULTS AND DISCUSSION

The results of the proximate analysis of the dried red cabbage, as shown in **Table 1**, agree with data reported in the literature [10].

Table 1. Proximate chemical composition of the dry red cabbage.

parameter	Moisture (%)	Total fat g/100g	carbohydrates g/100g	Glucose g/100g	Fructose, g/100g	Saccharose g/100g	Total sugars g/100g	proteins g/100g	fibers g/100g	Cellulose g/100g
Dry red cabbage pulp	8.9±2.1	0.50±0.04	49.5±5.2	8.0±1.0	9.1±1.3	11.2±2.1	28.3±5.5	14.6±1.0	7.3±0.8	11.9±1.5

In the **Figure 1.** typical TGA curve, obtained for the dried red cabbage at heating rates (5°C/min) are shown. All TGA curves obtained for different heating rates have similar thermal behavior with evident four weight loss in the temperature range from 25 to 700 °C. Generally, the first mass loss corresponds to the evaporation of water, the second and third to the thermal degradation of mono- and disaccharides (fructose, glucose, sucrose) [11], and to the thermal degradation of proteins [12] and fourth weight loss represents the thermal degradation of the cellulose [13]. The obtained percentages of mass loss cannot be mirrored to the composition of the sample (**Table 1**) as during the thermal decomposition of complex samples, numerous components interact during the simultaneous increase of temperature but some rough assumptions can be proposed [14].

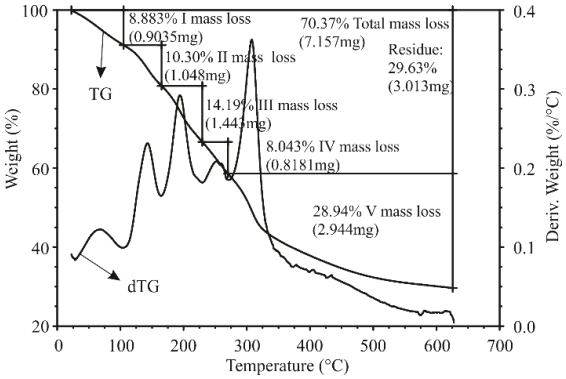


Figure 1. Typical TG/dTG curve of the dried red cabbage at heating rate of (5 °C/min).

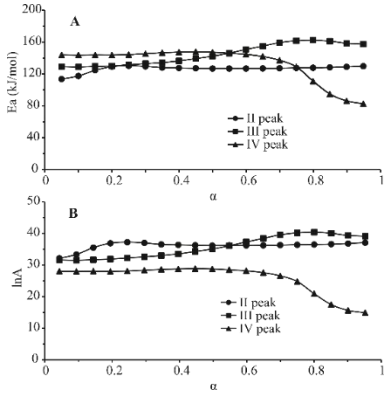


Figure 2. The dependence of **(A)** the activation energy (E_a) and **(B)** the natural logarithm of the prexponential factor on the conversion rate (α) for the thermal degradation process of dried red cabbage obtained by Freidman method.

In **Figure 2.A** the dependence of the activation energy (E_a) and **B** the natural logarithm of the prexponential factor on the conversion rate (α) dependence for the thermal degradation process of dried red cabbage, obtained form three DTG peaks and evaluated by Freidman method, is presented. In **Table 2.** kinetic parameters of the thermal degradation process of dried red cabbage obtained by Freidman method are presented. The obtained values for the activation energies (**Figure 2.** and **Table 2**.) are in accordance with the literature [15]. It is evident that the activation energy for the second peak, which corresponds to the degradation of mono- and disaccharides and proteins, didn't change with the conversion rate (α), suggesting the uniformity of the thermal process. The activation energy as a function of the conversion rate (α) obtained for the third peak showed a discrete increase, indicating reversible processes occurring not far from equilibrium [16]. For the fourth peak, the activation energy decreased with the conversion rate, suggesting the complexity of the ongoing process, as a decreasing dependence is normally followed by a plateau associated with the activation energy of the forward process [16]. The values obtained for lnA—the natural logarithm of the prexponential factor depending on the conversion factor had a similar trend as the values obtained for Ea/ conversion rate (α) dependence .

CONCLUSION

Determined proximate chemical composition of the dry red cabbage obtained after juicing agreed to the literature. While the mass loss percentages obtained from TGA curves do not directly reflect the complex composition of the sample's, as numerous components interact between each other during the thermal decomposition but some rough assumptions can be proposed. Kinetic analysis described

samples thermal degradation. The dependence of the activation energy on the conversion rate (α) indicated the complexity of the thermal processes, which is a consequence of the chemical composition of the sample.

Table 2. Kinetic parameters of thermal degradation process of dried red cabbage obtained by Freidman method. E_a—mean value of activation energy at conversion degree (α) from 0.1 to 0.9; lnA—the natural logarithm of the prexponential factor; $k_{0.5}$—thermal degradation rate constant at the conversion extent (α) value of 0.5.

	E_a (kJ/mol)	lnA	$k_{0.5}$ (min^{-1})
II peak	126.5 ± 4.6 [a]	36.1 ± 1.3 [b]	0.725
III peak	144.6 ± 13.0 [b]	35.7 ± 3.4 [b]	0.469
IV peak	133.0 ± 22.0 [ab]	25.8 ± 4.7 [a]	0.293

Acknowledgment
This work was supported by the Ministry of Science, Technological Development and Innovation of the Republic of Serbia (grant no 451-03-66/2024-03/200051).

REFERENCES

[1] M. M. Ozcelik, S. Aydin, E. Aydin, G. Ozkan, Food Sci Nutr 12 (2024) 1340–1355.
[2] K. Sakulnarmrat, D. Wongsrikaew, I. Konczak, LWT 137 (2021) 110473.
[3] J. H. Kwak, Y. Kim, S. I. Ryu, M. Lee, H. J. Lee, Y. P. Lim, J. K. Paik, Food Sci Nutr 8 (2020) 1898–1903.
[4] K. Kasarello, I. Köhling, A. Kosowska, K. Pucia, A. Lukasik, A. Cudnoch-Jedrzejewska, L. Paczek, U. Zielenkiewicz, P. Zielenkiewicz, Front Pharmacol 13 (2022).
[5] J. M. Sankhari, M. C. Thounaojam, R. N. Jadeja, R. V. Devkar, A. V. Ramachandran, J Sci Food Agric 92 (2012) 1688–1693.
[6] L. De Marchi, L. Salemi, M. Bellumori, R. Chignola, F. Mainente, D. V. Santisteban Soto, I. Fierri, M. Ciulu, G. Zoccatelli, Food Chem 440 (2024) 138272.
[7] S. Zlatanović, S. Ostojić, D. Micić, S. Rankov, M. Dodevska, P. Vukosavljević, S. Gorjanović, Thermochim Acta 673 (2019) 17–25.
[8] S. Vyazovkin, A. K. Burnham, J. M. Criado, L. A. Pérez-Maqueda, C. Popescu, N. Sbirrazzuoli, Thermochim Acta 520 (2011) 1–19.
[9] S. Vyazovkin, K. Chrissafis, M. L. Di Lorenzo, N. Koga, M. Pijolat, B. Roduit, N. Sbirrazzuoli, J. J. Suñol, Thermochim Acta 590 (2014) 1–23.
[10] M. Drozdowska, T. Leszczyńska, A. Koronowicz, E. Piasna-Słupecka, D. Domagała, B. Kusznierewicz, European Food Research and Technology 246 (2020) 2505–2515.
[11] N. Xu, C. Lu, T. Zheng, S. Qiu, Y. Liu, D. Zhang, D. Xiao, G. Liu, Mater Des 200 (2021) 109458.
[12] D. Jagadeesh, D. Jeevan Prasad Reddy, A. Varada Rajulu, J Polym Environ 19 (2011) 248–253.
[13] M. Mironova, I. Makarov, L. Golova, M. Vinogradov, G. Shandryuk, I. Levin, Fibers 7 (2019) 84.
[14] K. Singh, M. Risse, K. C. Das, J. Worley, Journal of Energy Resources Technology, Transactions of the ASME 131 (2009) 0222011–0222016.
[15] L. Luo, X. Guo, Z. Zhang, M. Chai, M. M. Rahman, X. Zhang, J. Cai, Energy and Fuels 34 (2020) 4874–4881.
[16] J. R. Prado, S. Vyazovkin, Thermochim Acta 524 (2011) 197–201.

IODIDE CONCENTRATION IN INFANT FOOD: INSIGHTS FROM A COMPARATIVE STUDY

N. Lugonja[1], B. Lončarević[1], V. Marinković[2], M. Lješević[1], A. Žerađanin[1], and J. Milić[1]

[1] *University of Belgrade, Institute of Chemistry, Technology and Metallurgy, Njegoševa 12, 11000 Belgrade, Serbia. (nikoleta.lugonja@ihtm.bg.ac.rs)*
[2]*Institute of Neonatology, Kralja Milutina 50, 11000 Belgrade, Serbia*

DOI: https://doi.org/10.46793/Phys.Chem24II.677L

ABSTRACT
Iodide in infant food is a crucial micronutrient for infants' development, as they are born with small amounts of stored intrathyroidal iodine. Human milk and infant formula are the primary sources of iodide for newborns, providing this essential element for both term and premature infants. This study aimed to monitor the concentration of iodide in infant food for term and premature infants, including human milk, infant formula, and cow milk. An iodide-ion-selective electrode was used to detect the iodide concentration in infant food samples. Results showed that premature colostrum and infant formula have the highest iodide concentration compared to mature milk samples. Over time, iodide levels undergo a significant decrease during lactation. Since premature infants are more vulnerable, their need for sufficient iodine for growth is higher, which is consistent with the obtained results.

INTRODUCTION
Human milk is the main food in infant nutrition, providing an excellent source of energy, protein, minerals, and vitamins. It supplies essential nutrients for the growth and development of infants and contains numerous components that help regulate their development. Breastfeeding premature infants offers many benefits, including improvements in digestion, nutrient absorption, and neural development, leading to rapid growth and mental development in children [1]. When breastfeeding is not possible or insufficient, it is necessary to provide infant formula (IF) with declared nutritional and biological values that approximate the composition of the mother's milk, thus serving as an adequate substitute. Infant formulas contain a modified ratio of proteins from cow's milk, along with added lactose, lipids, vitamins, and minerals. However, the complex composition and biological properties of human milk cannot be fully replicated in infant formula [2].

Iodine in infant food is a crucial micronutrient for normal physical and neurological growth and development. In food and iodized salt, iodine exists in several chemical forms, including sodium and potassium salts, inorganic iodine (I_2), iodate, and iodide, the reduced form of iodine [3]. Iodine rarely occurs as a free element but rather as a salt, hence it is often referred to as iodide rather than iodine. Babies are born with small amounts of stored intrathyroidal iodine and are particularly sensitive to iodine deficiency. Breastfed infants depend on this iodine to meet their physiological needs and iodine concentration in breast milk reflects the iodine status of lactating women. The recommended daily intake of enteral iodine for preterm infants per general guidelines is between 11 and 55 µg/kg/day. A daily intake for healthy preterm infants of at least 30 µg/kg is required to maintain a positive iodine balance. Achieving this iodine intake level may necessitate a human milk iodine concentration of 200 µg/L [4]. Most of the iodine in milk (80 to 90 %) is found in inorganic form (iodide), while 5 to 13 % is bound to protein by covalent bonds (as in thyroid hormones) or weak intermolecular bonds [5]. Cow's milk naturally has a low iodine concentration but becomes a rich source of iodine through standard farming practices, such as the addition of iodine salts to cattle feed [6].

The objective of the study was to track the levels of iodide concentration in infant foods, including human milk, infant formula, and cow milk, for both term and prematurely born infants. This monitoring is essential to ensure that this vulnerable group receives sufficient iodine intake.

METHODS

The study involved ten healthy mothers of preterm infants. Human milk samples were collected from mothers of preterm infants, delivered before 37 weeks of gestation, at the Institute of Neonatology, Belgrade, Serbia (E82501/4). The iodide content was determined in the human milk of mothers of preterm infants in three phases of lactation: colostrum, transient milk, and mature milk (MM). All milks were homogenized using an Ultrasonic homogenizer Sonopuls 2000.2 (Bandelin, Berlin, Germany) before measurement (Figure 1).



Figure 1. Human milk in different phases of lactation: 1-colostrum, 2-transient milk, 3-mature milk.

Infant formula for term infants from birth to 6 months of age from different manufacturers (IF1) on the Serbian market, and special infant formula (IFPre) for preterm and low birth weight infants, produced in Serbia, were examined. Formulas were prepared as a meal by dissolving 6-8 g of powder in 45 mL demineralized water, according to the manufacturer's instruction to obtain the final volume of 50 mL. Cow milk with 2.8 % of milk fat (Ultra-high-temperature processing - UHT, Imlek, Serbia) was used in the research.

Iodide content in infant food was determined using an Iodide ion selective electrode (Orion, Thermo Scientific). The iodide in each sample (50 mL) was measured at room temperature, after adding a small volume of nickel nitrate (ISA), an ionic strength adjustor to the sample before testing. After measurement, the electrode was rinsed (1 % EDTA and 1 % Tween) to stable electrode response throughout the testing. The iodide standard solution was 0.1 M NaI, and a standard curve was prepared in the range 0.80 - 1.20 mM of iodide (R^2 = 0.9903) at electrode potentials from -8.1 to -5 mV. The results for iodide in the milk samples are given in ppb (μg/100 mL of meal) expressed as mean values.

RESULTS AND DISCUSSION

The findings regarding iodide concentration in infant food are presented in Figure 2. A comparison of mean iodide concentration values in human milk at different lactation stages reveals that colostrum exhibits the highest iodide concentration. Conversely, as human milk matures, iodide concentration gradually declines, resulting in the lowest levels observed in mature milk compared to colostrum and transient milk.

The iodide concentration results for term and preterm infant formula samples are shown at Figure 2. The highest concentration 23.5 ± 0.5 µg/100 mL was found in IFPre, formulated specifically for preterm infants, whose nutritional needs differ from those of term infants. Infant formula for term infants (IF1) showed lower iodide content compared to IFPre. Infant formulas available in the market are primarily cow's milk-based but supplemented with a premix of vitamins and minerals to meet the requirements of growing and developing infants [2].

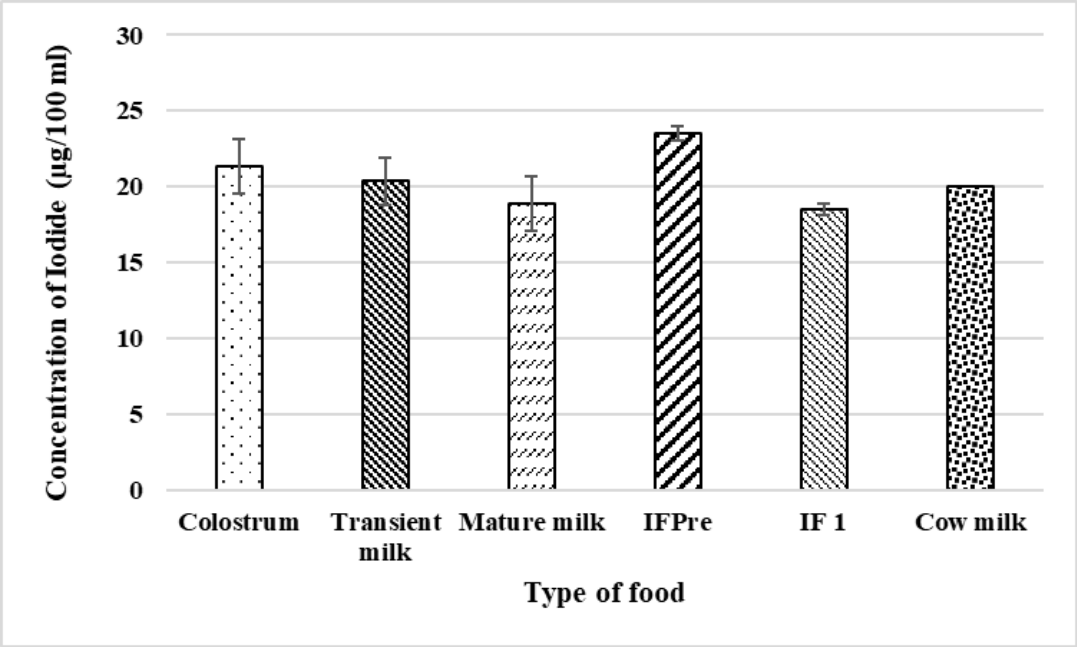


Figure 2. Iodide concentration in infant food (µg/100 ml): human milk, infant formula for preterm (IFPre) and term (IF1) infants, and cow milk.

Cow's milk is used in the nutrition of small children after one year. The values obtained for iodides in UHT cow's milk samples are similar to those in infant formula for term infants. Even though the soil is poor in this mineral, cow's milk on our market contains iodides, due to the supplementation of animal feed [6].

CONCLUSION

Based on the test results of iodide detected by ion-selective electrode in infant food samples, it can be concluded that preterm colostrum has the highest concentration, which follows the needs of premature babies. The iodide concentration decreased during the lactation period. Human milk for preterm infants should be supplemented with fortifier, to fulfill their needs. The iodide concentration in IF for term infants and cow's milk was similar, while in IF for preterm infants was higher for preterm infants.

Preterm infants require an adequate intake of iodine in the first few days as it is essential for their growth and development. The concentration of iodide in human milk varies based on the stage of lactation, time of day, and the mother's diet. If the mother consumes enough iodide, it will also benefit the child. Therefore, the mother's diet during the breastfeeding period is crucial.

Acknowledgment
This research has been financially supported by the Ministry of Science, Technological Development and Innovation of the Republic of Serbia (Contract No: 451-03-66/2024-03/200026).

REFERENCES

[1] N. M. Lugonja, V. Marinkovic, M. Pucarevic, S. Miletic, N. Stojic, D. Crnkovic, M. M. Vrvic, Foods 24;13(9) (2024) 1298.
[2] N. M. Lugonja, V. Marinkovic, D. Djurovic, R. Mileusnic Milenovic, J. Avdalovic, M. M. Vrvic, Hrana i ishrana 63 (2022) 17.
[3] D. K. Dror, L. H. Allen, Review. Adv Nutr. 9(suppl_1) (2018) 347S.
[4] N. Ureta-Velasco, K. Keller, D. Escuder-Vieco, J.C.E. Serrano, N.R. García-Lara, C.R. Pallás-Alonso, Nutrients 14;14(20) (2022) 4304.
[5] S. Liu, A. Sharp, X. Luo, et al., Brit. J. Nutrit. 131(2024) 286.
[6] https://www.unicef.org/serbia/en/reports/salt-iodisation-population-serbia.

CHEMICAL COMPOSITION AND ANTIMICROBIAL PROPERTIES OF ANISEED ESSENTIAL OIL

M. Petrović [1], D. Radić [1], M. Jovanović [1] and T. Šolević Knudsen [2]

[1]*Institute of General and Physical Chemistry, Studenstki trg 12-16, Belgrade, Serbia (mpetrovic@iofh.bg.ac.rs)*
[2]*Institute of Chemistry, Technology and Metallurgy, University of Belgrade, Njegoševa 12, 11000 Belgrade, Serbia*

DOI: https://doi.org/10.46793/Phys.Chem24II.681P

ABSTRACT

Essential oil obtained from aniseed (*Pimpinella anisum L.)* was investigated for its chemical composition and antimicrobial properties against some common food-born pathogens. According to GC-MS anlysis, eight compounds were identified and quantified in aniseed oil, representing 77.82 % of the total oil. The most abundant volatile compound contained in oil was *trans*-anethole, representing 61 % of the total identified compounds. γ-Himachalene, estragole, *cis*-anethole and α-himachalene were present in essential oil in several times lower concentrations. Concentrations between 0.12 mg/ml and 7.5 mg/ml were tested for antimicrobial properties. The minimum inhibitory concentration (MIC), as well as minimum lethal concentration (MLC) of the aniseed essential oil were determined by broth microdilution assay against six Gram-positive bacteria, seven Gram-negative bacteria strains and one yeast. The MICs and MLCs ranged from 0.12 mg/mL to 1.87 mg/mL, with Gram-positive bacteria being more sensitive to aniseed essential oil in comparison to Gram-negative bacteria.

INTRODUCTION

Anise (*Pimpinella anisum*) is a herbaceous annual plant, native to the Mediterranean region and primarily grown for its fruits, known also as aniseed. It has been reported that aniseed was used as traditional medicine in China as early as in the 5th century for a wide range of health issues. Namely, it has been used as an analgesic in migraine, as a carminative, aromatic, disinfectant and diuretic, as well as for treatment of epilepsy. Various bioactive properties of aniseed have been reported, such as antiperoxidative and antidiabetic, antioxidant, antimicrobial and others, as well as many pharmacological effects including hepatoprotective, anticonvulsant, anti-inflammatory, antispasmodic, bronchodilator, estrogenic, expectorant and insecticidal effects [1].

Aniseed is a medicinal, aromatic and spice herb, that is used in the pharmaceutical, food and cosmetics industries. Specifically, in the food industry, aniseed is among the favorable spices, often used for flavoring bread, biscuits, and cookies, as well as in the meat industry [2]. The most important constituent of aniseed essential oil is *trans*-anethole, responsible for its anise characteristic odor and aroma. Anethole is widely used as a flavor in alcoholic beverages such as ouzo (Greece) and Pernod (France), and in oral hygiene products. Its broad antimicrobial spectrum and sweet taste make it suitable for application in oral hygiene products [3]. Other constituents of aniseed essential oil belong to the group of coumarins, lipids, flavonoids, proteins, and carbohydrates [4].

Essential oils obtained from medicinal plants have been increasingly researched in terms of their potential application in the food industry, particularly as promising antimicrobial agents. Moreover, medicinal plant isolates have been reported as more effective in some cases against pathogenic microorganisms in comparison with conventional antimicrobial drugs [5]. Aniseed essential oil was reported to show antibacterial activity, as well as an antifungal effect [1].

The aim of this research is to investigate the volatile profile and antimicrobial properties of essential oil obtained from *Pimpinella anisum L.* fruits, known as aniseeds.

METHODS

Fruits of *Pimpinella anisum L.* (aniseed), donated from the "Bilje Borča" company, Belgrade, Serbia, were naturally dried and stored in tight-seal dark containers until needed. Approximately 40 g of air-dried and finely grounded anise seeds were subjected to hydrodistillation for 2 h using a Clevenger type apparatus. Obtained oil was dissolved in methylene chloride, and injected in HP5-MS capilar column of a gas chromatograph Agilent 7890N, coupled with a Hewlett-Packard 5972 mass spectrometer. Helium was the carrier gas (flow rate 1.5 cm^3/ min). Components of the volatile oil were identified based on their retention indices and their mass spectra using the Wiley and NIST Mass Spectral Libraries or literature data.

The broth microdilution method was used to determine the antimicrobial activity of plant isolates *in vitro* [6]. The final concentration of bacteria used for inoculation of microtiter wells was adjusted to 10^5 cfu/mL. Concentrations of essential oil in the range of 7.50 mg/mL – 0.12 mg/mL were tested. Minimal lethal concentration (MLC) was determined by sub-culturing content of the wells with no visible growth on agar plates and incubation at 37°C for 18h-24h for bacteria and 30°C for 24-48 h for fungi. No growth on the agar plate was reported as minimum lethal concentration (MLC). The MIC and MLC procedures were done in triplicates.

RESULTS AND DISCUSSION

Compounds identified in aniseed essential oil belong to the class of monoterpenes and sesquiterpenes (Table 1). The predominant components were *trans*-anethole (61.02 %), γ-himachalene (9.08 %), estragole (3.33 %), *cis*-anethole (2.55 %) and α-himachalene (1.29 %). The rest of the identified volatile compounds, *p*-cymene, limonene and linalool are present in minor percentages.

A comparison of the obtained results with literature data shows that trans-anethole content is significantly lower than those reported by other authors [1]. The yield and anethole content of aniseed, ranging approximately between 75 and 90 %, are affected by the genotype, the ecological conditions, and especially by agricultural practices such as irrigation, plant population, fertilizer, and planting date [1]. Corroborating to the results presented here, apart from *trans*-anethole, γ-himachalene and estragole were also detected in anise essential oil from Algeria, as well as linalool in minor concentration [7]. Similarly, γ-himachalene was present in the essential oil of Tunisian and Egyptian anise as the second most abundant compound following *trans*-anethole [8].

Table 1. Chemical composition of *Pimpinella anisum* essential oil.

№	Compound	Percentage in oil (%)
1.	*p*-Cymene	0.11
2.	Limonene	0.28
3.	Linalool	0.17
4.	Estragole	3.33
5.	*cis*-Anethole	2.55
6.	*trans*-Anethole	61.02
7.	α-Himachalene	1.29
8.	γ-Himachalene	9.08
Σ	Total identified	77.82

The results of the determination of antimicrobial activity against selected common food-borne pathogens are shown in Table 2. Gram-positive bacteria were more susceptible to anise essential oil (MIC and MLC values ranging from 0.12 mg/mL to 1.87 mg/mL) than Gram-negative bacteria (with

inhibitory and lethal concentrations ranging from 0.94 mg/mL to 1.87 mg/mL). Essential oil inhibited the growth of the yeast *Candida albicans* with MIC= 0.47 mg/mL, whereas the lethal concentration was 0.94 mg/mL.

Generally, higher resistance among Gram-negative bacteria could be ascribed to the presence of the outer membrane, surrounding the cell wall, which restricts diffusion of hydrophobic compounds through its lipopolysaccharide covering [9].

Low concentrations of aniseed essential oil inhibiting the growth of tested bacteria and yeast indicate promising antibacterial properties that can be beneficial in the food industry for the inactivation of pathogens in commercially produced food systems as well as for potential alternative to the chemical preservatives. The antimicrobial effect of aniseed essential oil could be ascribed to its main volatile compounds. Anethole isolated from the *Pimpinella anisum* fruit oil was shown to possess considerable antimicrobial activity against seven selected pathogenic microorganisms. Similarly as obtained here, the most promising results were obtained against *Staphylococcus aureus* and *Bacillus cereus* which were the most susceptible to the anethole [10]. The primary concern regarding antimicrobial agents, especially those used in the food industry, is their safety. Therefore, antimicrobial agents isolated from plants should be superior compared to non-natural ones.

Table 2. MICs and MLCs of *Pimpinella anisum* essential oil against some common food-borne pathogens.

Test microorganism			*Pimpinella anisum* essential oil (mg/mL)[a]
Gram-positive bacterias	*Listeria monocytogenes* ATCC 19111	MIC	0.94±0.00
		MLC	0.94±0.00
	Bacillus spizizeni ATCC 6633	MIC	0.94±0.00
		MLC	0.94±0.00
	Bacillus cereus ATCC 11778	MIC	0.12±0.00
		MLC	0.12±0.00
	Staphylococcus aureus ATCC 25923	MIC	0.12±0.00
		MLC	0.12±0.00
	Rhodococcus equi ATCC 6939	MIC	0.12±0.00
		MLC	0.12±0.00
Gram-negative bacterias	*Salmonella enteritidis* ATCC 13076	MIC	1.87±0.00
		MLC	1.87±0.00
	Shigella sonnei ATCC 29930	MIC	1.87±0.00
		MLC	1.87±0.00
	Proteus mirabilis ATCC 12453	MIC	0.94±0.00
		MLC	0.94±0.00
	Yersinia enterocolitica ATCC 27729	MIC	1.87±0.00
		MLC	1.87±0.00
Yeast	*Candida albicans* ATCC 10259	MIC	0.47±0.00
		MLC	0.94±0.00

[a] Data are expressed as a mean of three replicates ± standard deviation (n = 3).

CONCLUSION

Essential oil of *Pimpinella anisum* fruits, aniseeds, was characterized by GC-MS analysis. The most abundant compound the oil was *trans*-anethole, whereas γ-himachalene, estragole, *cis*-anethole and α-himachalene were also detected in significant amounts. Aniseed essential oil represents a good antimicrobial agent effective against selected food-borne pathogens, suggesting its promising potential for use in the food industry as an alternative to chemical preservatives.

Acknowledgment

This work was supported by the Ministry of Education, Science and Technological Development of the Republic of Serbia (grant no 451-03-47/2023-01/200051).

REFERENCES

[1] W. Sun, M. H. Shahrajabian, Q. Cheng, Cogent Biol., 5 (2019) 1673688.
[2] M. G.Aćimović, Lj. M. Kostadinović, S. J. Popović, N. S. Dojčinović, J. Agric. Sci. (Belgr.), 60 (2015) 237.
[3] I. Kubo, K. Fujita, K. Nihei, J. Sci. Food Agric. 88 (2008) 242.
[4] P. D. Picon, R. V. Picon, A. F. Costa, G. B. Sander, K. M. Amaral, A. L. Aboy, A. T. Henriques, BMC Complement. Altern. Med. 10 (2010) 1.
[5] H. C. Voon, R. Bhat, G. Rusul, Compr. Rev. Food Sci. Food Saf., 11 (2012) 34.
[6] A. Klačnik, S. Piskernik, B. Jeršek, S.S. Možina, J. Microbiol. Methods, 81(2010) 121.
[7] S. Saibi, M. Belhadj, E. Benyoussef, Anal. Chem. Lett., 2 (2012) 401.
[8] R. Bettaieb, I., S. Bourgou, W. A. Wannes, I. H. Selami, M. S. Tounsi, B. Marzouk, M-L. Fauconnier, R. Ksouri, Plant Biosyst. 152 (2018) 971.
[9] B. Speranza, M. R. Corbo in: Application of Alternative Food-Preservation Technologies to Enhance Food Safety & Stability, A. Bevilacqua, M. R. Corbo, M. Sinigaglia (Eds.), Bentham Publisher, 2010.
[10] M. J. Mohammed, J. Pharm. Res., 2 (2009) 915.

WHEAT AND RICE FLOUR ENRICHMENT WITH CELERY LEAFSTALKS POMACE

S. Gorjanović [1], F. Pastor [2], M. Dodevska [3], D. Micić [1] and S. Zlatanović [1]

[1] *Institute of General and Physical Chemistry, Studentski trg 12/V, 11158 Belgrade, Serbia (stasago@yahoo.co.uk, snezana.zlatanovic@gmail.com)*
[2] *University of Belgrade – Faculty of Chemistry, Studentski trg 16, 11158 Belgrade, Serbia*
[3] *Institute of Public Health of Serbia »Dr Milan Jovanovic Batut«, Dr Subotica Starijeg 5, 11000 Belgrade, Serbia*

DOI: https://doi.org/10.46793/Phys.Chem24II.685G

ABSTRACT

Pomace obtained from celery leafstalks alone or from its mixture with other vegetables and fruits, was processed into stable anti-grain flour (AGF) via dehydration (T≤55°C) and grinding at a small industrial scale. It maintained moisture below 10% and water activity (aw) below 0.4. Proximate composition and techno-functional properties, including water and oil binding capacities, were analyzed, and compared with standard wheat and rice flours. Celery pomace flour (CPF) as well as flour from celery mixed with apple, cucumber, kale, spinach, parsley, lettuce, and ginger (CPF1) or with apple, fennel, arugula, and ginger (CPF2), showed potential to enhance nutritional quality. Their addition to white wheat and rice flour resulted in significant enrichment in total dietary fiber. The amount of pomace required to adjust the carbohydrate to DF ratio to 10:1 in these flours was calculated.

INTRODUCTION

Celery (*Apium graveolens*) leafstalks are increasingly used to produce popular juice known for its health benefits. Celery based pomace, either from celery only or from celery mixtures with various fruits, vegetables and herbs, is generated in growing amount. This pomace is rich in bioactive molecules and dietary fiber (DF), which are essential for preventing non-communicable diseases caused by the lack of DF in modern diets. Despite its potential, celery pomace has been underutilized, and a sustainable method to stabilize it needs to be developed. In this study stable anti-grain four (AGF) was produced from celery pomace obtained from a trustworthy local juice manufacturer ColdPressok (Belgrade, Serbia) through cold pressing, without any enzymatic or heat treatment. An innovative technological process that includes dehydration below 55 °C and subsequent grinding was applied to decrease moisture content and water activity (aw), well enough to achieve good stability and storability, while preserving bioactive molecules. Obtained celery pomace flour was thoroughly characterized. The health benefits were assessed based on the total carbohydrates to total fiber ratio, a criterion increasingly used to evaluate the quality of whole grain products and processed foods in general. Additionally, the techno-functional properties of the flour were considered for their potential to improve intestinal peristalsis and hypolipidemic effects.

In this study, the amount of celery pomace flour required to reduce the carbohydrate to fiber ratio of white wheat (WF) and rice flour (RF) from approximately 30:1 and 50:1 to below 10:1 was calculated. The potential of celery pomace to fortify white WF and RF, thereby contributing to the prevention of obesity and diabetes, was also discussed.

METHODS

Flour production Celery leafstalk pomace, along with pomace obtained from celery mixed with apple, cucumber, kale, spinach, parsley, lettuce, and ginger or with apple, fennel, arugula, and ginger, was obtained at an industrial scale level from ColdPressok (Belgrade, RS). No treatments other than squeezing thoroughly washed raw material were applied. The pomace was collected aseptically immediately after squeezing. By applying a recently patented technological process pomace [1] was dehydrated at a small industrial scale level. The dehydrated pomace, with a water activity (aw) bellow 0.4 was ground to a particle size below 300 microns. The low moisture content of 5 wt % and aw enabled grinding of the dehydrated pomace and ensured good stability and storability of obtained flour. The proximate composition and techno-functional properties of CPF, CPF1 and CPF2, white WF and RF were determined.

Determination of proximate composition CPF, CPF1 and CPF2, as well as WF and RF were analyzed for moisture content, protein, fat, DF and ash content. The moisture and ash contents were estimated using gravimetric methods after drying on 105 °C, and incineration at 550 °C, respectively. The crude protein content was determined by the Kjeldahl method and the nitrogen factor used for protein calculation was 6.25, while the crude fats were determined using the extraction procedure on Soxhlet apparatus, with petroleum ether as a solvent, after the treatment with HCl. Nutritional components were determined by using the procedures described by the Association of Official Analytical Chemists. Soluble and insoluble DF was determined by the enzymatic-gravimetric procedure [2]. Total DF was calculated as the sum of the soluble and insoluble fiber [2]. Available carbohydrate content was calculated as: 100 - (fat (g) + ash (g) + moisture (g) + protein (g) + total fibre (g)). Determination of sucrose, D-glucose and D-fructose was performed according to the instruction manual by the spectrophotometric method using the enzymatic assay kit R-biopharm (R-BIOPHARM AG, Darmstadt). The water activity (aw) was determined by aw meter Novasina Lab Swift-aw, Novasina AG, Lachen, Switzerland, at 25 °C.

Calculation of energy value Total energy, calculated by multiplying determined carbohydrate, fat, protein and fibre content with their average energy values (fat 9 kcal/g, protein 4 kcal/g, carbohydrate 4 kcal/g and fibre 2 kcal/g), was expressed in kcal per 100 g of samples

Calculation of CPFs percentage required to be added into WF or RF to reach 10:1 carbohydrate to fiber ratio The ratio of carbohydrates to DF [3] is the most reliable criteria to recognize good whole grain food. Moreover, it could be used to estimate potential of celery-based pomace to enrich gluten free or common cereal flour. The amount of CPFs required to decrease the ratio of grain flour to 10:1 is calculated. Percentage of CPFs required to be added in mixture with chosen grain flour to reach carb:fiber 10:1 was calculated using following equation:

$$x = 100 \times \frac{CHF - 10 \times DFF}{10 \times DFP - CHP + CHF - 10 \times DFF}$$

x - percentage of CPFs added to standard flour to reach carb:fiber ratio 10:1 (g)
CHF - total carbohydrates content of standard flour (g/100g)
CHP - total carbohydrates content in CPFs (g/100g)
DFF - total dietary fiber content of standard flour (g/100g)
DFP - total dietary fiber content in CPF (g/100g)

Determination of Water and Oil Binding Capacity (WHC and OHC) For water holding capacity (WHC) and oil holding capacity (OHC) determination, 1 g of flour was mixed with 30 mL of distilled water and 10.0 mL of sunflower oil, respectively, and left for 24 h at room temperature. After centrifugation at 3600 rpm for 20 min, the supernatant was removed and the weight of the residue measured. Results were expressed as the weight of water bound or oil retained per gram of sample (g/g).

RESULTS

The proximate compositions of three prepared celery flour (CPF, CPF1 and CPF2) are compared with WF and RF.

Table 1. Proximate composition of tree types of anti-grain celery-based pomace flour (CPF, CPF1 and CPF2) in comparison to grain flour such as white wheat and rice flour (WF and RF).

Parameters (g/100g)	**CPF**	**CPF1**	**CPF2**	**WF**	**RF**
Fat	1.48±0.14	2.96±0.40	2.24±0.17	1.30±0.07	0.56±0.10
Total carbohydrate	63.53±0.41	70.10±0.85	75.67±0.62	75.46±0.34	80.85±0.28
Total sugar	5.24±0.23	4.22±0.30	11.82±0.58	0.14±0.03	0.13±0.02
Glucose	2.01±0.08	4.22±0.30	6.76±0.19	<0.1	<0.1
Fructose	1.53±0.09	<0.1	2.93±0.21	<0.1	<0.1
Sucrose	1.71±0.06	<0.1	2.14±0.18	0.14±0.03	0.13±0.02
Protein	15.50±0.42	13.80±0.28	10.20±0.25	9.6±0.16	6.74±0.19
Total fibre	46.89±1.88	51.10±1.63	47.68±1.07	2.50±0.27	1.61±0.17
Insoluble fibre	35.60±0.91	35.70±0.81	33.48±0.73	2.00±0.16	1.39±0.13
Soluble fibre	11.30±0.97	15.40±0.82	14.20±0.34	0.50±0.11	0.22±0.08
Carbohydrate/ fibre	**1.35**	**1.37**	**1.59**	**30.2**	**50.2**
Moisture	9.80±0.05	6.14±0.04	5.75±0.13	13.15±0.07	11.39±0.15
Ash	9.70±0.08	7.00±0.13	6.15±0.06	0.49±0.05	0.46±0.08
aw	0.41±0.01	0.29±0.01	0.28±0.01	0.65±0.01	0.58±0.01
Energy value (kcal/100g)	235.6	260.1	268.2	346.9	352.2

Total sugar (g/100g) = glucose (g/100g) +fructose (g/100g) +sucrose (g/100g)

Total carbohydrate (g/100g) = 100-(fat (g/100g) + protein (g/100g) + moisture (g/100g) + ash (g/100g))

As observed, the content of total dietary fiber is exceptionally high in all varieties of the obtained AGF. CPF contained 46.9±1.9 while CPF1 and CPF2 51.1±1.6 and 47.7±1.1 g/100 g. Content of TDF in WF and RF was only 2.5 ± 0.27 and 1.6 ± 0.17 g/100 g. Superior techno-functional properties of AGF, such as high WHC and OHC can be explained by high content of DF. Also, high WHC ascribed to all AGF samples exceeded highly common values for grain flour. WHC of approx. 9.21 g H_2O/g flour was ascribed to CPF 1 while 6.97 and 7.42 g/g flour to CPF1 and CPF2. WHC of WF and RF were found to be approx. 1.18 and 1.34 g/g flour. High values for OHC were also found for AGF. OHC for CPF was 1.96 g/g while 1.63 and 1.56. g/g for CPF1 and CPF2. OHC for WF and RF was much lower, 0.71 and 0.65 g/g flour. These values indicate that celery pomace flours (CPF, CPF1, and CPF2) have significantly higher WHC and OHC compared to traditional WF and RF. This property can be advantageous in various food applications where moisture retention and texture enhancement are desired.

To enable more comprehensive comparison between celery pomace flour and common wheat and rice flour carbohydrate to fiber ratio was used. As seen in Table 1 carb:fiber ratio in all CPFs is below 2. The lowest ratio of 1.35 is ascribed to CPF, the sample with the highest WHC and OHC. The ratio for WF and RF was found to be at least 20 folds higher, reaching 30 and 50. Obviously, the recommended carb:fiber ratio of up to 10-to-1 can be reached by addition of CPFs into grain flour. Addition of CPF in amount that does not exceed 15% can lower carb:fiber ratio of white WF and RF to 10 to 1. All three types of CPF can contribute content of DF significantly. Decrease of carb to fiber ratio in relation of CPF addition to rice flour was shown on Figure 1.

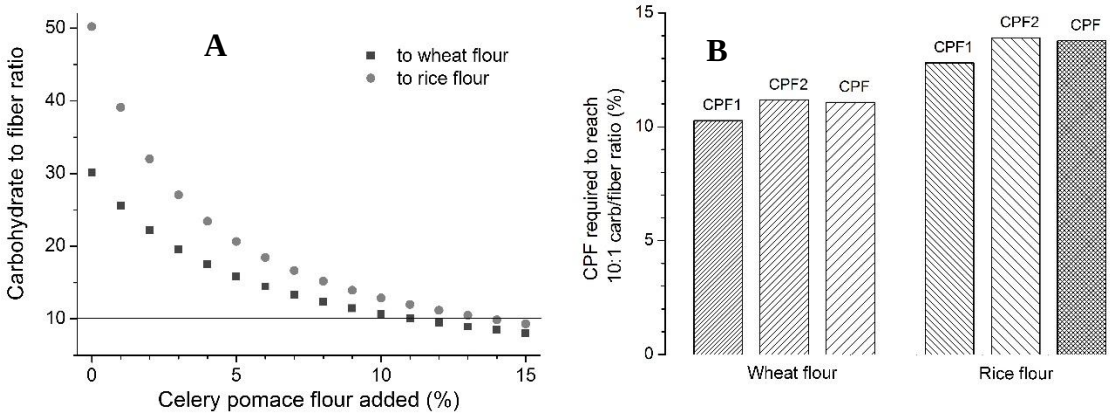


Figure 1. A) Decrease of carbohydrates to fiber ratio of white wheat and rice flour in relation to addition of celery-based flour (CPF) (%), **B)** percentage of CPF1, CPF2 and CPF required to be added in white wheat or rice flour to reach recommended 10:1 ratio.

Glycemic index and load (GI and GL) of bread made from composite flour made from CPF and white WF and RF is currently under investigation using *in vitro* methods, as well as standard *in vivo* determination. Both, GI and GL of bread from composite flour will be compared to bread from white WF and RF prepared according to same procedure.

CONCLUSION

Fortification of gluten free flour or standard grain flour with anti-grain flour obtained from minimally processed celery pomace can be a strategy to solve lack in dietary fiber in modern diet, potentially preventing obesity and diabetes associated with it. Due to its extremely high DF content, incorporating up to 15% pomace flour can achieve optimal ratio of total carbohydrates to total dietary fiber. Employment of composite flour obtained by mixing of common flour with anti-grain flour from celery pomace in production of popular bakery and confectionery might affect public health in a positive way. Relation of decrease of glycemic index and load related to addition of AGF into common flour is going to be established. *In vivo* and *in vitro* determination of GI and GL of bread prepared with and without CPF addition into white wheat and rice flour is currently under the progress.

Acknowledgments

This research was supported by the Science Fund of the Republic of Serbia. 7439 GRANT No. *From Waste to Food and Soil Enrichment - minimizing waste by applying circular economy in fruits/vegetables processing industry* – WasteBridge.

REFERENCES

[1] S. Zlatanović, S. Gorjanović, S. Ostojić, D. Micić, F. Pastor, A. Kalušević, J. Laličić-Petronijević, Method for Producing Gluten-Free Flour Made of Apple Pomace, WO/2020/027683, 2022.

[2] AOAC 991.43-1994(2000), Total, Soluble, and Insoluble Dietary Fibre: AOAC Official Method (2000).

[3] R. S. Mozaffarian, R. M. Lee, M. A. Kennedy, D. S. Ludwig, D. Mozaffarian, S. L. Gortmaker, Public Health Nutr., 16 (2013) 2255–2264.

ANTIOXIDANT ACTIVITY OF RED GRAPE SKIN EXTRACT FROM ŠUMADIJA DISTRICT

E. Avdović [1], D. Simijonović[1], S. Jovičić Milić[1], D. Stojković[1], D. Milenković[1], D. Dimić[2] and Z. Marković[1,3]

[1] University of Kragujevac, Institute for Information Technologies, Department of Science, Kragujevac, Jovana Cvijića bb, 34000 Kragujevac, Serbia, (edina.avdovic@pmf.kg.ac.rs)
[2]University of Belgrade, Faculty of Physical Chemistry, Studentski trg 12-16, 11000 Belgrade, Serbia
[3] Department of Natural Science and Mathematics, State University of Novi Pazar, Vuka Karadžića bb,36300 Novi Pazar, Serbia

DOI: https://doi.org/10.46793/Phys.Chem24II.689A

ABSTRACT

The aim of this study was to present the results of the antioxidant capacity of Merlot grape skin extract (**GSE**) originating from the Šumadija district. The extract was obtained utilizing the ultrasonic extraction technique in 50% ethanol. The antioxidant capacity of the **GSE** was determined using various spectroscopic methods such as DPPH, ABTS, and FRAP. Moreover, Folin–Ciocalteu method was used for determination of total phenolic contents in the **GSE**. The obtained results show that the ethanolic extract shows a good scavenging activity towards ABTS radicals, and a slightly weaker affinity to the DPPH radical. Also, this extract shows a reduction potential as measured by the FRAP assay, as well as a high concentration of phenolic compounds. These results indicate that the **GSE** exhibits remarkable antioxidant properties and very high TPC, suggesting its potential application in pharmacy and as a functional food.

INTRODUCTION

Antioxidants are compounds that help protect the body from damage caused by harmful molecules known as free radicals. They can be found in a variety of foods, such as fruits, vegetables, nuts, and whole grains. Antioxidants are also available in supplement form, but it is generally recommended to get them through a balanced diet.

The grape, a member of the *Vitis genus*, is well recognized as a key variety of vine utilized globally for the manufacture of wine. These plants play a vital role in agriculture and are grown on around 7.4 million hectares of land globally [1]. Vines and their fruits, particularly wine, have had substantial cultural and religious significance throughout history [2]. The advantages of including wine in the diet in moderation are well-established. This is demonstrated by a widely recognized phenomena called the "French paradox," which reveals that the people of France experience a lower incidence of cardiovascular ailments despite their dietary habits. This phenomenon can be attributed to the consumption of high-quality wine by the residents of this region, which is abundant in natural antioxidants.

In recent years, there has been a growing interest in using agro-industrial by-products since they contain a high number of bioactive compounds. These compounds have been found to have several health benefits, including reducing the risk of chronic diseases such as cancer, neurological diseases, and cardiovascular diseases [3,4]. Waste materials from the manufacture of wine, such as seeds and pomace, can be used to extract antioxidant chemicals, which offers substantial economic benefits. It is well-established that grape pomace contains significant amounts of antioxidant compounds, specifically polyphenols. On the other hand, grape skins contain anthocyanidins and anthocyanins,

which are natural pigments known for their antioxidant properties. These compounds inhibit lipoperoxidation and exhibit antimutagenic activity [5]. The phenolic content of grape skins is subject to variation based on factors such as cultivar, geographic origin, climate, and production practices, as well as exposure to illnesses such fungal infections. Polyphenols have garnered increasing attention due to their possible health advantages and pharmacological uses. In order to enhance the extraction yield, researchers have explored novel non-conventional techniques, including ultrasound (US), pulsed electric fields (PEF), and high-voltage electric discharges (HVED). These methods are considered environmentally sustainable and energy-efficient.

The aim of this research is to examine the antioxidant capacity of Merlot grape skin extract obtained from the Šumadija district. To achieve this goal, an ethanolic extract was prepared and different spectrophotometric methods were used to test its antioxidant capacity.

METHODS

The chemicals used in this study 2,2-diphenyl-1-picrylhydrazyl 1,1-diphenyl-2-picrylhydrazyl radical (DPPH), 2,2′-Azino-bis(3-ethylbenzothiazoline-6-sulfonic acid) diammonium salt) (ABTS), referent phenolic standards Nordihydroguaiaretic acid (NDGA), (S)-6-Methoxy-2,5,7,8-tetramethylchromane-2-carboxylic acid (Trolox)), gallic acid, ascorbic acid, potassium persulfate, iron(III) chloride, Folin Ciocalteu reagent, potassium ferricyanide, trichloroacetic acid, and methanol were procured from Sigma-Aldrich Chemicals. The UV-Vis measurements were performed on Perkin Elmer, Lambda 365 UV/Vis Spectrophotometer.

DPPH Radical Scavenging Assay

The scavenging activity of isolated extract towards DPPH radical was determined on similar way as described in reference [6] and it is based on the decrease in absorbance at 517 nm caused by the neutralization of radical. NDGA and quercetin were used as positive controls. IC_{50} values were determined for the tested extract and standards compounds, i.e. concentration of the extract necessary to reduce 50% of DPPH radical [7].

ABTS Radical Scavenging Assay

The ABTS test was performed according to the method described by Pontiki et al. [8] with slightly modifications. The decrease of absorbance was monitored at 734 nm. Trolox was used as positive control, and IC_{50} values were determined for extract and reference compound.

Determination of the ferric-reducing antioxidant power

The ferric-reducing antioxidant power (FRAP) method was performed according to the previously described procedure [9]. FRAP results are reported as value of the absorbance at 700 nm. In this case the ascorbic acid was used as positive control.

Determination of the total content of phenolic compounds

To determine the total phenol content (TPC) the Folin-Ciocalteu colorimetric method was applied [10]. Gallic acid was used as standard and the absorbance at 750 nm was measured. The TCPC was expressed as milligrams of gallic acid equivalents (GAE) per gram of dry Grape Skin Extract (GSE) (mg GAE/g GSE).

RESULTS AND DISCUSSION

The antioxidant potential of the ethanolic extract obtained from grape skin of Merlot variety (**GSE**) was estimated by using DPPH, ABTS, and iron-reducing antioxidant power. In addition, the **GSE** was subjected to determination of TPC by using Folin-Ciocalteu method. The results of these examinations are presented in **Table 1**. Familiar antioxidants such as trolox, quercetin, gallic acid, ascorbic acid and NGDA, were employed as standards. Upon comparing the antioxidant activity of **GSE** with the established standards, it was noted that the extract exhibited noteworthy antioxidant potential.

The results obtained from the DPPH test indicate that the **GSE** demonstrates a moderate level of antioxidant activity, with IC_{50} values of 86.4 µg/mL. The IC_{50} value is markedly greater than the IC_{50} value of the reference substances NDGA and quercetin. These findings indicate that while the antioxidant activity of the examined extract is not as strong as that of NDGA and quercetin, it nevertheless exhibits promise for further examination of its potential application. The extract has much higher efficacy against $ABTS^{\bullet+}$ radicals compared to its efficacy against DPPH radicals. Namely, demonstrated a significant ability to counteract $ABTS^{\bullet+}$ with IC_{50} values of 14.93 µg/mL, which is roughly three times greater than Trolox (1.3 µg/mL). These findings indicate that the examined extract exhibits more efficacy in scavenging ABTS•+ radicals as compared to DPPH radicals.

The FRAP method [11] is founded on the conversion of the Fe^{3+}–ferricyanide complex into iron in the form of Fe^{2+} by reduction. The absorbance at 700 nm for both the **GSE** and the antioxidant ascorbic acid are presented in **Table 1**. The compound's high redox potential is demonstrated by a rise in absorbance. Based on the absorbance of the extract, it can be concluded that the extract has a robust reduction potential (0.1599), which surpasses the reduction potential of ascorbic acid (0.1249).

The Folin Ciocalteu test revealed that the investigated extract contains 6580 mg GAE/g GSE. This result indicates that the **GSE** has a very high concentration of phenolic compounds, which are known for their ability to neutralize free radicals and prevent oxidative damage in the body.

Table 1. The antioxidant activity and total phenolic content of **GSE** and reference compounds.

Investigated extract and standards	**DPPH** IC_{50} (µg/mL)	**ABTS** IC_{50} (µg/mL)	**FRAP** (A_{700nm})	**TPC** (mg GAE/g GSE)
GSE	86.4 ± 3.3	14.9 ± 0.8	0.1599 ± 0.0063	6580 ± 4
NDGA	0.5 ± 0.1	–	–	–
Quercetin	1.9 ± 0.1	–	–	–
Trolox	–	1.3 ± 0.1	–	–
Ascorbic	–	–	0.1249 ± 0.0022	–

Abbreviations: mg GAE/g GSE – milligrams of gallic acid equivalents (GAE) per gram of dry Grape Skin Extract; A_{700nm} – Absorbance measured at 700 nm for **GSE** and referent standard ascorbic acid in sample where the concentration in the sample was 0.6 mg/mL; TPC – total phenolic content; FRAP – Ferric-reducing antioxidant power; Values are means ± SD of three measurements

CONCLUSION

This paper describes the investigation of the antioxidant capacity of Merlot **GSE** from the Šumadija region. The antioxidant potential and TPC of this extract were tested by various spectrophotometric tests such as DPPH, ABTS, FRAP and Folin Ciocalteu methods. The obtained results show that the ethanolic extract shows a good removal of ABTS radical, while it showed a slightly weaker affinity towards the DPPH radical. In addition, this extract shows reduction potential as measured by the FRAP assay, as well as that the extract includes a substantial concentration of phenolic compounds,

which are widely recognized for their ability to eliminate harmful free radicals and protect the body from oxidative harm. These results indicate a great potential of the extract for use in the pharmaceutical or food industry. Further studies could focus on optimizing extraction methods or exploring synergistic effects with other compounds to enhance its antioxidant properties.

Acknowledgment

This research was supported by the Science Fund of the Republic of Serbia, GRANT No. 11067, Promis 2023, Unleashing Nature's Potential: Using Grape Skin Extract and Sustainable Materials for Advanced Chronic Wound Therapy-**GraSP_MAT**; GRANT No. 14848, Proof of Concept, Unleashing nature's potential: Development of Additive-Free Prokupac Grape Skin Topping as Functional Food –**GraSP**.

REFERENCES

[1] Food and Agriculture Organization of the United Nations (FAO), FAO Production Yearbook, Food and Agriculture Organization of the United Nations, Rome, 56 (2002) 169.
[2] S. Lavee, Grapevine (Vitis Vinifera) Growth and Performance in Warm Climates, Springer, Dordrecht. Netherland, (2000) 343.
[3] A. Teixeira, N. Baenas, R. Dominguez-Perles, A. Barros; E. Rosa, D. A. Moreno, C. Garcia-Viguera, Int. J. Mol. Sci. 15 (2014) 15638.
[4] B. Salehi, S. Vlaisavljevic, C. O. Adetunji, J. B. Adetunji, D. Kregiel, H. Antolak, E. Pawlikowska, Y. Uprety, K. S. Mileski, H. P. Devkota, J. Sharifi-Rad, G. Das, J. K. Patra, A. K. Jugran, A. Segura-Carretero, M. D.D. M. Contreras, Trends Food Sci. Tech. 91 (2019) 362.
[5] R. Pedreschi, L. Cisneros-Zevallos, J. Agr. Food Chem, 54 (2006) 4557.
[6] C. Kontogiorgis, D. J. Hadjipavlou-Litina, Enzym. Inhib. Med. Chem. 18 (2003) 63.
[7] K. Marković, A. Kesić, M. Novaković, M. Grujović, D. Simijonović, E. H. Avdović, S. Matić, M. Paunović, M. Milutinović, D. Nikodijević, O. Stefanović, Z. Marković, RSC Advances 14 (2024) 4591.
[8] E. Pontiki, D. Hadjipavlou-Litina, K. Litinas, G. Geromichalos, Molecules 19 (2014) 9655
[9] I. F. F. Benzie, J. J. Strain, Anal. Biochem, 239 (1996) 70.
[10]Singleton, V.L., and J.A. Rossi. Am. J. Enol. Viticult. 16 (1965) 144.
[11]E. H. Avdović, Ž. Milanović, D. Simijonović, M. Antonijević, M. Milutinović, D. Nikodijević, N. Filipović, Z. Marković and R. Vojinović, Antioxidants 12 (2023) 2070.

Q *–Physico-Chemical Analysis*

PHYSICO-CHEMICAL INVESTIGATION OF XVI CENTURY FRESCO-PAINTINGS FROM MONASTERY CRNA REKA

B. Savić [1], J. Vujin [2], T. Tripković [3], J. Ciganović[4], I. R. Milošević[2], I. Živković[1] and T. Tomašević-Ilić [2]

[1] Faculty of Applied Arts, University of Arts Belgrade of Belgrade, Kralja Petra 4, 11000 Belgrade, Serbia
[2]Institute of Physics Belgrade, University of Belgrade, Pregrevica 118, 11080 Belgrade, Serbia (ttijana@ipb.ac.rs)
[3]Institute for the Protection of Cultural Monuments of Serbia, Radoslava Grujica 11, 11118 Belgrade, Serbia
[4]Vinca Institute of Nuclear Sciences-National Institute of the Republic of Serbia, University of Belgrade, Mike Petrovića Alasa 12-14, 11351 Belgrade, Serbia

DOI: https://doi.org/10.46793/Phys.Chem24II.695S

ABSTRACT
The 16th-century wall paintings of Monastery Crna Reka in Serbia are visibly deteriorating. Extensive wall degradation causes these frescoes to fall from their original positions and shatter into fragments. To address the proper restoration and conservation procedures, we examine the structure and morphology of the fragments. Micro-Raman spectroscopy and XRF revealed that the blue color on the wall paintings does not originate from blue pigments but results from the layer-by-layer technique of hematite and carbon black pigments by the artist, which, in combination with the mortar, gave a blue color sensation. Cross-sectional profiles and 3D maps obtained by profilometry show the surface morphology of these fragments, and can be consider as guidelines for further understanding of the various aspects of the painting's creation, monitoring future degradation process, and developing or applying protective coatings for Serbian frescoes.

INTRODUCTION

The 13th-century Monastery Crna Reka is located in southwestern Serbia, in the canyon of the Crna Reka river, on the rocky cliffs of mountain Mokra Gora. Its distinctive architecture renders it one of Serbia's most stunning cave-churches. The internal walls in Crna Reka were painted by the renowned artist Longin by al fresco-painting technique [1]. Despite having endured the passage of time without being demolished, exposure to various environmental factors upon natural aging has caused degradation of this unprotected monument, formation of micro and nanocracks, and eventually surface erosion. Such extensive degradation of the walls leads to the falling of fresco paintings. Preserving of this wall paintings which has been determined as the Heritage of the National Treasure category requires extensive restauration work. To ensure the long-term preservation of fresco paintings without altering their esthetics, it is essential to thoroughly understand their chemical structure and surface morphology [2]. Thus, conservators can make informed decisions on how to best maintain and protect frescoes against ongoing and future challenges. When Heritage samples must be analyzed, non-destructive techniques are the only option for obtaining information. The study by micro-Raman of cross sections is an effective tool capable of investigating the chemical structure of frescoes [3]. The use of cross sections can enable the identification of components in the artefacts from the support to the outermost layer. Combined with X-ray fluorescence (XRF), commonly used for the elemental characterization of heritage

objects due to its ability to detect a wide range of painting materials, in a non-destructive, sensitive, and efficient way, it can reliably identify the pigment compositions [4]. In paintings, surface topography reveals unintended stylistic elements embedded in the surface of the painting that may include the deposition and drying of the paint, patterns in the brushwork, physiological factors, and other aspects of the painting's creation [5]. This work aims to interpret the painting technique used by the artist and characterize the paint compounds using XRF and Raman spectroscopy.

METHODS

Sampling sites of wall paintings are determined according to standard sampling of the Heritage of the National Treasure category determined by Republic Institute for the Protection of Cultural Monuments, Law on Cultural Heritage and Ethical Sampling Guidance of Icon Heritage Science Group. Sampling of fresco painting was carried out from places with an unstable connection, where a conservation-restoration intervention of consolidation would otherwise be carried out. **Figure 1**. shows extensive degradation of frescoes and sampling sites.



Figure 1. Photographs of two sampling sites (A and B) and selected places prior to collection.

NT-MDT NTEGRA Spectra System with a 100x microscope objective, and a TE cooled CCD (1,024×256 pixels) detector, was used to obtain the Raman spectra. The 532-nm laser line of a He/Ne laser was employed for Raman excitation. The laser power was kept below 2 mW using density filters, to avoid sample degradation. A Thermo Niton XL3t portable analyzer was used for non-destructive elemental analysis, featuring multiple primary filters on its 50 kV X-ray tube to enhance sample excitation. The instrument was mounted on a stand, and a camera inside the analyzer head allowed for the definition of the sample surface area for analysis. The analysis time was set to 90 seconds. Using Niton's TestAllGeo and Mining calibration modes, the concentrations of 30 elements on the sample surfaces were determined semi-quantitatively. NITON Data Transfer software (NDT_REL_8.2.1) was used for the instrument control via computer and reading and processing of the recorded spectra. For the surface topography characterization, the non-contact optical profilometer Zygo NewView 7100 (Middlefield, CT, USA) was used.

For all measurements the samples were analyzed without any previous mechanical or chemical treatment being undertaken.

RESULTS AND DISCUSSION

Optical microscopy of the cross-section of the Crna Reka (CR) fresco painting fragment reveals a black and red layered structure on the surface of the fresco painting support (**Figure 2A-inset**). The red layer is positioned as a layer between two black layers on the white painting support. **Figure 2A**

depicts the Raman spectra of this untreated and unpolished cross-section sample. Bands at 227, 292, 405, 498, 611 and 657 cm^{-1}, characteristic for hematite (FeO3) [6], indicate that hematite was the main mineral used as a source of red pigments in these frescoes. The Raman spectra featured the origin of black layers on the support and on the surface. Broad bands at 1310 and 1591 cm^{-1} unequivocally indicate the presence of carbon-based compounds in this areas, attributed to carbon black. The band at 1310 cm-1 is due to sp^3-type C–C bonding, and the band at 1,597 cm^{-1} is due to sp^2-type C=C bonding. The absence of the symmetric stretching band of the phosphate group at 960 cm^{-1} excludes bone or ivory black pigments, suggesting that soot or powdered charcoal was the source of these black particles [7]. Strong bands at 285 cm^{-1} and 1081 cm^{-1}, and small band at 711 cm^{-1}, which was observed in the spectra, were attributed to calcite ($CaCO_3$) [8]. The Raman shift of bands related to black pigment and calcite indicate that the black paint could have been prepared by mixing the black pigment with lime or calcite. XRF spectra (**Figure 2B**) confirmed the results obtained by Raman spectroscopy. Although, the bluish is dominant color of the Monastery fresco paintings, XRF spectra indicates on the high presence of Ca and Fe of in all samples, without the presence of any element known to be used for blue pigments. Additionally, the presence of CaKα line in the XRF spectra and calcite in the Raman spectra indicates that the mortar on which it has been painted is a lime mortar, produced from limestone by heating calcium carbonate. This lime mortar has been used for millennia as pigments or primers, typically mixed with pigments in the fresco technique to bind the pigments.

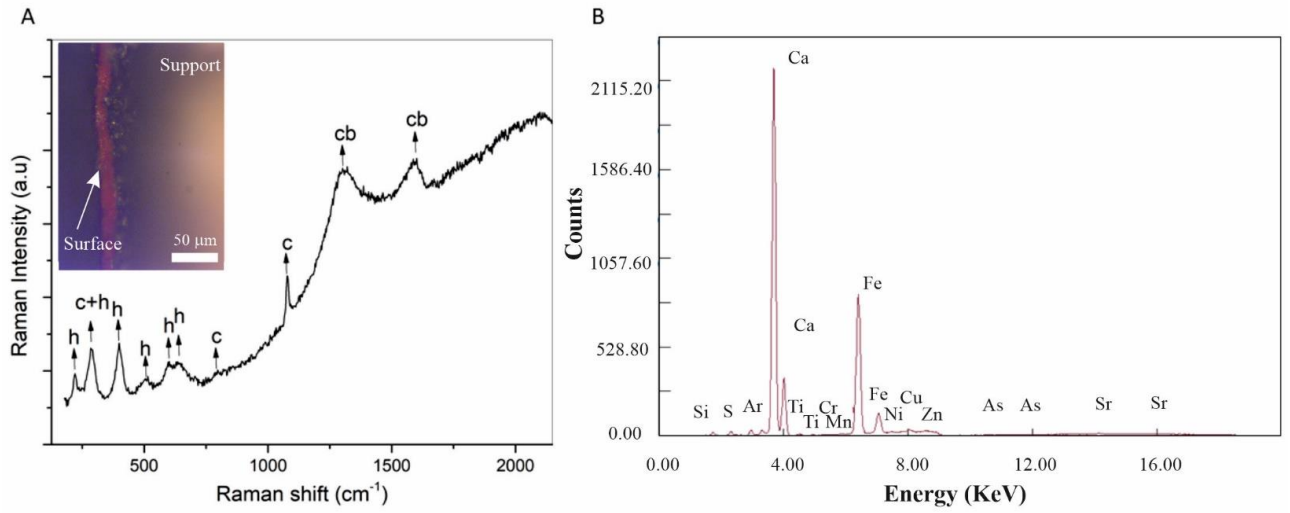


Figure 2. A) Representative Raman spectra of cross-section of the CR sample. Raman spectra featured the presence of hematite (h), calcite (c), and carbon black (cb) pigment; Optical Microscopy of unpolished and untreated cross-section of the CR sample. Scale bar is 50 µm. B) XRD spectra of the CR sample.

Figure 3 shows the surface morphology of the CR sample. High roughness is present across the entire surface. The areas with varying step heights, ranging from 4-10 µm, are likely the result of the deposition and drying of the paint during its creation. No patterns in the artist's brushwork were noticed. However, the surface inhomogeneity might result from degradation and requires further investigation. This should include examining other works by the artist and monitoring changes like cracking or flaking over time. Our findings provide a baseline record of the fresco's current condition. Conservators can use the established records to compare future observations, detect subtle changes and degradation progression, and determine the most suitable protective coating tailored to the specific needs of rough surfaces.

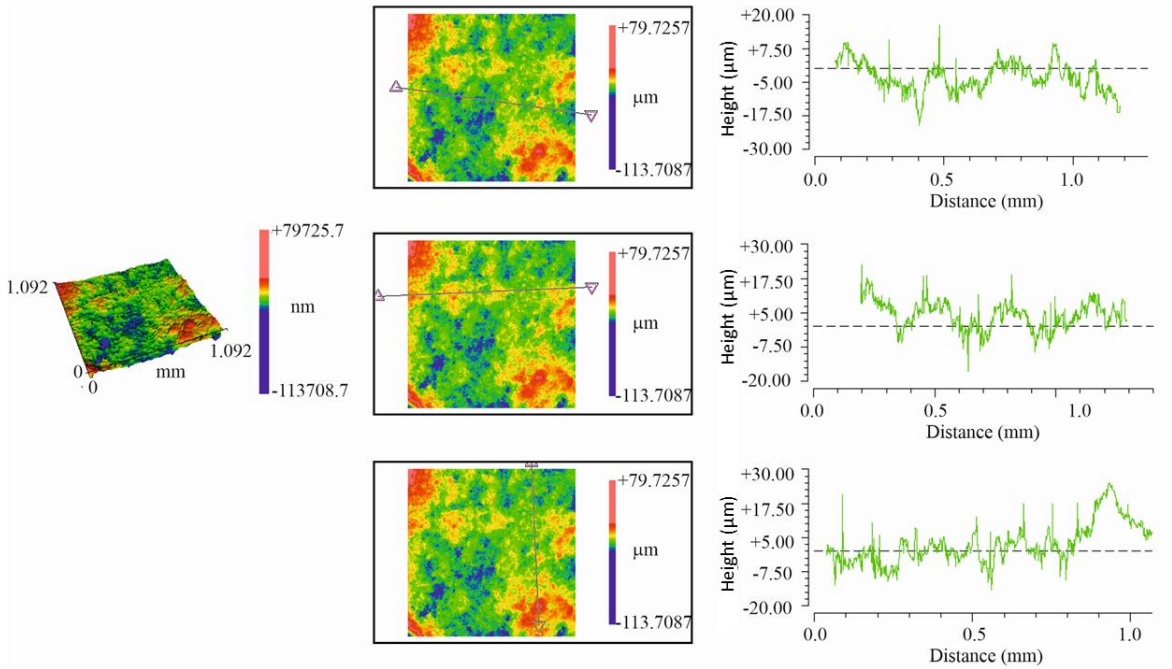


Figure 3. 3D and corresponding 2D maps with cross sectional profiles of CR sample.

CONCLUSION

The study of the cross sections indicates a layer-by-layer painting tecnique of fresco paintings from Crna Reka Monastery, and presents the characterisation of all layers (from the support to the most external) by micro-Raman spectroscopy. The following pigments were identified: hematite, carbon black, and calcite, and the composition was comfirmed by XRF measurements. Profilometry reveals the surface morphology of the paintings and provides information for future degradation monitoring of the frescoes.

Acknowledgment

This research was supported by the Science Fund of the Republic of Serbia, Grant No 7456, 2D Material-based Tiled Network Films for Heritage Protection-2DHeriPro, the Institute of Physics Belgrade through the Grant by the Ministry of Science, Technological Development and Innovations. Authors thank the Institute for the Protection of Cultural Monuments of Serbia for the collaboration. J. C. acknowledge Ministry of Science, Technological Development and Innovation of the Republic of Serbia through institutional funding (grant no: 451-03-66/2024-03/200017).

REFERENCES

[1] R. Stanić, Neka zapažanja o spomeničkim osobenostima Crnorečkog manastira i o programskim i stilskim odlikama zidnog slikarstva, u: Manastir Crna Rijeka i Sveti Petar Koriški, Naučni skup, Priština, Zubin Potok, Crna Rijeka, 25-26.V 1996, Priština, Beograd (1998) 163–179.
[2] P. Mora, Causes of deterioration of mural paintings, International Centre for the Study of the Preservation and the Restoration of Cultural Property, Rome (1974) 11–29.
[3] M.A. Ziemann et al., J. Raman Spectrosc. 52 (2020) 137–142.
[4] A. Harth, A. Herit Sci 12 (2024) 17.
[5] F. Ji et al., Herit Sci 9 (2021) 152.
[6] D. L. Argote et al., J. Archaeol. Sci. Rep. 32 (2020) 102375.
[7] A. Hernanz et al., J Raman Spectrosc 37 (2006) 492–497.
[8] S. Gunasekaran et al., J. Raman Spectrosc. 37 (2006) 892–899.

R *– Photochemistry, Radiation Chemistry, Photonics*

EFFECT OF MECHANICAL ACTIVATION ON PROCESSING OF $CoPd/TiO_2$ CATALYST PRECURSORS FOR CO HYDROGENATION

M. Shopska [1], M. Fabian [2], H. Kolev [1], K. Tenchev [1] and G. Kadinov [1]

[1] *Institute of Catalysis, BAS, acad. G. Bonchev St., Bldg 11, Sofia 1113, Bulgaria. (shopska@ic.bas.bg)*
[2] *Institute of Geotechnics, SAS, Watsonova 45, 04001 Kosice, Slovakia.*

DOI: https://doi.org/10.46793/Phys.Chem24II.701S

ABSTRACT
Precursors of (10%Co+0.5%Pd)/TiO_2 catalysts with application in CO hydrogenation obtained by impregnation were activated by high-energy ball milling. Activated precursors showed partial decomposition of supported nitrate salts during the milling, facilitation of the following complete decomposition of the residual amount of salts, and decrease in decomposition and reduction temperatures. The mechanical activation shortened the procedure about driven the systems to their active state.

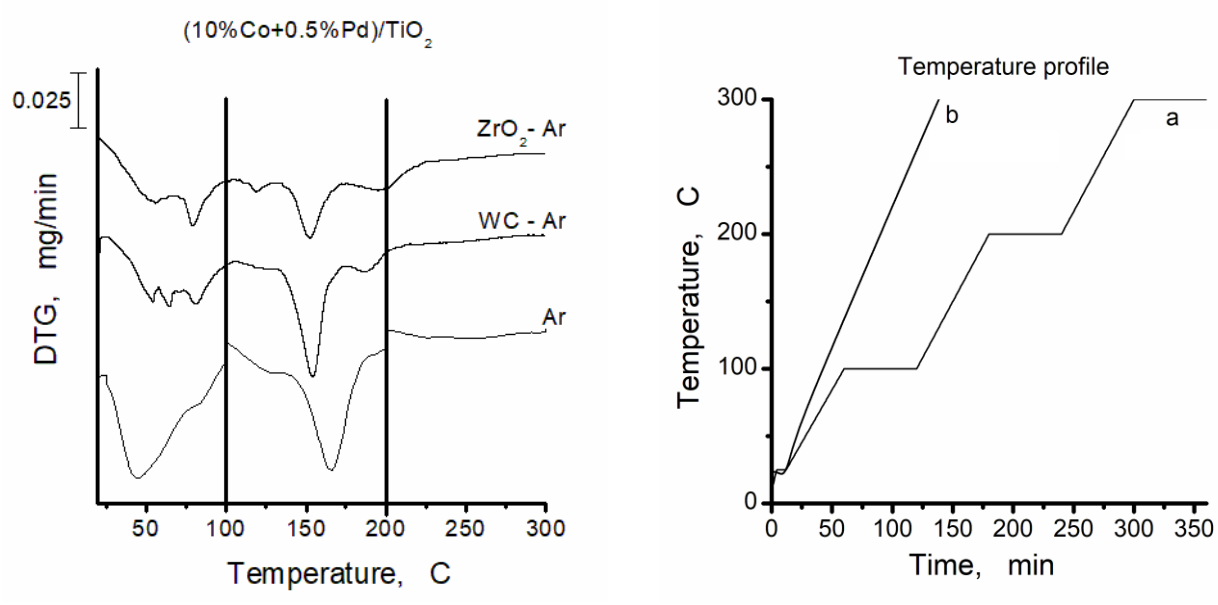
INTRODUCTION
Impregnation is the most wide used method for synthesis of catalysts. However, it produces wastewater and harmful gases. Drying, calcination and reduction of catalysts are time- and energy-consuming processes. Mechanical activation has relatively low impact on environment. Milling leads to increase of the substance inner energy. Treated system is metastable and through relaxation processes it reverses in equilibrium state [1]. Energy-rich systems could release the excessive energy in a suitable moment ensuring easier pass of some processes connected with catalyst formation as well as effect on chemical processes running on the surface. Application of milling on already synthesized systems influences on inactive substances creating specific reaction sites achieving an active state. Mechanical activation use often results in simplification of technology decreasing number of included stages. Present work reports investigations on the mechanical activation effect on obtained by impregnation precursors of (10%Co+0.5%Pd)/TiO_2 catalysts that have application in CO hydrogenation.

METHODS
(10%Co+0.5%Pd)/TiO_2 samples were synthesized by impregnation of titania support with nitrate salts of the both metals [2]. One part of the unprocessed material was milled 12 x 15 min (with pause of 10 min) at 450 rpm using ZrO_2 and WC balls and jars. 6-hour treatment in air or Ar flow at $T \leq 300$ °C was applied to the other part of the initial material to decompose the supported salts [2]. Infrared spectroscopy (IRS), x-ray photoelectron spectroscopy (XPS), differential thermogravimetry (DTG) and temperature-programmed reduction (TPR) were used to characterize all materials [2].

RESULTS AND DISCUSSION
Couple of bands at 1385 and 824 cm^{-1} characteristic about nitrate group was found in IR spectra of as synthesized and mechanically treated bimetallic samples. Comparison between spectra of CoO, Co_3O_4, carrier and mechanically treated samples showed changed band intensities in the spectra of activated materials compared to the spectrum of the support in range $\nu < 750$ cm^{-1}. Absorption at about 575 cm^{-1} was increased in the spectra of the mechanically activated precursors. The existence of CoO or Co_3O_4 could not be confirmed or rejected based on IR spectra. In view of the milling

mode, namely in air, the obtained results showed that most probably in the mechano-processed materials cobalt nitrate and Co_3O_4 existed together. IR spectra were used about tentative calculation for achieved decomposition extent of nitrate salts during milling. The band intensities characteristic of TiO_2 (507 cm^{-1}) and NO_3 group (1385 cm^{-1}) were used. Assessment was done by ratio $I(NO_3)/I(TiO_2)$ for every individual spectrum. Data showed that 33% of the supported salts decomposed using ZrO_2 milling instruments and 47% with WC ones.

Detected Co^{2+} and Pd^{2+} ions were registered by XPS study on surface of the samples, which contained supported nitrate salts without any processing and with mechanical treatment. Presence of Pd^0 and Co^{3+} as result of salts' decomposition during milling was not registered. This result could be due to their small amount or to adsorption of oxygen from air on the surface of the samples that reflected on the oxidation state of the metals. Analysis of N1s spectra showed that after mechanical impact part of supported nitrate salts were decomposed. In case of milling by WC instruments the amount of nitrate groups in samples decreased with 55% and by ZrO_2 balls it was with 41% of the initial level.



A B

Figure 1. DTG investigation of (10%Co+0.5%Pd)/TiO_2 system samples in Ar flow.
Plot A - Recorded DTG profiles: Ar - decomposition of supported nitrates using 6-hours procedure; ZrO_2-Ar and WC-Ar – mechanical treatment in air and DTG using 2.5-hours procedure; ZrO_2 and WC – milling instruments material.
Plot B - Course of the temperature in the processes of supported salts decomposition for samples without (a) and with (b) mechanical treatment.

DTG investigations of as prepared dry (10%Co+0.5%Pd)/TiO_2 sample precursor showed that the transformation of the supported salts in Ar occurred in three stages during the chosen 6-hour procedure of thermal treatment from T_{room} to 300 ºC (Figure 1, A(Ar), B(a)). About 60% of the total mass loss in the first stage at $T \leq 100$ ºC was due to processes of $Co(NO_3)_2.6H_2O$ partial dehydration and conversion of $Pd(NO_3)_2.2H_2O$ into Pd [3]. Calculated mass loss in the framework of the second stage (100 - 200 ºC) showed that decomposition of the cobalt nitrate into CoO (or Co_3O_4) went almost to the end. Additional process of lower intensity and insignificant mass loss

was registered at 230 ºC and was assigned to partial decomposition of surface species originated from CO_2 adsorption on the support [4]. The area of DTG peaks of mechanically activated samples was calculated and compared with that of DTG peaks of as prepared dry precursor (Figure 1, A(WC-Ar and ZrO_2-Ar), B(b)). The result was decreased areas after milling. This finding was result of partial decomposition of the supported salts during the treatment. The effect of WC balls application was stronger. Larger part of possible processes at T ≤ 100 °C had been realized during milling. Mass loss for different samples was about 51% (using ZrO_2 balls) and 64% (using WC balls) from the total mass loss. At T ≤ 200 °C the destruction process of the supported salts was realized at temperatures lower than those registered for as prepared precursor and the transformations went to the end. No processes were registered at T > 200 ºC.

Mechanically processed precursors were studied also by DTG with air flow. The aim was to be checked how far the oxidative atmosphere would affect the processes running at decomposition in full of the supported nitrates, respectively to the composition of samples. Comparative analysis showed that at T > 100 ºC the registered decrease in peak areas was (almost) the same in both systems using both atmospheres. It can be affirmed that the gas media effect was significant for the processes of dehydration and decomposition of the palladium salt.

TPR measurements of cobalt-palladium precursor decomposed in air by the 6-hour procedure of heating showed two temperature regions of the reduction (Figure 2, down plot). Based on comparison with TPR of Co_3O_4 and precursor of 1%Pd/δ-Al_2O_3 catalyst pretreated in air, we concluded that at T < 500 ºC Co_3O_4 was reduced and PdO particles did not exist. Part of Co_3O_4 was reduced at T < 250 ºC that was due to the presence of promotor element, namely Pd [5]. Other part of Co_3O_4 reduced independently at 300 < T < 500 ºC [6]. It could be supposed that in the low-temperature reduction region formation of bimetallic particles with Co-rich or plane Co surface occurs. The high-temperature peak of independent reduction of cobalt oxide phase could be explained based on the supposition that at a determined moment of the reduction there is no accessible Pd to produce activated hydrogen and to participate in further reduction of cobalt oxide phase.

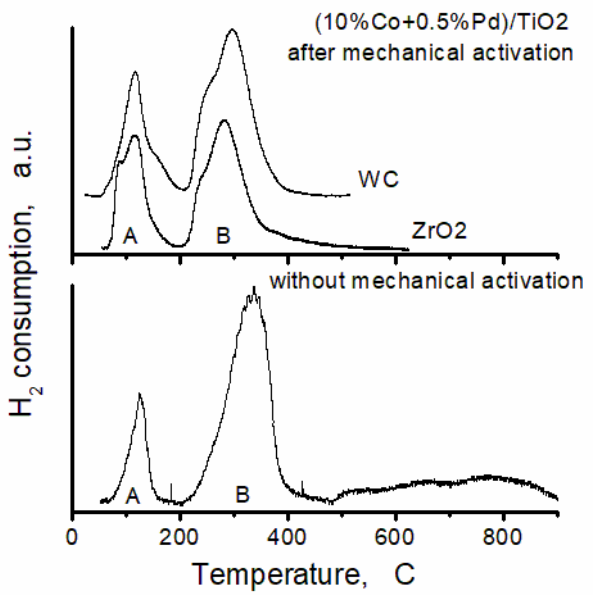


Figure 2. TPR profiles of (10%Co+0.5%Pd)/TiO_2 system samples treated in air by different procedures: down plot - 6-hours procedure; upper plot - 2.5-hours procedure; ZrO_2 and WC – material of milling instruments.

Based on TPR peaks area we supposed that about 25% of the cobalt oxide was reduced with stimulated participation of Pd. Low intensive reduction in the range 500 < T < 900 ºC (plateau) was registered, too. It could not be synonymously defined whether there went reduction of a phase similar to cobalt titanate or it was effect of strong metal-support interaction [7]. TPR curves of mechanically activated in Ar (not shown) or air (Figure 2, upper plot) precursors retained characteristic profile with two peaks. Decrease of high-temperature peak maximum with 40 - 60/50 - 60 °C and of low-temperature one with 10/0 °C was registered by DTG in air/Ar compared with those of the samples subjected to 6-hour thermal treatment. The data showed that the effect of the mechanical treatment was stronger in case of milling instruments produced of ZrO_2. Area of peaks A (T < 200 °C) and B (T > 200 °C) was calculated and obtained B/A ratios were compared. In result was found that the amount of the cobalt phase, which reduced at T < 200 °C under promotion of Pd has increased from 25% (in case of precursor not treated mechanically) to 40-50% (in case of mechano-activated precursors). It was supposed that mechanical treatment contributed to the process of bimetallic particles formation through fast decomposition a part of the supported salts (shortened time period from 6 to 2.5 hours for thermal treatment) and avoidance of mixed oxide phase formation.

CONCLUSION

Mechanical treatment lead to: decomposition of significant part of the supported salts; decrease in chemical transformation temperatures; shortening the duration of preliminary thermal treatment stage; increase of the low-temperature reducible oxide(s) amount; prevented formation of Co-Ti-O phases. Complete decomposition of supported salts in air or Ar had not significant effect on oxide composition and properties of the precursors.

Acknowledgment

Authors are grateful to Bulgarian and Slovak Academies of Sciences for financial support by grants IC-SK/02/2023-2024 and BAS-SAS-2022-06, respectively.

REFERENCES

[1] X. Liu, Y. Li, L. Zeng, X. Li, N. Chen, S. Bai, H. He, Q. Wang, Ch. Zhang, Adv. Mater., 34 (2022) 2108327.
[2] M. Shopska, H. Kolev, K. Aleksieva, I. Shtereva, K. Tenchev, S. Todorova, M. Fabian, G. Kadinov, Reac. Kinet. Mech. Catal. 134 (2021) 303.
[3] A. L. Lapidus, V. V. Maltsev, E. S. Shpiro, G. V. Antoshin, V. I. Garanin, Commun. AS USSR, chem. ser., 11 (1977) 2424.(in Russian)
[4] S. Todorova, V. Zhelyazkov , G. Kadinov, Reac. Kinet. Catal. Lett., 57 (1996) 105.
[5] A. Sarkany, Z. Zsoldos, G. Stefler, J. W. Hightower, L. Guczi, J. Catal., 157 (1995) 179.
[6] A. L. Lapidus, A. Yu. Krilova, V. V. Kazanskii, V. Yu. Borovkov, A. V. Zaitsev, G. V. Kozlova, A. Zukal, I. Rathouski, M. Yanchalkova, Commun. AS USSR, chem. ser., 11 (1991) 2444.(in Russian)
[7] A. Nobile, Jr., M. W. Davis, Jr., J. Catal., 116 (1989) 383.

IR-CATALYZED PHOTOREDOX C(sp3)-H BOND ALKYLATION OF N-BENZOXAZOLE AND N-BENZOTHIAZOLE TETRAHYDROISOQUINOLINES IN MICROFLOW REACTORS

B. P. Bondžić [1], A. Filipović [1], Z. Džambaski [1], M. Vučkovski [2] and A. M. Bondžić [2]

[1] *University of Belgrade-Institute of Chemistry, Technology and Metallurgy, National Institute of the Republic of Serbia, Njegoševa 12, 11000 Belgrade, Serbia. (bojan.bondzic@ihtm.bg.ac.rs)*
[2] *Vinča Institute of Nuclear Sciences, National Institute of the Republic of Serbia, University of Belgrade, P.O. Box 522, 11000 Belgrade, Serbia.*

DOI: https://doi.org/10.46793/Phys.Chem24II.705B

ABSTRACT

Functionalization of biologically important tetrahydroisoquinolines (THIQs) is achieved under visible light irradiation in the presence of Ir photocatalyst under microflow conditions. *N*-Benzoxazol and *N*-Benzthiazol substituted THIQs were alkylated at C1 position through Ir promoted C-H oxidation/organocatalyzed Mannich reaction sequence. Reactions were optimized in batch conditions regarding photo- and organocatalyst, temperature and light source and subsequently transferred to the custom-made polymeric type microreactor (polydimethylsiloxane polymer, PDMS). Application of the oxygen porous PDMS microreactor proved crucial regarding Ir catalyzed C-H oxidation step and overall reaction performance.

INTRODUCTION

1,2,3,4-tetrahydroisoquinoline (THIQ) natural products and related alkaloids belong to the well-known class of biologically active compounds that are considered a privileged structures in medicinal chemistry.[1] Several molecules possessing THIQ backbone were isolated from natural sources and have shown potent biological activity profiles. On the other hand, benzothiazoles, and benzoxazoles represent prominent structural motifs in a wide range of biologically active molecules and are attractive target structures in medicinal chemistry.[2] The benzoxazole moiety occurs in various compounds with antimicrobial, antitumor, herbicidal, antiretroviral, or protein inhibitory properties and is found in numerous ligands for biochemical receptors. Functionalization of (benz)azoles was previously achieved with a variety of transition-metal-catalyzed C−C and C−N coupling reactions using the copper, nickel, or palladium catalysis.[3]

Merger of these two functionalities (THIQ and benzoxazole) and subsequent functionalization of these hybrid compounds should provide good starting point for enhancement of their biological activity. To make the functionalization possible and more efficient we envisaged use of visible light promoted photoredox catalysis and application of microfluidic platforms in the cross dehydrogenative coupling (CDC) reactions. These reactions mostly employ high-valent transition-metal catalysts combined with co-oxidants such as tert-butylhydroperoxide (TBHP), H_2O_2, or molecular oxygen. Further development in the field of CDC couplings was achieved in line with the advance of photoredox catalysis in the past decade.

Synthesis of valuable organic molecules performed in flow attracted considerable attention in the past, while more recently one of the areas where flow systems have shown great potential is visible light promoted photoredox catalysis.[4] Microfluidic reaction platforms with high surface-area-to-volume ratios characteristic of these systems allow improved light utilization and better heat and mass transfer effects in photochemical transformations. With these advantages in mind, we applied

flow chemistry in cross dehydrogenative coupling functionalization of hybrid THIQ-Benzoxazole molecules.

METHODS

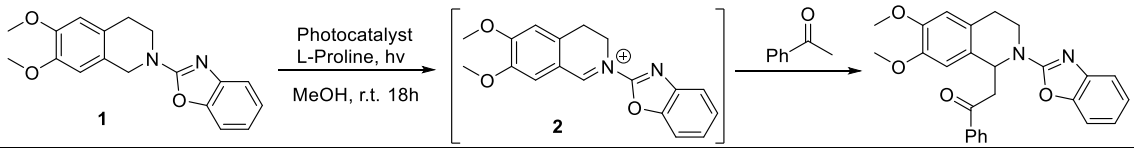
For PDMS microreactor fabrication we used SYLGARD silicone elastomer kit 184 obtained by Dow Corning Corporation. This two-part liquid component kit consisting of base and curing agents. Microchannels are designed with 3-D printer Wanhao Duplicator i3 Mini using transparent ABS (1,75mm) as a filament. For fabrication of FEP reactor the FEP tubing is wrapped in figure eights around glass tube so that a total of 100 cm (corresponding to 450 □L total volume) is used. For fabrication of silicone/glass microreactor photolithography was used along with wet-etching of pyrex glass and anodic bonding technique.

All reactions were monitored by thin-layer chromatography using Merck 60 F254 precoated silica gel plates (0.25 mm thickness). Preparative thin layer chromatography was performed using Merck 60 F254 silica gel purchased from Merck KGA. Column chromatography was carried out on silica gel (12-26, ICN Biomedicals) using petrol ether/ethyl acetate as eluents. 1H-NMR and 13C-NMR spectra used for structural characterization of compounds were measured on a Bruker Ultrashield Advance III spectrometer (1H at 500 MHz, 13C at 125 MHz) and Varian 400 sprectrometer (1H at 400 MHz, 13C at 100 MHz) using $CDCl_3$ as solvent with TMS as internal standard.

RESULTS AND DISCUSSION

We started our investigation by optimizing Mannich type reaction of benzoxazole functionalized THIQ **1** in the presence of L-proline as an organocatalyst. Effects of photocatalyst, additive and light source were investigated (Table 1). All tested photocatalysts showed activity, 1 equiv of TFA proved beneficial as well as application of blue LED light (Table 1). The best results were obtained with $[Ir(dtbbpy)(ppy)_2]PF_6$ catalyst under 455nm, blue LED, irradiation in the presence of 1 equiv. of TFA (Entry 3). As the solvent we used MeOH which allowed solubility of all reaction components.

Table 1. Optimization of visible light promoted Mannich reaction in batch conditions.

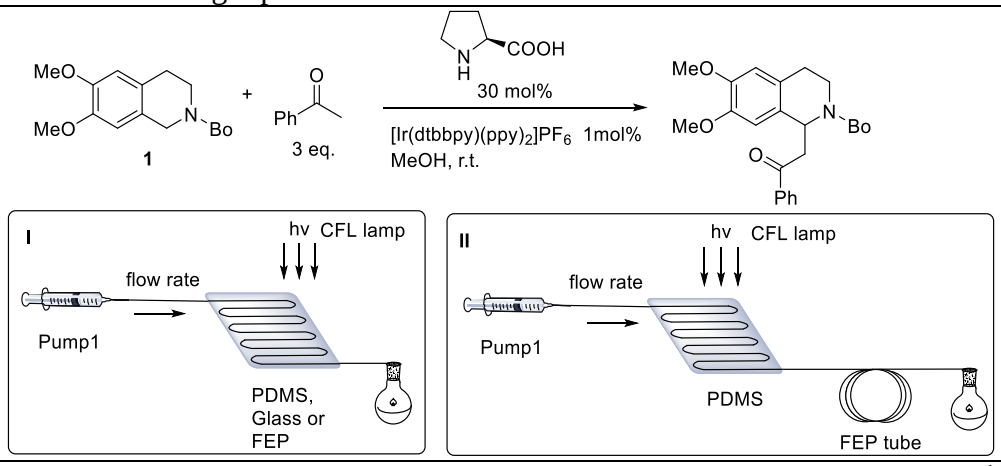


Entry	Photocatalyst	Light source	Additive	Yield (%)
1	$[Ru(bpy)_3]Cl_2$ 1 mol%	Blue LED	/	24
2	[Ir(dtbbpy)(ppy)2]PF6 1 mol%	Blue LED	/	38
3	$[Ir(dtbbpy)(ppy)_2]PF_6$ 1 mol%	Blue LED	TFA 1eq	68
4	$[Ir(dtbbpy)(ppy)_2]PF_6$ 1 mol%	CFL lamp	TFA 1eq	59
5	2,4,6-triphenylpyrylium tetrafluoroborate 5 mol%	Blue LED	TFA 1eq	47
6	9-Mesityl-3,6-di-*tert*-butyl-10-phenylacridinium tetrafluoroborate 5 mol%	Blue LED	TFA 1eq	65
7	9-Mesityl-10-methylacridinium perchlorate 5 mol%	Blue LED	TFA 1eq	59

a Reaction conditions: Tetrahydroisoquinoline (0.25 mmol, 1 equiv.), photocatalyst (0.0025 mmol, 1 mol%); L-Proline (0.075 mmol, 0.3 equiv.) and ketone (5 equiv.) were added to the solvent (1 mL) and pumped through microfluidic device irradiated with CFL or blue LED lamp, the residence time is shown in table; b Isolated yield after column chromatography.

Next, optimized conditions were transferred to microflow systems, using custom made microreactors (PDMS, FEP tube and glass/silicon, Table 2). Retention time of 2h in PDMS reactor proved beneficial as it allowed oxidation step to be completed and gave higher yield of desired product (Entry 2 compared to Entry 1, Table 2). Reaction in glass/silicon and FEP reactor didn't proceed efficiently (Entries 3 and 4, Table 2) giving less than 10% yield of the product. PDMS microreactor proved to be the best for this type of reaction due to its intrinsic gas porosity, atmospheric oxygen is required in the oxidation step to convert THIQ **1** into electrophilic iminium ion **2**. However, despite the fact that oxidation step was complete reaction intermediate **2** remained in the reaction mixture due to the slow second step of the reaction i.e. Mannich type addition of acetophenone enamine to intermediary iminium ion **2**. Therefore, reaction setup II was devised (Table 2) which included addition of FEP reactor at the exit of PDMS reactor thus allowing additional 4h of reaction time for addition step to go to completion (Entry 5, Table 2) thus providing excellent yield of 78%.

Table 2. Visible light photoredox Mannich reaction conducted in flow conditions.

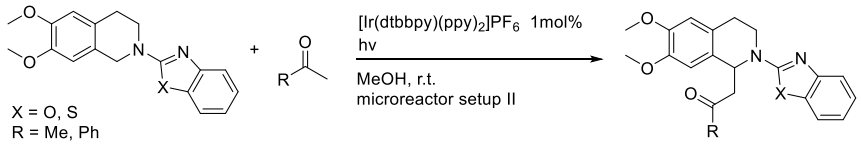


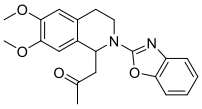
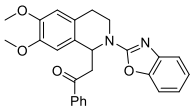
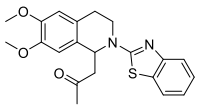
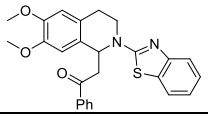
Entry[a]	Microreactor setup	Reactor type	Retention time (h)	Light source	Yield[b] (%)
1	I	PDMS	1	Blue led	42
2	I	PDMS	2	Blue led	51
3	I	GLASS	2	Blue led	<10
4	I	FEP	2	Blue led	<10
5	II	PDMS+FEP	2+4	Blue led	78

[a] Reaction conditions: tetrahydroisoquinoline (0.25 mmol, 1 equiv.), $[Ir(dtbbpy)(ppy)_2]PF_6$ (0.0025 mmol, 1 mol%); L-Proline (0.075 mmol, 0.3 equiv.) and ketone (5 equiv.) were added to the solvent (1 mL) and pumped through microfluidic device irradiated with CFL or blue LED lamp, the residence time is shown in table; [b] Isolated yield after column chromatography.

Optimized conditions have been applied to synthesize four new derivatives of functionalized THIQs (Table 3). As nucleophiles acetone and benzophenone were used while both benzoxazole and benzthiazole protected THIQs provided desired products in good yields under optimized conditions in microreactor setup II comprising of gas porous PDMS reactor for oxidation step and additional FEP microreactor attached to PDMS reactor which allowed subsequent addition step to go to completion.

Table 3. Visible light photoredox Mannich reaction conducted in flow conditions.



Entry[a]	Product	Residence time (h)	Light source	Yield (%)[b]
1		2+4	Blue led	72%
2		2+4	Blue led	78%
3		2+4	Blue led	84%
4		2+4	Blue led	81%

[a] Reaction conditions: tetrahydroisoquinoline (0.25 mmol, 1 equiv.), $[Ir(dtbbpy)(ppy)_2]PF_6$ (0.0025 mmol, 1 mol%); L-Proline (0.075 mmol, 0.3 equiv.) and ketone (5 equiv.) were added to the solvent (1 mL) and pumped through microfluidic device irradiated with blue LED light, the residence time of 2+4h was applied.; [b] Isolated yield after column chromatography.

CONCLUSION

We have successfully optimized and applied microfluidic procedure for the visible light promoted photoredox cross dehydrogenative coupling of benzoxazole and benzothiazole protected THIQs with ketones. The use of microfluidic setup in the Ir catalyzed visible light promoted photoredox oxidation of THIQs/Mannich reaction shortened the reaction times and improved yields of this process. Reactor setup consisting of custom made PDMS reactor for oxidation step in conjunction with attached FEP reactor for addition step proved advantageous in regard to reaction efficiency and yields.

Acknowledgment

This work was supported by the Ministry of Science, Technological Development, and Innovation of the Republic of Serbia (Agreement No. 451-03-66/2024-03/200017 and 451-03-66/2024-03/200026).

REFERENCES

[1] M. R. Bennett, M. L. Thompson, S. A. Shepherd, M. S. Dunstan, A. J. Herbert, D. R. M. Smith, V. A. Cronin, B. R. K. Menon, C. Levy, J. Micklefield, Angew. Chem. Int. Ed., 57 (2018) 10600.
[2] C. S. Demmer, L. Bunch, Eur. J. Med. Chem. 97 (2015) 778.
[3] L. Ackermann, S. Barfusser, J. Pospech, Org. Lett. 12 (2010) 724.
[4] Y. Su, N. J. W. Straathof, V. Hessel, T. Noël, Chem. Eur. J. 20 (2014) 10562.

STABILITY AND GAMMA RAYS-INDUCED CHANGES ON OPTICAL AND PHYSICOCHEMICAL FEATURES OF ZINC PHTHALOCYANINE

B. Vasiljević, J. Prekodravac, A. Radosavljević and D. Marinković

Vinča Institute of Nuclear Sciences, National Institute of the Republic of Serbia, University of Belgrade, P. O. Box 522, 11001 Belgrade, Serbia. (bojana.vasiljevic@vin.bg.ac.rs)

DOI: https://doi.org/10.46793/Phys.Chem24II.709V

ABSTRACT

This work presents detailed studies on the changes induced by gamma radiation on the optical, structural, morphological, and physicochemical properties of zinc phthalocyanine synthesized under microwave heating. Well-crystallized, with high yield and purity zinc phthalocyanine in β-form was obtained in a fraction of the time under the closed-vessel system of a microwave reactor. Gradual changes from blue to light yellow color of zinc phthalocyanine solution, with the increasing of the gamma radiation dose, were observed in the DMSO solution. High stability, in terms of morphology and dye structure, leads to promising new materials for a wide range of applications in advanced technology and medicine.

INTRODUCTION

Metallophthalocyanines (MPcs) are 18 π-electron conjugated aromatic, macrocyclic compounds that have drawn scientists` interest to study in a variety of fields, including sensing, photovoltaic optics, solar cells, optical storage devices, semiconductors, and high catalytic activity in redox processes [1,2]. MPcs were also proven to be useful as gamma (γ)-ray sensors in the field of gamma irradiation. Extensive research has shown that exposure to gamma radiation can change the optical and structural characteristics of MPcs thin films [3]. Because of the delocalization of excitation energy in the aromatic units, the MPc macromolecule acts as a stabilizer versus γ-irradiation inside the polymeric system [4].

Traditionally, the synthesis of MPcs has relied on multi-step processes involving distinct reaction steps and purification procedures. However, these conventional methods often encounter drawbacks such as decreased productivity, extended reaction times, and the production of by-products. In searching for synthetic methods that allow innovation and effectiveness of synthetic reactions, microwave chemistry gives enormous responses, reducing preparation costs and considerably reducing the environmental impact [5,6]. Fast, in-core, volumetric heating minimizes heat dissipation, allowing for the synthesis of compounds with increased yields and dramatically reduced reaction time. The literature on microwave-induced MPcs synthesis is meager, mainly performed in commercial microwave ovens, even if this implies unreproducible results [7] or in the presence of additional reactants [8].

In this study, we developed a simple and efficient procedure for synthesizing ZnPc. A greener and more economically friendly concept has been accomplished without an organic base catalyst. Detailed studies on the effect of gamma irradiation on the optical, structural, and morphological properties of ZnPc prepared by microwave heating are reported.

METHODS

Zinc (II) acetate dihydrate, $Zn(CH_3CO_2)_2x2H_2O$ (>99%,), 1,2-dicyanobenzene, $C_6H_4(CN)_2$ (≥98%), 2,2,6,6-tetramethylpiperidine, TMP (≥99%) and methanol (≥ 99%) were purchased from Sigma-

Aldrich, while *N*, *N*-dimethylformamide, DMF (>99%) were purchased from Alfa Aesar and dimethyl sulfoxide, DMSO (>99%) from Fisher Chemicals.

ZnPc was synthesized in a microwave reactor (noted as $ZnPc_{MW}$) as described in our previous work [9]. The starting compounds zinc (II) acetate dihydrate (0.63 mmol, 0.138 g), 1,2-dicyanobenzene (2.5 mmol, 0.320 g), and TMP (100 μL) were heated 1 mL of DMF at 200 ˚C, for 5 min in microwave reactor. The precipitate was filtered off and washed with 3% HCl, water, methanol, and dried. The resulting deep purple crystals remain after the processing of the reaction mixtures. Yield of $ZnPc_{MW}$ is 68 % (0.245 g). Synthesized crystals were irradiated by gamma rays with the source of Cobalt-60 at doses of 5, 10, and 25 kGy and noted as $ZnPc_{MW}$-5kGy, $ZnPc_{MW}$-10kGy, $ZnPc_{MW}$-25kGy, respectively. The solutions of $ZnPc_{MW}$ in DMSO as a solvent, with the concentration of $1x10^{-4}$M, were irradiated at a dose range of 1-25 kGy (1, 2, 3, 5, 7, 10,15, and 25 kGy).

Mono-mode microwave reactor Anton Paar Monowave 300 was used for microwave-assisted synthesis. The SmartLab® X-ray diffractometer (Rigaku, Japan) was utilized for X-ray diffraction (XRD) measurements, using Cu Kα radiation (λ = 1.542 Å). The patterns were collected at room temperature, within a 2θ range of 5–60° in a scan rate of 3°/min with a divergent slit of 0.5 mm, operated at 40 kV and 30 mA. Attenuated total reflectance Fourier transform infrared (ATR-FTIR) spectroscopic measurements were performed in the 400−4000 cm^{-1} range with a spectral resolution of 4 cm^{-1} at room temperature by Thermo Scientific Nicolet iS50 FT-IR spectrometer equipped with built-in all reflective ATR diamond. The ultraviolet-visible (UV-Vis) absorption spectra were recorded on a Shimadzu 1800 UV–Vis spectrophotometer equipped with a temperature controller in the range of 200–800 nm. Surface morphologies of the deposited samples were studied by Atomic Force Microscope (AFM), Quesant (Agoura Hills, CA, USA). The morphology of ZnPc was studied using a transmission electron microscope (TEM, Tecnai G2 F20, FEI) operated at a 200 kV accelerating voltage. All irradiations were carried out using the ^{60}Co gamma cell facility of the Laboratory for Radiation Chemistry and Physics "Gamma", Institute for Nuclear Sciences "Vinca".

RESULTS AND DISCUSSION

The powder XRD technique was utilized to analyze the crystal phase structure. The XRD measurement showed that the product was pure β-ZnPc crystal and that gamma radiation (25 kGy) did not affect the crystal phase (**Figure 1A**). The crystal morphology of $ZnPc_{MW}$ was characterized by AFM (Figure 1B), showing a stunning layered, rhombus-shaped crystal structure with a smooth surface. Samples irradiated by γ-rays with doses of 10 kGy (**Figure 1Bb**) showed no significant changes compared to unirradiated crystals (**Figure 1Ba**).

The HR-TEM $ZnPc_{MW}$ crystal micrographs with different magnifications are presented in **Figure 1C**. A high magnification of TEM images presented in **Figure 1Cb** revealed that the $ZnPc_{con}$-10kGy consists of particles in the range of 20-60 nm.

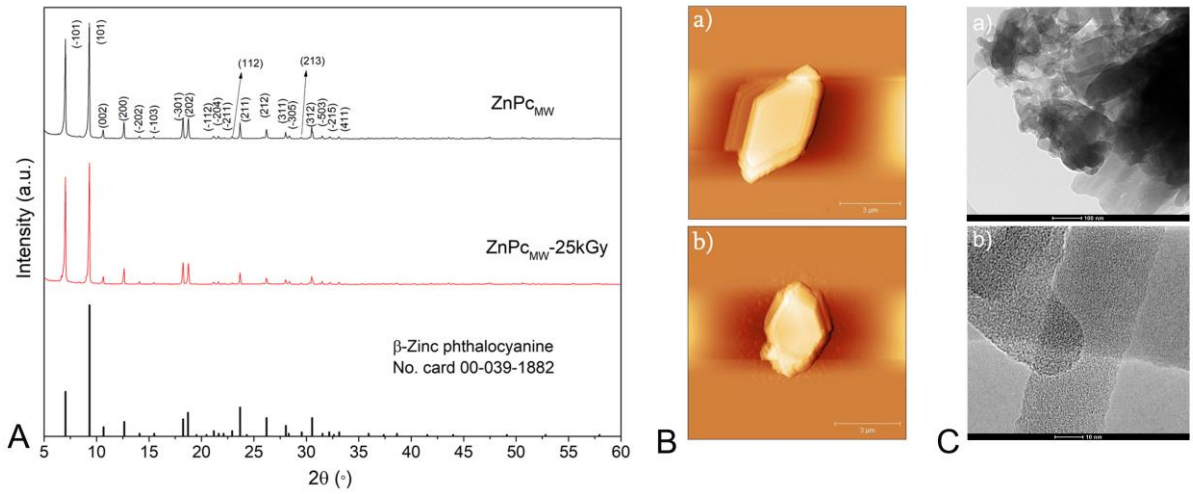


Figure 1. Morphology and structure of ZnPc$_{MW}$. (**A**) XRD patterns of pure crystals, (**B**) AFM image of crystals before (**a**) and after (**b**) gamma irradiation (ZnPc$_{con}$-10kGy), and (**C**) Low- (**a**) and high (**b**) resolution TEM image of ZnPc$_{con}$-10kGy.

The results presented in **Figure 2.** clearly showed that there were no differences in FTIR and UV-Vis spectra following varied dosages of irradiation. It can be assumed that the stability of ZnPc crystals over gamma radiation belongs to the delocalization of excitation energy in the double and aromatic units and due to the large ionic radius of Zn in the macromolecule structure.

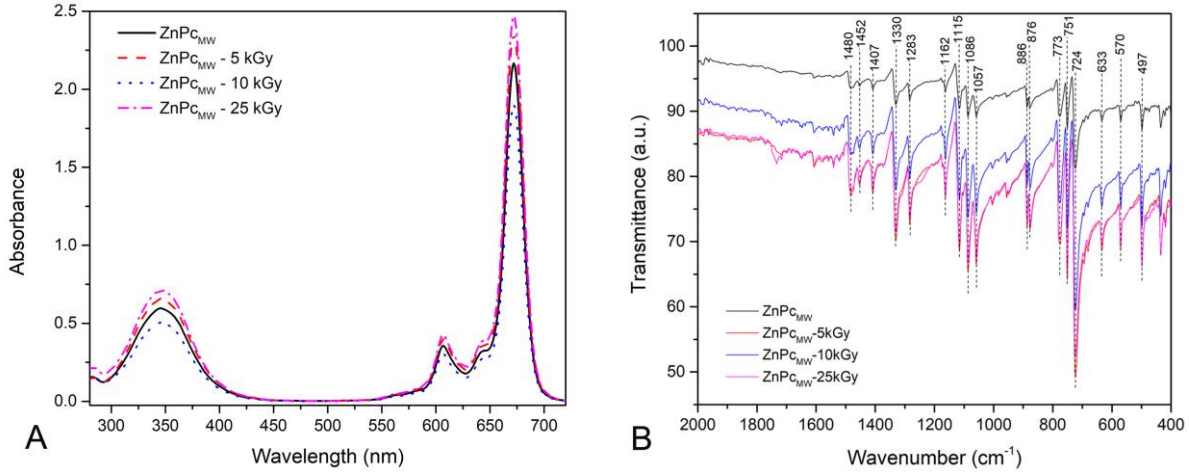


Figure 2. (**A**) UV-Vis and (**B**) FTIR spectra of gamma-irradiated crystals of ZnPc$_{MW}$ (5, 10, and 25 kGy).

The absorbance of synthesized dye solutions, subjected to increasing doses of gamma radiation was followed spectrophotometrically and the color decay curves were recorded. A moderate decrease in absorbance intensity is observed following the appropriate dose of irradiation for ZnPc$_{MW}$ in DMSO exposed to gamma irradiation at different doses (**Figure 3A**). Degradation percent (%) of absorption (calculated by formula A/A_0*100), approximately fitted by polynomial function (y = 112.69363 -10.33662*x +0.2536*x^2), for three main peaks are given in **Figure 3B**. As can be seen from **Figure 3C**. the color bleaching increases gradually with increasing absorbed dose up to 10 kGy [10], then it tends to saturate up to 25 kGy.

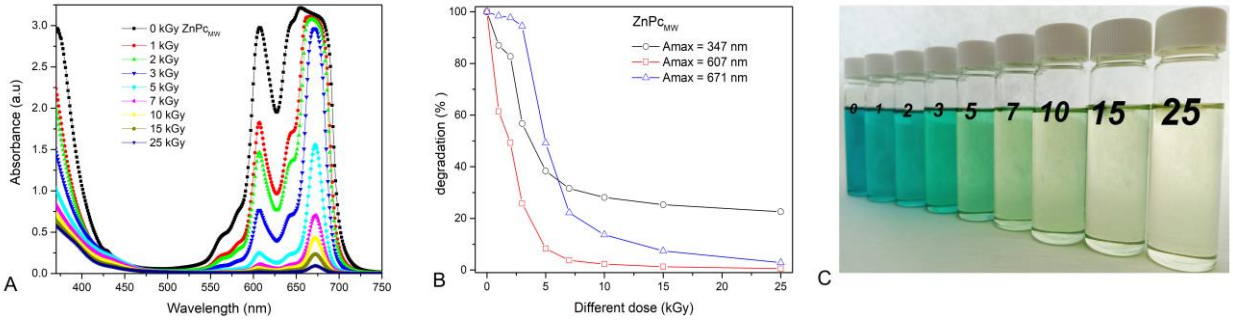


Figure 3. (**A**) UV-Vis spectra of unirradiated and gamma-irradiated (1-25 kGy) $ZnPc_{MW}$, (**B**) degradation (%) of absorption maxima at 347 nm, 607, and 671 nm, and (**C**) corresponding solutions color changes under different doses gamma irradiation (1-25 kGy).

From **Figure 3.** it could be concluded that gamma irradiation affects on the absorption intensity for the $ZnPc_{MW}$ studied system. The best effect is obtained for the peak at the absorption maximum of 607 nm, and the degradation is 99.46 % under a dose of 25 kGy. In this connection, the organic dye showed great potential as a novel sensor material for low-dose ionizing radiation, gamma rays.

CONCLUSION

Microwave chemistry proved to be highly effective in the synthesis of ZnPc in terms of purity and reaction speed. Detailed studies on the impact of gamma radiation on the optical and structural properties revealed high stability of synthesized ZnPc, in terms of morphology and dye structure. Microwave-synthesized ZnPc showed great potential to be used as a gamma radiation dosimeter for low-dose ionizing radiation, gamma rays.

Acknowledgment

The research was funded by the Ministry of Science, Technological Development and Innovation of the Republic of Serbia (grant number 451-03-66/2024-03/200017).

REFERENCES

[1] N. Morlanés, K. Takanabe, V. Rodionov, ACS Catal., 6 (2016) 3092.
[2] J. H. Zagal, S. Griveau, J. F. Silva, T. Nyokong, F. Bedioui, Coord. Chem. Rev., 254 (2010) 2755.
[3] N. Chaudhary, A. Singh, D. K. Aswal, A. K. Debnath, S. Samanta, S.P. Koiry, S. Sharma, K. Shah, S. Acharya, K.P. Muthe, S.C. Gadkari, Synth. Met., 231 (2017) 143.
[4] A. M. Abdel Ghaffar, T. E. Youssef, H. H. Mohamed, Mater. Chem. Phys., 178 (2016) 12.
[5] G. H. Elgemeie, R. A. Mohamed, J. Mol. Struct., 1173 (2018) 707.
[6] A. de la Hoz, Á. Díaz-Ortiz, P. Prieto, Handb. Environ. Chem., 32 (2015) 405.
[7] M. Seyyedhamzeh, N. Ganji, A. Shaabani, J. Porphyr. Phthalocyanines, 16 (2012) 1110.
[8] R. Ghadari, P.S. Saei, A. Sabri, Z. Ghasemi, F. Kong, J. Clean. Prod., 268 (2020) 20.
[9] B. R. Vasiljević, D. Milivojević, T. Barudžija, M. Budimir, D. Mijin, M. Marinović-Cincović, D. Marinković, Mater. Lett., 350 (2023) 134911.
[10] B. R. Vasiljević, D. Odobaša, I. Vujičić, M.B. Filimonović, K. Smits, D. Mijin, D. Marinković, Radiat. Phys. Chem., 222 (2024) 111816.

S *– Free Topic*

QSPR MODELING OF THE DIELECTRIC CONSTANT BASED ON MONTE CARLO OPTIMIZATION METHOD

A.M. Veselinović and J.V. Živković

University of Niš, Faculty of Medicine, Department of Chemistry,
Bulevar Dr Zorana Đinđića 81, 18000 Niš, Serbia. (aveselinovic@medfak.ni.ac.rs)

DOI: https://doi.org/10.46793/Phys.Chem24II.715V

ABSTRACT

Monte Carlo Optimization method has been used to develop QSPR models for the prediction of the dielectric constant of organic compounds. The QSPR models were developed from the dataset of 201 diverse compounds, splited in three random splits in training and test set and based on SMILES notation based molecular descriptors. By employing a variety of statistical methodologies, an assessment of the predictive capabilities and resilience of the established QSPR models was achieved. The demonstrated numerical values used for their validation underscore the strong suitability of these QSPR models. For the best model statistical quality is calculated with following characteristics r^2 = 0.7667, q^2 = 0.7597, s = 4.81 for training and r^2 = 0.8156, q^2 = 0.7973, s = 5.00 for test set. The Monte Carlo optimization technique effectively identified molecular fragments with defined impact on dielectric constant represented in QSPR modeling through the use of SMILES notation based descriptors.

INTRODUCTION

The static dielectric constant (ε), also known as relative permittivity, is a well-defined bulk property of materials. It reflects a material's ability to store electrical energy by separating opposing charges or aligning its molecular dipoles in an external electric field. Due to its ease of measurement, extensive experimental data for various organic and inorganic compounds are available. This property plays a crucial role in understanding chemical reactivity and equilibrium, particularly within the context of solvent effects. Solvent polarity is a critical factor influencing reaction rates and equilibria [1,2]. While the dielectric constant is frequently used as a practical indicator of solvent polarity, with nonpolar solvents having lower values than polar ones, it has limitations. Specific intermolecular interactions can influence solvent behavior beyond what the dielectric constant alone captures. Recognizing these limitations, researchers have proposed numerous alternative solvent polarity scales [3]. The ability to theoretically predict dielectric constants holds immense value in the design of novel materials. Such predictions, if fast and reliable across diverse molecules, can significantly accelerate research and development [4].

In recent years, a Monte Carlo optimization approach has emerged as a promising technique for Quantitative Structure-Property Relationship (QSPR) modeling. This method offers several advantages. It is conformation-independent, meaning it doesn't require specific molecular conformations, and utilizes optimal descriptors derived from both topological features and Simplified Molecular Input Line Entry System (SMILES) notation of the molecules [5,6]. This simplicity and efficiency make it a valuable alternative to traditional methods. Moreover, the approach can pinpoint specific molecular fragments (identified by SMILES notation descriptors) that influence the dielectric constant, aiding in the interpretation of the chemical basis for observed behavior. This study aims to achieve two key objectives the development of QSPR model for predicting dielectric constants using the Monte Carlo optimization method and identification of SMILES notation descriptors that correspond tao molecular fragments with positive or negative influences on the dielectric constant.

This combined approach will provide a valuable tool for understanding and predicting the relationship between molecular structure and dielectric properties, ultimately contributing to the design of new materials with tailored electrical characteristics.

METHODS

To initiate the development of suitable QSAR models, a total of 201 organic compounds, with defined dielectric constants, were taken from literature [7] and initially drawn using ACD/ChemSketch software version 11.0. These molecules were subsequently transformed into SMILES notation using the same software. Once we completed the construction of the relevant database, we proceeded to perform three distinct independent random divisions of the main molecule database into two sets: the training set, comprising 155 compounds (75%), and the test set, comprising 50 compounds (25%). The number of overlapping molecules in three independent test set was reduced to minimum according to published methodology [5]. We also assessed the normality of the activity distribution, following the method outlined in the published literature [5,6]. To create conformation-independent QSAR models, we utilized the CORAL software (CORrelation and Logic, http://www.insilico.eu/coral), which is founded on the Monte Carlo method and its algorithm, considering the relevant activity as a random occurrence. In this study, we employed all SMILES notation-based descriptors, encompassing local, global, and HARD-index descriptors. A notable characteristic of the resulting QSAR model, developed using the Monte Carlo method, is the calculation of correlation weight (CW), which assigns a numerical value to each of the optimal descriptors utilized and DCW, value calculated as sum of relevant CW according to Eq. 1. Further, the Monte Carlo method relies on two parameters: threshold (T) and the number of epochs (N_{epoch}). In the creation of QSAR models, we explored values ranging from 0 to 10 for T and from 0 to 70 for N_{epoch}. The process of identifying the most predictive combination of T and Nepoch was determined based on a methodology outlined in published references [5,6].

$$DCW(Threshold,N_{epoch}) = \Sigma CW(Sk) + \Sigma CW(SSk) + \Sigma CW(SSSk) + \Sigma CW(NOSP) + \Sigma CW(HALO) + \Sigma CW(BOND) + \Sigma CW(PAIR) \quad (1)$$

RESULTS AND DISCUSSION

The concept of the applicability domain (AD) plays a pivotal role in guiding the selection of molecules. To establish the AD, we followed a published methodology and confirmed that all molecules in this study fell within the defined AD range, with no outliers identified [5,6]. Utilizing the Least Squares method, we present the most optimal QSAR model, obtained from third split, for the dielectric constant, with respect to the T and N_{epoch} values, in the form of Equation 2.

$$\varepsilon = 5.9111(\pm 0.0236) + 1.4176(\pm 0.0058) \times DCW(1,7) \quad (2)$$

To assess the quality of the developed QSAR models, we employed the following methods: internal validation using the training set, external validation using the validation set, and data randomization through a Y-scrambling test. We accomplished this by employing various statistical parameters, including the correlation coefficient (r^2), cross-validated correlation coefficient (q^2), standard error of estimation (s), mean absolute error (MAE), Fischer ratio (F), root-mean-square error (RMSE), Rm2, and MAE-based metrics [5,6]. Ideality of Correlation (IIC) suggests that the method employed was successful in creating a QSAR model with good reproducibility, which was further validated using the concordance correlation coefficient (CCC) and the predictability of the developed QSAR was confirmed. Additionally, the model was classified as valid using MAE-based metrics. Results from Y-randomization, involving the random shuffling of Y values in 1000 trials across ten separate runs, that there was no chance correlation among the developed models. Calculated values for statistical metrics were for training set: $r^2 = 0.7667$; CCC = 0.8679; IIC = 0.8195; $q^2 = 0.7597$; s

= 4.81; MAE = 3.06; F = 490 and for test set: r^2 = 0.8156; CCC = 0.8558; IIC = 0.9030; q^2 = 0.7973; s = 5.00; MAE = 3.58 and F = 212. Developed QSAR model is visually depicted in **Figure 1**.

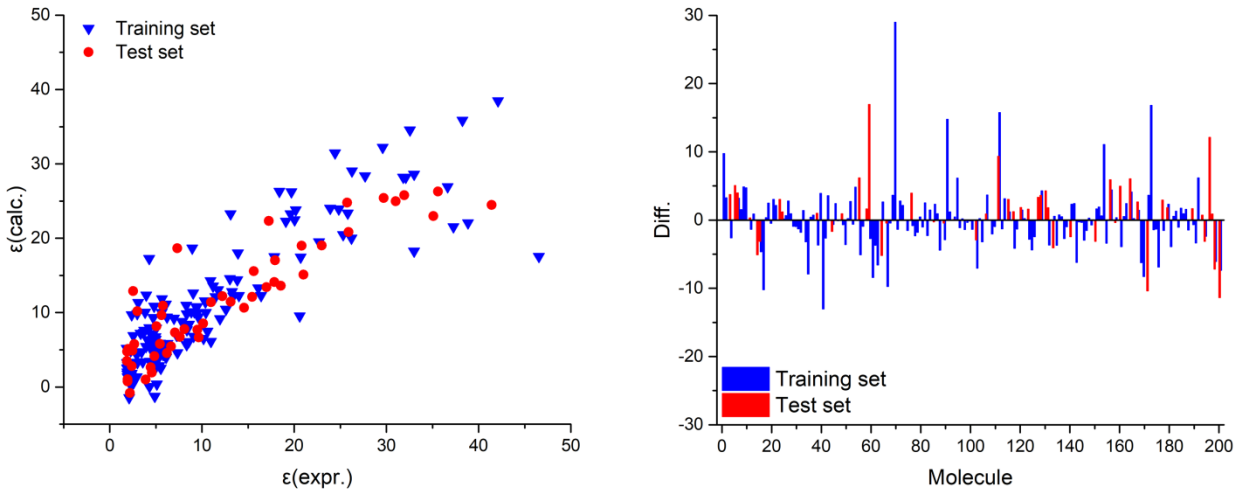
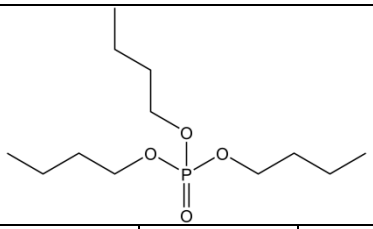


Figure 1. Graphical presentation of the best Monte Carlo optimization run (the highest value for r^2) for the developed QSAR model. (Ac(expr.) – experimental value for ε; Ac(calc.) – calculated value for ε using developed QSAR model; Diff. – Ac(expr.) - Ac(calc.)).

An illustration of the calculation of a molecule's summarized correlation weight (DCW) and the studied property (ε) is provided in Table 1.

Table 1. Example of DCW calculation.



SMILES notation:
CCCCOP(=O)(OCCCC)OCCCC
DCW = 2.77149
ε(calc.) = 9.8401

SAk	CW(SAk)	SAk	CW(SAk)	SAk	CW(SAk)
10001010000	0.4678	C...C...(...	0.3776	O...=...(...	-0.4536
(...(.....	-0.5997	C...C.....	0.0569	O...=.....	-0.9117
(..........	-0.4361	C...C...C...	-0.5338	O...C.....	1.2115
++++O---B2==	0.7773	C...O...(...	-0.5815	O...C...C...	2.08
++++O---P===	-1.7017	Cmax.0.....	2.2425	O...P...(...	-2.1038
++++P---B2==	-0.661	Nmax.0.....	1.0532	Omax.4.....	-0.686
=...(.....	-0.1495	NOSP0101000	0.3768	P...(.....	-0.6535
=..........	-0.4566	O...(...(...	-0.958	P...(...=...	1.2339
=...O...(...	-0.7338	O...(.....	-0.1986	P..........	1.5332
BOND1000000	2.4957	O...(.....	-0.1986	P...O.....	-0.7479
C...(.....	0.0359	O...(...C...	2.4459	P...O...C...	0.4284
C..........	-0.5695	O..........	0.6727	Smax.0.....	2.5778

One of the primary objectives of this study was to identify molecular fragments, characterized as the SMILES notation's optimal descriptors, that exert both positive and negative effects on the studied activity [5,6]. From all defined molecular descriptors especially interesting is analysis of ATOMPAIR global SMILES notation descriptor. This descriptor is defined as global SMILES notation descriptor since it describes molecule as whole. For an example ++++O---B2== descriptors detonates that molecule has oxygen and double bond. According to obtained results following ATOMPAIR descriptors have positive impact on dielectric constant: ++++B2--B3==, ++++F---B2==, ++++F---Br==, ++++F---Cl==, ++++F---O===, ++++CL--N===, ++++CL--O===, ++++Br--B2==, ++++Br--O===, ++++Cl--B2==, ++++N---B2==, ++++N---B3==, ++++N---O===, ++++N---S===. Interestingly, there are ATOMPAIRS with negative impact on dielectric constant like ++++Br--B2==, ++++O---P===, ++++P---B2== and ++++S---B2==.

CONCLUSION

The primary objective of this research is to create robust QSPR models capable of predicting the dielectric constant of various organic compounds with high predictability. This predictability is assessed through the use of various statistical parameters. The conformation-independent models, developed based on optimal descriptors derived from SMILES notation using the Monte Carlo optimization method. The application of a variety of statistical techniques allowed for the assessment of the predictive potential and robustness of the developed QSPR models. The validity of these models is confirmed by the numerical values obtained during their validation. The Monte Carlo optimization method effectively identified molecular fragments, which are employed as SMILES notation fragments in QSPR modeling, with both positive and negative effects on the dielectric constant of various organic compounds.

Acknowledgment

This work was supported by the Ministry of Education, Science and Technological Development of the Republic of Serbia (grant no 451-03-65/2024-03/200113).

REFERENCES

[1] C. Reichart, Solvents and Solvent Effects in Organic Chemistry, VCH, Weinheim, 1990.
[2] M. Karelson in Handbook of Solvents, Chapter 11, G. Wypych (Ed.), ChemTec Publishing, Toronto, 2001.
[3] J. Tomasi, B. Mennucci and C. Cappelli in Handbook of Solvents, Chapter 8, G. Wypych (Ed.), ChemTec Publishing, Toronto, 2001.
[4] A. R Katritzky, U. Maran, V. S. Lobanov and M. Karelson, J. Chem. Inf. Comput. Sci. 40 (2000) 18.
[5] A. M. Veselinović, J. B. Veselinović, J. V. Živković, G. M. Nikolić, Curr. Top. Med. Chem. 15 (2015) 1768.
[6] M. Zivkovic, M. Zlatanovic, N. Zlatanovic, M. Golubović, A. M. Veselinović, Mini Rev. Med. Chem. 20 (2020) 1389.
[7] S. Sild, M. Karelson, J. Chem. Inf. Comput. Sci., 42 (2002) 360.

QSPR MODELING OF MOLAR REFRACTIVITY BASED ON SMILES NOTATION MOLECULAR DESCRIPTORS

A.M. Veselinović and J.V. Živković

University of Niš, Faculty of Medicine, Department of Chemistry,
Bulevar Dr Zorana Đinđića 81, 18000 Niš, Serbia. (aveselinovic@medfak.ni.ac.rs)

DOI: https://doi.org/10.46793/Phys.Chem24II.719V

ABSTRACT

This study explores the application of the Monte Carlo optimization method for developing QSPR models that predict the molar refractivity of organic compounds. A dataset of 516 diverse compounds was utilized, randomly split into training and test sets. SMILES notation-based molecular descriptors served as the foundation for model development. A comprehensive assessment of the models' predictive capabilities and robustness was conducted using various statistical methodologies. The obtained validation metrics demonstrate the strong suitability of the established QSPR models. The best model achieved outstanding statistical quality, with R^2 values of 0.8985 and 0.8752 for the training and test sets, respectively. Additionally, the Q^2 values of 0.8971 and 0.8714 further support the model's generalizability. The Monte Carlo optimization technique effectively identified crucial molecular fragments impacting the molecular descriptors employed in the QSPR modeling process.

INTRODUCTION

The field of Quantitative Structure-Property Relationship (QSPR) studies aims to establish connections between a ligand's structural, physicochemical, and biological properties and its interaction with a receptor. A well-established concept is the correlation between ligand binding energy (reflecting the forces involved) and various physicochemical properties of different ligand regions. Identifying the appropriate physicochemical property for each force is crucial [1]. Furthermore, a molecule's properties are intrinsically linked to its structure. The molecular skeleton, defined by the number, type, and connectivity of atoms, lays the foundation for a molecule's 3D architecture. Molar refractivity (MR) is a vital physicochemical property commonly used in QSPR for its connections to lipophilicity, molar volume, and steric bulk [2-4]. However, individual atomic contributions to MR are not ideal for QSPR due to their insensitivity to changes in the chemical environment (e.g., substitutions).

In recent years, the Monte Carlo optimization method has emerged as a promising tool for QSPR modeling. This approach treats the analyzed property (e.g., MR) as a random event and utilizes conformation-independent methodologies. It leverages optimal descriptors derived from topological characteristics and SMILES notation, offering advantages in terms of simplicity and efficiency. Moreover, this method can pinpoint key molecular fragments (represented as SMILES descriptors) that influence the studied property, allowing for a connection to the chemical structure [5,6]. This study focuses on developing a conformation-independent QSPR model for predicting MR of organic compounds using the Monte Carlo optimization method. Additionally, we aim to identify SMILES-based descriptors associated with molecular fragments that impact MR. This combined approach offers a powerful strategy for decipherment and prediction of the structure-molar refractivity relationship in molecules. This knowledge will ultimately facilitate the rational design of novel materials with precisely controlled characteristics.

METHODS

A dataset of 516 organic compounds with reported molar refractivity was obtained from the literature [7]. We used ACD/ChemSketch v11.0 to draw the molecular structures and convert them to SMILES notation. The dataset was then randomly split into training (414 compounds, 75%) and test sets (142 compounds, 25%). Normality of the molar refractivity distribution was verified using established methods [5, 6]. CORAL software (http://www.insilico.eu/coral), based on the Monte Carlo method, was employed to develop conformation-independent QSPR models. All SMILES-based descriptors (local and global) were included. A key feature of the Monte Carlo method is the calculation of correlation weights (CWs) for each optimal descriptor, quantifying its importance. The sum of CWs (DCW) is calculated using Eq. 1. The method utilizes two parameters: threshold (T) and number of epochs (Nepoch). We explored T values from 0 to 10 and Nepoch values from 0 to 70 to identify the most predictive combination. The selection methodology followed established protocols [5,6].

$$DCW(Threshold,N_{epoch}) = \Sigma CW(Sk) + \Sigma CW(SSk) + \Sigma CW(SSSk) + \Sigma CW(NOSP) + \Sigma CW(HALO) + \Sigma CW(BOND) + \Sigma CW(PAIR) \quad (1)$$

RESULTS AND DISCUSSION

The applicability domain (AD) was established using a published methodology, ensuring all molecules fell within the defined range (no outliers) [5, 6]. The optimal QSPR model for molar refractivity, identified based on threshold (T) and number of epochs (N_{epoch}) values from the third split using the Least Squares method, is presented in Eq. 2.

$$MR = 7.4032(\pm 0.0262) + 2.1549(\pm 0.0023) \times DCW(2,5) \quad (2)$$

A comprehensive validation process was employed to assess model quality. This included internal validation using the training set, external validation using the test set, and a Y-scrambling test to assess for chance correlations. Various statistical parameters were used for evaluation, including correlation coefficient (r^2), cross-validated correlation coefficient (q^2), standard error of estimate (s), mean absolute error (MAE), Fischer ratio (F), root-mean-square error (RMSE), Rm^2, and MAE-based metrics [5, 6]. The Ideality of Correlation (IIC) and concordance correlation coefficient (CCC) indicated good model reproducibility. Additionally, the model's predictability was confirmed, and its validity was established using MAE-based metrics. Y-randomization (shuffling Y values in 1000 trials across 10 runs) confirmed the absence of chance correlation. Statistical results for the training set were: $r^2 = 0.8985$, CCC = 0.9465, IIC = 0.9032, $q^2 = 0.8971$, s = 3.80, MAE = 2.57, and F = 3646. The test set results were: $r^2 = 0.8752$, CCC = 0.9350, IIC = 0.9355, $q^2 = 0.8714$, s = 4.05, MAE = 3.01, and F = 982. The developed QSPR model is visually represented in Figure 1. An illustration of the calculation of a molecule's summarized correlation weight (DCW) and the studied property (MR) is provided in Table 1.

A key objective was to identify molecular fragments, represented by optimal SMILES descriptors, that influence the dielectric constant [5, 6]. Among these descriptors, the analysis of the ATOMPAIR global descriptor is particularly interesting. This descriptor considers the entire molecule, capturing the presence of specific atom pairs and their connectivity. For instance, the descriptor "++++O---B2==" indicates the presence of an oxygen atom and a double bond in molecule. Our results revealed that the following ATOMPAIR descriptors have a positive influence on the MR: ++++B2--B3==, ++++F---B2==, ++++F---Cl==, ++++CL--Br==, ++++CL--S===, ++++Br--B2==, ++++Br--B3==, ++++Br--N===, ++++Br--O===, ++++I---B2==, ++++I---O===, ++++Cl--B2==, ++++N---B2==, ++++N---O===, ++++N---S===, ++++O---B2==, ++++O---S=== and ++++S---B2==. Interestingly, there are ATOMPAIRS with negative impact on MR constant like ++++F---N===, ++++F---O===,

++++CL--N===, ++++CL--O===, ++++Br--S===, ++++N---B3==, ++++Cl--B3== and ++++O---B3==.

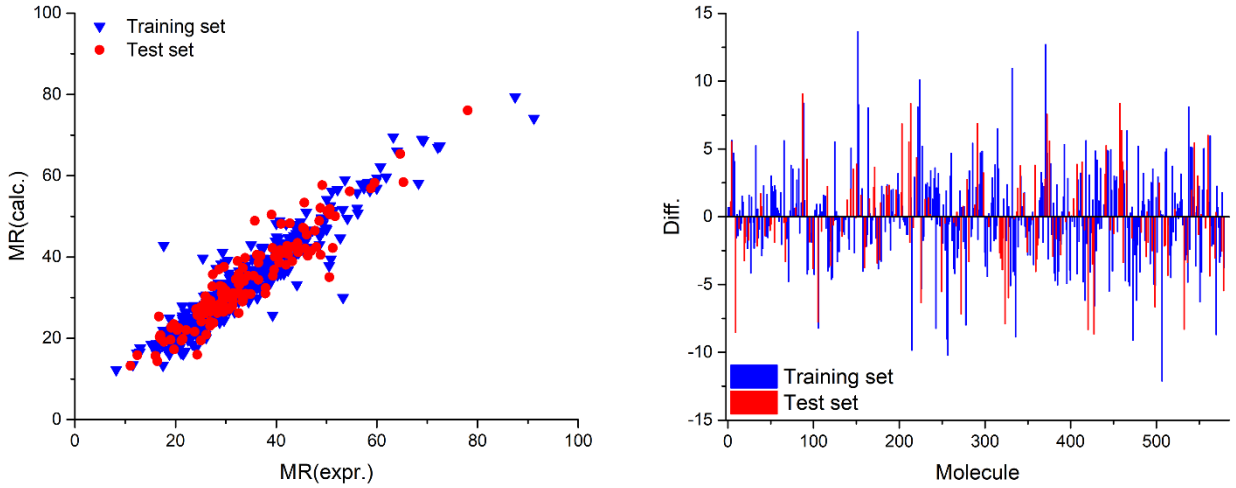
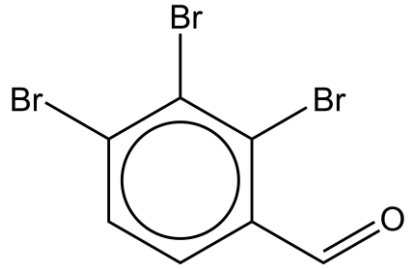


Figure 1. Graphical presentation of the best Monte Carlo optimization run (the highest value for r^2) for the developed QSAR model. (Ac(expr.) – experimental value for MR; Ac(calc.) – calculated value for MR using developed QSAR model; Diff. – Ac(expr.) - Ac(calc.)).

Table 1. Example of DCW calculation.



SMILES notation:
O=Cc1ccc(c(c1Br)Br)Br
DCW = 19.26342
MR(calc.) = 48.9133

SAk	CW(SAk)	SAk	CW(SAk)	SAk	CW(SAk)
10001000010	0.2196	Br..(.....	1.4134	c...C.....	1.1629
(.....	0.3492	Br..(...Br..	0.0481	c...c.....	0.2828
(...Br..(...	-0.061	Br.....	0.2817	c...C...=...	-0.2831
(...c...(...	0.4978	c...(.....	0.0952	C...c...1...	0.2168
++++Br--B2==	0.1452	c...(...c...	-0.1391	c...c...1...	0.2058
++++Br--O===	0.3529	C.....	0.4105	c...c...c...	0.3003
++++O---B2==	0.0858	c.....	0.3036	HALO00100000	0.1449
=.....	0.2009	C...=.....	0.371	NOSP01000000	0.2789
1.....	0.3253	c...1.....	0.4802	O.....	0.4838
1...c...(...	0.1786	c...1...c...	2.0831	O...=.....	-0.37
BOND10000000	0.2351	c...c...(...	0.3411	O...=...C...	-0.5102

CONCLUSION

In conclusion, this study successfully developed robust QSPR models for predicting the molar refractivity of various organic compounds using the Monte Carlo optimization method. These conformation-independent models, built on optimal SMILES notation descriptors, achieved high predictive accuracy as confirmed by strong statistical validation metrics. The Monte Carlo method

further provided valuable insights by identifying key molecular fragments within the SMILES notation that significantly impact the molar refractivity of the studied compounds. This approach offers a powerful tool for understanding the structure-property relationship in organic molecules and can ultimately facilitate the design of novel materials with tailored properties.

Acknowledgment
This work was supported by the Ministry of Education, Science and Technological Development of the Republic of Serbia (grant no 451-03-65/2024-03/200113).

REFERENCES

[1] J. C. Dearden, P. Rotureau, G. Fayet, SAR QSAR Environ Res., 24 (2013) 279.
[2] R. Ghavami, A. Najafi, B. Hemmateenejad, Can. J. Chem., 87 (2009) 1593.
[3] K. Roy, A. Saha, Indian J. Chem., 44 (2005) 1693.
[4] J. A. Padrón, R. Carrasco, R. F. Pellón, J. Pharm. Pharm. Sci., 5 (2002) 258.
[5] A. M. Veselinović, J. B. Veselinović, J. V. Živković, G. M. Nikolić, Curr. Top. Med. Chem. 15 (2015) 1768.
[6] M. Zivkovic, M. Zlatanovic, N. Zlatanovic, M. Golubović, A. M. Veselinović, Mini Rev. Med. Chem. 20 (2020) 1389.
[7] A. K. Ghose, G. M. Crippen, J. Chem. Inf. Comput. Sci., 27 (1987) 21.

THE APPLICATION OF SMILES NOTATION MOLECULAR DESCRIPTORS IN QSPR MODELING OF MICELLE–WATER PARTITION COEFFICIENT

J.V. Živković and A.M. Veselinović

University of Niš, Faculty of Medicine, Department of Chemistry,
Bulevar Dr Zorana Đinđića 81, 18000 Niš, Serbia. (aveselinovic@medfak.ni.ac.rs)

DOI: https://doi.org/10.46793/Phys.Chem24II.723Z

ABSTRACT

This study explores the development of robust QSPR (Quantitative Structure-Property Relationship) models for predicting micelle-water partition coefficients of organic compounds. The Monte Carlo (MC) optimization method was employed to construct conformation-independent models, utilizing SMILES notation descriptors and local molecular graph invariants. Three independent splits of a dataset containing 81 compounds with experimentally determined coefficients in sodium dodecyl sulfate (SDS) solutions were used for model development and validation. Rigorous statistical evaluation confirmed excellent predictive ability and robustness of the developed QSPR models. Additionally, key molecular fragments within SMILES descriptors influencing the micelle-water partition coefficient were identified. This work demonstrates the efficacy of the MC method for constructing conformation-independent QSPR models with strong predictive power for this crucial property.

INTRODUCTION

Lipophilicity, a key factor influencing drug action, is often expressed as the n-octanol-water partition coefficient (K_{ow}) [1,2]. However, K_{ow} may not accurately reflect the partitioning behavior of drugs within biological membranes. Micelle-water partition coefficients (K_{mw}) offer a superior alternative, mimicking the phospholipidic bilayer structure of biological membranes more closely [3]. However, experimentally determining K_{mw} can be expensive and time-consuming. To address this limitation, Quantitative Structure-Property Relationship (QSPR) models provide a valuable *in silico* approach for K_{mw} prediction [4]. QSPR establishes a mathematical relationship between a molecule's structure, encoded by molecular descriptors, and its properties.

This study explores the development of conformation-independent QSPR models using the Monte Carlo (MC) optimization method. The MC method offers a promising approach in QSPR modeling for several reasons. First, it treats the investigated property (K_{mw} in this case) as a random variable, allowing for a flexible modeling approach. Second, it utilizes conformation-independent descriptors derived from both the molecule's topology and its Simplified Molecular Input-Line Entry System (SMILES) notation. This offers advantages in terms of simplicity and efficiency compared to traditional methods that require complex conformational analysis. Notably, the MC method facilitates the identification of activity-influencing molecular fragments directly from SMILES notation descriptors, enabling a clear connection to the chemical structures of the studied compounds [5,6]. The present study focuses on developing a robust QSPR model for predicting K_{mw} using the MC optimization method. Our objectives are twofold - to develop a robust and conformation-independent QSPR model for predicting the micelle-water partition coefficient and to identify SMILES notation descriptors associated with molecular fragments that influence micelle-water partition coefficient, both positively and negatively.

METHODS

Micelle-water partition coefficients (K_{mw}) for 80 organic compounds encompassing aldehydes, amines, alcohols, ketones, ethers, and esters were obtained from the literature [7]. ACD/ChemSketch v11.0 software was used to draw the molecular structures, which were subsequently converted to SMILES notation. All K_{mw} values were determined under identical conditions in 4 mM SDS solutions and ranged from 1.27 (4-aminophenol) to 3.93 (2,3,5,6-tetrachloroaniline). The dataset was then randomly divided into three sets for model development and evaluation: training set (n = 40, 50%) - used for model generation; calibration test set (n = 20, 25%) - used for model calibration and test set (n = 20, 25%) - used for model evaluation. The normality of the K_{mw} values distribution was verified using established methods documented elsewhere [5,6]. Conformation-independent QSPR models were developed using the CORAL software (http://www.insilico.eu/coral), which is based on the Monte Carlo optimization method. All SMILES-based descriptors, including both local and global descriptors, were incorporated into the modeling process. A key feature of the Monte Carlo method is the calculation of correlation weights (CWs) for each optimal descriptor. These CWs quantify the relative importance of each descriptor in the model. The sum of CWs (DCW) is calculated using Eq. 1. To identify the most predictive combination of parameters, the model development process involved exploring a range of threshold (T) and number of epochs (Nepoch) values. T values from 0 to 10 and N_{epoch} values from 0 to 70 were investigated. The selection methodology followed established protocols outlined in previous publications [5,6].

$$DCW(Threshold,N_{epoch}) = \Sigma CW(Sk) + \Sigma CW(SSk) + \Sigma CW(SSSk) + \Sigma CW(NOSP) + \Sigma CW(HALO) + \Sigma CW(BOND) + \Sigma CW(PAIR) \quad (1)$$

RESULTS AND DISCUSSION

The applicability domain (AD) analysis confirmed that all molecules fell within the defined range established using a published methodology, ensuring no outliers were present in the dataset [5, 6]. The optimal QSPR model for molar refractivity was identified based on threshold (T) and number of epochs (N_{epoch}) values obtained from the third split using the Least Squares method. The specific equation for this model is presented in Eq. 2.

$$K_{mw} = 1.7245(\pm 0.0110) + 0.1094(\pm 0.0011) \times DCW(2,14) \quad (2)$$

A comprehensive validation process was employed to assess the quality of the developed model. Internal validation utilized the training set, while external validation employed the test set. Additionally, a Y-scrambling test was conducted to evaluate for the presence of chance correlations. Various statistical parameters were used for evaluation, including correlation coefficient (r^2), cross-validated correlation coefficient (q^2), standard error of estimate (s), mean absolute error (MAE), Fischer ratio (F), root-mean-square error (RMSE), Rm^2, and MAE-based metrics [5, 6]. The Ideality of Correlation (IIC) and concordance correlation coefficient (CCC) indicated good model reproducibility. The model's predictability and validity were further confirmed using MAE-based metrics. Y-randomization, involving shuffling Y values in 1000 trials across 10 runs, confirmed the absence of chance correlation. Statistical results for the training set were: $r^2 = 0.8927$, CCC = 0.9433, IIC = 0.8548, $q^2 = 0.8804$, s = 0.212, MAE = 0.168, and F = 316. The calibration set results were: $r^2 = 0.9052$, CCC = 0.9414, IIC = 0.6476, $q^2 = 0.8842$, s = 0.203, MAE = 0.157, and F = 172. The test set results were: $r^2 = 0.7734$, CCC = 0.8602, IIC = 0.8784, $q^2 = 0.7283$, s = 0.262, MAE = 0.198, and F = 61. The developed QSPR model is visually represented in Figure 1. An illustration of the calculation of a molecule's summarized correlation weight (DCW) and the studied property (MR) is provided in Table 1.

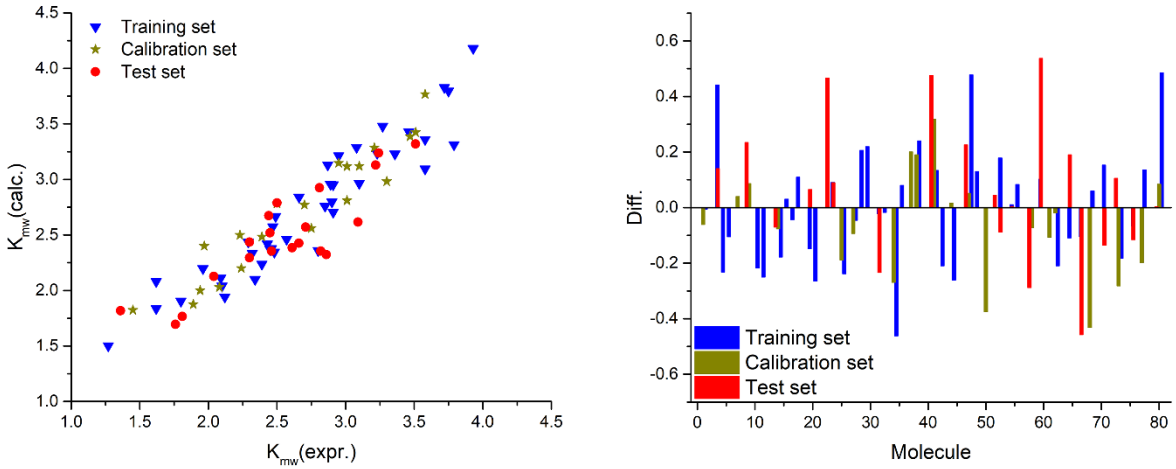
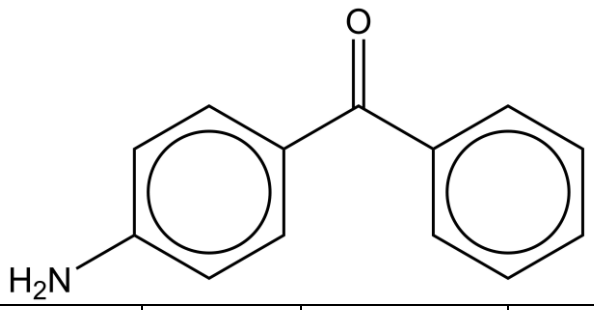


Figure 1. Graphical presentation of the best Monte Carlo optimization run (the highest value for r^2) for the developed QSAR model. (Ac(expr.) – experimental value for K_{mw}; Ac(calc.) – calculated value for K_{mw} using developed QSAR model; Diff. – Ac(expr.) - Ac(calc.)).

Table 1. Example of DCW calculation.

SMILES notation: Nc1ccc(cc1)C(=O)c1ccccc1 DCW = 8.14668 K_{mw}(calc.) = 2.6154					
SAk	CW(SAk)	SAk	CW(SAk)	SAk	CW(SAk)
N.....	-0.1967	BOND100000	0.1459	c...c...1...	0.4244
10011000000	5.3206	c...(.....	0.0891	c...c...c...	-0.0627
(.....	-0.0624	C...(.....	-0.058	c...N.....	-1.745
(...C...(...	1.5828	C...(...=...	0.6417	Cmax.1.....	-1.6412
++++N---B2==	-0.0515	C...(...1...	0.531	HALO00000	0.4853
++++N---O===	1.446	c...(...c...	-0.8668	N...c...1...	-1.2605
++++O---B2==	0.8953	c...(...O...	1.0633	Nmax.1.....	-0.7977
=...(.....	-0.0855	c.....	-0.7231	NOSP110000	-0.4962
=.....	0.3162	c...1...(...	0.1658	O...(.....	0.1686
=...O...(...	0.1202	c...1.....	0.5685	O.....	-0.2555
1...(.....	-0.4648	c...1...c...	1.0383	O...=...(...	-0.9441
1.....	1.5163	c...c...(...	-0.8322	O...=.....	0.7564
1...c...(...	0.5559	c...c.....	-0.6107	Omax.1.....	-0.6695

A key objective was to identify molecular fragments, represented by optimal SMILES descriptors, that influence the dielectric constant [5, 6]. Among these descriptors, the analysis of the ATOMPAIR global descriptor is particularly interesting. This descriptor considers the entire molecule, capturing the presence of specific atom pairs and their connectivity. For instance, the descriptor "++++O---

B2==" indicates the presence of an oxygen atom and a double bond in molecule. Our results revealed that the following ATOMPAIR descriptors have a positive influence on the K_{mw}: ++++CL--N===, ++++CL--O===, ++++Br--O===, ++++I---B2==, ++++N---O===, ++++O---B2==. ATOMPAIRS with negative impact on K_{mw} constant were: ++++I---O===, ++++N---B2==.

CONCLUSION

This study successfully employed the Monte Carlo optimization method to develop robust, conformation-independent QSPR models for predicting micelle-water partition coefficients (K_{mw}) of organic compounds. These models utilize optimal SMILES notation descriptors, effectively capturing conformation-independent characteristics crucial for K_{mw} prediction. Comprehensive evaluation using various statistical metrics confirmed the models' strong predictive potential and robustness, demonstrating their applicability for predicting K_{mw} within the defined applicability domain. This approach offers a significant advantage by enabling K_{mw} prediction without extensive experimental data, potentially accelerating drug discovery and reducing reliance on animal models. Furthermore, the use of SMILES notation-based descriptors provides a crucial benefit. These descriptors allow for clear mechanistic interpretation, enabling direct association with specific molecular fragments that influence K_{mw}. This mechanistic understanding offers valuable insights into the molecular basis of micelle-water partitioning and can guide the design of novel drug candidates with optimized K_{mw} properties. Overall, this work demonstrates the efficacy of the MC optimization method for constructing K_{mw} QSPR models with strong predictive ability.

Acknowledgment

This work was supported by the Ministry of Education, Science and Technological Development of the Republic of Serbia (grant no 451-03-65/2024-03/200113).

REFERENCES

[1] A. Viayna, S. Pinheiro, C. Curutchet, F. J. Luque, W. J. Zamora, J. Comput. Aid. Mol. Des., 35 (2021) 803.
[2] B. Morak-Młodawska, M. Jeleń, E. Martula, R. Korlacki, Int. J. Mol. Sci., 24 (2023) 6970.
[3] D. R. P. Loureiro, J. X. Soares, D. Lopes, T. Macedo, D. Yordanova, S. Jakobtorweihen, C. Nunes, S. Reis, M. M. M. Pinto, C. M. M. Afonso, Eur. J. Pharm. Sci., 115 (2018).
[4] K. A. Kelly, S. T. Burns, M. G. Khaledi, Anal. Chem., 73 (2001) 6057.
[5] A. M. Veselinović, J. B. Veselinović, J. V. Živković, G. M. Nikolić, Curr. Top. Med. Chem. 15 (2015) 1768.
[6] M. Zivkovic, M. Zlatanovic, N. Zlatanovic, M. Golubović, A. M. Veselinović, Mini Rev. Med. Chem. 20 (2020) 1389.
[7] M. H. Fatemi, F. Karimian, J. Colloid Interf. Sci., 314 (2007) 665.

FREE SH GROUPS IN MICROBIAL RESPONSE TO ANTIBIOTICS

K. Joksimović [1], J. Avdalović [1], A. Nikolić-Kokić [2], D. Jovanović [3], S. Miletić [1], K. Kasalica [1] and S. Spasić [1]

[1]*University of Belgrade, Institute of Chemistry, Technology and Metallurgy, National Institute of the Republic of Serbia*
Njegoševa 12, 11000 Belgrade, Serbia. (kristina.joksimovic@ihtm.bg.ac.rs)
[2] *University of Belgrade - Institute for Biological Research "Siniša Stanković", Bulevar despota Stefana 142, 11060 Belgrade, Serbia.*
[3] *City Institute for Public Health in Belgrade, Bulevar despota Stefana 54a, 11000 Belgrade, Serbia.*

DOI: https://doi.org/10.46793/Phys.Chem24II.727J

ABSTRACT

Glutathione (GSH) is the primary molecule responsible for maintaining homeostasis. It is a tripeptide made up of cysteine, glutamate, and glycine. The primary function in redox homeostasis is carried out by the unbound sulfhydryl (SH) group from glutathione (GSH). Microorganisms have swift responses to alterations in their environment, and the use of antibiotics can stimulate the development of bacterial resistance. Transcription factors such as SoxRS, OxyR, NFκB, AP-1, Nrf-2, and P53 are sensitive to variations in the redox state of cells, which is influenced by redox-reactive groups like thiols. Our study monitored alterations in the levels of free sulfhydryl (-SH) groups in *E. coli* and *S. aureus* following their exposure to streptomycin and amoxicillin. An observation was made that streptomycin reduces the concentration of free sulfhydryl (SH) groups in both *E. coli* and *S. aureus*. Conversely, amoxicillin enhances the concentration of free SH groups in *E. coli*, but further reduces the concentration of these groups in *S. aureus*.

There is a significant difference between Gram-positive and Gram-negative bacteria in this regard. These findings improve comprehension of the function of -SH groups in rectifying redox state imbalance in bacteria induced by antibiotics.

INTRODUCTION

The objective of this study was to assess the reaction of both gram positive and gram negative bacteria to antibiotics by examining the presence of free SH groups.

Glutathione's molecular structure is characterized by a gamma peptide linkage connecting the amino group of cysteine and the carboxyl group of glutamate, with the thiol group of cysteine playing a crucial role as an antioxidant. Glutathione plays a crucial role in maintaining the equilibrium of redox reactions inside cells. It also controls important cellular processes such as the cell cycle, apoptosis, defense mechanisms, and the metabolism of both internal and external substances. One of its key functions is assisting in the detoxification process by conjugating chemicals for removal. The user's text is a reference to a source or citation.

Bacteria utilize exogenous glutathione to mitigate oxidative damage. Bacterial pathogenicity in pathogens such as *Burkholderia pseudomallei* and *Listeria monocytogenes* is regulated by host glutathione. Within *B. pseudomallei*, it triggers the activation of the VirA histidine kinase sensor located on the cell membrane, resulting in the activation of the Type VI Secretion System. Within L. monocytogenes, it forms a binding interaction with the master virulence regulator PrfA, acting as an allosteric activator. The user's text is "[2]".

A research found that SBA-maleamic-Cu and SBA-imidazoline-Cu caused an increase in the formation of reactive oxygen species (ROS) in both *S. aureus* and *E. coli*. An electrochemical investigation indicated that these substances had an interaction with lysine or alanine, which might potentially hinder the formation of peptidoglycan in bacterial cell walls. The user's text is enclosed in tags.

The poor thiol reactivity in cells is a result of GSH's pKa value. However, high amounts of GSH enable reduction against oxidizing substances. The thioredoxin and glutathione systems are important thiol-dependent systems that play a crucial role in providing antioxidant capacity and participating in DNA synthesis and protein folding in bacteria. As a result, these systems have become targets for the creation of new antibiotics. Ebselen and auranofin, which are inhibitors of thioredoxin reductase, suppress the development of bacteria that do not have glutathione (GSH). A recent study discovered that the combination of ebselen and silver exhibited a potent impact on microorganisms that are resistant to many drugs. The user's text is "[4]".

Gram-negative bacteria utilize glutathione as their principal thiol redox buffer, whereas the majority of Gram-positive bacteria do not produce GSH. Actinomycetes synthesize mycothiol (MSH), a glutathione alternative, as well as mycothiol peroxidase, which safeguards cysteine from oxidation and controls reactive oxygen species. Corynebacterium diphtheriae utilizes MSH and thioredoxin as electron donors to facilitate the repair of sulfur oxidation through methionine sulfoxide reductase. Mycothiol-dependent enzymes in Gram-negative bacteria may utilize electron transfer from NADPH, providing an advantage compared to the GSH route. The user's text is "[5]".

Bacteria such as *Bacillus* and *Staphylococcus* produce a compound called bacillithiol (BSH). *Staphylococcus aureus* strains that do not have the BSH gene were shown to be more vulnerable to antibiotics and showed reduced survival rates in macrophage experiments. This suggests that these strains might be suitable targets for the development of new antibiotics.

METHODS

In this study we used *E. coli* and *S. aureus* as representatives of Gram positive and Gram negative bacteria. We exposed them to streptomicin and amoksicilin and measured free SH groups. The content of total thiols (protein and non-protein) and sulfhydryl groups was determined spectrophotometrically using a modified Ellman's method. [6]

In a test tube, the same volume (100 µl) of the sample, 1 M Tris buffer (pH 8), and DTNB reagent were mixed, and then ddH2O was added to a final volume of 1 ml. After incubating for 30 minutes at 25 °C, the absorbance was measured at 412 nm against a reagent blank. The obtained absorbance was corrected for the sample absorbance. The thiol concentration was determined based on the standard curve (y=0.00136x-0.00935, r=0.999) created with Cys solutions (concentrations ranging from 0.001 to 1 mM). The thiol content values in the serum were expressed in mmol/l. All determinations were performed in triplicate.

RESULTS AND DISCUSION

Our investigation found that both medicines caused a decrease in thiol groups in Gram-positive *S. aureus*. In contrast, amoxicillin caused an increase in free thiols in *E. coli*, a kind of Gram-negative bacteria. The findings of our investigation unequivocally demonstrate differences in the organization of thiol buffers in Gram-positive and Gram-negative bacteria. The different responses of these bacteria to amoxicillin can be attributed to these alterations.

Table 1. Determination of SH groups in mM.

	E.coli	*E.coli* + Streptomicin	*E.coli* + Amoksicilin	*S.aureus*	*S.aureus* + Streptomicin	*S.aureus*+ Amoksicilin
I	95,40	85,26	121,88	92,54	81,43	78,49
II	96,58	86,58	115,11	91,43	75,33	81,29
III	92,83	82,76	116,58	94,96	81,51	77,76

Gram-negative bacteria utilize glutathione as a tiny thiol molecule, whereas *Staphylococcus* species synthesize bacillithiol (BSH) to preserve redox equilibrium. Bacillithiol is also present in *Thermus thermophiles* and phototrophic *Chlorobiaceae*. *Staphylococcus aureus* utilizes coenzyme A (CoA) as an alternate sulfur-containing molecule, which is maintained in a reduced state by CoA disulfide reductase. [11]

Cysteine plays a vital role in the process of protein synthesis and maintaining a balance in redox reactions. It is either synthesized from scratch or obtained by recycling proteins through breakdown. During periods of oxidative stress, the body may not be able to produce enough cystine through new synthesis or breakdown of existing molecules. As a result, it has to import cystine from outside the cell using transporters such as SLC7A11/xCT. This transporter facilitates the transit of cystine by exchanging it with glutamate, which helps to maintain the balance of redox reactions and the proper functioning of cells. The dysregulation of SLC7A11/xCT is associated with several illnesses, such as cancer, that disrupt the balance of redox reactions, metabolic processes, immunological responses, and cell viability. The cystine/cysteine redox cycle promotes the development of cancer cells by sustaining a reducing extracellular environment.

CONCLUSION

Our investigation found that there were varying reactions in the levels of free SH groups in *E. coli* and *S. aureus* when treated with antibiotics. This phenomenon was shown to arise from the presence of distinct sources of free sulfhydryl (SH) groups in Gram-negative and Gram-positive bacteria. Glutathione is the primary provider of free SH groups in *E. coli*, but in *S. aureus*, bacithiol serves as the main source. This discovery allows for the enhancement of antibiotic action through the manipulation of redox activity.

Acknowledgment

This work was supported by the Ministry of Education, Science and Technological Development of the Republic of Serbia (grant no 451-03-66/2024-03/200026).

REFERENCES

[1] S. Gurung, O. V. Timmermand, D. Perocheau, A. L. Gil-Martinez, M. Minnion, L. Touramanidou, S. Fang, M. Messina, Y. Khalil, J. Spiewak, A. R. Barber, R. S. Edwards, P. L. Pinto, P. F. Finn, A. Cavedon, S. Siddiqui, L. Rice, P. G. V. Martini, D. Ridout, W. Heywood, I. Hargreaves, S. Heales, P. B. Mills, S. N. Waddington, P. Gissen, S. Eaton, M. Ryten, M. Feelisch, A. Frassetto, T. H. Witney, J. Baruteau. Science Translational Medicine, 16 (2024).

[2] J. W. K. Ku, Y.-H. Gan;. Redox Biology, 44 (2021) 102012.

[3] D. Díaz-García, P. R. Ardiles, M. Díaz-Sánchez, I. Mena-Palomo, I. del Hierro, S. Prashar, A. Rodríguez-Diéguez, P. L. Páez, S. Gómez-Ruiz;. Journal of Inorganic Biochemistry, 203 (2020)

[4] X. Ren, L. Zou, J. Lu, A. Holmgren; Selenocysteine in mammalian thioredoxin reductase and application of ebselen as a therapeutic. Free Radical Biology and Medicine ,127 (2018) 238–247.

[5] A. M. Reyes, B. Pedre, M. I. De Armas, M.-A. Tossounian, R. Radi, J. Messens, M. Trujillo; Antioxidants & Redox Signaling, 28 (2018) 487–504.

[6] P. H. W. Butterworth, H. Baum, J. W. Porter, Archives of Biochemistry and Biophysics, 118 (1967) 716–723.
[7] A. Crisafulli, F. Melis, F. Tocco, P. Laconi, C. Lap, A. Concu, Journal of Sports Medicine and Physical Fitness, 42 (2002) 409–417.
[8] D. A. Butterfield, J. Kanski, Peptides, 23 (2002) 1299–1309.
[9] N. J. Sucher, S. A. Lipton, Journal of Neuroscience Research, 30 (1991) 582–591.
[10] K. Ulrich, U. Jakob, Free Radical Biology and Medicine, 140 (2019) 14–27.
[11] S. Vesce, M. B. Jekabsons, L. I. Johnson-Cadwell, D. G. Nicholls, Journal of Biological Chemistry, 280 (2005) 38720–38728.

SURFACE MODIFICATION WITH 5-AMINOSALICYLIC ACID REDUCES NANOPARTICLE-INDUCED OXIDATIVE STRESS IN RAT SERUM

K. Bobić [1], J. Miletić Vukajlović [2], J. Martinović [1], I. Guševac Stojanović [1], N. Vukotić Todorović[1] and A. Todorović [1]

[1]*University of Belgrade, VINCA Institute of Nuclear Sciences - National Institute of the Republic of Serbia, Department of molecular biology and endocrinology, Mike Petrovića Alasa 12-14, 11000 Belgrade, Republic of Serbia. (katarina.bobic@vin.bg.ac.rs)*
[2]*University of Belgrade, VINCA Institute of Nuclear Sciences - National Institute of the Republic of Serbia, Department of physical chemistry, Mike Petrovića Alasa 12-14, 11000 Belgrade, Republic of Serbia.*

DOI: https://doi.org/10.46793/Phys.Chem24II.731B

ABSTRACT
Titanium dioxide nanoparticles (TiO_2 NPs) are emerging in many technologies, owing to their chemical stability, antibacterial and photocatalytic properties. However, they tend to accumulate in cells inducing oxidative stress, inflammation, and even apoptosis. The main goal of this study was to determine whether surface modification with 5-aminosalicylic acid (5-ASA) could reduce TiO_2 NPs toxicity. Therefore, female adult Wistar rats were orally treated in a single dose with 2.5 ml 0.01 M HCl (nanoparticle solvent); 1000 mg/kg of bare, commercially available TiO_2 or TiO_2 NPs surface-modified with 5-ASA (5-ASA/TiO_2 NPs). Oxidative stress parameters, including prooxidant/antioxidant balance (PAB), advanced oxidation protein products (AOPP), and lipid peroxidation (LPO) were measured in the serum. Treatment with 5-ASA/TiO_2 NPs showed potential to diminish LPO, but not AOPP or PAB, compared to bare TiO_2 NPs. It can be concluded that this modification only partially alleviates oxidative stress induced by TiO_2 NPs, and the underlying mechanisms remain unclear.

INTRODUCTION
Nanomaterials (structures with diameters less than 100 nm) have gained considerable attention in recent years, owing to their various traits and applications. Due to their chemical stability, antibacterial, photocatalytic, and photosensitizing properties, titanium dioxide nanoparticles (TiO_2 NPs) are among the most abundant nanomaterials in use. They are applied in pharmaceuticals, medicine, paints, wastewater treatment, food and beverages. TiO_2 NPs are used as an antibacterial coating in food packaging, food flavor enhancers, and colorant (E171) [1]. Beside the benefits that come with unique physical and chemical properties, these NPs demonstrated numerous adverse effects in both *in vitro* and *in vivo* experiments. TiO_2 NPs can be ingested orally, through skin or inhalation, enter circulation and distribute to liver, spleen, heart, reproductive organs, and even cross placental and blood-brain barriers. Furthermore, TiO_2 NPs can enter cells and produce reactive oxygen species (ROS) which can oxidize lipids and induce cell membrane damage, protein denaturation, and DNA damage [2], disrupting homeostasis, cell signaling, and functions.

European Commission Regulation of January 2022. banned the usage of TiO_2 as a food additive E171 [3] based on the EFSA's (European Food Safety Authority) updated research, concluding that the E171 contains up to 50% of nanosized particles and holds concerns about genotoxicity [4]. However, their use in medicinal products continues. Researchers are trying to find an equal substitute or to surface-modify TiO_2 NPs in order to reduce or even suppress their toxicity. Some scientists succeeded in this by attaching caffeic (CA) [5] or alpha-lipoic acid (ALA) [6] to the surface of TiO_2

NPs. Therefore, our goal was to investigate whether surface modification of TiO_2 NPs with 5-aminosalicylic acid (5-ASA), as known antioxidant, could optimize their properties.

METHODS

The synthesis and characterization of the surface-modified TiO_2 NPs have been described previously [7].

Experimental procedure:

All experimental procedures were performed in accordance with Directive 2010/63/EU of the European Parliament and authorized by the Veterinary Directorate of the Ministry of Agriculture, Forestry and Water Management of the Republic of Serbia, authorization protocol 323-07-03626/2021-05.

Adult Wistar female rats (n=12) were bred at VINCA Institute of Nuclear Sciences - National Institute of the Republic of Serbia, University of Belgrade. Rats, 2-3 per cage, were housed under standard conditions (12h light/dark cycle, 22 ± 2 °C, 55 % humidity) and provided with tap water and standard rat food *ad libitum*. On the first experimental day, the rats were divided randomly into three groups, with each group containing four animals that were administered acute oral treatment.

- → Animals in first group, control (C) received only solvent (2.5 ml 0.01 M HCl)
- → Animals in second group (TiO_2) received 1000 mg/kg TiO_2 NPs dissolved in HCl
- → Animals in third group (5-ASA/TiO_2) received 1000 mg/kg 5-ASA/TiO_2 NPs dissolved in HCl

All treatments were administered after 4 h of fasting, with a reusable stainless steel feeding needle, 16-G4", 3 mm ball diameter (Cadence Inc., USA), and 2 h later, the food and water were returned to the cages. The animals were then left to rest and were monitored daily for 14 days. They were decapitated on 14th day and trunk blood was immediately collected in vacutainers for serum separation. Blood samples were then centrifuged at 3500 rpm for 15 min (Heraeus Megafuge 2.0R, Germany), aliquoted, and stored at -80 °C until further analysis.

Spectrophotometric methods

The evaluation of the oxidative stress biomarkers, prooxidant/antioxidant balance (PAB), advanced oxidation protein products (AOPP), and lipid peroxidation (LPO) – levels of both malondialdehyde (MDA) and 4-hydroxy-2-nonenal (HNE), was also described by Todorovic et al. [7].

All data were expressed as mean percentage of control ± S.E.M. Results were analyzed with GraphPad Prism using One-way ANOVA followed by Tukey's post-hoc test, and statistical significance was set at $p < 0.05$.

RESULTS AND DISCUSSION

Recently published study by our group showed that surface-modification of TiO_2 NPs with 5-ASA can reduce toxic effects of TiO_2 NPs on biochemical and physiological parameters in rat ovaries, oviducts and uterus [7]. Dekanski et al. showed that exposure to TiO_2 NPs surface modified with CA does not induce pathological changes in liver, and biochemical parameters as indicators of liver function remained unaltered, indicating that toxic effects of TiO_2 NPs might be mitigated through used surface modification [5]. In addition, binding ALA functionalized with bovine serum albumin (BSA) to TiO_2 NPs' surface, showed selective cytotoxicity for cancer cells and negligible cytotoxicity for normal cells [6].

In this study, we focused on monitoring changes in several oxidative stress parameters in rat serum, as a general indicators of NPs' toxicity. As expected, PAB level was higher in TiO_2 group compared to the control ($p < 0.01$) (**Figure 1.**), showing disturbed oxidative balance shifted toward prooxidation. PAB level in 5-ASA/TiO_2 group was similar to those in the C group, but also remained

similar to the level in TiO_2 NPs treated group. This result indicates that 5-ASA partially reduced toxicity of TiO_2 NPs. In addition to general oxidative state in serum, our study monitored oxidation of biomolecules, including proteins (AOPP) and lipids (LPO). Compared to the control, AOPP levels of both 5-ASA/TiO_2 and TiO_2 groups were elevated ($p < 0.01$; $p < 0.05$ respectively), and mutually similar. On the other hand, level of LPO in 5-ASA/TiO_2 group was similar to that in the C group, and significantly lower in comparison to group treated with unmodified NPs ($p < 0.01$). Considering that proteins are more abundant than lipids in serum and react rapidly with oxidants, they are more susceptible to oxidation [8]. Therefore, this modification was not sufficient to reduce ROS levels enough to prevent oxidative damage to proteins, although the exact mechanism remains unclear.

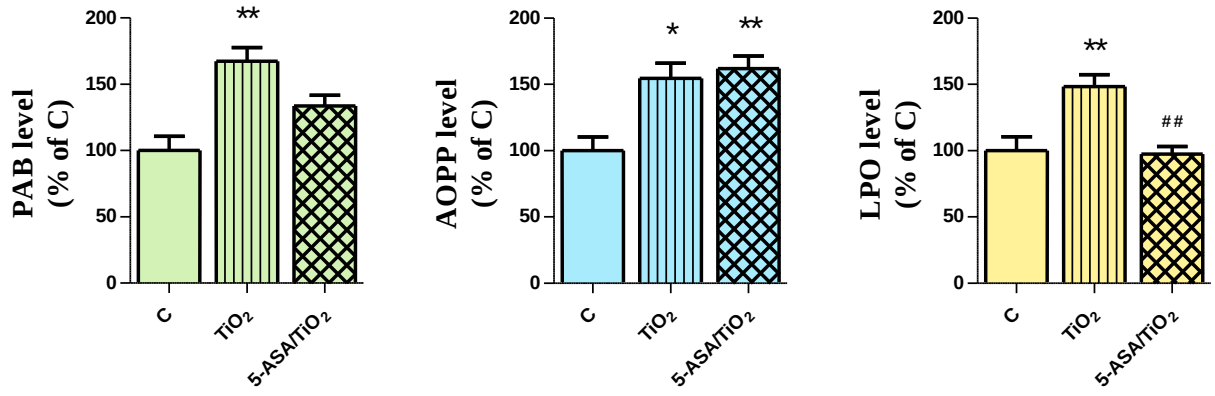


Figure 1. Effects of acute oral treatment with solvent (2.5 ml 0.01 M HCl), bare TiO_2 or TiO_2 nanoparticles surface-modified with 5-aminosalicylic acid (5-ASA/TiO_2) on oxidative stress parameters (prooxidant/antioxidant balance (PAB), advanced oxidation protein products (AOPP), and lipid peroxidation (LPO)) in serum of adult Wistar rats. Data are presented as the mean percentage of control ± SEM, * symbols indicate significant difference control *vs.* (un)modified TiO_2 groups (* $p < 0.05$, ** $p < 0.01$) while # represents the difference between TiO_2 and 5-ASA/TiO_2 ($^{\#\#}$ $p < 0.01$).

CONCLUSION

Based on the findings presented, it can be concluded that treatment with 5-ASA/TiO_2 NPs may potentially mitigate the detrimental effects of TiO_2 NPs on lipid oxidation, although it does not appear to have an impact on protein oxidation, since proteins are more prone to oxidation. The utilized modification is a newly reported method that may contribute to a better understanding of the toxic mechanisms involved, and potentially be used to improve surface modifications in a more beneficial direction.

Acknowledgment

This work was supported by the Ministry of Education, Science and Technological Development of the Republic of Serbia (grant no 451-03-66/2024-03/200017).

REFERENCES

[1] O. U. Akakuru, Z. M. Iqbal, A. Wu in: TiO2 Nanoparticles: Applications in Nanobiotechnology and Nanomedicine, A. Wu, W. Ren (Eds.) Wiley Online Library 2020.
[2] B. Song, J. Liu, X. Feng, L. Wei, L. Shao. Nanoscale Res. Lett. 10 (2015) 1.

[3] Official Journal of the European Union (2022) COMMISSION REGULATION (EU) 2022/63 of 14 January 2022 amending Annexes II and III to Regulation (EC) No 1333/2008o of the European Parliament and of the Council as regards the food additive titanium dioxide (E 171).
[4] EFSA, European Food Safety Authority, https://www.efsa.europa.eu/en/news/titanium-dioxide-e171-no-longer-considered-safe-when-used-food-additive, assessed on 24.5.2024.
[5] D. Dekanski, B. Spremo-Potparević, V. Bajić, L. Živković, D. Topalović, D. N. Sredojević, V. Lazić, J. M. Nedeljković, Food Chem. Toxicol. 115 (2018) 42.
[6] E. J. Diana, T. V. Mathew. Colloids Surf. B: Biointerfaces 220 (2022) 112949.
[7] A. Todorović, K. Bobić, F. Veljković, S. Pejić, S. Glumac, S. Stanković, T. Milovanović, I. Vukoje,J. M. Nedeljković, S. Radojević Škodrić, S. B. Pajović, Antioxidants. 13(2) (2024) 231.
[8] C. L. Hawkins, M. J. Davies, J. Biol. Chem., 294(51) (2019) 19683.

COMPARATIVE STUDY OF TIO2 AND SURFACE-MODIFIED TIO2 ON REDOX AND LIPID PARAMETERS IN HUMAN FIBROBLAST CELLS

J. Miletić Vukajlović [1], K. Bobić [2], J. Filipović Tričković [1], A. Valenta Šobot [1], J. Martinović [2], I. Guševac Stojanović [2] and S. Pejić [1]

[1] *University of Belgrade, VINČA Institute of Nuclear Sciences - National Institute of the Republic of Serbia, Department of physical chemistry, Mike Petrovića Alasa 12-14, 11000 Belgrade, Serbia. (jadranka@vin.bg.ac.rs)*

[2] *University of Belgrade, VINCA Institute of Nuclear Sciences - National Institute of the Republic of Serbia, Department of molecular biology and endocrinology, Mike Petrovića Alasa 12-14, 11000 Belgrade, Republic of Serbia.*

DOI: https://doi.org/10.46793/Phys.Chem24II.735MV

ABSTRACT

Titanium dioxide nanoparticles (TiO_2 NPs) find widespread application in both industrial and consumer goods, encompassing sectors such as cosmetics, pharmaceuticals, food and beverages, and more. This study investigated redox state parameters and lipid peroxidation parameter in human fibroblast cells treated with different concentrations of NPs. The NPs used included bare TiO_2 and TiO_2 modified with salicylic acid (SA). The parameter values were compared both with the control group and among the treated groups. Obtained results showed that all investigated NPs promoted oxidative stress in human fibroblast cells.

INTRODUCTION

Titanium dioxide (TiO_2) nanomaterials have a wide array of applications, ranging from everyday products, such as sunscreens, to sophisticated devices such as photovoltaic cells. Additionally, they are used in various environmental and biomedical applications, including photocatalytic degradation of pollutants, agriculture, water purification, biosensing, and drug delivery. Due to the widespread use of TiO_2 NPs in daily life, it is crucial to understand their toxicity and potential adverse effects on human health and the environment. Various experimental studies have indicated that exposure to TiO_2 NPs can be hazardous and lead to detrimental health outcomes [1]. Numerous in vitro studies have demonstrated that TiO_2 NPs exhibit cytotoxic and genotoxic effects, trigger apoptosis and inflammation, induce ROS production, and alter enzyme activity and gene expression [2]. Consistent with these in vitro findings, several in vivo studies have revealed that TiO_2 NPs, upon entering the bloodstream, can accumulate in vital organs, resulting in their injury. TiO_2 NPs penetrate the body via various exposure pathways and subsequently distribute to vital organs throughout the body. Gastrointestinal absorption of TiO_2 NPs as additives in toothpaste, lozenges, capsules, drug carriers, and similar products. [3] Considering the widespread use of TiO_2 NPs in cosmetics, dermal absorption stands out as another crucial mode of entry. According to several studies [3,4] TiO_2 NPs can penetrate trough different skin layers. Inhalation represents an additional pathway through which TiO_2 NPs enter the body and translocate to the central nervous system, mainly through sensory nerves.

Oxidative stress is believed to be a fundamental mechanism underlying the adverse biological effects induced by NPs. The involvement of oxidative stress in TiO_2-induced adverse effects is substantiated by evidence indicating an elevation in reactive oxygen species (ROS) production, lipid peroxidation, and depletion of cellular antioxidants. Various modifications have been reported to decrease the potential toxicity of TiO_2, including activated carbon coating [5], transition metal doping [6], metal ion implanting [7], or ascorbic acid [8] or polymer [9]. Salicylic acid (SA), also known as

2-hydroxybenzoic acid, is a phenolic compound synthesized by plants, playing direct and indirect roles in growth, development, thermogenesis, and disease resistance. SA is recognized pharmacological agent used for treating various conditions and reducing the risk of stroke, heart attack, and certain cancers. Thus, the aim of this study was to investigate the influence of TiO_2 nanoparticles on the redox status and lipid parameters of human lung fibroblasts, and their correlation with the occurrence of oxidative stress. Furthermore, this research sets itself apart by investigating the potential protective role of TiO_2 nanoparticles modified with salicylic acid (SA) against such citotoxic effects.

METHODS

Nanoparticles

In this experimental setup, commercially available TiO_2 NPs (Degussa P25 Titanium Dioxide Nanopowder, Sigma Aldrich Co., USA) and surface-modified TiO2 NPs with SA were utilized. The surface modification of TiO_2 NPs was conducted at the University of Belgrade, VINCA Institute of Nuclear Sciences, through a condensation reaction involving hydroxyl groups from both inorganic and organic components. Briefly, 3.5 g of TiO_2 was mixed with 602 mg of SA in 100 ml of water. The mixture was stirred for 24 h at 40°C, followed by centrifugation for 10 min at 4000 rpm (Sigma Laborzentrifugen GmbH, Germany), washing three times with dH_2O to remove excess ligands, and drying at 40°C in a vacuum oven (Owen GCA Corporation, USA). The characterization included visual inspection to estimate the color of the powders as an indicator of inorganic-organic compound formation (TiO_2/SA NPs powder exhibited a yellow color), as well as utilizing a Shimadzu UV-Visible UV-2600 spectrophotometer equipped with ISR-2600 Plus integrated sphere (Japan).

Cell and experimental procedures

MRC-5 human lung fibroblast cell suspension was used as a model to measure the impact of three different concentrations of TiO2 and TiO_2/SA NPs (10, 50, and 100 μg/ml).

MRC-5 (ATCC, Manassas, VA, USA) human lung fibroblast cell suspension at 1 x 106 cells per T25 cm2 flask was seeded in Dulbecco`s Modified Eagle`s Medium (DMEM, Gibco™, Thermo Fisher Scientific, USA), supplemented with 10% fetal bovine serum (FBS, Capricorn Scientific, Germany) and 1% antibiotic-antimycotic (Gibco™ Antibiotic-Antimycotic, Thermo Fisher Scientific, USA). The cells were grown under standard cell culture conditions at 37 °C and 5% CO2. After reaching confluency levels, cells were treated for 24 h with test samples. Untreated flask served as a negative control. Upon treatment, medium was removed, cells were washed with PBS, detached by trypsin, and settled by centrifugation for further experiments.

Statistical analyses

The oxidative status of the human lung fibroblast cell suspension was evaluated by measuring the levels of prooxidant-antioxidant balance (PAB), and end products of lipid peroxidation (LPO), as previously described [10]. The absorbance of reaction mixture for PAB was read at 450 nm, and for LPO at 586 nm on Perkin Elmer Wallac 1420 VICTOR2 Microplate Reader (UK). The results are expressed as a percentage of the mean values in group C ± SEM. Statistical analysis was conducted using one-way analysis of variance (ANOVA), followed by Tukey's multiple-comparison post hoc test. GraphPad Prism software version 5.0 (GraphPad Software, USA) was employed for all statistical analyses, with significance set at $p < 0.05$.

RESULTS AND DISCUSSION

In this study, the measured values of PAB level and the LPO in human fibroblast cells treated with TiO_2 and TiO_2/SA NPs are presented.

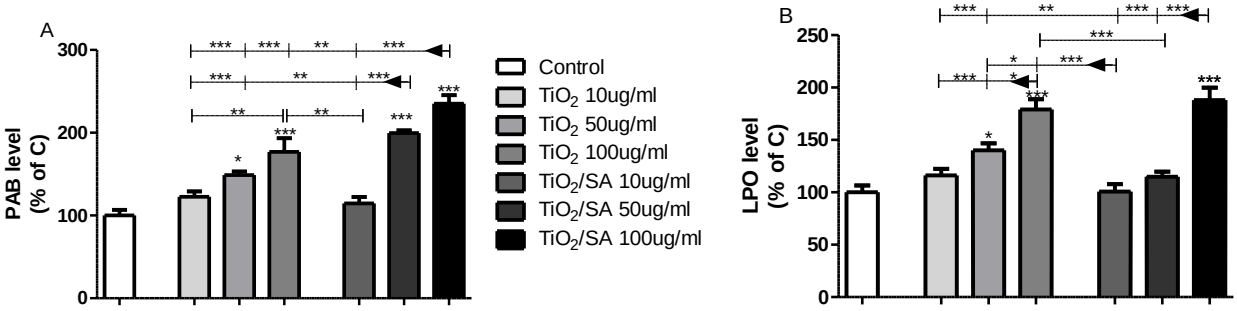


Figure 1. Levels of oxidative stress indicators: pro-oxidant and anti-oxidant balance (PAB) (A), and end lipid peroxidation products (LPO) (B) in human lung fibroblast cell suspension (C-control group, TiO_2 NPs (TiO_2 group), and surface-modified TiO_2 NPs with salicylic acid (SA) (TiO_2/SA group)). The symbol * above bars indicate a statistically significant difference between C and other experimental groups (* $p < 0.05$, ** $p < 0.01$, *** $p < 0.001$). The arrow on the line above the bar represents a point of comparison, both within the group, and between groups.

PAB level, as a general indicator of cell redox status, was estimated in human lung fibroblast cells 14 days after administration of bare TiO_2 NPs and TiO_2/SA NPs at three different concentrations (10, 50 and 100 μg/ml). Compared to the control (C) group statistically significant increase was observed in both groups, TiO_2 (50 μg/ml; $p < 0.05$ and 100 μg/ml; $p < 0.001$) and TiO_2/SA at concentration of 50 and 100 μg/ml ($p < 0.001$) (**Figure 1A**). Similar results were obtained in a mouse fibroblast cell model for different TiO_2 concentrations [12]. Cheng-Yu et al. [11] observed a notable rise in oxidative stress with increased TiO2 NPs concentration (>60μg/ml), characterized by elevated levels of ROS and LDH, alongside a decline in GSH and SOD in a mouse fibroblast cell model. Moreover, our findings also indicated statistically significant differences between TiO_2 and TiO_2/SA experimental groups and within groups. Contrary to the anticipation that nanoparticle modification would mitigate toxicity and, consequently, the onset of oxidative stress, our results indicated a notable elevation in PAB values within the TiO_2/SA group compared to the unmodified group (**Figure 1A**).

When considering the results obtained for LPO values, a statistically significant increase was detected at a concentration of 100 μg/ml for both groups ($p < 0.001$) and at TiO_2 50 μg/ml ($p < 0.05$) compared to the control (**Figure 1B**). A statistically significant reduction in LPO levels was observed in TiO_2/SA 50 μg/ml compared to TiO_2 NP. The results obtained for PAB indicate an increase in the shift towards pro-oxidative molecules, suggesting oxidative stress. However, lower values for LPO indicate that this oxidation does not primarily arise from lipids. Hence, the elevated levels of examined oxidative stress indicators in the TiO_2 and TiO_2/SA groups suggest heightened free radical generation and destabilization of antioxidant defense mechanisms, potentially culminating in oxidative stress, neuroinflammation, and cellular demise, as documented in previous studies [12]. Furthermore, Pan et al. [13] reported the effects of exposure of human dermal fibroblasts to TiO_2 NPs. It was shown that exposure to TiO_2 NPs impaired cell function, leading to reductions in cell area, proliferation, mobility, and collagen contractility. These NPs possess the capability to readily traverse cell membranes and become enclosed within vesicles. Pan et al. [14] also reported that particles coated with a polymer brush exhibited non-adherence to cell membranes, consequently preventing cellular penetration. This resulted in reduced ROS formation, thereby preserving normal cellular function which is contradictory to the results obtained in our study, where it was demonstrated that NP modification leads to an increase in oxidative stress parameters. The negative impact of nanoparticles was also demonstrated in a study by Lai et al. [2] where it was shown that exposure of

human neural and fibroblast cells to TiO_2 micro- and nanoparticles induces several modes of cell death.

CONCLUSION

Our study demonstrated that both TiO_2 NPs and surface-modified TiO_2/SA NPs induced oxidative stress in human lung fibroblast cells, as evidenced by increased levels of PAB and LPO. Contrary to expectations, surface modification with salicylic acid did not mitigate prooxidative effects, suggesting that such modifications might not reduce the cytotoxicity of TiO_2 NPs. These findings highlight the need for further investigation into the safety and potential health impacts of using modified NPs in various applications.

Acknowledgment

This work was supported by the Ministry of Education, Science and Technological Development of the Republic of Serbia (grant no 451-03-66/2024-03/200017).

REFERENCES

[1] S. Shabbir, MF. Kulyar, ZA. Bhutta, P. Boruah, M. Asif, BioNanoScience. 11 (2021) 621.
[2] JC Lai, MB Lai, S. Jandhyam, VV Dukhande, A. Bhushan, CK Daniels, SW Leung, Int J Nanomedicine 3 (2008) 533.
[3] AB da Silva, M. Miniter, W. Thom, RE Hewitt, J. Wills, R. Jugdaohsingh, JJ. Powell, Curr. Opin. Toxicol. 19 (2020) 112.
[4] S. Murugadoss, F. Brassinne, N. Sebaihi, J. Petry, SM. Cokic, KL.Van Landuyt, L. Godderis, J. Mast, D. Lison, PH. Hoet, S. Van Den Brûle, Part fibre toxicol. (2020) 1.
[5] J. Wang, G. Zhou, C. Chen, H. Yu, T. Wang, Y. Ma, G. Jia., Y. Gao, B. Li, J. Sun, Y. Li, F. Jiao, Y. Zhao, Z. Chai, Toxicol. Lett. 68 (2007a.) 176.
[6] K.B. Li, X.Z. Li, Chemosphere 48 (2002) 1103.
[7] S.K. Zheng, T.M. Wang, W.C. Hao, R. Shen, Vacuum 65 (2002) 155.
[8] A.P. Xagas, M.C. Bernard, A.H.L. Goff, N. Spyrellis, Z. Loizos, P. Falaras, J. Photochem. Photobiol. A: Chem. 132 (2000) 115.
[9] S.H. Bossmann, S. Gob, T.B. Siegenthaler, M. Andre, K.T. Ranjit, I. Willner, Fresenius J. Anal. Chem. 371 (2001) 621.
[10] S. Đurašević, G. Nikolić, A. Todorović, D. Drakulić, S. Pejić, V. Martinović, D. Mitić-Ćulafić, D. Milić, T. J. Kop, N. Jasnić, J. Đorđević, and Z. Todorović, Food Chem. Toxicol., 140 (2020) 111302.
[11] Y. Cheng-Yu, Z. Bang-Shang, W. Xue-Feng, L. Qing-Hua, Chem. Res. Toxicol. 21 (2008) 1871.
[12] Y. Ze, L. Zheng, X. Zhao, S. Gui, X. Sang, J. Su, N. Guan, L. Zhu, L. Sheng, R. Hu, and J. Cheng. Chemosphere, 92 (2013) 1183.
[13] Z. Pan, W. Lee, L. Slutsky, RA. Clark,|N. Pernodet, MH. Rafailovich, Small. 5 (2009) 511.

OXYGEN CONCENTRATION CONTROLS BIOFILM GROWTH INSIDE A NOVEL MICROFLUIDIC GRADIENT GENERATOR

A. Lončar [1], E. Secchi [2], J. Jimenez Martinez [3], H. Tabuteau [4], and T. Le Borgne [1]

[1] *Géosciences Rennes, UMR 6118, 263 av. General Léclérc, 35000 Rennes, France (aleksandar.loncar@univ-rennes.fr)*
[2] *ETH Zurich, Institute of Environmental Engineering, BioMatter Microfluidics Group, Laura Hezner-Weg 7, 8093 Zürich, Switzerland*
[3] *ETH Zurich, EAWAG, Subsurface Environmental Processes Group, Ueberlandstrasse 133 8600 Dubendorf, Switzerland*
[4] *L'Institut de Physique de Rennes, IPR UMR 6251, All. Jean Perrin Bât. 10B, 35000 Rennes*

DOI: https://doi.org/10.46793/Phys.Chem24II.739L

ABSTRACT

Bacterial biofilms are communities of bacteria suspended in extracellular substances, which protect the embedded colonies to ensure continued growth. They affect much of human life, colonizing the surfaces of implants, the lungs of cystic fibrosis patients and affecting biogeochemical cycles in the subsurface. Biofilm growth in these complex environments is poorly understood, as the varied nutrient concentrations give rise to chemical gradients, affecting how bacteria organize and mature. One such bacteria is *Pseudomonas putida*, an aerophilic subsurface organism that colonizes roots of many important agricultural plants. To investigate *P. putida* biofilm maturation in such conditions, we developed a novel microfluidic device capable of maintaining a stable oxygen gradient over time under flow. Our results suggest that oxygen gradients are correlated to gradients of biomass, indicating that *P. putida* biofilm growth is strongly connected to oxygen concentration and not a response to oxidative stress. Future experiments would attempt to determine the exact biochemical mechanism responsible for this growth response by utilizing bacterial mutants lacking in various metabolic capabilities.

INTRODUCTION

Biofilms are ubiquitous in Nature, with roughly 80% of all bacterial species exhibiting some form of biofilm development [1]. Bacteria in biofilms are embedded in a complex matrix made up of polysaccharides, lipids, proteins and extracellular DNA. These extracellular polymeric substances (EPS) protect bacteria from various extraneous factors, such as sudden changes in the chemical make-up of their environment, physical abrasion by fluid flow and antagonistic attacks by antibiotics [2]. Besides providing protection, biofilms are the main vehicle by which bacteria spread and multiply. Biofilm formation happens in four stages: (1) attachment, (2) microcolony formation, (3) maturation, (4) dispersal. After initial attachment to a surface, a mature biofilm is formed after 12-48h, depending on the species. This mature biofilm then releases new bacteria into the surrounding habitat, allowing bacteria to quickly colonize a surface [3]. However, the current understanding of the biofilm life cycle is based on studies mostly done in homogenous, nutrient rich environments, as mimicking naturally formed chemical gradients in a laboratory setting is challenging [4].

Pseudomonas putida is an aerobic, Gram-negative, rod-shaped bacteria that can generally be found in the rhizosphere. It can colonize roots and develop symbiotic relationships with important agricultural plants, protecting them from pathogens while deriving nutrition from decaying organic matter [5,6]. However, living in the subsurface exposes *P. putida* to gradients of many important

nutrients, such as oxygen, nitrogen and carbohydrates. This forces the bacteria to develop survival strategies, modifying the attachment rate and production of new cells [7].

Mimicking complex gradients has proven to be a difficult task in microfluidics [8]. The most common way of generating gradients under flow has been by use of a T-junction, a microfluidic device where two liquids with different concentrations of the solute of interest are injected inside of a T-shaped channel, creating a gradient in the middle as the solute diffuses from one liquid to the other [8,9]. However, T-junction gradient generators are only able to form a stable gradient over a small width (around 1000 μm) and only for small flow rates (0.1 – 1 μL/min), depending on the solute of interest. The time needed for these gradients to form is also large, as it relies mostly on diffusion [8–10].

For this reason, we developed a novel microfluidic device capable of on-chip oxygenation/deoxygenation of liquids and maintaining a stable, fast forming gradient over a wide spatial area and used it to study *P. putida* biofilm development under an oxygen gradient.

METHODS

Silicon wafer stencils were prepared using standard soft lithography techniques to imprint the design onto the wafer. Microfluidic chips were made by preparing a 10:1 mixture of SYLGARD 184 Silicone Elastomer Base and SYLGARD 184 Silicone Elastomer Curing agent (to from PDMS), pouring it over the stencil and curing it for 3 hours at 60°C. After curing, the PDMS chips were cut from the stencil, cleaned along with a microscope glass slide and exposed to plasma at HIGH RF for 40s in a Harrick Basic Plasma cleaner. The two pieces were then brought into contact and bonded over 8 hours at 80°C.

Pseudomonas putida was plated onto Luria Bertani (LB) agar and incubated for 24 hours at 30°C. Overnight cultures were prepared by transplanting one colony from the plate into 3 ml liquid LB and incubating for 18h at 30°C. Working cultures were prepared by soluting 50 μL of the overnight culture in 3 ml of fresh liquid LB and incubating for 5h at 30°C. The final OD of bacteria injected into the channel was 0.05. Bacteria were observed via fluorescence on an inverted microscope, LEICA DMI8, as they were genetically modified to produce green fluorescent protein (msfGFP).

RESULTS AND DISCUSSION

The design of the device (**Figure 1**) was optimized for enabling gas exchange and improving mixing. Two symmetrical 150 μm liquid channels were placed on either side of the main incubation chamber, surrounded by two 1000 μm gas channels. Sterile LB was flown through both liquid channels, while two gas channels were flushed with argon to deoxygenate the LB, and two gas channels were flushed with synthetic air to oxygenate it. Both liquids meet in the central chamber, where a porous media with a pore size of 300 μm blends the liquids via shear mixing and stabilizes the gradient. Bacteria were injected into the main chamber via a middle channel between the two liquid injection points.

The design was verified first by COMSOL Multiphysics 6.0 simulations to determine the length of the gas exchange portion, then by using an oxygen sensing optical fiber and fluorescein to verify the deoxygenation of the liquid and the shape of the gradient, respectively. The co-injection simulations injected two fluids, at 2.3E-4 mol/L and 0 mol/L O_2, respectively.

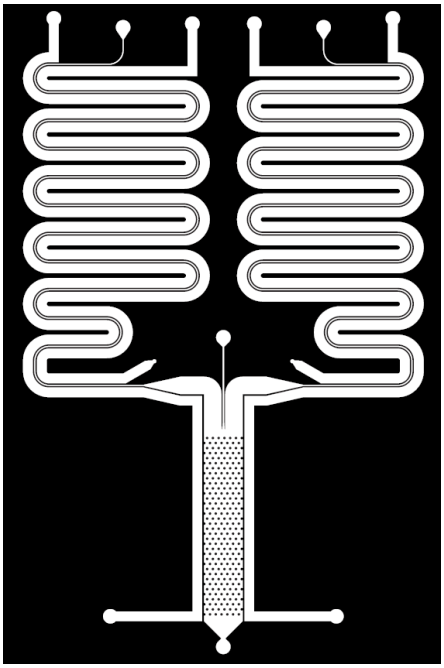


Figure 1 - Microfluidic device.

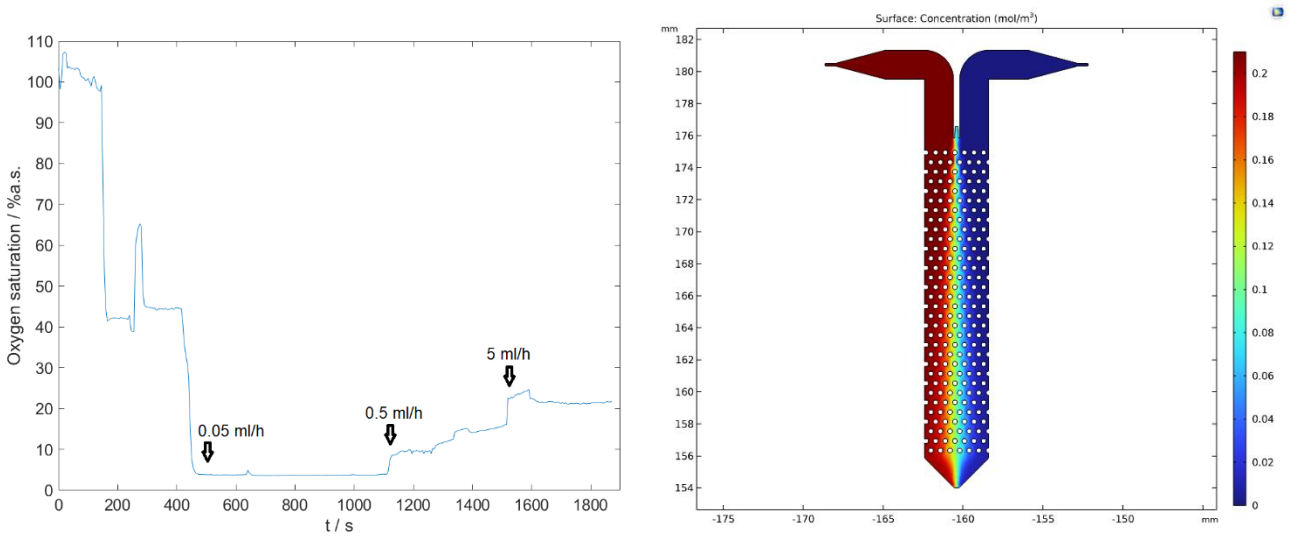


Figure 2 - Measurement of deoxygenation in liquid channel surrounded by argon for different flow rates (L), COMSOL simulation of an oxygen gradient in the device for Q = 0.2 ml/h (R).

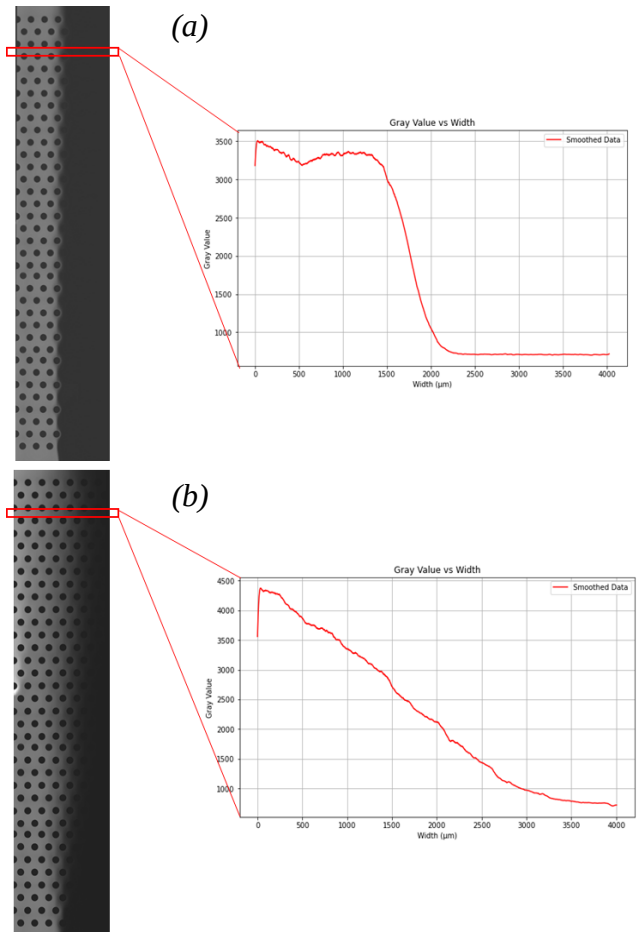


Figure 3 - Fluorescein mixing experiments for (a) Q = 0.5 ml/h (b) Q = 0.2 ml/h.

A stable gradient was established after t = 37s, for flow rates up to 0.5 ml/h (33.3 µL/min). To confirm this, an experiment was performed where an oxygen sensing optical fiber was inserted into the wider channel at the end of the gas exchange portion of the device, and 3 different flowrates were imposed, showing that oxygen was being effectively removed from the solution (**Figure 2**).

For verifying the shape of the gradient, a mock experiment using fluorescein was performed to show the enhanced mixing arising from the porous media. Fluorescein at a concentration of 1E-4 mol/L was injected from the left channel of the device, while pure DI water was injected from the right. Flow rates were varied from 1 ml/h to 0.1 ml/h by 0.05 ml/h increments. A stable, linear gradient was formed for a flow rate of 0.2 ml/h (**Figure 3**).

Using the determined flowrate of 0.2 ml/h, a *Pseudomonas putida* KT2440 biofilm was seeded and grown over a period of 12 hours inside of the main chamber. Oxygenated LB was injected from the right channel, while deoxygenated liquid was injected from the left. The biofilm development followed almost lineraly the shape of the oxygen gradient, implying that certain parts of the biofilm hoard resources, most likely through overconsumption. Unlike *Pseudomonas aeruginosa*, *P. putida* biofilms seemed to not develop as a stress response to oxygen limitation, but thrive even in high oxygen environments.

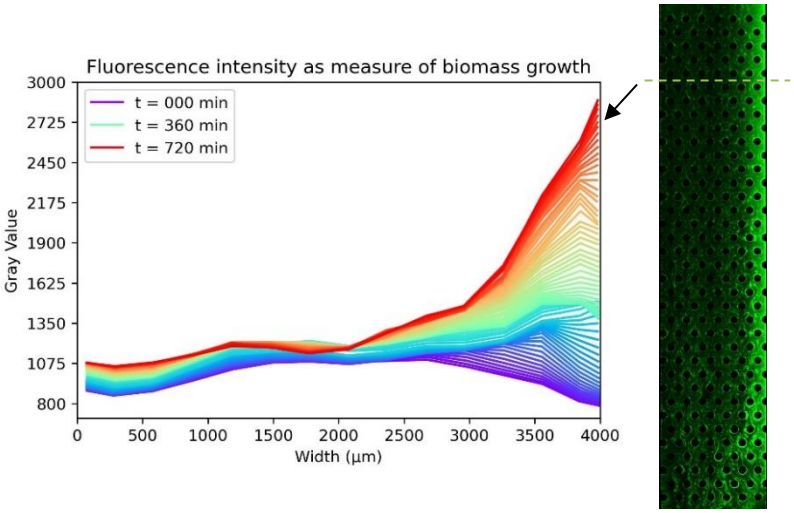


Figure 4 – Biofilm growth in main chamber after 12 hours, graph showing biomass over time for XZ plane cross-section.

CONCLUSION

Here we have shown a device that generates stable chemical gradients by combining approaches from microfluidics and porous media. Future experiments would attempt to leverage this device to investigate a wider array of topics, such as antibiotic resistance, double nutrient gradients and other avenues that might further understanding of biofilms.

Acknowledgment

AL, HT and TLB acknowledge that this project has received funding from the European Union's Horizon 2020 research and innovation program under the Marie Skłodowska-Curie grant agreement N°956457.

REFERENCES

[1] M.H. Muhammad, AL. Idris,X. Fan,Y. Guo, Y. Yu, X. Jin, et al., Front Microbiol, (2020) 11.
[2] HC. Flemming, TR. Neu, DJ.Wozniak, J Bacteriol, 189 (2007) 7945–7.
[3] K. Sauer, P. Stoodley, DM. Goeres, L. Hall-Stoodley, M. Burmølle, PS. Stewart, et al. Nat Rev Microbiol, 20 (2022) 608–20.
[4] J. Park, T. Bansal, M. Pinelis,MM. Maharbiz Lab Chip, 6 (2006) 611–22.
[5] G. Purtschert-Montenegro, G. Cárcamo-Oyarce, M. Pinto-Carbó, K. Agnoli, A. Bailly, L. Eberl, Nat Microbiol, 7 (2022) 1547–57.
[6] DC. Volke, P. Calero, PL. Nikel, Trends Microbiol, 28 (2020) 512–3.
[7] J. Jo, A. Price-Whelan, LEP Dietrich, Nat Rev Microbiol 20 (2022) 593–607.
[8] CJ. Wolfram, GW. Rubloff, X. Luo, Biomicrofluidics (2016) 10.
[9] B. Lin,A. Levchenko, Front Bioeng Biotechnol (2015) 3.
[10]EM. Lucchetta,JN. Lee, LA. Fu, NH. Patel, Ismagilov RF. Nature (2005) 434.

T *– Education*

MARIA GOEPPERT MAYER

T. Halaši[1], S. S. Kalamković[2], M. Ž. Kalamković[3] and J. M. Kalamković[4]

[1]*Faculty of Science, Department of Chemistry, Biochemistry and Environmental Protection, Methods of Teaching Chemistry, History of Chemistry, University of Novi Sad, Trg Dositeja Obradovića 3, 21000 Novi Sad, Serbia.* (*tibor.halasi@dh.uns.ac.rs*)
[2]*Primary School „Prva vojvođanska brigada", Seljačkih buna 51a, 21000 Novi Sad, Serbia*
[3]*School for elementary and secondary education with students' home "Milan Petrović", Novi Sad, Serbia*
[4]*Faculty of Technical Sciences, Biomedical Engineering, University of Novi Sad, Trg Dositeja Obradovića 6, 21000 Novi Sad, Serbia.*

DOI: https://doi.org/10.46793/Phys.Chem24II.745H

ABSTRACT
Maria Goeppert Mayer was a theoretical physicist who contributed significantly to the nuclear physics. She was awarded the Nobel Prize (1963) with collaborators for proposing the nuclear shell model of the atomic nucleus.

INTRODUCTION

Maria Goeppert (Maria Gertrud Kathe Mayer - Maria Göppert Mayer; Fig 1) was born on 28 June 1906 in Katowice Silesian city in Prussia, former German Empire (now Katowice is in Poland). She was the only child of Friedrich Göppert (a professor of pediatrics) and his wife Maria née Wolff. She lived in Göttingen from 1910 until her marriage. Just at a time when quantum mechanics is in its infancy and very attractive, after the Abitur (entrance exam) in Hanover in 1924, Maria first started studying mathematics, but very quickly she realized that she was more attracted to physics [1]. What's more, she aims to get a doctorate in physics. In 1930, Maria married Joseph Edward Mayer (1904-1983), an American Rockefeller, and moved to the United States. They had two children, Maria Ann (1933-2005, married to Donat Wenzel) and Peter Conrad (1938-2016, a graduate student of economics in Berkeley) [2]. Also (1930) in the doctoral thesis, Maria elaborated the theory of possible two-photon absorption of atoms. At Columbia University, she worked in 1937; it is interesting that she was not paid for that work. In 1946 Maier became a volunteer associate professor of physics at the University of Chicago and a senior physicist at Argonne National Laboratory [3]. Before, in December 1941, she took up her first paid professional position, teaching science part-time at Sarah Lawrence College [4]. In 1960, she was appointed full professor of physics at the University of California, San Diego. Maria was a famous and recognized scientist. She was a member of the National Academy of Sciences and a corresponding member of the Akademie der Wissenschaften in Heidelberg. She received honorary doctorates from Russell Sage College, Mount Holyoke College and Smith. It is interesting that the Crater Goeppert Mayer on Venus, which has a diameter of about 35 km, was named after Goeppert-Mayer. Maria died in San Diego, California on February 20, 1972. She was buried at *El Camino Memorial Park* in San Diego.



Figure 1. Maria Goeppert Mayer (1906 - 1972).



Figure 2. Maria Goeppert Mayer walking into the Nobel ceremony with King Gustaf VI Adolf of Sweden in 1963.

BIBLIOGRAPHY

Maria slowly developed into a chemical physicist and with Herzfeld (Karl Ferdinand Herzfeld, 1892-1978) worked in the field of quantum mechanics, on the spectrum of benzene, on the color of organic molecules. From 1931 to 1933, Maria collaborated with Max Born (1882-1970); together they were writing the articles for the "Handbuch der Phisik". Maria's good friends were Urey (Harold Clayton Urey, 1893-1981) and Fermi (Enrico Fermi, 1901-1954). At Fermi's urging, Maria investigated the valence shell of undiscovered transuranic elements. Using the Thomas–Fermi model, she predicted a new series like the rare earth elements. Between 1941 and 1945, Mayer with Teller (Edward Teller, 1908-2003), for the Manhattan Project at Columbia, work on the separation of isotopes of uranium. They were developing Teller's Super bomb. They were finding a way to separate the fissile isotope uranium-235 from natural uranium. They investigated the chemical and thermodynamic properties of uranium hexafluoride, as well as the possibility of separating isotopes by photochemical reactions. The method was impractical until the development of lasers and the separation of isotopes by laser excitation [3].

With the collaborators (J. Hansom D. Jensen and Eugene Wigner) [5], Maria developed a mathematical model for the structure of nuclear shells. Namely, the structure of the nucleus is like the structure of electrons in an atom. The fact that as Haxel (Otto Haxel, 1909-1998), Jensen (Johannes Hans Daniel Jensen 1907-1973) and Suess (Hans Eduard Suess, 1909-1993), whom she had never met, Maria gives the same explanation related to the structure of nuclear shells; at the same time, this helped convince her that the model correct. The model explains why a certain nucleus that have the magic number of nucleons (so-called Conventional nuclear magic numbers: 2, 8, 20, 50, 82, and 126 (Table 1) have abnormally high binding energy and zero electric quadrupole

moment (they are spherically symmetric). This periodicity in the properties of nuclei, which is like the periodic change in the properties of atoms, leads to the belief that nuclei have a structure of shells, like atoms. Namely, in atomic nuclei, nucleons (protons and neutrons) have a two-hexagonal interaction with each other. The binding potential energy between two nucleons (N-N) is a function of their inter-radial distance. The energy of the N-N bond, as well as the energy of nucleon separation, depends on the number of nucleons in the nucleus; the energy functions have maxima or discontinuities, respectively, for the values of some even numbers of nucleons (so-called magic numbers) for which the nucleus has a stable structure (Table 1), but also indicates the arrangement of nuclei in the form of structure shells.
[5]

The Shell Nuclear Model is only one of the models of the structure of the nucleus. Thus, there are several of them, such as the Liquid Drop Model, the Independent Particle Model, the Fermi Gas Model and the General Nuclear Model. All models have advantages and disadvantages. Nevertheless, the Shell Model has advantages over other models, because it successfully predicts the energy states of the nucleus, their shape, quadrupole electric moment and nuclear spin.

Table 1. The magic numbers of nuclides (protons and neutrons) of isotopes.

Number of protons	2	8	20	28	50	82	126
	^{4}He	^{16}O	^{40}Ca	^{58}Ni	^{112}Sn	^{204}Pb	
		^{17}O	^{42}Ca	^{60}Ni	^{114}Sn	^{206}Pb	
		^{18}O	^{43}Ca	^{61}Ni	^{115}Sn	^{207}Pb	
			^{44}Ca	^{62}Ni	^{116}Sn	^{208}Pb	
			^{46}Ca	^{64}Ni	^{117}Sn		
			^{48}Ca		^{118}Sn		
					^{119}Sn		
					^{120}Sn		
					^{122}Sn		
					^{124}Sn		
Number of neutrons	2	8	20	28	50	82	126
	^{4}He	^{15}N	^{36}S	^{48}Ca	^{86}Kr	^{136}Xe	^{208}Pb
		^{16}O	^{37}Cl	^{50}Ti	^{87}Rb	^{138}Ba	^{209}Bi
			^{38}A	^{51}V	^{88}Sr	^{139}La	
			^{39}K	^{52}Cr	^{89}Y	^{140}Ce	
			^{40}Ca	^{54}Fe	^{90}Zr	^{141}Pr	
					^{92}Mo	^{142}Nd	
						^{144}Sm	

Mayer received the Nobel Prize for Physics in 1963. She shared it with J. Hansom D. Jensen and Eugene Wigner [5] for their contribution to the development of the shell model which is related to the structure of atomic nuclei. The model was applied successfully for explanation the fluorescence, excited by two photons, in a europium-doped crystal. Maria was the second woman to

receive the Nobel Prize for Physics (Fig. 2), after Maria Salomea Skłodowska-Curie (1867-1934). The third woman to receive the Nobel Prize in Physics in 2018 is Donna Theo Strickland (1959-)

CONCLUSION

Maria's character and work are is an inspiration to scientists, especially women, to follow their research mission and push the boundaries in science, especial in physic world.

REFERENCES

[1]Biographical. Nobel Prize.org. Nobel Prize Outreach AB 2024. Sun. https://www.nobelprize.org/prizes/physics/1963/mayer/biographical/ (Accessed, May 19, 2024).
[2]Nobel Prize Awarded Women. Nobel Prize Official site. The Nobel Foundation. http://nobelprize.org/nobel_prizes/lists/women.html (Accessed May 19, 2024).
[3]The Nobel Prize in Physics 1963. Nobel Prize Official site. The Nobel Foundation. http://nobelprize.org/nobel_prizes/physics/laureates/1963/index.html (Accessed May 19 2024).
[4]Sarah Lawrence College - The College Archives (2024). Maria Goeppert Mayer: Revisiting Science at Sarah Lawrence College. https://www.sarahlawrence.edu/archives/exhibits/maria-goeppert-mayer-exhibit/ (Accessed, May 19, 2024).
[5]Maria Goeppert Mayer (1963). The shell model. Nobel Lecture, pp. 20-37, https://www.nobelprize.org/prizes/physics/1963/mayer/lecture/ (Accessed, May 19, 2024).

LOUIS DE BROGLIE

T. Halaši[1], S. S. Kalamković[2], M. Ž. Kalamković[3] and J. M. Kalamković[4]

[1]"Association of Cluster Chambers for Environmental and Sustainable Development", Novi Sad,Sebia. (tibor.halasi@dh.uns.ac.rs)
[2]Primary School „Prva vojvođanska brigada", Seljačkih buna 51a, 21000 Novi Sad, Serbia
[3]School for elementary and secondary education with students' home "Milan Petrović", Novi Sad, Serbia
[4]Faculty of Technical Sciences, Biomedical Engineering, University of Novi Sad, Trg Dositeja Obradovića 6, 21000 Novi Sad, Serbia.

DOI: https://doi.org/10.46793/Phys.Chem24II.749H

ABSTRACT
The physicist Louis de Broglie (*Louis Victor Pierre Raymond, 7th Duc de Broglie*) conducted revolutionary research in the field of quantum mechanics. In his doctoral thesis (1924), he pointed out the dual nature of matter, and for that discovery he received the Nobel Prize in Physics (1929).

BIOGRAPHY
Louis de Broglie (*Louis Victor Pierre Raymond, 7th Duc de Broglie*; Fig. 1) was a French physicist known for his groundbreaking work in quantum mechanics. De Broglie was Born in Dieppe, Seine-Maritime (France) on August 15. 1892. He came from a the famous aristocratic family of Broglie with a long history of military service. Despite his family's expectations for him to pursue a career in the military, de Broglie had a passion for science and what's more, it will become one of the most influential physicists of the 20th century.



Figure 1. Louis de Broglie (1892 - 1987). [1]

De Broglie's father was Louis-Alphonse-Victor, the 5th Duke de Broglie (1846–1906). His mother Pauline d'Armaille (1851–1928) was the granddaughter of Napoleon's general Philippe Paul, Count de Segur. De Broglie was the youngest, fifth child. His brothers and sisters were also well-known. His sister was Albertina (1872–1946), later Marchioness de Luppe. Brother Maurice (1875–1960) was a famous experimental physicist. Brother Philip (1881–1890) unfortunately passed away two years before Louis was born. Sister Pauline, Countess de Pange (1888–1972) was a renowned writer [1].

Louis loved reading. He was particularly interested in History, especially Politics. He had a good texts memory and read quickly. The ministers of the Third Republic of France especially fascinated him. De Broglie began his career in the humanities. Many thought he would become a great statesman in the future. DHe obtained his first degree (licence ès lettres) in History. Later, he switched to Mathematics and Physics, and obtained a degree (licence ès sciences) in Physics.
Lewis died a bachelor on March 19, 1987.

BIBLIOGRAPHY

He carried out his first research (20nd years of the last century) in the laboratory of his older brother Maurice. He studied the properties of the photoelectric effect as well as investigated the absorption of X-rays and this phenomenon describes using Bohr's theory (Niels Hendrik David Bohr, 1885–1962). He investigated the X-ray specters which are important for elucidating the structure of the inner electron shells of atoms. He did experiments with Alexandre Dauvillier (Alexandre Dauvillier, 1882–1979). Then the shortcomings of the existing schemes for the distribution of electrons in atoms were discovered. These deficiencies were remedied by Edmund Stoner (Edmund Clifton Stoner, 1899–1968). De Broglie was also involved in elucidating the insufficiency of Sommerfeld's formula (Arnold Johannes Wilhelm Sommerfeld, 1886–1951) for determining the position of lines in X-ray spectra. When the First World War began in 1914, de Broglie offered his services to the army in developing radio communication. The end of the war allowed de Broglie to continue his studies in Mathematics and in 1924 he presented his thesis on the wave nature of electrons in an atom. De Broglie's theory about the wave nature of matter was confirmed through electron diffraction.

Part of Louis de Broglie's research was experimentally confirmed by Davisson (Clinton Joseph Davisson, 1881–1958) and Germer (Lester Halbert Germer, 1896–1971). The entire work on the structure of the atom was completed in 1926 by Schrödinger (Erwin Rudolf Josef Alexander Schrödinger, 1887–1961). Schrödinger formulated the wave equations, which give the result of the probability of finding an electron near the nucleus. Later the concept of electron orbit stopped being used. His work led to the creation of a new branch of Physics known as Wave Mechanics, capable of explaining the wave nature of electrons in an atom.

How Lewis arrived at the idea of the dual nature of matter. He asked the question: "If light has particle properties in addition to wave properties, should particles of substance, such as, for example, electrons, also have wave properties in addition to particle properties?" The result of the answer was the de Broglie equation relates wavelength to particle momentum, that is,

$$\lambda = \frac{h}{p} = \frac{h}{\gamma m v} = \frac{h}{mv}\sqrt{1 - \frac{v2}{c2}}$$

where λ is the particle wavelength, h is Planck's constant, p is the momentum of the particle, m is the rest mass of the particle, v is the velocity of the particle, γ is the Lorentz factor and c is the speed of light in vacuum. This expression for the de Broglie wavelength is valid for relativistic particles as well as for particles moving at speeds much lower than the speed of light. De Broglie waves are not electromagnetic waves but have a specific nature for which no analogy can be found in nature. These waves, called matter waves, represent the particle itself. Their speed is not equal to the speed of light and is not constant.

Louis de Broglie became the youngest member of the *Academy of Sciences* in 1933, and in 1942. he became the permanent secretary of the said institution. He became a member of the French Academy on October 12, 1944, under exceptional circumstances. Louis de Broglie was an advisor to the French Atomic Energy Commission after 1945. He was awarded the Kalinga Prize of UNESCO in 1952. Prince de Broglie was awarded the Grand Cross of the *Legion of Honor* in 1961.

His most important publications are: Recherches sur la théorie des quanta (Research on the quantum theory), 1924; Ondes et mouvements (Waves and motions), Gauthier-Villars, 1926; La mécanique ondulatoire (Wave mechanics), Gauthier-Villars, 1928; Non-linear Wave Mechanics: A Causal Interpretation, 1960; Introduction to the Vigier Theory of elementary particles, 1963 and so on. In addition to his strictly scientific publications, he was the author of several books, including Matter and Light, On the Paths of Science, Certainties and Uncertainties of Science.

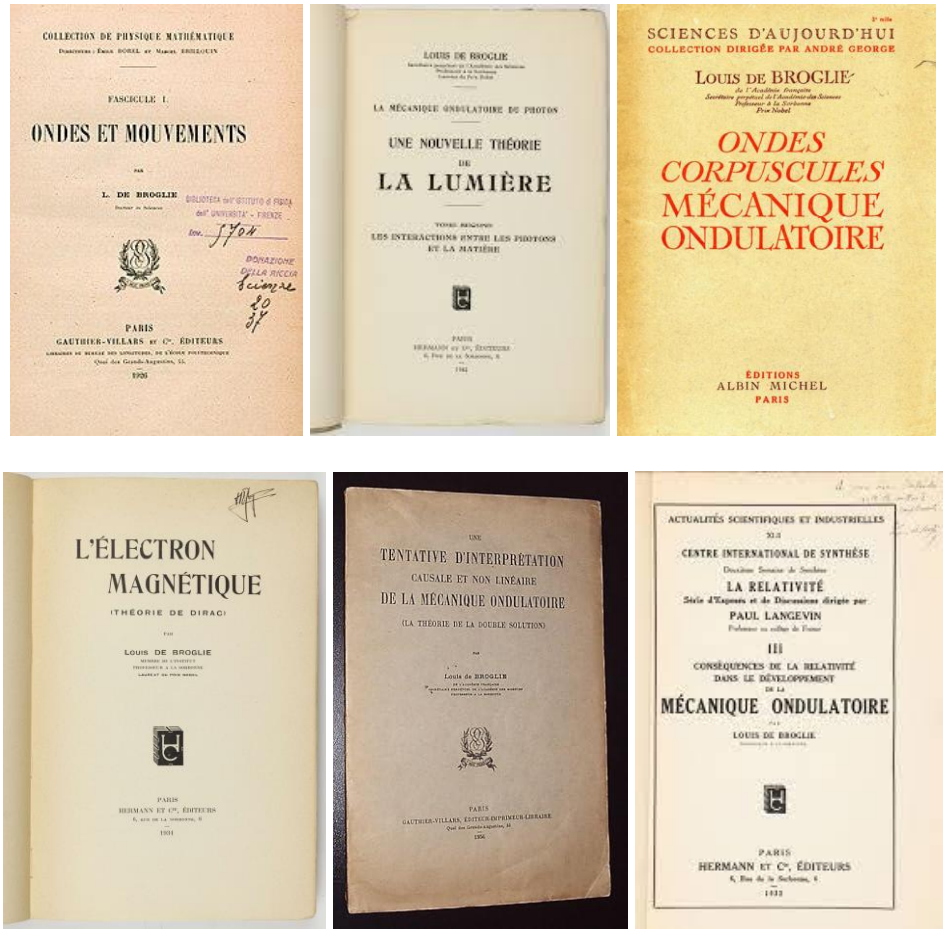


Figure 2. Some books title pages by Louis de Broglie.

NOBEL PRIZE

Physicist Orest Danilovich Khvolson (Оре́ст Дани́лович Хво́льсон, 1852–1934) nominated the de Broglie brothers for the Nobel Prize in 1925 and 1926 for their work in the field of X-rays. Only later, in 1929, did Lewis receive the Nobel Prize in Physics for the discovery of the dual nature of matter, more precisely more precisely the electrons.

EDUCATION WORK

De Broglie was not only a good scientist, but also an educator and mentor to many young physicists. He was a professor at the Sorbonne in Paris. His contribution to the development of the Henri Poincaré Institute, a renowned center for Theoretical Physics, is great [2].

CONCLUSION

Louis de Broglie is a pioneer and pivot in the world of Physics. He left behind a legacy with lots of innovative ideas have shaped our understanding of the atomic quantum realm. His outstanding and magnificent work inspires current researchers as well.

REFERENCES

[1] *Interenet Archive The Way Back Machine* http://www.academie-francaise.fr/immortels/base/academiciens/fiche.asp?param=580 (3/24/2024).

[2] J. Baggott. J. (2020). *The Quantum Cookbook: Mathematical Recipes for the Foundations for Quantum Mechanics*. De Broglie's Derivation of $\lambda = h/p$: Wave–Particle Duality, pp. 73-88. London: Oxford University Press, DOI: 10.1093/oso/9780198827856.001.0001.

INDEX

Abdelghany T.	No ORCID	139		
Aćimović D.	0000-0001-7506-9684	73	77	81
Adamović V.	0000-0002-9644-2430	531		
Ajduković M.	0000-0003-4219-6737	69	93	97
Albanese P.	0000-0002-0901-0956	549		
Aleksić M.	0000-0002-5332-7117	199	203	
Andreev S.V.	0000-0003-2405-9931	297		
Antanasković A.	0000-0003-4088-8748	447	459	531
Antić B.	0000-0002-5693-6401	635		
Antonijević Dj.	0000-0002-6955-7566	369	381	373
Antonijević Nikolić M.	0000-0003-4277-9780	577	663	
Avdalović J.	0000-0001-9917-7997	219	495	727
Avdović E.	0000-0003-2473-9603	689	53	
B. Čolović M.	0000-0001-5037-9985	603		
Bajuk-Bogdanović D.	0000-0003-2443-376X	539		
Banković P.	0000-0002-9732-7370	69	93	173
Basagni A.	0000-0001-9662-5125	413		
Basuki T.	No ORCID	65		
Becker T.J.	0009-0006-9815-405X	285		
Bekić B.	0009-0000-5522-3736	377		
Belaj F.	0000-0001-9749-2109	569		
Beljkas M.	0009-0000-5219-1257	647		
Beškoski V.	0000-0002-6372-4706	207	421	425
Biočanin V.	0000-0002-1607-4069	369	373	
Blagojević S.M.	0000-0002-0451-5912	417	551	
Blagojević S.N.	0000-0002-6085-138X	551		
Blagojević V.A.	0000-0001-8102-989X	257	261	265
Bobić K.	0000-0001-9575-0960	243	731	735
Boháč A.	No ORCID	203		
Bojić A.	0000-0002-9853-2747	349	353	357
Bojić D.	0000-0003-0737-4550	357		
Bondžić A.M.	0000-0002-7403-2318	627	631	705
Bondžić B.P.	0000-0002-8249-6091	627	631	705
Božić B.	0000-0001-9910-2741	269		
Bracanović I.	0000-0002-8526-8633	329	333	499
Brau F.	0000-0002-8715-5464	35		
Brdarić T.	0000-0003-2547-7123	73	77	81
Brković S.	0000-0002-8584-5648	187	191	195
Bubanja I.N.	0000-0002-3737-2532	155		
Budroni M.	0000-0003-1410-1745	35		
Bulatović S.S.	0000-0002-7861-4489	429	433	511
Čarapić M.	No ORCID	199		

Carević M.	0000-0002-7212-4438	309			
Čebela M.	0000-0001-6120-6924	557			
Cebzan A.	0009-0007-7640-5118	643			
Červený J.	0000-0002-5046-3105	127			
Ćetković D.	0000-0003-3444-1798	381			
Chibiryaev A.M.	0000-0002-4566-579X	17			
Choiński M.	0000-0001-6157-8963	151			
Ciganović J.	0000-0002-3860-4374	695			
Ćirić A.	0000-0003-0993-6094	365			
Čolović M.B.	0000-0001-5037-9985	607	611		
Čomor M.	0000-0002-7222-4500	309			
Čupić A.	0000-0003-4356-2962	507			
Čupić Ž.	0000-0002-4939-6718	143	151	167	
Ćurčić M.	0000-0002-4326-4036	385			
Cvjetinović Đ.	0000-0002-3523-4742	515			
Daković A.	0000-0002-7385-0458	455	491	659	
Danilović V.	0000-0001-9925-5457	369	373		
Davidović S.	0000-0001-7383-3976	317			
De Wit A.	0000-0002-3231-0906	35	147		
Đekić Lj.	0000-0003-0172-5305	365			
Despotović A.	0000-0001-9550-0240	369	373	381	
Dević G.	0000-0001-5606-3308	219	495		
Dimić D.	0000-0001-8127-5396	539	581	689	
Dimitrić Marković J.	0000-0003-4796-6251	581			
Dimitrijević A.	0000-0002-8346-9909	519	523	527	
Dimitrijević I.	No ORCID	491			
Dimitrov O.	0000-0002-5484-6488	397			
Djokovic N.	0000-0001-9972-3492	593	639	643	647
Djuric A.	0000-0002-4440-9890	593			
Dobričić V.	No ORCID	203			
Dodevska M.	0000-0001-6030-459X	685			
Dojčinović B.	0000-0003-1479-8060	97			
Đokić M.	0000-0001-7749-9768	507			
Dolan E.	No ORCID	289			
Đorđević D.M.	0000-0001-9797-663X	341	345		
Đorđević I.	0000-0001-5981-9385	597			
Đorđević M.	0000-0001-8068-8906	507			
Đorđević N.	0000-0003-4063-1635	243			
Đošić M.	0000-0002-0869-2182	531			
Dostanić J.	0000-0002-3934-0569	85	101		
Dožić A.	0000-0001-9691-4357	381			
Dragićević A.	No ORCID	239			
Dragović R.	0000-0002-4662-7808	507			
Dragović S.	0000-0003-0566-0182	503	507		

Drakulić D.	0000-0003-1448-9639	243		
Dražić B.	0000-0003-1723-3268	577	663	
Đukić D.	0009-0001-7863-1596	333		
Đuričić-Milanković J.	0000-0001-9624-8534	663		
Đurkić T.	0000-0003-1996-6676	483		
Džambaski Z.	0000-0002-3864-3904	627	631	705
Džunuzović J.V.	0000-0003-0681-9781	405	409	413
Džunuzović E.S.	0000-0002-7791-4076	405	409	413
Emel'yanenko V.N.	0000-0002-8230-4037	253		
Eraković Z.	0000-0001-8786-8328	479		
Eregić M.	0000-0002-1365-4631	479		
Fabian M.	0000-0002-8893-4195	701		
Facchini G.	0000-0003-4500-5748	35		
Farkas S.	No ORCID	293		
Filipović A.	0000-0002-8321-1289	627	631	705
Filipović N.	0000-0003-2261-8066	389		
Filipović Tričković J.	0000-0001-5450-0842	735		
Fišić N.	0009-0002-2261-2879	321		
Fronczak M.	0000-0002-8238-0232	59	101	
Gajić B.	0000-0001-8270-0198	507		
Gaković B.	0000-0002-5537-7804	393		
Gašić U.	0000-0001-5384-8396	667		
Gavrilovic Lj.	0000-0002-0815-4536	15		
Gavrilović Lj.	0000-0003-1453-9990	313		
Georgijević J.	0000-0003-1581-5539	187	195	
Gerić T.	0000-0002-9303-5231	313		
Glavinić U.	0000-0003-2143-1611	235		
Glišić S.	0000-0001-5691-1055	651	655	
Gojgić Cvijović G.	0000-0001-5598-0585	421	425	
Golubović L.	No ORCID	581		
Gordić V.	0009-0006-6382-6063	285		
Gorjanović S.	0000-0003-3676-5892	685		
Grigorov M.V.	0000-0002-9431-8874	587		
Grujić S.	0000-0003-4748-1391	483	487	
Grujičić M.	0000-0001-6276-2906	389		
Guševac Stojanović I.	0000-0001-5307-2970	243	735	731
Gvozdić E.	0000-0001-9181-0161	483		
Hadnađev-Kostić M.	0000-0001-8091-4213	85		
Halaši T.	No ORCID	745	749	
Hedrih A.	0000-0001-7598-900X	151		
Hey Hawkins E.	0000-0003-4267-0603	285		
Holló G.	0000-0001-9920-4801	293	549	
Horváth D.	0000-0003-3852-6879	129		
Horvath R.	0000-0001-8617-2302	549		

Huš M.	0000-0002-8318-5121	101		
Hutchinson E.	No ORCID	139		
Ilic A.	0009-0003-2466-0580	643		
Ilić M.	0000-0002-7102-1701	219	495	
Ilić V.	0000-0001-8110-1484	369	373	381
Ilić-Stojanović S.	0000-0003-2416-8281	479		
Itatani M.	0000-0003-1025-0452	549		
Ivanović T.G.	0000-0002-3459-7680	39		
Ivanović-Šašić A.	0000-0002-1600-5549	143	151	167
Ivković M.	0000-0003-4421-0002	49		
J. Dimitrić Marković	0000-0003-4796-6251	13		
J. Prins L.	0000-0001-6664-822X	3		
J. Žakula J.	0000-0001-7280-3273	611		
Janjetović K.	0000-0003-1387-480X	369	373	381
Janković B.	0000-0001-7520-1972	269		
Janković D.	0000-0003-3938-2790	573	635	
Janković M.	0000-0002-2255-7163	269		
Janošević Ležaić A.	0000-0003-4343-0572	89		
Ječmenica Dučić M.	0000-0002-6437-519X	81		
Jelenković B.	0000-0001-8276-1169	337		
Jelić I.	0000-0003-1406-2416	313		
Jelić M.	0000-0003-3723-4313	389		
Jevremović A.	0000-0003-3382-4287	321		
Jevtović V.	0000-0002-2180-8303	681		
Jia X.	0000-0003-0513-166X	215		
Jimenez Martinez J.	No ORCID	739		
Jocić A.	0000-0001-6731-8396	519	523	527
Joksimović K.	0000-0002-9371-4381	207	495	727
Jovanović Z.	0000-0003-1727-4852	389		
Jovanović D.	0000-0003-1665-7106	313		
Jovanović D.	0000-0002-9459-8271	627		
Jovanović D.	0000-0002-6567-1724	727		
Jovanović J.	0000-0002-7537-9591	417		
Jovanović M.	0000-0002-7312-443X	199		
Jovanović M.	0000-0001-9617-1151	681		
Jovanović S.	0000-0003-3577-5060	389		
Jovanović T.	0000-0001-5160-7732	565		
Jovanović V.	0000-0002-0446-7762	565		
Jović M.	0000-0002-3293-5797	503	507	
Jovičić Milić S.	0000-0001-9313-6983	53	689	
Jović-Jovičić N.	0000-0001-9940-9508	69	93	97
Kadinov G.	0000-0001-8604-7704	701		
Kalagasidis Krušić M.	0000-0003-0517-1952	85		
Kalamković J.M.	No ORCID	745	749	

Kalamković M.Ž.	No ORCID	745	749	
Kalamković S.S.	No ORCID	745	749	
Kalijadis A.	0000-0002-6897-4691	329	333	499
Kaluđerović G.N.	0000-0001-5168-1000	285		
Kamal K.M.	0000-0001-9855-157X	101		
Karić N.	0000-0002-7521-4340	463		
Kasalica K.	0000-0001-7731-2043	727		
Kazi S.S.	0009-0000-7133-2609	15		
Knyazev A.V.	0000-0002-2880-3484	253		
Kodranov I.	0000-0001-5871-1487	207		
Kokunešoski M.	0000-0003-1732-002X	317		
Kolev H.	0000-0002-4231-9306	701		
Kopitsyn D.	0000-0002-5791-4917	545		
Koričanac L.B.	0000-0001-5497-284X	603	607	611
Koskin A.P.	0000-0002-0091-2945	61		
Kostić M.	0000-0001-6488-5184	349	353	357
Kovačević M.	0000-0001-8858-6728	73	77	81
Kováčiková L.	No ORCID	203		
Krajišnik D.	0000-0002-5525-0109	659		
Krajnović T.	0000-0002-6938-6154	285		
Krmpot A.J.	0000-0003-2751-7395	213		
Krstić A.	0000-0001-7418-6723	329	333	499
Krstić D.Z.	0000-0002-9192-8087	603	607	611
Krstić J.	0000-0003-0321-0698	93	183	
Krstić M.	0000-0002-1134-8390	301	305	
Krstić M.	0000-0002-2109-0258	565		
Kuchierskaya A.	0000-0002-1167-7004	545		
Kukic E.	No ORCID	647		
Kumrić K.	0000-0002-9996-8243	479		
Kurunczi S.	0000-0002-6567-5231	549		
Kuzmanović M.	0000-0003-4731-7518	49	539	
Laban B.	0000-0002-7758-445X	557		
Lagzi I.	0000-0002-2303-5965	293	549	
Lahtela-Kakkonen M.	0000-0001-7163-7728	583		
Lau W.M.	0000-0002-2998-6470	139		
Laušević P.	0000-0001-8285-7064	187	191	195
Lazarević J.J.	0000-0001-8980-1688	377	595	
Lazarević N.	0000-0001-6310-9511	595		
Lazarević-Pašti T.	0000-0001-6220-2079	519	523	527
Le Borgne T.	No ORCID	739		
Lente G.	0000-0003-2022-2156	5		
Lješević M.	0000-0002-8164-6043	421	677	
Lončar A.	No ORCID	739		
Lončarević B.	0000-0002-2226-511X	421	425	677

Lončarević D.	0000-0002-2266-337X	85	101	
Lopičić Z.	0000-0002-7251-8699	447	459	531
Lugonja N.	0000-0002-5093-4448	421	425	677
Luo S-J.	No ORCID	215		
Maćešić S.	0000-0002-2317-7111	143	151	167
Macura S.	0000-0002-6054-5163	21		
Maharana S.N.	0000-0002-6561-7410	147		
Maksimović J.	0000-0001-7138-6666	151	163	167
Maksimović-Ivanić D.	0000-0002-8006-5079	285		
Maletić M.	0000-0002-4112-9316	463	467	471
Manić M.	0000-0002-2452-5798	507		
Manojlović D.	0000-0003-1388-6245	207		
Manojlović N.	0000-0001-9170-1790	167		
Marega C.	0000-0002-0485-4180	405	409	413
Marić S.	0000-0002-3982-2664	519	523	527
Marinković D.	0000-0002-6017-2109	709		
Marinković F.	0000-0003-3340-440X	535		
Marinković V.	No ORCID	677		
Marinović S.	0000-0002-2214-0157	69	93	183
Marinović-Cincović M.	0000-0001-6197-1511	565		
Markov P.	0000-0002-9383-0622	397		
Marković M.	009-0000-5619-237X	561		
Marković B.M.	0000-0001-7608-8289	429	433	511
Marković M.	0000-0001-6787-1933	455	491	659
Marković M.	0000-0001-7130-0623	539		
Markovic V.	No ORCID	639		
Marković Z.	0000-0001-5964-049X	53	689	
Martinović J.	0000-0001-8641-1051	243	731	735
Martyanov O.N.	0000-0001-9999-8680	17		
Masek O.	0000-0003-0713-766X	447		
Masnikosa R.	0000-0002-5220-4334	223	227	
Mašojević D.	0000-0002-7051-8628	317		
Matić Bujagić I.	0000-0001-8459-873x	483		
Meyer J.	No ORCID	15		
Micić D.	0000-0001-6905-8954	673	685	
Mićić S.	0009-0009-3654-0280	89		
Mihajlović-Lalić Lj.E.	0000-0003-4802-432X	569		
Mijatović S.	0000-0001-9509-9098	285		
Mijović M.	0000-0003-1884-6066	635		
Mikavica I.	0000-0001-9533-1360	459		
Miladinović J.M.	0000-0001-6259-8245	39		
Miladinović Z.P.	0000-0003-2086-9064	39		
Miladinović Z.R.	0000-0002-0019-8091	301	305	
Milanković V.	0000-0002-7706-9036	519	523	527

Milanović Z.	0000-0001-9953-3269	569	573	635
Milenković D.	0000-0001-7083-2257	53	689	
Miletić S.	0000-0002-7263-2686	495	727	
Miletić Vukajlović J.	0000-0002-9873-1906	243	731	735
Milić J.	0000-0001-7248-7602	219	495	677
Miličević D.	0000-0001-7746-0708	301		
Milinković S.	0009-0008-2545-702X	365		
Milojević-Rakić M.	0000-0002-3590-6094	321		
Milojković J.	0000-0002-6117-0703	447	459	531
Milošević K.	0000-0002-2746-6543	85		
Milošević I.R.	0000-0002-4463-5986	361	695	
Milošević M.	0000-0002-3869-5800	179	325	
Milutinović-Smiljanić S.	0000-0003-1357-4970	369	373	381
Mirković M.	0000-0003-2335-455X	329	333	
Mirković M.	0000-0002-3176-5554	569	573	635
Mitić D.	0000-0002-0650-8193	239		
Mitrić J.	0000-0002-1526-3976	595		
Mitrović J.	0000-0001-9634-7727	349	353	357
Mitrović S.	0000-0002-0442-4455	191	195	
Mladenova R.	No ORCID	397		
Mojović M.	0000-0002-1868-9913	231	235	239
Mojović Z.	0000-0003-4804-0776	175	179	309
Morozov E.V.	0000-0003-1561-3937	17		
Mraković A.	0000-0003-4569-5857	503		
Mravik Ž.	0000-0003-2327-5165	389	491	
Mudrinić T.	0000-0001-7467-8330	97	173	183
Murić B.	0000-0003-3003-1708	337		
Mušović J.	0000-0001-6985-2701	519	523	527
Najdanović S.	0000-0001-9383-4394	349	353	357
Nakarada Đ.	0000-0002-0154-6430	231	235	239
Nakashima S.	0000-0001-6870-802X	65		
Nastasijević B.	0000-0002-4529-1599	425		
Nastasović A.B.	0000-0002-8589-6437	511	429	433
Natić M.	0000-0002-6610-297X	667		
Nedić N.Ž.	0009-0002-5621-9223	511	429	433
Nedić-Vasiljević B.	0000-0003-1967-3937	93		
Negrojević L.	0000-0002-1550-6026	147		
Német N.	0000-0001-6800-1710	293		
Ng K.W.	0000-0003-2541-4763	139		
Nikodinović-Runić J.	0000-0002-2553-977X	421		
Nikolić G.M.	0000-0003-4827-4281	341	345	587
Nikolić J.	No ORCID	39		
Nikolic K.	0000-0002-3656-9245	199	639	643
Nikolić M.G.	0000-0002-6914-6011	341	345	637

Nikolić N.	0000-0002-7665-9480	325		
Nikolić N.	0000-0002-5730-7391	417		
Nikolić S.N.	0000-0002-2082-9954	213		
Nikolić-Kokić A.	0000-0002-1116-2035	727		
Novakovic K.	0000-0003-3763-2696	139		
Novaković T.	0000-0002-6407-9833	69	175	
Novikov A.	0000-0002-0887-6678	595		
Oasa S.	0000-0003-3800-590X	213		
Obradović J.	0009-0009-1423-2463	451		
Obradović M.	0000-0002-4769-2652	451		
Obradović M.	0000-0002-1349-1924	455	491	
Ognjanović M.	0000-0003-2889-4416	561	635	
Oljačić S.	0000-0001-9128-6072	615	623	647
Onjia A.	0000-0002-5694-7960	429	451	475
Ostojić S.	0000-0002-9853-1189	673		
Ožegović M.	0000-0001-7544-6785	455	491	
Pagnacco M.	0000-0002-1299-7974	163	417	
Panajotović R.	0000-0002-2174-0062	361		
Pantelić B.	0000-0003-1135-1474	219		
Pantelić D.	No ORCID	337		
Pantić B.	0000-0002-2852-9155	97	173	183
Parac-Vogt T.	0000-0002-6188-3957	603	607	611
Parlić J.	0009-0006-0501-0429	69	93	97
Pašti I.	0000-0002-1000-9784	539		
Pastor F.	0000-0003-0813-9085	785		
Pavićević K.	No ORCID	487		
Pavlović V.	0000-0002-1138-0331	333		
Peddis D.	0000-0003-0810-8860	23	289	
Pejčić M.	0000-0001-5379-6020	389		
Pejić N.	0000-0002-8148-8364	89	601	
Pejić S.	0000-0003-4573-2371	735		
Perić Grujić A.	0000-0002-2593-4796	463		
Perić K.	No ORCID	155		
Perić M.	0000-0001-8094-8464	669	573	
Permana S.	No ORCID	65		
Perović I.	0000-0003-4459-1044	187	191	195
Pešić J.	0000-0002-8600-7187	361		
Petković B.B.	0000-0002-2332-9170	557	561	565
Petković D.	0000-0001-5752-5367	389		
Petkovic M.	0000-0001-9637-1380	593		
Petronijević N.	0009-0000-9446-8664	421	425	
Petrović M.	0000-0001-7910-4213	681	667	
Petrović Đ.	0000-0002-1083-0265	479		
Petrović J.	0000-0002-3988-7644	515		

Petrović M.	0000-0002-7537-0327	349	353	357
Petrović R.	0000-0001-9511-5633	183		
Petrović S.	0000-0002-8894-692X	393		
Petrović S.P.	0000-0003-4763-904X	433		
Pijović Radovanović M.	0000-0002-2813-9560	187	191	
Pinheiro J.P.	No ORCID	15		
Pirić D.	0000-0003-4668-595X	223	227	
Plavsic M.B.	0000-0002-9872-5653	25	437	
Plavsic M.M.	0009-0009-8864-4364	25	437	
Popović D.Ž.	0000-0003-4008-5881	39		
Popović G.	0000-0002-4242-1132	615	619	623
Popović K.	0009-0007-5516-3711	663		
Popović M.	No ORCID	235		
Popović-Nikolić M.	0000-0002-8902-3211	615	619	623
Prašnikar A.	0000-0001-9194-6595	101		
Prekodravac J.	0000-0002-5692-0119	709		
Prijović Ž.	0000-0003-1069-2453	635		
Radić D.	0000-0002-0321-5213	681		
Radojević V.	0000-0001-9301-3983	385		
Radojičić T.	No ORCID	467		
Radosavljević A.	0000-0003-0307-3179	179	325	759
Radošević D.	0000-0002-3284-7201	651		
Radovic B.	0009-0006-1133-5705	643		
Radović M.	0000-0002-3972-313X	569	573	635
Radović-Vučić M.	0000-0001-6820-5844	349	353	
Radulović M.	No ORCID	231		
Rahnasto-Rilla M.	0000-0002-8882-747X	593		
Rakić A.	0000-0003-1489-6373	581		
Rakić T.	0000-0001-6959-3439	459		
Rančev S.	0000-0001-6105-0034	353		
Ranđelović A.	No ORCID	345		
Ranđelović D.	0000-0003-4976-7766	459		
Randjelović D.V.	0000-0003-0780-5058	207	413	
Ranković D.	0000-0001-9769-1423	49	539	663
Ranković M.	0000-0002-4752-6152	321		
Rašović A.	0000-0003-1740-9569	257	265	261
Recepoğlu Y.K.	0000-0001-6646-0358	275		
Ristanić M.	0000-0002-6084-7321	235		
Ristić M.	0000-0003-4644-5235	565		
Rmuš Mravik J.	0000-0002-0514-2150	389		
Rosić M.	0000-0001-7093-187X	557		
Rossi F.	0000-0002-1854-532X	293	549	
Rupar J.	0000-0001-5451-8516	89	203	321
Ruzic D.	0000-0002-0546-8265	593		

S. Konstantinović S.	0000-0002-3761-823X	249		
Sagbas B.	0000-0002-4491-0490	393		
Sakharov K.A.	0000-0002-3247-5743	297		
Šalipur H.	0000-0003-0587-2484	101		
Samaržija- Jovanović S.	0000-0003-3642-9741	565		
Sandić Z.P.	0000-0003-1998-7143	433		
Sari Yilmaz M.	0000-0003-0441-7586	333		
Savić B.	0009-0000-2873-6106	695		
Savić A.	0000-0002-2575-0436	239		
Savić J.	No ORCID	249		
Savić M.	0000-0002-6934-9193	635		
Savić N.	0000-0002-6593-3499	603	607	611
Savić Rosić B.	0000-0002-4632-7960	77		
Savić-Šević S.	0000-0002-6406-0745	337		
Savović J.	0000-0001-7828-6385	49		
Savraeva D.V.	0000-0002-5551-4792	297		
Schmitz G.	0000-0003-3860-0469	131		
Schreiber I.	0000-0001-6482-2722	127		
Schumann D.	0000-0001-5643-7701	515		
Schuszter G.	0000-0002-9170-9933	35	293	
Secchi E.	No ORCID	739		
Selivanova A.A.	0009-0004-3814-6811	297		
Semenov A.	0000-0003-0660-6233	595		
Semenov S.N.	0000-0002-5829-2283	129		
Senćanski J.	0000-0002-2020-0435	163	417	
Senćanski M.	0000-0002-7296-3223	651	655	
Seović M.	0000-0002-6341-4708	187	191	195
Shipochka M.	0000-0002-3188-5716	397		
Shopska M.	0000-0002-9714-2464	701		
Simić M.	0000-0001-9518-7709	73	77	81
Simijonović D.	0000-0002-3799-653X	53	689	
Simonović J.	0000-0003-4506-3470	369	373	
Simović-Pavlović M.	0000-0003-0766-059X	163		
Siogka C.	No ORCID	393		
Slimani S.	0000-0002-5830-1864	289		
Smičiklas I.	0000-0002-7384-7312	503	507	
Smiljanić D.	0000-0003-3560-1415	455	491	531
Šolević Knudsen T.	0000-0002-2419-153X	681		
Šoštarić T.	0000-0002-0359-4399	447	459	531
Spasenović M.	0000-0002-2173-0972	377		
Spasić S.	0000-0003-1731-3508	207	495	777
Spasojević J.	0000-0002-1520-5266	179	317	325
Srdic-Rajic T.	0000-0001-9840-6970	593		
Stajčić A.	0000-0002-5892-8819	385		

Stajčić I.	0000-0001-8278-4491	45	269	385
Stamboliev G.	0000-0002-2125-593X	305		
Stambolova I.	No ORCID	397		
Stamenović U.	0000-0001-8676-296X	317		
Stanić V.	0000-0001-9714-3769	313	627	
Stanimirović Z.	0000-0003-2657-8591	235		
Stanisavljev D.	0000-0003-1361-7977	155		
Stankov D.B.	0000-0002-6437-4015	49		
Stanković B.	0000-0003-1649-9005	535	599	
Stanković A.	0000-0002-1680-4260	635		
Stanković D.	0000-0001-7465-1373	569		
Stanković D.	0000-0001-7669-2865	573	635	
Stanković K.	0000-0002-8974-2558	479		
Stefanović I.S.	0000-0002-2679-0341	405	409	413
Stepanenko S.A.	0000-0001-6434-9891	61		
Stevanović G.	0000-0002-2239-2338	69	97	183
Stevanović J.	0000-0003-0906-5911	235		
Stevanović K.	0009-0002-7066-426X	163	651	655
Stoiljković M.	0000-0002-2794-3231	45	269	385
Stojanović D.	0000-0001-6308-7586	471		
Stojanović K.	0009-0003-3467-9875	73	77	81
Stojanović Z.	0000-0002-5989-0031	243		
Stojiljković V.	0000-0002-7005-8588	313	577	
Stojković D.	0000-0002-8258-7479	53	689	
Stojković Simatović I.	0000-0001-7836-4574	417		
Stolić P.	0000-0002-2574-4765	389		
Stoyanova D.	No ORCID	397		
Suljovrujić E.	0000-0001-8774-4341	301	305	
Suručić Lj.T.	0000-0003-4332-8690	429		
Sütő I.	No ORCID	129		
Tabuteau H.	No ORCID	739		
Tadić T.T.	0000-0003-4484-1568	429	433	511
Talip Z.	0000-0002-5095-799X	515		
Tanasković S.	0000-0002-3486-2800	313	577	663
Tasić T.	0000-0003-1988-4064	519	523	527
Tekić D.	0000-0003-2102-3116	519	523	527
Teletina K.	0009-0002-6867-2594	321		
Tenchev K.	0000-0002-9258-2559	701		
Tiiman A.	0000-0002-6136-1630	213		
Todorović A.	0000-0002-2074-1637	731		
Tolić Stojadinović Lj.	0000-0001-8438-5267	487		
Tomašević T.	0009-0003-4443-2040	361		
Tomašević T.	No ORCID	239		
Tomašević-Ilić T.	0000-0003-2870-0765	361		

Tomašević-Ilić T.	0000-0003-2870-0765	377	695	
Tosti S.	0000-0003-4832-6053	443		
Tóth Á.	0000-0001-8254-6354	129		
Traparić I.	0000-0001-6492-2360	49		
Tripković T.	0000-0002-9273-0267	695		
Trišović N.	0000-0002-9231-4810	283		
Trivunac K.	0000-0002-9251-744X	463	467	
Trohidou K.N	0000-0002-6921-5419	289		
Troter D.Z.	0000-0001-6340-5476	249		
Trukhan S.N.	0000-0001-8403-5902	17		
Turovtsev V.V.	0000-0002-4845-1017	253		
Uskoković P.	0000-0001-9543-1732	471		
Uskoković-Marković S.	0000-0003-2750-325X	595	659	
Valenta Šobot A.	0000-0002-8429-1399	735		
Valletti N.	0000-0002-4399-2682	293	549	
Vasić Anićijević D.	0000-0003-0566-3244	81	73	77
Vasić V.	0000-0002-1425-2183	227		
Vasilakaki M.	No ORCID	289		
Vasiljević B.	0000-0002-0335-1987	709		
Veličković S.	0000-0001-5605-6749	45	269	385
Velinov N.	0000-0001-9043-8521	349	357	
Veljković F.	0000-0002-4471-334X	45	269	385
Veljović S.	0000-0001-6408-9153	667		
Veselinović A.M.	0000-0001-9291-6654	715	719	723
Vesković J.	0009-0008-4000-7916	475		
Vlašković T.B.	0009-0006-2013-6388	557		
Vodnik V.	0000-0003-2944-6957	317		
Vranješ-Đurić S.	0000-0002-6340-2387	569	673	635
Vučković N.	No ORCID	203		
Vučkovski M.	0000-0001-6743-8320	631	705	
Vujasin R.	0000-0002-9859-5502	479		
Vujin J.	0000-0002-7081-8364	361	695	
Vukadinović A.	0000-0002-9352-8036	573	635	
Vukčević M.	0000-0003-0416-0741	463	467	471
Vukoje I.	0000-0001-9364-2616	179	317	325
Vukojević V.	0000-0003-0873-5653	213		
Vukotić Todorović N.	0000-0003-2806-1991	731		
Vulić T.	0000-0002-5107-9500	309		
Wurzer C.	0000-0002-8883-7600	447		
Xie M-H.	No ORCID	215		
Xu X.	0000-0001-9820-3153	215		
Yaacoub N.	0000-0002-5583-1165	289		
Yakovlev V.A.	0000-0001-5015-3521	61		
Yüksel A.	0000-0002-9273-2078	275		

Zautsau D.H.	0000-0002-4002-7019	253		
Zdolšek N.	0000-0002-2665-0111	187	191	195
Zemskov E.P.	0000-0001-8896-301X	159	425	727
Zlatanović S.	0000-0002-8450-602X	673	685	
Zlatović M.	0000-0003-4311-1731	329		
Zogović N.	0000-0003-4240-3193	369	373	381
Zverev S.A.	0000-0002-3232-9332	297		
Zvereva A.S.	0000-0002-1919-2810	297		
Žakula J.J.	0000-0001-7280-3273	603	607	
Žerađanin A.	0000-0001-5896-6025	207	425	677
Živković I.	0000-0001-7399-3945	695		
Živković J.V.	0000-0002-1130-2173	715	719	723
Živković S.	0000-0003-1499-1645	73		

List of reviewers	
Aleksandra Bajić	University of Novi Sad, Institute of food technology
Agota Toth	Department of Physical Chemistry and Materials Science, University of Szeged
Aleksandar Devečerski	University of Belgrade, Vinča Institute of Nuclear Sciences, National Institute of the Republic of Serbia
Aleksandar Veselinović	University of Niš, Faculty of Medicine
Aleksandra Daković	Institute for Technology of Nuclear and Other Mineral Raw Materials
Aleksandra Milutinović Nikolić	University of Belgrade, Institute of Chemistry, Technology and Metallurgy, National Institute of the Republic of Serbia
Aleksandra Nastasović	University of Belgrade, Institute of Chemistry, Technology and Metallurgy, National Institute of the Republic of Serbia
Alexander Knyazev	University of Nizhni Novgorod (UNN), Russia, Faculty of Chemistry
Ana Ivanović-Šašić	University of Belgrade, Institute of Chemistry, Technology and Metallurgy, National Institute of the Republic of Serbia
Ana Popović-Bijelić	University of Belgrade, Faculty of Physical Chemistry
Anđelka Hedrih	Mathematical Institute of the Serbian Academy of Sciences and Arts, National Institute of the Republic of Serbia
Andrew Clayton	Swinburne University of Technology, Australia
Anne De Wit	Faculté des Sciences, Nonlinear Physical Chemistry Unit, Belgium
Biljana Šljukić	University of Belgrade, Faculty of Physical Chemistry
Bojan Bondžić	University of Belgrade, Institute of Chemistry, Technology and Metallurgy, National Institute of the Republic of Serbia
Bojan Janković	University of Belgrade, Vinča Institute of Nuclear Sciences, National Institute of the Republic of Serbia
Bojana Marković	University of Belgrade, Institute of Chemistry, Technology and Metallurgy, National Institute of the Republic of Serbia
Bojana Nedić Vasiljević	University of Belgrade, Faculty of Physical Chemistry
Branislav Salatić	The Institute of Physics Belgrade, a National Institute of the Republic of Serbia
Branko Bugarski	Faculty of Technology and Metallurgy, University of Belgrade
Bratislav Obradović	Faculty of Physics, University of Belgrade
Davor Lončarević	University of Belgrade, Institute of Chemistry, Technology and Metallurgy, National Institute of the Republic of Serbia
Dejan Milenković	Institute for Information Technologies Kragujevac, University of Kragujevac
Dragomir Stanisavljev	University of Belgrade, Faculty of Physical Chemistry
Dunja Drakulić	University of Belgrade, Vinča Institute of Nuclear Sciences, National Institute of the Republic of Serbia
Dušan Dimić	University of Belgrade, Faculty of Physical Chemistry
Goran Janjić	University of Belgrade, Institute of Chemistry, Technology and Metallurgy, National Institute of the Republic of Serbia
Goran Nikolić	Faculty of Technology, Leskovac, University of Niš
Gordana Ćirić-Marjanović	University of Belgrade, Faculty of Physical Chemistry
Guy Schmitz	Université Libre de Bruxelles, Belgium
Igor Pašti	University of Belgrade, Faculty of Physical Chemistry
Irena Novaković	University of Belgrade, Institute of Chemistry, Technology and Metallurgy, National Institute of the Republic of Serbia

Irving Epstein	Brandeis University
István László	Budapest University of Technology and Economics
Itana Nuša-Bubanja	University of Belgrade, Faculty of Physical Chemistry
Ivan Stefanović	University of Belgrade, Institute of Chemistry, Technology and Metallurgy, National Institute of the Republic of Serbia
Jasmina Dimitrić-Marković	University of Belgrade, Faculty of Physical Chemistry
Jasna Džunuzović	University of Belgrade, Institute of Chemistry, Technology and Metallurgy, National Institute of the Republic of Serbia
Jelena Đorović Jovanović	Institute for Information Technologies Kragujevac, University of Kragujevac
Jelena Jovanović	Institute of General and Physical Chemistry
Jelena Miladinović	Faculty of Technology and Metallurgy, University of Belgrade
Jugoslav Krstić	University of Belgrade, Institute of Chemistry, Technology and Metallurgy, National Institute of the Republic of Serbia
Katarina Novaković	Newcastle University, School of Engineering
Ljiljana Mojović	Faculty of Technology and Metallurgy, University of Belgrade
Ljubiša Ignjatović	University of Belgrade, Faculty of Physical Chemistry
Maja Radetić	Faculty of Technology and Metallurgy, University of Belgrade
Mara Aleksić	Belgrade University, Faculty of Pharmacy
Marija Ajduković	University of Belgrade, Institute of Chemistry, Technology and Metallurgy, National Institute of the Republic of Serbia
Marija Mihailović	University of Belgrade, Institute of Chemistry, Technology and Metallurgy, National Institute of the Republic of Serbia
Matija Zlatar	University of Belgrade, Institute of Chemistry, Technology and Metallurgy, National Institute of the Republic of Serbia
Mila Ilić	University of Belgrade, Institute of Chemistry, Technology and Metallurgy, National Institute of the Republic of Serbia
Milan Kragović	University of Belgrade, Vinča Institute of Nuclear Sciences, National Institute of the Republic of Serbia
Milče Smiljanić	University of Belgrade, Institute of Chemistry, Technology and Metallurgy, National Institute of the Republic of Serbia
Milenko Plavšić	Faculty of Technology and Metallurgy, University of Belgrade
Milka Jadranin	University of Belgrade, Institute of Chemistry, Technology and Metallurgy, National Institute of the Republic of Serbia
Miloš Mojović	University of Belgrade, Faculty of Physical Chemistry
Mirjana Radenković	University of Belgrade, Vinča Institute of Nuclear Sciences, National Institute of the Republic of Serbia
Mirjana Žabić	Faculty of Technology, University of Banja Luka
Miroslav Kuzmanović	University of Belgrade, Faculty of Physical Chemistry
Miroslav Sovrlić	The Faculty of Medical Sciences, University of Kragujevac
Nadezda Vasilyeva	V.V. Dokuchaev Soil Science Institute, Moscow, Russia
Nataša Jović-Jovičić	University of Belgrade, Institute of Chemistry, Technology and Metallurgy, National Institute of the Republic of Serbia
Nataša Pejić	Belgrade University, Faculty of Pharmacy
Nebojša Nikolić	University of Belgrade, Institute of Chemistry, Technology and Metallurgy, National Institute of the Republic of Serbia
Nedeljko Manojlović	The Faculty of Medical Sciences, University of Kragujevac
Nenad Radić	University of Belgrade, Institute of Chemistry, Technology and Metallurgy, National Institute of the Republic of Serbia

Oleg N. Martyanov	Boreskov institute of catalysis Siberian branch of Russian Academi of sciences
Sanja Marinović	University of Belgrade, Institute of Chemistry, Technology and Metallurgy, National Institute of the Republic of Serbia
Sanja Panić	Faculty of Technology, University of Novi Sad
Sanja Sakan	University of Belgrade, Institute of Chemistry, Technology and Metallurgy, National Institute of the Republic of Serbia
Slavica Blagojević	Belgrade University, Faculty of Pharmacy
Slobodan Anić	University of Belgrade, Institute of Chemistry, Technology and Metallurgy, National Institute of the Republic of Serbia
Slobodan Cvetković	University of Belgrade, Institute of Chemistry, Technology and Metallurgy, National Institute of the Republic of Serbia
Sonja Grubišić	University of Belgrade, Institute of Chemistry, Technology and Metallurgy, National Institute of the Republic of Serbia
Sonja Jovanović	University of Belgrade, Vinča Institute of Nuclear Sciences, National Institute of the Republic of Serbia
Srđan Petrović	University of Belgrade, Institute of Chemistry, Technology and Metallurgy, National Institute of the Republic of Serbia
Srđan Rončević	University of Novi Sad, Faculty of Sciences
Stefan Pavlović	University of Belgrade, Institute of Chemistry, Technology and Metallurgy, National Institute of the Republic of Serbia
Stevan Blagojević	Institute of General and Physical Chemistry
Stevan Maćešić	University of Belgrade, Faculty of Physical Chemistry
Svetlana Mitrovski	University of Illinois, USA
Tamara Lazarević-Pašti	University of Belgrade, Vinča Institute of Nuclear Sciences, National Institute of the Republic of Serbia
Tatjana Novaković	University of Belgrade, Institute of Chemistry, Technology and Metallurgy, National Institute of the Republic of Serbia
Tihana Mudrinić	University of Belgrade, Institute of Chemistry, Technology and Metallurgy, National Institute of the Republic of Serbia
Uroš Anđelković	University of Belgrade, Institute of Chemistry, Technology and Metallurgy, National Institute of the Republic of Serbia
Vladana Vukojevic	Karolinska Institutet, Stockholm Sweeden
Vladimir Dobričić	Belgrade University, Faculty of Pharmacy
Vladimir Nikolić	Institute of General and Physical Chemistry
Vojkan Radonjić	University of Belgrade, Institute of Chemistry, Technology and Metallurgy, National Institute of the Republic of Serbia
Zara Zheleva	Institute of catalysis, Bulgarian Academy of Sciences
Željko Čupić	University of Belgrade, Institute of Chemistry, Technology and Metallurgy, National Institute of the Republic of Serbia
Zoran Šaponjić	Institute of General and Physical Chemistry
Zorica Mojović	University of Belgrade, Institute of Chemistry, Technology and Metallurgy, National Institute of the Republic of Serbia
Zorica Vuković	University of Belgrade, Institute of Chemistry, Technology and Metallurgy, National Institute of the Republic of Serbia

International Scientific Committee	
Ž. Čupić	University of Belgrade, Institute of Chemistry, Technology and Metallurgy, National Institute of the Republic of Serbia
V. Bukhtiyarov	Siberian Federal University
S. Minkovska-Dodova	The Institute of Catalysis (IC) of the Bulgarian Academy of Sciences (BAS)
B. Adnađević	University of Belgrade, Faculty of Physical Chemistry
S. Anić	University of Belgrade, Institute of Chemistry, Technology and Metallurgy, National Institute of the Republic of Serbia
A. Antić-Jovanović	University of Belgrade, Faculty of Physical Chemistry
A. Clayton	Swinburne University of Technology, Victoria, Australia
P. Banković	University of Belgrade, Institute of Chemistry, Technology and Metallurgy, National Institute of the Republic of Serbia
M. Fronczak	Lodz University of Technolog
Lj. Gavrilović	Institute for Energy Technology, Norway
M. Jeremić	University of Belgrade, Faculty of Physical Chemistry
E. Kiš	Faculty of Technology, Novi Sad
A.V. Knyazev	University of Nizhni Novgorod (UNN), Russia, Faculty of Chemistry
L.I. László	Budapest University of Technology and Economics
G. Lente	University of Pécs, Faculty of Sciences
S. Macura	Department of Biochemistry and Molecular Biology, Mayo Clinic, USA.
Z. Marković	State University of Novi Pazar
K. Novaković	Newcastle University, School of Engineering
V. Parmon	Boreskov Institute of Catalysis of the Siberian Branch of the RAS (Novosibirsk)
D. Peddis	Dipartimento di Chimica e Chimica Industriale, Università degli Studi di Genova; Istituto di Struttura della Materia-CNR, Monterotondo Scalo (RM)
M. Plavšić	Faculty of Technology and Metallurgy, University of Belgrade
L. J. Prins	University of Padova, Department of Chemical Sciences
J. Savović	Institute of Nuclear Sciences Vinča
G. Schmitz	Université Libre de Bruxelles, Belgium
I. Schreiber	University of Chemistry and Technology, Prague
L. Schreiberova	University of Chemistry and Technology, Prague
D. Stanisavljev	University of Belgrade, Faculty of Physical Chemistry
N. Stepanov	Lomonosov Moscow State University
Z. Šaponjić	Institute of General and Physical Chemistry
S. Tosti	ENEA Frascati Research Center, Fusion and Technologies for Nuclear Security Department
Á. Tóth	Department of Physical Chemistry and Materials Science, University of Szeged
N. Vasilyeva	Situational Analytical Center, Dokuchaev Soil Science Institute, Moscow, Russia
V. Vukojević	Karolinska Institutet, Stockholm Sweeden
A. De Wit	Faculté des Sciences, Nonlinear Physical Chemistry Unit, Belgium
A. Yüksel	Department of Chemical Engineering; Geothermal Energy Research and Application Center, Izmir Institute of Technology
M. Žabić	University of Banja Luka, Faculty of TechnologyA

CIP - Каталогизација у публикацији Народна библиотека Србије, Београд

544(082)
621.35(082)
577.3(082)
543.42(082)

INTERNATIONAL Conference on Fundamental and Applied Aspects of Physical Chemistry (17 ; 2024 ; Beograd)

Physical Chemistry 2024 : proceedings. Vol. 2 / 17th International Conference on Fundamental and Applied Aspects of Physical Chemistry, September 23-27, 2024 Belgrade, Serbia ; [organized by The Society of Physical Chemists of Serbia in co-operation with Institute of Catalysis Bulgarian Academy of Sciences ... [et al.]] ; [editors Željko Čupić, Slobodan Anić and Ana Ivanović-Šašić]. - Belgrade : Society of Physical Chemists of Serbia, 2024 (Belgrade : Jovan). - VI str., str. 406-769 : ilustr. ; 29 cm

Na nasl. str.: This conference is dedicated to the 100th anniversary of the birth of Professor Slobodanka Caca Veljković. - Tiraž 50. - Bibliografija uz svaki rad. - Registar.

ISBN 978-86-82475-46-0
ISBN 978-86-82475-44-6 (niz)

a) Физичка хемија -- Зборници b) Електрохемијско инжењерство -- Зборници
v) Биофизичка хемија -- Зборници g) Спектроскопија -- Зборници

COBISS.SR-ID 160311049